

Advances in Polymer Science 260

Thomas Basché  
Klaus Müllen  
Manfred Schmidt *Editors*

# From Single Molecules to Nanoscopically Structured Materials

 Springer

*Editorial Board:*

- A. Abe, Tokyo, Japan
- A.-C. Albertsson, Stockholm, Sweden
- G.W. Coates, Ithaca, NY, USA
- J. Genzer, Raleigh, NC, USA
- S. Kobayashi, Kyoto, Japan
- K.-S. Lee, Daejeon, South Korea
- L. Leibler, Paris, France
- T.E. Long, Blacksburg, VA, USA
- M. Möller, Aachen, Germany
- O. Okay, Istanbul, Turkey
- V. Percec, Philadelphia, PA, USA
- B.Z. Tang, Hong Kong, China
- E.M. Terentjev, Cambridge, UK
- M.J. Vicent, Valencia, Spain
- B. Voit, Dresden, Germany
- U. Wiesner, Ithaca, NY, USA
- X. Zhang, Beijing, China

## **Aims and Scope**

The series *Advances in Polymer Science* presents critical reviews of the present and future trends in polymer and biopolymer science. It covers all areas of research in polymer and biopolymer science including chemistry, physical chemistry, physics, material science.

The thematic volumes are addressed to scientists, whether at universities or in industry, who wish to keep abreast of the important advances in the covered topics.

*Advances in Polymer Science* enjoys a longstanding tradition and good reputation in its community. Each volume is dedicated to a current topic, and each review critically surveys one aspect of that topic, to place it within the context of the volume. The volumes typically summarize the significant developments of the last 5 to 10 years and discuss them critically, presenting selected examples, explaining and illustrating the important principles, and bringing together many important references of primary literature. On that basis, future research directions in the area can be discussed. *Advances in Polymer Science* volumes thus are important references for every polymer scientist, as well as for other scientists interested in polymer science - as an introduction to a neighboring field, or as a compilation of detailed information for the specialist.

Review articles for the individual volumes are invited by the volume editors. Single contributions can be specially commissioned.

Readership: Polymer scientists, or scientists in related fields interested in polymer and biopolymer science, at universities or in industry, graduate students.

Special offer:

For all clients with a standing order we offer the electronic form of *Advances in Polymer Science* free of charge.

Thomas Basché · Klaus Müllen · Manfred Schmidt  
Editors

# From Single Molecules to Nanoscopically Structured Materials

With contributions by

T. Basché · R. Berger · K. Binder · H.-J. Butt · M. Deserno ·  
G. Diezemann · G. Floudas · H. Frey · J. Gauss · J. Hedrich ·  
M. Helm · H.-P. Hsu · A. Janshoff · A. Köhn · U. Kolb ·  
K. Kremer · S.L. Kuan · F. Kuehn · A. Kühnle ·  
K. Landfester · H.J. Luhmann · M. Maskos · T. Metzroth ·  
I. Mey · A. Milchev · S. Muth · K. Müllen · W. Paul ·  
H. Paulsen · C. Peter · E. Pietrowski · V.G. Rostiashvili ·  
M. Sahl · F. Schmid · M. Schmidt · H.W. Spiess ·  
T.A. Vilgis · P. Virnau · T. Weil · Y. Wu · R. Zentel

 Springer

*Editors*

Thomas Basché  
Manfred Schmidt  
Johannes Gutenberg University Mainz  
Institute of Physical Chemistry  
Mainz  
Germany

Klaus Müllen  
Max Planck Institute for Polymer Research  
Mainz  
Germany

ISSN 0065-3195

ISBN 978-3-319-05827-6

DOI 10.1007/978-3-319-05828-3

Springer Cham Heidelberg New York Dordrecht London

ISSN 1436-5030 (electronic)

ISBN 978-3-319-05828-3 (eBook)

Library of Congress Control Number: 2014941445

© Springer International Publishing Switzerland 2014

This work is subject to copyright. All rights are reserved by the Publisher, whether the whole or part of the material is concerned, specifically the rights of translation, reprinting, reuse of illustrations, recitation, broadcasting, reproduction on microfilms or in any other physical way, and transmission or information storage and retrieval, electronic adaptation, computer software, or by similar or dissimilar methodology now known or hereafter developed. Exempted from this legal reservation are brief excerpts in connection with reviews or scholarly analysis or material supplied specifically for the purpose of being entered and executed on a computer system, for exclusive use by the purchaser of the work. Duplication of this publication or parts thereof is permitted only under the provisions of the Copyright Law of the Publisher's location, in its current version, and permission for use must always be obtained from Springer. Permissions for use may be obtained through RightsLink at the Copyright Clearance Center. Violations are liable to prosecution under the respective Copyright Law.

The use of general descriptive names, registered names, trademarks, service marks, etc. in this publication does not imply, even in the absence of a specific statement, that such names are exempt from the relevant protective laws and regulations and therefore free for general use.

While the advice and information in this book are believed to be true and accurate at the date of publication, neither the authors nor the editors nor the publisher can accept any legal responsibility for any errors or omissions that may be made. The publisher makes no warranty, express or implied, with respect to the material contained herein.

Printed on acid-free paper

Springer is part of Springer Science+Business Media ([www.springer.com](http://www.springer.com))

# Preface

Back in 2002 the German Research Foundation (Deutsche Forschungsgemeinschaft, DFG) has launched a Center of Research (Sonderforschungsbereich 625, SFB) with the title “From Single Molecules to Nanostructured Materials” at Johannes Gutenberg University, Mainz, together with the Max-Planck-Institute for Polymer Research, Mainz. Since 2002, more than 17 research groups were funded in order to theoretically and experimentally verify an ambitious concept comprising the design of nanostructured materials starting from a molecular basis, i.e. single molecules and single polymeric building blocks. The three overall objectives were as follows:

- To study the initial phases of self-organization
- To elucidate the formation of discrete aggregates from a defined number of molecules
- To establish complex structural hierarchies on the nanoscale and control the functions derived therefrom.

It is clear that this concept defines critical needs regarding materials and methods. Mostly synthetic polymers were at the core, however, biological polymers and small organic molecules were also considered. The disadvantage of polymers often lies in their pronounced conformational flexibility demanding a high entropy prize upon supramolecular structure formation. Shape-persistent macromolecules have helped to overcome this drawback and have therefore defined one focus of the SFB.

A second working principle relied on the defined functionalization of macromolecules and macromolecular assemblies. The basic idea was to chemically encode the building blocks, permitting better control of structure formation. The placement of ionic or hydrogen-bonding groups into well-defined positions, the definition of amphiphilic “patches” and the creation of directed as well as non-directed interactions have led to novel aggregate topologies in solution as well as on surfaces. Given the broad basis on both the macromolecule and the

particle side it became evident that a sophisticated toolbox of physical and theoretical methods was equally important, such methods including scanning probe and electron microscopy techniques, but also solid-state NMR spectroscopy, single molecule spectroscopy and scattering techniques.

Analogous considerations were initially made and obeyed throughout the project for the accompanying theoretical methods ranging from computer simulations on the basis of simplified models up to demanding *ab initio* procedures. The combined theoretical and spectroscopic analysis provided particularly valuable information on the structure and dynamics of complex assemblies as well as on fundamental questions regarding polymer chain statistics.

During the course of the project there were many scientific accomplishments, new ideas were explored and new challenges were created, all of which are summarized and reviewed in the present volume of *Advances in Polymer Science*.

We hope that the results accumulated by the SFB will stimulate new research projects not only locally in Mainz but also in the national and international polymer community.

On behalf of all our colleagues we wish to thank the DFG for its continuous and generous financial and administrative support. The invaluable judgments and critical advice of all the numerous voluntary reviewers involved in the SFB over the years are gratefully acknowledged.

Mainz, Germany  
July 2013

Thomas Basché  
Klaus Müllen  
Manfred Schmidt

# Contents

<b>Mechanical Properties of Single Molecules and Polymer Aggregates</b> .....	1
R. Berger, K. Binder, G. Diezemann, J. Gauss, M. Helm, H. -P. Hsu, A. Janshoff, T. Metzroth, I. Mey, A. Milchev, W. Paul, V.G. Rostiashvili, and T.A. Vilgis	
<b>Optical Properties of Assemblies of Molecules and Nanoparticles</b> .....	61
Thomas Basché, Andreas Köhn, Jürgen Gauss, Klaus Müllen, Harald Paulsen, and Rudolf Zentel	
<b>Structure Formation of Polymeric Building Blocks: Complex Polymer Architectures</b> .....	115
Kurt Binder, Hans-Jürgen Butt, George Floudas, Holger Frey, Hsiao-Ping Hsu, Katharina Landfester, Ute Kolb, Angelika Kühnle, Michael Maskos, Klaus Müllen, Wolfgang Paul, Manfred Schmidt, Hans Wolfgang Spiess, and Peter Virnau	
<b>Polymer Complexes in Biological Applications</b> .....	211
Jana Hedrich, Yuzhou Wu, Seah Ling Kuan, Frauke Kuehn, Eweline Pietrowski, Mike Sahl, Sandra Muth, Klaus Müllen, Heiko J. Luhmann, Tanja Weil, and Manfred Schmidt	
<b>Computational Studies of Biomembrane Systems: Theoretical Considerations, Simulation Models, and Applications</b> .....	237
Markus Deserno, Kurt Kremer, Harald Paulsen, Christine Peter, and Friederike Schmid	
<b>Index</b> .....	285

# Mechanical Properties of Single Molecules and Polymer Aggregates

**R. Berger, K. Binder, G. Diezemann, J. Gauss, M. Helm, H.-P. Hsu, A. Janshoff, T. Metzroth, I. Mey, A. Milchev, W. Paul, V.G. Rostiashvili, and T.A. Vilgis**

**Abstract** This chapter deals with the mechanical properties of single polymer chains, aggregates, and supramolecular complexes. The topics discussed cover a broad range from fundamental statistical mechanics of the equilibrium elastic properties of single polymer chains to details of the behavior of binding pockets in

---

R. Berger, V.G. Rostiashvili, and T.A. Vilgis  
Max-Planck-Institut für Polymerforschung, Ackermannweg 10, 55128 Mainz, Germany

K. Binder, and H.-P. Hsu  
Institut für Physik, Johannes Gutenberg Universität Mainz, Staudinger Weg 7, 55128 Mainz, Germany

G. Diezemann (✉), J. Gauss, and T. Metzroth  
Institut für Physikalische Chemie, Johannes Gutenberg Universität Mainz,  
Duesbergweg 10-14, 55128 Mainz, Germany  
e-mail: [diezemann@uni-mainz.de](mailto:diezemann@uni-mainz.de)

M. Helm  
Institut für Pharmazie und Biochemie, Johannes Gutenberg Universität Mainz, Staudinger Weg 5, 55128 Mainz, Germany

A. Janshoff, and I. Mey  
Institut für Physikalische Chemie, Johannes Gutenberg Universität Mainz,  
Duesbergweg 10-14, 55128 Mainz, Germany

Institut für Physikalische Chemie, Tammannstraße 6, 37077 Göttingen, Germany

A. Milchev  
Institut für Physik, Johannes Gutenberg Universität Mainz, Staudinger Weg 7, 55128 Mainz, Germany

Institute for Physical Chemistry, Academy of Sciences, Sofia 1113, Bulgaria

W. Paul  
Institut für Physik, Johannes Gutenberg Universität Mainz,  
Staudinger Weg 7, 55128 Mainz, Germany

Institut für Physik, Martin Luther Universität Halle, 06099 Halle, Germany

biomolecular assemblies as observed by force spectroscopy. The first section treats the equilibrium mechanical properties of single polymer chains in various environments, investigated via extensive simulations employing coarse-grained models that have proven extremely successful in many branches of polymer physics, namely the bond-fluctuation model and the self-avoiding walk model. Apart from the phase behavior and the adsorption properties, the mechanical pulling of a polymer chain from a surface has also been investigated. Molecular dynamics (MD) simulations of spring-bead models and analytical theory are used to describe the stochastic dynamics of the system. After these sections treating fundamental aspects of mechanical adsorption and translocation of polymer chains, we consider the adhesion of specific molecular systems to form networks of hydrogen bonds. In particular, we discuss all-atom force probe MD simulations of calixarene catenane systems, which have recently been synthesized. These simulations have been performed in close collaboration with corresponding experimental investigations utilizing atomic force spectroscopy (AFS) on the same systems, which will be reviewed together with other experimental determinations of the mechanical properties of supramolecular assemblies. Although these investigations can give insight into the reversible dynamics of hydrogen-bond networks, AFS can also be used in order to determine chemical equilibria under the impact of mechanical forces. Corresponding studies of this type are reviewed in the last section.

**Keywords** Chain collapse · Force probe molecular dynamics simulations · Force spectroscopy · Force-induced response · Polymer adsorption · Polymer translocation

## Contents

1	Phase Behavior, Structure, and Elastic Properties of Single Chains .....	3
1.1	Phase Behavior of Coarse-Grained Single-Chain Models .....	3
1.2	Force Versus Extension Behavior in the Good Solvent Regime .....	5
1.3	Single Chain Collapse Versus Adsorption .....	8
1.4	Adsorption of Single Chains .....	10
1.5	Manipulation of Single Chains: Force-Induced Detachment and Translocation Through Pores .....	17
2	Reversible Kinetics of Hydrogen-Bond Networks .....	27
2.1	Force Probe MD Simulations of Calix[4]arene Catenanes .....	28
2.2	Stochastic Modeling of Reversible Bond Breakage .....	31
3	Force Spectroscopy and Microscopy of Modular Macromolecules .....	33
3.1	Preferential Exclusion of Ectoin Enhances the Mechanical Stability of Fibronectin .....	33
3.2	Mechanically Interlocked Calix[4]arene Dimers Under External Force .....	39
4	Mechanical Properties of Nucleic Acids with Binding Pockets for Small Molecules .....	52
	References .....	52

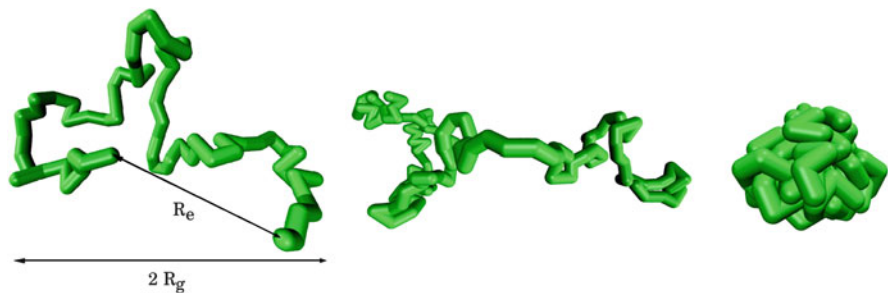


**Fig. 1** Snapshots of a polymer coil, generated by Monte Carlo simulation of the bond fluctuation model on the simple cubic lattice with a square well attraction of range  $\lambda = \sqrt{6}$  lattice spacings. For temperature  $T \rightarrow \infty$  the effective monomers (which block all eight sites of an elementary cube of the lattice from further occupation) interact with excluded volume forces and one has very good solvent conditions. Both the mean square end-to-end distance ( $R_e^2$ ) and the mean square gyration radius ( $R_g^2$ ) then scale with the number of effective monomers along the chain (henceforth denoted as “chain length”  $N$ ) as  $N^{2\nu}$ , with  $\nu \approx 0.588$  (*left*). When the temperature is finite, one reaches the  $\theta$ -temperature (*middle*) where the attractive interactions effectively “cancel” the repulsions,  $\nu = 1/2$  (*middle*). For  $T \ll \theta$  (*right*), the chain takes a compact configuration,  $\nu = 1/3$ . This compact configuration may either be a (fluid) globule or a (solid) crystal or an amorphous solid (glass). The snapshots all refer to  $N = 64$ . Adapted from Binder et al. [4]

## 1 Phase Behavior, Structure, and Elastic Properties of Single Chains

### 1.1 Phase Behavior of Coarse-Grained Single-Chain Models

Manipulation of single polymer chains has become a major direction of research in polymer science because such experiments can yield valuable insight into the relationship between the chemical structure and physical properties of macromolecules [1–3]. Such experiments do also depend on the conditions of the environment of the polymers, e.g., in an experiment where colloidal beads attached to the chain ends of a biopolymer are moved away from each other with laser tweezers. Then, the extension  $\langle X \rangle$  versus force ( $f$ ) relation will depend on the quality of the solvent in which the polymer has been dissolved. Also, the structure of a polymer adsorbed on a substrate from solution will depend on the solvent quality [4, 5].

When one addresses such questions via computer simulation of suitable models, knowledge of the phase behavior of the macromolecule in bulk solution (and how this is controlled by various parameters) is a necessary ingredient of the modeling study [4–14]. Figure 1 reminds the reader about the classic textbook view of this problem, with swollen coils (Fig. 1, left) under good solvent conditions, essentially Gaussian coils (Fig. 1, middle) under Theta solvent conditions, and collapsed dense globules in poor solvents (Fig. 1, right) [15]. However, this is not the whole story:

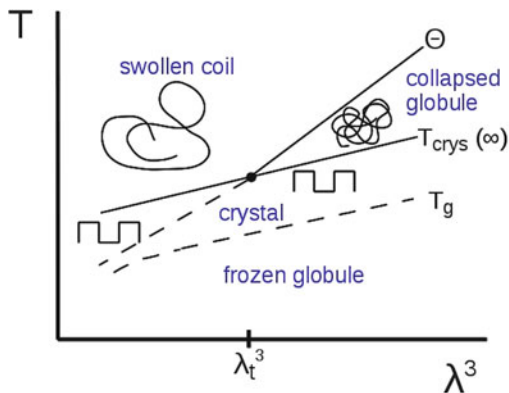


**Fig. 2** Schematic phase diagram of a single flexible polymer chain in the thermodynamic limit ( $N \rightarrow \infty$ ) as a function of temperature  $T$  and range of attractive monomer–monomer interaction  $\lambda$ . For  $\lambda > \lambda_t$ , there occurs a transition at  $T = \theta(\lambda)$  from the swollen coil to the collapsed fluid globule. At  $T_{\text{cryst}}(N = \infty)$  the globule crystallizes. Due to slow crystallization kinetics, this transition may be undercooled and at  $T_g < T_{\text{cryst}}(\lambda)$  the collapsed globule freezes into a glassy state. Since it was assumed that the transition lines vary linearly with the interaction volume  $\lambda^3$ ,  $\lambda^3$  rather than  $\lambda$  has been chosen as an abscissa variable. Adapted from Binder et al. [4]

although properties such as the asymptotic exponent ( $\nu$ ) describe how the size of the polymer scales with its chain length ( $N$ ) and do not depend on details of the monomer–monomer interaction, this is not true for the structure of the compact state. Both the bond fluctuation model [4–11] and a simple off-lattice model (tangent hard spheres with a square well attraction of range  $\lambda$ , in units of the sphere diameter  $\sigma$ ) [12–14] exhibit a phase diagram of the type shown in Fig. 2 [4]. Only for  $\lambda \geq \lambda_t$ , does one encounter the classic picture [15] of Fig. 1. For  $\lambda < \lambda_t$ , one does find a direct (first-order-like) transition from the swollen coil to the crystal; no  $\theta$ -like behavior can occur in thermal equilibrium. Thus, for  $\lambda = \lambda_t$  one encounters (in thermal equilibrium) a triple point, where swollen coils, collapsed fluid globules, and crystallized states of the polymer coexist. Sharp transitions of single chains can occur in the thermodynamic limit  $N \rightarrow \infty$  only; for chains of finite chain lengths  $N$ , the transition is rounded (and shifted) [6–11]. By “rounding” of a transition due to finite size  $N$  one means that the singularity that appears for  $N \rightarrow \infty$  (e.g., the divergence of the specific heat) is smeared out over some temperature region. The width of this region shrinks to zero as  $N \rightarrow \infty$ . But, one can provide theoretical arguments (and verify them by simulations) [6–10] that the extent of rounding and shifting scales like  $N^{-1/2}$  for the coil–globule transition. For the coil–crystal transition, the shift scales like  $N^{-1/3}$  and for the rounding like  $N^{-1}$ , so it is comparatively much sharper [12, 13]. In the simulations, the transitions are conveniently studied in the microcanonical (constant energy  $E$ ) ensemble rather than the conjugate canonical (constant temperature  $T$ ) ensemble [11, 14].

The models discussed so far assume that the macromolecules are fully flexible down to the smallest scales that are considered. This assumption is often not a good

approximation. If one includes local chain stiffness in the model, the swollen state and the Theta state in Fig. 1 still persist, whereas the compact states are modified. Bond vectors between neighboring monomers along the chain try to develop some local nematic-type order, but the chain connectivity constraint and the tendency to form compact structures are then in some conflict, which can, e.g., be resolved by the formation of toroidal structures [4, 16]. However, an exhaustive study of the phase diagram of a single chain as a function of stiffness, strength, and range of attractive effective monomer–monomer interactions, and chain length is still a task for the future.

## 1.2 Force Versus Extension Behavior in the Good Solvent Regime

In this subsection, we focus on long chains under good solvent conditions, where a rather universal behavior of the polymers (irrespective of the details of the model that is studied) [15] can be expected. Hence, we focus on the simplistic self-avoiding walk (SAW) model on the simple cubic lattice, but we include the effect of chain stiffness (introducing an energy penalty  $\epsilon_b$  whenever the SAW makes a  $90^\circ$  kink). This extension of the model is crucial when one has in mind the application to biopolymers (such as double-stranded DNA, which has a persistence length  $\ell_p = 50$  nm but a chain diameter of only  $D = 3$  nm) [1, 2]. This model can be studied very efficiently with the PERM algorithm (pruned-enriched Rosenbluth method) [17, 18], which allows the study of rather long chains (e.g., up to  $N = 50,000$ ). This algorithm directly estimates the partition function of the chain (and hence its free energy) as a function of  $N$ ,  $q_B = \exp(-\epsilon_b/k_B T)$  and the Boltzmann factor due to the force [ $\exp(f\ell_b/k_B T)$ , where the bond length  $\ell_b$  is simply the lattice spacing, taken as unit of length]. This model hence allows contact with the Kratky–Porod [19] worm-like chain (WLC) model, which is used as a standard model of semiflexible macromolecules [1, 2]. However, the Kratky–Porod model neglects excluded volume completely and hence necessarily fails (under good solvent conditions) for long chains.

Figure 3a shows a plot of  $3\langle R_g^2 \rangle / \ell_p L$ , where  $L = N\ell_b = N$  is the contour length of the semiflexible chain, versus  $n_p = L/\ell_p$ , the contour length in units of the persistence length, for zero stretching force,  $f = 0$  [20]. This representation is chosen such that the Kratky–Porod result reduces to a master curve, which saturates at unity for large  $n_p$ . It is seen that for  $n_p \leq 1$  all data coincide on a straight line, described by  $\langle R_g^2 \rangle = L^2/12$  (or  $3\langle R_g^2 \rangle / (\ell_p L) = 0.25(L/\ell_p)$ , respectively). This is the trivial result for rigid rods. For  $1 < n_p < 10$ , a gradual crossover towards the behavior of SAWs occurs,  $\langle R_g^2 \rangle / L \propto L^{2\nu - 1}$ , if the chains are rather flexible. If the chains are rather stiff, an intermediate Gaussian regime sneaks in (in  $d = 3$  dimensions only), before a second crossover to SAW-like behavior

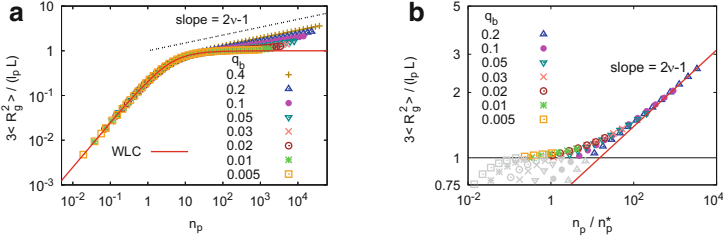


**Fig. 3** Log–log plot of the normalized mean square gyration radius  $3\langle R_g^2 \rangle / (\ell_p L)$  versus  $n_p = L/\ell_p$  (a) or versus  $n_p/n_p^*$  (b) where  $n_p^*$  has been chosen such that the data for large  $n_p$  coincide on the straight line with slope  $2\nu - 1$ , as indicated. Both parts include data for widely varying chain stiffness (note that  $\ell_p \approx q_b^{-1}/4$  for small  $q_b$  in  $d = 3$  dimensions). (a) The Kratky–Porod model for all  $L, \ell_p$  yields a unique master curve, denoted WLC. The horizontal part of this curve is also included in (b). Reprinted with permission from [20]. Copyright 2012, American Institute of Physics

occurs (at  $n_p = n_p^*$ , see Fig. 3b). Flory theory [21, 22] predicts that  $n_p^* \propto (\ell_p/D)^2$  whereas the simulations seem to suggest that  $n_p^* \propto (\ell_p/D)^{2.5}$  [22]. It is also important to note that in  $d = 2$  dimensions, a case relevant for polymers strongly adsorbed on planar substrates, no such intermediate Gaussian behavior occurs; instead, one crosses over from rigid rods to  $d = 2$  SAWs, with  $\langle R_g^2 \rangle \propto \ell_p^{1/2} L^{3/2}$ , irrespective of how large  $\ell_p$  is, as soon as  $n_p > 1$  [22]. The simulation results in Fig. 3 imply two successive crossovers, from rods to Gaussian random walks and from these simple random walks to swollen coils exhibiting SAW statistics, and are in very good agreement with experiments on semiflexible synthetic polymers [23]. For double-stranded DNA, however, the estimate  $\ell_p \approx 50$  nm implies that excluded volume effects become important only if  $L$  exceeds 100 nm. These deviations from the Kratky–Porod model also invalidate its predictions for the force versus extension curve [1, 2]:

$$\langle X \rangle / L \propto f \ell_p / k_B T \quad (\text{small } f), \quad 1 - \text{const} (f \ell_p / k_B T)^{-(1/2)} \quad (\text{large } f). \quad (1)$$

In  $d = 3$  dimensions, a useful interpolation formula between both regimes is:

$$\frac{f \ell_p}{k_B T} = \left[ \frac{1}{4} \left( 1 - \frac{\langle X \rangle}{L} \right)^{-2} + \frac{\langle X \rangle}{L} - \frac{1}{4} \right], \quad (2)$$

which will be used in later sections of this chapter for simplicity. So, irrespective of dimensionality, there is a wide regime of linear response and then the extension of the chain along the direction of the force ( $\langle X \rangle$ ) simply saturates at the contour length. However, in reality the regime of linear response is very restricted: One has  $\langle X \rangle / L \propto (\langle R_e^2 \rangle / L) f / k_B T$  until for  $f / k_B T \propto 1 / \sqrt{\langle R_e^2 \rangle}$  a crossover to

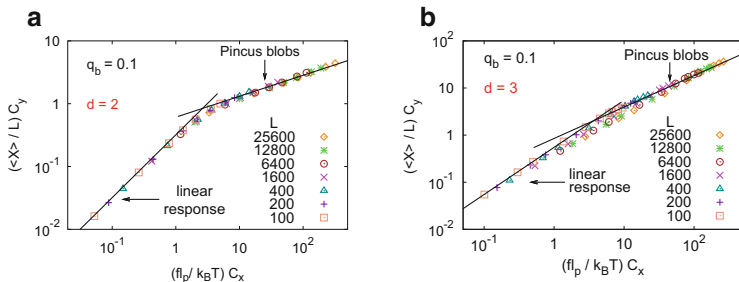


**Fig. 4** Log–log plot of scaled extension versus force curve,  $\langle X \rangle / L C_y$  versus  $(f \ell_p / k_B T) C_x$ , for moderately stiff chains ( $q_b = 0.1$ ), both in  $d = 2$  (a) and in  $d = 3$  (b). Contour lengths from  $L = 100$  up to  $L = 25,600$  are included. The two *straight lines* have the theoretical slopes appropriate for the linear response (for small  $f$ ) and for the nonlinear Pincus regime, respectively. (a) The scaling factors  $C_x = (L/\ell_p)^{3/4}$  and  $C_y = (L/\ell_p)^{1/4}$  are used according to our theory [20]; estimates for  $\ell_p$  were obtained independently from the initial decay of the bond vector autocorrelation function  $\langle \vec{a}_i \cdot \vec{a}_{i+s} \rangle$  as function of the index  $s$  along the chain. (b) In  $d = 3$ , the predicted scaling factors  $C_x = (L^3 \ell_b / \ell_p^4)^{1/5}$ ,  $C_y = [L^2 / (\ell_b \ell_p)]^{1/5}$  were used. Reprinted with permission from [22]. Copyright 2012, American Institute of Physics

a nonlinear regime (first proposed by Pincus [24]) occurs, where  $\langle X \rangle / L \propto (f \ell_p / k_B T)^{2/3} (\ell_p / R^*)^{1/3}$  with  $R^* \propto \ell_p^2 / D$  (in  $d = 3$ ). However, this Pincus regime is only observable for  $n_p > n_p^*$ . In  $d = 2$  dimensions, the nonlinear Pincus regime is described simply by  $\langle X \rangle / L \propto (f \ell_p / k_B T)^{1/3}$ , and this regime extends until saturation of  $\langle X \rangle$  at  $L$  starts. So, in  $d = 2$ , the Kratky–Porod model also fails completely with respect to the force–extension behavior, whereas in  $d = 3$  it holds for very stiff and thin chains (for which  $n_p^* \gg 1$ ), if they are not too long ( $n_p < n_p^*$ ).

The various crossover predictions and the numerical evidence that we have obtained for these crossovers are described in detail in two long papers [20, 22]; here we show only two examples that illustrate the crossover from the linear response to the Pincus regimes, both in  $d = 2$  and  $d = 3$  dimensions (Fig. 4). We stress that the widely used interpolation formula for the force versus extension curve quoted in Eq. (2) does not include the Pincus regime.

We emphasize that these deviations from the Kratky–Porod model that occur for semiflexible polymers both in equilibrium and in their response to stretching forces, were not properly noticed in most of the experiments. However, in analyzing data one normally does not have strictly monodisperse chains, and neither  $\ell_p$  nor  $L$  are independently known; both parameters are usually used as adjustable fitting parameters. Because  $\ell_p$  depends on  $d$ , and is also affected by solvent conditions, and for strongly stretched real chains other effects (related to the local chemical structure of the effective monomeric units) come into play, this failure is not surprising. However, some of the confusion over the actual values of  $\ell_p$  that

can be found in the literature for specific polymers can be attributed to such problems. But, it is reassuring that in a few recent experiments evidence for several crossovers in  $\langle X \rangle$  versus  $f$  curves and for the nonlinear Pincus behavior have been found [25].

The problem of understanding the persistence length and its consequences is also taken up by Butt et al. [26]: for bottle-brush polymers, there is the challenging problem of understanding how their stiffness depends on the grafting density and degree of polymerization of the grafted side chains.

### 1.3 *Single Chain Collapse Versus Adsorption*

The studies on single-chain adsorption on flat substrates were based on the same models used for the studies of single chains in the bulk, as described above. One issue that was addressed is the competition between adsorption, collapse, and crystallization of tethered single chains [5].

Figure 5 presents a tentative “diagram of states” for  $N = 64$  (we should speak about “phase diagrams” only in the limit  $N \rightarrow \infty$ , so the lines in the diagram of states are not sharp phase boundaries, but rather various signatures of smooth crossovers). Here, we use  $\beta_b = \epsilon/k_B T$  and  $\beta_s = \epsilon_s/k_B T$  as control parameters ( $\epsilon$  and  $\epsilon_s$  denote the strength of the attractive energy between monomers and between monomers and the substrate surface, respectively). Due to the competition between the structures identified in the bulk (Fig. 2) and various quasi-two-dimensional wall-attached structures, the phase diagram emerging in the limit  $N \rightarrow \infty$  for the bond fluctuation model of a polymer interacting with the surface (and allowing for variable solvent conditions) is still incompletely understood [5].

When we restrict attention only to the good solvent case, the PERM [17, 18] algorithm applied to the simple SAW model on the simple cubic lattice can be used again, and very long chains can be simulated (see Sect. 1.2). Although adsorption of single flexible polymers under good solvent conditions is a classical problem that has been studied for decades [27–32], very important aspects are still controversial. One such aspect is the value of the crossover exponent  $\phi$ , which controls the number of adsorbed monomeric units  $N_s$  right at the adsorption threshold. Although  $\phi = 1/2$  for Gaussian chains is well known, de Gennes [33] suggested a scaling relation  $\phi = 1 - \nu$ , which would imply  $\phi \approx 0.41$ . However, then it was shown that this scaling relation should hold only for a chain tethered to a freely penetrable interface, but not to an impenetrable surface [27, 28]. Early simulations [27] gave  $\phi \approx 0.59$ , but later investigations came up with different values; the smallest estimate so far is Grassberger’s [30] estimate of  $\phi \approx 0.48$ , but there has not yet been any consensus on a value of this exponent. Bhattacharya et al. [31] observed that, depending on the degree of interaction between different loops, one could get any value in the range  $0.39 \leq \phi \leq 0.59$ . Should one draw then the conclusion that this exponent is nonuniversal?

To test this question, the SAW tethered to an impenetrable wall has been studied, using a square well adsorption potential of depth  $U$  and range  $W$ . If universality

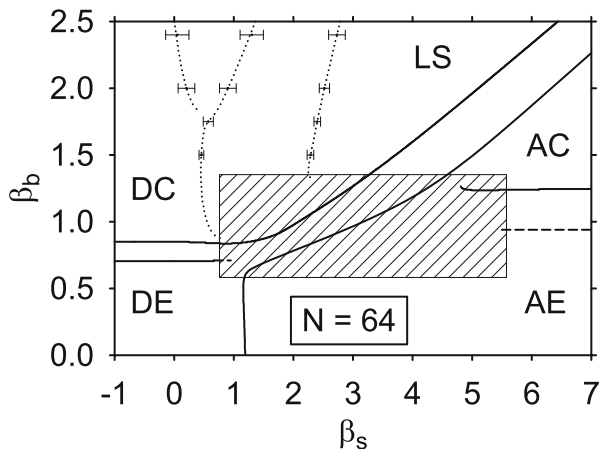


**Fig. 5** Diagram of states for a tethered chain, described by the bond fluctuation model on the simple cubic lattice, for chain length  $N = 64$ , in the plane of variables bulk coupling  $\beta_b$  and surface coupling  $\beta_s$ . The *solid lines* show the location of well-defined maxima in the fluctuation of surface contacts or bead–bead contacts, respectively; *broken* and *dotted lines* show the locations of less well-pronounced anomalies in these fluctuations. In the *hatched region*, the precise behavior is still uncertain. The states that compete with each other are desorbed expanded (*DE*, i.e., a three-dimensional mushroom); adsorbed expanded (*AE*, i.e., a  $d = 2$  SAW), desorbed collapsed (*DC*, as in Fig. 1b, but tethered to the grafting plane); adsorbed collapsed (*AC*, a compact but disordered structure with many surface contacts); and various crystalline layered structures (*LS*). Reprinted with permission from [5]. Copyright 2008, American Institute of Physics

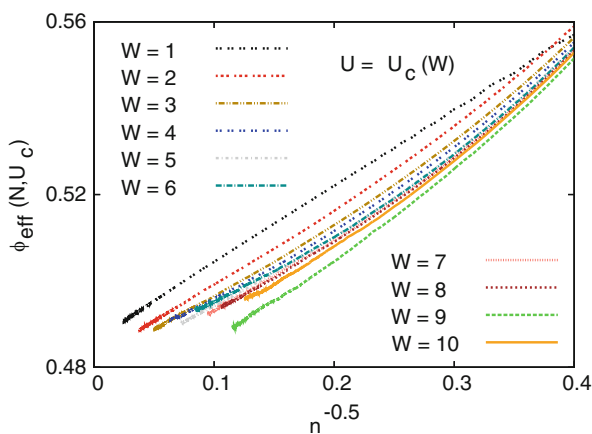


**Fig. 6** Plot of the effective crossover exponent  $\phi_{\text{eff}}(N)$  versus  $n^{-0.5}$  at  $U = U_c(W)$  for the different choices of  $W$ , as indicated. Note that  $\phi_{\text{eff}}(N, U, W)$  is defined as  $\phi_{\text{eff}}(N, U, W) = \ln \left\{ \frac{4\theta_s(2N, U, W)}{\theta_s(N/2, U, W)} / \ln 4 \right\}$ , where  $\theta_s$  is the fraction of adsorbed monomers at the surface. Reprinted with permission from [32]

holds, the location  $U_c(W)$  of the transition will depend on  $W$ , but not the critical exponents. Klushin et al. [32] showed that indeed all exponents are independent of the parameter  $W$ , but for the crossover exponent there occurs a correction term ( $\propto N^{-1/2}$ ), whose amplitude (which is not expected to be universal) strongly depends on  $W$ . However, if we introduce a blob picture such that  $N = ng$ , where  $g$  is the number of monomers per blob,  $n$  is the number of blobs, and the blob diameter ( $g^{\nu}$ ) is chosen equal to  $W$ , one finds that all systems behave rather similarly (Fig. 6) [32]. It also is evident that for smaller values of  $N$  the effective crossover exponent is distinctly larger than 0.5, whereas for  $N \rightarrow \infty$  the Grassberger [30] estimate  $\phi \approx 0.48$  is confirmed. The conclusion that  $\phi$  is universal is also confirmed by a study of the loop length distribution function at  $U = U_c(W)$ , which is found to satisfy a universal power law (in the limit  $N \rightarrow \infty$ ).

Another interesting question is the effect of chain stiffness on polymer adsorption. It has been found [34] that increase of  $\ell_p \rightarrow \infty$  causes a crossover in the character of the adsorption transition from second order (for finite  $\ell_p$ ) to first order as  $\ell_p$  diverges. This finding is compatible with mean field theories [35]. However, a complication that has not been analyzed before is the finding that the persistence length  $\ell_p$  is not only dependent on the bending potential, but also depends on the distance from the adsorption transition [34].

## 1.4 Adsorption of Single Chains

### 1.4.1 Copolymer Localization on Selective Liquid–Liquid Interfaces

The behavior of hydrophobic–polar (amphiphilic) copolymers (HP-copolymers) at a selective interface (the interface that divides two immiscible liquids, say, water and oil, each liquid being a good solvent for one type of monomer and bad for the other) is of great importance in the chemical physics of polymers. HP-copolymers are readily localized at such an interface because, under a sufficiently large degree of selectivity, the hydrophobic (H) and polar (P, hydrophilic) parts of a copolymer chain try to stay on different sides of the interface due to the interplay between the entropy loss in the vicinity of the interface and the energy gain in the proper solvent (cf. Fig. 7). Not surprisingly, during the last two decades the problem has attracted a lot of attention and has been looked at experimentally [37–39], theoretically [40, 41], and in computer experiments [42]. In earlier studies, attention was mostly focused on diblock copolymers [37, 38] due to their relatively simple structure, but the scientific interest shifted later to random HP-copolymers at penetrable interfaces [41, 43, 44]. In contrast, our investigations have focused mainly on unexplored aspects such as the impact of block size  $M$  on the static properties and on the localization kinetics of regular multiblock copolymers at the phase boundary between the two immiscible solvents. We showed that these are well described by a simple scaling theory [36, 45, 46] in terms of the total copolymer length

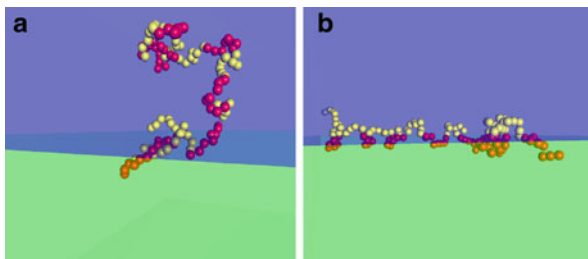


**Fig. 7** Snapshots of typical configurations of a copolymer with chain length  $N = 128$  and block length  $M = 8$  on the verge of adsorption threshold at  $\chi = 0.25$  (a) and in the strong localization limit  $\chi = 10$  (b). The value of the critical selectivity of this chain is  $\chi_c = 0.67$ . Reprinted with permission from [36]. Copyright 2005, American Institute of Physics

$N$  (the number of repeating units in the chain) and the block size  $M$  (the number of consecutive monomers of the same kind) as well as the selectivity parameter  $\chi$ , that is, the energy gained by a monomer when in the more favorable solvent.

Our scaling description is based on the idea that a multiblock copolymer can be treated as a “coarsened” homopolymer where a single HP-diblock plays the role of an effective segment. All such diblocks try to keep their H- and P-segments in the corresponding preferred environment. This leads to the diblock “polarization” at the interface and to a free energy gain, which produces an effective attraction energy  $E$ . This means that the energy gain  $\chi$  (i.e., the selectivity parameter) for a P-monomer in its own (polar) environment is equal to the corresponding energy gain for a H-monomer, provided the latter stays in the hydrophobic environment. An estimate for the effective attraction energy per diblock of length  $2M$  in the symmetric case yields  $E \propto -\chi^2 M^2$  [47], where the energy is measured in units of  $k_B T$ ,  $k_B$  denoting the Boltzmann constant. In terms of the selectivity parameter, there are three adsorption regimes that can be distinguished:

For  $\chi$  smaller than a critical value  $\chi_c$ , the interface is too weak to affect the polymer so that the macromolecule conformation is identical to that in the absence of an interface

For  $\chi \simeq \chi_c$ , the copolymer is captured by the interface yet is not strongly deformed (weak localization)

For  $\chi \simeq \chi_\infty > \chi_c$ , the interface is strong enough to induce a perfect flattening of the copolymer so that all the monomers are in their preferred environment (strong localization) (cf. Fig. 7b)

Various quantities, such as the fraction of repeating units (monomers) captured at the interface (which serves as an order parameter of the localization phase transition) and the components of the polymer radius of gyration parallel ( $R_{g\parallel}$ ) and perpendicular ( $R_{g\perp}$ ) to the phase boundary between the immiscible liquids, can be then studied in order to verify the predictions of the pertinent scaling analysis by comparison with results from Monte Carlo simulations [36, 45–47]. As an example, we show the changing degree of copolymer localization (Fig. 8a) and the ensuing

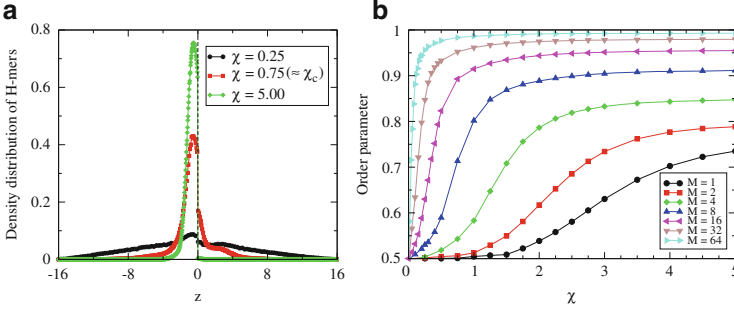


**Fig. 8** (a) Density distribution of hydrophobic monomers (*H-mers*) for a chain with  $N = 128$  and  $M = 8$  at different  $\chi$ . Here  $\chi_c = 0.67$ . (b) Fraction of polar and hydrophobic monomers (order parameter) in the polar (at  $z > 0$ ) and hydrophobic (at  $z < 0$ ) semispaces versus selectivity  $\chi$  for  $N = 128$  and different block sizes  $M$ . Reprinted with permission from [36]. Copyright 2005, American Institute of Physics

interface thickness as the selectivity  $\chi$  is varied (Fig. 8b). In fact, the copolymer localization at selective interface can be considered as a sharp phase transition in the limit  $N \rightarrow \infty$ ,  $M \rightarrow \infty$ , and  $\chi \rightarrow 0$ . As an appropriate variable  $\eta$  in the various scaling relations one may use the number of blobs,  $\eta \equiv \chi N^{(1-\nu)/2} M^{(1+\nu)/2}$  (here  $\nu \approx 3/5$  denotes the Flory exponent). At finite  $\chi$ , chain length ( $N$ ), and block length ( $M$ ), the transition looks like a smooth crossover, described by an order parameter in terms of the fraction of P- and H-monomers on both sides of the penetrable interface, (cf. Fig. 8b). Generally, in a very good agreement between theoretical predictions and our simulation data, one may conclude that the scaling theory correctly captures the most salient features related to the copolymer behavior at penetrable boundaries between selective solvents:

- The critical selectivity decreases with growing block length as  $\chi_c \propto M^{-(1+\nu)/2}$ , while the crossover selectivity to the strong localization regime obeys a simple relation  $\chi_\infty \propto 1/M$
- The size of the copolymer varies in the weak localization regime as  $R_{g\perp} \propto M^{-\nu(1+\nu)/(1-\nu)}$  and  $R_{g\parallel} \propto M^{[(\nu_2-\nu)(1+\nu)]/(1-\nu)}$ , where  $\nu_2 = 3/4$  is the Flory exponent in 2D space
- In the regime of strong localization, one obtains  $R_{g\perp} \propto M^\nu$  and  $R_{g\parallel} \propto M^{-(\nu_2-\nu)N^{\nu_2}}$ , respectively

For the most relevant case of strong localization, the kinetics of copolymer adsorption is of particular importance. A simple analytical theory based on scaling considerations has been proposed and shown to provide a faithful description for the relaxation of the initial copolymer coil into a flat-shaped layer [45]. This conformational change of a chain for  $\chi > \chi_\infty$  can be considered to be governed by an attractive force,  $f_{\text{attr}}^+ \approx -\chi_\infty N/R_{g\perp}$ , and an opposing force of confinement,  $f_{\text{conf}} \approx Na^{1/\nu}/R_{g\perp}^{1/\nu+1}$ , which yield a set of dynamic equations:

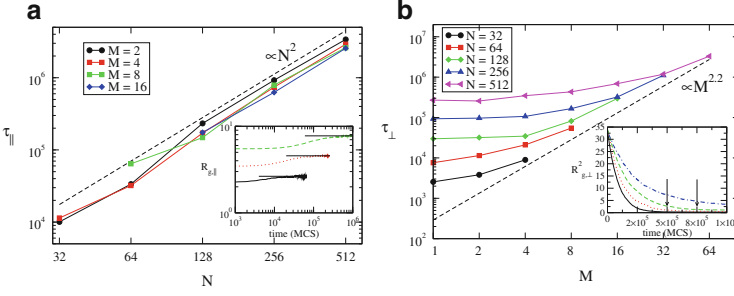


**Fig. 9** (a) Variation of  $\tau_{\parallel}$  with  $N$  for blocks of size  $M = 2, 4, 8,$  and  $16$ . The *inset* shows typical behavior of  $R_{\parallel}(t)$ . (b)  $\tau_{\perp}$  versus block length  $M$  for chains with  $32 \leq N \leq 512$ . Dashed line denotes the predicted slope of  $\approx 2.2$ . The *inset* shows typical relaxation of  $R_{g\perp}^2(t)$  for  $N = 256$ ,  $M = 2$ . Reproduced by permission from [45]. Copyright 2006, IOP Publishing

$$\zeta_0 N \frac{dR_{g\perp}}{dt} = -\frac{\chi_{\infty} N}{R_{g\perp}} + \frac{Na^{1/\nu}}{R_{g\perp}^{1/\nu+1}}, \quad \zeta_0 N \frac{dR_{g\parallel}}{dt} = \frac{\nu N^2}{R_{g\parallel}^3 R_{g\perp}} - \frac{R_{g\parallel}}{aN} \quad (3)$$

where the second equation in Eq. (3) describes the horizontal (or parallel to the interface) spreading due to steric repulsion (excluded volume effects), and  $\zeta_0$  denotes the monomer friction. One may find solutions for the set of equations of motion (3) and determine the characteristic times for relaxation perpendicular ( $\tau_{\perp}$ ) and parallel ( $\tau_{\parallel}$ ) to the interface (cf. Fig. 9). The observed agreement with simulation data is very good, and an important distinction between early and late stages of localization can be demonstrated. A careful analysis in terms of localization-induced coupling of (otherwise independent) Rouse modes reveals [47] a strong coupling of the first few modes as a consequence of the interplay between the interface and the regular block structure of the polymer. Summarizing, one may conclude that:

- The typical time for lateral diffusion in the case of strong localization varies as  $\tau \propto M^{2(\nu-\nu_2)} N^{2\nu_2+1}$  [36]
- The characteristic times for localization perpendicular and parallel to the interface at strong selectivity scale as  $\tau_{\perp} \propto M^{1+2\nu}$  and  $\tau_{\parallel} \propto N^2$ , respectively [45]
- The averaged components of the Rouse modes of a copolymer, adsorbed at a liquid–liquid interface, are not mutually orthogonal as in the bulk but significantly coupled for small indices  $p$ , with the coupling gradually vanishing as the mode number  $p$  grows [46]

Our studies have revealed that a selective liquid–liquid interface can be very sensitive with respect to the composition (most notably, the block size  $M$ ) and chain length  $N$  of a multiblock copolymer chain. This sensitivity suggests an interesting possibility to use selective liquid–liquid interfaces as a new type of chromatography, whereby one can “sieve” (i.e., separate and analyze) complex

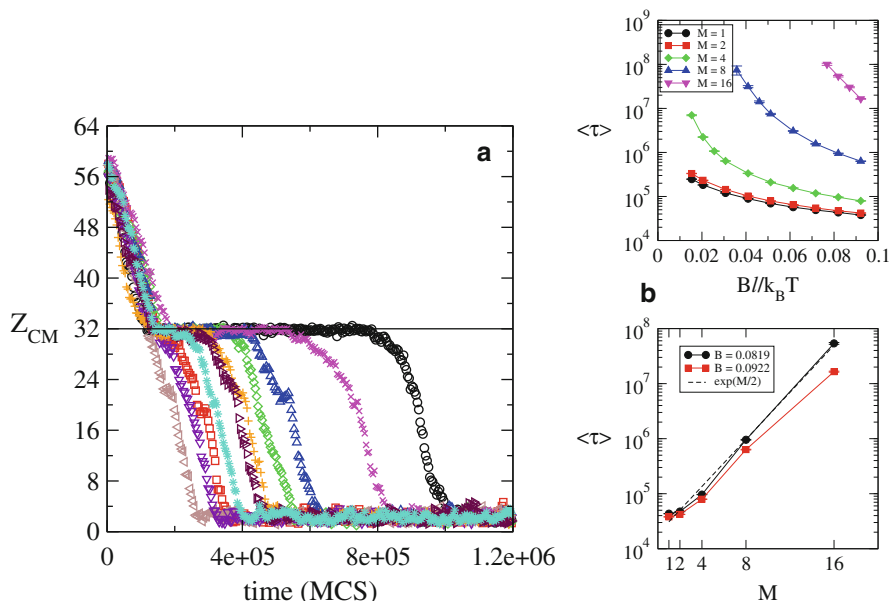


**Fig. 10** (a) Time transients of the chain center of mass motion  $Z_{CM}(t)$  during the drift of a copolymer with  $N = 256$  and  $M = 4$  at field intensity  $B = 0.031$  for 10 individual runs, indicating different capture times during crossing of the interface. The interface position is at  $Z = 32$ . Reprinted with permission from [47]. Copyright 2006 Wiley Periodicals, Inc. (b) Variation of the mean capture time  $\langle \tau \rangle$  with field strength  $B$  for copolymers of length  $N = 128$  and different block size  $M$ . Dashed line denotes an exponential fit. Reprinted with permission from [48]. Copyright 2006 American Chemical Society

mixtures of copolymers with respect to block size and chain length. Thus, a chain may be driven from an initial configuration, some distance away from the interface, into the other half of the container whereby it will pass through the penetrable interface. Depending on their length and composition, different chains will then be temporarily trapped at the plane separating the two solvents. One might expect that the characteristic “capture” time would strongly depend on the particular properties of the chain, so that for a given field intensity  $B$  some chains would stick for a long time at the interface, whereas others with different  $M$  and  $N$  will pass rapidly through it (cf. Fig. 10). This possibility has been considered both theoretically and by means of computer experiment in our investigations [47, 48], and the scaling of the typical “capture” times  $\tau$  with copolymer and block length  $N$  and  $M$  elucidated. For chains driven by an external field through a selective interface, one finds that the mean capture time  $\tau$  displays a non-Arrhenian dependence on the field intensity  $B$ , and increases almost exponentially with the block size  $M$  (cf. Fig. 10).

Finally, it is worth mentioning that in the rich behavior of copolymers at selective liquid–liquid interfaces we have not included results pertaining to random copolymers, where the range of sequence correlations plays a role similar to that

of the block size. Moreover, in our considerations we have largely ignored the possible effects of hydrodynamic interactions, even though the case of Zimm dynamics was accounted for in our scaling approach [47]. Also, the penetrable interface has been considered in the simplest approximation of zero thickness although the existence of some intrinsic width, capillary waves, etc. might add additional facets to the overall picture. Thus, a variety of details are relegated to further studies and the reported results should be seen as a first step into a fascinating field of phenomena that might offer a broad perspective for application and development.

### 1.4.2 Single Chain Adsorption: Statics and Kinetics

Adsorption of polymers on surfaces plays a key role in numerous technological applications and is also relevant to many biological processes. During the last three decades it has been constantly a focus of research interest. The theoretical studies of the behavior of polymers interacting with solid substrate have been based predominantly on both scaling analysis [49] as well as on the self-consistent field (SCF) approach [50]. The close relationship between theory and computer experiments in this field [27, 51] has proved especially fruitful. Most investigations focus on the determination of the critical adsorption point (CAP) location and on the scaling behavior of a variety of quantities below, above, and at the CAP.

The investigations mentioned above have been devoted exclusively to homopolymers, but the adsorption of copolymers (e.g., multiblocks or random copolymers) is still much less understood. Thus, for instance, the CAP dependence on block size  $M$  at fixed concentration of the sticking A-mers is still unknown, as are the scaling properties of regular AB-multiblock copolymers in the vicinity of the CAP. The main focus of our investigations [52] has been aimed at the adsorption transition of random and regular multiblock AB-copolymers on a rigid substrate. We have used two different models to establish an unambiguous picture of the adsorption transition and to test scaling predictions at criticality. The first model is an off-lattice coarse-grained bead-spring model of polymer chains that interact with a structureless surface by means of a contact potential, once an A-monomer comes close enough to be captured by the adsorption potential. The second model is the pruned-enriched Rosenbluth method (PERM) on a cubic lattice, which is very efficient, especially for very long polymer chains, and provides high accuracy of the simulation results at criticality. Notwithstanding their basic difference, both methods suggest a consistent picture of the adsorption of copolymers on a rigid substrate and confirm the theoretical predictions, even though the particular numeric values of the CAP are model-specific and differ considerably.

As one of the central results of our studies, one should point out the phase diagram of regular multiblock adsorption, which gives the increase in the critical adsorption potential  $\epsilon_c(M)$  with decreasing length  $M$  of the adsorbing blocks (cf. Fig. 11a). For very large block length,  $M^{-1} \rightarrow 0$ , we find that the CAP systematically approaches that of a homogeneous polymer. We demonstrate also

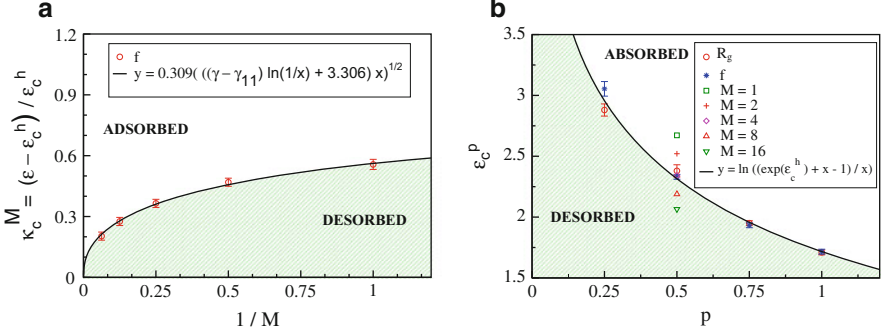


**Fig. 11** (a) Phase diagram showing the variation in critical adsorption strength  $\kappa_c^M = (\epsilon_c^M/\epsilon_c^h) - 1$  with block length  $M$ . (b) Critical adsorption potential (CAP) versus composition  $p$  for random copolymers. *Solid line* is a best fit of the theoretical prediction  $\epsilon_c^p = \ln[(\exp(\epsilon_c^h) + p - 1)/p]$ . Here, CAP  $\epsilon_c^h = 1.716$ . *Symbols* denote the CAP for multiblock copolymers with block size  $M$ . Reprinted (adapted) with permission from [52]. Copyright 2008 American Chemical Society

that the phase diagram, derived from computer experiment, agrees well with the theoretical prediction based on scaling considerations.

The phase diagram for random copolymers with quenched disorder that gives the change in the critical adsorption potential,  $\epsilon_c^p$ , with changing percentage of the sticking A-monomers,  $p$ , has also been determined from extensive computer simulations carried out with the two employed models (cf. Fig. 11b). We observed perfect agreement with the theoretically predicted result,  $\epsilon_c^p = \ln\left[\frac{\exp(\epsilon_c^h) + p - 1}{p}\right] \geq \epsilon_c^h$  (where  $\epsilon_c^h$  is the critical attraction energy of an effective homopolymer [53]), which has been derived by treating the adsorption transition in terms of the ‘‘annealed disorder’’ approximation. We show that a consistent picture appears of how some basic polymer chain properties of interest, such as the gyration radius components perpendicular and parallel to the substrate or the fraction of adsorbed monomers at criticality, scale when a chain undergoes an adsorption transition regardless of the particular simulation approach. An important conclusion thereby concerns the value of the universal crossover exponent  $\phi \approx 0.5$ , which is found to remain unchanged regardless of whether homopolymers, regular multiblock polymers, or random polymers are concerned.

The adsorption kinetics of a single polymer chain on a flat structureless plane has been examined in the strong physisorption regime [53]. Adopting the stem-flower model for a chain conformation during adsorption, and assuming the segment attachment process to follow a ‘‘zipping’’ mechanism, we developed a scaling theory that describes the time evolution of the fraction of adsorbed monomers for polymer chains of arbitrary length  $N$  at adsorption strength of the surface  $\epsilon/k_B T$ . To this end, we derived a master equation as well as the corresponding Fokker–Planck equation for the time-dependent probability distribution function (PDF) of the number of adsorbed monomers and for the complementary PDF of chain tails. Inherent in this derivation is the assumed condition of detailed balance, which makes it possible

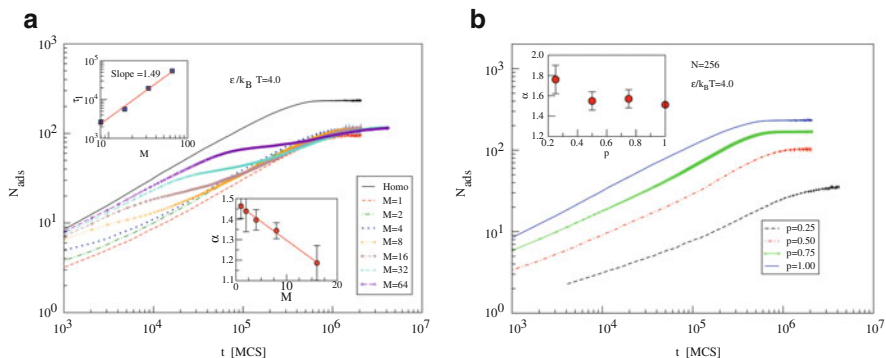


**Fig. 12** (a) Number of adsorbed segments  $N_{\text{ads}}(t)$  versus time  $t$  for regular AB copolymers with length  $N = 256$  and different block size  $M$ . The time interval of the transient “shoulders” is shown in the *upper inset*. The *lower inset* displays the variation in the scaling exponent  $\alpha$  for the time of adsorption  $\tau \propto N^\alpha$  with block length  $M$ . (b) The same plot for a random copolymer with  $N = 256$  and different composition  $p$ ;  $p = 1$  corresponds to the case of a homopolymer. The variation of  $\alpha$  with  $p$  is shown in the *inset*. Reprinted with permission from [53]

to relate the elementary steps of adsorption and desorption. From the numeric solution of the equivalent discrete set of coupled first-order differential equations, we find that the growth of the adsorbed fraction of monomers with time is governed by a power law,  $n(t) \propto t^{1/(1+\nu)}$ , while the typical time of adsorption  $\tau$  scales with the length of the polymer  $N$  as  $\tau \propto N^\alpha$ , with  $\alpha = 1 + \nu$ . In Fig. 12 we display the variation in the number of adsorbed segments  $N_{\text{ads}}$  with time  $t$  for regular copolymers with block size  $M$  and for random copolymers with percentage  $p$  of the “sticking” segments. The adsorption transients found in the Monte Carlo simulation are in good agreement with these predictions, if one takes into account the finite-size effects due to the finite length of the studied polymer chains. One could also conclude that, in the case of regular multiblock and random copolymers, the adsorption kinetics strongly resembles that of homopolymers.

It should be also mentioned that a lot of insight and information regarding the adsorption of single chains on a solid substrate can be gained from the PDFs of the various building units, trains, loops, and tails that an adsorbed chain is formed of. In the literature [53] one may verify that the theoretically derived and predicted exponential expression for the PDF of trains appears to comply very well with simulation data.

## 1.5 Manipulation of Single Chains: Force-Induced Detachment and Translocation Through Pores

### 1.5.1 Detachment of Adsorbed Polymer Chain: Statics and Dynamics

With the development of novel single macromolecule experiments, the manipulation of individual polymer chains and biological macromolecules is becoming an important method for understanding their mechanical properties and characterizing

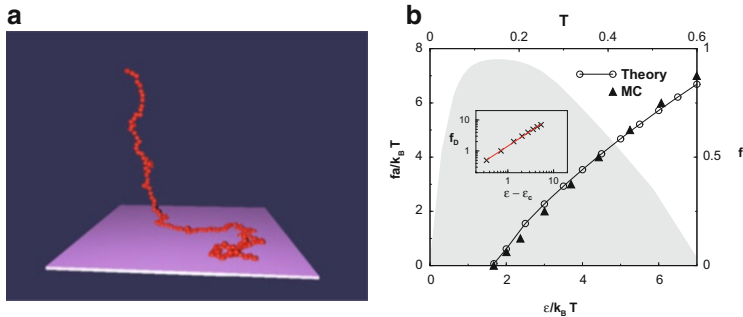


**Fig. 13** (a) Snapshot of an adsorbed polymer chain with length  $N = 128$ , partially detached from the plane by external force  $f_M = 6.13$  that keeps the end monomer at height  $h = 25\sigma$ . Reprinted with permission from [31]. Copyright 2009, American Chemical Society. (b) Critical detachment force  $f_D = f\sigma/k_B T$  versus surface potential  $\epsilon/k_B T$ . Triangles and circles denote MC and theoretical results, respectively. Inset shows a double-logarithmic plot of  $f_D$  against  $\epsilon - \epsilon_c$  with  $\epsilon_c = 1.67k_B T$ , yielding a slope of  $0.97 \pm 0.02$ , in agreement with the prediction  $f_D \propto (\epsilon - \epsilon_c)^{1/\phi}$ . The shaded area shows the same phase diagram but derived in units of  $f$  (right axis) versus temperature  $T$  (top axis). It appears reentrant. Reprinted with permission from [60]

the intermolecular interactions [54, 55]. Much of the related upsurge of interest into the statics and dynamics of single macromolecules at surfaces has been spurred by the use of atomic force microscopy [56, 57] (AFM) and optical/magnetic tweezers [58], which allow one to manipulate single polymer chains. There is a close analogy between the forced detachment of an adsorbed polymer chain (such as polyvinylamine and polyacrylic acid) adhering to a solid surface (such as mica or a self-assembled monolayer) when the chain is pulled by the end monomer and the unzipping of homogeneous double-stranded DNA [59].

In our investigations [31, 60, 61] along with computer experiments we use the grand canonical ensemble (GCE) approach of Kafri et al. [59] in order to treat the detachment of a single chain from a sticky substrate when the chain end is pulled by external force (cf. Fig. 13a). A central result is the overall phase diagram of the force-induced desorption transition for a linear self-avoiding polymer chain (cf. Fig. 13b). We demonstrate its reentrant character when plotted in terms of detachment force  $f_D$  against system temperature  $T$  [31, 60]. We find that, despite being of first order, the force-induced phase transition of polymer desorption is dichotomic in its nature, that is, no phase coexistence and no metastable states exist! This unusual feature of the phase transformation is unambiguously supported by our simulation data, e.g., through the comparison of the order parameter probability distributions in the immediate vicinity on both sides of the detachment line, whereby no double-peaked structure is detected.

We obtained these results by studying the various conformational building blocks, characterizing the structure of an adsorbed linear polymer chain, subject to a pulling force of fixed strength. The GC partition function of the adsorbed chain of length  $N$  at fugacity  $z$ ,  $\Xi(z) = \sum_{N=0}^{\infty} \Xi_N z^N = V_0(z)Q(z)[1 - V(z)U(z)]^{-1}$ , is

related to the GC partition functions  $U(z)$ ,  $V(z)$ , and  $Q(z)$  of loops, trains, and tails. Closed analytic expressions for the fraction of adsorbed segments (i.e., the order parameter of the desorption transition) and for probability distributions of trains, loops, and tails, cf. Eqs. (4) and (5), are derived in terms of the surface potential intensity both with and without external force. As an example, we refer here to the tail distribution without external force, which is given by:

$$P_{\text{tail}}(l) = \begin{cases} \frac{1}{l^\beta} \exp[-c_1(\epsilon - \epsilon_c)^{1/\phi} l], & \epsilon > \epsilon_c \\ \frac{A_1}{l^\beta} + \frac{A_2 N^{1-\gamma_1}}{l^\beta (N-l)^{1+\phi}}, & \epsilon = \epsilon_c \\ \frac{N^{1-\gamma_1}}{l^\beta (N-l)^{1+\phi}}. & \epsilon < \epsilon_c \end{cases} \quad (4)$$

The same for the loop distribution reads:

$$P_{\text{loop}}(l) = \begin{cases} \frac{1}{l^{1+\phi}} \exp[-c_1(\epsilon - \epsilon_c)^{1/\phi} l], & \epsilon > \epsilon_c \\ \frac{B_1}{l^{1+\phi}} + \frac{B_2 N^{1-\gamma_1}}{l^{1+\phi} (N-l)^\beta}, & \epsilon = \epsilon_c \\ \frac{N^{1-\gamma_1}}{l^{1+\phi} (N-l)^\beta}. & \epsilon < \epsilon_c \end{cases} \quad (5)$$

In Eqs. (4) and (5),  $A_1$ ,  $A_2$ ,  $B_1$ , and  $B_2$  are constants and  $\gamma_1 = 0.680$ ,  $\beta = 1 - \gamma_1$  are universal exponents. Among other things, we verify the gradual transition of the PDF of loops from power-law to exponential decay as one moves away from the CAP to stronger adsorption. We demonstrate that for vanishing pulling force,  $f \rightarrow 0$ , the mean loop size,  $L \propto (\epsilon - \epsilon_c)^{1 - (1/\phi)}$ , and the mean tail size,  $S \propto 1/(\epsilon - \epsilon_c)^{1/\phi}$ , diverge when one approaches the CAP. In contrast, for a non-zero pulling force,  $f \neq 0$ , we show that the loops on the average get smaller with growing force. Close to the detachment threshold,  $f \approx f_D$ , the tail length diverges as  $S \propto \left(1 - \frac{f}{f_D}\right)^{-1}$ . The simulation results for  $P_{\text{tail}}(l)$ ,  $P_{\text{loop}}(l)$  are in good agreement with the theoretical predictions. As expected, all these conformational properties and their variation with the proximity to the CAP are governed by a crossover exponent  $\phi$ . An important result in this work is the calculation of  $\phi$ , which provides insight into the background of the existing controversial reports about its numeric value. It is shown that the value of  $\phi$  may vary within the interval  $0.39 \leq \phi \leq 0.6$ , depending on the possibility that a single loop interacts with the neighboring loops in the adsorbed polymer. Since this range is model-dependent,

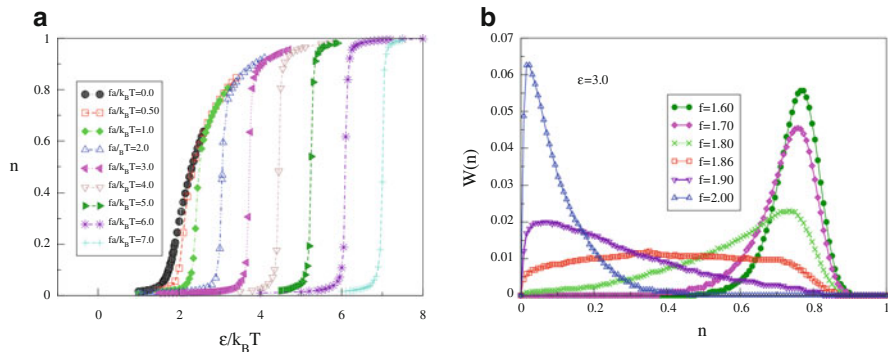


**Fig. 14** (a) Order parameter (fraction of detached monomers) versus surface potential  $\epsilon$  for different pulling forces. The chain is of length  $N = 128$ . (b) Order parameter distribution for pulling force  $f\sigma/k_B T = 6.0$  and different adhesion energy  $\epsilon/k_B T$ . The critical surface potential for this force is  $\epsilon_D = 6.095 \pm 0.03$  so that the values  $\epsilon/k_B T = 6.09$  and  $6.10$  are on each side of the detachment line. Reprinted with permission from [60]

one should not be surprised that different models produce different estimates of  $\phi$  in this interval.

In Fig. 14a one can see the isotherms of the order parameter,  $n = N_{\text{ads}}/N$ , against the surface attraction  $\epsilon$  for different pulling forces,  $f$ , which resemble closely those of a conventional first-order phase transition. However, as indicated by the corresponding PDF  $W(n)$  (cf. Fig. 14b), the adsorption–desorption first-order phase transition under pulling force has a clear dichotomic nature (i.e., it follows an “either/or” scenario): in the thermodynamic limit  $N \rightarrow \infty$  there is no phase coexistence! The configurations are divided into adsorbed and detached (or stretched) dichotomic classes. The metastable states are completely absent.

We would like to emphasize that our simulations have been carried out mainly within the framework of a constant-force ensemble, whereas one may also work in the constant-height ensemble whereby one uses the end-monomer height as an independent parameter and measures the force exerted by the chain on the end monomer, as we did in previous work [62]. Notwithstanding the equivalence of both ensembles, some quantities behave differently in each ensemble. So, for example, in the fixed-height ensemble one observes a constant-force plateau while the height of the chain end-monomer is varied. Most notably, the fraction of adsorbed monomers  $n$  varies steadily with changing  $h$ , whereas in the constant-force ensemble one observes a jump of  $n$  at a particular value of the force  $f$ . However, this should not cast doubt on the first-order nature of the phase transition, which can also be recovered within the constant-height ensemble, provided one expresses the control parameter  $h$  in terms of the average force  $\langle f \rangle$ . This interesting aspect has been considered in detail by Skvortsov et al. [63].

Last but not least, we would like to point out a very recent investigation [64] in which we show that the change of detached monomers with time is governed by a differential equation that is equivalent to the nonlinear porous medium equation,

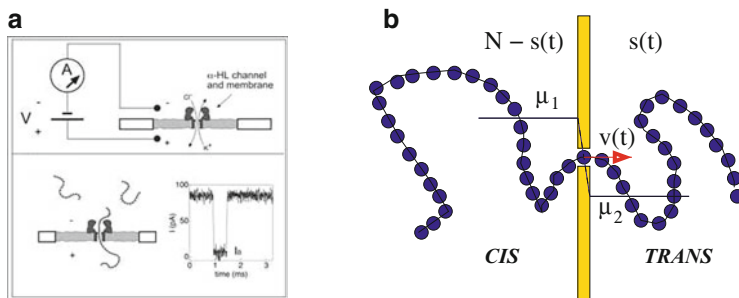


**Fig. 15** (a) DNA translocation through a protein pore in  $\alpha$ -hemolysin. When the DNA enters the pore, the ionic current is blocked. This current blockage is used to detect the residence time of DNA bases in the pore [67]. (b) Chain translocation through a nanopore. The instantaneous translocation coordinate is  $s(t)$  and the bead velocity in the pore is  $v(t)$ . The driving force is due to a chemical potential gradient within the pore,  $f = (\mu_1 - \mu_2)/k_B T$ . Adapted from [68]. Reproduced by permission of IOP Publishing. All rights reserved

employed widely in transport modeling of hydrogeological systems. Depending on the pulling  $f$  and restoring  $\varphi$  forces, one can discriminate between a “trumpet” ( $1/N^{\nu} \ll \varphi < f < 1$ ), “stem-trumpet” ( $\varphi < 1 < f$ ), and “stem” ( $1 < \varphi < f$ ) regimes of desorption. Remarkably, in all these cases the time dependence of the number of desorbed monomers  $M(t) = N - N_{\text{ads}}(t)$  and the height of the end monomer (i.e., the monomer that experiences the applied external pulling force)  $h(t)$  follow an universal  $\sqrt{t}$ -law (even though this is not a diffusion phenomenon). There is, however, a common physical background with the well-known Lucas–Washburn  $\sqrt{t}$ -law of capillary filling [65], as with the ejection kinetics of a polymer chain from a cavity (virus capsid) [66]. In these seemingly different phenomena there is always a constant driving force (meniscus curvature or polymer entropy) that acts against a gradually changing drag force (friction) in the course of the process.

### 1.5.2 Polymer Translocation Through Narrow Pores in the Membranes and Escape from Long Pores

The translocation of a polymer is the process during which a flexible chain moves through a narrow pore of size comparable with that of a chain segment to go from one (*cis*) side of a membrane to the other (*trans*) side, as shown in Fig. 15. This phenomenon is important in many biological and chemical processes, such as viral injection of DNA into a host and RNA transport through a nanopore of the nuclear membrane, and appears highly promising as a possible nanotechnological application, e.g., for drug delivery [67, 69], rapid DNA sequencing [67, 70, 71], gene therapy, etc.

During the last decade, polymer translocation has thus turned into a very active area of research with a variety of theoretical, simulational, and experimental studies examining this process under different conditions [68]. Different driving

mechanisms for the translocation processes have been a subject of intense discussion, e.g., electric fields [72], chemical potential gradients [73], selective adsorption on one side of the membrane [74, 75], and related ratchet mechanisms [76]. In addition, entropic barriers, segment crowding at the pore orifice, and, most notably, the interplay between topological connectivity of the chain and geometric constraints imposed by the pore, make the problem rather intricate and complex. Moreover, since polymer translocation is such an ubiquitous phenomenon, it remains questionable whether a single universal scenario is operative under all circumstances, so detailed studies of its various aspects are necessary.

It is convenient and customary to describe the translocation process by a single variable  $s$ , called the translocation coordinate, which denotes the sequential number of the monomer located in the pore at time  $t$ , and tells how much of the polymer has passed meanwhile through the pore (cf. Fig. 15b). As a rule, once the initial monomer has already threaded through the hole, among the principal quantities of interest are the mean translocation time  $\tau$ , and its dependence on polymer length  $N$  and on the driving force magnitude  $f$ . In fact,  $\tau$  is one of the few dynamic quantities that are accessible in current experiments [67, 70, 71]. Assuming that  $\tau \propto N^\alpha f^{-\delta}$ , one of the objectives is to provide a plausible explanation for the observed values of the exponents  $\alpha$  and  $\delta$ . Important information is obtained from the probability distribution function of translocation times,  $Q(t)$ , and also from the time dependence of the mean squared displacement (variance) of the translocation coordinate  $\Delta(t) \equiv \langle \Delta s^2(t) \rangle = \langle s^2 \rangle - \langle s \rangle^2$ . Both quantities play essential roles in numerous efforts to elucidate a typical hallmark of the translocation process. Namely, its dynamics is anomalous with  $\langle \Delta s^2(t) \rangle \propto t^\beta$ , where  $\beta < 1$  (i.e., the dynamics is subdiffusive) for the force-free (i.e.,  $f = 0$ ) case and  $\beta > 1$  (i.e., super-diffusive) for the force-driven polymer translocation. This is well established at present [77–80].

There are different possibilities for how the forced translocation can be effected. For example, Milchev et al. [74, 75] studied the possibility that the monomer–membrane interaction is attractive on the *trans* side, while it is assumed to be repulsive on the *cis* side. Assuming that a few monomers of a chain have already passed through the pore and experience the favorable membrane–monomer interaction on the *trans* side, two questions that are asked are: (1) How likely is it that the rest of the chain will follow from the *cis* to the *trans* side, depending on chain length  $N$  and the distance  $T/T_c - 1$  from the adsorption transition that happens on the *trans* side at  $T = T_c$ ? (2) How does the time needed for complete translocation depend on these parameters?

Milchev et al. [74, 75] found that it makes a big difference whether one studies the case in which in equilibrium a chain is not yet absorbed on the *trans* side (and still in a mushroom state when the chain gets through the pore) or whether adsorption occurs. In the first case, the problem is similar to unbiased translocation (which occurs by thermal fluctuations only [81, 82]), i.e., for any finite fraction of monomers that have already passed to the *trans* side there is still a non-zero probability that the whole chain returns to the *cis* side (and diffuses away). In this case, the translocation time is found to scale as  $\tau \propto N^{2\nu + 1} \approx N^{2.2}$ , i.e., the time is simply of the order of the Rouse time of a single chain in a good solvent (note that the Monte Carlo modeling of Milchev et al. [74, 75] uses implicit solvent

and there cannot be any effects due to hydrodynamic interactions). In any case, this result already shows that the relation  $\tau \propto N^2$  [81, 82] (derived on the assumption that the problem can be reduced to a quasi-one-dimensional problem of diffusion over an entropic barrier, taking the numbers of monomers at the *trans* side as “reaction coordinate”) cannot hold in general. Indeed, Dubbeldam et al. [77, 78] have shown that different power laws can be obtained by a model in which ordinary diffusion is replaced by fractional Brownian motion, which leads to anomalous diffusion.

When one studies translocation driven by adsorption for temperatures where in equilibrium the chain is adsorbed on the *trans* side in a “pancake configuration,” one finds that a finite number of monomers adsorbed on the *trans* side (of order 10) suffices to pull the remaining chain through the hole in the membrane in almost all cases. The relaxation time was found to scale like  $\tau \propto N^{1.7}$ , but is not clear whether this exponent can be theoretically explained [74, 75].

The standard model for forced translocation uses a biasing force on any monomer that has entered the pore, driving it from the *cis* to the *trans* side (see [83] and references therein). Estimates for the various exponents describing the translocation dynamics have been given [83], but in this study (as well as in other work that can be found in the literature) it is not clear whether the asymptotic scaling regime really has been reached or whether one observes “effective exponents” due to slow crossovers. In addition, a rather fundamental problem [83, 84] is a strong conformational asymmetry of the part of the chain that is still on the *cis* side and the part that is already on the *trans* side: the former part is under stretch because parts of the chain very distant (along the contour) from the pore have not yet relaxed. Translocation happens too fast for the chain configurational degrees of freedom to reach local equilibrium. So, the radius of the *cis* part is relatively too large.

Conversely, the configuration of the *trans* part is somewhat too dense and, hence, the radius is too small [83, 84]. Although some aspects of this phenomenon have been discussed by Sakaue [85, 86], we feel that a complete theory of translocation that properly incorporates all these out-of-equilibrium effects still needs to be developed.

In the wake of these developments, our studies of translocation dynamics have been focused on the generic case of unbiased translocation [77, 79, 80] in the absence of driving force,  $f = 0$ , and on the case when the chain threading through a pore is driven by applied force [78, 87–89]. In our original efforts to capture the essence of the problem, we employed diverse methods (scaling theory, fractional calculus, Monte Carlo and molecular dynamics simulations). We found that the relevant dynamic variable, the transported number of polymer segments  $s(t)$ , displayed an anomalous diffusive behavior both with and without an external driving force being present [77–80]. A closed analytic expression for the probability,  $W(s, t)$ , of finding  $s$  translocated segments at time  $t$  in terms of chain length  $N$  and applied drag force  $f$  was derived from the fractional Fokker–Planck equation and shown to provide analytic results for the time variation of the statistical moments  $\langle s(t) \rangle$  and  $\langle s^2(t) \rangle$ . It was shown that in the absence of driving force, the time  $\tau$  needed for a macromolecule of length  $N$  to thread from the *cis* into

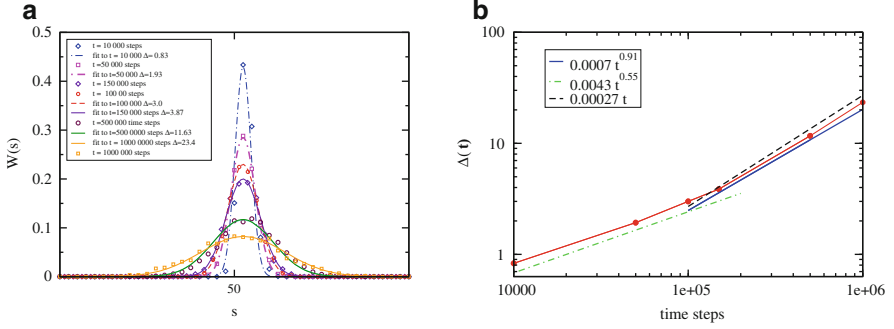


**Fig. 16** (a) The probability distribution of translocation coordinate  $W(s, t)$  at five different time moments (*symbols*) along with Gaussian fits (*lines*) with variance  $\Delta$ . (b) Increase of the variance  $\Delta(t)$  with elapsed time  $t$ , indicating a crossover from short-time subdiffusive behavior  $\propto t^{0.55}$  to late time nearly normal diffusive behavior  $\propto t^{0.91}$ . Reprinted with permission from [87]

the *trans* side of a cell membrane scales like  $\tau \propto N^{2\nu+2-\gamma_1}$  with the chain length. Thus, the anomalous dynamics of the translocation process has been related to a universal exponent that contains the basic universal exponents of polymer physics, the Flory exponent  $\nu$ , and the surface entropic exponent  $\gamma_1$ . If a driving force is present, our results suggested a scaling  $\tau \propto f^{-1} N^{2\nu+1-\gamma_1}$ , in good agreement with Monte Carlo (MC) and molecular dynamics (MD) simulation data.

While validating the sub- or superdiffusive behavior of  $\langle \Delta s^2(t) \rangle$ , several new findings revealed that the probability distribution of the translocation coordinate  $s$ , i.e.,  $W(s, t)$ , stays Gaussian for different time moments. Moreover, the long time tail of the translocation time distribution was found to have an exponential form, challenging the power-law behavior [77, 78] predicted within the fractional Fokker–Planck equation. In an effort to reconcile the new findings with the observed sub- or superdiffusive variation of  $\Delta(t) = \langle \Delta s^2(t) \rangle$ , we recently suggested a new governing equation [87, 88], based on the fractional Brownian motion (fBm) approach (cf. Fig. 16 for the force-free case).

Starting from the Langevin equation  $ds(t)/dt = v(t)$  where, by assumption, the translocation velocity  $v(t)$  follows Gaussian statistics, we derived a Fokker–Planck equation for the distribution  $W(s, t)$ :

$$\frac{\partial}{\partial t} W(s, t) = - \frac{\partial}{\partial s} [K(s) W(s, t)] + \mathcal{D}(t) \frac{\partial^2}{\partial s^2} W(s, t) \quad (6)$$

where the average velocity is  $\langle v(t) \rangle \equiv K(s)|_{s=s(t)}$  and the time-dependent diffusion coefficient  $D(t) = \int_0^t G(t, t') dt'$ , with  $G$  being the second moment (velocity autocorrelation function)  $G(t_1, t_2) \equiv \langle [v(t_1) - \langle v(t_1) \rangle][v(t_2) - \langle v(t_2) \rangle] \rangle$ , assuming a (constant) friction coefficient,  $\xi_0$ . In the simplest case of the unbiased process (i.e.,  $f = 0$ ), Eq. (6) can be solved to:

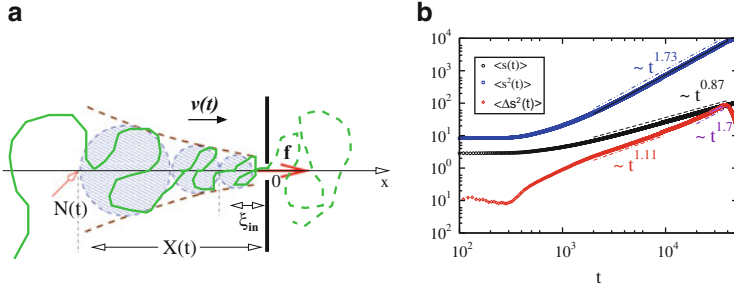


**Fig. 17** (a) Dynamic response of a driven polymer translocation upon switching the pulling force  $f$ . At time  $t$  the tension force has passed the  $N(t)$  monomer and is at distance  $X(t)$  from the membrane while  $M(t)$  monomers have already moved into the *trans* side of the separating membrane. The chain portion to the *right* of  $X(t)$  is moving with mean velocity  $v(t)$ . (b) First and second moments of the translocation coordinate  $\langle s \rangle$  and  $\langle s^2 \rangle$ , and the variance  $\langle \Delta s(t)^2 \rangle = \langle s^2 \rangle - \langle s \rangle^2$  for a polymer chain with length  $N = 100$  and driving force  $f = 5.0$ . Reprinted with permission from [89]

$$W(s, t) = \frac{1}{\sqrt{2\pi Dt^\beta}} \exp \left[ -\frac{(s - s_0)^2}{4Dt^\beta} \right] \quad (7)$$

where  $D$  is a constant. Therefore, the distribution  $W(s, t)$  is indeed Gaussian, albeit with a width proportional to the variance  $\Delta(t)$  (cf. Fig. 16), which in this case follows a subdiffusive behavior (i.e.,  $\beta < 1$ ). This result reproduces the MC simulation findings reported recently by Kantor and Kardar [90].

In an effort to lean on a solid physical background in order to describe faithfully the more complex (far from equilibrium) case of a driven translocation, following the pioneering work of Sakaue [85, 86], we considered the propagation of a tensile front along the polymer chain backbone upon pulling [89]. As shown schematically in Fig. 17a, when a pulling force is instantaneously switched on, tension starts to propagate along the chain backbone and progressively alters the polymer conformation. Eventually, after some characteristic time, a steady state is reached and the whole polymer starts moving with constant velocity. We find that:

- The translocation starts with the formation of initial Pincus blob (i.e., the first blob is generated immediately at the pore entrance). The characteristic time for blob initiation is given by  $\tau_{\text{init}} \propto a\xi_0/f$ . Our MD simulation results essentially support the scaling prediction  $\tau_{\text{init}} \sim 1/f$ .
- The initiation is followed by a tensile force transmission along the chain backbone that is governed by the local balance of driving and drag forces. For forces in the interval  $N^{-\nu} \ll af/k_B T < 1$  this leads to the so-called trumpet regime (see Fig. 17a). The corresponding translocation time is given by  $\langle \tau \rangle \propto C_1 f^{1/\nu - z} N^{1+\nu} + C_2 f^{2-z} N^{2\nu}$ , where the dynamic exponent  $z = 2 + 1/\nu$  for Rouse dynamics and  $z = 3$  for Zimm dynamics.  $C_1$  and  $C_2$  are numerical model-dependent constants. As a result, different scaling of  $\tau$  is observed,

depending on chain length  $N$  and driving force strength  $f$ . Thus, one expects a crossover from  $N^{2\nu}/f^{1/\nu}$  to  $N^{1+\nu}/f$ , i.e., the translocation exponent  $\alpha$  grows with increasing force  $f$  from  $\alpha \approx 1.18$  to  $\alpha \approx 1.59$ .

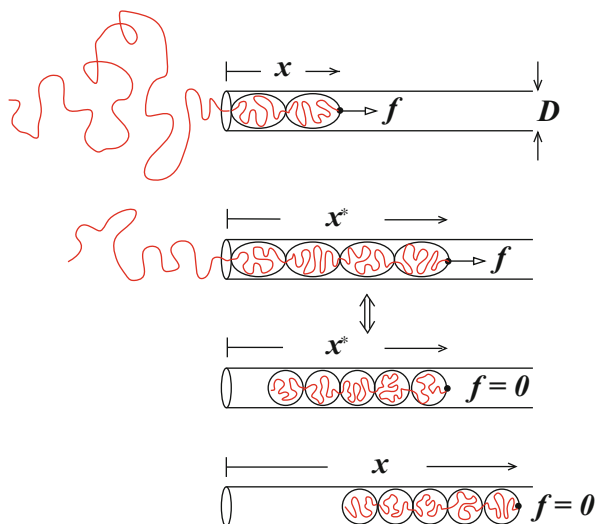
- For strong forces, the translocation time can be estimated as  $\langle \tau \rangle = C_1 \tau_0 N^{1+\nu} / \tilde{f}_a + C_2 \tau_0 N^{2\nu} / \tilde{f}_a$  where the first term dominates under condition  $N^{1-\nu} \gg C_2/C_1$ . Therefore, the translocation scaling exponent grows from  $\alpha = 2\nu$  to  $\alpha = 1 + \nu$  as the chain length  $N$  increases. This is in agreement with the results of MD and MC simulations. A scaling relation very close to  $\langle \tau \rangle \propto N^{2\nu} / \tilde{f}_a$  has been found experimentally [91] in the case of translocation of long double-stranded DNA through a silicon oxide nanopore. In this experiment the translocation exponent was  $\alpha = 1.27$ , which is close to our theoretical prediction.
- Even if the mentioned approach appears to yield physically plausible and qualitatively correct results, generally, the MD simulation findings yield systematically smaller values for the translocation exponent, e.g.,  $\alpha \approx 1.11$  and  $\alpha \approx 1.47$  for weak and strong forces, respectively. As we show below, this shortcoming of the theory stems most probably from neglecting the role of fluctuations during the translocation process, which is common to most theoretical treatments so far.

In our most recent work, we investigated the impact of thermal fluctuations on the driven translocation dynamics, theoretically and by means of extensive MD simulation [88]. Indeed, the role of thermal fluctuations is by no means self-evident. Our theoretical consideration is based on the Fokker–Planck equation (FPE) Eq. (6), which has a nonlinear drift term and a diffusion term with a time-dependent diffusion coefficient  $\mathcal{D}(t)$ .

Our MD simulation reveals that the driven translocation process follows a superdiffusive law with a running diffusion coefficient  $\mathcal{D}(t) \propto t^\gamma$ , where  $\gamma < 1$ . Therefore, although in the unbiased translocation case, the diffusion is Brownian (or slightly subdiffusive), in the biased regime the process becomes superdiffusive, i. e., the variance  $\langle \Delta s^2 \rangle \propto t^\theta$ , where  $1 < \theta < 2$  (cf. Fig. 17b). Moreover, the exponent  $\theta$  increases with the growth of the driving force  $f$ , namely,  $\theta = 1.5$  for  $f = 1$ , and  $\theta = 1.84$  for  $f = 10$ . This finding is then used in the numerical solution of the FPE, which yields an important result: for comparatively small driving forces, fluctuations facilitate the translocation dynamics. As a consequence, the exponent  $\alpha$ , which describes the scaling of the mean translocation time  $\langle \tau \rangle$  with the length  $N$  of the polymer,  $\langle \tau \rangle \propto N^\alpha$ , is found to diminish. Thus, taking thermal fluctuations into account, one can explain the systematic discrepancy between the theoretically predicted duration of a driven translocation process, considered usually as a deterministic event, and measurements in computer simulations.

Finally, a related interesting problem occurs when a force acts on a chain end of a flexible macromolecule, which is dragged into a nanotube with repulsive walls (Fig. 18). Since in a nanotube of diameter  $D$ , the chain (under good solvent conditions) forms a string of blobs,  $g \propto N^{1/\nu}$  monomers per blob, and each blob costs a free energy of  $k_B T$ , there is a free energy cost of order  $N/g \propto ND^{-1/\nu}$  that needs to be overcome by the force. Klushin et al. [92] showed, by a phenomenological scaling

**Fig. 18** Flexible polymer chain with one end dragged into a nanotube in a quasi-equilibrium process. The coordinate  $x$  of the end where the force acts is taken as a reaction coordinate. At  $x = x^*$  the free part of the chain is suddenly sucked into the nanotube. Reprinted with permission from [92]. Copyright 2008 American Chemical Society



theory and by simulation, that the process has discontinuous features: after a critical fraction of the chain is drawn into the tube, the rest moves into the tube, releasing the tension that is still present as long as part of the chain is still outside the nanopore.

## 2 Reversible Kinetics of Hydrogen-Bond Networks

The discussion so far has focused on the general properties of single polymer chains, but in many applications and experimental realizations of the forced desorption or unfolding of biomolecules the specific nature of the adhesion bonds under study determine specific material properties. In many situations, one is confronted with an adhesion cluster that is stabilized by a number of parallel bonds. One important class of noncovalent adhesion bonds is provided by hydrogen bonds (H-bonds). The most common situation that is encountered in many experimental investigations of the mechanically forced opening of adhesion bonds via dynamic force spectroscopy (DFS) employing atomic force microscopes or optical tweezers is the following: The system under study consists of adhesion complexes that are pulled in order to investigate the rupture events. Often, the rupture event is irreversible in the sense that reversing the pulling direction does not give rise to rebinding. Recently, reversible bond breakage has also been studied in different systems [93, 94] and one particular study will be reviewed in the following section (Sect. 2.2) [95]. In Sect. 2.1, we will report on the results of force probe MD simulations on dimers of calix[4]arene catenanes that show very interesting reversible H-bond network dynamics. In addition, we briefly review the theoretical treatment of the stochastic dynamics of reversibly binding systems under different protocols of external force application.

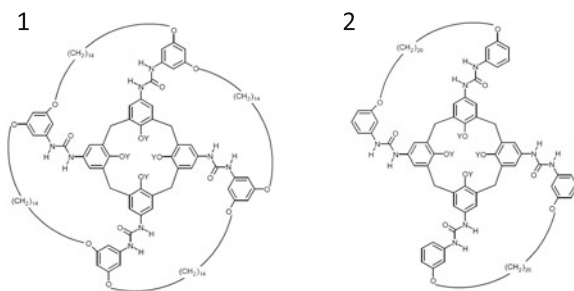


**Fig. 19** Structure of the calix[4]arene monomers. Note the shorter loop length in the tetra-loop (1) compared to the bis-loop (2) system. *Y* indicates CH<sub>3</sub>. Reprinted with permission from [98]. Copyright (2011) American Chemical Society

## 2.1 Force Probe MD Simulations of Calix[4]arene Catenanes

Catenanes constitute a family of molecules that are interesting because of their potential incorporation into molecular motors or switches [96] and, in particular, the specially designed calix[4]arene catenanes that have been synthesized recently have interesting properties [97]. We have investigated exactly the same systems that are also the subject of experimental DFS investigations reviewed in Sect. 3, namely dimers of two calix[4]arenes with the structures presented in Fig. 19 [98] using mesitylene as an aprotic solvent. Structure 1 has four aliphatic loops of 14 CH<sub>2</sub> groups and structure 2 has two longer loops consisting of 20 CH<sub>2</sub> groups. In the dimers, the loops are intertwined building catenane structures, which in equilibrium form a compact aggregate stabilized by 16 H-bonds formed between urea groups located at the upper rim of the calixarene monomers (UU-bonds). If one pulls the dimer along the direction connecting the calixarene “cups,” this compact structure opens but the monomers cannot dissociate completely due to the mechanical lock provided by the intertwined loops. These systems therefore are ideally suited for a study of reversible binding. All force probe MD simulations were performed in the so-called force ramp mode, meaning that the force increases linearly with time,  $F(t) = k_c \cdot v \cdot t$ , with the pulling velocity  $v$  and the stiffness of the pulling device  $k_c$ . These simulations reveal that, after opening the compact structure, a new set of H-bonds forms between the urea groups of one monomer and the ether groups of the other monomer (UE-bonds). In the system with four loops, this structure cannot be opened by further pulling the system because of the rather short loop length. In Fig. 20, the structure of the closed and open configuration of the tetra-loop system is shown along with a sketch of the H-bonds present in the respective states. The pulling direction in the force probe MD simulation is indicated by the arrow in the closed structures shown in the upper part of Fig. 20.

If one reverses the pulling direction after the system has undergone the transition to the open structure, one observes a rebinding into the closed state for pulling

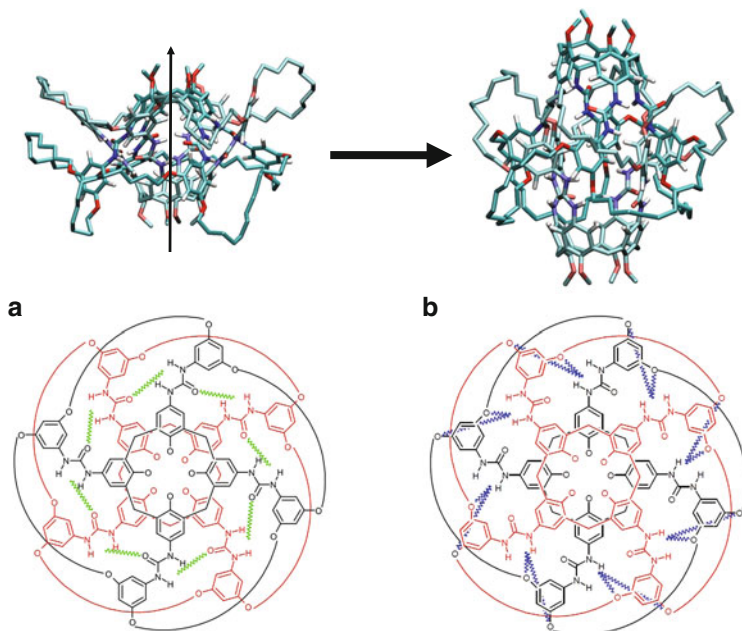


**Fig. 20** *Top:* Examples of the configurations of the (a) closed ( $t = 0$ ) and (b) open ( $t = 17$  ns) structures of the tetra-loop system from a pulling simulation with  $v = 0.1$  nm/ns. *Bottom:* Representations of the tetra-loop calix[4]arene dimer. The loops consist of 14  $\text{CH}_2$  groups; the endstanding  $\text{CH}_3$  groups linked to the oxygen atoms are not shown. (a) UU-bonds relevant in the closed state are indicated in *green*. (b) UE-bonds stabilizing the open state are drawn in *blue*. Reprinted with permission from [98]. Copyright (2011) American Chemical Society

velocities  $v$  that are not too large. This is exemplified in Fig. 21, which shows typical force versus extension curves for the tetra-loop system calculated for different pulling velocities. The hysteresis hallmarking the nonequilibrium nature of the simulations is evident immediately. From the dependence of the hysteresis on the pulling velocity it becomes clear that the system will not rebind for large  $v$  if the force is relaxed after the opening transition. Thus, if one considers the time scale set by  $v$ , the system appears irreversible on a fast time scale and reversible on a slower time scale.

Because the rupture event is a stochastic process, the rupture forces are distributed in a certain range. Therefore, as in the experimental studies, we performed a large number of simulations and analyzed the rupture force distributions and the rejoin force distributions. The mean values as a function of the pulling velocity represent the so-called force spectrum. Experimentally, often a logarithmic dependence of the mean rupture force on  $v$  is observed, but the data collected by Schlesier et al. [98] allow no definite conclusion regarding this dependence.

As mentioned above, we also performed simulations on a bis-loop system undergoing two transitions. The first transition is from a compact, closed structure stabilized by a maximum of 16 UU-bonds to an intermediate reminiscent of the open structure of the tetra-loop system. In the second transition, this UE-stabilized structure opens upon further increase of the external force and an open structure

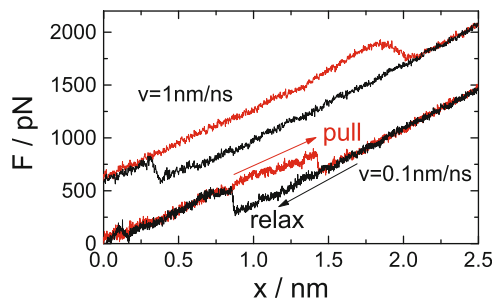


**Fig. 21** Representative force versus extension ( $x = v \cdot t$ ) curves for the tetra-loop system for the pull mode (*red*) and the relax mode (*black*). The *upper curves* are for  $v = 1$  nm/ns ( $v = -1$  nm/ns in the relax mode) and are shifted by 600 pN for clarity. The *lower curves* are for  $v = 0.1$  nm/ns ( $v = -0.1$  nm/ns). Reprinted with permission from [98]. Copyright (2011) American Chemical Society

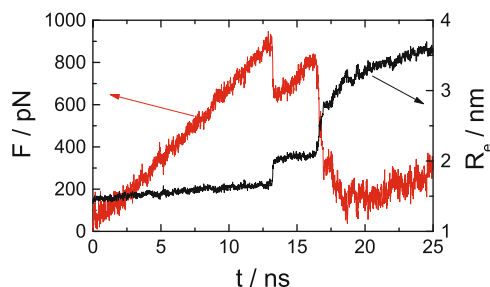


**Fig. 22** Measured force  $F = k \cdot q$  and  $R_e$  for the bis-loop system as a function of simulation time for  $v = 0.1$  nm/ns for a representative simulation run. Reprinted with permission from [98]. Copyright (2011) American Chemical Society

devoid of any H-bonds forms. In this structure, the dimer cannot dissociate completely due to the mechanical lock imposed by the aliphatic loops. Figure 22 shows the measured force  $F$  and the end-to-end distance,  $R_e$ , as a function of simulation time for the system along the arrow shown in Fig. 21. The two steps in the force with the concomitant step-like increase in the end-to-end distance are clearly visible. In contrast to the tetra-loop system, the bis-loop system shows only irreversible opening of the structures and no rejoining for the pulling velocities used in the simulations. However, an analysis of the life-time of the intermediate state revealed that this structure might well be of relevance for the interpretation of the experiments.

All simulations discussed so far have been performed using one particular force field, the GROMOS G53A5 force field [99]. Because it is well known that the choice of the force field has a strong impact on the results of MD simulations, we performed force probe MD simulations of the tetra-loop calix[4]arene dimer using three different frequently used force fields [100]. The most important

conclusion to be drawn from a comparison of the GROMOS G53A5, OPLS-AA [101], and AMBER GAFF [102] force fields is that there are only quantitative differences in the results regarding rupture forces, rebinding ability, and structural quantities. Thus, the fact that one imposes quite strong nonequilibrium conditions on the system does not give rise to additional problems in MD simulations (at least for the force fields studied).

## 2.2 Stochastic Modeling of Reversible Bond Breakage

As discussed above, the reversible opening of adhesion bonds or the reversible unfolding of biomolecules has been investigated in the recent past with increasing intensity. The fact that both the opening and the rejoining events can be observed in favorable examples opens the way to more detailed information regarding the energy landscape of the system under study. The analysis of experimental DFS data showing irreversible rupture events is usually based on the phenomenological Bell model [103]. In this model, it is assumed that the application of an external force  $F$  to the system results in a decrease in the activation energy for bond rupture,  $E_A$ , by an amount  $(F \cdot x)$ . Here,  $x$  denotes the distance from the free energy minimum of the closed structure to the transition state. Thus, the escape rate simply reads as  $k(F) = k_0 e^{\beta F x}$  ( $\beta = 1/T$  with the Boltzmann constant set to unity). Assuming first-order kinetics for the escape from the closed state, one can calculate the rupture force distribution if the time-dependence of the force,  $F(t)$ , is known.

The time-dependence of the force is determined by the protocol applied in the actual application of DFS. One common way to perform the experiments or simulations is the force-ramp mode, in which the applied force increases with a constant velocity,  $F(t) = k_c \cdot v \cdot t$ , where  $k_c$  denotes the force constant of the pulling device. The other protocol, called force-clamp mode, consists in the application of a constant external force,  $F(t) = F_{\text{ext}}$ . In the force-ramp case, one finds the logarithmic dependence of the mean rupture force and  $v$  quoted above. The simple model appears to work quite well for small pulling velocities but fails if one pulls fast. In this situation, more detailed calculations of the rupture force distributions via the computation of the mean first passage time in model free-energy landscapes give more reliable results [104].

The impact of reversible rebinding on the rupture force distributions has been investigated only recently [105, 106] and showed that one reaches equilibrium between the closed and open structure for vanishing pulling velocity and gave the results of the Bell model for fast pulling. We have analyzed the behavior of both the rupture force and rejoin force distributions for the stochastic dynamics in a double-well potential and have considered the dependence of the shape of the distributions and the mean forces on system parameters such as the pulling device stiffness  $k_c$  for the force-ramp protocol [107] (cf. Fig. 23). It was shown that it should be possible to extract the equilibrium constant defined by the kinetic rates for bond rupture and rejoining from the equilibrium forces, i.e., the mean forces obtained in the limit of

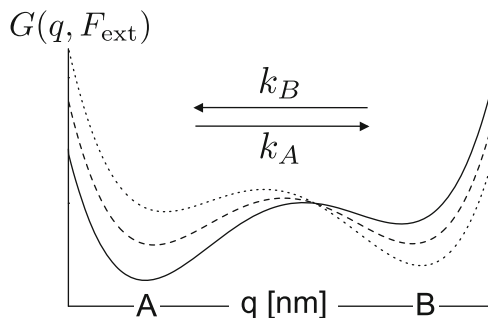


**Fig. 23** Free energy  $G(q, F_{\text{ext}})$  as a function of the reaction coordinate defined as the pulling direction for various values of the applied force. For larger applied force, the *right-hand* “B” minimum becomes deeper (*dashed* and *dotted* lines) and the equilibrium constant  $K(F_{\text{ext}})$  decreases. Reprinted with permission from [108]. Copyright 2010 by the American Physical Society

vanishing pulling velocity. Also, the impact of a soft worm-like chain (WLC) polymeric linker has been treated in an approximate manner using an effective compliance of the composite system. It was found that not only the rupture force distribution but also the rejoining force distribution is affected in a specific way, depending on the parameters of the WLC model. Given the fact that the WLC model might fail (cf. the discussion on this point in Sect. 1.2), this can be of importance when analyzing DFS experiments. Additionally, it was found that in equilibrium the impact of the linker on the equilibrium rupture forces vanishes. This finding, however, depends on the specific model used to treat the system composed of the double-well potential and the linker.

If the reversible dynamics of bond rupture is considered in the force clamp mode, one can exploit an analogy to the treatment of single molecule fluorescence to treat the statistical properties of the transition events [108, 109]. If one considers two states, A (closed) and B (open) with rates  $k_A = k(A \rightarrow B)$  and  $k_B = k(B \rightarrow A)$ , the equilibrium constant is given by  $K = k_B/k_A$ . Due to the strong exponential dependence of the kinetic rates on the external force, in the Bell model given by  $k_A(F) = k_A e^{\beta F \cdot x_A}$  and  $k_B(F) = k_B e^{-\beta F \cdot x_B}$  one can vary  $K$  over a broad range. This fact opens the possibility of very detailed analysis of two-state kinetics. In particular, an analysis of the Mandel parameter [109] and the waiting time distributions [108] should allow the investigation of deviations from simple Markovian kinetics. Different event counting schemes can be utilized, depending on the value of the equilibrium constant, in order to study the possible effect of dynamic or static disorder on the kinetics. As shown in Fig. 24, in the so-called cycle counting scheme only  $B \rightarrow A$  transitions are counted, and in the event-counting scheme every transition is considered. In particular, in situations where  $K$  differs strongly from unity, the cycle-counting scheme may be advantageous due to resolution problems. In favorable cases, an analysis of the moments of the corresponding waiting times will allow deciding whether the system can be described as a two-state system or whether a more complex scheme is required for successful modeling of the kinetics.

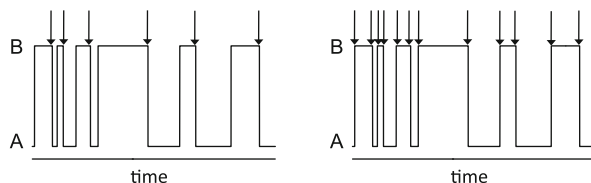


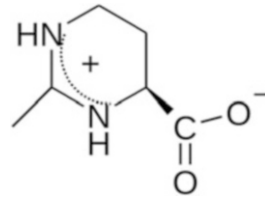
**Fig. 24** Example trajectories showing the two different ways of counting, as indicated by the arrows. *Left*: cycle-counting (only B→A transitions are counted), *Right*: event-counting (all transitions are counted). Reprinted with permission from [108]. Copyright 2010 by the American Physical Society

### 3 Force Spectroscopy and Microscopy of Modular Macromolecules

With the advent of nanotechnology, there has been a strong increase in interest in the physics of small systems far from equilibrium. Mechanically driven transformations, as carried out by single-molecule stretching experiments or observed for molecular machines, offer a unique way to study fundamental theories of statistical mechanics associated with fluctuation-dissipation theorems. Here, we describe the mechanics of unfolding fibronectin in the presence of osmolytes as a model for proteins present in the extracellular matrix. Stretching of single proteins is done by force spectroscopy, giving insight into the structure of fibronectin. We found that preferential exclusion of osmolytes enhances the stability of proteins. Furthermore, we describe the mechanics of oligo calix[4]arene catenanes as a model system that permits the control of the spatial boundaries for separation of hydrogen bonds by mechanically arresting the unbound state with tailored loop entanglement. Thereby, we can investigate hydrogen bond breakage both close to equilibrium and also far from equilibrium by adjusting the separation velocity using a linear force ramp. The loops permit the reversible rupture and rejoining of individual nanocapsules. Experiments carried out by force spectroscopy using an atomic force microscope are backed up by MD simulations and stochastic modeling and reveal the presence of an intermediate state between the closed and open state of a single nanocapsule.

#### 3.1 Preferential Exclusion of Ectoin Enhances the Mechanical Stability of Fibronectin

Production of osmolytes plays a pivotal role in the adaptation of organisms to high salt conditions. Compatible solutes may act as stabilizing agents, which protect cells from denaturing [110–113]. Among the various compatible solutes, ectoine (1,4,5,6-tetrahydro-2-methyl-4-carboxylic acid; Fig. 25), a zwitterionic

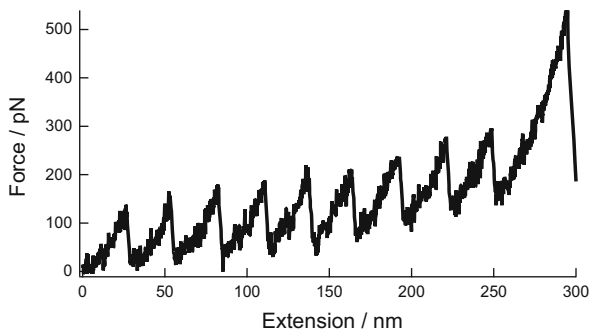
**Fig. 25** Chemical structure of ectoine

cyclic amino acid, is the most common solute found in the cytosol of aerobic heterotrophic bacteria where it increases the thermotolerance [114, 115]. In general, it has been suggested that the presence of osmolytes increases the stability of proteins and preserves enzymatic activity in an aqueous environment. These properties make the compounds potential candidates for biotechnological applications ranging from food processing to protection of tissue from environmental stress factors such as UV irradiation [116]. Timasheff and coworkers [117] argue that the main factor in stabilizing protein structure by large quantities of osmolytes dissolved in water originates from the increase in surface tension of the water, thus leading to a preferential exclusion of the osmolytes from the protein–water interface. The increase in surface tension is in accordance with Gibbs’ isotherm and forces the protein to adopt a more compact protein structure that reduces the surface area exposed to the aqueous phase without perturbing its native function.

Intrigued by this mechanism of protein stabilization, we wanted to prove this hypothesis of protein stabilization by employing single-molecule stretching experiments using proteins. We deliberately chose proteins from the extracellular matrix because they would be exposed to external stresses in the most profound way. AFM and particularly single-molecule force spectroscopy can provide insights into the stability of single ligand–receptor pairs and the elastic properties of individual macromolecules [118–120]. Besides stretching of simple homopolymers, a variety of different biological macromolecules ranging from polysaccharides to modular proteins such as titin and spectrin have been investigated by means of force–extension curves [118, 121, 122]. Most of the pioneering work in this area stems from the group of Gaub and coworkers [123, 124]. Force-induced unfolding of proteins is particularly interesting for unraveling the structure–function relationships of protein filaments involved in the mechanical function of cells and extracellular matrix. Stretching of modular proteins such as titin [123], tenascin [125], spectrin [126], and fibronectin [127] at different loading rates can be used to gather information about the energy landscape of the folded structure. Thereby, Müller and coworkers [128] were able to remove individual domains of single bacteriorhodopsin molecules from a solid supported membrane, giving unfolding fingerprints displaying the structural integrity of the protein under investigation [129].

Previously, we were able to measure the mechanical unfolding of single native fibronectin to reveal the detailed composition of the protein, known to consist

**Fig. 26** Typical force extension curve of native fibronectin. The *sawtooth pattern* is indicative of successive unfolding of individual protein domains. Reproduced from [131] by permission of the PCCP Owner Societies



of three types of subunits FN-I, FN-II, and FN-III that differ in the number of amino acids (45, 60, and 90, respectively) [127]. Fibronectin contains 220 kDa subunits linked into dimers and polymers by disulfide bonds. Fibronectin binds to the cell surfaces via integrins and other extracellular molecules, thereby mediating cell adhesion [130]. Stretching of the molecule results in a subsequent unfolding of the globular domains FN-I, FN-II, and FN-III, which all adopt a beta-sandwich structure. Each unfolding event is accompanied by a specific lengthening of the filament, which corresponds to the number of amino acids forming an individual subunit. This complete and subsequent noncooperative unfolding of subunits results in a typical sawtooth pattern of the force–extension curve (Fig. 26). Evans and Ritchie found that the force of each subsequent unfolding event rises by a constant factor due to simple statistical reasons [132].

Here, we report on single-molecule stretching of native fibronectin and the influence of the compatible solutes ectoine and sarcosine on the mechanical properties, as revealed by the unfolding of the individual subunits and the overall persistence length of the macromolecule [131]. In accordance with the preferential exclusion model, we found a significant stabilization of the protein structure in the presence of osmolytes but not an increase in unfolding forces.

### 3.1.1 Stretching of Native Fibronectin

Figure 26 shows a typical force–extension curve of a single native fibronectin dimer stretched in between a force probe such as an AFM tip and the substrate. Analysis of the force–extension curves is simplified by the fact that the subunits unfold independently from each other, whereas the individual unfolding process of a single protein domain is entirely cooperative and occurs as an all-or-nothing process. This behavior gives rise to the characteristic sawtooth profile, as first described by Rief et al. [123]. Since fibronectin is composed of three different classes of subunits, differing mainly in the number of amino acids, the different events can be easily assigned by monitoring the unfolding forces and elongation lengths after bond rupture.

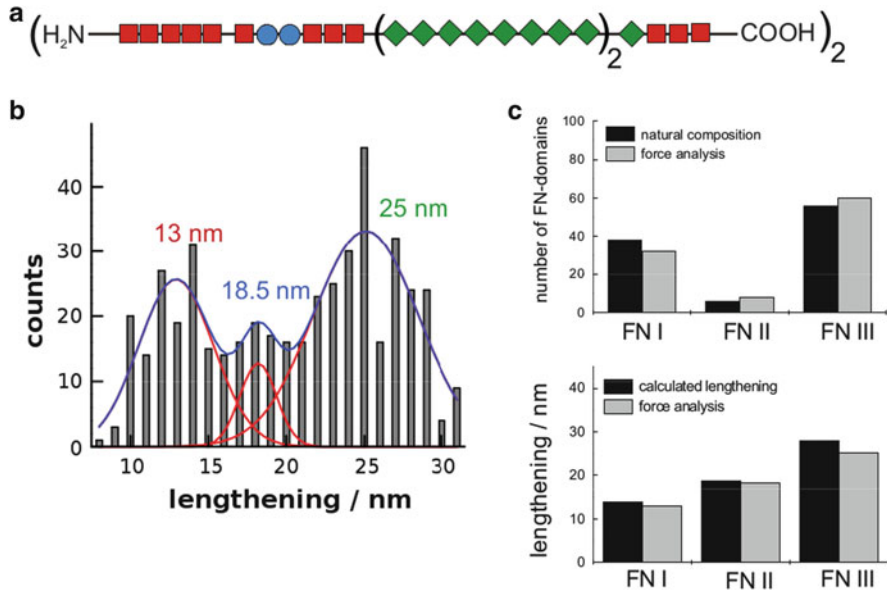
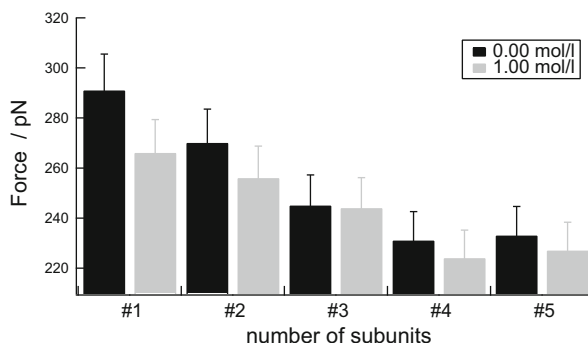


**Fig. 27** (a) Structure of fibronectin composed of (■) FN-I (45 aa), (●) FN-II (60 aa), and (◆) FN-III (90 aa) domains. Cell binding to integrins is mainly provided by FN-III domains, which carry the RGD sequence, whereas attachment to collagen and fibrin is realized by FN-I subunits. (b) Histogram showing the lengthening of different domains due to subsequent unfolding of the modular filament fibronectin. Three Gaussian peaks were fitted to the data with peak maximums at  $12.9 \pm 0.6$  nm representing FN-I,  $18.2 \pm 0.9$  nm for FN-II, and  $25.1 \pm 0.5$  nm for FN-III units. The integral of the corresponding Gaussian curves is related to the percentage of subunit occurrence in native fibronectin, i.e., 153.7 for FN-I, 38 for FN-II, and 280.5 events for FN-III subunits. (c) Statistical analysis of occurrence and lengthening, as obtained from force extension curves. Reproduced from [131] by permission of the PCCP Owner Societies

Of the three different domains, the FN-I domains possess the least amount of amino acids and hydrogen bonds and thus exhibit generally lower unfolding forces of about 50–100 pN, while showing an average lengthening of only about 13 nm (Fig. 27). FN-II domains are composed of 60 amino acids, thus showing intermediate unbinding forces and a lengthening of about 18.5 nm [127]. Figure 26 also shows the prominent unfolding events of FN-III domains, with an average lengthening of 25 nm and unfolding forces ranging from 100 to 200 pN depending on the number of units stretched and the overall compliance of the system. A higher compliance reduces the unfolding force. Notably, the unfolding force is a function of the contour length and therefore of the number of subunits between tip and substrate. Besides, the probability of bond breakage decreases with decreasing number of subunits between tip and sample and thereby displays smaller forces. Figure 27 summarizes the results from many pulling events and also shows a compilation of the expected and measured lengthening of each type of subunit and their occurrence. From structural data of native fibronectin, we expected to

**Fig. 28** Unfolding force of FN-III domains as a function of domain number and presence of ectoine. Reproduced from [131] by permission of the PCCP Owner Societies



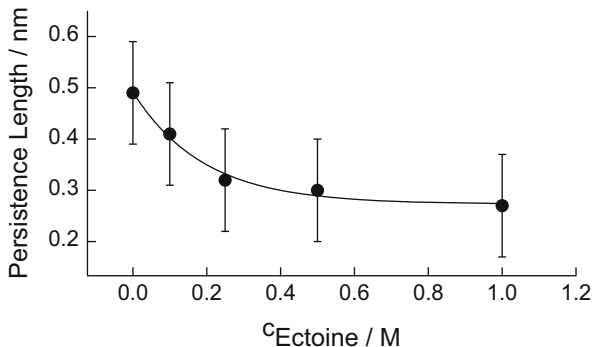
find a distribution showing three maxima. Fitting of three Gaussian curves to the histogram data (Fig. 27b) results in domain lengthening corresponding well to the expected changes in contour length for FN-I, FN-II, and FN-III domains.

#### Influence of Ectoine on the Unfolding Force of FN-III

The major question was whether bacterial osmolytes increase the stability of proteins and nucleic acids by preferential exclusion of ectoine from the interface. First, we investigated the influence of the presence of ectoine and sarcosine on the unfolding force of the individual FN-III subunits of native fibronectin. After recording the force–extension curves and quantifying the unfolding forces (as shown in Fig. 28), we classified the unfolding forces according to their unfolding history (five groups) and compiled the data in a histogram. The unbinding force decreases with increasing number of folded domains between tip and sample, as expected from stochasticity. Although we accounted for the history of unfolding, no significant impact of ectoine or sarcosine on the unfolding force was observed. Although differences in the unfolding forces in the presence of osmolytes might be obscured by changes in the persistence and contour length, it is conceivable that neither ectoine nor sarcosine affect the inner structure of the protein domains but have larger impact on the whole filament by compacting the structure, as expected from the interpretation following Timosheff [110, 111, 117]. Thus, we concluded that the impact of osmolytes on the compliance of the whole molecule should be more significant than on the unfolding forces. Hence, we elucidated whether the tendency of the molecule to adopt a more coiled structure is enhanced by the addition of compatible solutes.

In order to study the influence of bacterial osmolytes on the compliance of the protein we described the force as a function of the extension by a conventional WLC model. This model has provided reasonable results in many studies where the Scanning Force Microscopy (SFM) or optical tweezers have been used to stretch long proteins, even though it fails in some important situations (as discussed in

**Fig. 29** Persistence length of fibronectin as a function of ectoine concentration. A lower persistence length implies a higher tendency to form coils. Reproduced from [131] by permission of the PCCP Owner Societies



Sect. 1). Nevertheless, systematic shifts in molecular properties determined with the help of the WLC model remain correct, although the absolute values might be erroneous. The force is given by rearranging Eq. (2):

$$f = \frac{k_B T}{l_p} \left[ \frac{1}{4} \left( 1 - \frac{x}{L} \right)^{-2} + \frac{x}{L} - \frac{1}{4} \right] \quad (8)$$

The parameter of interest in the context of preferential exclusion is the persistence length  $l_p$  as a measure for the elasticity of the protein. Note that for a worm-like polymer  $l_p \sim \kappa R^4$ , with  $\kappa$  being the bending modulus and  $R$  the radius of the cross-section of the filament. Higher values indicate a tendency to form more extended rod-like structures. For instance, the persistence length of double-stranded DNA is about 50 nm, whereas the persistence length of a single-stranded DNA or polypeptide is only about 0.5–1 nm. WLC fits were carried out for a large number of fibronectin molecules under different conditions. Figure 29 shows the mean persistence length as a function of the osmolyte (ectoine) concentration. The persistence length significantly decreases from 0.5 to 0.29 nm with increasing concentration of ectoine [131]. This implies that the tendency of the molecule to adopt a more condensed (i.e., coiled conformation) increases due to preferential exclusion of ectoine from the interface. Control experiments with sodium chloride at a high concentration of 4 M do not show any significant change in persistence length.

In conclusion, bacterial osmolytes such as ectoine and sarcosine stabilize extracellular matrix proteins, as revealed in mechanical single-molecule experiments, not by increasing intramolecular forces as one might expect but by thermodynamically forcing the molecule into a more compact structure and thus increasing the entropic spring constant of the molecule due to preferential exclusion of the corresponding osmolyte. The unfolding energy in the presence of ectoine increases accordingly.

### 3.2 *Mechanically Interlocked Calix[4]arene Dimers Under External Force*

Thermal fluctuations in macroscopic systems close to a local equilibrium are merely a source of noise that can usually be neglected in everyday physics. In contrast to macroscopic systems, small systems are largely influenced by thermal fluctuations. At macroscopic scales, the experimental outcomes are essentially independent of the repetition of thermodynamic manipulations following the identical protocol, but the situation is different at microscopic scales, where outcomes from repetitions of an identical experimental protocol vary substantially [133]. Recent theoretical developments in nonequilibrium physics have shown how, by using these fluctuations, it is possible to recover free energy differences and energy landscapes from experiments carried out far from equilibrium [104, 134–137]. The methods usually require large sampling of rather rare events, which poses a great challenge to experimentalists. Experiments suitable for verifying modern theories of nonequilibrium statistical mechanics like the fluctuation theorem and the Jarzynski relation need to fulfill two fundamental requirements [138]. On the one hand, manipulative devices such as optical/magnetic tweezers or force microscopes with a bendable cantilever are needed that allow fixing a single state variable such as a defined force or distance, while other variables are allowed to fluctuate [139]. Moreover, since sampling of rare events is necessary to obtain the free energy from out-of-equilibrium experiments, a large number of repetitions are required to reconstruct the underlying potential. Therefore, stable experimental set-ups and special molecules with defined states are needed to permit a large number of realizations with variable outcome.

Therefore, tunable model systems of sufficient smallness are required that can be subjected to defined external mechanical perturbations, giving access to both the equilibrium and nonequilibrium regimes. This allows verification of the free energy differences computed from nonequilibrium conditions by switching the system into quasi-equilibrium conditions, providing the free energy differences directly.

Although supramolecular assemblies are ideally suited to study the physics of small systems under external load, only a few are appropriate for the study of reversible and irreversible transformations. Most examples are from biomolecules such as proteins and nucleic acids [93, 140]. Along these lines, Bustamante and coworkers were the first to establish a reversible model system to apply Jarzynski's relation to compute the free energy difference from out-of-equilibrium experiments [141].

Recently, a supramolecular model system was successfully established that allows the assessment of different regimes of externally stimulated stochastic barrier crossing, ranging from quasi-equilibrium to nonequilibrium bond breakage. This has been achieved by creating a modular molecule that prevents irreversible bond rupture by mechanically limiting the separation distance using entangled loops (Fig. 30) [95]. The mechanical lock limits the distance of the two binding partners, raising

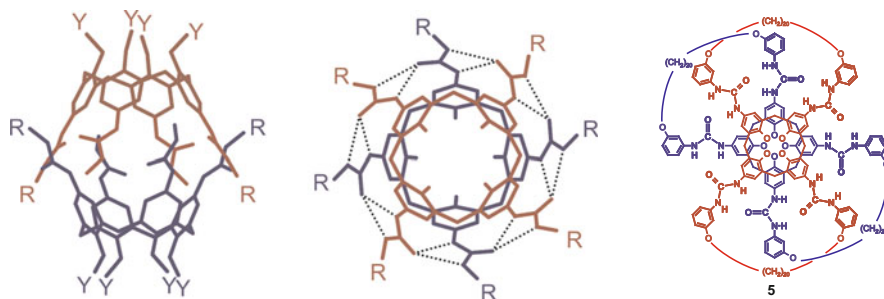


**Fig. 30** A single nanocapsule consisting of two intramolecular entangled bis-loop tetra-urea calix[4]arenes. The dimer is connected by 16 hydrogen bridges, of which 8 are strong and 8 are weak. Reproduced with permission from [95]

the rebinding probability especially at low loading rates. Re-formation of dimeric capsules is observed even during separation. Oligomerization of the dimeric calix[4]arene catenanes provides an intrinsic control that single molecules have indeed been extended and that the observed rupture events correspond to individual breakage of the calixarene capsules. Essentially, we found that calixarene dimers separate under an external force ramp independently, but stochastically generate a characteristic sawtooth pattern. The rupture forces are velocity dependent and re-formation of hydrogen bonds is observable at low loading and relaxation rates. MD simulations in conjunction with stochastic modeling suggests that an intermediate structure arises due to steric reasons (*vide infra*).

### 3.2.1 Force Spectroscopy of Single bis-Loop Tetra-Urea Calix[4]arene Catenanes

Modular long-chain molecules can be stretched with different loading rates to study the unfolding and refolding of intramolecular hydrogen bonds in entangled bis-loop tetra-urea calix[4]arene catenanes.<sup>1</sup> One nanocapsule consists of two calixarene monomers, which are connected via 16 hydrogen bonds to form a dimer (Fig. 30). The hydrogen bridges are formed by four urea groups located at the upper ring of each calixarene monomer. Between two monomers, eight hydrogen bonds are classified as strong (N–O distance, 0.286 nm) and eight as weak (N–O distance, 0.329 nm) [143]. Together with the spacers, each bimolecular capsule exhibits a length of about 4 nm in the initial or unified state and approximately 6 nm in the elongated or ruptured state after the disjoining of intramolecular hydrogen bonds, as demonstrated by MD simulations (*vide infra*). The nanocapsules are oligomerized via covalent coupling between the amino and carboxyl

<sup>1</sup>This chapter contains and describes the results obtained in the framework of the Ph.D. thesis of Matthias Janke [142]. Figs. 30, 32, 33, 34, 35, 36, 37, 38, and 39 are taken from this work.

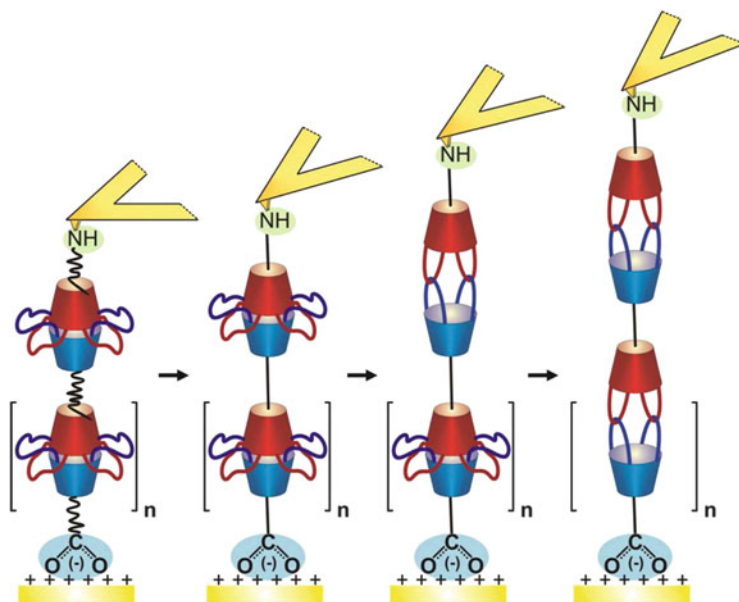


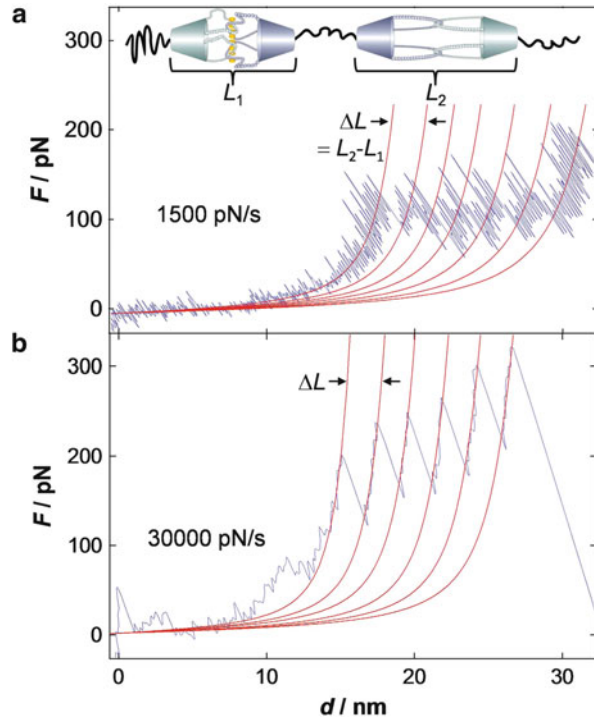
**Fig. 31** Envisioned single-molecule stretching experiment involving oligomeric calixarene catenanes. The molecule is noncovalently attached to the (Trimethylammoniumundecanethiol) functionalized and thereby positively charged gold substrate via terminal carboxyl groups. By touching the surface with the functionalized tip, a molecule is randomly picked up by forming a covalent bond between the terminal amino group and the succinimidy ester groups of the functionalized cantilevers. By increasing the distance from the surface, the molecule is continuously stretched until intramolecular breakage of the hydrogen bridges occurs. Reproduced with permission from [95]

groups, forming amide bonds located at the terminus of each spacer, resulting in long-chain molecules with four to six connected capsules on average. The relevant force scale in these experiments usually ranges between 10 and 150 pN. An illustration of the envisioned experiment is shown in Fig. 31.

### Force–Extension Curves of Calixarene Catenane Oligomers

Stretching experiments with oligomerized calixarene catenanes exhibit a characteristic sawtooth pattern in which the individual rupture events are separated by merely 1–2 nm due to the presence of the mechanical lock provided by the entangled loops. Figure 32 shows two stretching curves from experiments carried out at different loading rates, together with corresponding elastic WLC fits to the data. A persistence length of about 0.4 nm is indicative of a single polymer chain such as a polypeptide or single-stranded DNA. The difference in the contour length  $\Delta L$  mirrors the length extension between two successive rupture events and is a function of the loop length. The sawtooth pattern of the extension curves

**Fig. 32** Stretching and subsequent rupturing of an individual oligo calixarene catenane at two different velocities: (a) 1,500 and (b) 30,000 pN/s. The lines represent worm-like chain (WLC) fits to the data with a persistence length  $l_p$  of approx. 0.4 nm. The changes in the contour length  $\Delta L$ , as obtained from the fitting procedure, are of about 1–2 nm. These abrupt extensions represent the elongation of single capsules after breakage of the intramolecular hydrogen bonds, as illustrated in the *inset* of (a). The markers inside the tight capsule on the *left* represent intact hydrogen bridges



mirror independent breaking of individual capsules, similar to observations in the case of fibronectin. During a pulling experiment, the tension inside a long-chain molecule is identical throughout the entire contour length. An abrupt extension of the chain caused, e.g., by a sudden opening of one of its nanocapsules, leads to a rapid drop in tension. This release in tension is detected by the cantilever, which shows a sudden drop in deflection. The probability of capsule opening depends on the number  $n$  of available closed capsules prior to pulling and therefore decreases after elongation of each capsule. As a consequence, the subsequent rupture event occurs at larger force, as observed for unfolding of fibronectin or titin [123, 127]. The force of each subsequent rupture event rises with a factor of  $f_\beta/n$ , where  $f_\beta$  is the thermal activation parameter and  $n$  represents the number of previous ruptured bonds [132].

The number of capsules in between the substrate and the AFM tip can be directly counted from the number of events displayed in the stretching curve, e.g., in Fig. 32a six capsules are stretched and in Fig. 32b five capsules. This is in good agreement with the estimated number of capsules computed from the longest contour length,  $L$  (35 nm in Fig. 32a and 28.5 nm in Fig. 32b), divided by the theoretically expected length of an elongated capsule of about 6 nm. Therefore, it is safe to assume that all capsules break upon extension. Besides, the rupture forces rise with increasing loading rate, which is discussed in greater detail below.

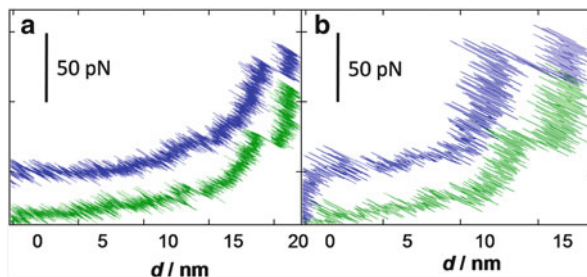


**Fig. 33** Examples of force–distance curves showing distinct refolding events in the retracting curve (*green*). Measurements were carried out with a loading rate of (a) 60 and (b) 300 pN/s. On purpose, an offset of 30 pN was applied between trace (pulling, *blue*) and retrace (relaxation, *green*) to improve visibility

### Reversibility of Pulling Experiments

Due to the mechanical lock provided by two entangled loops, the opening of the nanocapsules can be reversed because the two binding partners are not separated “infinitely” as in many other experiments involving single-molecule pulling. In contrast, the mechanical lock keeps the two capsules close together so that rebinding is a likely scenario. Thus, re-formation of hydrogen bridges is possible and rejoining of capsules should be observed in the retracting curves. An example of clearly visible rejoining events upon relaxation is shown Fig. 33. The hysteresis between pulling and relaxation increases with higher loading rates. As a consequence, assignable rejoining events of capsules are only found at lower pulling velocities. Importantly, the rebinding events are usually less clearly pronounced than the rupture events and therefore the retraction curve usually displays a less obvious sawtooth pattern. Stretching of a molecule frequently results in a separation from either the tip or the substrate, which prevents an investigation of rejoining events of the capsules. Successful stretching and relaxing cycles of a clamped single molecule are often called “fishing” experiments. Figure 34 displays a successful fishing experiment, in which the maximal stretching distance is increased gradually between the individual force curves until the molecule loses contact in force curve number 31.

In contrast to the force-induced unfolding of modular proteins such as titin, tenascin, spectrin, or fibronectin, the rupture events of calixarene dimers show no wear off, i.e., no reduction in the number of unfolding capsules in the subsequent stretching cycle. Interestingly, we found that even while pulling on the molecule, rejoining of previously separated capsules into intact tight capsules occurs. This has also been described by Schlierf and Rief for protein folding from and unfolding into an intermediate state [144]. Rejoining of the dimers is identifiable by a pronounced force plateau in the extension curves (Fig. 34, cycles 4 and 26–28). Such a plateau has also been described by Bustamante and coworkers for ribozyme unfolding and is found in MC simulations [145]. However, in contrast to the work of Bustamante, a substantial hysteresis between extension and relaxation of the oligomer remains in

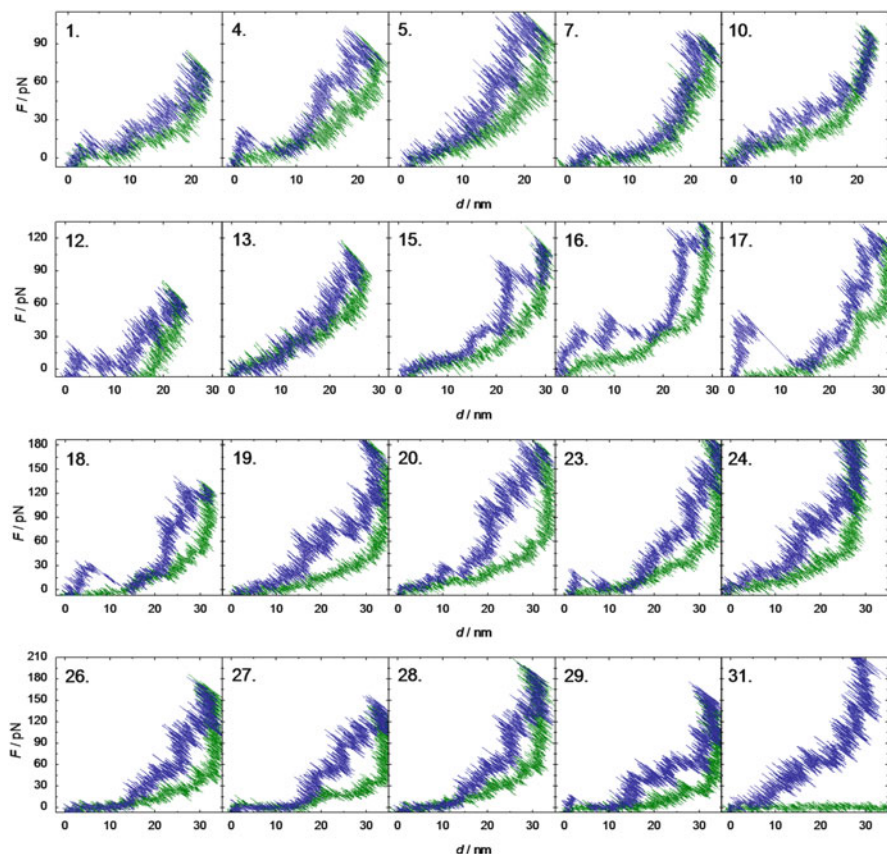


**Fig. 34** Sequence of stretching (*upper traces*) and relaxing (*lower traces*) curves (1–31) of a single calixarene catenane oligomer at a loading and relaxing rate of 300 pN/s. The distance between tip and sample was gradually increased between each cycle, leading to higher forces. In *cycle 31* the molecule eventually lost contact with either the substrate or the cantilever. Note that rejoining of capsules during relation is frequently observed

our experiments, indicating that the system is still far from equilibrium at a loading rate of 300 pN/s. Information about the energy landscape of the 16 hydrogen bonds in a dimer can be obtained from velocity-dependent measurements supported by MD simulations and stochastic calculations (*vide infra*).

#### Analysis of the Force–Distance Curves

A comprehensive quantitative analysis of rupture and rejoining events of experiments with calixarene catenanes was carried out by identifying the force and extension of each rupture event, as well as the rejoining forces, and then compiling

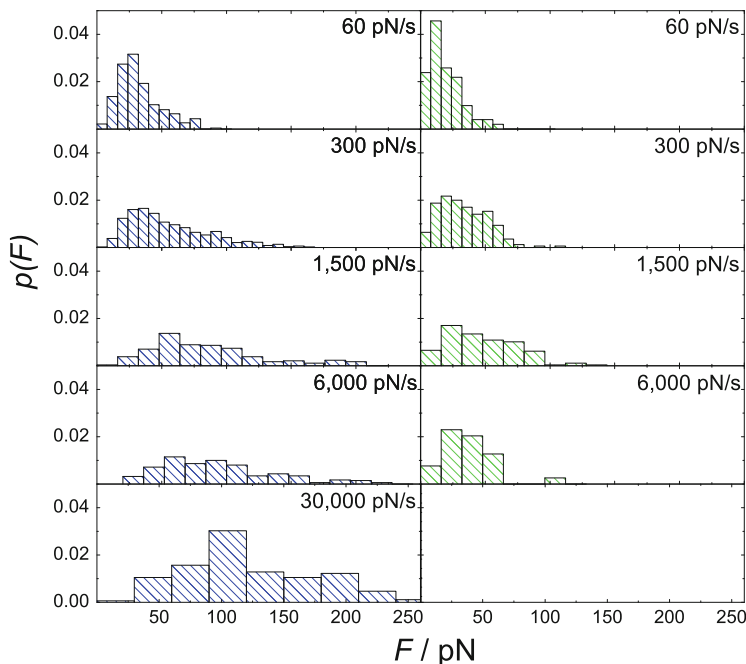
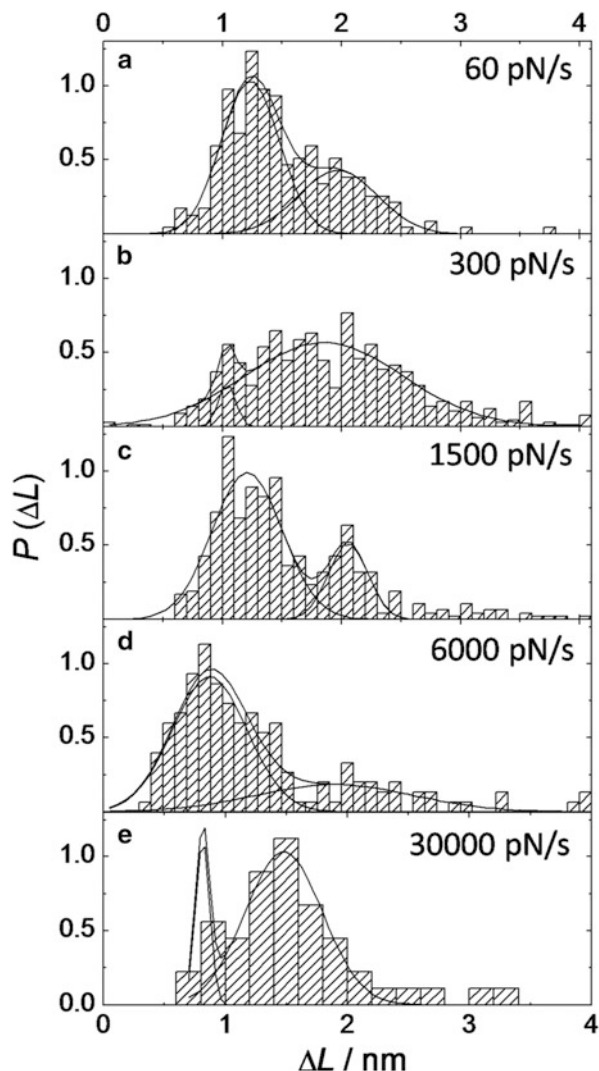


**Fig. 35** Histograms of rupture force (*left*) and rejoining force (*right*) obtained at different loading rates (from *top to bottom*: 60, 300, 1,500, 6,000, and 30,000 pN/s)

the data in histograms. Figure 35 shows that the average rupture forces  $\langle F_{\text{rup}} \rangle$  increase with loading rate and that the normalized rupture force histograms broaden significantly. In contrast, the mean rejoining forces  $\langle F_{\text{rejoin}} \rangle$  decrease with increasing loading rate while the width broadens. Rejoining of capsules is no longer observed at loading rates larger than 6,000 pN/s, supporting the idea that the pulling process is irreversible. Figure 36 shows the distribution of  $\Delta L$  obtained from rupture events as a function of the loading rate. Mostly, a bimodal distribution is apparent, especially at lower loading rates, where a lot of data could be acquired due to better measurement conditions. The maxima are located at around 1 and 2 nm, indicating the presence of a sufficiently stable intermediate. The appearance of such an intermediate state during pulling is also observed in MD simulations (vide infra) and has been considered and examined by stochastic modeling.

To determine a correlation between length extension and rupture force, all events are classified into a lengthening of about 1 ( $\pm 0.4$ ) or 2 ( $\pm 0.4$ ) nm. As expected, events with a capsule elongation of 2 nm exhibit slightly higher average rupture forces (Fig. 37).

**Fig. 36** Histograms of the individual extensions  $\Delta L_1$ ,  $\Delta L_2$  found per rupture event as a function of loading rate by fitting two Gaussian functions to the data: (a) 60 pN/s,  $\Delta L_1 = (1.2 \pm 0.49)$  nm,  $\Delta L_2 = (2 \pm 0.66)$  nm; (b) 300 pN/s,  $\Delta L_1 = (1.0 \pm 0.1)$  nm,  $\Delta L_2 = (1.9 \pm 1.3)$  nm; (c) 1,500 pN/s,  $\Delta L_1 = (1.2 \pm 0.58)$  nm,  $\Delta L_2 = (2.1 \pm 0.33)$  nm; (d) 6,000 pN/s,  $\Delta L_1 = m$  ( $0.9 \pm 0.6$ ) nm,  $\Delta L_2 = (1.9 \pm 1.33)$  nm; (e) 30,000 pN/s, no data analysis possible



### Impact of the Solvent on Rupture Forces

All force–distance experiments were conducted in mesitylene (1,3,5-trimethylbenzene) solution. Mesitylene is a good solvent for calixarenes and has a high boiling point, which is desirable for single-molecule experiments. The dimeric calixarene capsules have a cavity size suitable for the inclusion of solvent molecules such as mesitylene. Because hydrogen bridges inside the capsules can be influenced by the dielectric permittivity of the guest molecules, it is important to test whether impurities of the solvent may affect the experimental result. Toluene is probably the most likely contamination. Control experiments were conducted with 5 vol% toluene as an

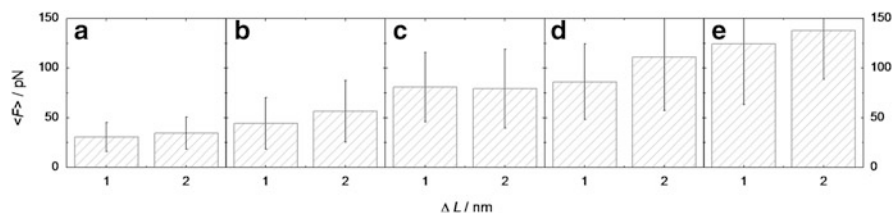


**Fig. 37** Rupture forces corresponding to  $\Delta L \approx 1 \text{ nm}$  and  $\Delta L \approx 2 \text{ nm}$  as a function of loading rate: (a) 60, (b) 300, (c) 1,500, (d) 6,000, and (e) 30,000 pN/s. Generally, rupture forces increase with pulling velocity and differences in rupture forces become more distinct with higher loading rate

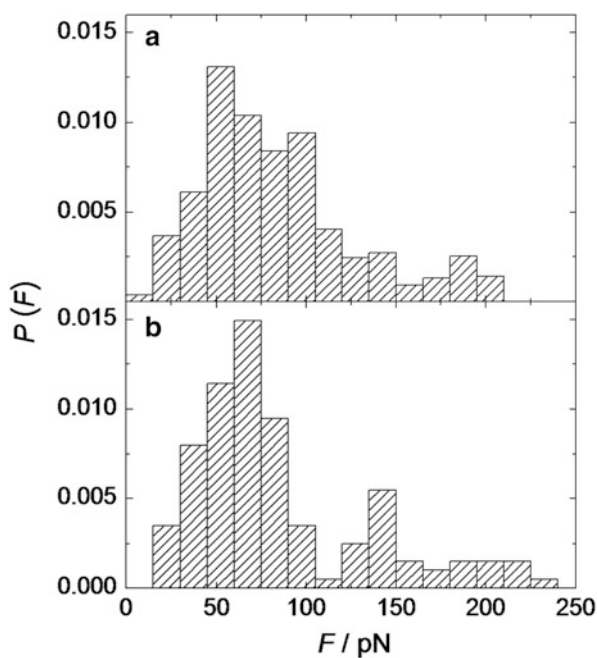


**Fig. 38** Rupture force histograms (loading rate 1,500 pN/s) obtained in (a) pure mesitylene and (b) mesitylene with toluene (5 vol%) as an additive

additive. Figure 38 shows rupture force distributions for experiments carried out in pure mesitylene (Fig. 38a) and with 5 vol% toluene (Fig. 38b). The histograms are virtually identical, as expected, since mesitylene and toluene have the same dielectric constant ( $\epsilon_r = 2.4$  at room temperature).

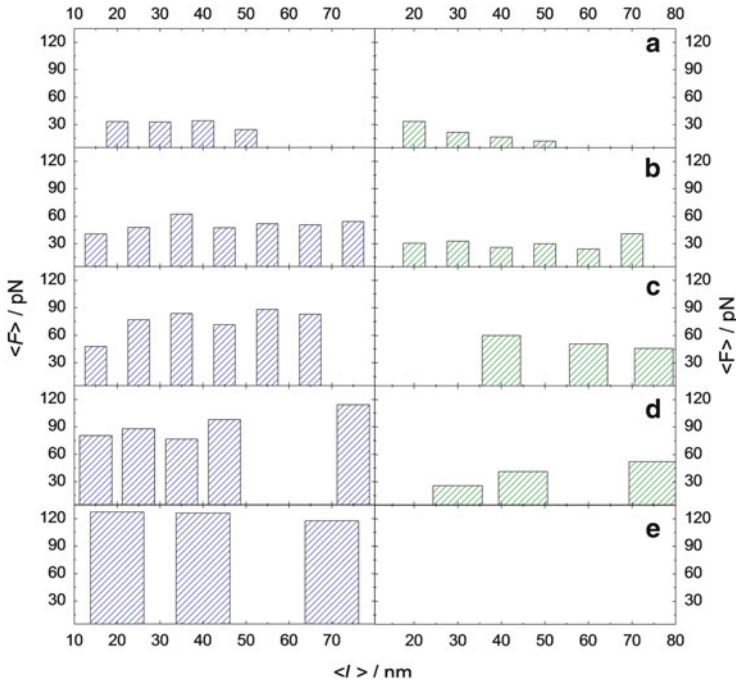


**Fig. 39** Average rupture and rejoining forces (rupture, *left*; rejoining, *right*) as a function of contour length at different loading rates: (a) 60, (b) 300, (c) 1,500, (d) 6,000, and (e) 30,000 pN/s (no rejoining events are found)

### Effect of the Linker and Contour Length on Capsule Breakage

The elastic response of a molecular system is directly coupled to the mechanical properties of the transducer. Evans and Ritchie studied the effect of a soft molecular linkage on the strength of a weak connecting bond [132]. Based on theoretical considerations, Friedsam et al. illustrated the effect of a soft spacer on rupture force histograms [146]. Due to the presence of polymer spacers with a certain length distribution, the rupture force histograms were broadened significantly. Thormann et al. investigated the impact of either a bovine serum albumin (BSA) linker or poly(ethylene)glycol (PEG) spacer on the well-known biotin–streptavidin bond [147]. In the case of the BSA linker, they observed a soft response of the BSA that leads to a broadening in the distribution of the rupture forces. The PEG linker causes a reduction in average unbinding forces in comparison to calculations without a soft spacer. Due to the soft linker, the force ramp inclines towards lower forces compared to a linear force ramp. Hence, the molecular system spends more time at low forces, which increases rupture probability at low forces.

If the molecules are rather stiff  $\kappa_{\text{linker}} \gg \kappa_c$ , with  $\kappa_c$  denoting the stiffness of the transducer and  $\kappa_{\text{linker}}$  the stiffness of the linker, the rupture force is approximately independent of the molecule length and elastic properties, and the spring

constant of the cantilever dominates the force ramp in the experiment. Polymer linkers display a nonlinear compliance that requires more sophisticated treatment to correctly describe the elastic properties of the molecular chain. Figure 39 shows that no correlation between contour length and average forces was found experimentally. This is attributed to the considerably small length of the decylene ( $C_{10}H_{20}$ ) spacers. Regardless of this finding, only molecules in a contour length interval of 10–30 nm were selected for further analysis to avoid unnecessary histogram broadening.

### Comparison with Theory

The profound understanding of breakage and rebinding of hydrogen bridges under external load is a major goal in understanding the function of complex biological structures. Calix[4]arene catenanes are an ideally suited model system for studying reversible binding, experimentally with dynamic force spectroscopy (DFS) and theoretically by means of MD simulations (described in detail in Sect. 3.1).

Theories based on diffusive barrier crossing with a fluctuating cantilever assume either a one-well potential, when no rebinding is taken into account, or a two-well potential when rebinding is included [107–109, 148, 149]. Here, a similar approach was used to evaluate the rates of barrier crossing and location of barriers using stochastic models to capture the force spectra obtained experimentally. In order to extract relevant parameters from the energy landscape of the calixarene dimer, it is mandatory to first estimate the number of dominant states and barriers. The following scrutiny is based on data analysis recently published by Janke et al. [95]. First, it is instructive to analyze the increase in length  $\Delta L$  of the molecule upon rupture, extracted from fitting a WLC function to the data as done before (vide supra) and compare this result, at least qualitatively, with MD simulations (Fig. 40a–c). Figure 40c shows a single pulling trajectory obtained from MD simulations displaying two distinct length jumps. The first sudden length increase can be attributed to H-bond breakage because it exceeds the typical reach of H-bonds (0.3 nm), and the second smaller sudden jump is assigned to the opening of an intermediate conformation. A more comprehensive study has been published by Schlesier et al. [98].

Both the experimentally obtained histogram (Fig. 40a) and the histogram compiling data from MD simulations (Fig. 40b) display the same bimodal distribution in  $\Delta L$  centered at 1 and 2 nm, indicative of an intermediate state. The breakage of the H-bonds does not follow a specific sequence nor does it display the signature of cooperativity. It was found that the intermediate state was reasonably stable (>10 ns) in prolonged simulations at elevated temperature (460 K) under constant force. Possible conformations of the strained dimers captured by MD simulations at various times with the intermediate state at 1 ns are shown in Fig. 40d. Assignment of an intermediate state is often difficult and usually interfered indirectly from nonlinear force spectra [150]. A nonlinear relationship between  $\langle F_{\text{rup}} \rangle$  and  $\ln(dF/dt)$  does not necessarily imply the presence

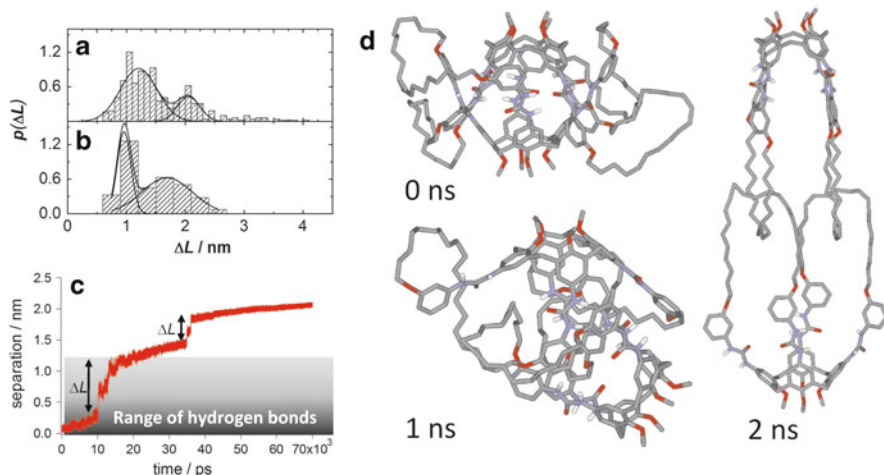


**Fig. 40** Comparison of experimental results with MD simulations and stochastic modeling [95]. Histograms of dimer separation  $\Delta L$  from (a) force experiments (1,500 pN/s) and (b) MD simulations. Fitting of two Gaussian functions to the corresponding histograms  $p(\Delta L)$  provides mean separations  $\Delta L$  at  $1.2 \pm 0.01$  and  $2.05 \pm 0.02$  nm for experimental force curves and  $0.9 \pm 0.14$  and  $1.7 \pm 0.05$  nm for MD simulations. (c) Separation of two calixarene monomers as a function of time, obtained from a single run. (d) Snapshots of a calix[4]arene dimer under harmonic load at various times. At 1 ns the intermediate state is shown. Reproduced with permission from [95]

of additional energy barriers, but could be rather a consequence of an intrinsic feature of diffusive barrier crossing with a fluctuating cantilever [149]. Figure 41a schematically shows the assumed energy potential with idealized cusp-like barriers. Stochastic analysis was carried out to propose parameters of a three-well-potential, such as the location of the energy barriers  $q_{TA}$  and  $q_{TB}$ , the position of the intermediate state  $q_I$ , the height of the energy barriers  $V_{TA}$  and  $V_{TB}$ , and the corresponding transition rates at zero force. Solution of the master equation provides the force-dependent populations of the corresponding states:

$$\frac{d}{dF} n_X(F) = \left( \frac{dF}{dt} \right)^{-1} \left[ - \sum_{Y(\neq X)} k_{XY}(F) n_X(F) + \sum_{Y(\neq X)} k_{XY}(F) n_Y \right] \quad (9)$$

where  $n_X(F)$  is used to provide approximate values for the aforementioned parameters of the three-well-potential. This can be accomplished by fitting the resulting probability distributions to the rupture and rejoining histograms recorded at different loading rates (Fig. 41b, c). Optimization of parameters provided locations for the first barrier at approximately  $q_{TA} \approx 0.3$  nm and the second at  $q_{TB} \approx 1.1$  nm. The probability densities  $p(F)$  are plotted for a loading rate of 1,500 pN/s along with the experimental force histograms of rupture and rejoining forces. The rupture force histogram displays two clear maxima corresponding to

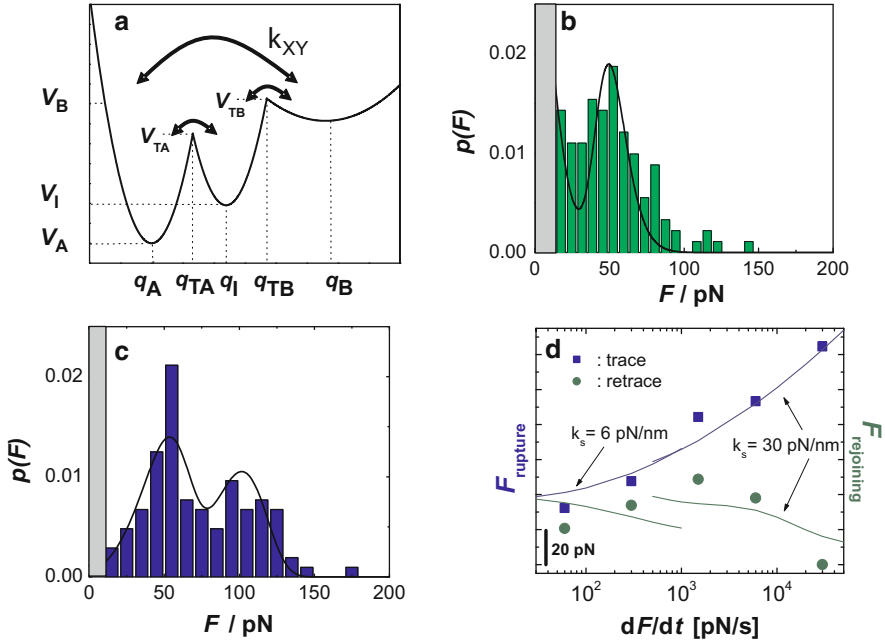


**Fig. 41** Stochastic modeling of capsule breakage and rejoining suggests a three-well potential with a stable intermediate state. (a) Harmonic three-well potential centered at  $q_A$ ,  $q_I$ , and  $q_B$  separated by two cusp-like barriers at  $q_{TA}$  and  $q_{TB}$ , with the corresponding rate constants at zero force  $k_{XY}(0)$ . Histograms of (b) rejoining force and (c) rupture force obtained at 1,500 pN/s, together with results from stochastic modeling (lines) in which the parameters of Eq. (9) were fitted to the data. The two clearly discernible peaks imply the presence of an intermediate. The gray box on the left indicates the force resolution due to thermal fluctuations of the cantilever. (d) Force spectrum showing mean rupture and rejoining forces computed from the histograms displayed in Fig. 35. The blue lines represent the mean rupture force obtained from stochastic modeling, and the green lines denote the mean rejoining forces. The lines are not continuous because two different cantilevers with force constants of 0.006 and 0.03 N/m were used. Reproduced with permission from [95]

the two barriers at  $q_{TA}$  and  $q_{TB}$ . Force spectroscopy data is shown in Fig. 41d. Mean rupture and rejoining forces are plotted as a function of loading rate on a semilogarithmic scale. Close to the equilibrium, rupture and rejoining forces converge to a constant force that is independent of the loading rate indicative of equilibrium conditions. A linear dependence of the average rupture force as a function of  $\ln(dF/dt)$ , as suggested by Bell, is only observed at high loading rates [103]. Because two different cantilever spring constants (0.006 and 0.03 N/m) were used, the curves are not continuous.

With the advent of nanotechnology, interest in the physics of small systems far from equilibrium has strongly increased. Suddenly, tiny systems in which thermal fluctuations prevail could be easily conceived and realized. Mechanically driven transformations, as carried out by single-molecule stretching experiments

or observed for molecular machines, offer a unique way to study fundamental theories of statistical mechanics associated with fluctuation-dissipation theorems. Here, we describe the mechanics of two modular polymers, i.e., fibronectin and oligomeric calix[4]arene catenanes under external force. Whereas fibronectin is a native protein that displays irreversible rupture of protein domains upon extension, the linked calix[4]arene catenanes allow re-formation of separated bonds on experimental time scales due to mechanical locks. In this context, two fundamental questions were addressed. First, to what extent can proteins be stabilized by exposure to compatible solutes and, second, can we investigate H-bond breakage both close to equilibrium and also far from equilibrium using a single molecule. We found that, addressing the first question, it is possible to drive the system into a more coiled conformation but not to enhance the stability of the domains. Preferential exclusion of compatible solutes such as ectoine forces the protein into a more globular conformation, which is displayed by a reduced persistence length. Calixarene catenanes mechanically arrest the system in close vicinity after rupture. The loops therefore permit the reversible rupture and rejoining of individual nanocapsules formed by the calix[4]arene catenanes. Addressing the second question, experiments carried out by force spectroscopy using an atomic force microscope in conjunction with MD simulations and stochastic modeling revealed the presence of an intermediate state between the closed and open state of a single nanocapsule. In summary, entangled nanocapsules are ideal model systems for investigating the strength of hydrogen bonds on a single molecule level with adjustable reversibility. Reversibility can be tuned by changing the loop length, as demonstrated by MD simulations. Longer loop lengths drive the system out of equilibrium by widening the potential, making rejoining highly improbable. The system offers the opportunity to study the energy landscape of a single (chemical) reaction as a function of molecular design and external force, making it an ideal test bed for modern theories of nonequilibrium statistical mechanics.

## **4 Mechanical Properties of Nucleic Acids with Binding Pockets for Small Molecules**

Mechanical properties of biopolymers such as nucleic acids, in particular of DNA, have become of high interest in material science. As a programmable scaffold, biopolymers can be designed to self-assemble into a variety of two- and three-dimensional structures and thus form an interesting platform for bottom-up assembly of nanoscale structures [151]. In addition to structures that can be predicted and rationally designed by engineering standard interactions of the Watson–Crick type, nucleic acids can establish noncanonical interactions to form complicated three-dimensional structures, including catalytic pockets and high affinity binding pockets for small molecules. Although such binding pockets cannot yet be rationally

engineered, they can be obtained with high efficiency by applying a combinatorial technique termed SELEX. The products of SELEX are so-called aptamers, i.e., nucleic acids that bind to a given target with high affinity. Thus, identified aptamers hold great interest, e.g., in analytics, diagnostics, and potentially in material science. However, as opposed to canonical Watson–Crick-based DNA structures [152], their mechanical properties have hardly been investigated at all [153].

One particularly interesting problem in the context of aptamer science is the detection of the binding of small molecules to macromolecules, and the impact of binding on the mechanical properties of nucleic acid structures. Previous approaches to this problem suffer from the need to chemically alter either the macromolecule or the small molecule (hereafter called the “analyte”) in order to allow proper detection. Because even the smallest alterations to the chemical structure of an analyte induce significant changes to its physicochemical properties, we have devised a new approach to measure the interaction of nucleic acid aptamers and small molecules by atomic force spectroscopy (AFS). The approach combines both of the above-mentioned structural features of DNA, fusing the structural domain of an aptamer to the faithfully hybridizing stretches of Watson–Crick helices. Rather than immobilizing the interaction partners in a traditional AFS experiment on opposing surfaces (i.e., an aptamer on the AFM tip and the small molecule on a substrate surface), we split an aptamer structure into two parts and equipped both halves with flanking regions that would recognize the respective other half by Watson–Crick base pairing. Neither half of the aptamer alone retains sufficient structure for binding the analyte; instead, the fully competent binding pocket is transiently generated during the short period of an AFS measurement cycle, in which both components are in spatial proximity. Measurements in the absence and in the presence of an analyte should then reveal whether this period is sufficiently long to allow detectable binding events. Previous experiments had shown that transient binding motifs could in principle be assembled from DNA strands *in situ*. Thus, binding of a third DNA strand to a transient double-stranded DNA, as well as binding of intercalating small molecules to such a triple helix, could indeed be detected by force spectroscopy [154, 155]. As binding resulted in an increase of the most probable rupture force in each case, this was also anticipated for the new aptamer approach. However, it was entirely unclear whether the rather complicated binding pockets would form in a fast and reproducible manner, and whether the binding of a single analyte molecule would be strong enough to be detectable.

For a proof of concept, we used a DNA aptamer that binds adenosine monophosphate (AMP) [156]. The sequence of the DNA aptamer was 3-ACT GGAAGGAGGGATGC-GCATCTAGGAGGTCCAGT-5 and provided two binding pockets (underlined bases) for AMP. The structure suggests a contribution of base stacking as well as of a total of five H-bonds to the binding derived from NMR analysis [157]. Furthermore, the aptamer structure is symmetric and thus provides binding pockets for two molecules of AMP, whose binding is highly cooperative [157, 158]. For the force spectroscopy measurements, the DNA sequence was split symmetrically in length between C–G. Then, the split sequences were equipped with a poly-A tail at the 5-ends, a six-carbon spacer to

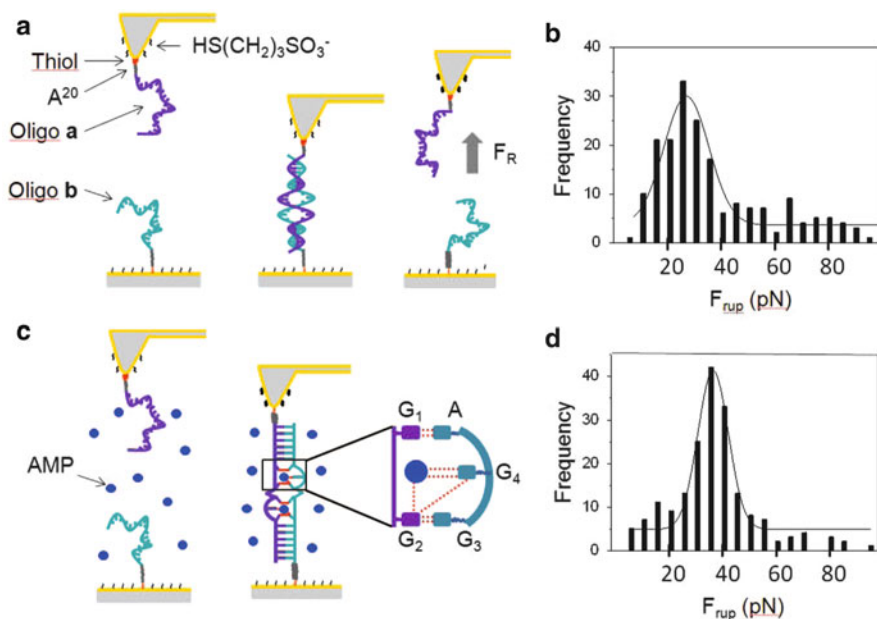


**Fig. 42** (a) Outline of the split AMP aptamer experiment. The adhesion force between the AFS tip and the sample surface was minimized by the additional immobilization of HS(CH<sub>2</sub>)<sub>3</sub>SO<sub>3</sub>Na. Both parts of the oligonucleotide aptamer (oligo-a and oligo-b) were immobilized by thiol linkers to the gold-coated tip and sample surface, respectively. Upon withdrawal of the tip away from the surface at a speed of 400 nm/s the rupture force  $F_{rup}$  was measured. Force–distance curves were repeated 1,000 times. (b) Plot of the measured rupture forces in a histogram. The fit of the data with a Gaussian distribution leads to the most probable rupture force, here  $27.3 \pm 8.4$  pN. For the Gaussian fit we have ignored rupture forces  $>40$  pN. (c) When AMP target molecules were added to the buffer solution, AMP molecules entered the binding pockets and eight additional hydrogen bonds were formed at each pocket (dotted lines). (d) In the presence of AMP, the most probable rupture force was  $38.8 \pm 5.2$  pN. Reprinted with permission from [156]. Copyright (2011) American Chemical Society

allow for enough flexibility and sufficient spatial distance from the surface, and a terminal thiol group for immobilization on a Au surface. One strand was immobilized on the AFS tip (oligo-a, 3-ACTGGA-AGGAGG-AGATGC-A20-SH-5) and the other strand was immobilized on the substrate (oligo-b, 5-SH-A20-TGACCT-GGAGGA-TCTACG-3) (Fig. 42a, left). Now, upon moving the AFS tip close to the sample surface, oligo-a and oligo-b can partially hybridize and the binding pockets form (Fig. 42a, center). In the absence of AMP, a most probable force  $F_{rup}$  of 27 pN at a pulling speed of 400 nm/s between both oligonucleotides was measured (Fig. 42b). This rupture force was associated with the H-bonds formed by 12 base pairs in the hybridized system and was consistent with the measurements of Strunz et al. [152] under comparable conditions. When the buffer solution was changed to a buffer containing AMP (Fig. 42c), the analyte molecules could enter the binding pockets. At a concentration of 100  $\mu$ M, which

is much greater than  $K_d$  of the target molecule AMP, we found an increase in the most probable rupture force to 39 pN (Fig. 42d). The increase in rupture force can be associated with 16 additional hydrogen bonds, i.e., eight additional hydrogen bonds per binding pocket (dotted lines in Fig. 42c, right). Then, the target molecule AMP was washed away by rinsing with pure buffer solution. The most probable rupture force returned to the values corresponding to the initial experiment in buffer, within the given experimental error. We concluded that the increase in rupture force was due to binding of AMP molecules to the transiently formed binding pockets of the bipartite aptamer.

The approach of splitting the aptamer sequences into a bipartite structure should be widely applicable for the detection of various small molecules, even cocaine [159, 160]. In order to prove the universality of the concept we used a DNA aptamer (sequence CCCTCTGGGTGAAGTAACTTCATAATAGGAACAGAGGG) that binds cocaine via a hydrophobic pocket formed by a noncanonical three-way junction [161]. Splitting this sequence into complementary parts results in an asymmetric length of the oligonucleotides (oligo-a, 5-HS-A20AATAGGAACAGAGGG-3 and oligo-b, 5-HS-A20-CCCTCTGGGTGAAGTAACTTCAT-3). Preliminary data from AFS experiments performed in a similar way to the experiments outlined above revealed most probable rupture forces of  $40 \pm 14$  pN in the absence and  $62 \pm 19$  pN in the presence of cocaine (Fig. 43). However, these measurements showed that only 60% of the rupture events can be associated with a cocaine molecule bound into the binding pocket. Thus, either formation of the binding pocket during measurement of the force–distance curve was hindered or the dissociation constant of this bipartite system deviated significantly from the literature value of 100  $\mu$ M.

In general, the split aptamer concept enables us to study concentration dependencies of the target molecules. Thus, the binding constants of the target and the split aptamer systems as well as the selectivity of molecular interactions are accessible on a single-molecule level. In order to investigate whether the dissociation constant of the split systems differs from that of the non-split, ideal aptamer we have performed rupture force experiments using concentrations ranging from 0.01 to 100  $\mu$ M [156]. For each concentration we have analyzed the corresponding histograms by fitting simultaneously two Gaussian distributions to the peaks corresponding to only oligo hybridization and to AMP binding, respectively. We found that with increasing concentration of AMP, the peak corresponding to AMP binding became more pronounced, i.e., more rupture events at higher forces were present. Simultaneously, the peak corresponding to only oligo hybridization was composed of fewer rupture events. At a concentration of  $3.7 \pm 2.5$   $\mu$ M, we observed the same amount of events. Thus, there is a 50% probability that AMP was bound in the binding pockets formed by the split aptamer at this concentration. Therefore, this concentration was attributed to the dissociation constant of the AMP binding aptamer. This value, which was obtained on a single-molecule level, is in agreement with a measurement performed by ultrafiltration ( $6 \pm 3$   $\mu$ M) [164].

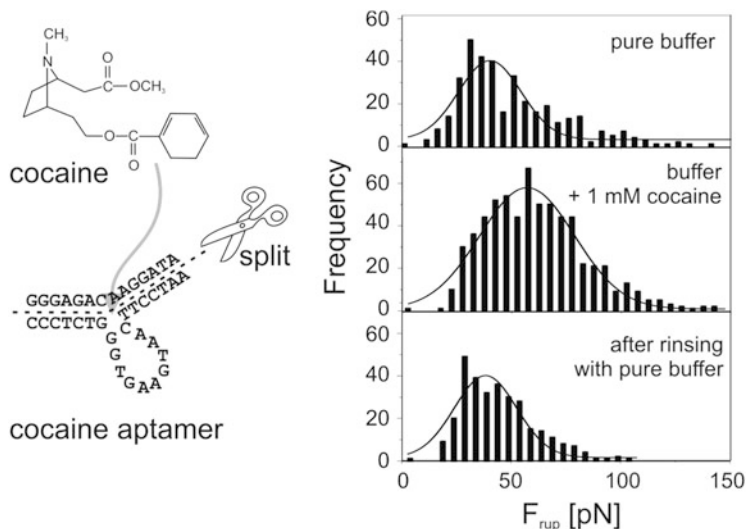


**Fig. 43** *Left*: The split aptamer concept applied to the detection of cocaine. The binding constant of the cocaine–aptamer complex is approximately  $100\ \mu\text{M}$  [162]. The *line* indicates the split of the aptamer resulting in two oligos. *Right*: Histograms display the results performed in pure buffer solution (*top*), with 1 mM cocaine in the buffer solution (*middle*), and after rinsing cocaine away with pure buffer (*bottom*). Each set of data was fitted with a Gaussian distribution. Data adapted from the PhD thesis of Huong Nguyen [163]

In summary, our approach has established a number of highly interesting new findings for DNA aptamers. In addition to the proof-of-principle demonstration that binding of single analyte molecules alters the force spectra of split aptamers to a significant degree, we have developed the split aptamer concept into a generally applicable tool. Interesting open questions include the expansion to the RNA world with its huge variety of different and more complex three-dimensional structures. Investigation of the RNA aptamer, optimized for tetracycline binding [165], would be the first step into transferring the knowledge we acquired.

## References

1. Lavery R, Lebrun A, Allemand J-F, Bensimon D, Croquette V (2002) *J Phys Condens Matter* 14:R383
2. Strick TR, Dessinges M-N, Charvin G, Dekker NH, Allemand J-F, Bensimon D, Croquette V (2003) *Rep Prog Phys* 66:1–45
3. Gallyamov MO (2011) *Macromol Rapid Comm* 32:1210
4. Binder K, Paul W, Strauch T, Rampf F, Ivanov V, Luettemer-Strathmann J (2008) *J Phys Condens Matter* 20:494215
5. Luettemer-Strathmann J, Rampf F, Paul W, Binder K (2008) *J Chem Phys* 128:064903
6. Rampf F, Paul W, Binder K (2005) *Europhys Lett* 70:628

7. Binder K, Baschnagel J, Müller M, Paul W, Rampf F (2006) *Macromol Symp* 237:128
8. Rampf F, Binder K, Paul W (2006) *J Polym Sci B Polym Phys* 44:2542
9. Paul W, Strauch T, Rampf F, Binder K (2007) *Phys Rev E* 75:060801(R)
10. Paul W, Rampf F, Strauch T, Binder K (2007) *Macromol Symp* 252:1
11. Paul W, Rampf F, Strauch T, Binder K (2008) *Comput Phys Commun* 179:17
12. Taylor MP, Paul W, Binder K (2009) *Phys Rev E* 79:050801(R)
13. Taylor MP, Paul W, Binder K (2009) *J Chem Phys* 131:114907
14. Taylor MP, Paul W, Binder K (2010) *Phys Procedia* 4:151
15. DeGennes P-G (1979) *Scaling concepts in polymer physics*. Cornell University Press, Ithaca
16. Ivanov VA, Paul W, Binder K (1998) *J Chem Phys* 109:5659
17. Grassberger P (1997) *Phys Rev E* 56:3682
18. Hsu H-P, Grassberger P (2011) *J Stat Phys* 144:597
19. Kratky O, Porod G (1949) *J Colloid Sci* 4:35
20. Hsu H-P, Paul W, Binder K (2012) *J Chem Phys* 137:174902
21. Schaefer DW, Joanny JF, Pincus P (1980) *Macromolecules* 13:1280
22. Hsu H-P, Binder K (2012) *J Chem Phys* 136:024901
23. Norisuye T, Fujita H (1982) *Polym J* 14:143
24. Pincus P (1976) *Macromolecules* 9:386
25. Saleh OA, McIntosh DB, Pincus P, Ribbeck N (2009) *Phys Rev Lett* 102:068301
26. Binder K, Butt H-J, Floudas G, Frey H, Hsu H-P, Landfester K, Kolb U, Kühnle A, Maskos M, Müllen K, Paul W, Schmidt M, Spiess HW, Virnau P Structure formation of polymeric building blocks: complex polymer architectures. *Adv Polym Sci*, in press doi:10.1007/12\_2013\_230
27. Eisenriegler E, Kremer K, Binder K (1982) *J Chem Phys* 77:6296
28. Eisenriegler E (1993) *Polymers near surfaces*. World Scientific, Singapore
29. Descas R, Sommer J-U, Blumen A (2004) *J Chem Phys* 120:8831
30. Grassberger P (2005) *J Phys A Math Gen* 38:323
31. Bhattacharya S, Rostiashvili VG, Milchev A, Vilgis TA (2009) *Macromolecules* 42:2236
32. Klushin LI, Polotsky AA, Hsu H-P, Markelow DA, Binder K, Skvortsov AM (2013) *Phys Rev E* 87:022604
33. DeGennes P-G (1976) *J Phys (France)* 37:1445
34. Hsu H-P, Binder K (2013) *Macromolecules* 46:2496
35. Birshtein TM, Zhulina EB, Skvortsov AM (1979) *Biopolymers* 18:1171
36. Corsi A, Milchev A, Rostiashvili VG, Vilgis TA (2005) *J Chem Phys* 122:094907
37. Rother G, Findenegg GF (1998) *Colloid Polym Sci* 276:496
38. Omarjee P, Hoerner P, Riess G, Cabuil V, Mondain-Monval O (2001) *Eur Phys J E* 4:45
39. Taubert A, Napoli A, Meier W (2004) *Curr Opin Chem Biol* 8:598
40. Sommer JU, Daoud M (1995) *Europhys Lett* 32:407
41. Chatellier X, Joanny J-F (2000) *Eur Phys J E* 1:9
42. Lyatskaya Y, Gersappe D, Gross NA, Balazs AC (1996) *J Chem Phys* 100:1449
43. Chen ZY (1999) *J Chem Phys* 111:5603
44. Chen ZY (2000) *J Chem Phys* 112:8665
45. Corsi A, Milchev A, Rostiashvili VG, Vilgis TA (2006) *Europhys Lett* 73:204
46. Corsi A, Milchev A, Rostiashvili VG, Vilgis TA (2006) *Macromolecules* 39:1234
47. Corsi A, Milchev A, Rostiashvili VG, Vilgis TA (2006) *J Polym Sci B* 44:2572
48. Corsi A, Milchev A, Rostiashvili VG, Vilgis TA (2006) *Macromolecules* 39:7117
49. de Gennes P-G (1987) *Adv Coll Int Sci* 27:189
50. Fleer GJ, Scheutjens JM, Cohen-Stuart TCMA, Vincent B (1993) *Polymers at interface*. Chapman and Hall, London
51. Milchev A, Binder K (1996) *Macromolecules* 29:343
52. Bhattacharya S, Hsu H-P, Milchev A, Rostiashvili VG, Vilgis TA (2008) *Macromolecules* 41:2920

53. Bhattacharya S, Milchev A, Rostiashvili VG, Grosberg AY, Vilgis TA (2008) *Phys Rev E* 77:061603
54. Strick T, Allemand J-F, Croquette V, Bensimon D (2001) *Phys Today* 54:46
55. Celestini F, Frisch T, Oyharcabal X (2008) *Phys Rev E* 70:012801
56. Kikuchi H, Yokoyama N, Kajiyama T (1997) *Chem Lett* 11:1107
57. Rief M, Oersterhelt F, Heymann B, Gaub HE (1997) *Science* 275:1295
58. Smith SB, Cui Y, Bustamante C (1996) *Science* 271:795
59. Kafri Y, Mukamel D, Peliti L (2002) *Eur Phys J B* 27:135
60. Bhattacharya S, Milchev A, Rostiashvili VG, Vilgis TA (2009) *Phys Rev E* 79:030802 (R)
61. Milchev A, Rostiashvili VG, Bhattacharya S, Vilgis TA (2011). Polymer chain adsorption on a solid surface: scaling arguments and computer simulations. In: Michailov M (ed) *Nanophenomena at surfaces*. Springer series in surface sciences, vol 47. Springer, Berlin Heidelberg, p 185
62. Bhattacharya S, Milchev A, Rostiashvili VG, Vilgis TA (2009) *Eur Phys J E* 29:285
63. Skvortsov AM, Klushin LI, Birshtein TM (2009) *Polym Sci A (Moscow)* A 51:1
64. Paturej J, Milchev A, Rostiashvili VG, Vilgis TA (2012) *Macromolecules* 45:4371
65. Dimitrov DI, Klushin L, Milchev A, Binder K (2008) *Phys Fluids* 20:092102
66. Milchev A, Klushin L, Skvortsov A, Binder K (2010) *Macromolecules* 43:6877
67. Meller A (2003) *J Phys Condens Matter* 15:R581
68. Milchev A (2011) *J Phys Condens Matter* 23:103101
69. Nakane JJ, Akeson M, Marziali A (2003) *J Phys Condens Matter* 15:R1365
70. Meller A, Nivon L, Branton D (2001) *Phys Rev Lett* 86:3435
71. Kasianowicz JJ, Brandin E, Branton D, Deamer DW (1996) *Proc Natl Acad Sci USA* 93:13770
72. Slonkina E, Kolomeisky AB (2003) *J Chem Phys* 118:7112
73. Wei D, Yang W, Jin X, Liao Q (2007) *J Chem Phys* 126:204901
74. Milchev A, Binder K, Bhattacharya A (2004) *J Chem Phys* 121:6042
75. Milchev A, Binder K (2005) *Computer Phys Commun* 169:107
76. Slatex GW, Guo HL, Nixon GI (1997) *Phys Rev Lett* 78:1170
77. Dubbeldam JLA, Milchev A, Rostiashvili VG, Vilgis TA (2007) *Phys Rev E* 76:010801 (R)
78. Dubbeldam JLA, Milchev A, Rostiashvili VG, Vilgis TA (2007) *Eurphys Lett* 79:18002
79. Dubbeldam JLA, Milchev A, Rostiashvili VG, Vilgis TA (2009) *J Phys Condens Matter* 21:098001
80. Dubbeldam JLA, Milchev A, Rostiashvili VG, Vilgis TA (2009) *Ann N Y Acad Sci* 1161:95
81. Sung W, Park PJ (1996) *Phys Rev Lett* 77:783
82. Muthukumar M (1999) *J Chem Phys* 111:10371
83. Bhattacharya A, Morrison WH, Luo K, Ala-Nissli T, Ying S-C, Milchev A, Binder K (2009) *Eur Phys J E* 29:423
84. Bhattacharya A, Binder K (2010) *Phys Rev E* 81:041804
85. Sakaue T (2007) *Phys Rev E* 76:021803
86. Sakaue T (2010) *Phys Rev E* 81:041808
87. Dubbeldam JLA, Rostiashvili VG, Milchev A, Vilgis TA (2011) *Phys Rev E* 83:011802
88. Dubbeldam JLA, Rostiashvili VG, Milchev A, Vilgis TA (2013) *Phys Rev E* 87:032147
89. Dubbeldam JLA, Rostiashvili VG, Milchev A, Vilgis TA (2012) *Phys Rev E* 85:041801
90. Chatelain C, Kantor Y, Kardar M (2008) *Phys Rev E* 78:021129
91. Storm AJ, Storm C, Chen J, Zandbergen H, Joanny J-F, Dekker C (2005) *Nano Lett* 5:1193
92. Klushin LI, Skvortsov AM, Hsu H-P, Binder K (2008) *Macromolecules* 41:5890
93. Liphardt J, Onoa B, Smith S, Tinoco I, Bustamante C (2001) *Science* 292:733
94. Gebhardt JCM, Bornschrögl T, Rief M (2010) *Proc Natl Acad Sci USA* 107:2013
95. Janke M, Rudzevich Y, Molokanova O, Metzroth T, Mey I, Diezemann G, Marszalek PE, Gauss J, Böhmer V, Janshoff A (2009) *Nat Nanotechnol* 4:225
96. Sauvage J-P, Dietrich-Buchecker C (1999) *Molecular catenanes, rotaxanes, and knots*. Wiley-VCH, Weinheim

97. Wang L, Vyotsky M, Bogdan A, Bolte M, Böhmer V (2004) *Science* 304:1312
98. Schlesier T, Metzroth T, Jahnshoff A, Gauss J, Diezemann G (2011) *J Phys Chem B* 115:6445
99. Oostenbrink C, Villa A, Mark AE, van Gunsteren WF (2004) *J Comput Chem* 25:1656
100. Schlesier T, Diezemann G (2013) *J Phys Chem B* 117:1862
101. Jorgensen WL, Maxwell DS, Tirado-Rives J (1996) *J Am Chem Soc* 118:11225
102. Cornell WD et al (1995) *J Am Chem Soc* 117:5179
103. Bell GI (1978) *Science* 200:618
104. Dudko OK, Hummer G, Szabo A (2008) *Proc Natl Acad Sci USA* 105:15755
105. Seifert U (2002) *Europhys Lett* 58:792
106. Li F, Leckband D (2006) *J Chem Phys* 125:194702
107. Diezemann G, Janshoff A (2008) *J Chem Phys* 129:084904
108. Diezemann G, Schlesier T, Geil B, Janshoff A (2010) *Phys Rev E* 82:051132
109. Diezemann G, Janshoff A (2009) *J Chem Phys* 130:041101
110. Arakawa T, Timasheff SN (1983) *Arch Biochem Biophys* 224:169
111. Arakawa T, Timasheff SN (1985) *Biophys J* 47:411
112. Yancey PH, Clark ME, Hand SC, Bowlus RD, Somero GN (1982) *Science* 217:1214
113. Santoro MM, Liu Y, Khan SMA, Hou LX, Bolen DW (1992) *Biochemistry-US* 31:5278
114. Galinski EA, Pfeiffer H-P, Trüper HG (1985) *Eur J Biochem* 149:135
115. Galinski EA (1995) *Adv Microb Physiol* 37:273
116. Knapp S, Ladenstein R, Galinski EA (1999) *Extremophiles* 3:191
117. Timasheff SN (1992) *In water and life*. Springer, Berlin
118. Janshoff A, Neitzert M, Oberdörfer Y, Fuchs H (2000) *Angew Chem Int Ed* 39:3212
119. Bizzarri AR, Cannistraro S (2010) *Chem Soc Rev* 39:734
120. Puchner EM, Gaub HE (2009) *Curr Opin Struct Biol* 19:605
121. Fisher TE, Carrion-Vazquez M, Oberhauser AF, Li H, Marszalek PE, Fernandez JM (2000) *Neuron* 27:435
122. Noy A (ed) (2008) *Handbook of molecular force spectroscopy*. Springer, Berlin
123. Rief M, Gautel M, Oesterhelt F, Fernandez JM, Gaub HE (1997) *Science* 276:1109
124. Rief M, Grubmüller H (2002) *ChemPhysChem* 3:255
125. Oberhauser AF, Marszalek PE, Erickson HP, Fernandez JM (1998) *Nature* 393:181
126. Rief M, Pascual J, Saraste M, Gaub HE (1999) *J Mol Biol* 286:553
127. Oberdörfer Y, Fuchs H, Janshoff A (2000) *Langmuir* 16:9955
128. Müller DJ, Baumeister W, Engel A (1999) *Proc Natl Acad Sci USA* 96:13170
129. Kedrov A, Janovjak H, Sapra KT, Müller DJ (2007) *Annu Rev Biophys Biomol Struct* 36:233
130. Yamada KM (1983) *Annu Rev Biochem* 52:761
131. Oberdörfer Y, Schrot S, Fuchs H, Galinski E, Janshoff A (2003) *Phys Chem Chem Phys* 5:1876
132. Evans E, Ritchie K (1999) *Biophys J* 76:2439
133. Bustamante C, Liphardt J, Ritort F (2005) *Phys Today* 58:43 doi:10.1063/1.2012462
134. Hummer G, Szabo A (2010) *Proc Natl Acad Sci USA* 107:21441
135. Hummer G, Szabo A (2001) *Proc Natl Acad Sci USA* 98:3658
136. Crooks GE (2000) *Phys Rev E* 61:2361
137. Jarzynski C (1997) *Phys Rev Lett* 78:2690
138. Harris NC, Song Y, Kiang C-H (2007) *Phys Rev Lett* 99:068101
139. Neuman KC, Nagy A (2008) *Nat Methods* 5:491
140. Stigler J, Ziegler F, Gieseke A, Gebhardt JCM, Rief M (2011) *Sci Signal* 334:512
141. Alemany A, Ribezzi-Crivellari M, Ritort F (2013) Recent progress in fluctuation theorems and free energy recovery. In: Klages R, Just W, Jarzynski C, Schuster HG (eds) *Nonequilibrium statistical physics of small systems: fluctuation relations and beyond*. Wiley-VCH, Weinheim, p 155
142. Janke M (2008) *Atomic force microscopy of biomimetic systems*. Ph.D. thesis, Mainz
143. Vysotsky MO, Bolte M, Thondorf I, Böhmer V (2003) *Chem Eur J* 9:3375

144. Schlierf M, Rief M (2005) *J Mol Biol* 354:497
145. Onoa B, Dumont S, Liphardt J, Smith SB, Tinoco I, Bustamante C (2003) *Science* 299:1892
146. Friedsam C, Wehle AK, Křhner F, Gaub HE (2003) *J Phys Condens Matter* 15:S1709
147. Thormann E, Hansen PL, Simonsen AC, Mouritsen OG (2006) *Colloids Surf B* 53:149
148. Lee G, Khadar A, Yong J, Peter A, Vann B, Marszalek PE (2006) *Proc Natl Acad Sci USA* 104:20719
149. Hummer G, Szabo A (2003) *Biophys J* 85:5
150. Merkel R, Nassoy P, Leung A, Ritchie K, Evans E (1999) *Nature* 397:50
151. Rothmund PWK (2006) *Nature* 440:297
152. Strunz T, Oroszlan K, Schafer R, Guntherodt HJ (1999) *Proc Natl Acad Sci USA* 96:11277
153. Neupane K, Yu H, Foster DA, Wang F, Woodside MT (2011) *Nucleic Acids Res* 39:7677
154. Ling L, Butt HJ, Berger R (2004) *J Am Chem Soc* 126:13992
155. Ling L, Butt H-J, Berger R (2006) *Appl Phys Lett* 89:113902
156. Nguyen T-H, Steinbock L, Butt HJ, Helm M, Berger R (2011) *J Am Chem Soc* 133:2025
157. Lin CH, Patel D (1997) *J Chem Biol* 4:817
158. Nonin-Lecomte S, Lin HC, Patel JD (2001) *Biophys J* 81:3422
159. Baker BR, Lai RY, Wood MS, Doctor EH, Heeger AJ, Plaxco KWJ (2006) *J Am Chem Soc* 128:3138
160. Liu J, Lu Y (2006) *Angew Chem Int Ed* 45:90
161. Neves MAD, Reinstein O, Saad M, Johnson PE (2010) *Biophys Chem* 153:9
162. Swensen JS, Xiao Y, Ferguson BS, Lubin AA, Lai RY, Heeger AJ, Plaxco KW, Soh HT (2009) *J Am Chem Soc* 131:4262
163. Nguyen T-H (2013) Rupture forces of split aptamers. Ph.D. thesis, Mainz
164. Niazi JH, Lee SJ, Kim YS, Gu MB (2008) *Bioorg Med Chem* 16:1254
165. Müller M, Weigand JE, Weichenrieder O, Süss B (2006) *Nucleic Acids Res* 34:2607

# Optical Properties of Assemblies of Molecules and Nanoparticles

**Thomas Basché, Andreas Köhn, Jürgen Gauss, Klaus Müllen, Harald Paulsen, and Rudolf Zentel**

**Abstract** Organic dye molecules, colloidal semiconductor quantum dots, and light-harvesting complexes have been employed as optically active building blocks to create complex molecular assemblies via covalent and non-covalent interactions. Taking advantage of the chemical flexibility of the dye and quantum dot components, as well as recombinant protein expression and the ordering capability of cholesteric phases, specific optical function could be implemented. Photophysical phenomena that have been addressed include light-harvesting, electronic excitation energy transfer (EET), and lasing. Optical single-molecule experiments allow control of energy transfer processes in individual molecular dyads and triads. Quantitative insights into the mechanism of EET have been provided by combining the results from single-molecule spectroscopy and quantum chemistry.

**Keywords** Cholesteric phases · Energy transfer · Fluorophores · Light-harvesting complex · Organic dye molecules · Quantum chemistry · Semiconductor quantum dots · Single-molecule spectroscopy

---

T. Basché (✉), A. Köhn and J. Gauss  
Institut für Physikalische Chemie, Johannes Gutenberg-Universität Mainz,  
Duesbergweg 10-14, 55099 Mainz, Germany  
e-mail: [thomas.basche@uni-mainz.de](mailto:thomas.basche@uni-mainz.de)

K. Müllen  
Max Planck-Institut für Polymerforschung, Ackermannweg 10, 55128 Mainz, Germany

H. Paulsen  
Institut für Allgemeine Botanik, Johannes Gutenberg-Universität Mainz, Müllerweg 6,  
55099 Mainz, Germany

R. Zentel  
Institut für Organische Chemie, Johannes Gutenberg-Universität Mainz, Duesbergweg 10-14,  
55099 Mainz, Germany

## Contents

1	Introduction .....	62
2	Preparation and Photophysical Properties .....	63
2.1	Multichromophoric Systems Tailored for Energy Transfer Applications .....	63
2.2	Complexes from Colloidal Semiconductor Quantum Dots and Organic Dye Molecules .....	74
2.3	Biological–Chemical Hybrids Built from Light-Harvesting Complexes .....	81
2.4	Dye Molecules in Cholesteric Phases: Towards Lasing Applications .....	86
3	Single-Molecule Studies of Electronic Excitation Energy Transfer .....	93
3.1	Flexibility of Donor–Acceptor Dyads .....	93
3.2	Control of the Energy Transfer Pathway by Dual Pulse Excitation .....	94
3.3	Read-Out of the Spin State of a Single Molecule by the Emission from Proximate Fluorophores .....	97
3.4	Rates and Mechanism of Energy Transfer .....	98
4	Theoretical Description of Vibronic Spectra and Electronic Coupling .....	101
4.1	Vibronic Spectra of PMI and PDI Chromophores .....	103
4.2	Electronic Coupling in Donor–Acceptor Dyads .....	105
	References .....	107

## 1 Introduction

The evolution of specific properties resulting from the formation of complex molecular assemblies is an important and longstanding issue in contemporary science. In this chapter, the controlled organization of organic, inorganic, and biological components into molecular assemblies via covalent and non-covalent (e.g., electrostatic) interactions is presented. The central issue in these studies is control of the photophysical properties of the constructs, which are determined by the nature of the building blocks and by their organization into assemblies on different length scales. Although electronic excitation energy transfer (EET) between molecules or molecules and colloidal semiconductor quantum dots (QDs) is of chief importance, the effect of helical superstructures on the emission of dye molecules has also been considered. Stationary and time-resolved absorption and emission spectroscopy proved to be valuable tools for characterization of the properties of such molecular assemblies. A synthetic challenge has been to provide complex donor–acceptor dyads and triads with high structural perfection with respect to the distance and orientation of the chromophores. As described in Sect. 2.1, rylene tetracarboxydiimide building blocks in conjunction with rigid oligo(phenylene) bridges offer a versatile approach for electronic and geometrical control of EET processes. A further advantage of this class of dye molecules are their favorable properties for single-molecule spectroscopy (SMS). Following proper functionalization by dicarboxyl anchors, rylene dyes have also been attached to QDs. Owing to the chemical flexibility of the dye as well as the QD components, various options exist for tuning the spectral parameters of QD/dye hybrids, as

illustrated in Sect. 2.2. Although the observation of EET qualitatively provided clear evidence for the formation of such complexes, more detailed studies have revealed that Förster theory seems to give a reasonable description of the process. Besides QD/dye hybrids, well-defined QD oligomers have been prepared by a novel route involving ultracentrifugation as the final separation step, paving the way towards QD molecules. In Sect. 2.3, it is shown that rylene dyes also can serve as energy donors and/or acceptors in hybrid constructs with light-harvesting complexes (LHCII) from green plants. Eventually, LHCII in such constructs may sensitize electron injection into a semiconductor layer via an acceptor dye. The use of recombinant versions of LHCII afforded the incorporation of anchors such as hexahistidine tags for specific interaction with QDs, in which case complex formation was again signaled by EET. Another way of arranging emitters is presented in Sect. 2.4, which describes the use of cholesteric phases for the formation of helical superstructures of dye molecules. Lasing was observed in free-standing cholesteric films after introduction of the emitters. Section 3 is devoted to the visualization of EET between individual molecules in donor–acceptor dyads. Time- and frequency-resolved single-molecule techniques have been employed to address the mechanism of EET and have allowed quantification of deviations from a Förster description. Successful attempts to reverse the energy flow in individual aggregates demonstrated how aggregate function could be modified. The turning on and off of EET could be used to read out the spin state of a single molecule. The chapter closes with theoretical efforts (Sect. 4) on the description of photophysical parameters and processes. Quantum chemical *ab-initio* methods have been applied for the determination of electronic transition energies, the vibronic structure of emission spectra and electronic coupling strength between molecules. Indeed, the stringent combination of synthetic chemistry, SMS and quantum chemistry has delivered quantitative insights into electronic coupling in molecular assemblies.

## 2 Preparation and Photophysical Properties

### 2.1 *Multichromophoric Systems Tailored for Energy Transfer Applications*

#### 2.1.1 Linear and Kinked Donor–Acceptor Dyads

##### PDI–TDI Dyads

In 2004, the first work was reported directed toward single-pair electronic EET in a dyad built from perylene diimide (PDI) as donor, terrylene diimide (TDI) as acceptor and a *p*-terphenyl spacer (dyad **1**, Fig. 1) as bridging group [1]. Since then, several more single-molecule as well as computational studies on this compound have been carried out to investigate the prevailing energy transfer

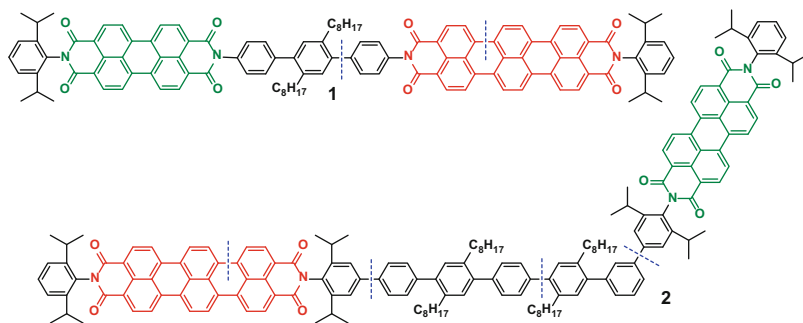
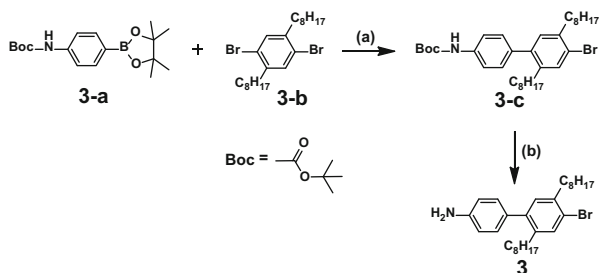


**Fig. 1** Molecular structures and retrosynthesis of the linear dyad **1** and kinked dyad **2** with PDI (green) and TDI (red)

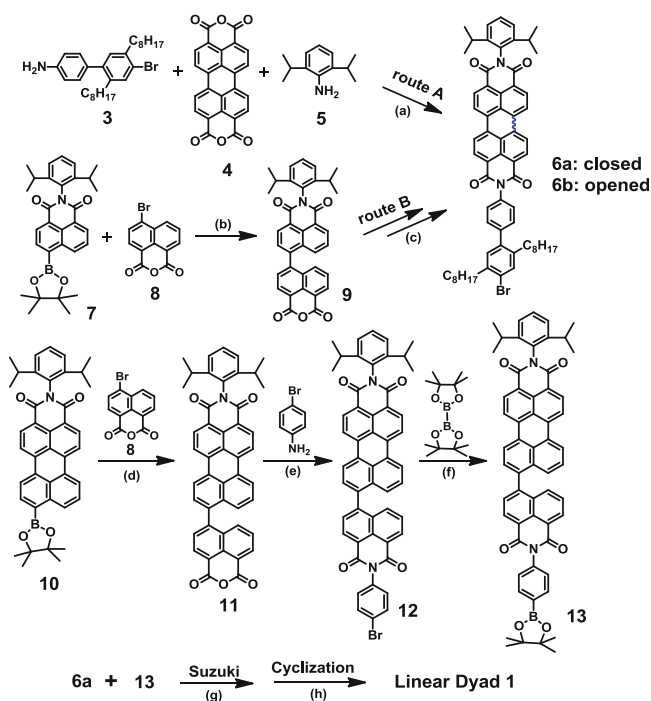
(EET) process, to evaluate the limits of Förster theory and to reverse the EET [2–4]. In this section, we summarize the synthesis of multichromophores including dyads, triads, dendritic and star-shaped systems, with an emphasis on the structural design and the systematic comparison of different synthetic approaches. Single-molecule investigations of these compounds focusing on EET are described in Sect. 3. It must be emphasized that valid photophysical answers cannot simply be obtained from trivial or even commercially available chromophores but must be built on conceptual and synthetic breakthroughs. Herein, optimized reaction pathways are discussed with respect to solubility, reactivity, and accessibility of the building blocks used. Key reactions used are imidization, Suzuki coupling and cyclization of biaryl intermediates to ribbon-type arenes. In most cases, the initial synthetic target is the asymmetric introduction of different functional groups into the perylene diimide and terrylene diimide by imidization. Combined with rigorous purifications, this optimized multichromophore synthesis is the basis for creative photophysics.

To begin with, we take the donor–acceptor (D–A) dyad **1** (Fig. 1) as an example to illustrate the importance of arranging the best reaction sequence. For the synthesis of the linear dyad **1**, the major challenge is to balance solubility and reactivity of the building blocks. Our synthetic strategy for dyad **1** consists of the synthesis of the PDI unit (**6a**), the open-form of TDI (**13**), and the linker (**3**) (Scheme 1) together with their final combination to form dyad **1**. The concept outlined in Scheme 2 comprises selective imidization of perylene **4** for introducing a functional group at the imide nitrogen position, a coupling reaction connecting **6a** and **13** and, finally, a cyclization reaction giving rise to the terrylene moiety.

There are several possibilities for combining these three moieties to give dyad **1** such as routes A and B shown in Fig. 2. In route A, the critical step is the cyclization which, however, causes complete hydrolysis of the PDI part (arrow in Fig. 2, compound **1-a**) under basic reaction conditions. On the other hand, regarding route B, by using the unsymmetrical compounds PMI–PMA and TMI–TMA as the building blocks to avoid the cyclization, it was not possible to achieve the target compound **1** via statistical imidization. It thus needs to be decided which chromophore, PDI or TDI, should be connected to the linker first. Both PDI and TDI tend to



**Scheme 1** Synthesis of linker **3**. (a)  $[\text{Pd}(\text{PPh}_3)_4]$ ,  $\text{K}_2\text{CO}_3/\text{H}_2\text{O}$ , toluene,  $80^\circ\text{C}$ , 16 h, 65%; (b) 10% TFA, dichloromethane, room temperature, 0.5 h, 90%



**Scheme 2** Synthesis of the linear dyad **1**. (a) Imidazole/propionic acid (10:1, v/v),  $140^\circ\text{C}$ , 4 h (26%); (b)  $[\text{Pd}(\text{PPh}_3)_4]$ ,  $\text{K}_2\text{CO}_3/\text{H}_2\text{O}$ , toluene,  $80^\circ\text{C}$ , 16 h; (c) propionic acid,  $150^\circ\text{C}$ , 16 h; (d)  $[\text{Pd}(\text{PPh}_3)_4]$ ,  $\text{K}_2\text{CO}_3/\text{H}_2\text{O}$ , toluene,  $80^\circ\text{C}$ , 16 h, 72%; (e) 4-bromo-aniline, propionic acid,  $150^\circ\text{C}$ , 16 h, 88%; (f)  $[\text{PdCl}_2(\text{dppf})] \cdot \text{CH}_2\text{Cl}_2$ , bis(pinacolato)diboron, 1,4-dioxane, KOAc,  $70^\circ\text{C}$ , 16 h, 78%; (g)  $[\text{Pd}(\text{PPh}_3)_4]$ ,  $\text{K}_2\text{CO}_3/\text{H}_2\text{O}$ , toluene,  $80^\circ\text{C}$ , 16 h, 40%; (h) ethanolamine,  $\text{K}_2\text{CO}_3$ ,  $160^\circ\text{C}$ , 0.5 h, 20%. Route A one-pot imidization. Route B base-promoted coupling reaction between naphthalene monoimide derivatives

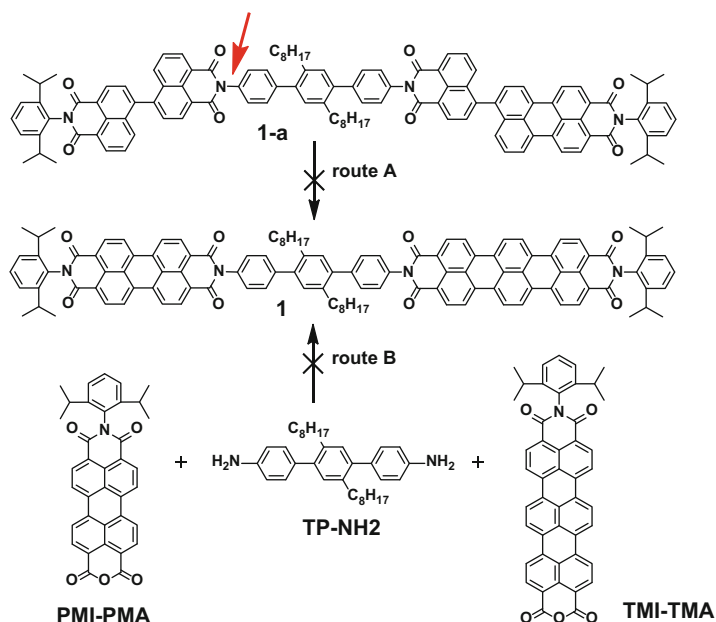


**Fig. 2** Preliminary approaches for synthesis of dyad **1**. The *arrow* indicates the position of hydrolysis of the PDI part in **1a**

form strong  $\pi$ - $\pi$  stacking aggregates, which result in poor solubility in organic solvents. It is thus understandable that the use of the solubilizing group ( $C_8H_{17}$ ) is decisive for the success of synthesis of dyad **1**. The overall yield in route A is very low, whereas in route B compound TMI-TMA displays very low reactivity in the final imidization. Thus, we show a more convenient synthetic pathway for the three building blocks and the target dyad **1** as described below.

### Synthesis of the Linker

Alkyl-substituted oligophenylenes are very well suited as rigid spacers. Bifunctional *p*-terphenyls are well established and have been used as spacers in various molecular architectures [5]. We used a phenylene derivative, 1,4-dibromo-2,5-dioctylbenzene (**3-b**), functionalized in an AB pattern as a starting material for the bridge compound **3**. Due to the solubilizing effect of the alkyl-substituted phenylene moiety, the chromophores can be solubilized when connected to the linker. Building the *p*-terphenyl spacer in a stepwise fashion requires two functional groups in the compound **3** (i.e., the bromo group for Suzuki coupling and the amine group for imidization). The synthesis of **3** started from **3-b**, which was coupled with *tert*-butyl-*N*-[4-(4,4,5,5-tetramethyl-1,2,3-dioxaborolan-2-yl)phenyl]carbamate (**3-a**) via a Suzuki reaction. After removing the *N*-*tert*-butoxycarbonyl (Boc) protecting group from this product (**3-c**), 4-aniline-2,5-dioctylbenzene bromide (**3**) was obtained (Scheme 1).

### Synthesis of the PDI Unit **6a** (Donor)

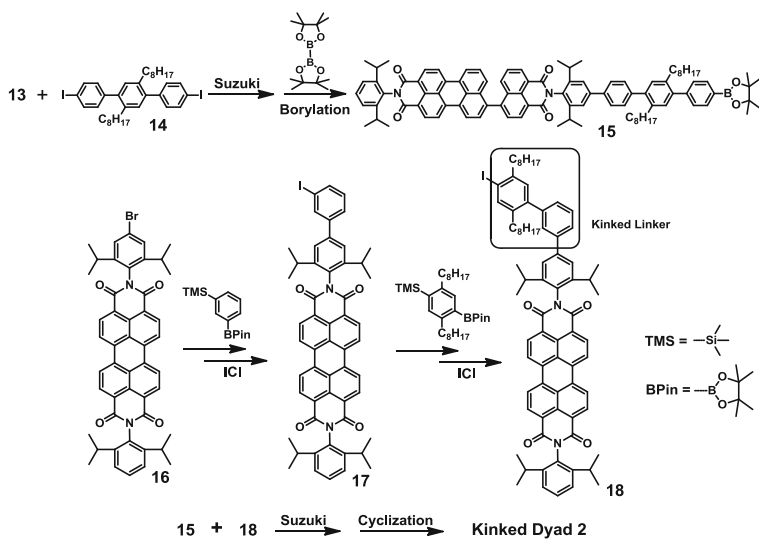
Several methods have been reported for the monofunctionalization of PDI [6] including one-pot imidization (route A) or a base-promoted coupling reaction between naphthalene monoimide derivatives (route B) [7], as shown in Scheme 2. We found the one-pot imidization reaction (route A) to be more practical than route B: route B consisted of five steps and the open-form product **6b** was labile under the basic reaction conditions required to produce the closed product **6a**. The one-pot imidization, route A, was simple and **3** could easily be recovered via column chromatography because the use of an excess amount of **3** was necessary. Concerning the solubility and reactivity of perylene tetracarboxylic acid dianhydride (PDA) **4**, the imidization of **4** was, first, carried out with 2,6-diisopropylaniline (**5**) in imidazole; then **3** in propionic acid solution was added to produce the closed product PDI **6a**.

### Synthesis of the TDI unit **13** (Acceptor)

The key concept for the synthesis of the TDI building block is the introduction of a boronic ester group with a TDI moiety (compound **13**) for the final coupling reaction with PDI. Starting from *N*-(2,6-diisopropylphenyl)-9-(4,4,5,5-teramethyl-1,3,2-dioxaborolan-2-yl)perylene-3,4-dicarboximide (**10**), building block **13** was synthesized in the multistep sequence shown in Scheme 2 (steps d–f). For the selective cross-coupling of boronic ester **10** with 4-bromonaphthalene-1,8-dicarboxylic anhydride (**8**), the introduction of a bromo substituent at the *N*-aryl group (i.e., **12**) should come after the [Pd(PPh<sub>3</sub>)<sub>4</sub>]-catalyzed coupling reaction (Scheme 2, step d). An excess amount of the naphthalene derivative must be used during the coupling reaction (Scheme 2, step d) in order to favor the hetero-coupling of **10** and **8** over the homo-coupling of **10**. Next, the monosubstitution (Scheme 2, step e) of **11** was accomplished by condensation of the anhydride moiety with 4-bromo aniline in propionic acid. Compound **12** was treated with bis(pinacolato)diboron to form its boronic ester derivative **13** (Scheme 2, step f).

### Synthesis of the Linear Dyad **1**

Finally, the open form of the dyad (dyad **1-a**) was synthesized by Suzuki coupling of the PDI part **6a** and the TDI part **13** (Scheme 2, step g). The dyad **1-a** was obtained in 60% yield after gel permeation chromatography (GPC). Due to its extended aromatic core, terylene diimide shows a much lower solubility than its smaller homologue perylene diimide. Concerning the poor solubility of the TDI unit, the cyclization reaction was performed as the last step (Scheme 2, step h). As shown in Fig. 2, the perylene part is susceptible to hydrolysis, so the cyclization had to be performed rapidly (within 30 min). Cyclization using K<sub>2</sub>CO<sub>3</sub> as base in ethanalamine completed the synthesis of the dyad **1**. Besides unreacted **1-a**, the



**Scheme 3** Synthesis of the kinked dyad 2

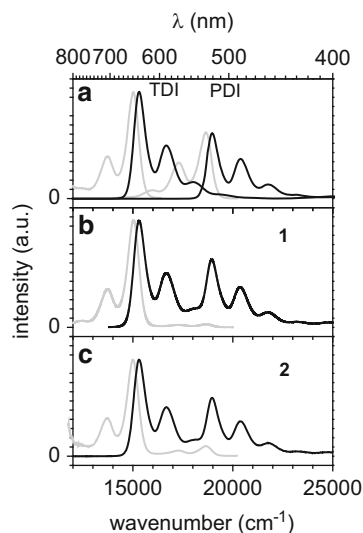
main byproducts in the synthetic step h (Scheme 2) are compounds PMI–PMA and **11**, which both have quite polar anhydride groups and thus readily stick on the silica gel column during purification. Target compound **1** was purified by column chromatography on silica gel using a mixture of toluene, dichloromethane and methanol as eluent to yield dyad **1** in 20% isolated yield for the cyclization reaction. The relatively low yield is due to the formation of hydrolyzed byproducts PMI–PMA and **11**.

### Synthesis of the Kinked Dyad 2

Based on a facile synthetic route to linear dyad **1**, the synthesis of the kinked dyad **2** with a longer spacer becomes possible [8, 9]. Adopting the same strategy but using a longer linker **14** for connection with the open form of TDI unit **13** and a kinked linker (i.e., *meta*-substituted biphenyl; Scheme 3) to combine with the PDI **16**, the kinked dyad **2** was synthesized as shown in Scheme 3.

The terphenyl-substituted open TDI part **15** was synthesized by selective Suzuki coupling of **13** and diiodo-terphenyl **14** followed by borylation with bispinacolate diboron. The unsymmetrical PDI substituted with 3'-(4-iodo-2,5-dioctyl)-1, 1'-biphenyl **18** was obtained by multistep synthesis. The intermediate **17** was synthesized by Suzuki coupling of bromophenyl-PDI **16** with 3-(trimethylsilyl) phenyl pinacolate boronic ester and further halogenation using ICl, transforming the trimethylsilyl group to iodide. **17** underwent another Suzuki coupling with 2,5-dioctyl-4-(trimethylsilyl)phenyl pinacolate boronic ester and halogenation with ICl to furnish **18** with a kinked linker. By using the same procedure for the

**Fig. 3** Absorption (*black lines*) and emission ensemble spectra (*grey lines*) of (a) PDI and TDI, (b) dyad **1** and (c) dyad **2**. All compounds were dissolved in toluene. Reprinted with permission from [9]. Copyright 2008 American Institute of Physics



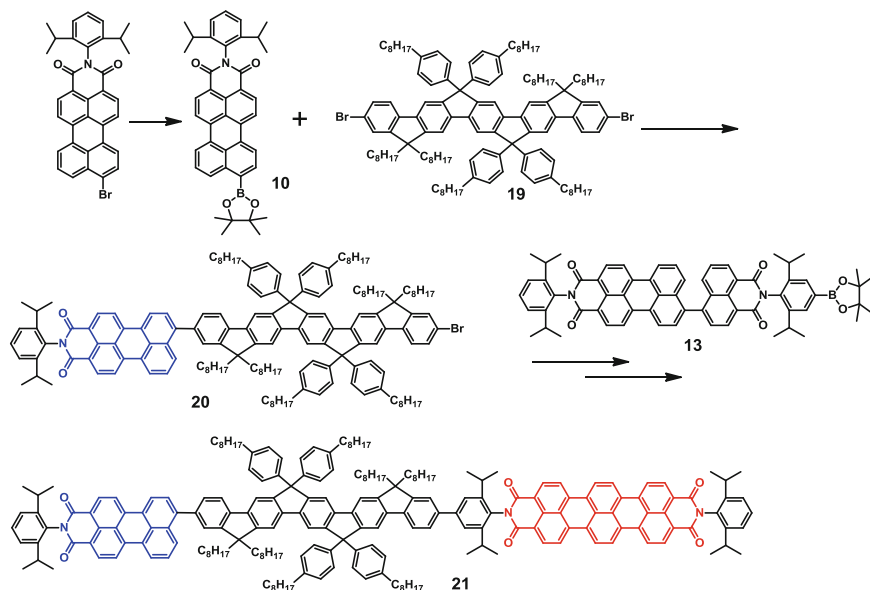
synthesis of linear dyad **1**, the kinked dyad **2** was obtained via Suzuki coupling of **15** and **18**, followed by a mild cyclization with the weak base  $K_2CO_3$  in ethanolamine.

In Fig. 3, the bulk absorption and emission spectra of PDI, TDI and the dyads **1** and **2** are shown. Within the experimental accuracy, no differences in the absorption spectra of the free chromophores and the chromophores attached to the oligophenylene bridges are discernible. Based on additional observations [9] it was concluded that there is no significant  $\pi$ -conjugation between the bridge and the chromophores and that interchromophore coupling in the dyads was weak. The emission spectra of both dyads (Fig. 3), besides the vastly dominating TDI contribution, also show PDI emission. Estimates of the EET efficiencies within the framework of Förster theory [10–12] indicated that PDI emission should occur for **2** but not for **1** (see below). Because PDI emission was not observed in single-molecule experiments it may be due to residual amounts of precursors **6a** and/or **13**.

The rate constants of EET have been calculated for **1** and **2** using the Förster expression [10–12], a brief derivation of which can be found in Sect. 4:

$$k_{\text{EET}}^{\text{Förster}} = \frac{1}{\tau_D} \left( \frac{R_0}{R_{\text{DA}}} \right)^6 \quad \text{with} \quad R_0^6 = \frac{9 \ln 10}{128 \pi^5 N_A} \frac{\phi_D \kappa^2}{n^4} \int_0^\infty \frac{f_D(\tilde{\nu}) \alpha_A(\tilde{\nu})}{\tilde{\nu}^4} d\tilde{\nu} \quad (1)$$

Employing Förster radii of  $R_0 = 7.6$  nm (**1**) and  $R_0 = 7.1$  nm (**2**), these values translate into EET rate constants and efficiencies of  $1.1 \times 10^{11} \text{ s}^{-1}$  and 0.998 for dyad **1** and  $7.3 \times 10^9 \text{ s}^{-1}$  and 0.965 for dyad **2**, respectively [9]. Please note that the spectral overlap – the integral in the equation for  $R_0$  and often denoted by  $J$  – is the same for both dyads and the numbers given are valid for toluene solutions under ambient conditions.



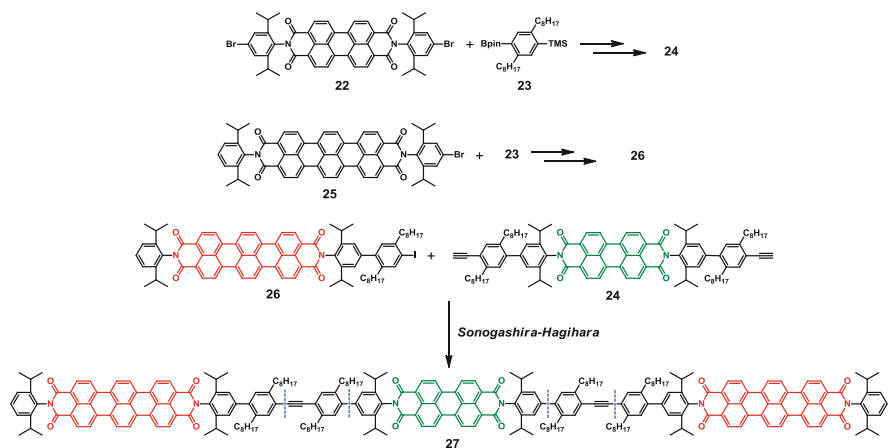
**Scheme 4** Synthesis of model dyad PMI-*p*Ph-Ph-TDI **21**

### PMI-TDI Dyad

To enhance the bridge-mediated contributions to the electron coupling in the electronic energy transfer process between the donor and the spacer in the dyad system, we designed a dyad **21** in which a perylene monoimide (PMI) donor was connected with a terylene diimide (TDI) acceptor through a ladder-type pentaphenylene (pPh) spacer [13]. The synthesis of the rigid ladder-type pPh spacer **19** is described elsewhere [14]. As discussed above, the facile synthesis of the PMI-boronic ester **10** and the open form TDI boronic ester **13** made the route to the target dyad **21** quite straightforward. As illustrated in Scheme 4, selective onefold Suzuki coupling of spacer **19** with **10** afforded the PMI-pPh-Br **20**, which was then subjected to a further Suzuki coupling with **13**. The precursor resulting from the Suzuki coupling was further cyclized to give the target dyad **21**.

### PDI-TDI-PDI Triad

Besides the dyads, we also prepared the novel linear triad **27** (Scheme 5) with PDI as donor and TDI as acceptor [15]. The synthesis of this acceptor-donor-acceptor (A-D-A) multichromophore was accomplished by the Sonogashira coupling of an asymmetric TDI **26** and a bifunctional PDI **24**. To begin with, the bifunctionalized dibromophenyl-PDI **22** was synthesized by imidization of PDA **4** and 4-bromo-2,6-diisopropylaniline. After Suzuki coupling, halogenation and Sonogashira coupling,



**Scheme 5** Synthesis of TDI–PDI–TDI (A–D–A type) triad **27**

the 5-(2-ethynyl-1,4-dioctyl) phenyl end-capped PDI **24** could be obtained from **22**. The asymmetrically functionalized TDI **25** was obtained by cyclization of its open form **12** (Scheme 2) and the asymmetric TDI **26** was synthesized by using Suzuki coupling with 2,5-dioctyl-4-(trimethylsilyl)phenyl pinacolate boronic ester **23** and then followed by halogenation with ICl to convert the trimethylsilyl group into the corresponding iodide **26**. Further Sonogashira coupling of **24** and **26** afforded the triad **27** in relatively low yield, mainly due to the poor solubility of rylene diimides **24** and **26**, although *n*-octyl-chains had been attached to the spacer units. To address these problems, several modifications can be addressed: (1) instead of using the Sonogashira coupling, a Suzuki-type aryl–aryl coupling can be performed due to much higher yields in the rylene–dye coupling reactions; and (2) to prevent aggregation, a branched alkyl chain can be introduced into the imide-position of the TDI building block.

### 2.1.2 Dendrimer-Based and Star-Shaped Multichromophores

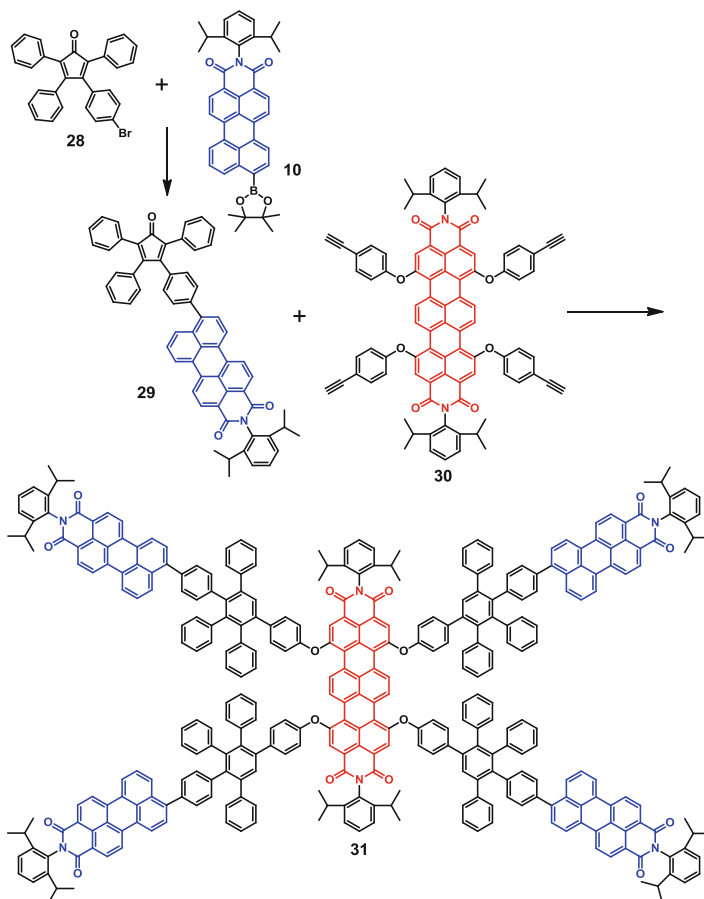
Dendrimers are a class of macromolecules with a precisely controllable branched structure, consisting of three structural units: a core, a hyperbranched scaffold and an external surface [16]. Dendrimers have been shown to possess unusual physical and chemical properties that differ significantly from those of linear oligomers and polymers. By using a fluorescent chromophore as the core of a dendrimer, one can apply fluorescence spectroscopy to study structural aspects and the conformational mobility of dendrimers in solution [17, 18]. At the same time, the dendritic shell provides a unique nanometer-sized environment for the spatial isolation of the chromophore, making them interesting materials for investigations by SMS. The synthesis of dendrimers with fluorescent chromophores attached to the rim serves as an efficient way to obtain a well-defined number of chromophores in a confined volume [19–25]. Not only can the number of chromophores be easily controlled,

but the interactions between the chromophores can also be governed by changing the structure of the branches or of the cores. Another essential advantage of the dendrimer-based design of multichromophores is the complete suppression of aggregation between the dye molecules. Here we take two dendrimers as examples to illustrate how to functionalize TDI and PMI for multichromophoric dendrimer synthesis.

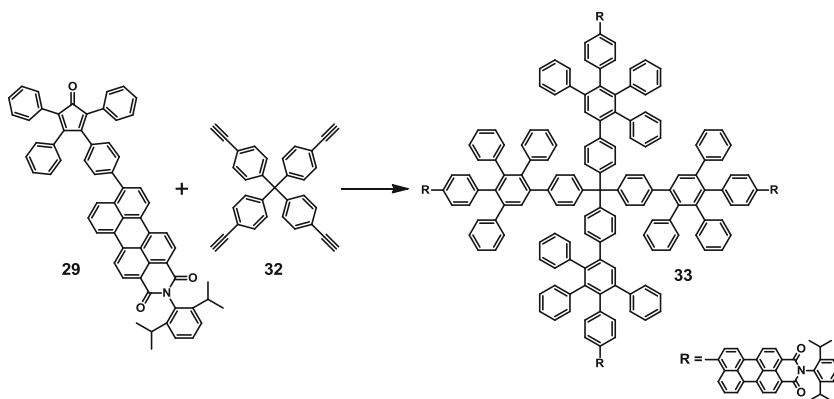
The 4PMI-TDI based dendrimer **31** [26, 27] consists of a terylene diimide (TDI) unit acting as energy acceptor in the core and four perylenemonoimide (PMI) units as energy donors on the periphery. These chromophores (TDI and PMI) were chosen because of their photostability, high extinction coefficients at convenient absorption wavelengths ( $\lambda_{\text{max}} = 495$  nm and  $\lambda_{\text{max}} = 673$  nm for PMI and TDI, respectively), high fluorescence quantum yields, and good overlap between the emission of PMI and the absorption of TDI. This provides an optimal basis for efficient intramolecular Förster energy transfer. The synthetic approach rests upon the Diels–Alder cycloaddition of a tetraphenylcyclopentadienone (Cp) system containing the dye molecule PMI with the ethynyl functionalized TDI. The monobromo-Cp **28** was firstly coupled with the PMI-boronic ester **10** to generate the PMI-containing Cp **29**, which underwent a fourfold Diels–Alder reaction with a tetraethynyl-functionalized TDI **30** to afford the target multichromophoric dendrimer **31** in 92% yield (Scheme 6). The number of bromo groups in compound **28** determined the final number of PMIs in the dendrimer. Moreover, with this strategy, various chromophore pairs at the rim and the core of the dendrimer could be established.

Scheme 7 presents another example of a first-generation polyphenylene dendrimer (G1-4PMI **33**) having a rigid tetrahedral core with four PMI chromophores at the rim [28, 29]. Target compound **33** was synthesized by the efficient Diels–Alder reaction of tetrakis(4-ethynylphenyl)methane (**32**) with the PMI-decorated cyclopentadienone **29** (Scheme 5) in 90% yield [30]. Moreover, to systematically study the energy transfer in such multichromophoric systems, the number of PMI chromophores could be varied from one to four along the branches of the dendrimer in the direction of the corners of a tetrahedron [30], [31, 32]. In this way, one could achieve better control over the orientation of the polyphenylene building blocks around the central core. For asymmetric functionalization of the periphery of a polyphenylene dendrimer, a stepwise Diels–Alder reaction of the triisopropylsilyl (TIPS)-protected tetraphenyl methane and Cp with or without PMI branches was used [30].

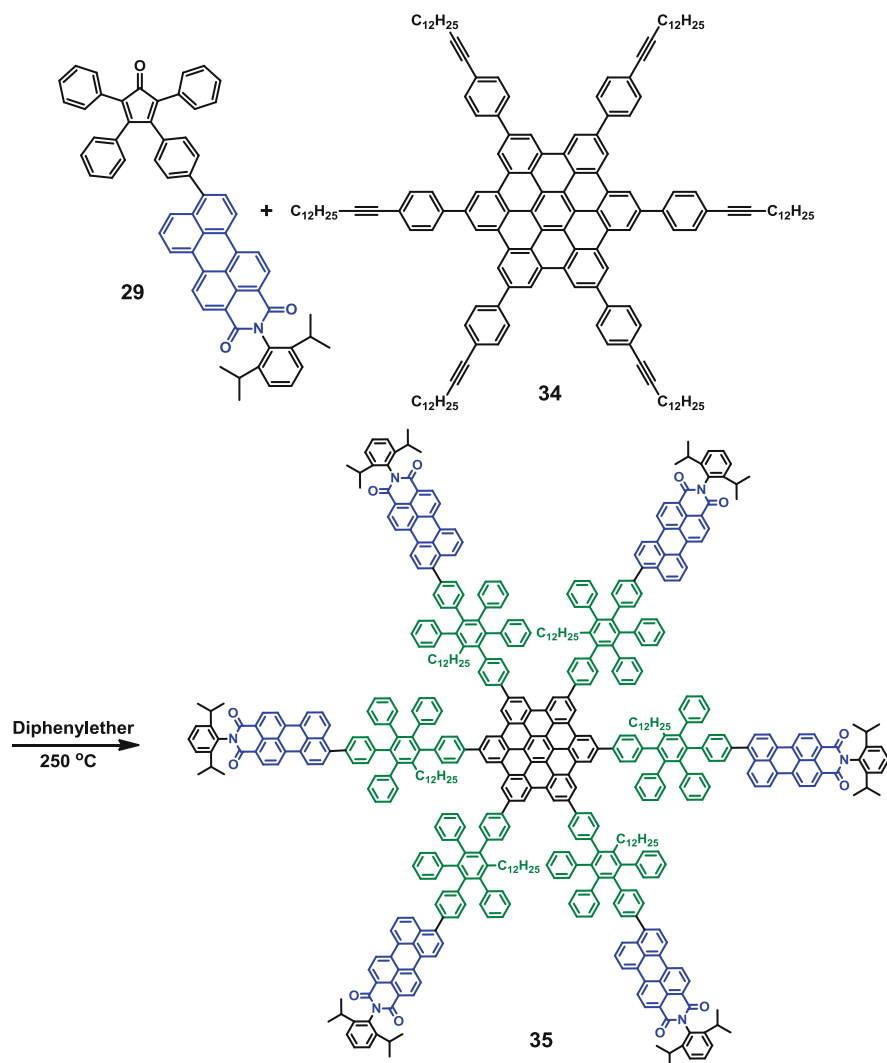
PMI-substituted hexa-*peri*-hexabenzocoronene (HBC) **35** was designed as model compound for intermolecular energy and electron transfer studies because of its  $D_{6h}$  symmetry, electronic and self-assembling properties [33–35]. The multichromophore (HBC-6PMI) **35** has six PMI chromophores attached to HBC via a 3'-dodecyl-4',5',6'-triphenyl-1,1':2',1''-terphenyl spacer unit (Scheme 8). HBC-6PMI **35** was obtained by Diels–Alder reaction of hexa-[4-(tetradec-1-yn-1-yl)phenyl]-HBC **34** [36] and well-established building block PMI-decorated Cp **29** (as discussed above) in diphenyl ether at 250°C in 58% yield [33–35]. Indeed, electronic excitation of the HBC core of this molecule resulted in efficient energy transfer to the PMI shell [37, 38].



**Scheme 6** Synthesis of 4PMI-TDI based dendrimer multichromophore **31**



**Scheme 7** Synthesis of model dyad G1-4PMI **33**



**Scheme 8** Synthesis of star-shaped HBC-6PMI **35**

## 2.2 Complexes from Colloidal Semiconductor Quantum Dots and Organic Dye Molecules

Inorganic–organic hybrid materials composed of colloidal semiconductor nanocrystals or QDs and  $\pi$ -conjugated organic dyes are being increasingly considered for optoelectronics and sensing applications [39–41]. The surface chemistry of the QDs is a crucial issue here because the dye molecules have to be attached to the QD surface by appropriate functional ligands. In an early attempt, it was found that the

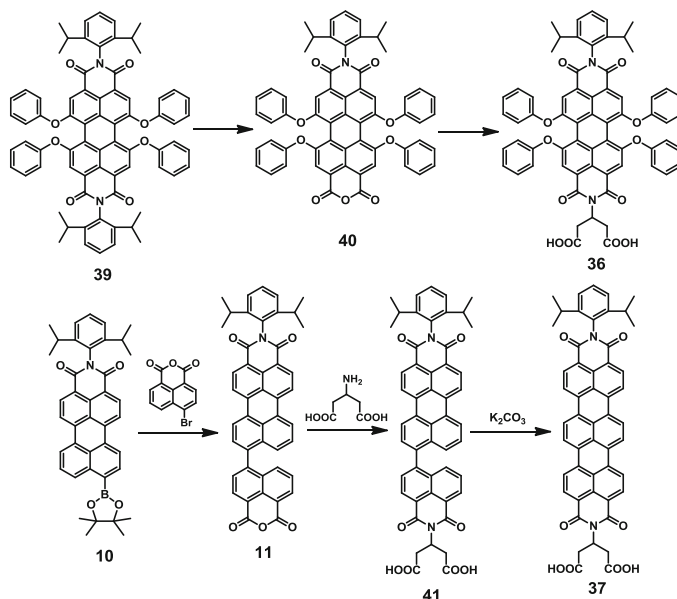
emission of CdSe/ZnS QDs was completely quenched by unspecific complex formation with a diazaperylene dye not bearing a suitable binding functionality [42]. Suitable anchor groups for CdSe or ZnS QDs are provided by amines, oxides and thiols, which have different affinities for the QD surface and alter the fluorescence properties to different degrees. Amines often lead to an increase in the fluorescence but bind only weakly to the QDs. The opposite is true for thiols, which bind more strongly but typically reduce the fluorescence of the particles. To overcome the weak binding of amines, Potapova et al. [43] used a dye-labeled polymer ligand with multiple amine anchor groups, which formed stable complexes with CdSe/ZnS QDs. Other approaches used functionalized peptides and proteins to attach dyes to QDs [44–46]. As discussed below, carboxylic groups enable stable binding of dye molecules to QDs. In most of the conjugates the QD (dye) acts as an energy donor (acceptor) and EET signals complex formation. In a few cases the opposite arrangement has also been considered, one example of which is given in Sect. 2.3. The EET from QD to dye in several instances was satisfactorily modeled in terms of the Förster mechanism [47, 48], although deviations have also been reported [49].

### 2.2.1 Semiconductor Quantum Dots

Several types of QDs have been employed in the assembly of QD/dye complexes. In early attempts [42, 43] CdSe/ZnS core–shell QDs have been used, which were synthesized following established protocols [50, 51]. Later, a synthetic route for multishell QDs was developed [52] in which the shell composition of the CdSe core was gradually changed from CdS to ZnS in the radial direction. The resulting particles had a high crystallinity, large fluorescence quantum yields of up to 80% and increased photochemical and colloidal stability. Moreover, the presence of the passivating shell mediated the impact of ligand exchange on the fluorescence properties of the multishell QDs. The particles discussed so far represent type-I core–shell QDs in which electron and hole are confined in the core after light absorption. In addition, type-II core–shell QDs [53–55] of composition CdTe/CdSe/ZnS were provided for complex formation with light-harvesting complexes as described in Sect. 2.3. In these particles, the hole is confined to the core while the electron largely resides in the shell.

### 2.2.2 Functionalized Organic Dye Molecules

Furnishing organic dyes with carboxylic groups yields stable complexes with QDs [56]. Thus, we designed a family of rylene dyes **36–38** bearing  $\beta$ -glutamic acid groups at the imide positions for stable complexation with QDs. In the case of **36** (Scheme 9) [57], the starting perylene dye **39** was partially saponified under basic conditions to give monoanhydride **40**. Imidization of **40** with  $\beta$ -glutamic acid in *N*-methyl-2-pyrrolidone (NMP) afforded **36**. On the other hand, using the open form



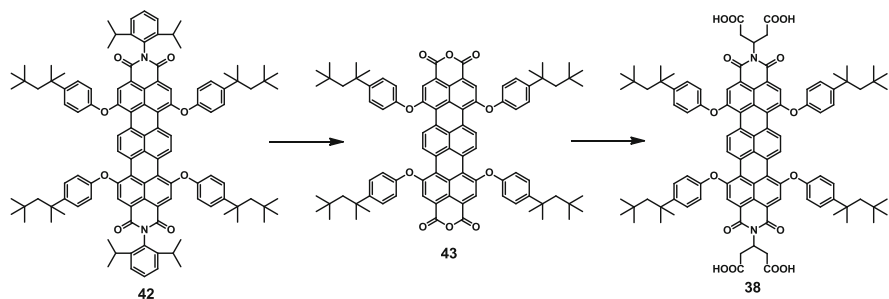
**Scheme 9** Synthesis of dicarboxylic acid anchor functionalized PDI **36** and TDI **37**

(**11**) instead of the closed form of TMI–TMA was necessary to achieve enough solubility for reactivity and purification for dye **37** (Scheme 9). As described previously, **11** was obtained by Suzuki coupling of **10** and 4-bromonaphthalene-1,8-dicarboxylic anhydride **8**. Imidization of **11** and  $\beta$ -glutamic acid gave the precursor **41**, which was later converted to the glutamic acid-tailored TDI **37**.

On the other hand, when two glutamic acids were attached to the dye molecules, the possibility arose of connecting two or more nanoparticles with rylene dyes. Thus, the designed TDI **38** with two dicarboxylic acid anchors at the imide nitrogen atoms was synthesized by the same procedure as described above. The dianhydride **43** was obtained by complete saponification of TDI **42** [7]. Further imidization of **43** and  $\beta$ -glutamic acid afforded TDI **38** [58] (Scheme 10). The complexation between TDI **38** and QDs led to the formation of QD dimers and trimers, for which energy transfer from the QDs to the TDI “bridge” was observed.

### 2.2.3 Quantum Dot/Dye Complexes

Complexes between **36** and **37** and CdSe/CdS/ZnS QDs [57] were formed by sonicating a mixture of dye (in methanol) and QD (in chloroform) after addition of a weak base. The QD/dye complexes were precipitated, washed, and redissolved in chloroform to yield clear solutions. A chelate-type binding of the bidentate anchor to the zinc ions on the QD surface (as sketched in Fig. 4b) was proposed, providing high stability of the complexes. The complexes could also be transferred from the organic into the aqueous phase via ligand exchange [57].



**Scheme 10** Synthesis of tetracarboxylic acid functionalized TDI **43**

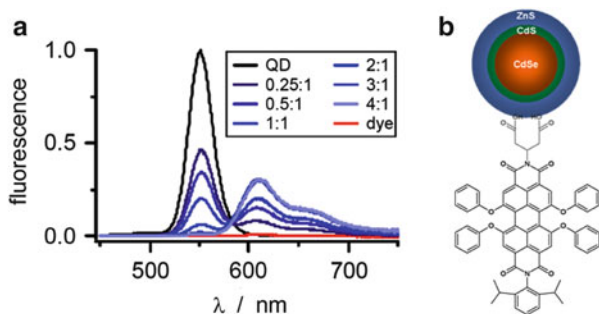


**Fig. 4** (a) Fluorescence spectra of dye **36**/QD complexes in chloroform as a function of the dye/QD ratio. The excitation wavelength was 390 nm. (b) Complex formation between **36** and CdSe/CdS/ZnS core-shell QDs (not to scale)

In Fig. 4a, a series of emission spectra obtained for different dye **36**/QD ratios is shown [57]. With increasing dye amounts, the QD emission was successively quenched and the sensitized dye emission increased, indicating efficient EET in the complexes. This observation was supported by fluorescence decay curves of QDs within the complexes, in which an additional fast component due to EET appeared.

In Fig. 5a QD quenching expressed as  $F_0/F - 1$  from the series in Fig. 4a is plotted versus the dye/QD ratio (where  $F_0$  and  $F$  are the fluorescence intensity of QD in the absence and presence of the dye, respectively). Because reduced donor emission and sensitized acceptor emission and strong spectral overlap between QD emission and dye absorption was observed, the quenching of QD emission was described by the following expression with transfer efficiency  $E$ :

$$\frac{F_0}{F} - 1 = \frac{E}{1 - E} \quad \text{with} \quad E = \sum_{d=0}^{d_{\max}} a(d) \cdot \frac{d}{d + (r/R_0)^6} \quad (2)$$

where  $d$  is the number of dye molecules bound to QD and  $a(d)$  is the QD fraction with  $d$  bound dye molecules according to a binomial distribution. The ratio  $(r/R_0)$  is

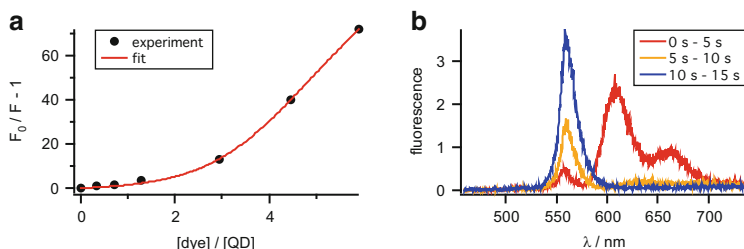


**Fig. 5** (a) Stern–Volmer plot of QD fluorescence quenching in complex with dye **36**. (b) Sequence of single complex emission spectra of dye **36**/QD in PMMA. Reprinted with permission from [57]. Copyright 2008 American Chemical Society

one of the fitting parameters, where  $r$  is the donor–acceptor distance and  $R_0$  the Förster radius, which was 5.3 nm. The model described the experimental data of dye **36**/QD complexes in Fig. 5a reasonably well, resulting in  $(r/R_0) = 0.63$ . Using  $R_0 = 5.3$  nm, one obtains  $r = 0.63 \times 5.3 = 3.4$  nm. From the binding model (Fig. 4b) a center-to-center distance of 3.3 nm was estimated. The fairly good agreement between spectroscopic and geometrical data indicated that a Förster approach provided a reasonable description of EET in the complexes [57].

Individual complexes immobilized in PMMA could be studied by confocal fluorescence microscopy. In the series of emission spectra shown in Fig. 5b, the first spectrum is dominated by the emission of the dye ( $\lambda_{\max} \sim 600$  nm) while QD emission ( $\lambda_{\max} \sim 560$  nm) is weak. During recording of this spectrum, the dye bleached, resulting in QD emission only in the second spectrum. The third and subsequent spectra (not shown), exclusively showed QD emission. The strongly varying emission intensities of QD in the second and third spectrum were caused by QD blinking [59]. For all cases studied, dye bleaching was more efficient than QD bleaching, demonstrating the superior photostability of QDs.

By furnishing rylene dyes with dicarboxylate anchors, a versatile route for the preparation of extraordinarily stable dye/QD complexes has been established. It was pointed out that, by proper choice of dye and QD components, a broad spectral range from the visible up to the near infrared could be covered and the efficiency of EET easily tuned.

## 2.2.4 Quantum Dot Oligomers

Distance-dependent excitation and charge transfer are strong motivations for the study of QD oligomers. Recent experiments have even provided first indications for wavefunction overlap in oligomers of small CdTe QDs [60]. Yet, due to the few successful examples for the preparation of defined QD oligomers, studies of electronic coupling have remained rather elusive. The main challenges in the preparation of discrete QD assemblies are to find effective coupling mechanisms and to separate particular QD oligomers from a possibly wide distribution of products. DNA approaches have been found successful for assembling QDs into

dimers and higher oligomers [61]. Alternatively, small bi-functional molecules like bis(acyl hydrazide) [62] or 1,6-hexanedithiol [60] have been used to generate discrete QD oligomers, which could be purified up to a level of ~70% by size-selective precipitation. Xu et al. [58] have recently shown that density gradient ultracentrifugation is an efficient tool for separating directly coupled or dye-bridged QD dimers and trimers from QD monomers and higher oligomers.

Colloidal QDs dispersed in organic solvents are capped by hydrophobic ligands such as long-chain amines or oleic acid. By adding a bad solvent (methanol) to a solution of QDs in a good solvent (toluene) the QDs will precipitate, and can be separated from the solvent mixture by standard centrifugation. By this procedure, ligands may detach from the QD surface, leading to the onset of aggregation. Consequently, by repeating the precipitation/dissolution cycles many times and depending on the binding strength of the ligands, a larger and larger fraction of the material may aggregate and finally becomes insoluble in the good solvent. It has been shown that the degree of aggregation induced by the precipitation/dissolution cycles could be controlled, yielding a distribution of directly coupled QD oligomers in the good solvent [58]. Subsequently, dimers and trimers were separated and enriched by density gradient ultracentrifugation. CdSe/CdS/ZnS core-shells particles were used in this study.

The density gradient in the ultracentrifugation tube was built with cyclohexane/CCl<sub>4</sub> mixtures, with the gradient from bottom to top adjusted from 90–40% with respect to the CCl<sub>4</sub> volume ratio. On top of the gradient solution, 0.1–0.2 mL of the QD solutions were applied. A typical ultracentrifugation took ~10 min at 56,000 rpm and, under the right conditions [58], led to the appearance of several bands. After ultracentrifugation, material was removed from the various bands by a pipette and after further dilution their composition examined by transmission electron microscopy (TEM). By this approach, monomer, dimer, and trimer fractions could be separated from higher oligomers residing at the bottom of the tube. The purity of the various fractions could be increased by a second round of ultracentrifugation, yielding purities of up to 90%.

Besides directly coupled QD oligomers, dye-bridged variants could be assembled by employing the bi-functional TDI spacer **38**. This type of QD oligomer was prepared by mixing QDs dissolved in toluene and **38** dissolved in methanol to yield a QD-to-dye ratio of typically 1:3. After ultracentrifugation, several bands appeared along the tube and TEM images of the various fractions showed that again monomers, dimers, and trimers could be separated. Spectroscopic investigations in bulk solution indicated that EET from the QDs to the dye “bridge” occurred [58].

In Fig. 6, high resolution TEM images of a directly coupled QD dimer and a QD dimer crosslinked by TDI are shown. The two QDs are in close contact in the first case, but there is a clear interparticle distance in the second case caused by the dye bridge. By analyzing approximately 20 dimers for each case, it was found that the QDs touched each other in ~95% of the directly coupled dimers. In contrast, for the **38** cross-linked dimers, a clear separation between the QDs was found in ~70% of the images. The observation of close contact in directly coupled dimers gave further support to the assumption that in this case loss of ligands is responsible for the formation of oligomers.

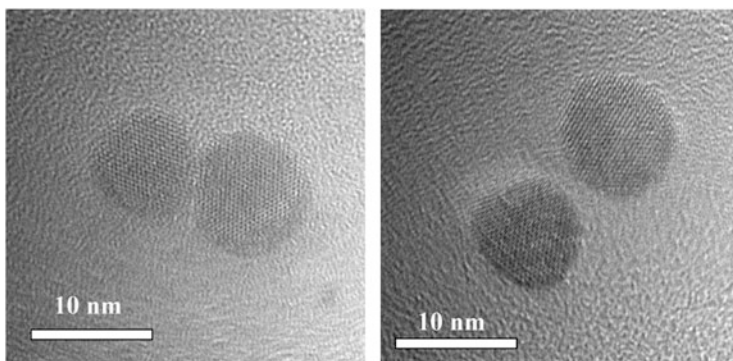


**Fig. 6** Typical high-resolution TEM images of a directly coupled QD dimer (*left*) and a dye **38** linked QD dimer (*right*)

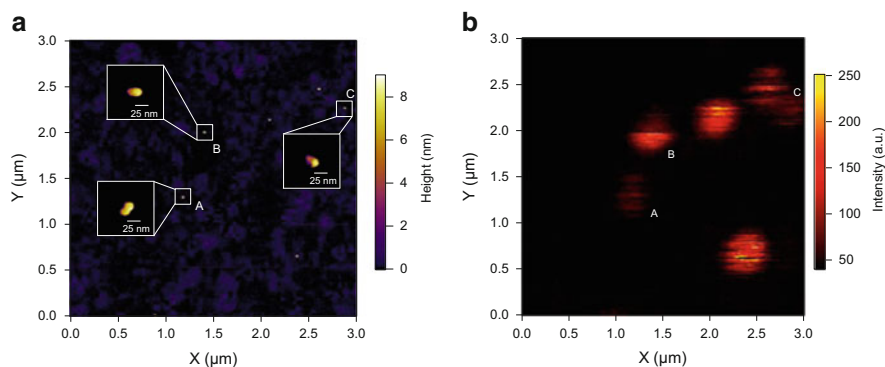


**Fig. 7** (a) AFM height image of QD dimers linked by dye **38**. Three selected dimers are marked as A, B and C. (b) Confocal fluorescence image of the same area of the sample. The lateral resolution of the AFM was estimated to be  $\sim 8$  nm. Adapted with permission from [58]. Copyright 2011 American Chemical Society

Although this work had shown that QD oligomers could be substantially enriched by ultracentrifugation, their purity still was not 100%. Another way to achieve 100% purity – at least in spectroscopic investigations – was to study single oligomers. Figure 7a shows an image of isolated dye-linked QD dimers taken with an atomic force microscope (AFM). For these experiments, the dimers were deposited on glass substrates from a solution with very low concentration. The AFM image unambiguously proved that individual ODs within a dimer could be resolved with this technique. Employing confocal fluorescence microscopy, the emission of the same set (A, B, C) of dimers could be simultaneously imaged (Fig. 7b). The stripes in the fluorescence spots were due to QD blinking [59]. Emission spectra taken from single dimers were found to be composed of contributions from QD and **38** [58].

The simple and effective two-step procedure (assembly/separation) outlined here was also successfully applied to other types of QDs (CdSe, CdSe/ZnS) and seems to be applicable to a wide range of ligand-stabilized colloidal nanoparticles. Moreover, it opens the way to a detailed study of electronic coupling in, e.g., quantum dot molecules.

## **2.3 *Biological–Chemical Hybrids Built from Light-Harvesting Complexes***

### **2.3.1 Hybrid Constructs of Light-Harvesting Complex II (LHCII) and Quantum Dots**

Biological photosynthesis as well as artificial constructs for solar energy conversion such as photovoltaic devices are dependent on the efficient absorption of solar light. In natural systems, this is accomplished by the presence of light-harvesting complexes (i.e., protein complexes containing a number of pigments that are able to absorb the incident light, ideally over the entire spectrum) and then to conduct the excitation energy towards reaction centers where energy conversion takes place. QDs have widely been used as artificial light harvesters in chemical constructs, due to their efficient absorption and their exceptional photochemical stability [63]. Numerous attempts have been made to combine QDs with biological systems to improve their performance. Thus, QDs have been used in combination with isolated reaction centers to replace their biological light-harvesting units [64–66]. Alternatively, QDs have been added to improve the light-harvesting capacity of biological complexes such as cyanobacterial phycobilins [67, 68], cyanobacterial phycoerythrin [69, 70] and purple-bacterial light-harvesting proteins LH1 and LH2 [70]. In these combinations with biological light-harvesting complexes, the QDs were intended to serve as energy donors to one or several biological pigment(s). The efficiency of this energy transfer was difficult to compare with the expected one because the interactions between QDs and protein complex were not defined enough to predict distances between the components.

We have been working with a recombinant version of the major light-harvesting complex (LHCII) in green plants. The advantage of the recombinant origin of this complex was the possibility to modify the apoprotein structure such that it contained defined anchors for the interaction with QDs, such as hexahistidine tags tightly interacting with  $Zn^{2+}$  in the outer ZnS shell [71]. The main pigments in LHCII, chlorophylls *a* and *b*, absorb very well in the blue and red spectral range but only poorly in the green one. To try and fill this “green gap”, we used CdSe/ZnS QDs emitting at 600 nm, binding via the C-terminal hexahistidine tag in trimeric recombinant LHCII. When LHCII was added to the QDs at various ratios between 0.25 and 3, the fluorescence emission of the QD donor concomitantly decreased up to about 70% quenching (Fig. 8). At the same time, only a small amount of

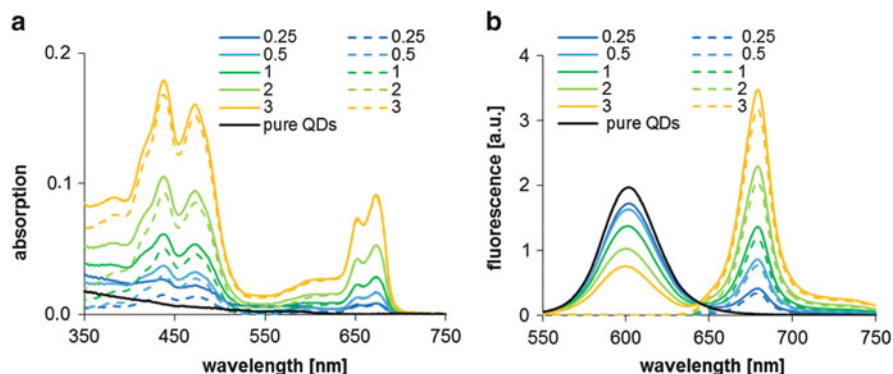


**Fig. 8** Energy transfer from CdSe/ZnS QDs to LHCII. Spectra of QD/LHCII hybrid complexes (*solid lines*) and LHCII references (*dashed lines*). A spectrum of pure QDs is shown as black solid line. LHCII/QD ratios of 0.25, 0.5, 1, 2 and 3 were chosen. QD concentration was 15 nM. (a) Absorption spectra. (b) Emission spectra, excitation wavelength was 360 nm

sensitized acceptor (chlorophyll) emission was observed, which only marginally increased with rising LHCII:QD ratios. Since the fluorescence quantum yields of LHCII and QD are 0.2 and 0.25, respectively, the integral of sensitized acceptor (chlorophyll) emission would be expected to be 80% of the integral of quenched donor (QD) emission according to Förster theory. Consequently, energy transfer does seem to take place between QD and LHCII but clearly there is an additional mechanism by which the presence of LHCII quenches the QD fluorescence emission. A similar effect has been described for the combination of CdSe/ZnS QDs and LH1/LH2 from purple bacteria [70].

The addition of QD absorption in the “green gap” to the absorption of LHCII was measurable but small (Fig. 9). The limited extent of the QD contribution is due to the fairly large extinction coefficient of LHCII in comparison to QDs, the trimer containing no less than 42 chlorophyll and 12 carotenoid molecules.

Much higher energy transfer efficiencies were obtained when LHCII was combined with type-II CdTe/CdSe/ZnS QDs. These had their emission maximum at 750 nm and, thus, served as acceptors of LHCII excitation energy (Fig. 10). Energy transfer efficiencies were as high as 40–65%, depending on the mode of interaction between the components [72]. The hexahistidine tag in the LHCII apoprotein has been exchanged with a number of other binding anchors such as an oligo-cysteine motif or a ZnS affinity tag to improve the binding strength between the protein complex and QDs even further.

### 2.3.2 Hybrid Constructs of LHCII and Rylene Dyes

Organic dyes have been more successful than QDs in attempts to fill in the “green gap” in LHCII absorption. One example is rhodamine maleimide attached to one or three cysteines engineered into the LHCII apoprotein [73]. Another example is a

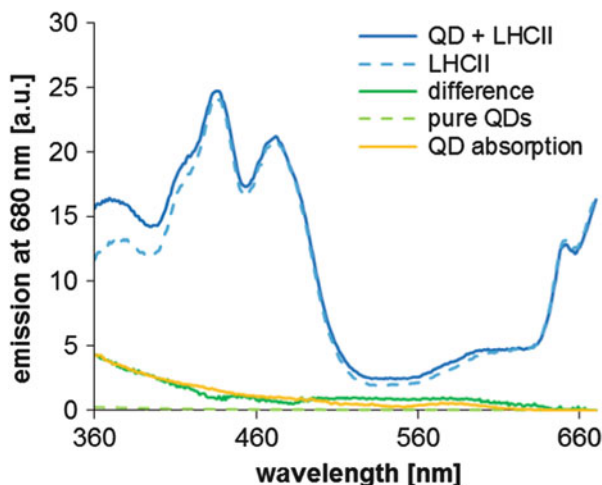


**Fig. 9** QD contribution to light utilization of LHCII. Excitation spectra of QD/LHCII hybrid complexes (*blue solid line*), pure LHCII (*blue dashed line*) and pure QD (*green dashed line*). For comparison, the difference spectrum of the hybrid complexes and pure LHCII (*green solid line*) as well as the adjusted absorption spectra of pure QDs (*solid yellow line*) are shown. QD concentration, 15 nM; LHCII/QD ratio, 1

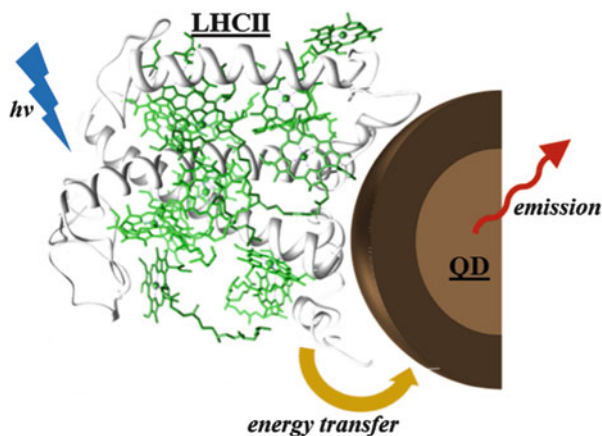
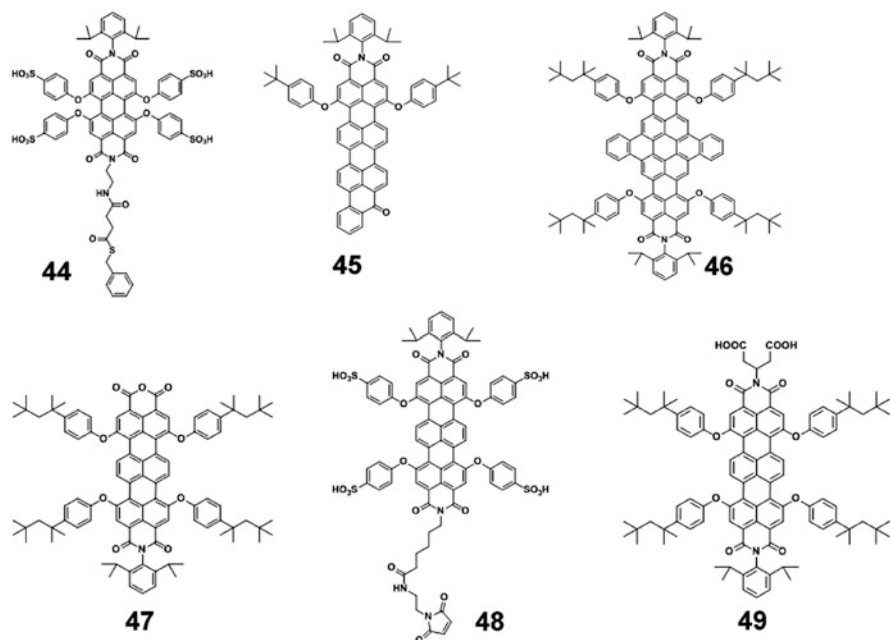


**Fig. 10** Scheme of an LHCII transferring its excitation energy to CdTe/CdSe/ZnS QDs

perylene diimide thioester **44** that was attached to an N-terminal cysteine in LHCII by way of “chemical ligation” [74]. As described above for QDs, constructs were also made with dyes whereby LHCII in fact served as a light-harvester by transferring its excitation energy to an acceptor dye. In earlier work we had seen that significant EET took place from LHCII to benzoylterrylene-3,4-dicarboximide (BTI, **45**) [75]. The transfer efficiency was limited to 70% at room temperature,



**Scheme 11** Rylene dyes synthesized by the group of K. Müllen that were used for ligation with LHCII

presumable due to efficient back transfer from BTI to LHCII. Based on this result, efforts have been made in two directions: (1) to design energy acceptor dyes that undergo even more efficient energy transfer with LHCII as a donor than BTI, and (2) find acceptor dyes that are capable of charge separation and thus would make, together with LHCII, efficient sensitizers in Graetzel-type photovoltaic cells. To this end, several rylene dyes synthesized in the laboratory of K. Müllen have been screened (Scheme 11).

The quaterylene dye dinaptho quaterylene diimide (DNQDI, **46**) exhibits two distinct absorption maxima at 653 and 707 nm, making it an ideal candidate for accepting excitation energy from the LHCII. However, the dye's pronounced hydrophobicity makes it difficult to attach it to the LHCII apoprotein. Moreover, the labeled protein lost its ability to fold spontaneously into a pigmented complex. A terrylene monoimide monoanhydride maleimide (TMIMA, **47**) dye was attached to the LHCII apoprotein (LHCP). The dye's extinction maximum was at 672 nm in DMF, providing a reasonably good overlap with the fluorescence emission maximum at 680 nm of LHCII. The attachment of the maleimide-functionalized dye to the sulfhydryl group of a cysteine in the protein's N-terminal domain led to a strong blue shift in the absorption of the dye to 624 nm, so it was no longer useful as an energy acceptor for the LHCII (data not shown). A terrylene diimide dye without a monoanhydride function but also containing a maleimide group (TDI-mal, **48**) was successfully attached to the apoprotein and the protein could be reconstituted

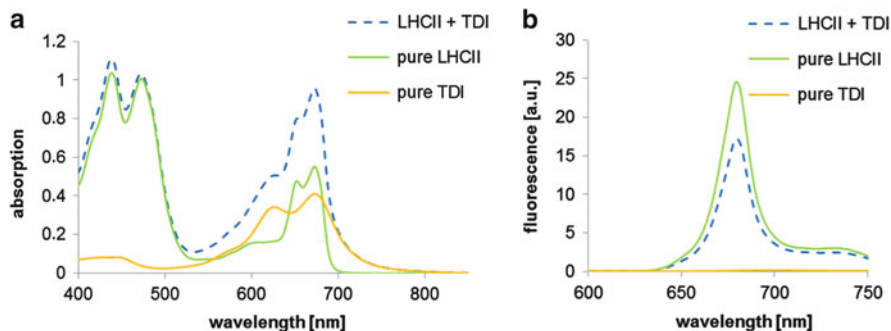


**Fig. 11** Energy transfer measurements of LHCII-TDI<sub>GS</sub> samples: (a) Absorption spectra and (b) fluorescence emission spectra with excitation at 470 nm. 1  $\mu$ M LHCII was mixed with 5  $\mu$ M TDI<sub>GS</sub> in 0.2% lauryl maltoside (LM) (dotted blue line). Pure LHCII (solid green line) and pure dye (solid yellow line) at the same concentration in 0.2% LM. The fluorescence was measured at an absorption of <0.1 at 470 nm

and trimerized without loss of function. With a labeling efficiency of almost 100%, the energy transfer efficiency was only 24% (data not shown), possibly also due to efficient back transfer of the excitation energy. In contrast to TMIMA, TDI-mal does not contain an anhydride or other functional group that helps to attach the dye to semiconductor materials such as TiO<sub>2</sub> in photovoltaic applications. Therefore, a glutamic acid-functionalized rylene dye (TDI-GS, **49**) with an absorption maximum at around 673 nm was synthesized (Fig. 4). In comparison to the TDI-mal ( $\epsilon_{666\text{nm}} = 16,630 \text{ M}^{-1} \text{ cm}^{-1}$  in THF), the extinction coefficient of TDI-GS is much higher ( $\epsilon_{666\text{nm}} = 77,000 \text{ M}^{-1} \text{ cm}^{-1}$  in THF) and according to Förster theory the expected energy transfer in hybrid complexes with LHCII and TDI-GS should be higher than in hybrid complexes of LHCII and TDI-mal. On the other hand, the TDI-GS cannot be covalently attached to the LHCII. To test the energy transfer between LHCII and TDI-mal at least qualitatively, measurements were made with the protein complex and the dye colocalized in detergent micelles.

The dye was solubilized under sonication in an aqueous solution of 10% (w/v) of lauryl maltoside (LM) and then added to LHCII at a ratio of 5 dye molecules per LHCII and a final detergent concentration of 0.2%. As shown in Fig. 11, the emission of LHCII was quenched by about 30% in the presence of the dye. The acceptor (TDI-GS) emission was difficult to detect due to the low fluorescence quantum yield of this dye in the aqueous environment (below 1%). Therefore, sensitized acceptor fluorescence could not be measured, which would have been a good indication for Förster-type energy transfer. Even so, a 30% donor (LHCII) fluorescence quenching makes TDI-GS a promising candidate for energy transfer. Because TDI-GS has been shown to be a useful sensitizer in Graetzel cells [76], LHCII may help to improve its sensitizing efficiency if it is co-adsorbed with the dye on the TiO<sub>2</sub> surface of the cell. Experiments along these lines are in progress.

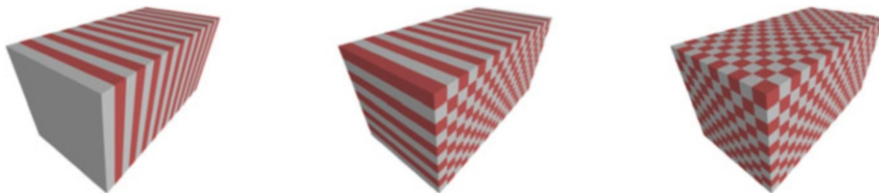


**Fig. 12** Representation of 1D, 2D, and 3D photonic crystals. The *different colors* represent areas of a different refractive index

## 2.4 Dye Molecules in Cholesteric Phases: Towards Lasing Applications.

As shown in the previous sections, the optical emission of complex dye and QD aggregates can be tuned by arranging donor and acceptor in close proximity (distances up to 10 nm). It can, however, also be manipulated by feedback mechanisms, which scatter photons back to the emitting center, create standing waves in the material and thus lead to enhanced stimulated emission or even lasing. Such materials are called “photonic crystals” [77–81].

Photonic crystals, in general, are materials with a periodic variation of the refractive index, whereby the wavelength of the photons, to be manipulated, determines the periodicity of the refractive index modulation. They offer the possibility to influence light emission by structures in the 100 nm range. Such materials can be realized (see Fig. 12) as 1D photonic crystals (Bragg-stacks, but also cholesteric liquid crystals), 2D photonic crystals (realized, e.g., in regularly patterned surfaces) and as 3D photonic crystals (mostly artificial opals). 3D photonic crystals offer a significant advantage over 1D or 2D photonic crystals as they allow it to create standing waves in all three directions of space. As a result, a “full band-gap” may evolve in 3D photonic crystals if the magnitude of the refractive index modulation is very high. In this case, light propagation is prohibited in all directions of the Brillouin zone. This “immobilizes” photons, changes the density of states inside the photonic material, and allows a modification of light emission, including an increase in the lifetime of excited states. In addition, properties like lasing at a very low threshold are predicted [82]. It must, however, be noted such a “full band-gap” has been realized so far only for the IR region. It has not yet been achieved for the visible range, because this would require the use of optically transparent materials (down to 400 nm) with a refractive index approaching 3, which is hardly achievable [83].

Thinking about applications of lasers and today’s trends in technology there is a conflict evident. Electronic devices are getting smaller and smaller while lasers remain, due to their resonators and other optical elements, big if they are constructed in the traditional way. Fabry–Perot resonators and their folded or ring versions are complex, expensive and difficult to assemble. In the competition of engineering towards very small lasers, many different architectures have been

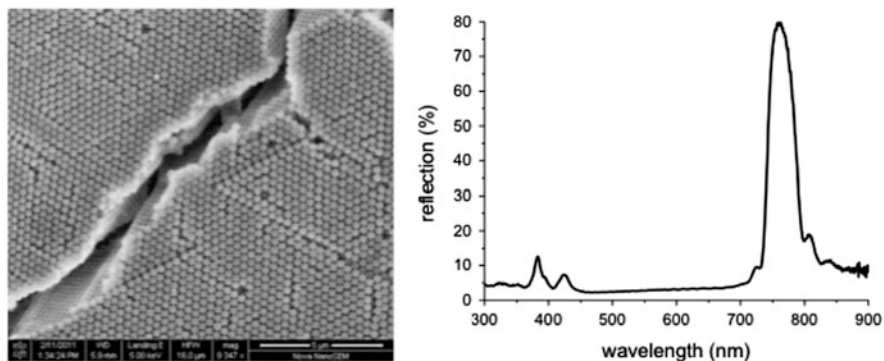


**Fig. 13** SEM picture of a typical photonic crystal made from monodisperse colloids (sample similar to those in [81, 86]) and the resulting selective reflection at 780 nm

created. External cavities have been decreased in size or replaced by other structures. In this context, periodic dielectric structures (photonic crystals) become essential. The most common type of miniature laser is, however, still the laser diode utilized in all types of disk drives. It is similar to an LED, in which the inner surfaces of the diode housing are metallized to creating a resonator, resulting in laser emission. For high power output laser diodes, many of these cells are combined to bars achieving demands up to 70 W [84].

Although many diode lasers work as multimode lasers, the distributed feedback (DFB) and distributed Bragg reflector (DBR) lasers show a mode selection because of their periodic structure. The mode selectivity is generated by the optical properties of the periodic structures because only the modes that are associated with a standing wave/stop band are amplified. DFB structures are photonic structures, which are doped throughout the volume with chromophores (in an optimal case at the maxima of the standing waves), whereas DBR lasers have a miniature Fabry–Perot cavity in which the dye is localized, and the mirrors are replaced by periodic gratings [85].

Artificial opals [77–81] consist of monodisperse spheres that have been crystallized into a cubic densest packing (see Fig. 13). They are the prototype of a 3D photonic crystal (Fig. 12) and possess stop bands (but not a full band-gap) in all three directions of space. They act as very strong feedback media because of the strong difference in refractive index between the spheres (silica or polymer) and the voids consisting of air and reflect 80% or more of light perpendicular to the surface (see Fig. 13) [81]. From their synthesis it is easy to incorporate fluorescent dyes [81, 86] or even highly fluorescent nanoparticles [81, 87] within the colloids (place of highest refractive index, maxima of the standing waves). Although artificial opals look most promising as feedback media for lasing application [88, 89], very few successful lasing experiments are described. This difficulty is, most probably, related to the strong difference in refractive index between spheres and voids, which leads to strong multiple scattering. This offers the potential to achieve a

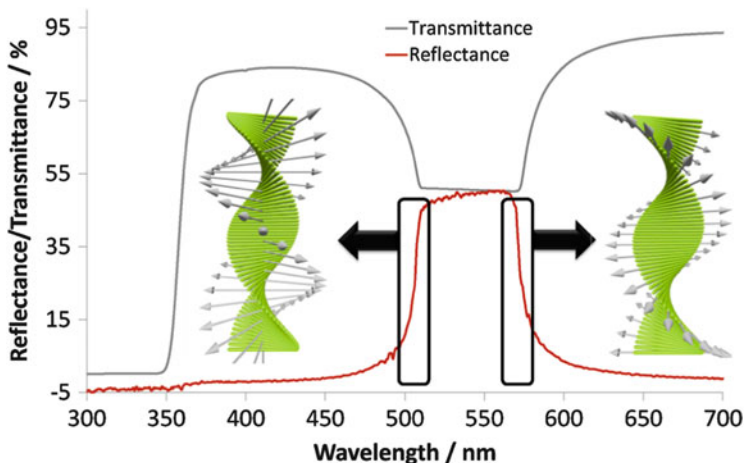


**Fig. 14** Transmittance and reflection of linearly polarized light by a low molar mass cholesteric material. Lasing happens at the band-edges (*black boxes* at 500 and 580 nm), where the density of states is highest. There, two standing waves evolve: out-of-phase (*left*) and in-phase (*right*). See [101, 102, 105] for details

“full band-gap”, but only for a “perfectly crystallized” opal. In real opals, defects exist and they cause very strong diffuse scattering, which is detrimental for lasing. As a result of this problem, two types of lasers have mostly been realized with opals so far. One type consists of “opaline gels”, in which the voids are filled with a liquid [90]. This reduces the difference in refractive index and thereby reduces diffuse scattering from the defects. Alternatively, defect lasing is reported. This relies on the use of an optimized (dye-containing) isotropic polymer film within the opal, which creates a defect state within the band-gap [91, 92]. Amplified spontaneous emission [92] and lasing [93] from this mode has been reported.

### 2.4.1 Liquid Crystal Lasers

The cholesteric liquid crystalline phase is the chiral modification of the nematic phase, in which the liquid crystalline director twists in a helical way (Fig. 14). It acts thus as a 1D photonic structure for light, whose wavelength in the material matches the pitch of the helix. As the helical structure is chiral, this applies however, only to light of the appropriate handedness. Thus, 50% of unpolarized light is reflected (this corresponds to the photonic stop band), whereas 50% is transmitted (this is the light of the opposite handedness). Cholesteric phases can thus act as feedback media for lasers. This was first recognized and patented in 1973 [94]. From then it took almost seven more years until the first experimental proof of lasing from a dye-doped cholesteric material was published [95]. After an additional eight years it was proven that lasing happens at the band edges (see Fig. 14) [96].

It is the advantage of the cholesteric phase that its pitch and thereby the wavelength of the emitted laser light can be tuned by various external stimuli (usually the temperature). Lasers relying on a cholesteric feedback medium have usually a very narrow linewidth and their emission is circularly polarized. With this concept, rather small lasers can be constructed [97, 98]. They are usually pumped by pulsed solid-state lasers although, after first attempts [99], continuous pump conditions were recently successfully established [100]. Lasing has been mostly observed from low molar mass cholesteric mixtures because they show excellent alignment. The state of the art is reviewed in [98, 101, 102].

The key concept of cholesteric laser is best explained by the density of optical modes or density of states (DOS) [97] known from the physics of solid state lasers. The cholesteric phase provides resonance through its periodic structure. Light propagation only occurs for allowed (or cavity) modes, whose number is proportional to the density of states [103]. Inside the photonic band gap of a cholesteric phase, the DOS is equal to zero and emission is suppressed but enhanced at the band-edges [104]. Here, the photon velocity decreases to zero while the photon dwell time increases to infinity because of multiple reflections from the periodical structure. The details of lasing depend now on the width of the band-gap, which is mostly determined by the birefringence  $\Delta n$  and by the orientation of the fluorescent dyes parallel or perpendicular to the director. The stimulated emission of the gain material in a DFB laser at frequencies where the DOS reaches its maxima can be considered as a standing wave. For one of the standing waves (in-phase), the polarization direction is always parallel to the director (Fig. 14, right) and feels the extraordinary refractive index of the liquid crystal. It has a lower energy, which corresponds to the low energy band-edge. For cholesteric materials with a wide band-gap resulting from a large  $\Delta n$ , the threshold for the low energy band-edge is considerably lower than at the other band-edge, where the polarization direction is perpendicular to the director (out-of-phase standing wave; Fig. 14, left). Lasing may thus be found first at the low energy band-edge, but at sufficient high pumping power it becomes possible at both edges [105].

In addition to band-edge lasing, defect mode lasing is possible [97]. A defect in the photonic structure creates fine bands of allowed transmissions inside the photonic band gap. A defect may result from an isotropic or anisotropic layer between adjacent cholesteric layers, but also from phase shifts [106], particle stabilized defects [107], deformation of the cholesteric helix [108] or local polymerization [109]. The threshold of such defect modes are low and can be as low as a few nanojoules per pulse [110].

#### 2.4.2 Crosslinked Polymeric Cholesterics as Lasing Material

Today's challenge is the search for robust cholesteric materials with a low threshold value for lasing, but a high tolerance for pumping. As mentioned above, lasing from cholesteric structures is mostly the domain of low molar mass liquid crystals. That is because it is essential to obtain a monodomain, which is as defect-free as

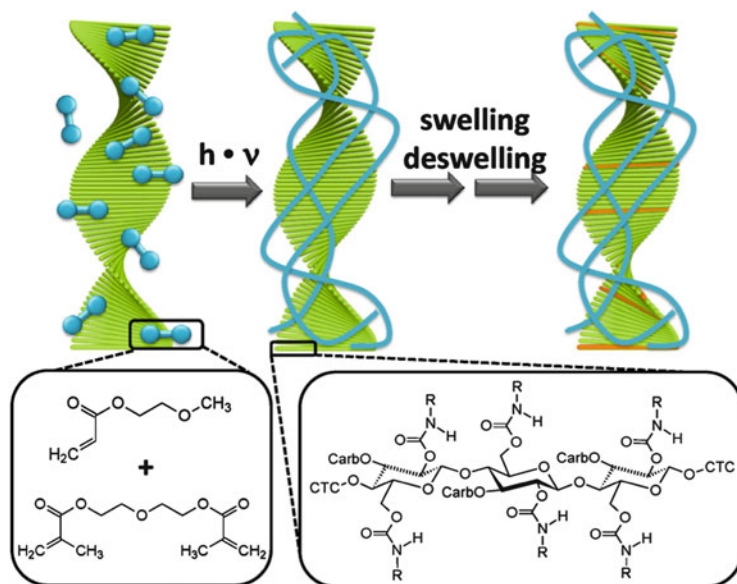


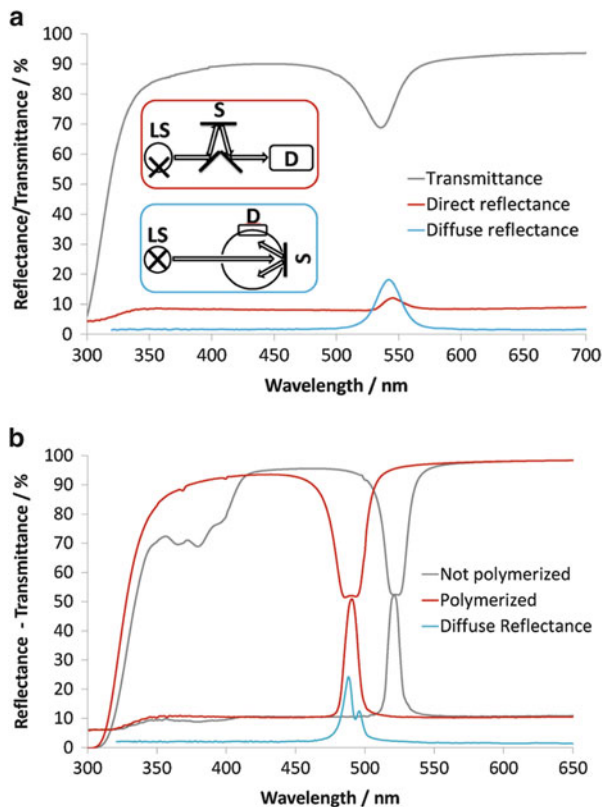
**Fig. 15** Representation of the optimized system. Cellulose carbanilates are used as long mesogens [112]. They form a lyotropic cholesteric phase in mono- and bis-acrylates as solvents. Their photochemical polymerization freezes the helical cholesteric structure. Later on, fluorescent materials can be incorporated into this matrix by swelling and deswelling

possible, and low molar mass liquid crystals are easy to orient. This is necessary to obtain optimal optical properties, which include maximal reflection perpendicular to the substrate and very little scattering.

On the other hand, polymerized (or even crosslinked) cholesteric films would also be very interesting. At first, polymerization/crosslinking allows the permanent stabilization of any selective reflection adjusted beforehand. Thus the cholesteric material can be used afterwards independent of the environmental temperature. But, more importantly, crosslinking stabilizes the helical structure against disturbance by temperature fluctuations during pumping. It thereby strongly increases the maximal tolerable pumping power. In addition, crosslinked systems give flexible films [111, 112] and they make it easy to prepare samples for working in the defect mode. But, it is only possible to benefit from these advantages if a high quality of orientation can be obtained.

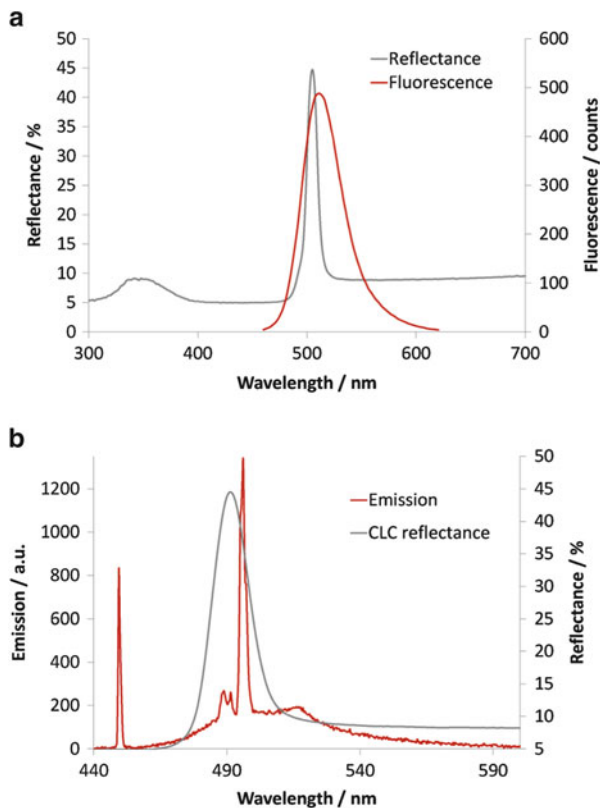
There is another reason for being interested in the use of cholesteric phases prepared by large mesogens. This is related to the use of large, highly fluorescent structures like oligomers optimized for organic LEDs or fluorescent quantum rods. To obtain a low threshold value for lasing, these structures have to be oriented well in the cholesteric phase, with their dipole transition moments parallel to the local director to benefit from the standing wave evolving (see Fig. 14). To achieve this, it seems desirable to work with lyotropic cholesteric phases consisting of long mesogens in a polymerizable solvent (see Fig. 15). Such long mesogens give a

**Fig. 16** Optical properties of different lyotropic cholesteric phases of cellulose carbanilates. (a) Unoptimized older system [111, 112]. LS: Light source, S: Sample, D: Detector. (b) Newly optimized system [115]



high order parameter and they look adequate for the orientation of large elongated fluorescent dyes. Now, such cholesteric phases from chiral polymers are known and opalescent films have been described [111–114]. However, their optical properties are, so far, rather poor. This can be seen from Fig. 16a [115]. Transmission spectra show a band gap, but much less than 50% of the light is stopped from transmission. Reflection measurements look even worse. Most importantly, only a tiny amount of light is reflected perpendicular to the surface, and much more is reflected in a diffuse way. This is obviously the result of a broad distribution of the helical axes. On the other hand, the concept of Fig. 15 looks attractive under another aspect. Working with crosslinked films offers the possibility to incorporate the fluorescent materials after the polymerization/crosslinking step by swelling. This is highly advantageous because the fluorescent materials may (1) reduce the order in the cholesteric material and (2) interfere with the photopolymerization used to prepare the crosslinked films. It was thus the challenge to optimize synthesis and processing to obtain high quality cholesteric materials [115]. This was done using cellulose tricarbonylates [111–114], which show a length of the polymer chain of about 80–150 nm.

**Fig. 17** Properties of crosslinked cholesteric films for possible lasing applications. **(a)** Match of fluorescence of dye and stop band. **(b)** Lasing of circularly polarized light



By careful choice of the polymerizable solvent, by hydrogen bond influencing additives, but especially by the synthetic realization of a very high degree of substitution of the cellulose based polymer, we succeeded in reducing the viscosity of the lyotropic solution considerably [115]. The proper use of mechanical stirring in combination with a tuned substrate treatment and film preparation method and subsequent polymerization allowed, finally, the preparation for the first time of free-standing cholesteric films of a high optical quality such as known from low molar mass systems (see Fig. 16b). They showed selective reflection with a half width of only 20 nm, 50% of transmission, nearly no scattering and nearly 50% perpendicular reflection.

In addition, a method was developed by which fluorescent material can be introduced into the films after film preparation (see Fig. 15). It is thus possible to match fluorescence and cholesteric stop band (Fig. 17a). On such materials, lasing can be observed in analogy to low molar mass cholesteric systems [116]. Whereas a broad fluorescence is observed below the lasing threshold, a very sharp laser peak (100% right-hand circularly polarized) is observed above the threshold value at the long wavelength bend-edge (Fig. 17b).

### 3 Single-Molecule Studies of Electronic Excitation Energy Transfer

Lately, the quest for investigating electronic coupling at the single molecule level has led to a number of experimental and theoretical studies. Specific topics that have been addressed include the investigation of coherent coupling and localization, superradiant emission, singlet–singlet annihilation and the origin of collective “off” states [117–123]. In this section, single-molecule experiments conducted with D–A compounds described in Sect. 2.1 are presented. As already outlined in Sect. 2.1, the D–A-model systems have been specifically designed to gain quantitative and novel information by SMS on the rate and mechanism of electronic EET. One important factor has been to arrange the donor(s) and acceptor(s) via fairly rigid oligo (phenylene) bridges at fixed distances and orientations. The chromophores PMI, PDI and TDI were chosen because they possess favorable properties for SMS, with large absorption cross-sections, high emission quantum yields and low photobleaching yields. In the dyads and triads, the donor and acceptor chromophores can be selectively excited, and all the chromophores give rise to sharp zero-phonon lines at cryogenic temperatures, which is a crucial prerequisite for extracting EET times from line width measurements. These outstanding characteristics of the multichromophores have fostered a number of novel single-molecule results, which are discussed in the next section.

#### 3.1 Flexibility of Donor–Acceptor Dyads

Following the discussion in Sect. 2.1, we will start with a presentation of the results that have been gained for the dyads **1** and **2**. An important parameter in the description of EET is the mutual orientation of the transition dipoles, typically expressed by the orientation factor  $\kappa$ . In Förster theory [12] this orientation factor appears squared [see Eq. (1)] and  $\kappa^2$  assumes values of 4 for collinear aligned transition dipoles and 1 for parallel transition dipoles. From early single-molecule measurements on dyad **1** [1], it was known that the two transition dipoles are not aligned in a truly collinear fashion. In these experiments, which used annular illumination to extract the 3D orientation of the transition dipoles of PDI and TDI, an average deviation from a collinear alignment by  $22^\circ$  was found. Later experiments used rotation polarization of the excitation light rather than annular illumination. In these studies, which allowed faster data acquisition, the PDI and TDI chromophores were selectively excited in alternate fashion by two laser sources [124]. The new results nicely confirmed the original distribution concerning the relative orientation of transition dipoles. Moreover, it was found that the flexibility of the oligo(*p*-phenylene) spacer is the origin of the deviations from collinearity; each *p*-phenylene group on average contributes  $12^\circ$  to the deviation. The experimental results were supported by quantum chemical calculations from

which a comparable flexibility was predicted (see Sect. 4.2). These results are also consistent with experimental data obtained for dyad **2** and with earlier studies of the persistence length of poly(*p*-phenylenes) [125–127].

### 3.2 Control of the Energy Transfer Pathway by Dual Pulse Excitation

The reversible switching of the transition frequency [128] or the turning on and off of EET [129] by light irradiation are prominent examples for the controlled modification of the optical response of single molecules. In this section, experiments will be described that allowed control of the EET process in single molecules of dyad **1**. In particular, the direction of EET could be partially reverted in the sense that the former donor became the acceptor and vice versa [4]. The experiments were based on selective excitation of both PDI and TDI in **1** by short light pulses of different color and with variable time delay. Different excitation and energy transfer scenarios were created and monitored by the corresponding fluorescence signals.

In Fig. 18a, the relevant photophysical processes that may occur in **1** are depicted. Exciting TDI to its  $S_1$  state leads to TDI fluorescence. On the other hand, photons absorbed by PDI are rapidly transferred to TDI, also resulting in TDI fluorescence. The latter energy transfer pathway will be denoted as EET. Obviously, due to energetic reasons, it is not possible to transfer excitation energy from TDI to PDI after exciting TDI to its  $S_1$  state. The situation is different if two excitations are present at the same time. Then, the EET pathway is not available anymore because TDI is already in the excited state. Under these conditions, singlet–singlet annihilation (SSA) as well as donor fluorescence may arise. In SSA, energy is transferred from one electronically excited state to the other, resulting in a higher excited state and a ground state (see Fig. 18a). The higher excited singlet state ( $S_n$ ) typically quickly relaxes to the first excited singlet state ( $S_1$ ), effectively quenching one photon. Please note that EET as well as SSA are both manifestations of resonant electronic EET.

In the experiments, red (635 nm) and green (523 nm) pulsed laser sources were utilized to selectively excite TDI and PDI, respectively. Whereas the red laser was set to maximum power to saturate the  $S_0 \rightarrow S_1$  transition of TDI, the green excitation intensity had to be set considerably lower to prevent fast photobleaching of PDI. Three different pulse sequences were implemented (A, B, C) as depicted in Fig. 18b. In the course of period A, only green pulses were used for excitation. In the second sequence (B), the green and red lasers were fired and both chromophores were excited successively with a time delay of 12.5 ns (3–4 times longer than the fluorescence decay times of the chromophores). The third sequence (C) was optimized to prepare both chromophores in the excited state at the same time. Applying the excitation cycle to single TDI molecules yielded fluorescence time

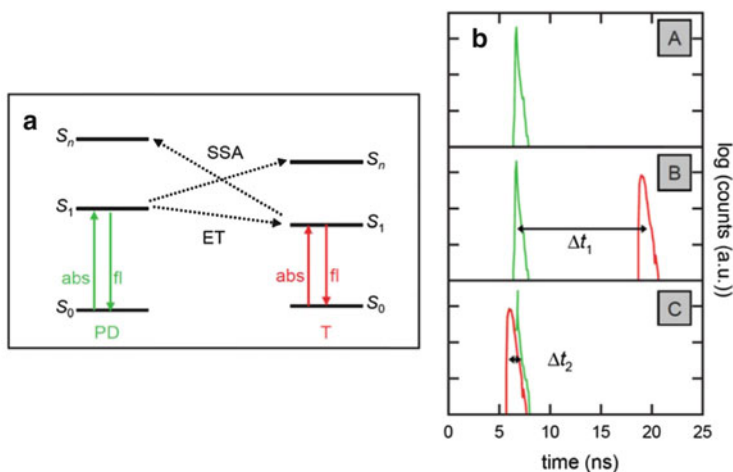


**Fig. 18** (a) Relevant photophysical processes upon photoexcitation of **1**. Excitation of PDI leads to energy transfer to TDI (ET) and acceptor fluorescence. If both chromophores are in the first excited singlet state ( $S_1$ ), then in principal donor fluorescence as well as singlet–singlet annihilation (SSA) could occur. (b) Instrumental response functions of the three excitation sequences. During sequence A the molecules were excited by the green laser only. During sequences B and C excitation occurred with red and green laser pulses and different time delays  $\Delta t_1 = 12.5$  ns and  $\Delta t_2 = -0.7$  ns, respectively

traces as displayed in Fig. 19b. Trivially, the PDI channel detected no signal. On the TDI channel, nearly no fluorescence was observed during sequence A, since the green laser pulses merely had a chance to excite TDI. As expected, during sequences B and C the fluorescence signal was almost constant. In Fig. 19c, a section of an experimental time trace of molecule **1** is displayed. It was found that the fluorescence intensity recorded at the TDI channel significantly changed depending on the excitation sequence. By solely exciting the donor with the green laser (sequence A), efficient EET took place. Thus, only TDI emission was observed. Switching on the red laser in scenario B led to stronger TDI fluorescence. (Note that the red laser had a higher intensity than the green one.) Both the red and green excitation energies are emitted via TDI since only a single excitation was present in the molecule at a given time. In contrast, by applying sequence C, both chromophores were excited at virtually the same time. Although the number of exciting photons was equal to sequence B (Fig. 19c), a significant decrease in the TDI fluorescence intensity was detected. On the PDI channel, fluorescence was not detected during any of the three excitation sequences.

It was concluded that the radiative losses observed for **1** stem from efficient SSA induced by pulse sequence C. From the experimental data the efficiency of the process was calculated to be  $\sim 86\%$ , which was in reasonable agreement with theoretical estimates [4]. As depicted in Fig. 18a, the SSA process may occur in two directions. Since in both cases TDI fluorescence would be recorded, a simple spectral distinction was impossible. Considering the spectral overlaps and

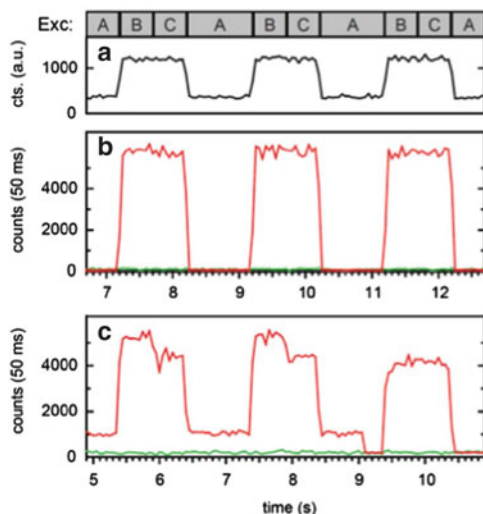


**Fig. 19** *A*, *B* and *C* correspond to the excitation sequences described in Fig. 18b. (a) The excitation cycle monitored from reflected excitation light of both lasers. The fluorescence time traces (b, c) match the excitation cycle depicted in (a). (b) Fluorescence time trace of a single TDI molecule. (c) Section of an experimental time trace of **1**. The emission at the TDI channel (red) showed a strong dependence on the excitation scenario. During pulse sequence *C*, the intensity decreased significantly compared to scenario *B* because of efficient SSA. The PDI channel (green, magnified 10 times) detected no fluorescence at any time. At  $\sim 9.1$  s the donor chromophore (PDI) underwent photobleaching. Consequently, an emission pattern similar to that of single TDI molecules (c.f. b) was observed

photostability issues [4] it was concluded that the energy is preferentially transferred to PDI, thus promoting it to a higher singlet state. Indeed, by applying pulse sequence *C* the energy transfer pathway in **1** has been reversed. Each green excitation that is created at the PDI site will promote PDI to a higher excited state by annihilating a red excitation from the TDI site. By this means, energy effectively flows from the former acceptor to the former donor.

The concept of controlling the energy flow in a single molecule can be extended to compound **27** (Scheme 5) in which a central PDI moiety is connected to two TDI chromophores via rigid bridges. Upon excitation of PDI, EET can occur to both TDI molecules, a situation that harbors the potential to channel the energy flow to only one of them. In a first study [15], the SSA between the two peripheral TDI chromophores of **27** has been quantified by time-resolved photon coincidence measurements. Despite the fairly long intermolecular distance (see Scheme 5), SSA was found to be three times faster than the fluorescence lifetime of TDI. Considering the spectral overlap for SSA and EET from an excited to a ground state TDI chromophore, it was inferred that for any arrangement of the chromophores both processes occur on a similar time scale.

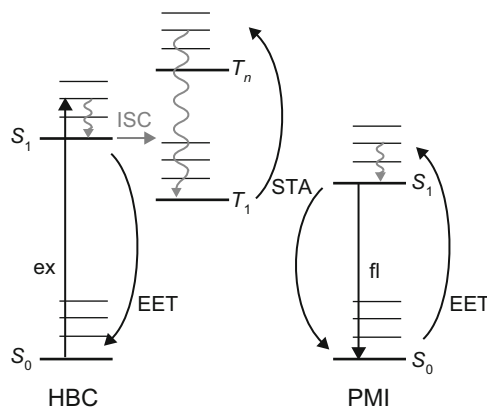


**Fig. 20** Energy level scheme and electronic transitions in **35**. Upon excitation (*ex*) of HBC, either singlet energy transfer (*EET*) to the PMI periphery or intersystem crossing (*ISC*) to the HBC triplet state ( $T_1$ ) occurs. In the case of *EET*, PMI fluorescence (*fl*) is observed while population of  $T_1$  leads to a dark state. After *ISC*, singlet–triplet annihilation (*STA*) may quench excited singlet states ( $S_1$ ) of the PMI periphery through energy transfer to  $T_1$ . Subsequently, in this example, the higher excited triplet state ( $T_n$ ) decays non-radiatively

### 3.3 Read-Out of the Spin State of a Single Molecule by the Emission from Proximate Fluorophores

The 2D graphene-type molecule hexa-*peri*-hexabenzocoronene (HBC) has gained considerable interest because of its self-assembling and photophysical properties. The large intersystem crossing rate and long triplet state ( $T_1$ ) lifetime in the range of seconds are prohibitive for direct single-molecule observation. Yet, at the single molecule level it may be highly interesting to take advantage of the long population storage times in  $T_1$ . By covalently linking fluorescent acceptor molecules (PMI) to HBC giving rise to **35** [37], efficient *EET* from HBC to PMI leads to strong PMI fluorescence. A Jablonski diagram of the relevant electronic processes in **35** is given in Fig. 20.

In single-molecule experiments with **35** it was found that, after selective excitation of HBC, the PMI emission was interrupted by dark intervals whose length of several seconds was in good agreement with the triplet state lifetime of HBC [38]. Hence, the intermittency was induced by population of the HBC triplet state from which the *EET* path to the PMI molecules in the shell is blocked. Accordingly, the presence or absence of PMI emission permitted read out of the spin state of a single HBC molecule.

In addition, it was found that during the lifetime of the HBC triplet state, additional selective excitations of the PMI chromophores were quenched by singlet–triplet annihilation as sketched in Fig. 20 [38]. This result establishes a direct link to Sect. 3.2 because the energy transfer pathway in **35** has been reversed. The energy now flows from PMI to HBC. In this respect, the HBC core could be viewed as a switch for the PMI fluorescence operating via intersystem crossing.

### 3.4 Rates and Mechanism of Energy Transfer

At cryogenic temperatures, the combination of confocal microscopy and frequency-selective SMS is a powerful tool for the investigation of multichromophoric aggregates because it allows for individually addressing molecules whose spatial distance is much smaller than the optical resolution of the imaging system [130, 131]. Such experiments strongly rely on the occurrence of sharp zero-phonon transitions and an inhomogeneous broadening much larger than the homogeneous width of the former. These features open up a number of interesting perspectives for the study of proximate and interacting molecules.

To image individual multichromophoric assemblies, a home-built low-temperature laser scanning confocal microscope was used, which is described in detail elsewhere [28]. Excitation spectra of single molecules within an individual multichromophore are measured by using a ring-dye laser pumped by an argon ion laser as tunable light source. Excitation spectra are obtained by scanning the laser across the molecular absorption lines while detecting the red-shifted emission from either the same chromophore or from chromophores to which the excitation energy has been transferred. Typically, excitation spectra have been recorded at a temperature of 1.4 K. In principal, any temperature between 1.4 K and room temperature is accessible with the cryostat in which the sample and part of the microscope are inserted.

As has been shown recently, for systems exhibiting weak electron–phonon coupling, the rate constant of EET can be extracted from the widths of the sharp purely electronic zero-phonon lines (ZPLs) of donor chromophores observed at low temperatures [2, 9, 26]. Under these conditions the homogeneous line width of a ZPL is composed of the following contributions:

$$\Delta\nu_{\text{hom}} = \frac{1}{2\pi T_1} + \frac{1}{\pi T_2^*} + \frac{1}{2\pi \tau_{\text{EET}}} \quad (3)$$

The first two terms are the contributions from the lifetime of the excited state  $T_1$  (population decay) and pure dephasing processes  $T_2^*$ ; the third term results from the EET, which is treated as an  $T_1$ -type energy relaxation process that causes line broadening of the donor excitation spectrum. In case the third contribution dominates the line width, EET time constants are easily accessible from the simple relation  $\Delta\nu = (2\pi\tau_{\text{EET}})^{-1}$ . Actually, it has to be checked for every particular case that the pure dephasing and lifetime contribution can be neglected compared to the EET contribution. In addition, it has to be assured that the excitation lines are not power broadened and that the band width of the dye laser is substantially smaller than the width of the ZPL. With a laser band width of 2 GHz, which corresponds to the broad band mode of a ring dye laser, line widths are accessible in the range from 5 to roughly 500 GHz, corresponding to EET rates between  $3 \times 10^{10}$  and  $3 \times 10^{12} \text{ s}^{-1}$ .

The determination of single donor EET rate constants from the line widths of low temperature excitation spectra as described above was first accomplished for the multichromophoric poly(phenylene) dendrimer **31**, in which the TDI acceptor is residing in the dendrimer core and the donors are located at the rim of the structure [26]. In this study it was shown that frequency-selective high resolution spectroscopy at low temperature allows the elucidation in great detail of complex energy transfer processes in individual multichromophoric assemblies by controllably interrogating the donors as well as the acceptors. In particular, the EET time constants for individual donors within the dendrimer could be determined. In a room temperature single-molecule study of the same dendrimer it had previously been shown that the acceptor rise time, which corresponds to an average over the energy transfer times of the four donors, could be accessed by time-resolved fluorescence spectroscopy [27]. A similar type of time-resolved experiment has been performed for dyad **2**. In particular, the EET time constants were accessed by analyzing differences in the fluorescence rise/decay time profiles of the acceptor, recorded successively for a dyad prior to and after bleaching of the donor [8]. These investigations had already indicated that the distribution of EET times obtained for single dyads cannot be reproduced by a purely Förster-type description of the EET process.

The study of **1** allowed addressing coupling mechanisms and more principal photophysical aspects of the EET process. Metivier et al. have determined the distribution of EET time constants for single molecules of **1** embedded in PMMA [2]. The EET times were in the range of several picoseconds, which translated into an EET efficiency of almost 100%. Accordingly, in emission spectra of **1** only acceptor emission was observed. These results were similar to those obtained for the dendrimer **31**, which actually was not too surprising because the chromophores and mutual distances were comparable in both systems. Again, a large discrepancy was found between the experimentally determined distribution of EET rates of **1** and a distribution that was calculated within the Förster model (see Fig. 21a). The details for the calculation can be found in the literature [2, 9]. Considering the average values obtained from the experimental ( $\langle k_{\text{EET}}^{\text{exp}} \rangle = 3.2 \times 10^{11} \text{ s}^{-1}$ ) and the calculated distributions ( $\langle k_{\text{EET}}^{\text{Förster}} \rangle = 3.9 \times 10^{10} \text{ s}^{-1}$ ), it is seen that the discrepancy amounts to a factor of  $\sim 8$ . Figure 21a also displays the expected distribution of EET times due to the conformational flexibility of **1** (see Sect. 3.1). This distribution is appreciably smaller than the distribution of EET times caused by the variations in spectral overlaps, which originates in the inhomogeneous broadening of the optical transitions.

Besides the obvious discrepancy between the measured distributions of EET rates and those calculated according to Förster theory (illustrated in Fig. 21a), the validity of the Förster model was further checked by plotting the experimentally determined EET rates  $k_{\text{EET}}^{\text{exp}}$  against the spectral overlaps of individual molecules of **1**, which according to the standard Förster expression of the EET rate should yield a linear dependence (see Eq. (1), [12]). The dashed line in Fig. 21b represents a linear fit to the data. Although the slope of this line showed good agreement with

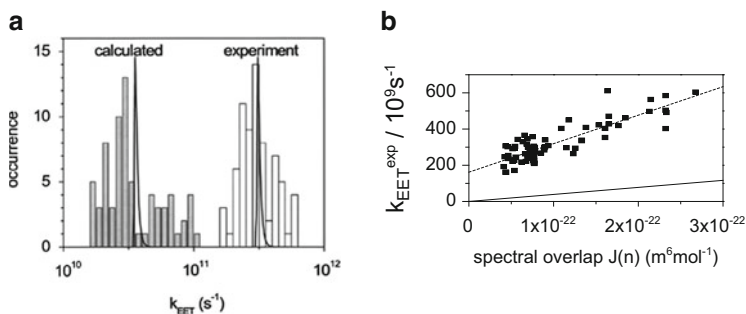
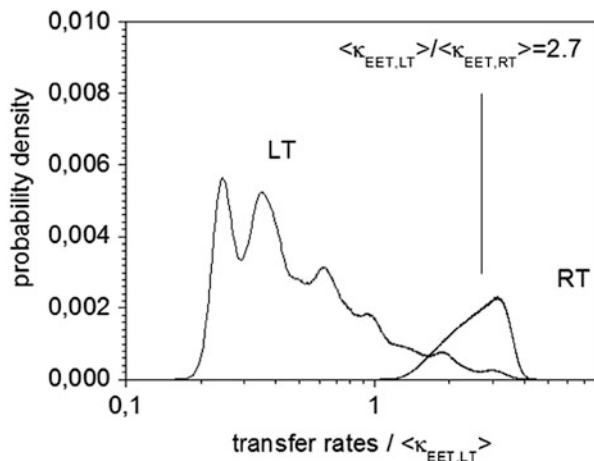


**Fig. 21** (a) Distribution of single-molecule energy transfer rates of **1** obtained at 1.4 K. The *open bars* represent the rates determined from donor (PDI) excitation spectra, while the *filled bars* are calculated from the spectral overlaps according to Förster theory. The *solid lines* show a simulated rate distribution solely originating from different molecular conformations. This distribution has been scaled to fit both histograms. (b) Experimentally determined energy transfer rates plotted vs. the calculated spectral overlaps  $J$ . The *solid line* has been calculated by Förster theory. The *dashed line* represents a linear fit to the data

the data – thereby indicating a Förster type contribution – clearly an offset remained. The solid line in Fig. 21b corresponds to the result of a pure Förster calculation using the corresponding parameters of **1** at 1.4 K. The findings discussed above have triggered a number of theoretical activities to understand the origin of the discrepancies between experiment and theory [3, 132, 133]. The results of a quantum chemical study of **1** [3] are discussed in Sect. 4.

A different situation was encountered for dyad **21**, which was also studied by SMS and quantum chemical calculations [13]. In **21** the through-bond coupling of the PMI chromophore (donor) to the ladder-type pentaphenylene (pPh) bridge led to appreciable shifts and modifications of the PMI-centered electronic transitions while no significant changes were noticeable for the TDI chromophore. Similar to the cases of dyads **1** and **2**, the TDI chromophore in **21** was bound to the bridge via the imide nitrogen. The distribution of EET times for **21** was again determined by low temperature single-molecule excitation spectroscopy. Simulations of the EET time distribution within the framework of Förster theory, assuming PMI as donor and TDI as acceptor, gave EET times which were eight- to tenfold larger than the measured values. Simulations in which PMI-pPh was treated as the effective donor instead of PMI nicely reproduced the experimentally determined EET times. TD-DFT calculations showed that the electronic excitation on the PMI (donor) significantly gave rise to a partial charge transfer character and induced an approximately threefold increase in the electronic coupling strength. Recalling that the EET rate scales with the squared electronic coupling, a decrease in the EET time by a factor of about nine was predicted theoretically in full agreement with the spectroscopic results [13]. Moreover, it was concluded that in **21** the breakdown of the Förster dipole approximation is due to the presence of the bridge and not because of higher multipole contributions.

**Fig. 22** Comparison of the distributions of energy transfer rates ( $\kappa_{\text{EET}}$ ) at room temperature (*RT*) and 1.4 K (*LT*) calculated within Förster theory. Reprinted with permission from [9]. Copyright 2008 American Institute of Physics



Finally, it is interesting to compare how the distributions of EET rates develop when the temperature is changed. As seen in Fig. 22, at low temperature the distribution of EET rates is significantly broader and shifted to smaller values compared to room temperature. The narrowing of the spectra at low temperature induces strong modifications of emission and absorption spectral shapes and results in many different spectral configurations where the spectral overlap can be more or less favored. On average, the EET slows down by approximately a factor of three when the temperature is lowered to 1.4 K.

The differences between the low and room temperature spectral overlaps are strongly related to the temperature-dependent relative intensities of ZPLs and phonon side bands. If a lowering of the temperature led to atomic-like line spectra (no phonon side bands), constellations could be envisioned in which spectral overlap would completely vanish or become very large due to accidental degeneracy of sharp and intense lines carrying a lot of oscillator strength. This aspect is interesting historically. In his original work on concentration quenching of dye molecules in solution, Perrin had assumed (by classical arguments) that energy is exchanged between atomic-like resonant transitions [134]. Accordingly, he obtained interaction distances that were much too large. It was one of Förster's achievements to include vibronic coupling and the concomitant redistribution of oscillator strength between many transitions [12].

## 4 Theoretical Description of Vibronic Spectra and Electronic Coupling

Quantum chemical model calculations are useful tools for gaining further insight into the atomistic details of the photophysical properties considered in this chapter. We will describe a number of studies that have helped to develop a better understanding of the optical spectra of rylene dyes and the EET processes in simple donor–acceptor dyads such as **1** and **2**.

Since particular attention is given to the phenomenon of EET, a few details will be outlined. The incoherent EET process describes the coupling of a deexcitation of a donor molecule ( $D^* \rightarrow D$ ) and the excitation of an acceptor molecule ( $A \rightarrow A^*$ ) (see for example [135]). The rate of this process can be calculated from Fermi's golden rule:

$$k_{\text{EET}} = \frac{2\pi}{\hbar} \sum_k \sum_l p_{D^*A,k} |\langle \Psi_{D^*A,k} | \hat{H}_{DA} | \Psi_{DA^*,l} \rangle|^2 \delta(E_{D^*A,k} - E_{DA^*,l}) \quad (4)$$

where  $\Psi_{D^*A,k}$  and  $\Psi_{DA^*,l}$  are the wavefunctions of the initial and final states, respectively, with energies  $E_{D^*A,k}$  and  $E_{DA^*,l}$ . The indices  $k$  and  $l$  are the vibrational quantum numbers and  $p_{D^*A,k}$  is a Boltzmann factor. The operator  $\hat{H}_{DA}$  describes the coupling between the states.

The usual approximations for this expression involve the Born–Oppenheimer approximation and the assumption of localized electronic and nuclear wavefunctions. With this, the matrix element in Eq. (4) can be expressed as:

$$\begin{aligned} \langle \Psi_{D^*A,k} | \hat{H}_{DA} | \Psi_{DA^*,l} \rangle &= \langle \psi_{D^*} \psi_A | \hat{H}_{DA} | \psi_D \psi_{A^*} \rangle \langle \chi_{D^*,k} | \chi_{D,l} \rangle \langle \chi_{A,k} | \chi_{A^*,l} \rangle \\ &= V_{DA} F_{D,kl} F_{A,kl}. \end{aligned} \quad (5)$$

Here,  $\psi_{D^*}, \dots$  are electronic wavefunctions, while  $\chi_{D^*,k}, \dots$  are the corresponding nuclear wavefunctions. In the second equality, we have introduced the electronic coupling matrix element  $V_{DA}$  and the Franck–Condon integrals  $F_{D,kl}$  and  $F_{A,kl}$  of the donor and acceptor, respectively. This allows rewriting Eq. (4) as:

$$k_{\text{EET}} = \frac{2\pi}{\hbar} |V_{DA}|^2 \mathcal{D}_{\text{EET}}. \quad (6)$$

In this equation, the Franck–Condon factors (the squared Franck–Condon integrals) and the resonance condition [the delta function in Eq. (4)] have been absorbed into the spectral density  $\mathcal{D}_{\text{EET}}$  [135]. It can be factored into the line-shape functions for donor emission and acceptor absorption (this is only possible due to the assumption of local vibrational modes). In addition, the dipole approximation can be made for the electronic coupling matrix element:

$$V_{DA} \approx \frac{\boldsymbol{\mu}_D \cdot \boldsymbol{\mu}_A}{R_{DA}^3} - \frac{(\boldsymbol{\mu}_D \cdot \mathbf{R}_{DA})(\boldsymbol{\mu}_A \cdot \mathbf{R}_{DA})}{R_{DA}^5} \quad (7)$$

using the dipole transition matrix elements  $\boldsymbol{\mu}_D = \langle \psi_{D^*} | \hat{\boldsymbol{\mu}} | \psi_D \rangle$  (and similar for the acceptor), the interchromophoric separation vector  $\mathbf{R}_{DA}$  and its modulus  $R_{DA}$ . As realized by Förster [11, 12], the dipole approximation allows calculation of the transfer rate from experimentally available quantities like the absorption spectrum  $\alpha_A(\tilde{\nu})$  (where  $\tilde{\nu}$  is the wave number) of the acceptor and the fluorescence lifetime  $\tau_D$ , quantum yield  $\phi_D$ , and the normalized emission spectrum  $f_D(\tilde{\nu})$  of the donor. This results in the famous Förster expression [11] for the EET rate [see also Eq. (1)]:

$$k_{\text{EET}}^{\text{Förster}} = \frac{1}{\tau_{\text{D}}} \left( \frac{R_0}{R_{\text{DA}}} \right)^6 \quad (8)$$

The Förster radius  $R_0$  with:

$$R_0^6 = \frac{9 \ln 10}{128 \pi^5 N_{\text{A}}} \frac{\phi_{\text{D}} \kappa^2}{n^4} J; \quad J = \int_0^\infty \frac{f_{\text{D}}(\tilde{\nu}) \alpha_{\text{A}}(\tilde{\nu})}{\tilde{\nu}^4} d\tilde{\nu} \quad (9)$$

depends on the spectral overlap  $J$ , which was used in the discussion in Sect. 3. It is proportional to the spectral density  $\mathcal{D}_{\text{EET}}$  in Eq. (6). In addition to the above defined symbols, the orientation factor  $\kappa$  appears in Eq. (9) [which results from the orientation dependence of the dipolar interaction described in Eq. (7)] and the refractive index  $n$ , which has been introduced as a screening factor due to the medium in which donor and acceptor are embedded [136].

#### 4.1 Vibronic Spectra of PMI and PDI Chromophores

Due to their direct relation to the spectral overlap integral, see Eq. (9), the emission and absorption spectra of the dye molecules are of interest in the context of EET processes. The simplest way to model excitation spectra employs the calculation of vertical energy separations, i.e., the separation of the Born–Oppenheimer potential energy surfaces of the initial state and the final state at the equilibrium structure of the initial state. This energy separation is expected to coincide with the absorption maximum, as rationalized by the Franck–Condon principle (see for example [135]). This assumption is not always appropriate, rylene dyes being a prominent example. These dyes feature a strong 0–0 transition and a pronounced vibronic progression that is even visible in solution at room temperature (see for example [137]). A detailed simulation of the vibrational substructure of the absorption and emission bands is necessary to understand the details of the spectrum.

The absorption and emission spectra of PMI and PDI showed pronounced differences. The ensemble spectra of PMI at room temperature were much broader and showed less vibrational structure than those of PDI.

In order to investigate this difference, high resolution vibronic spectra were measured by low-temperature SMS [137]. In order to avoid aggregation and to achieve better solubility, the dyes were synthesized with bulky ligands in the N-position (2,4-di-*tert*-butyl-phenyl ligands). For the single-molecule spectra, PMMA films containing PMI or PDI were prepared.

Quantum chemical calculations were performed for the fully substituted molecules as well as for model compounds with hydrogen or phenyl groups in the N-position. Interactions with the environment were not accounted for. The equilibrium structures of the singlet ground state  $S_0$  and the first excited singlet state  $S_1$  were determined by density functional theory, using the B3LYP functional

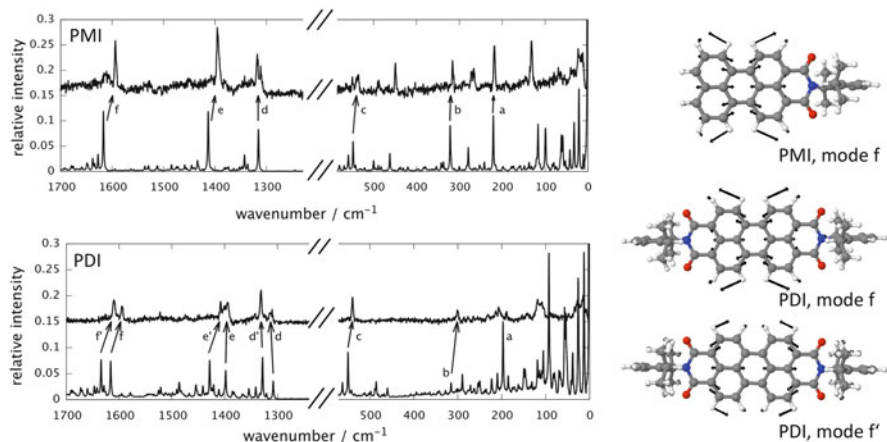


**Fig. 23** Comparison of experimental and calculated emission spectra of a PMI (upper left) and a PDI derivative (lower left), and representations of the normal modes (right). Relative frequencies with respect to the 0–0 transition are given. The experimental spectra are representative single-molecule emission spectra at  $T = 1.2$  K. Reproduced (in part) with permission from [137]. Copyright 2010 American Chemical Society

[138] and the SVP [139] and TZVP [140] basis sets. In addition, wavefunction methods with second-order treatment of electron correlation effects were used, specifically MP2 (Møller–Plesset perturbation theory to second order) for the ground state and ADC(2) (algebraic-diagrammatic construction to second order) for the excited state [141, 142]. SVP basis sets were used in these cases.

The dipole transition moment is rather large for both PMI and PDI (8 and 9 Debye units, respectively) and does not change significantly upon distortion of the molecule from the  $S_0$  to the  $S_1$  structure. Hence, the Franck–Condon approximation is appropriate for calculating the vibrational substructure of the absorption and emission bands.

To this end, harmonic vibrational frequencies for both  $S_0$  and  $S_1$  states were determined using density functional theory at the B3LYP level and SVP basis sets. The Franck–Condon factors were determined taking full account of mode mixing effects (Dushinsky rotation) [143].

The calculated spectra agreed very well with the experimental results (see Fig. 23) and allowed an assignment to specific molecular vibrations. Two main systems of vibronic bands were found. One involved molecular vibrations between 200 and 600  $\text{cm}^{-1}$ . These were mainly breathing modes of the perylene backbone. The second system extended from 1,300 to 1,650  $\text{cm}^{-1}$ . Here, predominantly C–C stretch modes were involved (mixed with CH deformation modes; see Fig. 23). The second series of transitions was mainly responsible for the vibronic progression seen in ensemble spectra. They did not involve the imide groups, which explained the similarity of the monomer spectra when the substitution pattern at N is changed, or if the molecules are part of a multichromophoric species.

The selected high-resolution spectra and the simulated spectra (as shown in Fig. 23) did not directly reveal any reason why the appearance of PMI and PDI bulk spectra was so different. The calculations showed, however, that PMI has a significant static dipole moment in the  $S_0$  state (around 6 Debye units), which increases by 1 Debye unit upon excitation into the  $S_1$  state. By symmetry, PDI has no dipole moment in either state. This pointed to strong linear electron–phonon coupling in the case of PMI, which was in line with the measured Debye–Waller factors for PMI ( $\alpha_D = 0.15$ ) and PDI ( $\alpha_D = 0.4$ ).

Efforts to provide a quantitative model for the coupling of vibronic transitions to the phonons of the host material have been undertaken recently. The theory and first results will be published elsewhere.

## 4.2 Electronic Coupling in Donor–Acceptor Dyads

As outlined before, D–A dyads **1** and **2** allowed detailed investigation of EET mechanisms, in particular since they provide a well-defined geometrical arrangement of the chromophores. Experimental investigations have found much higher transfer rates than predicted by Förster theory [2, 9] (see also Sect. 3). To explain this finding, a number of hypotheses have been investigated both experimentally and by theoretical modeling.

One issue is the potential flexibility of such dyads, which might lead to significantly shorter interchromophoric distances than expected from a naïve linear structure. This idea was examined in the case of **1** [124]. Quantum chemical calculations, employing density functional theory, were carried out to check the influence of strong perturbations like point charges or strong uniform electric fields. Neither the transition energy nor the transition dipole moment were found to change significantly, even for very strong fields ( $10^7$ – $10^9$  V/m). In particular, the orientation of the transition dipole remains along the long chromophore axis in all cases. The transition properties also remain nearly unchanged when the molecular structure is distorted. Hence the orientations of the transition dipoles can be unequivocally used as a probe for chromophore orientation. This information is accessible in single-molecule experiments as described in [124] and reveals some flexibility of **1**, with an average relative angle of  $22^\circ$  between donor and acceptor.

As shown in [3], this cannot explain the large rates because the decreased interchromophoric distance is counteracted by a reduced orientation factor due to the deviation from the optimal collinear arrangement. As a further point, the validity of the dipole approximation, Eq. (7), was investigated [3]. To this end, the electronic coupling matrix element in Eq. (6) was calculated from the Coulomb integral over the one-particle transition densities of the donor  $\gamma_D(\mathbf{r}, \mathbf{r}')$  and the acceptor  $\gamma_A(\mathbf{r}, \mathbf{r}')$ :

$$V_{\text{DA}} \approx \int \gamma_{\text{D}}(\mathbf{r}_1, \mathbf{r}_1) \frac{1}{|\mathbf{r}_1 - \mathbf{r}_2|} \gamma_{\text{A}}^*(\mathbf{r}_2, \mathbf{r}_2) d^3\mathbf{r}_1 d^3\mathbf{r}_2. \quad (10)$$

The equation is valid for sufficiently separated chromophores, which is the case for **1** and **2**. If the wavefunctions of donor and acceptor start to penetrate each other, exchange and charge-transfer contributions must also be taken into account [144].

The transition densities were calculated using both density functional theory and a second-order coupled-cluster model, CC2 [142]. The electronic couplings calculated with Eq. (10) turned out to be slightly larger than those from the dipole approximation, but the effect on the rates is only of the order of 30%, which does not explain the experimental findings reported in [2, 9].

More important is bridge-mediated energy transfer. It turned out that the coupling to the oligo-phenyl bridge significantly enhanced the energy transfer. This mechanism can be understood as a participation of excited states on the bridge unit (denoted  $B(i)$ ) in the following, where  $i$  runs over all electronic bridge states). Perturbation theory yields the following expression for the total effective electronic coupling [145]:

$$V_{\text{DA}}^{\text{eff}} = V_{\text{DA}} + \sum_i \frac{V_{\text{DB}(i)} V_{\text{B}(i)\text{A}}}{(\Delta E_{\text{D}} - \Delta E_{\text{B}(i)})}. \quad (11)$$

In this equation,  $V_{\text{DB}(i)}$  and  $V_{\text{B}(i)\text{A}}$  are the electronic coupling matrix elements between donor and bridge unit and bridge unit and acceptor, respectively;  $\Delta E_{\text{D}}$  and  $\Delta E_{\text{B}(i)}$  are vertical excitation energies. The relative sign of the direct and the bridge-assisted contribution decides whether the presence of the bridge results in an enhancement or a screening of the direct contribution. For dyad **1**, the transition dipoles of the two chromophores are arranged collinearly. This will in all cases lead to the same sign for both contributions in Eq. (11) and thus to enhanced electronic coupling matrix elements.

In [3], the bridge contributions were modeled by considering the coupling of the combined donor/bridge system with the acceptor. Figure 24 shows that the bridge effect is mainly due to a non-resonant coupling to the bridge (see the small features on the bridge unit in Fig. 24a), whereas coupling to charge transfer excitations seemed not to play a role (absence of any features on the bridge unit for the difference density (Fig. 24b)). The bridge contributions resulted in an enhanced coupling, which increased the rates by a factor of  $|V_{\text{DA}}^{\text{eff}}|^2/|V_{\text{DA}}|^2 \approx 3$  in the case of **1** [2]. The results were largely interpreted in terms of the polarizability of the bridge, which effectively reduced the distance between donor and acceptor. Notably, the dipole field emitted by the donor was only weakly enhanced by the polarizability of the bridge, whereas higher multipole fields were much more strongly boosted [3]. Remarkably, these investigations have revealed that it does matter what kind of dielectric is between the donor and the acceptor. By taking into account the full Coulomb coupling and the bridge-mediated contribution, the slope of the line fitted to the experimental data (see Fig. 21b) could be reproduced reasonably well.

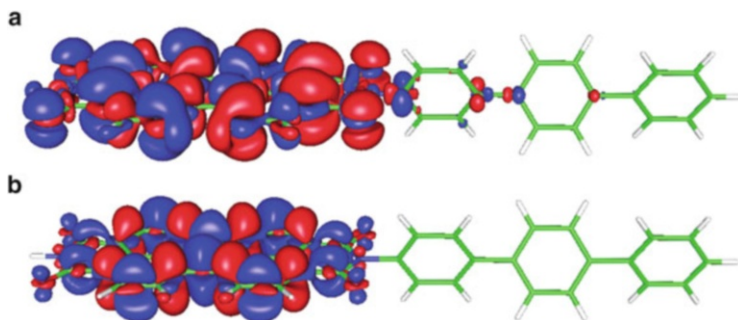


**Fig. 24** Coupling of a *p*-terphenyl to the PDI chromophore (*left*). Shown are the isosurfaces of (a) the transition density and (b) the difference density. The calculations were performed with the CC2 method and a SVP basis set. Reproduced with permission from [3]. Copyright 2008 American Institute of Physics

The theoretical calculations, however, could not account for the apparent offset seen in Fig. 21b. It has been speculated that this off-set might be traced back to a coherent coupling mechanism contributing to the optical line width [9]. Finally, theoretical results for **1** in PMMA have yielded an excellent agreement between the Förster screening factor  $1/n^4$  and a screening factor obtained by considering a cavity enclosing the dyad inside the PMMA dielectric environment [132].

**Acknowledgement** The contributions of our co-workers Burkhard Fückel, Long Chen, Gregor Diezemann, Gerald Hinze, Ting Ren, Daniel Wenzlik, Mara Werwie and Xiangxing Xu are gratefully acknowledged.

## References

1. Hübner CG, Ksenofontov V, Nolde F, Müllen K, Basché T (2004) Three-dimensional orientational colocalization of individual donor–acceptor pairs. *J Chem Phys* 120:10867
2. Metivier R, Nolde F, Müllen K, Basché T (2007) Electronic excitation energy transfer between two single molecules embedded in a polymer host. *Phys Rev Lett* 98:047802
3. Fückel B, Köhn A, Harding ME, Diezemann G, Hinze G, Basché T, Gauss J (2008) Theoretical investigation of electronic excitation energy transfer in bichromophoric assemblies. *J Chem Phys* 128:074505
4. Fückel B, Hinze G, Nolde F, Müllen K, Basché T (2009) Control of the electronic excitation energy transfer pathway between two single fluorophores by dual pulse excitation. *Phys Rev Lett* 103:103003
5. Tour JM (1994) Soluble oligo- and polyphenylenes. *Adv Mater* 6:190
6. Wicklein A, Lang A, Muth M, Thelakkat M (2009) Swallow-tail substituted liquid crystalline perylene bisimides: synthesis and thermotropic properties. *J Am Chem Soc* 131:14442
7. Nolde F, Qu J, Kohl C, Pschirer NG, Reuther E, Müllen K (2005) Synthesis and modification of terrylenediimides as high-performance fluorescent dyes. *Chem Eur J* 11:3959
8. Hinze G, Haase M, Nolde F, Müllen K, Basché T (2005) Time-resolved measurements of intramolecular energy transfer in single donor/acceptor dyads. *J Phys Chem A* 109:6725

9. Hinze G, Metivier R, Nolde F, Müllen K, Basché T (2008) Intramolecular electronic excitation energy transfer in donor/acceptor dyads studied by time and frequency resolved single molecule spectroscopy. *J Chem Phys* 128:124516
10. Förster T (1946) Energiewanderung und Fluoreszenz. *Naturwissenschaften* 33:166
11. Förster T (1948) Zwischenmolekulare Energiewandlung und Fluoreszenz. *Ann Phys* 2:55
12. Förster T (1965) Delocalized excitation and excitation transfer. In: Sinanoglu O (ed) *Modern quantum chemistry, part III: Action of light and organic crystals*. Academic, New York, p 93
13. Curutchet C, Feist FA, Van Averbeke B, Mennucci B, Jacob J, Müllen K, Basché T, Beljonne D (2010) Superexchange-mediated electronic energy transfer in a model dyad. *Phys Chem Chem Phys* 12:7378
14. Zhou G, Baumgarten M, Müllen K (2007) Arylamine-substituted oligo(ladder-type pentaphenylene)s: electronic communication between bridged redox centers. *J Am Chem Soc* 129:12211
15. Fückel B, Hinze G, Nolde F, Müllen K, Basché T (2010) Quantification of the singlet–singlet annihilation times of individual bichromophoric molecules by photon coincidence measurements. *J Phys Chem A* 114:7671
16. Fischer M, Vögtle F (1999) Dendrimers: from design to application—a progress report. *Angew Chem Int Ed* 38:884
17. Pollak KW, Leon JW, Fréchet JMJ, Maskus M, Abruña HD (1998) Effects of dendrimer generation on site isolation of core moieties: electrochemical and fluorescence quenching studies with metalloporphyrin core dendrimers. *Chem Mater* 10:30
18. Matos MS, Hofkens J, Verheijen W, De Schryver FC, Hecht S, Pollak KW et al (2000) Effect of core structure on photophysical and hydrodynamic properties of porphyrin dendrimers. *Macromolecules* 33:2967
19. Gilat SL, Adronov A, Fréchet JMJ (1999) Light harvesting and energy transfer in novel convergently constructed dendrimers. *Angew Chem Int Ed* 38:1422
20. Adronov A, Gilat SL, Fréchet JMJ, Ohta K, Neuwahl FVR, Fleming GR (2000) Light harvesting and energy transfer in laser-dye-labeled poly(aryl ether) dendrimers. *J Am Chem Soc* 122:1175
21. Devadoss C, Bharathi P, Moore JS (1996) Energy transfer in dendritic macromolecules: molecular size effects and the role of an energy gradient. *J Am Chem Soc* 118:9635
22. Jiang D-L, Aida T (1997) Photoisomerization in dendrimers by harvesting of low-energy photons. *Nature* 388:454–456
23. Jiang D-L, Aida T (1998) Morphology-dependent photochemical events in aryl ether dendrimer porphyrins: cooperation of dendron subunits for singlet energy transduction. *J Am Chem Soc* 120:10895
24. Saito T, Jiang D-L, Aida T (1999) A blue-luminescent dendritic rod: poly(phenyleneethynylene) within a light-harvesting dendritic envelope. *J Am Chem Soc* 121:10658
25. Choi M-S, Aida T, Yamazaki T, Yamazaki I (2001) A large dendritic multiporphyrin array as a mimic of the bacterial light-harvesting antenna complex: molecular design of an efficient energy funnel for visible photons. *Angew Chem Int Ed* 40:3194
26. Metivier R, Kulzer F, Weil T, Müllen K, Basché T (2004) Energy transfer rates and pathways of single donor chromophores in a multichromophoric dendrimer built around a central acceptor core. *J Am Chem Soc* 126:14364
27. Gronheid R, Hofkens J, Köhn F, Weil T, Reuther E, Müllen K, De Schryver F (2002) Intramolecular Förster energy transfer in a dendritic system at the single molecule level. *J Am Chem Soc* 124:2418
28. Christ T, Kulzer F, Weil T, Müllen K, Basché T (2003) Frequency selective excitation of single chromophores within shape-persistent multichromophoric dendrimers. *Chem Phys Lett* 372:878
29. Hofkens J, Maus M, Gensch T, Vosch T, Cotlet M, Köhn F, Herrmann A, Müllen K, De Schryver F (2000) Probing photophysical processes in individual multichromophoric dendrimers by single-molecule spectroscopy. *J Am Chem Soc* 122:9278

30. Weil T, Wiesler UM, Herrmann A, Bauer R, Hofkens J, De Schryver FC, Müllen K (2001) Polyphenylene dendrimers with different fluorescent chromophores asymmetrically distributed at the periphery. *J Am Chem Soc* 123:8101
31. Maus M, Mitra S, Lor M, Hofkens J, Weil T, Herrmann A, Müllen K, De Schryver FC (2001) Intramolecular energy hopping in polyphenylene dendrimers with an increasing number of peryleneimide chromophores. *J Phys Chem A* 105:3961
32. Vosch T, Hofkens J, Cotlet M, Köhn F, Fujiwara H, Gronheid R, Van Der Biest K, Weil T, Herrmann A, Müllen K, Mukamel S, der Auweraer V, De Schryver F (2001) Influence of structural and rotational isomerism on the triplet blinking of individual dendrimer molecules. *Angew Chem Int Ed* 40:4643
33. Schmidt-Mende L, Fechtenkötter A, Müllen K, Moons E, Friend RH, MacKenzie JD (2001) Self-organized discotic liquid crystals for high-efficiency organic photovoltaics. *Science* 293:1119
34. Grimsdale AC, Müllen K (2005) The chemistry of organic nanomaterials. *Angew Chem Int Ed* 44:5592
35. Wu J, Pisula W, Müllen K (2007) Graphenes as potential material for electronics. *Chem Rev* 107:718
36. Wu J, Watson MD, Zhang L, Wang Z, Müllen K (2003) Hexakis(4-iodophenyl)-perihexabenzocoronene- a versatile building block for highly ordered discotic liquid crystalline materials. *J Am Chem Soc* 126:177
37. Wu J, Qu J, Tchegobtareva N, Müllen K (2005) Hexa-peri-hexabenzocoronene/perylenedicarboxymonoimide and diimide dyads as models to study intramolecular energy transfer. *Tetrahedron Lett* 46:1565
38. Fückel B, Hinze G, Wu J, Müllen K, Basché T (2012) Probing the electronic state of a single coronene molecule by the emission from proximate fluorophores. *ChemPhysChem* 13:938
39. Huynh WU, Dittmer JJ, Alivisatos AP (2002) Hybrid nanorod-polymer solar cells. *Science* 295:2425
40. Medintz IL, Clapp AR, Mattoussi H, Goldman ER, Fisher B, Mauro JM (2003) Self-assembled nanoscale biosensors based on quantum dot FRET donors. *Nat Mater* 2:630
41. Medintz IL, Uyeda HT, Goldman ER, Mattoussi H (2005) Quantum dot bioconjugates for imaging, labeling and sensing. *Nat Mater* 4:435
42. Schmelz O, Mews A, Basché T, Herrmann A, Müllen K (2001) Supramolecular complexes from CdSe nanocrystals and organic fluorophores. *Langmuir* 17:2861
43. Potapova I, Mruk R, Hübner C, Zentel R, Basché T, Mews A (2005) CdSe/ZnS nanocrystals with dye-functionalised multi-anchor polymer-ligands. *Angew Chemie* 44:2437
44. Willard, DM, Carillo LL, Jung J, Van Orden A (2001) CdSe-ZnS quantum dots as resonance energy transfer donors in a model protein-protein binding assay. *Nano Lett* 1:469
45. Baer R, Rabani EJ (2008) Theory of resonance energy transfer involving nanocrystals: the role of high multipoles. *Chem Phys* 128:184710
46. Fernandez-Arguelles M, Yakovlev A, Sperling RA, Luccardini C, Gaillard S, Sanz Medel A, Mallet JM, Borchon JC, Feltz A, Oheim M, Parak WJ (2007) Synthesis and characterization of polymer-coated quantum dots with integrated acceptor dyes as FRET-based nanoprobles. *Nano Lett* 7:2613
47. Clapp AR, Medintz LR, Mattoussi H (2006) Förster resonance energy transfer investigations using quantum-dot fluorophores. *Chem Phys Chem* 7:47
48. Clapp AR, Medintz IL, Mauro JM, Fisher BR, Bawendi MG, Mattoussi H (2004) Fluorescence resonance energy transfer between quantum dot donors and dye-labeled protein acceptors. *J Am Chem Soc* 126:301
49. Dayal S, Lou Y, Samia ACS, Berlin JC, Kenney ME, Burda C (2006) Observation of non-förster-type energy-transfer behavior in quantum dot-phthalocyanine conjugates. *J Am Chem Soc* 128:13974
50. Murray CB, Norris DJ, Bawendi MG (1993) Synthesis and characterization of nearly monodisperse CDE (E=S, SE, TE) semiconductor nanocrystallites. *J Am Chem Soc* 115:8706

51. Hines MA, Guyot-Sionnest P (1996) Synthesis and characterization of strongly luminescing ZnS-Capped CdSe nanocrystals. *J Phys Chem* 100:468
52. Xie R, Kolb U, Li J, Basché T, Mews A (2005) Synthesis and characterisation of highly luminescent CdSe-core CdS/Zn0.5Cd0.5S/ZnS multi shell nanocrystals. *J Am Chem Soc* 127:7480
53. Kim S, Fisher B, Eisler H-J, Bawendi MG (2003) Type-II Quantum Dots: CdTe/CdSe(Core/Shell) and CdSe/ZnTe(Core/Shell) Heterostructures. *J Am Chem Soc* 125:11466
54. Xie R, Zhong X, Basché T (2005) Synthesis, characterization, and spectroscopy of type-II core/shell semiconductor nanocrystals with ZnTe cores. *Adv Mater* 17:2741
55. Xie R, Kolb U, Basché T (2006) Design and synthesis of colloidal nanocrystal heterostructures with tetrapod morphology. *Small* 2:1454
56. Liu Y, Kim M, Wang Y, Wang YA, Peng X (2006) Highly luminescent, stable, and water-soluble CdSe/CdS core-shell dendron nanocrystals with carboxylate anchoring groups. *Langmuir* 22:6341
57. Ren T, Mandal PK, Erker W, Liu Z, Avlasevich Y, Puhl L, Müllen K, Basché T (2008) A simple and versatile route to stable quantum dot-dye hybrids in nonaqueous and aqueous solutions. *J Am Chem Soc* 130:17242
58. Xu X, Stöttinger S, Battagliarin G, Hinze G, Mugnaioli E, Li C, Müllen K, Basché T (2011) Assembly and separation of semiconductor quantum dot dimers and trimers. *J Am Chem Soc* 133:18062
59. Gomez DE, Califano M, Mulvaney P (2006) Optical properties of single semiconductor nanocrystals. *Phys Chem Chem Phys* 8:4989
60. Koole R, Liljeroth P, Donega CD, Vanmaekelbergh D, Meijerink A (2006) Electronic coupling and exciton energy transfer in CdTe quantum-dot molecules. *J Am Chem Soc* 128:10436
61. Antelman J, Wilking-Chang C, Weiss S, Michalet X (2009) Nanometer distance measurements between multicolor quantum dots. *Nano Lett* 9:2199
62. Peng XG, Wilson TE, Alivisatos AP, Schultz PG (1997) Synthesis and isolation of a homodimer of cadmium selenide nanocrystals. *Angew Chem Int Ed* 36:145
63. Smith AW, Nie S (2010) Semiconductor nanocrystals: structure, properties, and band gap engineering. *Acc Chem Res* 43(2):190
64. Govorov AO (2008) Enhanced optical properties of a photosynthetic system conjugated with semiconductor nanoparticles: the role of Förster transfer. *Adv Mater* 20(22):4330
65. Nabiev I, Rakovich A, Sukhanova A, Lukashev E, Zagidullin V, Pachenko V, Rakovich YP, Donegan JF, Rubin AB, Govorov AO (2010) Fluorescent quantum dots as artificial antennas for enhanced light harvesting and energy transfer to photosynthetic reaction centers. *Angew Chem Int Ed* 49(40):7217
66. Maksimov EG, Kurashov VN, Mamedov MD et al (2012) Hybrid system based on quantum dots and photosystem 2 core complex. *Biochem Mosc* 77(6):624
67. Schmitt F (2010) Temperature induced conformational changes in hybrid complexes formed from CdSe/ZnS nanocrystals and the phycobiliprotein antenna of *Acaryochloris marina*. *J Opt* 12(8):84008
68. Schmitt F, Maksimov E, Suedmeyer H, Jeyasangar V, Theiss C, Paschenko V, Eichler H, Renger G (2011) Time resolved temperature switchable excitation energy transfer processes between CdSe/ZnS nanocrystals and phycobiliprotein antenna from *Acaryochloris marina*. *Photonic Nanostruct* 9(2):190
69. Maksimov EG, Gostev TS, Kuz'minov FI, Sluchanko NN, Stadnichuk IN, Pashchenko VZ, Rubin AB (2010) Hybrid systems of quantum dots mixed with the photosensitive protein phycoerythrin. *Nanotechnol Russia* 5(7-8):531
70. Schmitt FJ, Maksimov EG, Hatti P, Weissenborn J, Jeyasangar V, Razjivin AP, Pashchenko VZ, Friedrich T, Renger G (2012) Coupling of different isolated photosynthetic light harvesting complexes and CdSe/ZnS nanocrystals via Förster resonance energy transfer. *Biochim Biophys Acta Bioenerg* 1817(8):1461
71. Erker W, Bogasch S, Xie RG, Grundmann G, Paulsen H, Basché T (2010) Assemblies of semiconductor quantum dots and light-harvesting-complex II. *J Lumin* 130(9):1624

72. Werwie M, Xu X, Haase M, Basché T, Paulsen H (2012) Bio serves nano: biological light-harvesting complex as energy donor for semiconductor quantum dots. *Langmuir* 28(13):5810
73. Gundlach K, Werwie M, Wiegand S, Paulsen H (2009) Filling the "green gap" of the major light-harvesting chlorophyll *a/b* complex by covalent attachment of Rhodamine Red. *Biochim Biophys Acta Bioenerg* 1787(12):1499
74. Peneva K, Gundlach K, Herrmann A, Paulsen H, Müllen K (2010) Site-specific incorporation of perylene into an N-terminally modified light-harvesting complex II. *Org Biomol Chem* 8(21):4823
75. Wolf-Klein H, Kohl C, Müllen K, Paulsen H (2002) Biomimetic model of a plant photosystem consisting of a recombinant light-harvesting complex and a terrylene dye. *Angew Chem Int Ed* 41(18):3378
76. Li C, Liu M, Pschirer NG, Baumgarten M, Müllen K (2010) Polyphenylene-based materials for organic photovoltaics. *Chem Rev* 110:6817
77. Yablonovitch E (1987) Inhibited spontaneous emission in solid-state physics and electronics. *Phys Rev Lett* 58:2059
78. John S (1987) Strong localization of photons in certain disordered dielectric superlattices. *Phys Rev Lett* 58:2486
79. Busch K, Lölkes S, Wehrspohn RB, Föll H (2004) Photonic crystals – advances in design. Fabrication and characterization. Wiley-VCH, Weinheim
80. Wehrspohn RB, Kitzerow H-S, Busch K (2008) Nanophotonic materials, photonic crystals, plasmonics and metamaterials. Wiley-VCH, Weinheim
81. Lange B, Fleischhaker F, Zentel R (2007) Chemical approach to functional artificial opals. *Macromol Rapid Commun* 28:1291
82. John S, Quang T (1995) Localization of superradiance near a photonic band-gap. *Phys Rev Lett* 74:3419
83. Müller M, Zentel R, Maka T, Romanov SG, Sotomayor Torres CM (2000) Photonic crystal films with high refractive index contrast. *Adv Mater* 12:1499
84. Kneubühl FK, Sigrist MW (1999) *Laser*. Teubner Studienbücher, Stuttgart
85. Dodabalapur A, Chandross EA, Berggren M, Slusher RE (1997) Applied physics: organic solid-state lasers: past and future. *Science* 277:1787
86. Müller M, Zentel R, Maka T, Romanov SG, Sotomayor Torres CM (2000) Dye-containing polymer beads as photonic crystals. *Chem Mater* 12:2508
87. Fleischhaker F, Zentel R (2005) Photonic crystals from core-shell colloids with incorporated highly fluorescent quantum dots. *Chem Mater* 17:1346
88. Gorelik VS (2008) Optics of globular photonic crystals. *Laser Phys* 18:1479
89. Romanov SG, Maka T, Sotomayor Torres CM, Müller M, Zentel R (1999) Photonic band-gap effects upon the light emission from a dye-polymer-opal composite. *Appl Phys Lett* 75:1057
90. Furumi S, Kanai T, Sawada T (2011) Widely tunable lasing in a colloidal crystal gel film permanently stabilized by an ionic liquid. *Adv Mater* 23:3815
91. Fleischhaker F, Arsenaault AC, Kitaev V, Peiris FC, von Freymann G, Manners I, Zentel R, Ozin GA (2005) Photochemically and thermally tunable planar defects in colloidal photonic crystals. *J Am Chem Soc* 127:9318
92. Fleischhaker F, Arsenaault AC, Schmidtke J, Zentel R, Ozin G (2006) Spin-coating of designed functional planar defects in opal film: generalized synthesis. *Chem Mater* 18:5640
93. Shi LT, Jin F, Zheng ML, Dong XZ, Chen WQ, Zhao ZS, Duan XM (2011) Threshold optimization of polymeric opal photonic crystal cavity as organic solid-state dye-doped laser. *App Phys Lett* 98:093304
94. Goldberg, L.S, Schnur, J.M. (1973) Tunable internal-feedback liquid crystal-dye laser. US patent No. 3,771,065.
95. Ilchishin IP, Tikhonov EA, Tishchenko VG, Shpak MT (1980) Generation of a tunable radiation by impurity cholesteric liquid crystals. *JETP Lett* 32:24
96. Ilchishin IP, Tikhonov EA, Tolmachev AV, Fedoryako AP, Shpak MT (1988) Harmonic distortion of the nematic liquid crystal structure with induced gyrotropy which manifests in the distributed feedback laser. *Ukrainskii Fizicheskii Zhurnal* 33:1492
97. Blinov LM, Bartolino R (2010) Liquid crystal microlasers. Transworld Research Network, Kerala, p 1

98. Coles H, Morris S (2010) Liquid-crystal lasers. *Nat Photon* 4:676
99. Coles H, Morris S, Ford AD, Hands PJW, Wilkinson TD (2010) Red-green-blue 2D tuneable liquid crystal laser devices for displays. In: Blinov LM, Bartolino R (eds) *Liquid crystal microlasers*. Transworld Research Network, Kerala, p. 241
100. Munoz A, McConney ME, Kosa T, Luchette P, Sukhomlinova L, White TJ, Bunning TJ, Taheri B (2012) Continuous wave mirrorless lasing in cholesteric liquid crystals with a pitch gradient across the cell gap. *Opt Lett* 37:2904
101. Haase W, Podgornov F, Matsuhisa Y, Ozaki M (2008) Lasing in dye-doped chiral liquid crystals: influence of defect modes. In: Wehrspohn RB, Kitzerow H-S, Busch K (eds) *Nanophotonic materials: photonic crystals, plasmonics and metamaterials*. Wiley-VCH, Weinheim, p 239
102. Ozaki M, Matsuhisa Y, Yoshida H, Ozaki R, Fujii A (2008) Photonic crystals based on chiral liquid crystals. In: Wehrspohn RB, Kitzerow H-S, Busch K (eds) *Nanophotonic materials, photonic crystals: plasmonics and metamaterials*. Wiley-VCH, Weinheim, p 251
103. Moreira M, Relaix S, Cao W, Taheri B, Palfy-Muhoray P (2010) Mirrorless lasing and lasing thresholds in cholesteric liquid crystals. In: Blinov LM, Bartolino R (eds) *Liquid crystal microlasers*. Transworld Research Network, Kerala, p 223.
104. Schmidtke J, Stille W (2003) Fluorescence of a dye-doped cholesteric liquid crystal film in the region of the stop band: theory and experiment. *Eur Phys J B Condensed Matter Complex Syst* 31:179
105. Ozaki M, Matsuhisa Y, Yoshida H, Ozaki R, Fujii A (2007). Photonic crystals based on chiral liquid crystal. *Phys Status Solidi A Appl Mater Sci* 204:3777
106. Kopp VI, Genack AZ (2002) Twist defect in chiral photonic structures. *Phys Rev Lett* 89:033901
107. Zapotocky M, Ramos L, Poulin P, Lubensky TC, Weitz DA (1999) Particle-stabilized defect gel in cholesteric liquid crystals. *Science* 283:209
108. Matsui T, Ozaki M, Yoshino K (2004) Tunable photonic defect modes in a cholesteric liquid crystal induced by optical deformation of helix. *Phys Rev E* 69:061715
109. Yoshida H, Lee CH, Fujii A, Ozaki M (2007) Tunable chiral photonic defect modes in locally polymerized cholesteric liquid crystals. *Mol Cryst Liq Cryst* 477:255
110. Ozaki M, Ozaki R, Matsui T, Yoshino K (2003) Twist-defect-mode lasing in photopolymerized cholesteric liquid crystal. *J Appl Phys II Lett* 42:L472
111. Zentel R, Müller M, Keller H (1997) Solid opalescent films originating from urethanes of cellulose. *Adv Mater* 9:159
112. Müller M, Zentel R (2000) Cholesteric phases and films from cellulose derivatives. *Macromol Chem Phys* 201:2055
113. Sato T, Shimizu T, Kasabo F, Teramoto A (2003) Isotropic-cholesteric phase equilibrium in solutions of cellulose tris(phenyl carbamate). *Macromolecules* 36:2939
114. Norisuye T, Tsuboi A, Sato T, Teramoto A (1997) Solution properties of cellulose tris (3,5-dimethyl-phenylcarbamate). *Macromol Symp* 120:65
115. Wenzlik D, Zentel R (2013) High optical quality films of liquid crystalline cellulose derivatives in acrylates. *Macromol Chem Phys*. doi:[10.1002/macp201300354](https://doi.org/10.1002/macp201300354)
116. Wenzlik D. (2013) PhD thesis, Johannes Gutenberg-Universität Mainz, Germany
117. Christ T, Petzke F, Bordat P, Herrmann A, Reuther E, Müllen K, Basché T (2002) Investigation of molecular dimers by ensemble and single molecule spectroscopy. *J Lumin* 98:23
118. Hettich C, Schmitt C, Zitzmann J, Kuhn S, Gerhardt I, Sandoghdar V (2002) Nanometer resolution and coherent optical dipole coupling of two individual molecules. *Science* 298:385
119. Vosch T, Cotlet M, Hofkens J, Van Der Biest K, Lor M, Weston KD, Tinnefeld P, Sauer M, Latterini L, Müllen K, De Schryver FC (2003) Probing Förster type energy pathways in a first generation rigid dendrimer bearing two perylene imide chromophores. *J Phys Chem A* 107:6920
120. Hübner CG, Zumofen G, Renn A, Herrmann A, Müllen K, Basché T (2003) Photon antibunching and collective effects in the fluorescence of single bichromophoric molecules. *Phys Rev Lett* 91:093903

121. Lippitz M, Hübner CG, Christ T, Eichner H, Bordat P, Herrmann A, Müllen K, Basché T (2004) Coherent electronic coupling versus localization in individual molecular dimers. *Phys Rev Lett* 92:103001
122. Hernando J, van der Schaaf M, van Dijk EMHP, Sauer M, Garcia-Parajo MF, van Hulst NF (2003) Excitonic behavior of rhodamine dimers: a single-molecule study. *J Phys Chem A* 107:43
123. Hernando J, Hoogenboom JP, van Dijk EMHP, García-López JJ, Crego-Calama M, Reinhoudt DN, van Hulst NF, García-Parajó MF (2004) Single molecule photobleaching probes the exciton wave function in a multichromophoric system. *Phys Rev Lett* 93:236404
124. Fückel B, Hinze G, Diezemann G, Nolde F, Müllen K, Gauss J, Basché T (2006) Flexibility of phenylene oligomers revealed by single molecule spectroscopy. *J Chem Phys* 125:144903
125. Farmer BL, Chapman BR, Dudis DS, Adams WW (1993) Molecular-dynamics of rigid-rod polymers. *Polymer* 34:1588
126. Petekidis G, Vlassopoulos D, Galda P, Rehahn M, Ballauff M (1996) Determination of chain conformation of stiff polymers by depolarized Rayleigh scattering in solution. *Macromolecules* 29:8948
127. Vanhee S, Rulkens R, Lehmann U, Rosenauer C, Schulze M, Köhler W, Wegner G (1996) Synthesis and characterization of rigid rod poly(p-phenylenes). *Macromolecules* 29:5136
128. Kulzer F, Kummer S, Matzke R, Bräuchle C, Basché T (1997) Single-molecule optical switching of terylene in p-terphenyl. *Nature* 387:688
129. Irie M, Fukaminato T, Sasaki T, Tamai N, Kawai T (2002) A digital fluorescent molecular photoswitch. *Nature* 420:759
130. Betzig E (1995) Proposed method for molecular optical imaging. *Optics Lett* 20:237
131. van Oijen AM, Köhler J, Schmidt J, Müller M, Brakenhoff GJ (1998) 3-Dimensional super-resolution by spectrally selective imaging. *Chem Phys Lett* 292:183
132. Curutchet C, Mennucci B, Scholes GD, Beljonne D (2008) Does Förster theory predict the rate of electronic energy transfer for a model dyad at low temperature? *J Phys Chem B* 112:3759
133. Chen H-C, You ZQ, Hsu CP (2008) The mediated excitation energy transfer: effects of bridge polarizability. *J Chem Phys* 129:084708
134. Perrin F (1929) La fluorescence des solutions. Induction moléculaire – polarisation et durée d'émission – photochimie. *Annales de physique* 12:169
135. May V, Kühn O (2010) Charge and energy transfer dynamics in molecular systems. Wiley-VCH, Weinheim
136. Knox RS, van Amerongen H (2002) Refractive index dependence of the Förster resonance excitation transfer rate. *J Phys Chem B* 106:5289
137. Diehl FP, Roos C, Jankowiak H-C, Berger R, Köhn A, Diezemann G, Basché T (2010) Combined experimental and theoretical study of the vibronic spectra of perylenecarboximides. *J Phys Chem B* 114:1638
138. Becke A (1993) A new mixing of Hartree–Fock and local density-functional theories. *J Chem Phys* 98:1372
139. Schäfer A, Horn H, Ahlrichs R (1992) Fully optimized contracted Gaussian basis sets for atoms Li to Kr. *J Chem Phys* 97:2571
140. Schäfer A, Huber C, Ahlrichs A (1993) Fully optimized contracted Gaussian basis sets of triple zeta valence quality for atoms Li to Kr. *J Chem Phys* 100:5829
141. Schirmer J (1982) Beyond the random-phase approximation: a new approximation scheme for the polarization propagator. *Phys Rev A* 26:2395
142. Hättig C (2005) Structure optimizations for excited states with correlated second-order methods: CC2 and ADC(2). *Adv Quantum Chem* 50:37
143. Jankowiak H-C, Stuber JL, Berger R (2007) Vibronic transitions in large molecular systems: rigorous prescreening conditions for Franck–Condon factors. *J Chem Phys* 127:234101
144. Harcourt RD, Scholes GD, Ghiggino KP (1994) Rate expressions for excitation transfer. II. Electronic considerations of direct and through-configuration exciton resonance interactions. *J Chem Phys* 101:10521
145. Scholes GD, Harcourt RD (1996) Configuration interaction and the theory of electronic factors in energy transfer and molecular exciton interactions. *J Chem Phys* 104:5054

# Structure Formation of Polymeric Building Blocks: Complex Polymer Architectures

**Kurt Binder, Hans-Jürgen Butt, George Floudas, Holger Frey, Hsiao-Ping Hsu, Katharina Landfester, Ute Kolb, Angelika Kühnle, Michael Maskos, Klaus Müllen, Wolfgang Paul, Manfred Schmidt, Hans Wolfgang Spiess, and Peter Virnau**

**Abstract** This chapter describes macromolecules with a complex structure, their defined aggregation in solution, their adsorption to surfaces, and their possible aggregation on surfaces. The term “complex structure” implies that the macromolecules show different, distinct structural elements or building blocks on a supra-atomic length scale. Key to understanding the complex structure of macromolecules, their aggregation, and adsorption to surfaces are intra- and intermolecular interactions such as van der Waals, electrostatic,  $\pi$ - $\pi$  interactions, and hydrogen bonds.

**Keywords** Biopolymers · Conformation · Copolymers · Cylindrical brush · Dendrimer · Liquid crystal · NMR spectroscopy · Organic electronics · Polyelectrolyte · Polymer · Self-assembly

---

K. Binder, H.-P. Hsu, and P. Virnau  
Institute of Physics, Johannes Gutenberg University, Mainz 55099, Germany

H.-J. Butt (✉), K. Landfester, K. Müllen, and H.W. Spiess  
Max Planck Institute for Polymer Research, Ackermannweg 10, Mainz 55128, Germany  
e-mail: [butt@mpip-mainz.mpg.de](mailto:butt@mpip-mainz.mpg.de)

G. Floudas  
Department of Physics, University of Ioannina, Ioannina 45110, Greece

H. Frey  
Institute of Organic Chemistry, Johannes Gutenberg University, Mainz 55099, Germany

U. Kolb, A. Kühnle, and M. Schmidt  
Institute for Physical Chemistry, Johannes Gutenberg University, Mainz 55099, Germany

M. Maskos  
Institute for Physical Chemistry, Johannes Gutenberg University, Mainz 55099, Germany  
Institut für Mikrotechnik Mainz IMM, Carl-Zeiss-Strasse 18-20, Mainz 55129, Germany

W. Paul  
Institute for Physics, Martin Luther Universität, Halle 06120, Germany

## Contents

1	Introduction .....	119
2	Polyphenylene Dendrimers .....	122
2.1	Introduction .....	122
2.2	Synthesis of PPDs .....	123
2.3	Dissociation of Charged PPDs and Ion Transport .....	124
2.4	PPDs as Light-Harvesting, Light-Emitting, and Photoswitchable Multichromophores .....	128
2.5	PPDs as Hosts and Drug Carriers .....	130
2.6	PPDs as Building Blocks for Self-Assembly .....	131
2.7	Conclusions .....	132
3	Cylindrical Brush Polymers .....	132
3.1	Introduction .....	132
3.2	Simulations of Single Brushes .....	133
3.3	Experiments on Individual Brushes .....	135
3.4	Intramolecular Phase Separation Within Cylindrical Copolymer Brushes with Incompatible Side Chains .....	142
3.5	Simulations of Cylindrical Bottlebrush Polymers .....	146
3.6	Complex Formation of Polymer Brushes .....	152
3.7	Complexes Formed in Between Polyelectrolytes in Aqueous Solution .....	156
3.8	Complex Formation Between Weakly Charged Polyelectrolytes in Organic Solvents .....	161
3.9	Adsorption to Surfaces .....	162
3.10	Conclusions .....	165
4	Supramolecular Structure Formation by Directed Interactions .....	165
4.1	Introduction .....	165
4.2	Solid-state NMR Techniques for Analyzing Structure and Dynamics .....	166
4.3	Self-Assembly and Dynamics of Polypeptides .....	168
4.4	Polymers with Different Building Blocks .....	170
4.5	Interplay of Undirected and Directed Interactions .....	171
4.6	Columnar Structures from Discotic Liquid Crystals .....	174
4.7	Conclusions .....	176
5	Block Copolymers and Confinement .....	176
5.1	Diblock Copolymers Confined in Miniemulsion Droplets .....	177
5.2	Junction-Point Reactive Block Copolymers for Surface Modification .....	183
5.3	Nanoparticles Confined in a Polymersome Shell Layer .....	188
5.4	Conclusion .....	193
6	Towards Synthesis on an Insulating Surface .....	194
6.1	Introduction .....	194
6.2	Proof of Concept: Dehalogenation and Covalent Coupling on an Insulating Surface .....	196
6.3	Towards Hierarchical Structure Formation: Exploring Two-Step Reactions .....	200
	References .....	202

## Abbreviations

$\alpha$	Degree of dissociation
$\delta$	Shell thickness of nanocapsule
$\epsilon$	Energy of interaction between monomers
$\lambda$	Wave length
$\eta$	Viscosity

$\nu$	Exponent characterizing end-to-end distance
$\rho$	Density of polymers or particles in solution
$\sigma$	Grafting density of side chains to backbone
$\chi$	Flory–Huggins interaction parameter
$\lambda_B$	Bjerrum length
$\sigma_{\text{calc}}$	Calculated conductivity
$\sigma_{\text{DC}}$	DC-conductivity of an ion-containing medium
$\sigma_{\text{exp}}$	Measured DC-conductivity
$D_{+}, D_{-}$	Calculated diffusion coefficient of the free cation/anion
$D_{+}^{\text{exp}}, D_{-}^{\text{exp}}$	Diffusion coefficient as measured by NMR
$\langle z_b \rangle$	Average distance of a backbone monomer of an adsorbed bottle brush from the surface
$\vec{A}_{\text{FM}}$	Atomic force microscopy
$\vec{l}_s$	Bond vectors are grafted to the backbone
BPCPPCA	2-(4-Bromophenyl)-6-(4-chlorophenyl)pyridine-4-carboxylic acid
BPDCA	Biphenyl-4,4'-dicarboxylic acid
BTA	Benzene-1,3,5-tricarboxamides
$d$	Exponent describing kinetics of aggregation
$D$	Diameter of drop
$D_0$	Diffusion coefficient of the neutral complex
DCBA	2,5-Dichloro benzoic acid
DEER	Double electron–electron resonance
$D_{\text{exp}}$	Experimental diffusion coefficient
DIBA	2,5-Diiodo benzoic acid
DISA	3,5-Diiodo salicylic acid
DLS	Dynamic light scattering
DMF	<i>N,N</i> -Dimethylformamide
DQNMNR	Double-quantum nuclear magnetic resonance spectroscopy
DS	Dielectric spectroscopy
DSC	Differential scanning calorimetry
$e_{\rightarrow}$	Elementary charge
$\vec{R}_{e,b}$	End-to-end vector of the backbone
$\vec{R}_e$	End-to-end vector of side chain
$\vec{l}_b$	Effective bond vectors of main chain
$E_C$	Coulomb attractive energy
EPR	Electron paramagnetic resonance
$E_{\sigma}$	Activation energy for ion transport
FCS	Fluorescence correlation spectroscopy
HBC	Hexa-peri-hexabenzocoronenes
$I$	Scattering intensity
IBA	4-Iodo benzoic acid
$k_B$	Boltzmann constant
$L$	Contour length
$L_0$	Thickness of block copolymer lamellar

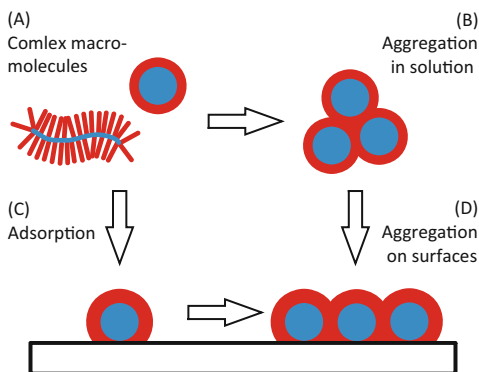
LC	Liquid crystalline
$l_d$	Domain size
LED	Light emitting diode
$l_k$	Kuhn length
$l_m$	Length per repeat unit of the main chain
$l_p$	Persistence length
$M_0$	Molar mass of one repeat unit in the main chain
MAO	Methylaluminoxanes
MAS	Magic angle spinning
MFA	Methyl formamide
$M_L$	Molar mass per length of main chain
$M_n^{sc}$	Number-average side chain molar mass
$M^{sc}$	Side chain molar mass
$N$	Degree of polymerization
$N_b$	Number of effective monomers in main chain
NICS	Nucleus independent chemical shift
NMR	Nuclear magnetic resonance
NOE	Nuclear Overhauser effect
$N_s$	Number of effective monomers in side chain
OPBA	Oligo( <i>p</i> -benzamides)
$P$	Main chain degree of polymerization
PAH	Polycyclic aromatic hydrocarbons
PAMAM	Poly(amido amine)
PBI	Perylene bisdiimide
PBLG	Poly( $\gamma$ -benzyl-L-glutamate)
PDI	Perylene diimide
PEG	Poly(ethylene glycol)
PEI	Poly(ethylene imine)
PEO	Poly(ethylene oxide)
$p_i$	Number density of the <i>i</i> th type of charge carrier
PLL	Poly-L-lysine
PLP	Poly(L-proline)
PMA	Polymethacrylate
PMMA	Poly(methyl methacrylate)
PPD	Polyphenylene dendrimer
$p_s$	Total ion concentration
PS	Polystyrene
$P_{sc}$	Side chain degree of polymerization
PSS	Poly(styrene sulfonate)
PVP	Poly-2-vinylpyridinium
$P_w$	Weight average degree of polymerization
$q$	Scattering vector
QD	Quantum dot
$q_i$	Charge of the <i>i</i> th type of charge carrier

$r_c$	Distance separating a point-like cation from a point-like anion
$R_c$	Core radius of a spherical brush
$R_{cs}$	Cross-sectional radius
$R_g$	Radius of gyration
$R_{gc}$	Cross-sectional radius of gyration of brush polymer
$R_h$	Hydrodynamic radius
$S$	Dynamic order parameter
$s$	Number of bonds along the backbone
SANS	Small angle neutron scattering
SAXS	Small-angle X-ray scattering
$s_{blob}$	Number of monomers per blob
SDS	Sodium dodecyl sulfate
SLS	Static light scattering
$T$	Temperature
$t$	Time
TBA <sup>+</sup>	Tetrabutylammonium cation
TEM	Transmission electron microscopy
$T_g$	Glass transition temperature
THF	Tetrahydrofuran
$T_\Theta$	Theta temperature
$W(r)$	Potential of mean force for two particles at distance $r$
WAXS	Wide-angle X-ray scattering
$x_{anion}$	Mole fraction of anionic charges
XPS	X-ray photoelectron spectroscopy
$Z^+/Z^-$	Charge ratio
$\epsilon_0$	Permittivity of free space
$\epsilon_r$	Dielectric permittivity
$\mu_i$	Mobility of the $i$ th type of charge carrier
$\sigma_0$	Limiting conductivity

## 1 Introduction

This chapter is organized according to the complexity of structure formation (Fig. 1) and along the dominating interactions. First we focus on van der Waals attraction, electrostatic interactions, and possible phase separations. They depend on distance but are not specifically oriented. When hydrogen bonds or  $\pi$ - $\pi$  interactions come into play, more complex macromolecular architectures are formed due to the directionality. Although phase separations are often driven by interactions including H-bonds (e.g., the phase separation between water and hydrocarbons), we have included them in the first part because the resulting supramolecular structures are not dominated by the orientation of the H-bonds. As a further “interaction” we include geometrical constraints. In the simplest case,

**Fig. 1** Overview of the topics in this chapter



such a constraint is formed by the adsorbing surface. As a real volumetric constraint we include the confinement of block copolymers to small spherical drops.

We start with two examples: polyphenylene dendrimers (PPDs) and linear brush polymers. Dendrimers (Sect. 2) are three-dimensional, mostly spherical macromolecules that are built around a core with multiple branching points. Among this intensively studied class of polymers, PPDs are distinguished because they are shape-persistent due to the stiffness of the polyphenylene arms and their steric interactions. Herein, PPDs with widely different functions, caused by different chemical groups at their surface, in their scaffold, and in their core, are described. Since PPDs are perfectly monodisperse and possess a defined shape, they are ideal for addressing fundamental questions of polymer science. One example is the charging of PPDs in organic liquids. Embedding an ionic core in a nonpolar PPD shell immediately highlights the dissociation of ion pairs in nonpolar liquids: how does the degree of dissociation depend on the size of the ions and the dielectric permittivity of the solvent? As examples for functionality, two classes of PPDs are described: first, PPDs as light harvesting, light-emitting, and photoswitchable multichromophores and second, by designing the interior and surface solution properties, PPDs as hosts for specific molecules and as carriers and for drug transport.

As a second example cylindrical brush polymers, often called bottle brushes, are described (Sect. 3). Cylindrical brush polymers usually consist of a flexible main chain, densely grafted by flexible, stiff or dendritically branched side chains. The latter are known as dendronized polymers and have been frequently investigated by both theory and experiment. In the present review, we focus on brush polymers with linear side chains.

The main conformation of cylindrical brush polymers is governed by two opposing forces: The steric repulsion of the densely grafted side chains leads to stretching of the side chains and of the main chain, whereas the entropy elasticity causes both main and side chains to adopt a coiled conformation. Thus, the shape of cylindrical brush polymers emerges from a subtle balance of repulsive and entropic forces. In more detail, the directional persistence of the main chain is primarily governed by the grafting density, the length and the solvent quality of the side chains, as well as by the electrostatic interaction in the case of charged side chains. Bottle brushes have been analyzed experimentally, theoretically, and by simulations.

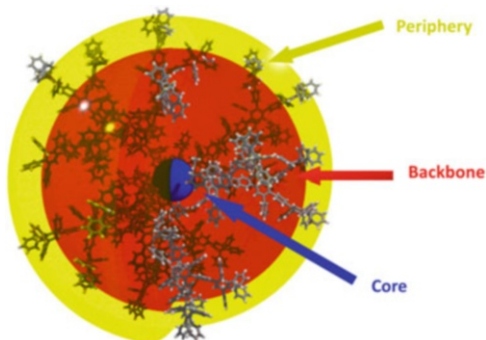
More specific and oriented interactions, such as hydrogen bonds and shape-dependent  $\pi$ - $\pi$  interactions offer the possibility to control supramolecular organization in a much more defined way. This is exemplified in Sect. 4. In fact, the same interactions that dominate the shape of complex macromolecules are also responsible for the formation of defined aggregates and for the adsorption to surfaces. They govern self-assembly at the two levels: the internal structure of the building blocks and the self-assembly of the building blocks. In a simplified manner, the first role can be viewed as “intramolecular” and the second role as “intermolecular”. These intra- and intermolecular roles of different interactions are discussed for all types of macromolecules.

Another type of “interaction” is confinement. We focus on the confinement of block copolymers and the resulting microphase separation. As one example, the structure of polystyrene-*block*-poly(methyl methacrylate) (PS-*b*-PMMA) in the confinement of droplets in miniemulsions is described. To better understand microphase separation, experimental results are compared to self-consistent field theory simulations. Then, we consider block copolymers bound to a solid surfaces and their response to different environmental conditions (Sect. 5). As a third example of structures and confinement, the incorporation of quantum dots into the hydrophobic region of polymersomes is demonstrated.

In the last section (Sect. 6) we focus on molecules adsorbed to surfaces. Creating complex polymer architectures on surfaces is important for applications such as (bio)sensors and molecular electronics. However, molecular self-assembly usually relies on weak, reversible interactions leading to inherently fragile structures. To provide stability as well as enhanced electron transport properties we explore the possibility of creating covalently linked molecular structures on bulk insulator surfaces.

In order to better understand the structure and dynamics of polymers, the formation of complex architectures, and to further improve the function of a specific material, a whole range of complementary characterization techniques was required. For example, complex formation of polyelectrolytes has been studied intensely with light and small angle neutron scattering (SANS). Techniques were not only applied but also improved and new techniques have been developed. One example is solid-state NMR. NMR not only yields information on the atomic structure but also provides dynamic information. Typically, NMR results are complemented by wide and small angle X-ray scattering (WAXS and SAXS, respectively) and computer simulations. Another example is high-resolution atomic force microscopy (AFM). In recent years non-contact AFM has been developed, which allows imaging of crystalline structures and defects at the atomic level. So far, however, most studies have been limited to comparatively small organic molecules deposited under well-controlled ultrahigh vacuum conditions. Therefore, the technique is constantly being further developed to extend it to “soft” organic materials and to “real” environments such as in liquids.

**Fig. 2** Representation of polyphenylene dendrimers (PPDs) with functional groups in the core, scaffold, and on the rim



## 2 Polyphenylene Dendrimers

### 2.1 Introduction

One of the key features in the synthesis of semirigid macromolecules such as dendrimers is to keep the entropy price low in all kinds of hierarchical structure formation. Dendrimers as unique macromolecules with three-dimensional (3D) shape have found multiple applications [1]. However, in spite of their multifunctional character and their remarkable aesthetic appeal [2], there remain conceptual and experimental problems: How perfectly can they be synthesized [3, 4] and are they really spherical? Many dendrimers described in the literature are not shape-persistent because they are made from conformationally flexible building blocks [5, 6]. They change their shape under the influence of external forces or the prevailing environment. Polyphenylene dendrimers (PPDs) [7–9] introduced here adopt a special role because they (1) possess a high degree of structural perfection, (2) are extremely stable even under harsh conditions, and (3) determine a perfect nanosite definition for active groups either in the core, in the scaffold, or on the rim (Fig. 2) [10]. Examples of such active groups are chromophores, catalysts, and electrolyte functions.

The design principle for PPDs is the build-up from twisted, tightly packed benzene rings. Slight liberation of these rings causes some entropy gain upon solvation, so that the dendrimers become soluble. Solubility can even increase from generation to generation. On the other hand, the phenylene arms of the dendrons cannot undergo back-bending. This is what makes these 3D objects shape-persistent [11].

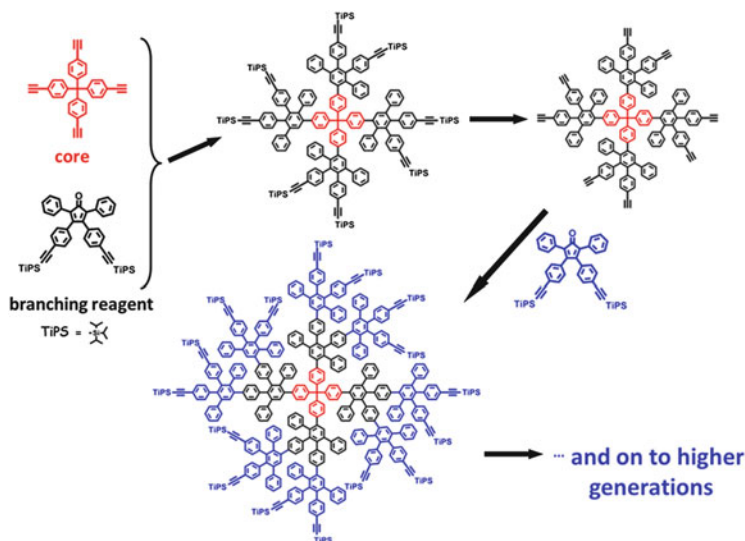


**Fig. 3** Synthesis of PPDs via the divergent route using a protected AB<sub>2</sub>-branching segment and a tetraphenyl methane core

## 2.2 Synthesis of PPDs

We have succeeded in divergent growth [12] from generation to generation up to nine generations (G<sub>9</sub>) [13, 14]. The synthetic breakthrough depended upon the use of AB<sub>2</sub> and AB<sub>4</sub> branching reagents, which comprise both a diene and two or four, respectively, ethynyls as dienophile units for repetitive Diels–Alder cycloaddition (Fig. 3). The dienophiles are blocked by attachment of bulky tri-isopropylsilyl groups [15].

Thus, when the branching reagents are heated together with any multi-ethynyl-substituted core molecule, cycloaddition upon extrusion of carbon monoxide occurs and pentaphenyl benzene moieties are formed. The number of surface ethynyl functions is thus doubled when going to the next generation with the branching reagent. It is the use of multiple irreversible Diels–Alder reactions that leads to a high degree of structural perfection in dendrimer synthesis, a structural perfection so far not reached by other dendrimers. We have verified the structural perfection of PPDs with molecular weights of 1.8 MDa and diameters in excess of 30 nm (Fig. 4). Gel permeation chromatography (GPC), mass spectrometry (MS), and NMR spectroscopy are combined to give a unified view of polymer characterization. Apart from this synthetic achievement, and the importance of this work for precision polymer synthesis in general, there is the additional opportunity of functionalizing the PPDs either inside or outside. The perfect nanosite definition mentioned above proves its value upon incorporation of different functions [7].

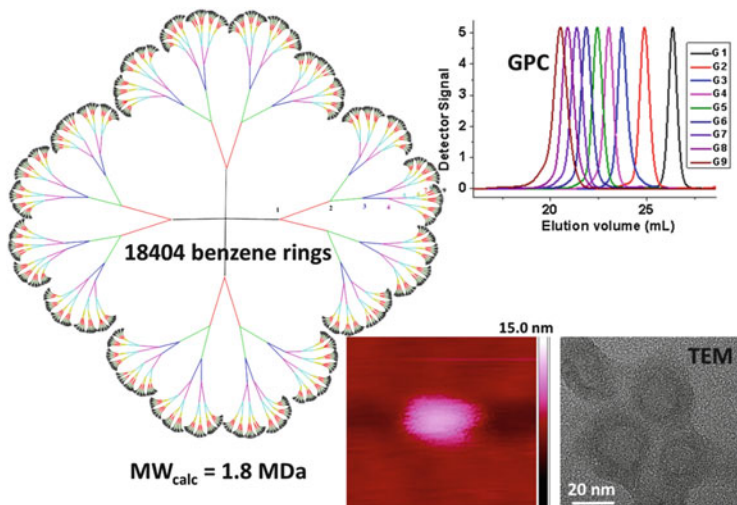


Fig. 4 Structure, GPC chromatograms, and AFM and TEM images of the G9 PPD

### 2.3 Dissociation of Charged PPDs and Ion Transport

What is particularly challenging and what also defines a tight connection with bottle brush polymers is the incorporation of electrolyte functions. Loading charges on the surface of the dendrimer, e.g., via sulfonate groups, can make a nonpolar polymer water soluble. The same can be achieved by core-shell synthesis when polyacrylate or polylysine chains are grafted from the surface of the dendrimer [16–19]. What is particularly useful for grafting by controlled radical polymerization is that one can perfectly control the number of initiator groups and thus the number of resulting arms [16]. Since these PPDs are water-soluble their ability to cross cellular membranes can be studied (Sect. 2.5).

Alternatively, a single charge, for example in the form of a borate anion [20] or a phosphonium cation, can be placed in the core of the dendrimer. This furnishes organosoluble salts, whereby the ion inside the rigid capsule is spatially separated from the counterion. It is clear that these objects open new pathways in polyelectrolyte studies, for example, by dielectric spectroscopy. More specifically, there is now a chance to independently study dissociation and ion mobility as a function of ion size [21] (Fig. 5). Dissociable, shape-persistent dendrimers allow the analysis of the fundamental question of how charges arise in nonpolar liquids.

In nonpolar solvents, ion dissociation is hindered because of the Coulomb attractive energy [22], which for two monovalent charges is:

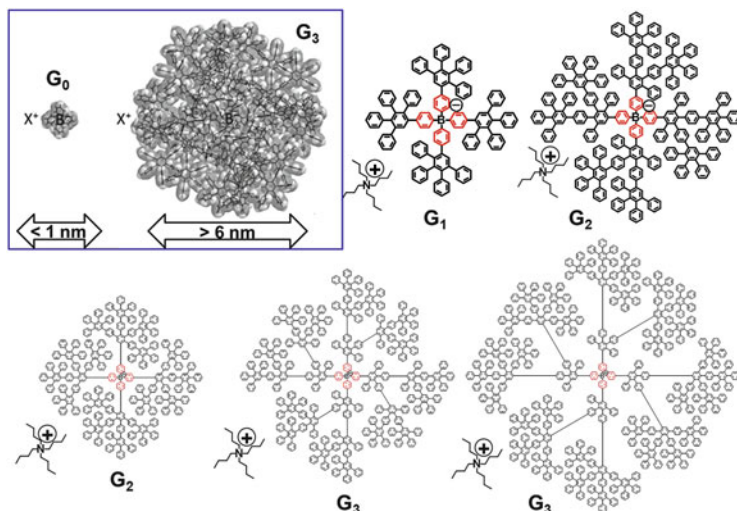


**Fig. 5** Increasing size of tetraphenylborate anions via dendronization with polyphenylenes.  $G_1$ ,  $G_2$ ,  $G_3$  first, second, and third generation, respectively

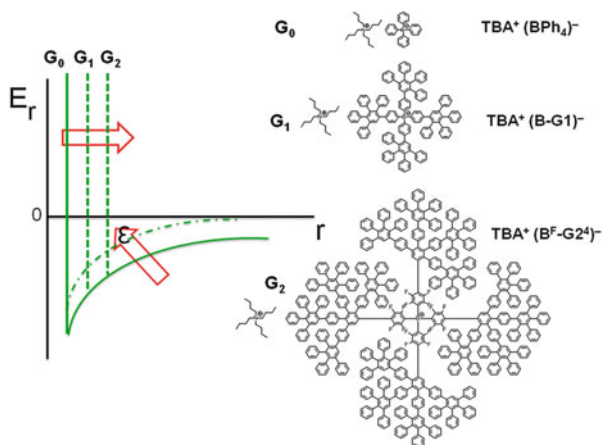
$$E_C = \frac{e^2}{4\pi\epsilon_0\epsilon_r r_c} \quad (1)$$

Here,  $e$  is the elementary charge,  $\epsilon_0$  is the permittivity of free space,  $r_c$  is the distance separating a point-like cation from a point-like anion and  $\epsilon_r$  is the dielectric permittivity of the surrounding medium. The “escape distance” from the Coulomb energy is set by the Bjerrum length,  $\lambda_B = e^2/4\pi\epsilon_0\epsilon_r k_B T$ , giving the characteristic separation between two ions at which Coulombic interactions are balanced by the thermal energy. Here,  $k_B$  is the Boltzmann constant and  $T$  the temperature. In liquids of low polarity, such as toluene or even tetrahydrofuran (THF), the Bjerrum length is 20.4 and 7.4 nm, respectively. Ion dissociation in such solvents is limited unless the ion size approaches the escape distance set by  $\lambda_B$ .

Figure 6 schematically describes the effect of solvent polarity and ion size on the Coulomb potential. It shows that increasing the dielectric permittivity of the solvent raises the attractive part of the potential, making the potential less attractive and facilitating ion dissociation. On the other hand, increasing the ionic size effectively shifts the repulsive part of the potential to length scales that approach the Bjerrum length promoting ion separation. With respect to electric conductivity and charge transport, one has to take into account the balance between ion dissociation (promoted by the bulky ions) and mobility (inhibited by the large ions). With respect to the latter, extensive research on increasing the size and bulkiness of molecular anions has led to a new class of compounds known as weakly coordinating anions [23].

With the recent synthesis of ionic dendrimers (Fig. 6) [20] a number of large and rigid molecular ions with dimensions approaching the Bjerrum length in nonpolar

**Fig. 6** *Left:* Effective Coulomb energy (solid line) showing the effect of increasing dielectric permittivity of the medium (dashed-dotted line) and the effect of increasing the anion size (dashed lines). *Right:* Dendritic molecules as a function of the anion generation. All molecules share the same cation, i.e., TBA<sup>+</sup>



solvents have become available. In addition to the increase in anion size, another approach emphasized the effect of delocalization of the anion charge [21]. It is thought that the spreading of the anion charge to a larger area is responsible for the weaker coordination. However, it is still unknown how the large size, shape, and selective anion functionalization with fluoro-substituted phenylene groups at the anion core and dendritic corona affect the dissociation and eventually the transport properties of ions. To study ion transport, dielectric spectroscopy is the method of choice because of its inherent ability to provide both the degree of ion dissociation and the transport properties through the measured DC conductivity. Herein we report on the ion dissociation and transport properties of a series of tetrabutylammonium salts (TBA<sup>+</sup>) of rigidly dendronized anions with various sizes (with diameters up to 5 nm) in solution and as a function of the solvent polarity [21].

The DC conductivity of an ion-containing medium is expressed as the sum of the individual contributions of all charge carriers,  $\sigma_{\text{DC}} = \sum_{i=1}^n p_i \mu_i q_i$ . Here,  $p_i$ ,  $\mu_i$ , and  $q_i$  are the number density, the mobility, and the charge of the  $i$ th type of charge carrier, respectively. An underlying assumption is that all charge carriers move independently of each other with a constant mobility. In the present case there are two monovalent charge carriers, i.e., the cations (TBA<sup>+</sup>) and respective anions. Therefore, the DC conductivity of the fully dissociated ions can be expressed as  $\sigma_{\text{DC}} = p_+ \mu_+ e + p_- \mu_- e$ . Measured DC conductivities (with values of  $\approx 10^{-5}$  S/cm) for the different dendrimers in THF conform to  $\sigma_{\text{DC}} = \sigma_0 \exp(-E_\sigma/k_B T)$ , where  $\sigma_0$  is the limiting conductivity and  $E_\sigma$  is the activation energy for ion transport. Furthermore, a linear concentration dependence of the DC conductivity was found, which implies an increasing number of mobile charge carriers at a fixed degree of ion dissociation. The degree of ion dissociation can be extracted from the ratio of the measured DC conductivity  $\sigma_{\text{exp}}$  and the calculated conductivity  $\sigma_{\text{calc}}$  that assumes complete ion dissociation as  $\alpha = \sigma_{\text{exp}}/\sigma_{\text{calc}}$ , also known as the Haven ratio [24]. The denominator can be calculated from the mobility,  $\mu_i = e/6\pi\eta r_i$ :

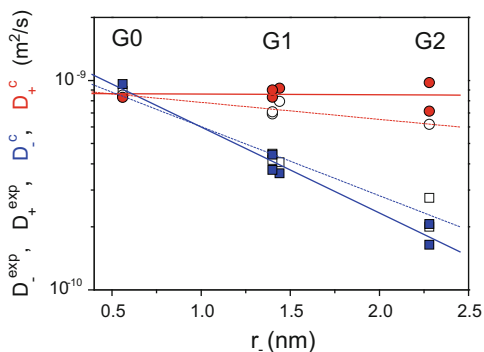


**Fig. 7** NMR anion ( $D_{-}^{\text{exp}}$ , open squares) and cation ( $D_{+}^{\text{exp}}$ , open black circles) diffusion coefficients plotted for the different generations (G0, G1, and G2) as a function of the anion size. The calculated anion ( $D_{-}^{\text{c}}$ , filled blue squares) and cation ( $D_{+}^{\text{c}}$ , filled red circles) diffusion coefficients corresponding to free ions are also plotted for comparison. The solid and dashed lines through the calculated and measured data, respectively, are guides for the eye

$$\sigma_{\text{calc}} = \frac{p_s^e}{6\pi\eta} \left[ \frac{1}{r^+} + \frac{1}{r^-} \right] \quad (2)$$

Here,  $\eta$  is the viscosity of the surrounding liquid,  $r^{+/-}$  are the ionic radii, and  $p_s$  is the total ion concentration from the stoichiometry. The measured DC conductivity differs from the calculated conductivity because the paired charges do not contribute to the current.

Further information is provided by diffusion-ordered spectroscopy (DOSY)-NMR. With DOSY-NMR the diffusion coefficient,  $D_{\text{exp}}$ , can be measured. The measured diffusion coefficients, however, are not the diffusion coefficients of the free ions. They represent some average of the fully dissociated and paired states. Nevertheless, knowledge of the measured (NMR) diffusion coefficients together with the degree of ion dissociation allows calculation of the diffusion coefficients of the free ions [21].

Figure 7 compares the measured and calculated diffusion coefficients for different anion sizes and generations at 25°C. The NMR diffusion coefficients underestimate/overestimate the respective cation/anion diffusion coefficients with regard to the free ions. However, when coupled with independent conductivity measurements they result in the transport properties of the unassociated species.

Ion dissociation is promoted by fluoro-substitution away from the boron position in the corona. This shows that the reduction of the electrostatic interactions is more effective in producing weakly coordinating anions than the mere delocalization of the anion charge produced by fluorination of the core. In the absence of fluoro-substitution, steric effects gain importance and result in a higher dissociation.

Charging of PPDs in nonpolar solvents is not only interesting from the fundamental physics point of view. On the chemical side, the encapsulation of a borate anion leads to so-called weakly coordinating anions [23, 25]. In many

chemical reactions, including dissociation and solvolysis, one is interested in weak anion–cation interactions [20]. A well-known case is metallocene-catalyzed olefin polymerization, where chain growth occurs at a zirconocenium cation. The necessary counteranion should only weakly interact with the extremely sensitive catalyst center and this is why methylaluminumoxanes (MAO) as anionic species without nucleophilic power have become so important. Huge excesses of MAO are often applied and this has prompted the use of tetraphenylborate as stoichiometrically applied counterions. It is clear that our dendritic borates are much larger, giving the possibility to leave the positively charged catalyst as unperturbed as possible during polyolefin synthesis.

#### **2.4 PPDs as Light-Harvesting, Light-Emitting, and Photoswitchable Multichromophores**

Rylene dyes can be tuned so that absorption and emission cover the whole spectrum of visible light and extend far into the near infrared. It is then logical to incorporate these dyes at the core, in the scaffold, or on the rim of a PPD [26–28]. In that way, one can precisely control the steric and electronic conditions for a Förster resonant energy transfer and for light-induced electron transfer. The resulting dendrimers are unique multichromophoric light-harvesting systems [29–32] and have become important objects, even for single molecule spectroscopy [33–35]. Using, for example, a perylene-3,4,9,10-tetracarboxylic diimide chromophore as a core, one obtains nanosized emitters with constant fluorescence wavelength, but increasing diameter. These dyes have served as probes for studying the dynamics of solid polymers by defocused widefield imaging. Another good case can be made for using PPDs as active components of light-emitting diodes (LEDs). A well-known troublesome problem is to match the concentration of holes and electrons and to keep the recombination zone away from the electrode. This is normally accomplished by complex multilayer devices. The dendrimers, in a sense, also represent a layer-by-layer design, but now with molecular precision. More specifically, we have synthesized PPDs with a triphenylamine-based hole-capturing layer on the surface [36], an inner layer of triphenylenes where excitons are formed upon charge recombination, and a central core of pyrene that removes the excitons from the area of charge recombination by a rapid energy transfer (Fig. 8) [37]. The light is finally emitted from the inner core. The advantages of this design in terms of device stability and efficiency define a topic of future research.

An additional challenge appears when multiple azobenzenes are introduced into otherwise rigid scaffolds and PPDs thus become stimulus-responsive, molecularly defined nanoparticles [38, 39]. One might argue that incorporation of azobenzenes into polymers or polymer nanoparticles is a well-known concept for changing structures (Fig. 9).

When combined with the rigid PPDs, however, this seemingly conventional method proves of special value. Only two examples will be mentioned. Light-induced transition from the *trans*- to the *cis*-isomer of the dendronized borate anion

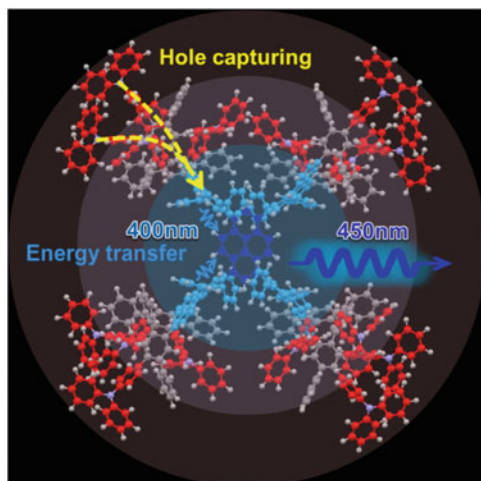


**Fig. 8** Dendrimer for light-emitting diodes. Design of a PPD incorporating triphenylamines, triphenylene, and pyrene in defined positions

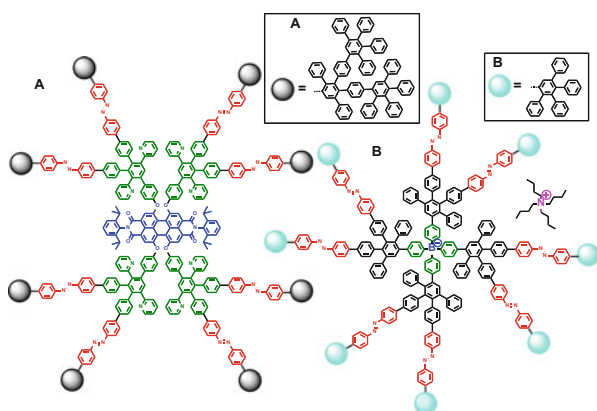


**Fig. 9** PPDs with inserted azobenzene units and different cores: (a) perylendiimide, (b) borate

(Fig. 10a) changes the size of the 3D molecule with high precision. This affects the transport through porous materials. More importantly, the ion conductivity of such salts now becomes photoswitchable. Another case is the related structure with a perylenediimide core. Figure 10b illustrates that the space inside the dendrimer is suitable for the uptake of guest molecules. After forming the *cis*-isomer, the guest molecule is firmly entrapped and can only be released upon back-isomerization to the *trans*-isomer. It is tempting to think of such PPDs as vehicles carrying a payload of drugs, but now with the additional advantage of controlled uptake and release.

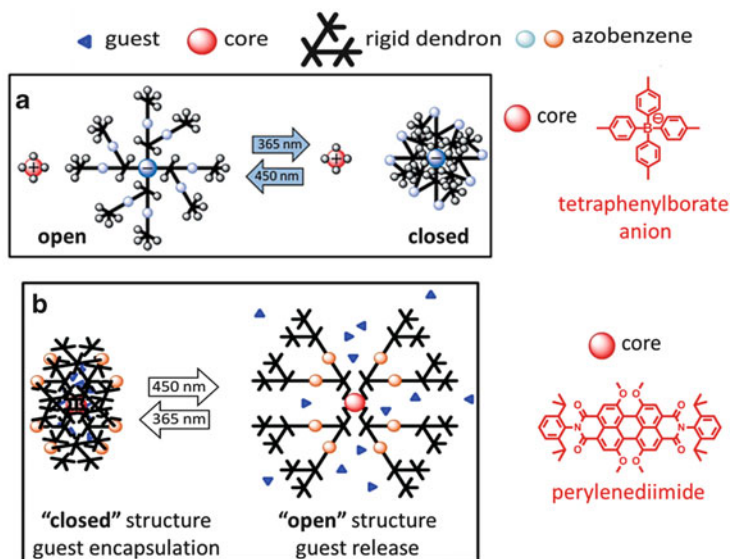
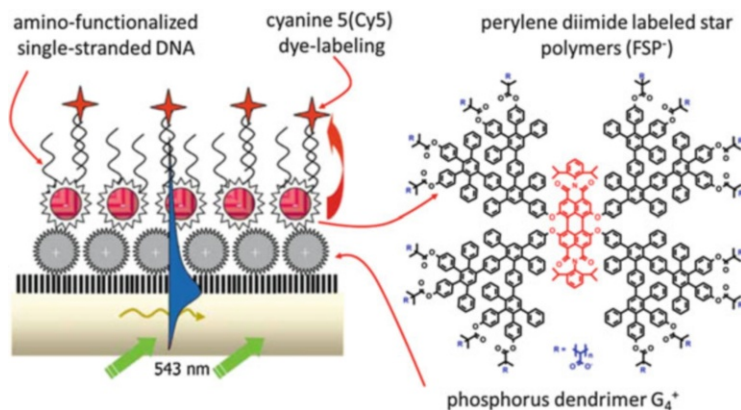


Fig. 10 PPDs with photoswitchable structures

## 2.5 PPDs as Hosts and Drug Carriers

Another example of designing the interior for suitable guest-uptake is the use of the dendrimers as receptors for analyzing vapors and for sensing of guest molecules [40–42]. Thus, hazardous explosives [43] such as triacetone triperoxide, which has been used in terroristic attacks, can be trapped with high sensitivity and selectivity and can be detected by an ultra-microbalance that carries the dendrimer on its tip. Indeed, the limit of detection has now reached the picogram range. A challenging task is to understand the steric (size and nature of the voids) and electronic (incorporation of pyridine and imidazole units for activating charge-transfer interactions or hydrogen bonding with the guest) conditions and use this as a guideline for improved receptor design. There are many other useful applications of the PPDs as host or encapsulating species [44, 45] whose detailed description is beyond the scope of this text. One example is the growth of metal nanoparticles inside the rigid dendrimer by reduction of metal salts, thus preventing the particles from undesirable aggregation.

The PPDs thus create a perfect nanoenvironment with increasingly complex function. Admittedly, they define enormous tasks for precision polymer synthesis, but if really sophisticated function is targeted it is worthwhile to take on this challenge in view of the wealth of otherwise inaccessible chemical, physical, and biological properties [10, 46]. Further, there is much to learn when comparing multifunctional dendrimers based upon covalent build-up, with assemblies depending upon weak intermolecular forces. This is indeed another benefit of the structural perfection of the PPDs, that they also allow the fabrication of increasingly complex supramolecular structures.



**Fig. 11** Representation of a DNA biosensor prepared via layer-by-layer deposition of positively and negatively charged dendrimers

## 2.6 PPDs as Building Blocks for Self-Assembly

The PPDs can, indeed, serve as building blocks for assembly processes. Long fibers are obtained when their solutions are cast on substrate surfaces [47–49]. Here again, the shape-persistence of PPDs proves of special value because the extended arms can interdigitate, activate  $\pi$ - $\pi$  interactions between benzene rings, and thus lead to a directional growth of the fibers. There are various ways to further control these self-assembly processes: by alkyl groups or electrolyte functions on the dendrimer surfaces [50] even including desymmetrization by forming amphiphilic Janus-type particles, by introduction of perfluorobenzenes into the interior, or by applying additional templating effects of the surfaces. Different, but equally powerful, cases of assembly processes are the formation of films for highly sensitive DNA detection via layer-by-layer deposition of PPDs (Fig. 11) with oppositely charged surfaces, or cell nucleus staining utilizing electrolyte–electrolyte interactions with histones [51–53].

Although the role of PPDs for cell uptake and drug delivery [16, 54, 55] has already been mentioned, it is important to stress the three key advantages in this regard: (1) the creation of perfect cavities for host–guest interactions, (2) the incorporation of fluorophores at defined positions for monitoring uptake experiments by fluorescence microscopies, and (3) the modification of the dendrimer surface for both water-solubility and transport through membranes [56]. With this in mind, an even more complex design should be introduced. The surface of a dendrimer is again equipped with electrolyte functions for water solubility, but now patches of polar and unipolar domains are formed. It is clear that the shape-persistence of the scaffold proves of key importance for defining the patches. Indeed, the cell uptake of such PPDs has been shown promising for doxorubicin delivery [57]. Even more, the holy grail of delivery experiments has been approached by looking at epithelial cells and, remarkably enough, transport through the blood–brain-barrier could be accomplished. It is not remote to thus

consider the “patched” PPDs as synthetic substitutes of transport proteins, which are also characterized by polar and unipolar surfaces areas of varying size [58].

Dendrimers are without doubt a unique case of 3D macromolecules. In this class, PPDs stand out because of the rigidity of the dendrons, which excludes back-bending. This leads to a pronounced rigidity of the shape, which can be further controlled by choice of the core and the branching points.

## 2.7 Conclusions

This brief overview illustrates that PPDs (1) are a challenging case of precision macromolecular synthesis; (2) define ample questions for supramolecular studies such as guest uptake, aggregation in solution, and controlled deposition on surfaces; (3) stimulate many functional investigations into sensing and optoelectronics, cell biology, and nanomedicine; and (4), as justified above, are suited for the fabrication of real devices such as ultrastable LEDs. In the meantime, a firm dendrimer community has been established for which the function of these macromolecules stands in the foreground. It is, indeed, worthwhile to push the limits of complex dendrimer functions even if polymer nanoparticles or hyperbranched polymers are sometimes claimed to do the same job, but at lower cost. In any case, PPDs are unique among the dendrimers due to their structural perfection, stability, and shape-persistence.

## 3 Cylindrical Brush Polymers

### 3.1 Introduction

Like the PPDs, cylindrical brush polymers owe their properties to a very special macromolecular design. Attaching many side chains to a polymer backbone is another way of creating a spatially defined rigidity. The length and grafting density of the side chains on a polymer backbone has a profound and tunable influence on the structure and dynamics of the macromolecules. A further option is to introduce ionic charges on the side chains, leading to novel polyelectrolyte structures. PPDs and cylindrical brush polymers, special examples of unconventional polymer topologies, thus jointly offer two challenging possibilities: studying intra- and intermolecular structural changes in cases of controllable rigidity and gaining insight into unprecedented polyelectrolytes.

Bottlebrush polymers contain a long flexible macromolecule as a backbone to which side chains, which may also be flexible, are grafted [59, 60]. The idea then is that via suitable choices of parameters such as the grafting density, solvent quality, and side chain molecular weight the local stiffness of this cylindrical molecular brush can be controlled. The qualitative picture one draws is that of a wormlike

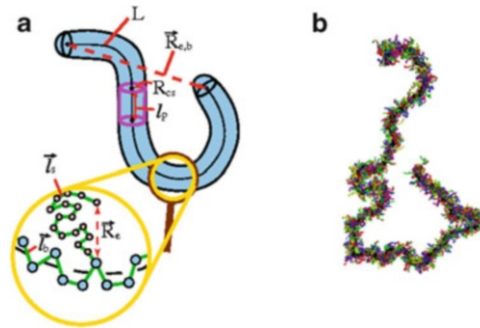


**Fig. 12** (a) Explanation of the multiple length scales for molecular bottle brush polymers. A coarse-grained continuum description depicts the polymer as a flexible spherocylinder with a cross-sectional radius  $R_{cs}$  and a contour length  $L$  along the axis of the coarse-grained cylinder, which is straight over a length  $l_p$ , the persistence length. A less coarse view (*lower* part of the figure) depicts the backbone as a self-avoiding walk of  $N_b$  effective monomers (subscript  $b$  indicates the backbone) connected by effective bond vectors  $\vec{l}_b$ . Side chains with  $N_s$  effective monomers and bond vectors  $\vec{l}_s$  are grafted to the backbone with grafting density  $\sigma$ . End-to-end vectors of the backbone  $\vec{R}_{e,b}$  and a side chain  $\vec{R}_e$  are also indicated. (b) Snapshot of a typical conformation of a simulated bottle brush polymer, using the athermal bond fluctuation model, with  $N_b = 1,027$ ,  $N_s = 24$ , and very good solvent conditions. From Hsu et al. [61]

chain, described by effective parameters such as the contour length  $L_{cc}$  of the backbone chain, the persistence length  $l_p$ , and the cross-sectional radius  $R_{cs}$  (Fig. 12) [61]. But, the quantitative understanding of this picture has been rather controversial: scaling relations for the dependence of these parameters on the degree of polymerization  $N_s$  of the side chains were proposed (e.g. [62]), which turned out at variance with both experiments (e.g., [63]) and simulations (e.g., [64]); moreover, results from experiments on the persistence length of brushes having chemically similar (or even identical) structures disagreed with each other [63].

### 3.2 Simulations of Single Brushes

Getting this information experimentally is difficult [63] because one needs to do scattering experiments over a range of several decades of scattering wave number, and this has to be done under extremely dilute conditions (see Sect. 3.3 for experiments). However, the simulations [61, 64–66] revealed that the problem is more subtle, simply because the notion of persistence length is well-defined only for semiflexible Gaussian chains [66]. For polymers under good solvent conditions, the applicability of the Gaussian chain statistics (that is also implied by the Kratky–Porod model of wormlike chains [67]), which rather generally is taken to

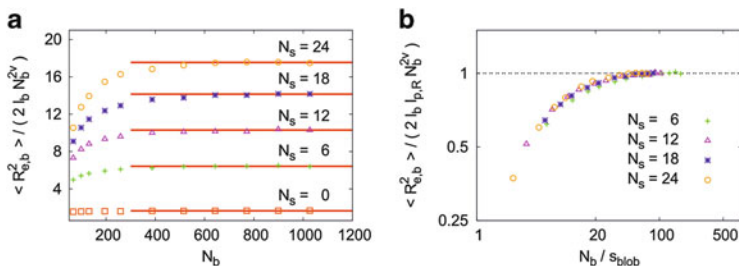


**Fig. 13** (a) Rescaled mean-square end-to-end distance  $\langle R_{e,b}^2 \rangle / (2 l_b N_b^{2\nu})$ ,  $\nu \approx 0.588$ , of the bottle brush polymer under good solvent condition plotted for grafting density  $\sigma = 1$  and several choices of the side chain length  $N_s$ . (b) Rescaled mean-square end-to-end distance, taking the straight line ordinate values from the left plot as ordinate unit, and rescaling the backbone chain length  $N_b$  with the number of monomers per blob  $s_{\text{blob}}$ , as described in the main text. From [61]

be the “gold standard” for stiff polymers [68], is rather restricted. So it turns out that the exponential decay of the bond autocorrelation function  $\langle \cos(\theta(s)) \rangle$  for bonds along the backbone  $s$  steps of length  $l_b$  apart,  $\langle \cos(\theta(s)) \rangle \sim \exp(-s l_b / l_p)$ , is delicate. Such an exponential decay can only be found for a rather small number of steps [66],  $s < l_p / l_b$ , but is not asymptotically for  $s \rightarrow \infty$ , where the decay always follows a power law  $\langle \cos(\theta(s)) \rangle \propto s^{-\beta}$  with  $\beta = 2 - 2\nu \approx 0.824$  under good solvent conditions but  $\beta = 3/2$  for theta solvents [66]. A Gaussian behavior (as predicted by the Kratky–Porod model) occurs only for polymers in 3D space that are both very stiff and very thin, namely for the contour lengths  $L$  in the range  $l_p \ll L \ll (l_p / R_{cs})^2 l_p$  [70]. Only in this regime (and in the rather trivial regime  $L < l_p$ , where the polymer resembles a rigid rod of length  $l_p$ ) would the Kratky–Porod model be applicable. As we shall see below, for bottlebrush polymers the persistence length ( $l_p$ ) is not very much larger than their cross-sectional radius ( $R_{cs}$ ), and then the Kratky–Porod model fails.

However, for bottlebrush polymers where the backbone chain and the arms are flexible, the chain stiffness is a consequence of chain thickness. The simulations give rather clear evidence [61, 66, 70] that the chains do get stiffer with increasing chain lengths of the side chains (Fig. 13a). However, there is a monotonic increase of the mean square end-to-end distance of the backbone with backbone chain length  $N_b$ , from the rod-like behavior at small  $N_b$ , where we find  $\langle R_{e,b}^2 \rangle / N_b^{2\nu} \propto N_b^{2-2\nu} \approx N_b^{0.824}$  (since rods scale as  $\langle R_{e,b}^2 \rangle \propto N_b^2$ ), to coils swollen by the excluded volume forces  $\langle R_{e,b}^2 \rangle \propto N_b^{2\nu}$  with  $\nu \approx 0.588$  [68]; hence, for  $\langle R_{e,b}^2 \rangle / N_b^{2\nu}$  horizontal plateaus result, as is evident from the data.

It turns out that there is a simple rescaling possible, by which all curves superimpose (at least approximately) on a master curve (Fig. 13b):  $N_b$  is rescaled by  $s_{\text{blob}}$ , the number of monomers per blob, motivated by the idea that the bottlebrush polymer is viewed as a pearl-necklace chain of blobs, the blob radius being the cross-sectional radius of the cylindrical brush. From this condition,  $s_{\text{blob}}$  is easily derived numerically from the simulation data.

It was also found [69] that in two dimensions (relevant for strongly adsorbed semiflexible polymers), excluded volume effects are much stronger than in three dimensions. This is not just because the exponent  $\nu$  in the relation  $\langle R_{e,b}^2 \rangle \propto N_b^{2\nu}$ ,  $\nu = 3/4$  [68] differs more strongly from the Gaussian value  $\nu = 1/2$  than the value  $\nu = 0.59$  in three dimensions. As mentioned above, for very stiff and thin polymers in three dimensions, a regime of Gaussian behavior occurs for chains of intermediate length, in between the rod regime (for short chains) and the self-avoiding walk regime (for long chains). In two dimensions, however, there is never a Gaussian regime intermediate between the rod regime ( $\langle R_{e,b}^2 \rangle \sim N_b^2$ ) and the swollen coil regime ( $\langle R_{e,b}^2 \rangle \sim N_b^{2\nu} = N_b^{3/2}$ ), rather the two regimes join smoothly for  $N_b l_b = l_p$ . It is also interesting to note that for a given energy of local bond bending, the persistence length  $l_p$  depends distinctly on the conditions in which the polymer exists: for an adsorbed stiff thin chain,  $l_p$  is about 2.4 times larger than when the same chain is not yet adsorbed. Also, the solvent conditions matter and this has been demonstrated by a simulation [71] of a bead-spring model of a bottlebrush polymer, comparing good solvent conditions (a temperature about 30% higher than the Theta temperature) with Theta conditions. At the Theta temperature, the persistence length is smaller, as expected, because the cross-sectional radius is also smaller.

### 3.3 Experiments on Individual Brushes

The main conformation of cylindrical brush polymers is governed by two opposing forces: The steric repulsion of the densely grafted side chains leads to stretching of the side chains and of the main chain, whereas the entropy elasticity causes both main and side chains to adopt a coiled conformation. In the case of rigid side chains, the arguments above apply to the main chain only. Rigid side chains were investigated by analytical theory as well as by simulations, but experimental data are rare (see below). An increase in main chain stiffness with the length of the side chains was one major goal of experimental investigations. Usually, the Kratky–Porod wormlike chain model is applied to fit experimental data such as form factors, dimensions such as the radius of gyration ( $R_g$ ) and the hydrodynamic radius ( $R_h$ ), and intrinsic viscosities. For a reliable application of the wormlike chain model, the contour length,  $L$ , needs to be known. Typically  $L = l_m P$ , with  $P$  being the (main chain) degree of polymerization and  $l_m$  the length per repeat unit. For vinyl main chains,  $l_m = 0.25$  nm. There was considerable discussion about whether  $l_m = 0.25$  nm also applies to cylindrical brush polymers, because AFM investigations resulted in smaller cylinder lengths than expected by the weight-average degree of polymerization,  $P_w$ , determined by static light scattering (SLS), even if corrected for main chain polydispersity [72–74]. It was speculated that within the cylindrical geometry the main chain was locally coiled, but persistent on larger length scales. This picture seemed to be supported by simulations, which showed a bimodal decay of the bond angle correlation function [66, 70, 75–77].

Another “caveat” was raised by theory, which revealed the main chain stiffness to decrease from the middle of the chain towards the ends. This relates to the fact that the steric repulsion between the side chains becomes less at both ends due to the hemispherical volume accessible. In addition, the motion of segments near the chain ends is less restricted [66, 70, 75–77]. Accordingly, application of the wormlike chain model with uniform chain stiffness is somewhat questionable, but for long main chains this effect is most probably not pronounced.

### 3.3.1 Polymethacrylate-Polystyrene Brushes in Toluene and Cyclohexane

A series of cylindrical brush polymers was synthesized with a polymethacrylate (PMA) main chain and polystyrene (PS) side chains of various side chain molar masses,  $M^{\text{sc}}$ , or side chain degrees of polymerization,  $6 < P^{\text{sc}} < 33$ . The aim was to experimentally investigate the length per repeat unit,  $l_{\text{m}}$ , the Kuhn statistical segment length,  $l_{\text{k}}$ , and the side chain extension in terms of the cross-sectional radius of gyration,  $R_{\text{gc}}$ , as well as the segment distribution within the cylindrical cross-section. The full scattering envelope was measured by a combination of SLS and SANS. The cross-sectional radius of gyration was determined from the cross-sectional Guinier plot, i.e.,  $\ln(qI(q))$  versus  $q^2$ , with  $I(q)$  being the absolute scattering intensity and  $q$  the scattering vector. The resulting  $R_{\text{gc}}$  values are shown in Fig. 14 for measurements in the very good solvent toluene and in the poor solvent cyclohexane. Fits to the scaling law  $R_{\text{gc}} = k(M_{\text{n}}^{\text{sc}})^a$  [78, 79] yields values in toluene,  $a = 0.61 - 0.67$ , and in cyclohexane,  $a = 0.56$ . Here,  $k$  is a fitting constant and  $M_{\text{n}}^{\text{sc}}$  is the number average molar mass of the side chains. However, these results should be taken with caution due to the small side chain molar masses investigated, but they are qualitatively in good agreement with the simulation results of the previous section.

From the Holtzer plot of  $qI(q)$  versus  $q$  [63], the mass per length,  $M_{\text{L}}$ , was determined, which translates into the length per monomer unit:

$$l_{\text{m}} = M_0/M_{\text{L}} \quad (3)$$

with  $M_0$  as the molar mass of one repeat unit (Fig. 15a, b). In cyclohexane,  $l_{\text{m}} = 0.207$  nm (solid black line in Fig. 15) is obtained, which is significantly lower than  $l_{\text{m}} = 0.25$  nm, the usual value for vinylic chains. The situation in toluene is less clear: The average over all values yields  $l_{\text{m}} = 0.241$  (solid red line in Fig. 15). A least square fit indicates a decrease of  $l_{\text{m}}$  with increasing side chain molar mass (dotted red line in Fig. 15). For small side chains  $l_{\text{m}} = 0.26$  is obtained. The experimental uncertainty is, however, too large to allow for an unambiguous interpretation. In addition, the factorization of the scattering envelope into main and side chain form factors might not be justified if the cross-terms between side and main chain scattering are not negligible [64].

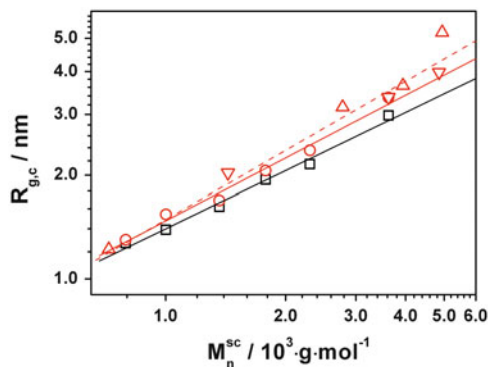


**Fig. 14** Cross-sectional radius of gyration versus side chain molar mass  $M_n^{\text{sc}}$  measured in D8-toluene (red circles) and in D12-cyclohexane (black squares). Data from [63]. The red triangles show additional SANS and SAXS results of PMA-PS samples measured in toluene [80, 81]. The solid black line represents a power law fit to the data in cyclohexane, the solid red line to the data in toluene [63], and the dashed red line a power law fit to all data in toluene

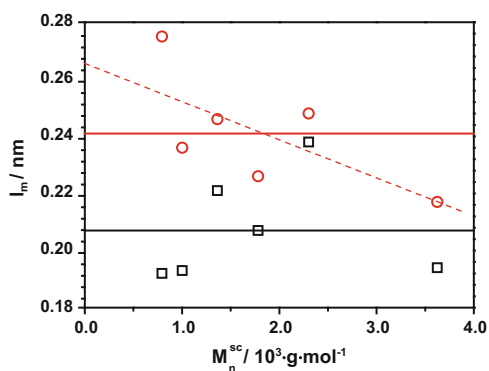


**Fig. 15** Cylinder length per monomer as function of side chain molar mass for the samples measured in D8-toluene (red circles) and in D12-cyclohexane (black squares) as determined by Holtzer analysis. The solid lines indicate the mean values of  $l_m = 0.241$  nm and of  $l_m = 0.207$  nm, the dotted red line represents a least square fit to the red circles. From [63]

Utilizing the  $l_m$  values derived from the Holtzer plateau, the full scattering envelopes were fitted by the Pedersen–Schurtenberger expression for wormlike chains including polydispersity effects (Fig. 16) [63].

A fit of the data shown in Fig. 16 according to:

$$l_k = l_{k0} + k(M_n^{\text{sc}})^n \quad (4)$$

yields  $l_{k0} = 5.28$  nm,  $n = 1.79$  for the data in toluene and  $l_{k0} = 5.66$  nm,  $n = 1.42$  for cyclohexane. In the equation above,  $l_{k0}$  represents the “intrinsic” Kuhn length of

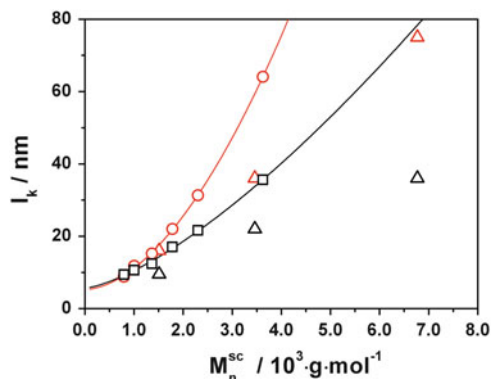


**Fig. 16** Kuhn lengths as function of side chain molar mass for samples measured in D8-toluene (red circles, [63]; red triangles, [82–86]) and for the samples measured in cyclohexane (black squares, this work; black triangles, [82–86]). The lines represent the respective fits according to Eq. (4) (data of [63] only)

the bare backbone without any side chains, which is expected to lie close to the Kuhn length of polyethylene ( $l_k = 1.5$  nm). The extrapolated  $l_{k0}$  values are much larger. This discrepancy has not been explained so far. Since the exponents  $n$  vary significantly with the value of  $l_{k0}$  and a range of exponents were postulated by various theories and simulations ( $1.375 < n < 1.875$ ), a detailed discussion does not seem to be meaningful in view of the fact that the experimentally accessible side chain lengths are far too small to show asymptotic scaling properties.

The analysis of the experimental data so far is based on three assumptions: (1) Most seriously, the concept of the persistence length is applicable. Simulations indicate that for good solvent conditions the effective persistence lengths actually diverge with increasing backbone molecular weight. As a consequence, no intrinsic persistence lengths may be derived, only molar mass-dependent apparent persistence lengths. (2) The form factor can be factorized into a main chain part and a cross-sectional part. Simulations have shown that such a factorization may introduce systematic errors [64]. (3) The Pedersen–Schurtenberger expression was derived for values of  $R_{gc}/l_k = 0.1$ , which is smaller than observed for the present cylindrical brush polymers.

Therefore, it may be elucidating to express the chain stiffness as function of the cross-sectional radius of gyration. As discussed in [87] for bottlebrushes under good solvent conditions, a mapping of the scaling function in Fig. 13b to the scaling function of the mean square radius of gyration of moderately stiff linear chains appears to be possible. It leads to the following empirical relation:

$$l_p = 3R_{gc} \quad (5)$$

where  $l_p$  is the persistence length. In Fig. 17, a direct comparison of the experimental data with the simulation results is shown. The length unit of the lattice model

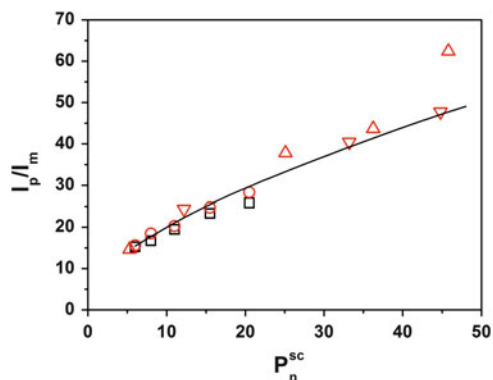


**Fig. 17** Comparison of the experimental and simulated persistence lengths normalized to the length of one repeat unit,  $l_p/l_m$ , as function of the number-average side chain degree of polymerization  $P_n^{sc}$ . Both the simulated and the experimental persistence lengths were derived from the simulated or measured cross-sectional radii of gyration,  $R_{gc}$ , according to Eq. (5): simulation (*solid curve*), measurements in toluene (*red circles and triangles*), measurements in cyclohexane (*black squares*)

simulation was converted into physical units by taking the lattice spacing to be equivalent to 0.2 nm. The agreement is good, given the ambiguity in properly establishing the correlation of the simulation model to the chemical details of the experimental system.

### 3.3.2 Polymer Brushes with Poly-L-lysine Side Chains

In order to address the question of whether or not the specific side chain conformation influences the main chain conformation, cylindrical brush polymers with poly-L-lysine (PLL) side chains were synthesized [88]. Here, we will discuss in some detail the cylindrical brush sample CB-PLL55, which comprises 960 main chain repeat units and an average of 55 lysine repeat units in one side chain sample. Typically, PLL forms a random coil in aqueous solution. In aqueous 0.5 M NaClO<sub>4</sub> solution, however, it is known to adopt one of the most prominent structures of polypeptides: an  $\alpha$ -helix (see also Sect. 6.1) [89]. Upon reduction of the charge density by changing the pH to  $>9.8$  and/or increasing the temperature or by addition of surfactant, a  $\beta$ -sheet structure is favored. Thus, cylindrical brushes with PLL side chains seemed to be ideal candidates for investigating the influence of a coil to  $\alpha$ -helix to  $\beta$ -sheet transition of the side chains on the main chain conformation. Indeed, circular dichroism (CD) measurements confirmed that all three side chain conformations also occur in the side chains of cylindrical brush polymers (Fig. 18).

The fit of the CD spectra reveals a helix content of approximately 90%. Although we could not quantify the  $\beta$ -sheet content in absolute numbers, addition of the anionic surfactant sodium dodecyl sulfate (SDS) caused the  $\beta$ -sheet content to increase with

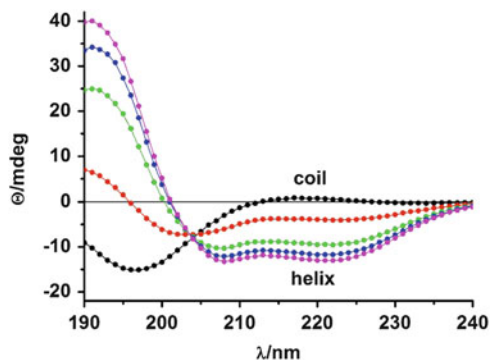


**Fig. 18** CD spectra of the cylindrical PLL brush in aqueous solution for different concentrations of  $\text{NaClO}_4$ . The *solid lines* represent the fits to the data by the program Dichroweb:  $\text{H}_2\text{O}$  (*black circles*), 0.1 N  $\text{NaClO}_4$  (*red circles*), 0.25 N  $\text{NaClO}_4$  (*green circles*), 0.5 N  $\text{NaClO}_4$  (*blue circles*), 1.0 N  $\text{NaClO}_4$  (*magenta circles*). Adapted from [88]

increasing SDS/lysine ratio (Fig. 19). For a molar ratio SDS/lysine  $>4$ , aggregation and eventually precipitation was observed.

Unfortunately, quantitative light scattering results could not trace the effect of the coil-to-helix side chain transition on the main chain conformation, because the concomitant increase in ionic strength has a larger impact on the overall dimensions, i.e., leads to a significant decrease. Like many other polyelectrolytes, CB-PLL55 approaches the phase boundary at high ionic strength (“salting out”), which is known to depend on specific interactions with the added salt. This attraction at high salt is qualitatively confirmed by AFM pictures, which show strongly curved cylinders in both NaBr and  $\text{NaClO}_4$  solutions, which is a clear indication of intramolecular attraction.

In contrast, the AFM pictures as well as cryo-TEM of sample CB-PLL55 prepared from 5 mM NaBr aqueous solution (Fig. 20) show extended cylinders. The cylinders exhibit undulations of the cross-section that are reminiscent of the “pinned clusters” [74, 91] postulated by scaling arguments. The occurrence of pearl-necklace-type structures, where pinned clusters of side chains alternate with regimes that are almost free of side chains, has also been seen in simulations of bottlebrushes, provided one has poor solvent conditions. These clusters are formed by collective collapse of several neighboring side chains [92]. We return to this problem in Sect. 3.5.

It is to be concluded so far, that the coil-to-helix transition of the side chains have no precisely detectable effect on the main chain conformation, since the effects of solvent quality/electrostatic screening are dominating.

The situation is entirely different if the side chains adopt a  $\beta$ -sheet structure. Here, the AFM-pictures in the dry state and measured in solution reveal a helical conformation of the cylinder (Fig. 21). The pitch of the helix lies in the regime of 15–25 nm, which cannot be explained by helix formation on a molecular (i.e.,

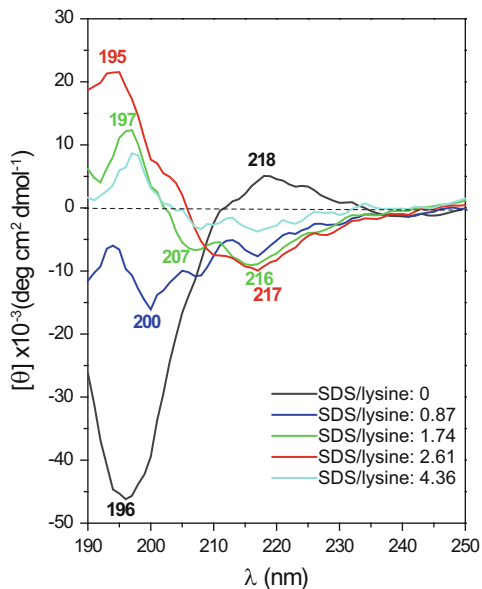


**Fig. 19** CD spectra of PLL brush and of PLL–SDS complexes prepared with increasing SDS content. From [90]

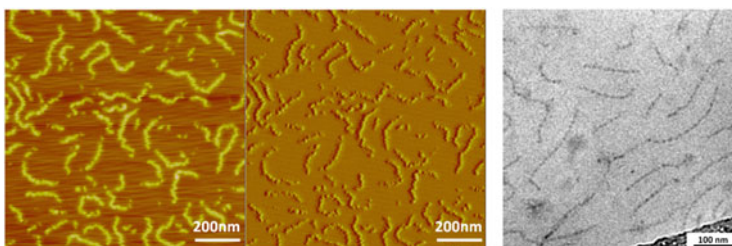


**Fig. 20** AFM micrographs of sample CB-PLL55 in 0.005 M NaBr solution (*left* height, *middle* amplitude) and cryo-TEM picture (*right*). From [88]

monomeric) length scale. Rather, the twist of the  $\beta$ -sheet formed by the PLL side chains was postulated to force the main chain into a helix. Although a detailed molecular picture on how the side chains arrange to form the  $\beta$ -sheet structure is still missing, Fig. 21 may well illustrate the simplified origin of the formation of the cylindrical helix. Accordingly, the presented system constitutes an example of an intramolecular hierarchical structure formation.

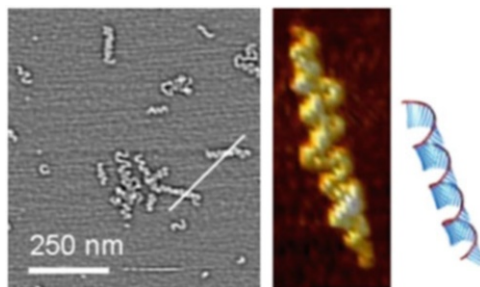


**Fig. 21** AFM picture (in aqueous solution on a mica surface) showing helical cylindrical brush–SDS complexes (*left*), 3D presentation of a single helix (*middle*), and drawing of the helix induced by  $\beta$ -sheet formation of the side chains (*right*). From [90]

### 3.4 Intramolecular Phase Separation Within Cylindrical Copolymer Brushes with Incompatible Side Chains

In addition to the side chain conformation, chemically different side chains attached to the same main chain may also have a pronounced impact on the main chain conformation, particularly if the respective side chains are incompatible. Demixing of the side chain is hampered by the fact that the chemically different side chains are bound to the same main chain, leading to highly frustrated single chain structures. In order to experimentally address this point, the phase separation within statistical cylindrical brush copolymers comprising PMMA and poly-2-vinylpyridinium (PVP) side chains was investigated [93, 94]. The samples were prepared by radical copolymerization of methacryloyl end-functionalized PMMA ( $M_n^{\text{sc}} = 3,700$  g/mol) and PVP ( $M_n^{\text{sc}} = 5,100$  g/mol) macromonomers. Copolymer brushes with two different compositions were synthesized and characterized as shown in Table 1. Subsequent quaternization of the PVP side chains with ethylbromide was conducted in order to enhance incompatibility.

AFM pictures taken from the nonquaternized copolymer brushes after spin-casting a dilute solution in chloroform onto mica revealed the usual wormlike conformation (Fig. 22). However, the same preparation of the quaternized samples yielded cylindrical brushes with pronounced and regular curvatures. The shorter contour length sample 22PVP47-*co*-78PMMA35-QEB50 almost exclusively formed horseshoe structures (Fig. 23) and the longer copolymer brush 73PVP47-*co*-27PMMA35-QEB70 showed a meander-like conformation (Fig. 23). This behavior was interpreted as intramolecular phase separation of the PMMA and quaternized PVP side chains, as sketched in Fig. 24.

Later, some attempts were made to quantify the curvature of sample 21PVP47-*co*-79PMMA44 as function of the degree of quaternization and of the quaternization agent, i.e., ethyl versus benzyl bromide [94]. With increasing degree of quaternization of the PVP side chains, the curvature radius varies from  $R_{\text{curv}} = 27$  nm

**Table 1** Light scattering results of the copolymermacromonomers in DMF, and AFM results (weight and number-average contour lengths,  $L_w$  and  $L_n$ ) of the samples spincast from  $\text{CHCl}_3$  solution onto mica

Polymacromonomer <sup>a</sup>	$M_w \times 10^{-6}$ ( $\text{g mol}^{-1}$ )	$R_g$ (nm)	$R_h$ (nm)	$L_w$ (nm)	$L_n$ (nm)
22PVP47-co-78PMMA35	1.2	29.9	19.4	52	32
22PVP47-co-78PMMA35-QEB50	–	33.1	20.7	–	–
73PVP47-co-27PMMA35	4.54	54.9	40.1	143	75
73PVP47-co-27PMMA35-QEB70	–	58.8	42.5	–	–
21PVP47-co-79PMMA44	2.5	35	27	–	–
50PVP47-co-50PMMA44	1.9	27.2	19.9	–	–

<sup>a</sup>Sample code: w%PVP( $P_n^{\text{SC}}$ )-co-w%PMMA( $P_n^{\text{SC}}$ )-degree of quaternization(QEB) in %

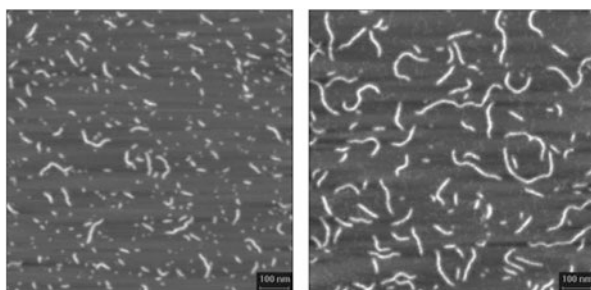


**Fig. 22** AFM micrograph (height image) of 22PVP47-co-78PMMA35 (*left*) and of sample 73PVP47-co-27PMMA35 (*right*) spincast from  $\text{CHCl}_3$  solution onto mica. From [93]

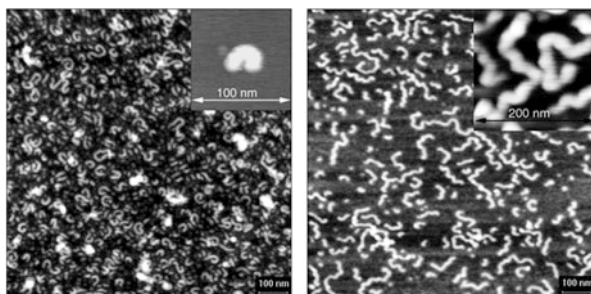


**Fig. 23** AFM micrographs (height image,  $2 \times 2 \mu\text{m}^2$ ) of the quaternized cylindrical brush copolymers. *Left*: 22PVP47-co-78PMMA35-QEB50 spincast from  $\text{CHCl}_3$  solution onto mica, the *inset* shows the magnification of a single horseshoe-shaped brush. *Right*: 73PVP47-co-27PMMA35-QEB70 spincast from aqueous solution onto mica. The *inset* shows the magnification of meandering cylindrical brushes. From [93]

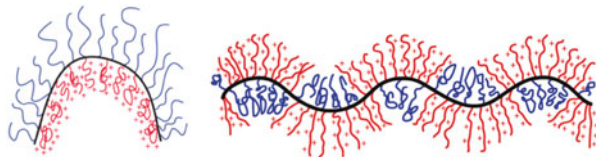


**Fig. 24** Sketch of postulated phase-separated side chains in a horseshoe brush (*left*) and in a meandering brush (*right*) [93]

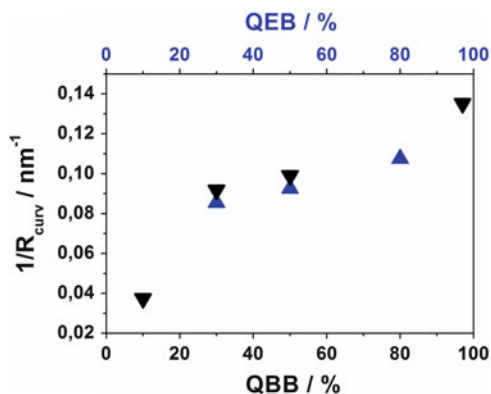


**Fig. 25** Inverse radius of curvature determined from AFM pictures as function of the degree of quaternization for sample 21PVP47-*co*-79PMMA44. *QBB* degree of benzylation, *QEB* degree of ethylation. Data taken from [94]

(10% benzylated) down to  $R_{\text{curv}} = 7.4$  nm (100% benzylated). Figure 25 shows no pronounced difference in  $R_c$  for the ethylated and benzylated samples.

Finally, an interesting behavior was observed for sample 50PVP47-*co*-50PMMA44-QBB20, i.e., a cylindrical copolymer brush with 50% PMMA and 50% PVP side chains, which were quaternized to 20% with benzyl bromide. The AFM pictures taken from spin-cast solutions in chloroform are shown in Fig. 26. Almost exclusively two or three cylindrical brushes are observed to align parallel to each other, which is also seen for the ethylated sample 50PVP47-*co*-50PMMA44-QEB58 (Fig. 27).

It should be noted that aggregate formation could be confirmed by light scattering in chloroform solution for the quaternized samples derived from 50PVP47-*co*-50PMMA44, thus qualitatively confirming the conclusion drawn from the AFM pictures.

Evidence for intramolecular phase separation was not only provided by the AFM pictures, but also from X-ray investigations on melt extruded samples [95]. Whereas the unquaternized sample 73PVP47-*co*-27PMMA35 did not show any scattering peak, the quaternized sample 73PVP47-*co*-27PMMA35-QEB70 did show a peak, which indicates a mean distance between more or less ordered structures of

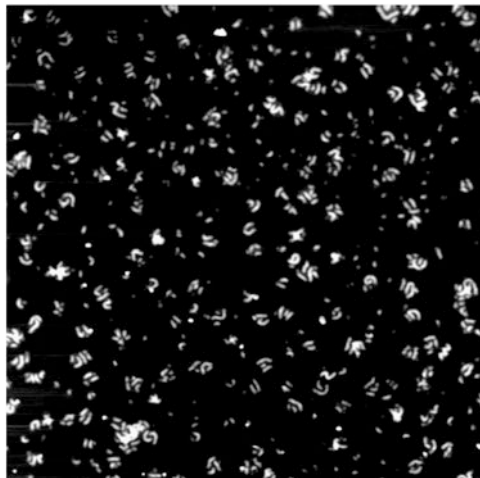


**Fig. 26** AFM picture of sample 50PVP47-*co*-50PMMA44-QBB20 spincast from chloroform solution onto mica. Scale:  $2 \times 2 \mu\text{m}^2$ . From [94]

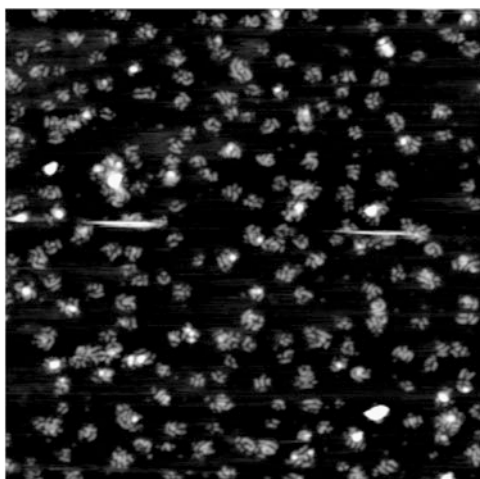


**Fig. 27** AFM picture of sample 50PVP47-*co*-50PMMA44-QEB58 spincast from chloroform solution onto mica. Scale:  $2 \times 2 \mu\text{m}^2$ . From [94]

17.25 nm (Fig. 28). Such distance is not compatible with a correlation between single cylinders but rather of cylinder bundles, as sketched in Fig. 29.

In summary, there is ample evidence for the occurrence of intramolecular phase separation in cylindrical copolymer brushes. Since the phase separation is restricted to a length scale of a few nanometers, direct proof is extremely difficult to achieve. In addition, the computer simulations outlined in Sect. 3.5 will show that statistical

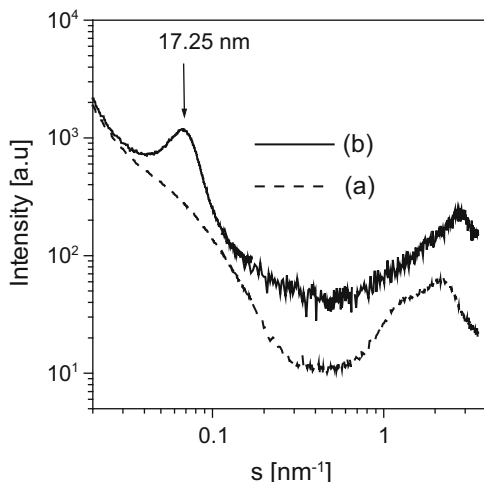


**Fig. 28** X-ray scattering intensity versus scattering vector of sample 73PVP47-co-27PMMA35 (a) nonquaternized and (b) quaternized with ethyl bromide (70%) [95]

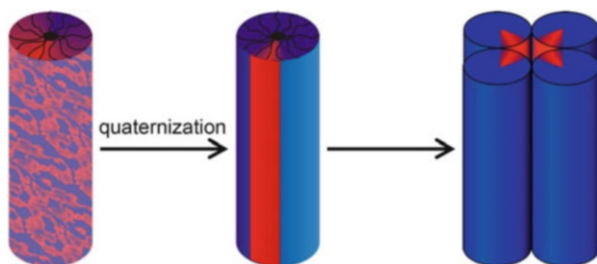


**Fig. 29** Proposed scenario for the intramolecular phase separation and subsequent ordering, in order to explain the X-ray scattering peak corresponding to a mean distance of 17.25 nm of correlated scattering objects [95]

fluctuations in a quasi-one-dimensional (quasi-1D) system most probably destroy any long-range order.

### 3.5 Simulations of Cylindrical Bottlebrush Polymers

For the simulations we consider cylindrical bottlebrush polymers, where two types (A, B) of flexible side chains of length  $N_A$ ,  $N_B$  are densely grafted to a backbone. The degree of (in)compatibility between these constituents can be characterized by a Flory–Huggins parameter  $\chi_{AB}$ , and the solvent quality is described by Flory–Huggins parameters  $\chi_{AA}$ ,  $\chi_{BB}$ , as usually done in the phenomenological

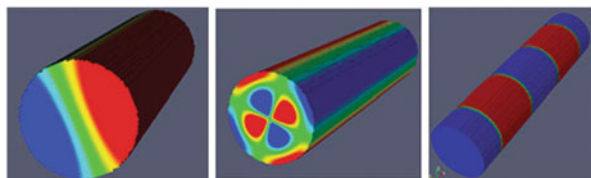


**Fig. 30** Schematic phase morphologies of binary cylindrical bottle brushes: Janus cylinder (*left*), Janus dumbbell (*middle*) and lamellar-like (*right*) morphologies. The *red* and *blue* domains are filled by the A and B monomers; interfacial regions are *green*. From [99]

theory of copolymers (or of binary polymer mixtures, respectively) in the presence of solvent [96–98].

Here, we only consider the simplified case where the backbone of the bottle brush polymer is very stiff, so that the bottle brush polymer can be approximated as a rigid cylinder, at least over a large-enough length scale of interest along the cylinder axis that physical effects due to possible bending of the cylinder must be negligible. We shall address the most symmetric case,  $N_A = N_B = N_s$  and  $\chi_{AA} = \chi_{BB} = \chi$ , for the sake of simplicity. An important observation [99] is that for large  $N_s$  the problem is in fact equivalent (at least to a very good approximation) to the problem of mesophase formation of symmetrical block copolymers of chain length  $2N_s$  confined into a cylinder of radius  $R$  with “neutral walls” (i.e., there is no enthalpic preference of the cylinder walls to either A or B). When the solvent quality is poor, then the monomer density in the cylinder can be taken to be essentially homogeneous, and the interfacial thickness of the polymer–solvent interface (at the cylinder surface) is of the order of a few monomer diameters.

First of all, we emphasize that there is a negligible difference between the situation in which A-chains and B-chains (each chain has  $N_s$  effective monomers) are grafted alternatively with one chain end to the rigid backbone, and that in which  $A_xB_{1-x}$  copolymers (with  $x = 1/2$ , each chain being twice as large) are grafted with their junctions to the backbone, such that the total number of monomers is identical. Secondly, if these junctions were not grafted to the backbone, but free to move in the cylinder, there would be only a minor entropy gain [99]. Hence, the theory of block copolymer mesophase formation in cylindrical confinement [100, 101], where no constraint on the location of these A–B junctions exists, can be generalized to the present problem [99].

Figure 30 shows the possible mesophase orderings that one might expect [99]. Early work [102, 103] has focused on the possibility of microphase separation in the form of “Janus cylinders” [104], i.e., the cylinder splits into two halves, with a planar A–B interface (containing the cylinder axis, taken to be the  $z$ -axis henceforth).

However, it was speculated that other structures could come into play, depending on the ratio  $\chi_{AB}$  [105]. If A–B contacts are much more unfavorable than monomer–solvent contacts, the formation of a planar A–B interface is unfavorable and instead of a simple cylinder one expects the formation of a double cylinder (i.e.,

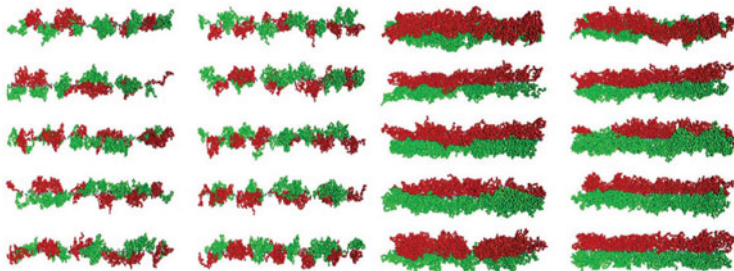


**Fig. 31** Snapshot picture of bottle brush polymers at  $\epsilon_{AB} = 1/2$ ,  $N_s = 35$ ,  $T = 1.5$  and  $\sigma = 0.57$  (left) and  $\sigma = 1.5$  (right). A and B monomers are distinguished by different colors. From [99]

one cylinder contains the A chains and the other the B chains, both cylinders touch along the straight backbone of the bottlebrush [105]. More complicated morphologies such as Janus-dumbbell morphologies are also conceivable (Fig. 31).

In addition, even for one-component bottle brush polymers under poor solvent conditions it is known from experiment [74], theory [74], and simulation [92]) that mesophase formation in the  $z$ -direction along the backbone may occur; namely, the formation of a pearl-necklace structure, where monomer-rich clusters along the backbone alternate with regions almost free of monomers. It is conceivable to obtain a generalization of this structure for the two-component case, where A-rich and B-rich regions alternate along the backbone (Fig. 30). This is a variant of the lamellar structure, well known from block copolymer melts in the bulk [99, 106]. A weak segregation theory along the lines of Leibler [107] has been worked out for this problem, taking into account both the complications of cylindrical confinement and the constraint that the copolymers are tethered to the backbone, and succeeded in showing that for a range of conditions it is in fact the lamellar-like order of Fig. 30 that dominates. However, since this Leibler-type theory [99] is essentially a linear stability analysis around the homogeneous state, it cannot account for strongly nonlinear effects, which are expected to dominate in strongly segregated situations. Therefore, Erukhimovich et al. [99] complemented their study by molecular dynamics simulations of a bead-spring model, choosing side chain lengths of  $N_s = 20, 35$ , and  $50$ , and working with backbone chain lengths  $L$  such that  $50$  side chains were always grafted. Choosing the interaction of nonbonded beads of the same type as a simple Lennard–Jones potential, with parameters  $a = 1$  and  $\epsilon = 1$  setting the scale of length and temperature, the Theta temperature of isolated chains would be about  $T_\Theta \approx 3.0$ . The Lennard–Jones energy between unlike pairs of beads ( $\epsilon_{AB}$ ) and the grafting density ( $\sigma$ ) along the backbone were parameters that could be varied ( $\epsilon_{AB} = 1/2, 3/4, 7/8, 15/16$ , and  $1$ ), the value of  $1$  corresponding to a single-component bottlebrush. Figure 31 shows typical snapshots of the bottle brushes at  $\epsilon_{AB} = 1/2$ ,  $T = 1.5$  and two grafting densities,  $\sigma = 0.57$  and  $\sigma = 1.51$ . One can see that for the smaller grafting density a lamellar-like microphase separation is preferred, whereas for large grafting density

the order along the  $z$ -axis is more uniform, more or less compatible with the Janus cylinder-type morphology.

These conclusions have been strengthened by an analysis of suitable correlation functions and structure factors [99]. These results show (Fig. 31) that a cylindrical bottle brush is a quasi-1D object and, as expected for any kind of 1D system, from basic principles of statistical thermodynamics, statistical fluctuations destroy any kind of long-range order in one dimension [108]. Thus, for instance, in the lamellar structure there cannot be a strict periodicity of local composition along the  $z$ -axis, rather there are fluctuations in the size of the A-rich and B-rich domains; as one proceeds along the  $z$ -axis, these fluctuations are expected to add up in a random fashion. However, in the molecular dynamics simulations of Erukhimovich et al. [99] no attempt could be made to study such effects quantitatively because the backbone contour length  $L$  was not very large in comparison with the domain size  $l_d$  of an A-rich (or B-rich, respectively) domain.

Because a periodic boundary condition in the  $z$ -direction was used to eliminate effects due to the free chain end of the backbone, axial correlations could only be studied over distances  $z$  distinctly smaller than  $L/2$ , to avoid finite size effects. Another complication was that the density distribution in radial direction is still nonuniform for the rather short side chain lengths accessible in the simulations. Also, very long-lived fluctuations occurred, which created strong deviations from the average circular shape of the cross-section of the bottle brush in the  $xy$ -plane perpendicular to the backbone. These fluctuation phenomena not only concern the lamellar-like phase, where the translational symmetry along the  $z$ -axis is broken, but they also affect the Janus cylinder structure or the phase where the cylinder cross-section has a Janus dumbbell shape (Fig. 30). Here one expects that the orientation of A–B interfaces randomly changes when one proceeds along the  $z$ -axis [105, 109, 110]. This problem has been investigated by us with large scale Monte Carlo simulations of a lattice model of bottlebrush polymers [105, 109, 110], applying the pruned-enriched Rosenbluth method (PERM) [111, 112]. By this method, precise results could be obtained for bottle brush polymers using three choices of the side chain length ( $N_s = 6, 12, \text{ and } 18$ ) and three choices of the backbone contour length ( $L = 32, 48, \text{ and } 64$  lattice spacings, respectively), studying various solvent conditions. Clearly, these side chain lengths are very short, but they do correspond to the range that is relevant experimentally [93, 113].

When a phase separation into a Janus cylinder structure occurs, e.g., where the upper half of the cylinder contains the B-rich phase and the lower half the A-rich phase, we have a planar AB interface (Fig. 32a) and the quantity that we wish to record is the vector normally oriented to this interface for any monomer of the backbone. Studying the orientational correlations of this vector will yield the desired information on possible fluctuations of interface orientation (Fig. 32b). Since the AB interface at nonzero temperature is not a sharp dividing surface, but rather has a finite width, a numerical characterization of the local orientation of this interface normal is difficult. Therefore, an essentially equivalent but numerically unambiguous characterization of this Janus cylinder-type ordering has been

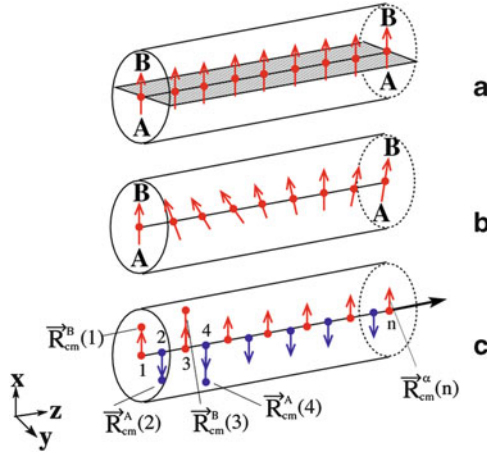


**Fig. 32** (a) Perfect phase separation of side chains in a binary (A, B) copolymer bottle brush with alternating grafting sequence ABAB... of side chains along the backbone into a Janus cylinder structure implies formation of an AB-interface phase (*shaded*) between the A-rich part (*bottom*) and the B-rich part (*top*) of the cylindrical brush. The local orientation of the interface can be characterized by a unit vector oriented normal to it (*arrows*). (b) At nonzero but low temperatures, phase separation will occur locally, but entropy will lead to long wavelength fluctuations of the orientation of this unit vector, destroying axial long-range order along the  $z$ -direction of the bottle brush backbone. (c) Construction of unit vectors  $\vec{R}_{\text{cm}}^{\alpha}(j)$  defined as projections of the vector from the grafting site of a chain to its center of mass position into the  $xy$ -plane. Here the grafting sites are labeled as  $j = 1, 2, \dots$  and  $\alpha = A$  or B.  $\vec{S}_{\text{cm}}^{\alpha}(j)$  then is a unit vector along  $\vec{R}_{\text{cm}}^{\alpha}(j)$ . From [109]

achieved by calculating the unit vector  $\vec{S}_n^{\alpha}$  ( $\alpha = A$  or B) from each grafting site  $n$  of the backbone to the projection of the center of mass position,  $\vec{R}_{\text{cm}}^{\alpha}(n)$  of the grafted chain (Fig. 32c). Because A-chains and B-chains are grafted alternatively to the backbone in our model, the correlation function of interest is:

$$C_n \equiv \left( \left\langle \vec{S}_i^A \cdot \vec{S}_{i+n}^A \right\rangle + \left\langle \vec{S}_{i+1}^B \cdot \vec{S}_{i+1+n}^B \right\rangle \right) / 2, \quad i = 1, 3, \dots \quad n = 2, 4, \dots \quad (6)$$

Note that we use an even number of backbone monomers and periodic boundary conditions along the backbone, so there is translational invariance. From this correlation function, a correlation length  $\xi$  then is extracted from a fit to:

$$C_n = \text{const} \left( e^{-n/\xi} + e^{-(N_b-n)/\xi} \right) \quad (7)$$

Figure 33a shows a plot of the inverse correlation length  $\xi^{-1}$  versus the inverse Flory–Huggins parameter  $\chi_{AB}^{-1}$  for the three side chain lengths studied, in the case of poor solvent conditions  $q = \exp(-\varepsilon/k_B T) = 1.5$ , (where  $\varepsilon$  is the energy that is

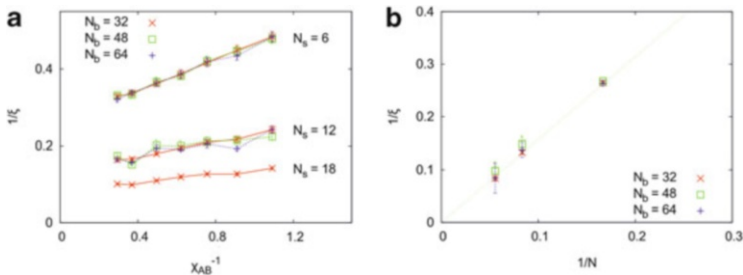


**Fig. 33** (a) Plot of inverse correlation length for Janus-cylinder-type order versus  $\chi_{AB}^{-1}$  (with  $\chi_{AB} = z_c [\epsilon_{AB} - (\epsilon_{AA} + \epsilon_{BB})/2]/k_B T$ ,  $z_c = 6$  being the coordination number of the simple cubic lattice) for the three side chain lengths  $N_s = 6, 12,$  and  $18$ . These data do not depend significantly on the backbone chain length  $N_b$ , as seen from the coincidence of data for  $N_b = 32, 48,$  and  $64$ , respectively. From [109]. (b) Inverse correlation length  $\xi^{-1}$  in the limit of  $\chi_{AB} \rightarrow 0$  plotted versus  $1/N_s$  for a poor solvent. The *straight line* suggests an asymptotic behavior  $\xi \approx N_s$  in this limit. From [109]

won if two lattice sites are occupied by monomers of the same kind.). Even for  $\chi_{AB} \rightarrow \infty$  (i.e., the strong segregation limit), the correlation length seems to remain finite for finite  $N_s$ . But actually there is a significant increase of this correlation length with increasing side chain length, because, as  $N_s \rightarrow \infty$  the diameter of the cylindrical bottle brush would become macroscopic, and then long-range order of the Janus cylinder-type occurs.

For real binary bottlebrushes, changes of solvent quality have been shown to lead to very interesting structure formation, such as meander-like or horseshoe-like structures [93]. For a theoretical modeling of such phenomena, it is necessary to take into account both the flexibility of the backbone (and hence a finite persistence length of the bottlebrush [71]) and differences in solvent quality for A and B side chains. Although we have studied the effect of solvent quality on the effective stiffness of the bottle brush for homopolymer bottle brushes with flexible backbone [71], an analogous study for binary bottle brushes would be very demanding, and hence has not yet been attempted with the methods described in this section.

The main results of this section are that binary bottle brush polymers show microphase separation but the range over which this mesophase ordering occurs is always finite, due to the quasi-1D character of these cylindrical brushes. The correlation range over which such order is possible increases with increasing side chain length and grafting density (and with increasing monomer density inside the cylindrical brush caused by decreasing solvent quality and resulting expulsion of solvent molecules from the brush). Apart from “Janus cylinder” and “Janus dumbbell” type structures, lamellar-like ordering (with almost regular alternation of A-rich and B-rich clusters along the backbone) may also occur, in particular for medium values of the grafting density.

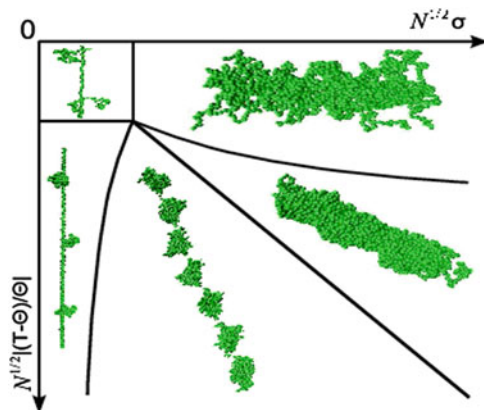


**Fig. 34** Schematic phase diagram of a bottle brush polymer with a rigid backbone under poor-solvent conditions, in the plane of variables scaled grafting density and scaled distance to the Theta temperature [92]. The lines separating the different regions have been proposed by mean field arguments [74]. They are not to be understood as quantitative estimates of phase transition lines, but rather as rough estimates of smooth crossovers. Representative simulation snapshots visualize the different microphases

### 3.6 Complex Formation of Polymer Brushes

The same interactions that dominate the shape of complex macromolecules are also responsible for the formation of defined aggregates and for the adsorption to surfaces, which is described in Section 3.9. As one example, cylindrical brushes are again described. The interaction of side groups with the solvent determines the structure of the macromolecules and the interactions between them as well as with surfaces.

Poor solvent conditions for the side chains grafted to, e.g., a linear polymer (bottle brushes) will lead to intermolecular aggregation; however, interestingly, they can also lead to intramolecular microphase separation within a homopolymer chain. Consider a bottle brush polymer with a very stiff backbone (in the simulations [92] it was modeled as a rigid rod) placed into poor solvent conditions. The resulting structures then depend on solvent quality and grafting density of the side chains, as exhibited in Fig. 34.

For low grafting densities, isolated side chains collapse onto the backbone of the bottle brush. For high grafting densities, a homogeneous cylindrical brush collapses onto itself. For intermediate grafting densities, however, the translation invariance along the backbone is broken upon side-chain collapse, and a microphase-separated pearl-necklace structure is formed.

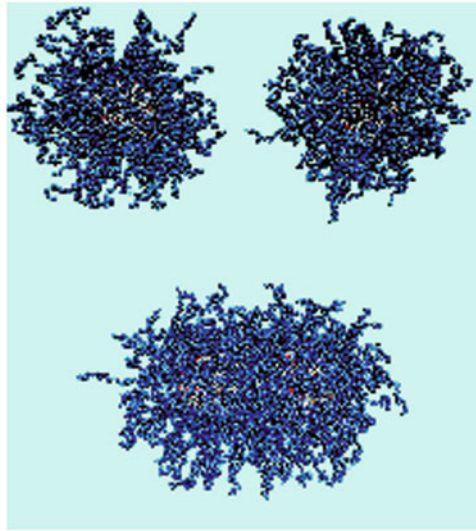
A similar breaking of the symmetry of the high temperature (good solvent) phase upon side-chain collapse also occurs for an even simpler kind of brush structure, a spherical polymer brush, and there it also leads to a specific form of intermolecular aggregation. Spherical polymer brushes formed from (spherical) nanoparticles to

which flexible polymers are grafted are interesting building blocks for various nanostructured materials [114, 115]. Since it is possible to vary parameters such as the radius (denoted as  $R_c$ ) of the solid nanoparticle that forms the core of the spherical polymer brush, the grafting density of the macromolecules, their chemical nature, their degree of polymerization, and the chemical nature of the matrix (solvent or polymer melt) in which the spherical polymer brushes are embedded, a rich behavior can be expected [116, 117].

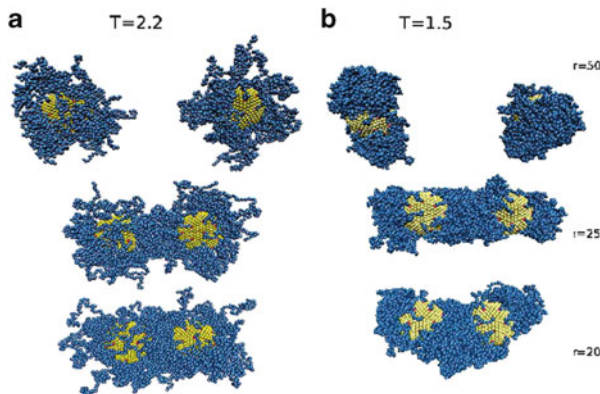
In the theoretical modeling [117–120] to be briefly described here, only limited aspects of this broad field were addressed, namely the case where the density of the nanoparticles in the system is sufficiently dilute such that only the structure of isolated spherical brushes or their pairwise interactions are of interest; dense aggregates formed from more than two spherical brushes were not considered. Two complementary techniques were used, molecular dynamics computer simulation [121] and analytical calculations based on density functional methods [122] and the self-consistent field theory of polymers [123]. We also restrict attention to the case where the grafting density is high enough such that under good solvent conditions the close approach of two nanoparticles (to a distance of a few diameters of the effective monomers) is prohibited by the large entropic penalties; hence, the direct van der Waals attraction of the nanoparticles can always be neglected. Note that for the standard bead-spring model of flexible polymers that is used here [121], every effective monomer represents 3–5 chemical monomers, so one can associate the effective monomer diameter (which is taken as length unit here  $a = 1$ ) to a physical size of 1 nm, while the radius  $R_c$  of the nanoparticle typically was about  $8a$ . Choosing a number  $N$  of effective monomeric subunits of the grafted chains from  $N = 20$  to  $N = 80$ , the thickness of the brush coating on the nanoparticles also is a few nanometers, comparable to  $R_c$ . Thus, our studies are neither in the limit where the spherical polymer brush can be considered as a many-arm star polymer, nor in the limit  $R_c \rightarrow \infty$  where the brush coating can be described in terms of a planar polymer brush.

Figure 35 [118] shows typical configurations of two nanoparticles (with a total number of 92 grafted chains containing  $N = 40$  effective monomers per chain) under good solvent conditions, for distances between them of  $r = 55$  and  $r = 20$ . In this case, the potential of mean force  $W(r)$  between the two particles is uniformly repulsive: although it is practically zero in the first case, i.e., the particles are essentially noninteracting, it is  $200 k_B T$  for  $r = 20$ . Such a close approach of the brushes, where the two polymeric shells strongly interpenetrate, therefore cannot occur simply by thermal fluctuations.

However, the situation is different when the solvent quality varies (Fig. 36). Note that we have treated only implicit solvent in the simulations, whereas in the analytical calculations spherical brushes embedded in concentrated polymer solutions could also be treated, to check the extent to which this case resembles a dilute solution under Theta solvent conditions [120]. Figure 36 shows that in poor solvents conditions, for moderate grafting density, the nanoparticle is no longer coated by a uniform polymer layer but the system prefers to form a dumbbell-shaped object. At both the “north pole” and the “south pole” of the nanoparticle



**Fig. 35** Snapshot pictures of two spherical polymer brushes with 92 chains, with number of effective subunits  $N = 40$  grafted to a nanoparticle with radius  $R_c = 7.9$  Lennard-Jones diameters (grafting density  $\sigma = 0.118$ ). Particles making up the nanoparticle are shown in *grey* and *red* (if they are grafting sites); effective monomers of the chain molecules are shown in *blue*. The *upper* picture refers to a separation of  $r = 55$  between the core centers, and the *lower* picture to  $r = 20$ . Effective monomers interact with the repulsive Weeks-Chandler Anderson potential. Adapted from [118]



**Fig. 36** Same as Fig. 35, but effective monomers interact with a Lennard-Jones potential, which leads to a Theta temperature at  $T_\Theta = 3.0$ , for temperatures  $T < T_\Theta$ : (a)  $T = 2.2$  and (b)  $T = 1.5$ .  $R_c = 7$ ,  $N = 60$ , and three core-core separations are chosen:  $r = 50$  (*upper* picture),  $r = 25$  (*middle* picture), and  $r = 20$  (*lower* picture). Adapted from [120]

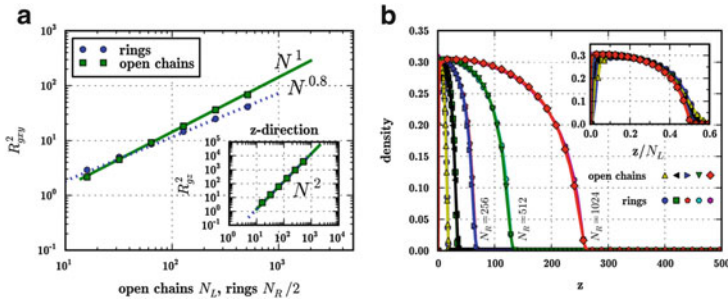


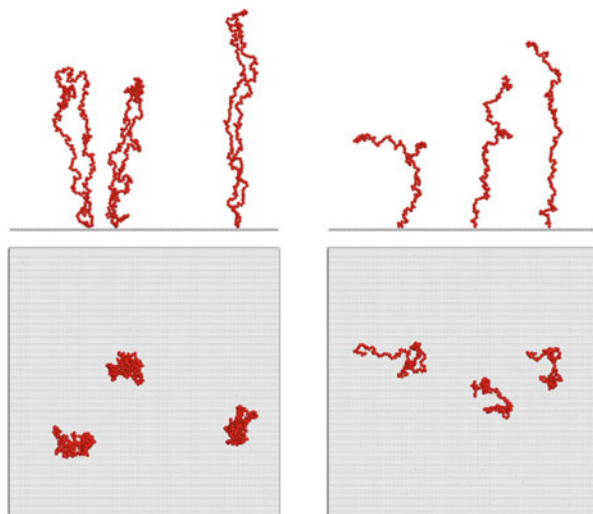
**Fig. 37** (a) Comparison of density profiles for brushes composed of linear (open) chains and ring chains. A grafted ring polymer typically has the same profile as a linear chain of half length at twice the grafting density. *Inset*: Scaled plot. (b) Scaling of the transverse components of the radius of gyration for ring brushes and brushes composed of linear chains. *Inset*: Scaling of the component perpendicular to grafting plane. From [124]

there is a polymer-rich cluster, while the “equator” stays almost free of polymers (of course, the orientation of the north–south axis through the particle is random, resulting from fluctuations when cooling the particle down to a temperature of about  $T = T_{\Theta}/2$ ,  $T_{\Theta}$  being the Theta temperature of the solution). Such inhomogeneous structures, a kind of irregular mesophase where polymer-rich “dimples” alternate with regions that are almost free of polymers, are also known from flat polymer brushes [116]. When two such inhomogeneous spherical polymer brushes approach each other, rather elongated rod-like aggregates may form (Fig. 36b). However, a quantitative analysis shows that in this case  $W(r)$  has a deep minimum, of the order of at least  $-100 k_B T$ , so it is clear that Fig. 36b depicts frozen nonequilibrium structures [120].

A very special type of segregation between polymers in brushes also occurs when ring polymers are densely grafted on substrates. The non-crossability constraint of non-concatenated ring polymers causes the effect, even under good-solvent conditions, that the polymers are much more strongly segregated from each other, unlike brushes made of linear chains, where chains laterally interpenetrate much more strongly.

Numerical simulations performed on graphic processing units (GPUs) reveal that density profiles of these peculiar brushes are almost identical to those of linear brushes (at twice the grafting density and half the chain length), and that the radius of gyration scales linearly with  $N$  in the direction perpendicular to the grafting plane [124, 125]. The transverse components, however, differ considerably between the two. The radius of gyration scales like  $N^{0.4}$  (as opposed to  $N^{0.5}$  for regular brushes composed of linear polymers, Fig. 37), and if one looks at individual chains from the top, ring brushes are clearly much more segregated (Fig. 38). Intriguingly, this phenomenon can also be observed in semidilute solutions of ring polymers [126, 127]. There, the inability to interpenetrate other chains due to the lack of an adequate reptation mechanism also leads to a stronger segregation of individual chains and the same scaling behavior that was observed for transverse components is found for the complete chain ( $N^{0.4}$  or even  $N^{0.33}$  in the thermodynamic limit, versus  $N^{0.5}$  for linear polymers).

**Fig. 38** Snapshots of individual chains taken from a brush composed of ring chains (*left*) and linear chains (*right*); *side views* and *top views* are shown. From [124]



### 3.7 Complexes Formed in Between Polyelectrolytes in Aqueous Solution

The complex formation of oppositely charged macromolecules is a long-standing subject of interest in polymer science. Whereas complexes comprising linear flexible polyions [128–133] as well as linear polycations and DNA [134–143] are frequently reported, studies on the influence of chain topology are mostly restricted to dendrimers of various generations [144–147]. Only two reports deal with the complexation of DNA and polymers with dendritically branched side chains [148, 149]. We confine discussion to complexes formed by wormlike polyions with large persistence length, such as anionically and cationically charged cylindrical brush polyions and cationic cylindrical brush polymers and DNA. Particular emphasis is given to question of equilibrium versus nonequilibrium complexes.

The complexes formed by excess polycations and DNA have found interesting applications in gene transfection because the complexed DNA is believed to be protected against degradation and the complexes exhibit a more or less pronounced cationic charge, which facilitates cell uptake (Sect. 5). Here, the structure of the complexes should be elucidated with respect to molar mass, radius of gyration  $R_g$ , and hydrodynamic radius  $R_h$  [150]. This is not easily achieved because complexes are known to be stable only if they coexist with the non-complexed excess component, i.e., either polycation or DNA. The situation is well illustrated by Fig. 39, where the apparent molar mass of the mixture measured at a small but finite concentration is plotted versus the mass fraction of DNA,  $w_{\text{DNA}} = m_{\text{DNA}} / (m_{\text{DNA}} + m_{\text{polycation}})$  with  $m_{\text{DNA}}$  and  $m_{\text{polycation}}$  being the respective mass fractions of DNA and polycation. The data of the various polycations utilized and of DNA are summarized in Table 2 in terms of chain topology, contour length, total charge,

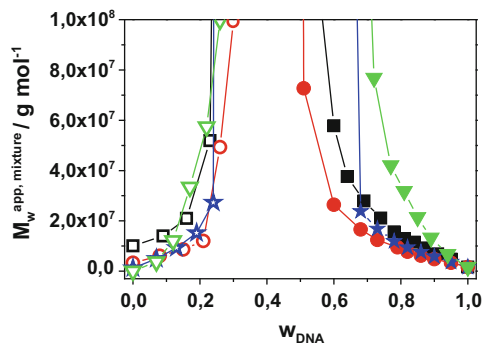


**Fig. 39** Apparent molar mass ( $M_w$ ) as function of weight fraction  $w_{\text{DNA}}$  for the various polycation topologies: PVP26 (filled squares, open squares), PVP47 (filled circles, open circles), PEI (filled stars, open stars), and PAMAM (filled inverted triangles, open inverted triangles); DNA excess and polycation added (closed symbols), polycation excess and DNA added (open symbols). From [150]

**Table 2** Characteristics of the polycations and of DNA utilized for complex formation

Polyion	Topology	Size	$M_w/M_n$	Charges/ molecule ( $Z^{+/-}$ )	Charge density
PVP26	Cylindrical brush polymer	Contour length $L = 610$ nm	5.3	$\langle Z^+ \rangle_n = 5,500$	$48 \text{ N}^+/\text{nm}$
PVP47	Cylindrical brush polymer	Contour length $L = 100$ nm	3.9	$\langle Z^+ \rangle_n = 2,800$	$100 \text{ N}^+/\text{nm}$
PEI28	Cylindrical brush polymer	Contour length $L = 90$ nm	2.7	$\langle Z^+ \rangle_n = 1,800$	$55 \text{ N}^+/\text{nm}$
PAMAM-G5	Dendrimer	Hydrodynamic radius $R_h = 3.4$ nm	$\sim 1$	$Z^+ = 127$	$(19 \text{ N}^+/\text{nm})$
pUC19- supercoiled DNA	Supercoiled DNA	Contour length $L = 930$ nm	1	$Z^- = 5,372$	$5.9 \text{ P}^-/\text{nm}$

and charge density and in Table 3 in terms of molar mass and dimensions. The cylindrical brush polymers have the same PMA main chain but differ in side chain length, which results in different number of chemical charges per main chain repeat unit as well as in different chemistry of the cationic side chains, i.e., ethylpyridinium (PVP) versus ethyleneimine (PEI) side chains. One commercial fifth generation poly(amido amine) (PAMAM) dendrimer sample was included for comparison.

For all polycations, the well known divergence of molar mass is observed in the regime more or less close to charge stoichiometry, indicating agglomeration. In order to determine molar mass and dimensions of the pure complexes by SLS and DLS, the

**Table 3** Light scattering characterization of the investigated polymers

Polymer	Solvent	$M_w$ (g mol <sup>-1</sup> )	$R_g$ (nm)	$R_h$ (nm)	$R_g/R_h$
pUC19	Aq. 5 mM phosphate buffer	$1.66 \times 10^6$	65.6	43.6	1.5
PVP26	Aq. 10 mM NaBr	$10.1 \times 10^6$	87.2	48.2	1.8
PVP47	Aq. 5 mM phosphate buffer	$3.48 \times 10^6$	45.8	33.1	1.4
PEI*HCl	Aq. 0.1 M HCl	$1.19 \times 10^6$	46.8	26.5	1.8
PAMAM-G5	MeOH + 10 mM LiBr	$2.80 \times 10^4$	–	3.4	–

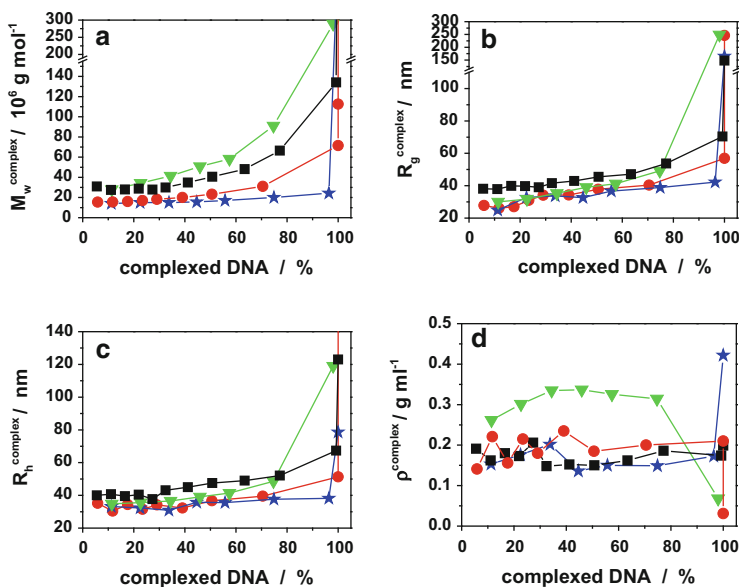


**Fig. 40** (a) Molar masses, (b) radii of gyration, (c) hydrodynamic radii, and (d) densities of the complexes as function of the complexed DNA fraction for the various polycations: PVP26 (*filled black squares*), PVP47 (*filled red circles*), PEI (*filled blue stars*), and PAMAM (*filled inverted green triangles*). From [150]

weight fraction of the respective excess component needs to be known. This was achieved by gel electrophoresis in case of excess DNA and by GPC in case of excess polycation. As described in detail elsewhere[150], it is straightforward to extract the characterization data of the pure complexes from SLS and DLS of the mixture, i.e., complexes coexisting with excess DNA (Fig. 40a–d) and for excess polycation (Fig. 41a–d). It is found that at large excess of one component, the molar mass and dimensions of such “primary” complexes do not depend on the mixing ratio. Only if the fraction of excess DNA becomes less than 20% or if excess polycation is less than 10% does bridging of primary complexes set in, which eventually results in macroscopic phase separation. Although the complexes consist of several DNA and polycation molecules the sizes are significantly smaller as compared to pure DNA, i.e., the complexes are compacted for all cylindrical brush polycations to a density in

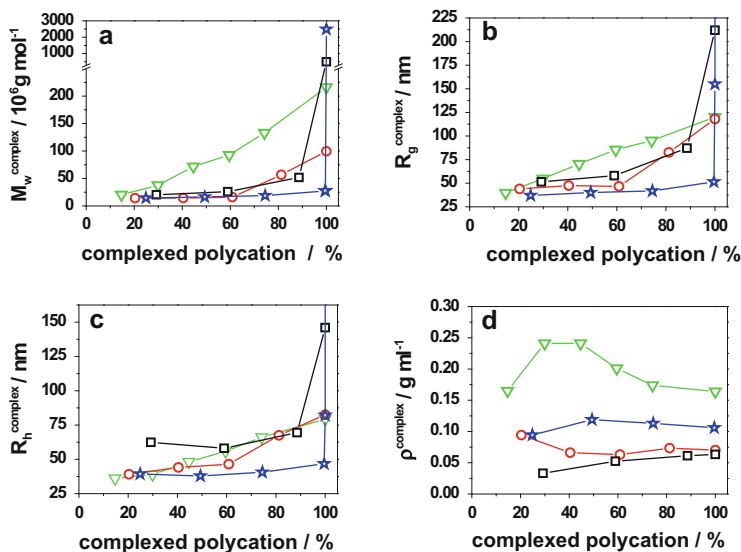


**Fig. 41** (a) Molar masses, (b) radii of gyration, (c) hydrodynamic radii, and (d) densities of the complexes as function of the complexed polycation fraction: PVP26 (*open black squares*), PVP47 (*open red circles*), PEI (*open blue stars*), and PAMAM (*open inverted green triangles*). From [150]

solution,  $\rho = 3M_w/(4\pi R_h^3)$ , of  $0.15 < \rho < 0.25 \text{ g/cm}^3$  for excess DNA and somewhat less compacted for excess polycation, i.e.,  $0.05 < \rho < 0.1 \text{ g/cm}^3$ . For the PAMAM dendrimers, the density is even larger, i.e.,  $\rho = 0.3 \text{ g/cm}^3$  for excess DNA and  $\rho = 0.2 \text{ g/cm}^3$  for excess PAMAM. Approximately five to ten DNA molecules are in one primary complex if the complexes are formed at excess DNA, whereas three DNA molecules are in one complex if formed at excess polycation.

Another result concerns the charge stoichiometry within one complex. For excess DNA,  $Z^+/Z^- = 0.8$  whereas for excess polycation  $Z^+/Z^- = 3$ . It should be noted that these numbers do not represent the effective charge but the chemical charge of the complexes, which may include sterically shielded charges in the interior of the cylindrical brushes and ignores possible reduction of charges by counterions (Manning condensation, ion pair formation).

In summary, the complexes of DNA with the various cylindrical brush polycations form primary complexes of constant size as long as no intercomplex bridging occurs, whereas for PAMAM the complex mass and size increase monotonically with increasing content of the minority component. It should be noted that all complexes constitute nonequilibrium structures because size and stability depend significantly on the preparation conditions. For instance, dropping the minority component into the excess component under stirring, which was applied for the experiments described above, yields more stable and smaller complexes than those prepared by rapid mixing in a stopped-flow device. Also, the sequence of mixing matters. Adding the excess component to the minority component, which is avoided in the experiments above, seems to be problematic because the titration

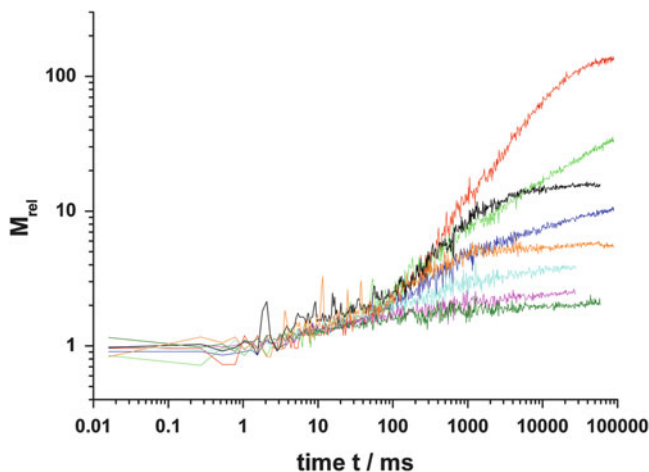


**Fig. 42** Relative molar mass  $M_{\text{rel}}(t)$  as function of time for complexes formed at different charge fractions  $x_{\text{anion}}$ . From top to bottom:  $x_{\text{anion}} = 0.398$  (red), 0.332 (green), 0.498 (black), 0.284 (blue), 0.665 (orange), 0.249 (light blue), 0.199 (magenta), and 0.166 (dark green). From [151]

passes through the “unstable regime” in which phase separation is known to occur. Rapid mixing and vigorous stirring might avoid macroscopic phase separation, but the problem is obvious.

Recently, a light scattering stopped-flow cell was developed with a dead time of less than 5 ms, thus allowing for kinetic measurements of the apparent molar mass starting at 10–50 ms after mixing [151]. With such a device, the complexation kinetics of DNA with a cylindrical brush polymer with PVP side chains was investigated. The results are summarized in Fig. 42 for different mixing ratios, expressed by the mole fraction of anionic charges  $x_{\text{anion}}$ . For  $x_{\text{anion}} < 0.25$  stable complexes are observed to form on a time scale of 60–70 ms. For  $0.2 < x_{\text{anion}} < 0.4$  the complexes first grow on much larger time scale up to a maximum of 10 s for  $x_{\text{anion}} = 0.4$ , followed by a power law behavior, i.e.,  $M_{\text{rel}} \approx t^d$ . Here  $M_{\text{rel}}$  is the increase in molar mass relative to the bare mixture of polycation and DNA, the time  $t$ , and the exponent  $d \ll 1$ . However, no theoretical explanation for  $d < 1$  has been derived so far.

Many more and more detailed investigations of the kinetics of complex formation are needed in order to develop a deeper understanding of such nonequilibrium processes. These first experiments merely demonstrate the potential and the need to elucidate the kinetics of nonequilibrium structure formation.

Besides investigating nonequilibrium complexes, it is equally challenging to direct electrostatically driven complex formation into equilibrium. One vision was to obtain anisotropic complexes by mixing rod-like polycations and polyanions, such as anionic and cationic cylindrical brushes or cationic cylindrical brushes and DNA. In aqueous solution “scrambled egg” structures were always obtained by mixing cylindrical brush polymers with polystyrene sulfonate and with PVP side chains as well as by mixing cylindrical brushes with PVP or PLL side chains with

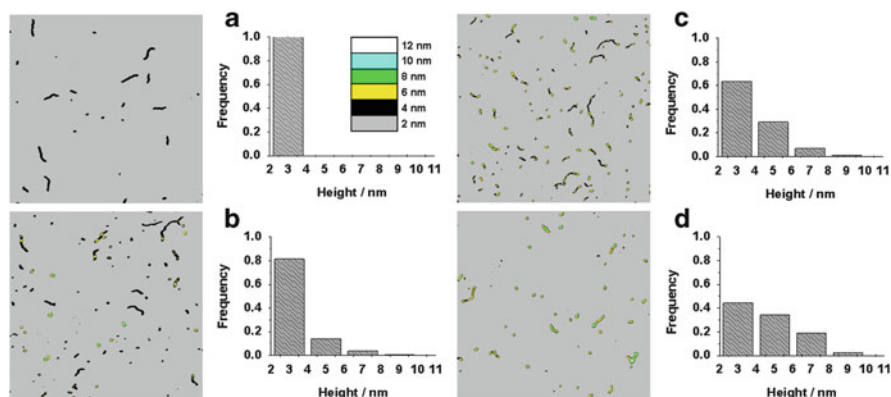


**Fig. 43** AFM pictures and analysis of results for the complexes (spincast on freshly cleaved mica) between cylindrical brushes with PSS-surfactant side chains and with PEI-PEO side chains with increasing mass fraction  $w$  of cylindrical brushes with PEI-PEO side chains: (a)  $w = 0$ , (b)  $w = 0.33$ , (c)  $w = 0.7$ , and (d)  $w = 0.87$ . From [152]

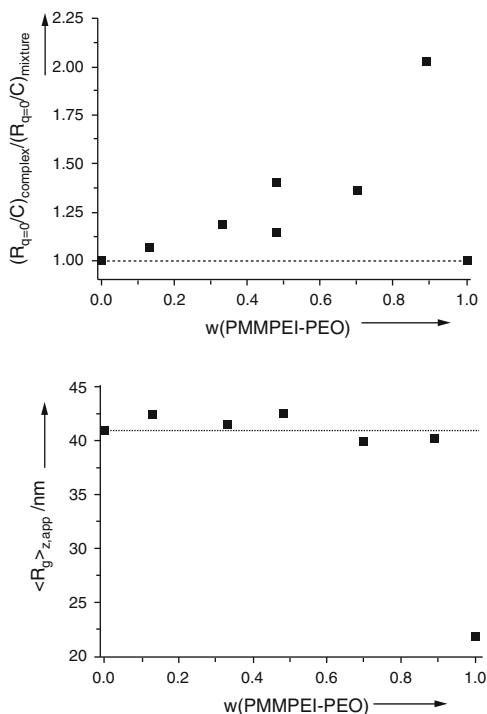
plasmid and linear double-stranded DNA. It was speculated that strong electrostatic interactions prohibit the formation of well-organized structures. Addition of salt did not change much except that the complexes became larger and eventually unstable due to the well-known salting-out phenomenon.

### 3.8 Complex Formation Between Weakly Charged Polyelectrolytes in Organic Solvents

One strategy is to strongly reduce the ionic charges of the components. This was accomplished by excluding water as the solvent due to solubility problems and favoring solvents like alcohols, *N,N*-dimethylformamide (DMF), etc. Two examples utilizing cylindrical brush polymers as templates for single brush complexes have been successful so far [152, 153].

A polyelectrolyte/surfactant complex consisting of cylindrical brush polymers with polystyrene sulfonate side chains and dodecyltrimethylammonium bromide (DOTAB) was dissolved in DMF. In DMF some of the surfactant groups dissociate. For the polymer/surfactant aggregate, this leads to slightly anionically charged cylindrical brush polyions. The weak cation was a cylindrical brush with a PMA main and PEI side chains. The side chains were grafted by six PEG2000 chains per PEI side chain. Upon mixing in DMF, both light scattering and AFM revealed the larger PSS-C12 brush to act as a single molecule template for complexation of shorter PEI-PEG brushes (Fig. 43), i.e., several PEI-PEG brushes were complexed by one single PSS-C12 brush. Upon increasing the fraction of PEI-PEG brushes, the height of the complexes increased. At the same time, the molar mass measured by SLS was shown to strongly increase at constant radius of gyration (Fig. 44). Since

**Fig. 44** *Upper graph:* Reduced light scattering intensity  $(R(q=0)/c)_{\text{complex}}$  measured at one small but finite concentration and extrapolated to zero scattering vector of the complexes between cylindrical brushes with PSS-C12 side chains and with PEI-PEO side chains. Values are normalized by the respective calculated scattering intensity of the mixture,  $(R(q=0)/c)_{\text{mixture}}$ , as function of the weight fraction of the cylindrical brush with PEI-PEO side chains. *Lower graph:* Apparent radii of gyration measured at one small but finite concentration. From [152]



the sequence of mixing did not affect the results, the complexes are most probably equilibrium structures.

Similar results were obtained for mixtures of a cylindrical brush polymer with PSS-C12 side chains and fifth generation PAMAM dendrimers. In methanol large aggregates were obtained, whereas in both DMF and methyl formamide (MFA), single cylinder complexes were identified by AFM and by light scattering. Obviously, not only the effective charge (via the dielectric constant) governs electrostatically driven structure formation but also subtle solubility effects. Additionally, the nature of the solvent (protic versus aprotic) plays a role.

It should be mentioned that no equilibrium structures (neither in methanol nor in DMF) have been obtained so far with plasmid and various linear DNA–surfactant complexes and cylindrical PVP brushes [154].

### 3.9 Adsorption to Surfaces

The same interactions that determine intramolecular structure and aggregation also play a role in adsorption to surfaces. When a simple linear macromolecule interacts with a surface and becomes adsorbed, its structure changes from the 3D “mushroom” conformation to the (quasi)-2D “pancake” conformation [155]. In the

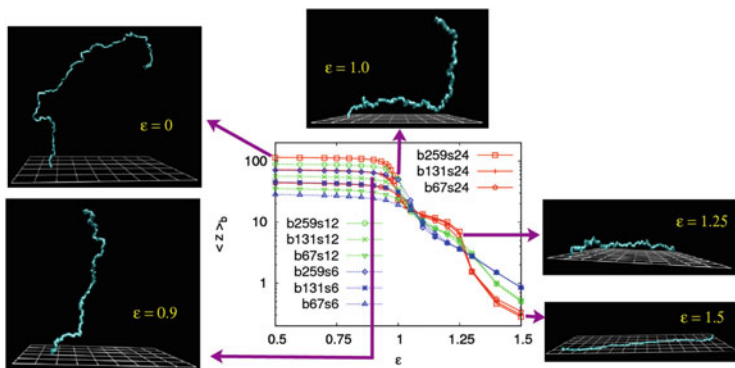


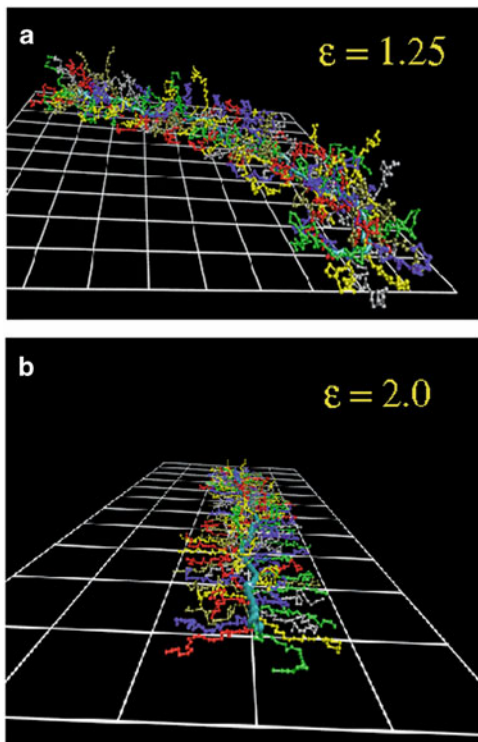
**Fig. 45** Average distance  $\langle z_b \rangle$  of a backbone monomer from the adsorbing surface plotted versus adsorption energy  $\epsilon$  (in units of the thermal energy  $k_B T$ ) for several choices of the backbone chain length  $N_b$  and side chain length  $N_s$  (denoted as  $b N_b s N_s$ ). For  $N_b = 131$ ,  $N_s = 24$ , typical snapshots of the backbone chain are shown for five values of  $\epsilon$ . Note that the simulation refers to the bond fluctuation model, where every monomer takes all sites of an elementary cube of the simple cubic model, but only the  $z$ -coordinate of the four lower sites of the cube is counted for computing  $\langle z_b \rangle$ . Note also the logarithmic scales of the figure. Adapted from [157]

weakly adsorbed case, the chain in the pancake is an irregular sequence of “trains” (strictly 2D pieces of the chain attached to the planar substrate) alternating with “loops” (and “tails” at the chain ends) [123].

For the adsorption of macromolecules with complex architecture, such as bottle brush polymers, it is an intriguing question how the above picture of polymer adsorption changes; after all, most manipulations of macromolecules with external devices (e.g., AFM tips) presuppose that the macromolecule is situated at a suitable surface [156], rather than freely diffusing in the 3D space of a more or less dilute polymer solution.

The coarse-grained view of a bottle brush in 3D space is often similar to the wormlike chain model [59–61]: a more or less randomly bent cylinder with cross-sectional radius  $R_{cs}$ , contour length  $L$  along the contour axis, and persistence length  $l_p$  (meant to describe the local chain stiffness). Obviously, it is not completely clear how such a structure changes when the macromolecule interacts with an adsorbing surface. Do we expect a wormlike structure, where (like for a real living worm) the local cross-section of the worm is still spherical? If so, only a few monomers on the periphery of the bottle brush touch the substrate. However, it could also be that the bottle brush becomes adsorbed to the surface somewhat more strongly, so its local cross-section could look like a sphere cap rather than like a sphere. This situation is analogous to droplets at walls under incomplete wetting conditions [158]. If the picture of a sequence of trains and loops is still valid, the structure in the trains and loops could well be different. Finally, when the adsorption strength is very pronounced, the bottle brush can become forced into a quasi-2D flat configuration attached to the substrate. Then locally it would look like a comb, with spikes stretching away from the backbone at both sides. Given the fact that, in reality, the chemical structure of the backbone will differ from the chemical

**Fig. 46** Snapshot pictures of adsorbed bottle brushes for the case  $N_b = 131$ ,  $N_s = 24$  and two values of  $\varepsilon$ : (a)  $\varepsilon = 1.25$  and (b)  $\varepsilon = 2.0$ . Different side chains are in different colors (the backbone is in light blue). Adapted from [157]



structure of the side arms, many model parameters may come into play when a simulational modeling of this problem is attempted. However, for the sake of simplicity this possible difference in chemistry has been ignored [157, 159]; thus, in the modeling results (cf. Fig. 45) [157] a single parameter  $\varepsilon$  occurs (units chosen such that  $k_B T = 1$ ) that describes the strength of the short-range adsorption potential.

The simulations have revealed a two-stage adsorption process for a bottle brush polymer (Fig. 45): In the first stage, the configuration changes from mushroom-like structures where only very few monomers near one backbone end are bound to the surface (state with  $\varepsilon = 0.9$  in Fig. 45) to a weakly bound wormlike chain ( $\varepsilon = 1.25$  in Fig. 45). We find that for an adsorbed bottle brush a more realistic picture than a worm is a “millipede”: many “arms” (i.e., side chains of the bottle brush polymer) touch the substrate, all along the backbone, but the latter is still elevated. The typical distance  $\langle z_b \rangle$  of the backbone from the surface is still of the order of 10 lattice spacings (in the bond fluctuation model that is used here, bond lengths vary from 2 to  $\sqrt{10}$  lattice spacings, and the number of effective monomers in a side chain in Fig. 45 varies from  $N_s = 6$  to  $N_s = 24$ ). At the transition from the mushroom to the millipede structure (near  $\varepsilon \approx 1.3$ ), a second transition to a strongly adsorbed state occurs,  $\langle z_b \rangle$  is of order unity, and the backbone monomers

become more or less completely attached to the wall. But, even in the weakly adsorbed regime, such as  $\varepsilon = 1.25$ , one finds clear evidence that the backbone extension exhibits a scaling with the number of backbone monomers  $N_b$  compatible with 2D self-avoiding walks,  $L \propto N_b^{2\nu(2d)} = N_b^{3/2}$  [68]. The snapshots in Fig. 45 show only the backbone chain, whereas Fig. 46 shows snapshots of a rather short bottle brush ( $N_b = 131$ ,  $N_s = 24$ ) in the weakly adsorbed ( $\varepsilon = 1.25$ ) and strongly adsorbed ( $\varepsilon = 2.0$ ) cases. Note that for  $N_b = 131$  and  $\varepsilon = 2.0$ , the rod regime still holds and the contour length  $L$  of the (coarse-grained) cylindrical macromolecule does not exceed the persistence length  $l_p$ . Note also that the side chains are not fully adsorbed linear “spikes”, but rather exhibit an irregular sequence of loops and trains: so the picture of a comb lying flat on the surfaces is not yet appropriate.

### 3.10 Conclusions

Cylindrical brushes constitute a hybrid between a branched polymer and a molecular object. Their shape is strongly anisotropic but both main and side chains preserve their intrinsic flexibility, although with strongly reduced degrees of freedom. The presented simulations demonstrate that the established wormlike chain models are not applicable for the determination of chain stiffness, which could well be the origin of diverging experimental results in the past. Particularly valuable is the finding that a global relation between the main chain stiffness and the cross-sectional diameter of the brushes is much more promising than subtle bond angle correlation functions in order to obtain a good measure of the directional persistence.

The unique structure of cylindrical brushes makes them ideal candidates to (1) experimentally and theoretically study the phase separation in quasi -1D molecular objects, (2) investigate the properties of polyelectrolyte complexes of shape-persistent polyions, (3) elucidate the adsorption on planar surfaces, and eventually (4) develop novel cationic carriers for gene transfection, as described in detail in Sect. 4.

## 4 Supramolecular Structure Formation by Directed Interactions

### 4.1 Introduction

The formation of intermolecular structure of the cylindrical brushes described in the previous section is mainly governed by their anisotropic shape, which enables them to form even lyotropic phases. Other driving forces are of ionic and/or entropic

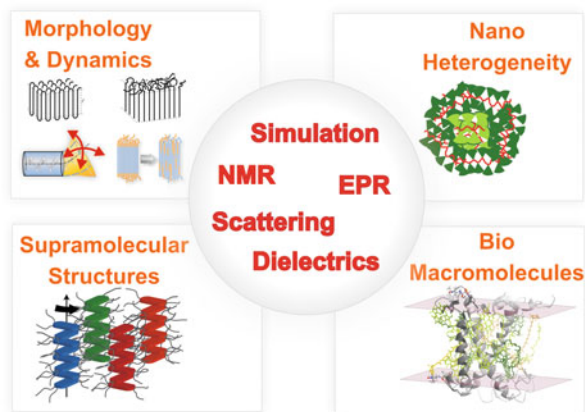
origin or comprise thermodynamic phase separation, which typically do not induce preferred directions. One exception is the intramolecular  $\beta$ -sheet formation of the side chains in cylindrical brush structures with PLL side chains, which originate from intramolecular hydrogen bonds. The latter belongs to the class of interactions that induce a certain orientation. Such directional interactions are the main subject of this section, where more complex and highly ordered supramolecular structures are described on the basis of hydrogen bonds and shape-dependent  $\pi$ - $\pi$  interactions. Here the investigations are focused on the interplay of both types of interactions occurring in the same system.

A particularly valuable tool for studying intra- and intermolecular interactions is solid-state NMR. Advanced solid-state NMR, combined with X-ray scattering and computer simulation, provides site-selective and noninvasive information of noncovalent interactions such as hydrogen bonding and  $\pi$ - $\pi$  interactions. For this reason, we first briefly introduce the NMR techniques and then describe specific applications to macromolecular and supramolecular systems, including hybrids of synthetic polypeptides, hybrids containing synthetic polymers, polymers with incompatible segments, and systems containing rigid rods or rings.

## ***4.2 Solid-state NMR Techniques for Analyzing Structure and Dynamics***

Signals originating from hydrogen-bonded protons are well separated in  $^1\text{H}$  magic-angle spinning (MAS) NMR spectra, typically resonating between 8 and 20 ppm [160]. The  $^1\text{H}$  chemical shift includes semiquantitative information about the strength of the hydrogen bonds. In addition, the  $^1\text{H}$  chemical shift is also a sensitive probe with respect to ring currents associated with aromatic moieties [161]. This is observed as a low field shift of the chemical shift compared to the corresponding liquid state signal and may thereby serve as a direct indication of  $\pi$ - $\pi$  interactions. Likewise, the low field shift can be simply related to the packing via so-called nucleus independent chemical shift (NICS) maps [162]. This augments the well-known sensitivity of  $^{13}\text{C}$  NMR chemical shifts to local conformation [163]. Detailed packing information is obtained from distance measurements between specific proton sites at adjacent building blocks via high resolution double quantum (DQ) solid-state NMR under MAS. Disk-shaped moieties that stack into columnar structures known as discotic liquid crystals have been studied extensively. In the liquid crystalline (LC) phase, the disks rotate about the column axis. A particularly simple way of characterizing such restricted molecular dynamics is provided by the dynamic order parameter  $S$ , where  $0 \leq S \leq 1$ . It is defined as the ratio between the motionally averaged and the static anisotropic NMR interaction, e.g., dipole-dipole coupling, anisotropic chemical shift, or quadrupole coupling [160]. For the rotation of disks in a perfectly packed column,

**Fig. 47** Overview of systems, phenomena, and techniques for elucidating the interplay between structure and dynamics in macromolecular and supramolecular systems



$S = 0.5$  for  $^{13}\text{C}$ - $^1\text{H}$  dipole–dipole coupling, or  $^2\text{H}$  quadrupole coupling, centered around the C–H (C–D) bond direction. Imperfections of the packing in the LC phase, where disks are inclined to the column axis, lead to a reduction,  $S < 0.5$ . Thus,  $S$  provides both dynamic and structural information. In general, solid-state NMR can provide site-selective information about the amplitude and time scales of molecular motions over broad ranges of length and time [164].

Advances in the synthesis, characterization, and understanding of macromolecular and supramolecular systems have led to an enormous variety and complexity in the field of soft matter science [165]. The traditional separations in terms of structure versus dynamics, crystalline versus amorphous, or experiment versus theory are increasingly overcome. As far as characterization of such materials is concerned, no experimental or theoretical/simulation approach alone can provide full information. Instead, a combination of techniques is called for and conclusions should be backed by results provided by as many complimentary methods as possible [166]. Combining scattering or NMR spectroscopy with computer simulation is well established today in the study of structure and dynamics of biomacromolecules [167]. Prominent examples of such an approach in the supramolecular field involve the combination of X-ray scattering, spectroscopy and computer simulation to elucidate the packing in newly synthesized columnar systems [168]. The versatility of magnetic resonance techniques, in particular solid-state-type NMR, in elucidating the interplay between structure and dynamics in these systems is evident from the examples provided below. Yet none of the results in the examples are based on a single technique (Fig. 47).

The methods for determining structure and dynamics of supramolecular systems based on 2D DQNMNMR as reviewed, e.g., in [161, 164, 169] are now widely employed in soft matter and life sciences alike. Recently, a new systematic strategy for revealing the local packing in semicrystalline  $\pi$ -conjugated polymers was introduced [170]. Our strategy takes advantages of a multi-technique approach in which unit-cell parameters are derived from X-ray scattering, and molecular constraints are determined from solid-state NMR spectroscopy. The parameters

derived from this strategy include the space group, which is one of the first steps in a conventional approach to solving a crystal structure, distance constraints from  $^1\text{H}$  DQNMNMR, and chemical shifts. These experimental results are unified by quantum-chemical calculations, enabling the verification of specific packing models *in silico* and quantification of  $\pi$ -stacking effects. This approach can be compared with that employed for solution structures of biomacromolecules through distance constraints (nuclear Overhauser effect, NOE) and NMR chemical shifts [171]. This, however, requires a large number of NOE constraints, whereas in a crystalline solid the periodicity described by the space group gives access to the full 3D structure from only a few constraints. Thus, our strategy, which we propose to term “multi-technique crystallography”, can be applied in general to provide quantitative insights into the packing of semicrystalline polymers with specific intermolecular packing features, such as hydrogen bonds or stacking of aromatic moieties.

Based on work at the Max Planck Institute for Polymer Research [172, 173], pulsed electron paramagnetic resonance (EPR) has experienced a remarkable revival worldwide [174]. In particular, pulsed double electron–electron resonance (DEER) spectroscopy in combination with site-directed spin labeling [175] is extensively used today in studies of the structure of proteins, including their function as carriers of small molecules, and of nucleic acids. Moreover, it is used to probe large, complex biomacromolecules and their assemblies as well as 1361 protein folding [176].

### 4.3 *Self-Assembly and Dynamics of Polypeptides*

Polypeptides, i.e., macromolecules composed of amino acids, are probably the best known example of molecular structures determined by intramolecular hydrogen bonds [177]. Resembling biomacromolecules, they are considered for use in drug delivery and gene therapy and thus have been subject of intensive studies [178]. In addition, it is known that the superb performance of biological polypeptide-based materials such as hair or spiders’ silk is due to a hierarchical superstructure over several length scales, where structure control is exerted at every level of hierarchy [179]. The two most common local conformations of polypeptides, known as secondary structures, are the  $\alpha$ -helix, stabilized by intramolecular hydrogen bonds, and the  $\beta$ -sheet, stabilized by intermolecular bonds. These secondary structures can be probed directly by solid-state NMR [163] and their packing can be obtained by X-ray analysis [180]. Different chain conformations can also be distinguished by simple circular dichroism (CD) measurements [177], employed in Sect. 3.3.2. In addition, the  $\alpha$ -helical structure posts a permanent dipole moment along its backbone and can, therefore, be classified as type-A polymer in Stockmayer’s classification [181]. This dipole moment can be measured precisely using dielectric spectroscopy (DS) and can be used as a probe of the persistence length of the secondary structure [182]. Over the years, we have studied various

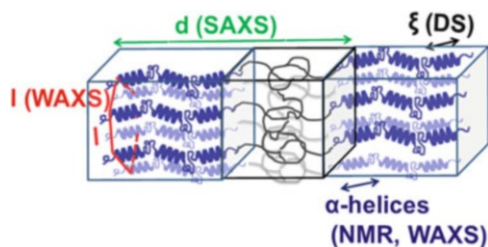


**Fig. 48** Assembly of a lamellar-forming polypeptide-coil diblock copolymer depicting the main techniques employed in our studies. Small-angle X-ray scattering (SAXS) is employed for the domain spacing,  $d$ .  $^{13}\text{C}$  NMR and wide-angle X-ray scattering (WAXS) are employed to identify the type of the peptide secondary structure ( $\alpha$ -helical in the schematic). WAXS is further employed to specify the lateral self-assembly of  $\alpha$ -helices within the polypeptide domain (a hexagonal lattice is indicated). Dielectric spectroscopy (DS) and site-specific NMR techniques are employed for the dynamics. Furthermore, the most intense DS process provides the persistence length,  $l_p$ , of  $\alpha$ -helical segments [181]

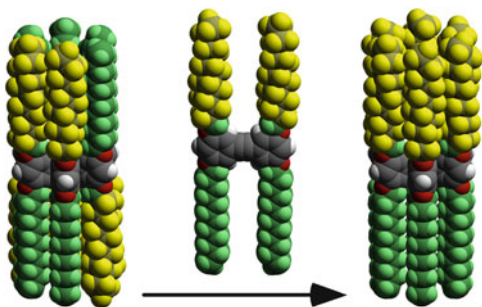
polypeptides by different NMR techniques, X-ray scattering, and dielectric spectroscopy in order to better understand their hierarchical self-assembly (Fig. 48).

As shown in an extended review [181], the concerted application of these techniques has shed light on the origin of the glass transition, the persistence of the  $\alpha$ -helical peptide secondary motif, and the effects of topology and packing on the type and persistence of secondary structures. Protein function and applications often depend on these issues. With respect to the freezing of the dynamics at the liquid-to-glass transition temperature ( $T_g$ ), it was found that the origin of this effect is a network of broken hydrogen bonds. It is the diffusion of these defects along the chain that give rise to the strongly non-Arrhenius dynamics associated with  $T_g$ . Glass formation is largely independent of the presence or absence of side groups and is decoupled from the solvent dynamics. The selective probing of the  $\alpha$ -helical motifs by NMR elucidated the geometry of the respective dynamic processes. Not surprisingly, the presence of defects in hydrogen-bonded regions also has consequences on the persistence length of  $\alpha$ -helices. Using poly( $\gamma$ -benzyl-L-glutamate), PBLG, as an example, it was shown that helices are objects of rather low persistence in the bulk as well as in concentrated solutions in helicogenic solvents [183].

Copolyptides, on the other hand, with their inherent nanometer length scale of phase separation, provide means of manipulating both the type and persistence of peptide secondary structures. As examples we refer to the partial annihilation of  $\alpha$ -helical structural defects due to chain stretching, to the induced chain folding of  $\beta$ -sheets in block copolypeptides with incommensurate dimensions, and to the destabilization of  $\beta$ -sheets in peptidic blocks having both secondary motifs [184–186]. These effects should be taken into account when such peptides are going to be employed in applications such as drug delivery.

Polypeptide star polymers with a large hydrocarbon core were found to exhibit several unanticipated properties. First, with the aid of a polyphenylene (see also Sect. 2) core scaffold it was shown that there is a distinct change in the

**Fig. 49** Incompatible segments, CF<sub>2</sub> (yellow), CH<sub>2</sub> (green), and aromatics (red), can be forced into proximity by limiting conformational freedom



peptide secondary structure from coil/ $\beta$ -sheet conformations to  $\alpha$ -helices that is accompanied by an abrupt increase in the hydrodynamic radii. This change in secondary structure and its consequences on the diffusion of the conjugates can be crucial in the efficient design of multiple antigen peptides. Second, the bulk studies revealed a strong effect of the polyphenylene core on the peptide secondary motifs that could not be envisaged from their linear analogues. The time-scale and the amplitude of polypeptide molecular motion could be measured by combining dielectric spectroscopy with advanced NMR techniques [187].

Proline residues are of exceptional significance in protein conformation and protein folding because proline is the only amino acid where the nitrogen bears no amide hydrogen, preventing hydrogen bonding. Furthermore, the bulky pyrrolidine ring restricts the available conformations. Therefore, polypeptides with proline residues offer a unique possibility to unravel the interplay between hydrogen bonding and geometric packing effects. A recent multi-technique study of diblock copolymers of PBLG and poly(L-proline) (PLP) investigated their hierarchical self-assembly. Both blocks possess helices stabilized solely either by hydrogen bonds (PBLG) or by steric hindrance (PLP) and are further packed in two different hexagonal cells. An intriguing *trans*–*cis* conformational change of PLP upon confinement was observed that mimics the isomerization of isolated proline residues in proteins. These *cis*-PLP conformations reside primarily at the PLP–PBLG interface, alleviate the packing frustration, and permit PBLG and PLP helices to pack with their bulk properties [188].

#### 4.4 Polymers with Different Building Blocks

Precise 3D nanoscale morphological control of the solid state in the 5–10 nm range using semiflexible chains is a demanding challenge [189]. The development of strategies for increasing the intricacy within self-assembled nanostructures outside of biology or analogous *de novo* examples is hindered by the ability to predict the complex competition of intra- and intermolecular interactions at the molecular level. With this in mind, fluorocarbon units were incorporated into polymers. This offers ways of combining a low friction coefficient, high rigidity, extremely low surface energy, hydrophobicity, chemical inertness, and thermal resistance, which make them

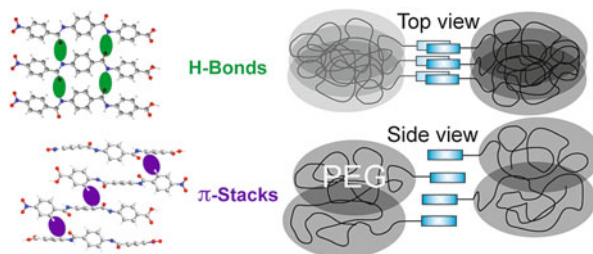


**Fig. 50** Packing of rod-coil copolymers. The rigid rods are held together by intermolecular hydrogen bonds. The space between the stacks is filled by the PEG side chains adopting a Gaussian coil-like conformation

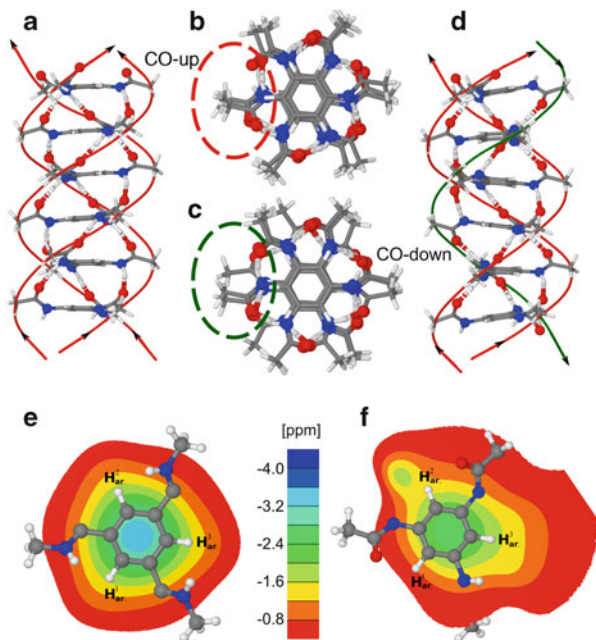
useful for a wide range of applications. Last, but not least, partially fluorinated compounds provide unique tools for tailoring self-assembly via the fluorophobic effect. In particular, in systems containing fluorocarbon/hydrocarbon amphiphiles tethered to cores with only rotational degrees of freedom, these incompatible segments can be forced into proximity (Fig. 49). The lack of sufficient conformational mobility leads to kinetically trapped phases, stabilized by favorable interactions with neighboring molecules [190, 191]. Here,  $^{13}\text{C}$  and  $^{19}\text{F}$  NMR both in solution and in solid state are especially informative for unraveling the self-organization.

#### 4.5 Interplay of Undirected and Directed Interactions

Rod-coil block copolymers represent an interesting class of diblock copolymers due to their particular aggregation behavior. The interactions between various segments and geometric effects are responsible for nanoscale phase separation and liquid crystallinity. The ability to self-assemble on the nanometer length scale has promoted these systems for possible applications such as light-emitting diodes (LEDs) and organic photovoltaics and also for the preparation of nanometer-scaled architectures. Therefore, rod-coil block copolymers with an oligomeric rod segment are of particular interest because their aggregation might depend on the length of the respective building blocks [192, 193]. With this in mind, we have investigated copolymers built of oligomeric rod blocks of oligo(*p*-benzamides) (OPBA) and a poly(ethylene glycol) (PEG) coil (Fig. 50). An interesting feature of solid OPBAs is their rigidity resulting from packing due to hydrogen bonding and  $\pi$ - $\pi$  interactions. Both are noncovalent interactions, and their influence on the structure of the studied system is not yet fully understood.

Insight into aggregation and local packing of both OPBAs and OPBA-based rod-coil copolymers can be obtained from advanced high-resolution solid-state NMR. It was found that longer OPBAs form hydrogen-bonded layered  $\beta$ -sheet-like aggregates, which are remarkably stable and apparently reflect an equilibrium structure [194]. This structure is retained after PEG attachment, forming a rod-coil

**Fig. 51** Helical BTA stacks: (a, b) CO-centered and (c, d) N-centered. The tilted stacking leads to a splitting of the CH signals in  $^1\text{H}$  MAS NMR spectra, as indicated by the NICS maps (e, f) [197]



copolymer. At  $59^\circ\text{C}$  a transition to a LC phase of the rod-coil copolymer is observed by DSC. From solid-state NMR studies, this has been ascribed to melting of the PEG coil, where the aggregates of the OPBA rods are preserved. Because of the pre-organization in the LC phase, an improvement of the local order is observed for the OPBA rods in the copolymer.

C3 symmetric benzene-1,3,5-tricarboxamides (BTAs) are known to form helical supramolecular assemblies with columnar mesophases [195]. The driving forces for self-organization can vary from system to system despite equivalent, hydrogen-bonding central building blocks [195]. Solid-state NMR combined with X-ray scattering, optical spectroscopy, and computer simulation provides insight in the subtleties of the organization of the moieties [196]. When three bulky side groups, such as 3,3'-diamino-2,2'-bipyridines, are attached to BTAs, the self-assembly of the disk-like molecules is mainly driven by steric interactions between neighboring molecules, where surprisingly hydrogen bonding along the columns has almost no influence on the final supramolecular structure. This results in a complicated helical arrangement with a pitch angle between  $13^\circ$  and  $16^\circ$ , in accord with quantum chemical calculations. In contrast, in BTAs with short chiral, aliphatic side chains, the supramolecular organization sensitively depends on the local hydrogen bonding. Unlike the common symmetric co-planar helical arrangement of carbonyl-centered BTAs found in supramolecular polymers in gels (Fig. 51a, b), NH-centered BTAs adopt an asymmetric helical arrangement in the solid (Fig. 51c, d) [197].

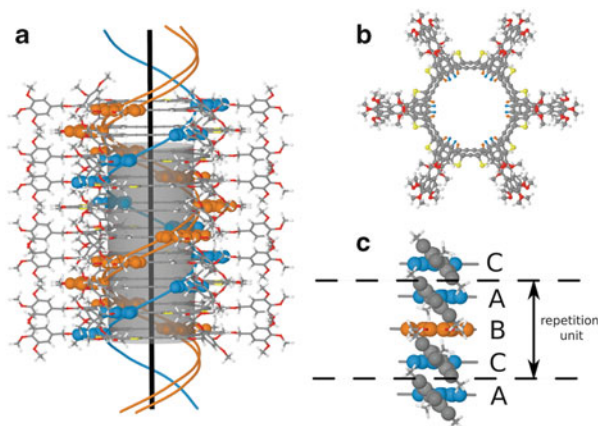


**Fig. 52** a) Sketch of empty helical stacks formed by shape-persistent macrocycles. b) A pitch angle of  $\approx 60^\circ$  between adjacent macrocycles was determined from 2D double quantum NMR correlation spectra in agreement with NICS maps. c) Side-chain packing [201]

Supramolecular organization is also able to create tubular molecular structures [198, 199]. Tube stabilization utilizing strong bonds, e.g., by metal–ligand interactions or by surfactant-templated synthetic procedures, leads to fixed structures in the final material. To generate more flexible tubes one can take advantage of dissipative forces. A recent example is the self-assembly of shape-persistent low symmetry arylene-ethynylene-butadiynylene macrocycles into flexible molecular channels, with dissipative forces between aromatic moieties with different electron affinities [200]. From solid-state NMR experiments combined with chemical shift calculations it was possible to show that the channels are indeed empty [197]. The decisive role of the length of the dendritic side chains was unraveled, as well as the formation of a six-membered ring with weak intramolecular contact involving a proton site on an aromatic group of the group and a flexible ethylene oxide linker of the side group. The formation of a LC phase then leads to the immediate and controllable formation of self-repairing nanochannels. These channels have an inner diameter of well over 1 nm in the LC phase. The channels are further stabilized by a helical arrangement, with a pitch of about  $60^\circ$  between individual macrocycles as identified from  $^1\text{H}$  solid-state NMR experiments and NICS calculations (Fig. 52). Such artificial channels can function as size-selective or even as molecular-selective pores for chemical sensing or directed transport of nanosized objects [200, 201].

In addition to the structure of supramolecular objects, the dynamics of the building blocks themselves or molecules trapped in cages and channels is of great importance [166, 202]. For instance, the guest dynamics of dimeric capsules of tetratolyl urea calixarene filled with different aromatic guests such as benzene, fluorobenzene, and 1,4-difluorobenzene was studied. Upon inclusion, all guest moieties exhibit

complexation-induced chemical shifts varying from 3 to 5 ppm. All guest molecules undergo distinct motions, ranging from mere  $C_6$ -rotations of benzene at low temperatures to rather ill-defined  $180^\circ$  phenyl flips of fluorobenzene. In addition, by combination of both computed NICS maps and explicit  $^{19}\text{F}$  and  $^2\text{H}$  ab initio chemical shift calculations by density functional theory, the preferred orientation of the guest molecules within the host was derived. Although benzene populates the center plane formed by the stabilizing hydrogen bonds of the urea units, fluorobenzene prefers an equatorial position. In the case of 1,4-difluorobenzene, an axial position is suggested. Off-centered orientations towards the “walls” of the host, however, can be safely ruled out [203].

## 4.6 Columnar Structures from Discotic Liquid Crystals

The disk-shaped polycyclic aromatic hydrocarbons (PAH) form  $\pi$ -stacks and are currently of broad scientific interest due to their potential application as conducting molecular wires [204]. Charge mobility can occur parallel to the stacking axis. Critical for the charge-carrier properties are disk size, shape, and periphery [205]. We have studied two such disk-shaped molecules that form molecular wires in their crystalline and LC phases. We determined the packing and specific molecular dynamics of the disks, including the intriguing kinetics of self organization and self-healing.

The most prominent examples of such molecular  $\pi$ -stacks are based on hexa-peri-hexabenzocoronenes (HBC) [160, 204]. Here, the kinetics of phase transformation from the high temperature discotic liquid crystalline mesophase to the crystalline phase at lower temperatures has been studied in a model dipole-functionalized HBC derivative. Complementary structural (X-ray diffraction, solid-state NMR) and dynamic (solid-state NMR, DS) methods were employed. These experiments revealed long-lived metastability, slow kinetics, as well as an intermediate state that involves a change in unit cell prior to crystallization. The barrier properties for the unit cell transformation and crystallization amount to 1 and 2.5 eV, respectively. Although crystallization bears some similarity to nucleation and growth, the LC to crystalline transformation is more complex and involves fractional exponents. In addition, the selective probing of the alkyl chains and disk dynamics by NMR allowed identifying the role of the latter on inducing crystallization [206].

Among the different discotic liquid crystals, perylenediimide (PDI) derivatives have received considerable attention, originally because of their industrial applications as pigments. Efforts to optimize pigment colors resulted in high-grade industrial applications including automotive coatings [207]. These applications made use of the high tinctorial strength, light and weather stability, insolubility, and chemical inertness of PDIs. Other major applications of PDI derivatives are as organic electronics in all-organic photovoltaic solar cells and field-effect transistors. These applications rely on the high charge carrier mobilities that made PDI the best n-type semiconductors available to date [208]. Central to these applications of HBCs

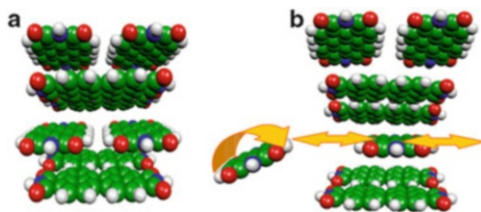


**Fig. 53** Drawing of the PBI columns as revealed from solid-state NMR and computer simulation. (a) Tetramer motif stacking into columns. (b) Molecular reorganization: One PDI leaves the columns, flips over, and enters a column again [210]

and PDIs is their ability to organize efficiently in different packing motifs and, in particular, their degree of intra- and intermolecular order. The degree of structural perfection strongly affects their properties (absorbance, fluorescence, and charge transport) and results in applications in organic field-effect transistors, light-emitting diodes, and organic solar cells.

In a systematic investigation of the self-assembly, dynamics, and kinetics of phase formation of donor–acceptor substituted perylene derivatives, the role of the strong dipole associated with the diphenylamine-functionalized perylenemonomimides molecules was elucidated. The close packing manifested itself in strong heteronuclear dipolar couplings, which were exploited in solid-state NMR. The structural investigation revealed that the self-assembly and thermodynamic properties of perylene derivatives are significantly different from those of the corresponding HBC compounds. Perylenes, with a small  $\pi$ – $\pi$  overlap, form a crystalline phase as well, but the residues do not tilt with respect to the columnar axis. Because such a tilt is absent in perylenes, the intercolumnar thermal expansion is always positive, being similar to the intracolumnar thermal expansion. This constitutes a primary difference between the self-assembly motifs of the crystalline phase of perylenes and those of the HBCs. The phase formation involves a delicate balance of short-range interactions and packing. Our results suggest that branched chains substituted away from bay positions are important as space-filling agents within the alkyl domains for the formation of the crystalline phase.

The solid-state NMR experiments unraveled the role of intramolecular hydrogen bonding in stabilizing the crystalline phase as well as the influence of non-hydrogen-bonded moieties on the twist angle between successive monomers [209].

With respect to the dynamics, both solid-state NMR and DS revealed a relatively immobile core within the crystalline phase. Perylene derivatives that do not crystallize undergo an isotropic liquid-to-glass transformation at a temperature that was found to depend on the number of methylene units in the alkyl chains. The phase transformation kinetics from the high temperature isotropic phase to the crystalline phase at lower temperatures revealed a long-lived metastable state as a result of the soft potential. The crystalline phase is formed via nucleation and growth. The transformation kinetics is controlled by the nucleation barriers. The existence of slow molecular dynamics and of very slow phase transformation suggests that care should be taken in establishing the equilibrium phases of discotic liquid crystals.

Furthermore, these issues could influence the charge carrier mobilities that are required for applications as photovoltaic solar cells and field-effect transistors [209].

This is indeed the case for perylene bisdiimides (PBI) functionalized with dendritic groups. These dendronized PBIs self-assemble into a complex helical column generated from tetramers containing a pair of molecules arranged side-by-side and another pair in the next stratum of the column, turned upside-down and rotated around the column axis at an intratetramer angle that is different from that of the intertetramer angle (Fig. 53). In most cases, the intratetramer stacking distance in this column is 4.1 Å, while the intertetramer distance is 3.5 Å. The architecture of this complex helical column, the structure of its 3D periodic array, and its kinetically controlled self-organization with such a long intratetramer distance are not ideal for the design of supramolecular structures with high charge carrier mobility. In fact, the mobility of electrons is only moderate. However, in some cases heating above 100°C into the LC phase optimizes the packing, resulting in shorter intertetramer distances and much higher charge mobilities [210]. This is accompanied by substantial narrowing of the  $^1\text{H}$  NMR lines. Computer simulation showed that this narrowing of the NMR spectra indicates a complex reorganization mechanism, where the PBI molecules leave the supramolecular column, flip over, and reenter a column at a later time (Fig. 53) [210].

## 4.7 Conclusions

The examples briefly reviewed here demonstrate that the interplay of synthesis, multi-technique characterization and computer simulation is crucial for the development of functional materials based on supramolecular organization of carefully designed building blocks. Local conformation, intrinsic mobility, incompatibility, and well-established noncovalent interactions such as hydrogen bonds or  $\pi$ - $\pi$  interactions can govern self-assembly in highly specific ways. Moreover, complex molecular dynamics is relevant for generating stable structures with desired properties such as high charge carrier mobility. In contrast, ill-defined sample preparation can lead to partially disordered structures with inferior properties. Magnetic resonance, both NMR and EPR, can provide unique detailed information about all these aspects over large ranges in space and time. Therefore, these techniques play an important role in the generation of functional organic materials.

## 5 Block Copolymers and Confinement

This section deals with the influence of amphiphilicity on the formation of block copolymer structures. These block copolymers are either confined in the spherical shape of a nanodroplet or on a surface. Whereas in the first case, the fundamental aspects of mesoscopic structure formation are the focus of attention, we concentrate in the second case on a specific function, i.e., switchable wettability due to the

in-chain attachment and self-assembly of a block copolymer on a surface. As a third example we describe the inverse effect: vesicles formed by block copolymers and dispersed in aqueous medium confine quantum dots in the hydrophobic interior of the lamellae.

### 5.1 Diblock Copolymers Confined in Miniemulsion Droplets

As a first example, we consider block copolymers confined in droplets as obtained by the miniemulsion process. It is well known that block copolymers self-assemble into periodic nanostructures such as lamellae, hexagonally coordinated cylinders, cubic lattices of spheres, and the gyroid morphology [189, 211]. This phase behavior can be adjusted by different parameters such as temperature or the chemical composition [212, 213]. Block copolymers have been investigated extensively in bulk. The influence of a 2D or 3D confinement on the sub-100-nm scale has, however, only been examined in a limited way. In the 2D confinement of a film, a deviation of the lamellar thickness from the value of the bulk material is induced [214]. By confining a block copolymer in a porous silica matrix, both cylindrical and lamellar structures were observed [215]. Electrospinning and subsequent annealing of the obtained fibers also lead to cylindrical structures [216]. Onion-like block copolymer morphologies were obtained in spherical particles using spray coating [217]. Using emulsion techniques and subsequent solvent evaporation techniques, onion-like particles from poly(styrene-*b*-isoprene) and poly(styrene-*b*-methyl methacrylate) (PS-*b*-PMMA) were created [218]. Lamellar, hexagonal, and bicontinuous phases in nanoparticles could be realized with a triblock copolymer [219].

Nanoparticles consisting of different molecular weight PS-*b*-PMMA copolymers and nanocapsules made of the same copolymers, but additionally with hexadecane as liquid core material, were prepared by using a combined miniemulsion and solvent evaporation technique [220]. The morphology of block copolymer assemblies was investigated in dependence of the nanoconfinement. We introduced two nanoconfinement parameters: the diameter  $D$  of the droplet throughout the synthesis and the shell thickness  $\delta$  of the nanocapsules with a liquid as core.  $D$  was controlled by varying the concentration of the surfactant in the miniemulsion, while  $\delta$  was controlled by the ratio of hexadecane to copolymer.

For the investigation of the influence of the molecular weight of the polymer on the morphology of the block copolymer, we used PS<sub>76</sub>-*b*-PMMA<sub>79</sub> and PS<sub>838</sub>-*b*-PMMA<sub>945</sub>, where the numbers correspond to the average numbers of units of styrene and methylmethacrylate [221].

For the formation of solid copolymer nanoparticles without a liquid core, PS-*b*-PMMA was used as a model system. In order to be able to form nanoparticles, the block copolymer was dissolved in chloroform and the solution was miniemulsified in water by adding the SDS. In this case, homogeneous droplets were formed. After evaporation of the chloroform, nanoparticles consisting entirely of block copolymer

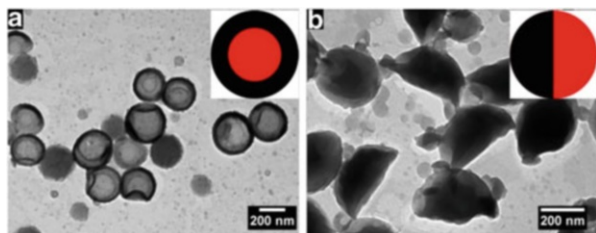


**Fig. 54** TEM micrographs of nanobjects made of PS<sub>838</sub>-*b*-PMMA<sub>945</sub> and hexadecane (ratio 1:1) with increasing amount of SDS. Their morphology changes from (a) nanocapsule (low coverage of SDS, 0.67 wt%) to (b) a Janus-like structure (high coverage of SDS 3.33 wt%). The insets represent the morphology in aqueous phase with the copolymer (*black*) and hexadecane (*red*); the latter is evaporated in the electron microscope and therefore not visible on the TEM micrograph [221]. Reproduced by permission of The Royal Society of Chemistry

were obtained. Phase separation of the block copolymer took place during solvent evaporation.

Nanocapsules consisting of the block copolymer as shell and with a liquid as core could be obtained by adding hexadecane, which is a nonsolvent for the copolymer. The block copolymer was dissolved in a mixture of chloroform and hexadecane. During evaporation of the chloroform there is a phase separation of the block copolymer and the hexadecane, and a microphase separation of the block copolymer itself. For the successful formation of nanocapsules, the interfacial tensions for the polymer/water and water/hexadecane interfaces are important.

The presence of the surfactant SDS influences nanocapsule formation in two ways: With increasing SDS concentration, the nanocapsules become smaller. At the same time, with decreasing size of the nanocapsule, the coverage of the nanobjects (before evaporation of the solvent, the nanodroplets; after the evaporation, the nanoparticles or nanocapsules) by SDS increases, leading to a decrease in the interfacial tension of droplet/water and copolymer/water. The interfacial tension between copolymer and water ( $\approx 0.035$  N/m) without surfactant is considerably smaller than the interfacial tension between hexadecane and water ( $\approx 0.054$  N/m). Thus, in the case of a low concentration of SDS and subsequent coverage of the nanobjects by SDS, the interfacial tension of the copolymer/water interface is lower than that of the hexadecane/water interface; therefore as the thermodynamically most stable structure, nanocapsules are expected to be formed (Fig. 54a).

In the case that the concentration of SDS is high enough to give full coverage of the interfaces with surfactant, there are similar interfacial tensions for the polymer/water and hexadecane/water interfaces and Janus-like particles consisting of PS-*b*-PMMA and liquid hexadecane are formed in the aqueous phase. After drying (and therefore complete removal of the liquid hexadecane), a half-spherical morphology is obtained as verified by electron microscopy (Fig. 54b). Please note that in this case, the copolymer is seen as one phase.

The size of the nanoparticles and nanocapsules can be controlled by varying the amount of SDS in the miniemulsion process. For solid nanoparticles using the block copolymer PS<sub>838</sub>-*b*-PMMA<sub>945</sub> without hexadecane, the diameter decreases with

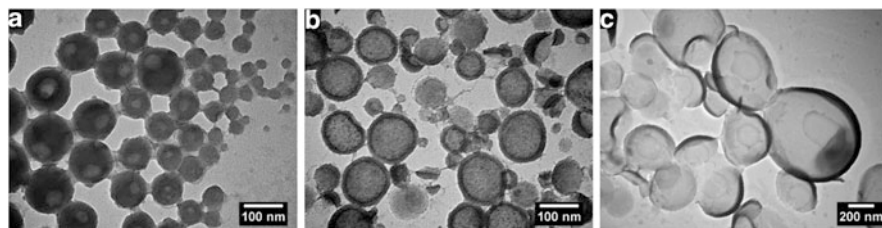


**Fig. 55** TEM micrographs of capsules consisting of PS<sub>838</sub>-*b*-PMMA<sub>945</sub> with increasing amount of hexadecane to copolymer: (a) 0%, (b) 40%, and (c) 80%. The SDS concentration was constant at 0.67 wt% compared to the dispersed phase. The capsules become more unstable as the wall thickness decreases with increasing amount of hexadecane [221]. Reproduced by permission of The Royal Society of Chemistry

increasing amount of surfactant (0.17–3.33 wt% compared to the dispersed phase) from about 250 nm down to 80 nm. For the nanocapsules with the same block copolymer, but additionally with hexadecane, the diameter of the nanocapsules was in the range of 470 nm (for the lowest amount of surfactant of 0.17 wt%) down to 200 nm (with a high concentration of SDS of 3.33 wt%). For the lower molecular weight block copolymer PS<sub>76</sub>-*b*-PMMA<sub>79</sub>, a decrease of the diameter from about 260 to 100 nm upon the same increase in SDS was observed. Since the diameter of the droplet determines the size of the particle or capsule obtained after solvent evaporation, the particle diameter is directly related to the amount of surfactant. For PS<sub>838</sub>-*b*-PMMA<sub>945</sub>, the average wall thickness varies between 68 and 20 nm and for PS<sub>76</sub>-*b*-PMMA<sub>79</sub> between 36 and 12 nm (Fig. 55). A thinner shell leads to unstable capsules that easily collapse. The theoretical wall thickness is in good agreement with the observed wall thicknesses.

After having evaluated the structure of the nanoobjects and considering the copolymer as one phase, the microphase structure of the copolymer within the nanoparticles and nanocapsules can be elucidated. The theoretical lamellar thickness  $L_0$  of PS-*b*-PMMA can be calculated for PS<sub>76</sub>-*b*-PMMA<sub>79</sub> to be 13.1 nm and for PS<sub>838</sub>-*b*-PMMA<sub>945</sub> to be 64.4 nm. For PS<sub>76</sub>-*b*-PMMA<sub>79</sub>, the product  $\chi N$  having a value of 6.5 is in the weak segregation limit. Therefore, no well-defined lamellar structures were expected for the low molecular weight PS<sub>76</sub>-*b*-PMMA<sub>79</sub>. In contrast, for high molecular weight PS<sub>838</sub>-*b*-PMMA<sub>945</sub>, the product  $\chi N$  equals 71 and the polymer is located in the strong segregation limit. A lamellar morphology is expected. When confined to spherical nanoparticles, this corresponds to an onion-like morphology. In cross-section cuts of stained particles in an epoxy matrix, this onion-like structure was indeed observed (Fig. 56e, f) using no hexadecane and low surfactant concentration. The lamellar thickness was 60 nm, in good agreement with the theoretical value of 64.4 nm. Because PMMA possesses a slightly lower interfacial tension with water than PS, it is expected that PMMA forms the outer layer. The XPS survey spectra revealed, as expected, only the elements carbon and oxygen. In addition, sulfur was found, but in low concentrations of less than 0.4 atomic %. High-resolution scans over carbon and oxygen were performed to determine the experimental oxygen/carbon ratio from which the molar PMMA

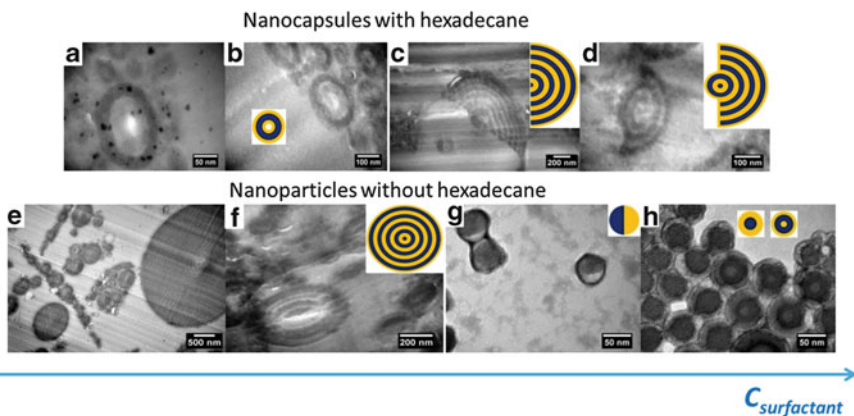


**Fig. 56** Final structure of nanoparticles (without hexadecane) and nanocapsules (with hexadecane) obtained with  $\text{PS}_{838}\text{-}b\text{-PMMA}_{945}$  after evaporation of hexadecane. The copolymer is in the strong segregation limit; PS (blue), PMMA (yellow). (a, b) Nanocapsules with hexadecane and low surfactant concentration show an onion-like morphology in cross-section cuts. (c, d) With hexadecane and high surfactant concentration, an onion-like structure is obtained at the geometrical center of the original Janus-like nanoparticle of hexadecane and polymer. In the outer regions, a bent structure is observed, which we attribute to volume conservation effects. (e, f) Without hexadecane and at low surfactant concentration, TEM micrographs show a lamellar structure in cross-sections of both large and small nanoparticles with good agreement between measured and theoretical layer thickness. (g) For higher concentrations of surfactant and therefore smaller nanoparticles, Janus-like block copolymer nanoparticles are obtained with diameters below the theoretical layer thickness. (h) For slightly larger nanoparticles, core-shell and onion-like morphologies form. Figure modified from [221]. Reproduced by permission of The Royal Society of Chemistry

surface concentration can be determined. For the onion-like particles, the surface consists of 87.1% PMMA.

For nanoparticle diameters below  $\sim 60$  nm (higher surfactant concentrations), e.g., below the theoretical layer thickness, Janus-like particles were observed (Fig. 56g). Particles with slightly larger diameters showed a core-shell structure, and a further small increase in diameter yielded an onion-like morphology (Fig. 56h). Because these particles are small enough to be sufficiently transparent to electrons they could be directly deposited onto a carbon support for TEM. Embedding in an epoxy matrix and thin sectioning was not needed. Therefore, the contrast is high enough to distinguish PS, PMMA, and the surrounding area. In agreement with the XPS results on larger particles, PMMA is located on the outside for both core-shell and onion-like morphologies.

As for the Janus-like particles, the entropic penalty for bending the block copolymer domains is higher than the penalty for creating an interface of the PS domain with water. However, a slight increase in the diameter is sufficient for turning the Janus-like particles into core-shell particles. Core-shell particles suffer from a higher entropic penalty due the bending of the lamellae but gain interfacial energy because the PS domain is not exposed to water. The results indicate that  $D \approx L_0$  represents the turning point for the conflicting energy contributions. Half-



**Fig. 57** Nanocapsules of  $PS_{76}\text{-}b\text{-}PMMA_{79}$  (weak segregation limit) show a structured surface in SEM and TEM images. In both cases, the small patches consist of PS, since it appears bright in the SEM and dark in the TEM. The patchy structure is also visible in TEM micrographs of stained cross-sections of (a) nanocapsules and (b) half-spherical nanoparticles and in (c) SEM and (d) TEM micrographs of nanoparticles consisting of  $PS_{76}\text{-}b\text{-}PMMA_{79}$ , indicating that it is not only a surface phenomenon [221]. Reproduced by permission of The Royal Society of Chemistry

spherical particles obtained from Janus-like particles of polymer and hexadecane showed an onion-like morphology at the center of the particle, whereas the outside of the particle consisted of bent lamellae.

Nanocapsules made of high molecular weight  $PS_{838}\text{-}b\text{-}PMMA_{945}$  and hexadecane show an onion-like morphology (Fig. 55a, b). The PMMA located on the outside of the capsules is not visible in the cross-section cuts, but XPS measurements confirm that the surface is mainly PMMA (94.8%). Due to the elongation of the capsules during the cutting process, the exact layer thickness is difficult to estimate. However, it still corresponds well to the theoretical layer thickness of about 60 nm but no clear conclusion can be drawn about whether there is an increase in the lamellar thickness of the copolymer due to the strong double confinement in the shell.

At higher concentrations of SDS and in the presence of hexadecane, an onion-like morphology was observed at the center of the nanoparticle, whereas the outside of the nanoparticle consisted of bent lamellae (Fig. 56c, d). We attribute this to a conservation of volume of the two polymer blocks: the volume can be conserved quite easily by a slight change in lamellar thickness in the outer regions of the nanoparticle, resulting in bent lamellae. In the center of the nanoparticle, the degree

of curvature of the block layers is much higher; therefore the layers adopt an onion-like morphology to conserve the total volume.

In the case of nanocapsules consisting of low molecular weight PS<sub>76</sub>-*b*-PMMA<sub>79</sub>, patchy structures were observed in SEM and TEM (Fig. 57). In SEM, these patches with a diameter of 15 nm appear bright whereas they appear dark in TEM. The patchy structure is due to the weak phase separation characteristic for values of  $10.5 > \chi N > 6$ . The same patchy structures were also observed on the nanoparticles made of low molecular weight PS-*b*-PMMA. XPS measurements on nanoparticles and nanocapsules made of low molecular weight PS-*b*-PMMA show that both PS and PMMA are located on the surface. PMMA constitutes the main part (74.8% on nanocapsules and 77.7% on nanoparticles), which is probably due to the higher polarity of the PMMA. From the XPS measurements it can be deduced that the surface of the PS<sub>76</sub>-*b*-PMMA<sub>79</sub> nanoparticles contains slightly more PMMA than PS<sub>76</sub>-*b*-PMMA<sub>79</sub> nanocapsules does, whereas more PMMA is observed on nanocapsules than on nanoparticles for P(S<sub>838</sub>-*b*-MMA<sub>945</sub>). Patchy structures were not only observed on the surface of the nanoparticles and nanocapsules, but also on the inside (Fig. 57). The images show that there is no well-defined lamellar structure as observed in nanoparticles and nanocapsules made of high molecular weight PS-*b*-PMMA. There is an irregular sequence of brighter and darker domains, which can be assigned to PMMA and PS, respectively. Nanoparticles, half-spherical nanoparticles, and nanocapsules show this structure. Roughly, the size of these domains can be determined to be between 10 and 20 nm. They exhibit approximately the same size as the patches observed on the surface of the nanoparticles and nanocapsules with SEM and TEM. In the case of the nanocapsules, cross-sections were prepared. Therefore, the patches outside of the nanocapsules are due to cuts apart from the equator of the capsules through the capsular wall.

The examples show the influence of the confinement on polymers. Nanoparticles and nanocapsules of PS-*b*-PMMA with different molecular weights were prepared. Their morphology could be precisely tuned by changing the amount of surfactant and hexadecane in double confinement. Also, the wall thickness of the capsules could be controlled by the amount of hexadecane employed during formation using a miniemulsion process with subsequent solvent evaporation.

In order to better understand the experimentally observed microphase separation of block copolymers in confinement, it is instructive to consider an even simpler system theoretically. Therefore, we consider a mixture of 50% A and 50% B monomers in spherical confinement. The resulting structures depend on the interfacial tensions between the two species and the respective tensions between the monomers and the wall. One would expect a Janus-type structure, as observed in simulations of simple binary mixtures [222, 223], if the tensions towards the confining wall are equal (resulting in a contact angle of 90° according to Young's equation). Alternatively, core-shell structures emerge if one type of particle is strongly preferred and wets the wall. Sickle-like structures arise for finite contact angles of less than 90°.



**Fig. 58** Mean-field density profiles obtained from self-consistent field theory simulations. A- versus B-rich domains are displayed for a blend of A- and B-homopolymers (**a**) and for AB-diblock-copolymer melts (**b**, **c**). In each case, all A-, and B-blocks contain equal numbers of monomers. Here, spherical confinement is implemented by blending either A- and B-homopolymers (**a**), or AB-diblock-copolymers (**b**, **c**) with C-homopolymers. The C-homopolymers act as a very bad solvent, thus enforcing the formation of A-, and B-rich spherical domains. In this case, the geometry of the confined polymer phases is studied in two dimensions. Whether Janus (**a**), core-shell (**b**), or onion (**c**) particles form depends on the number of monomers per block, and the interactions between different monomer species. From (**a**) to (**c**), the length of A-, and B-sequences steadily decreases; the sequences in (**a**) are roughly four times as long as in (**b**), and are about 15 times as long as in (**c**). To form Janus particles, the A–C versus B–C interactions need to be equal. To form layered structures, there has to be a significant difference

The same basic structures can be expected in melts that consist of 50% A and 50% B homopolymers (Fig. 58a) or even AB diblock copolymers (Fig. 58b). The situation changes somewhat for AB diblocks if the typical length of the polymer (as, e.g., expressed by its radius of gyration) is much smaller than the radius of the confining sphere. Now, the system is essentially forced to form additional interfaces as it can, e.g., no longer form a core-shell structure due to spatial constraints. Consequently, additional layers and onion-like structures emerge (Fig. 58c).

Finally, we would like to give a short outlook on the structure of a single homopolymer chain confined to a very small miniemulsion droplet. Advanced Monte Carlo methods [224] were applied to a simple coarse-grained model of polystyrene in spherical confinement [225]. The polymer chain becomes highly knotted once the confining droplet shrinks (e.g., by evaporation of the solvent) beyond the typical size of the polymer (in good solvent conditions) [225–227]. These simulations may hence lead the way to the synthesis of knotted and unknotted ring polymers in extremely small miniemulsion droplets when the termini of the polymer are chemically linked.

## 5.2 *Junction-Point Reactive Block Copolymers for Surface Modification*

Extending the concept of confining block copolymers at interfaces, we describe the synthesis and surface properties of a special type of diblock copolymer. These amphiphilic block copolymers are covalently attached to a surface as a consequence of a reactive moiety at the junction point of the two incompatible blocks. This block

copolymer topology results in a homogeneous, ultrathin polymer film that introduces the possibility to switch the surface polarity thermally or by contact with a solvent. The synthetic route described here for junction-point reactive block copolymers is of a general nature. The resulting materials can be used for tailoring of the surface wettability of a variety of flat surfaces and curved surfaces such as nanoparticles. An important feature of this approach is that attachment to the interface is the final step of the approach, permitting the tailoring of the block copolymer structure in homogeneous solution prior to the final surface attachment, in pronounced contrast to established “grafting from” routes.

Ultrathin polymer films capable of stimuli-responsive wetting are particularly interesting because they permit reversible switching in surface properties from hydrophilic to hydrophobic and thus offer potential applications in the field of self-cleaning [228], “smart” coatings [229, 230] and also for microfluidic devices [231]. Y-shaped polymer brushes consisting of two incompatible polymer chains that are covalently linked to the surface with an in-chain anchor group have only been the subject of a few studies. The main advantage of these structures is the homogeneous distribution of both incompatible polymer chains over the surface, due to the suppression of segregation processes. In the few reported approaches, these Y-shaped polymer brushes have been obtained by grafting-from [232] (attachment of a difunctional initiator to the substrate) or grafting-to [233] (grafting via junction-point functionalized block copolymers) strategies. Theoretical studies were carried out by Zhulina and Balazs [234]. Tsukruk and coworkers used carboxy-terminated PS and poly(*tert*-butyl acrylate) attached to 3,5-dihydroxybenzoic acid as an AB<sub>2</sub> anchoring moiety [233, 235]. Wang et al. presented a hydrosilylation grafting-to process to link block copolymers to silicon surfaces via a Si–H junction point [236].

To synthesize junction-point reactive block copolymers we combined carbanionic and oxyanionic polymerization with new bifunctional termination strategies based on tailored epoxide building units. As a precondition for the junction-point reactive block copolymers, a semicontinuous strategy for the rapid preparation of multihydroxyl functional polystyrenes has been established. It relies on the high stability of the acetal-protecting groups of the respective protected glycidyl ethers towards strong bases [237a]. The synthesis is carried out in a continuously operating microstructured reaction device for living carbanionic polymerization. The reaction is terminated with specifically tailored glycidyl ethers, followed by deprotection of the introduced end group moieties. Based on the termination with functional epoxide derivatives, a series of block copolymers bearing a single in-chain amino functionality was synthesized via anionic polymerization of styrene and ethylene oxide [237b]. By means of both a conventional and a continuous setup, living polystyrene was quantitatively end-functionalized with an oxirane (DBAG, dibenzyl-aminoglycidol; Fig. 59) prior to the polymerization of the PEO segment. The in-chain amine was conjugated with a fluorescent dye, evidencing full junction-point functionalization (Fig. 59).

As a consequence of this work, a general strategy for the synthesis of reversibly stimuli-responsive Y-shaped polymer brushes and their surface attachment has been developed (Fig. 60) [237c]. The preparation of the respective junction-point reactive block copolymers relies on a combination of carbanionic and oxyanionic

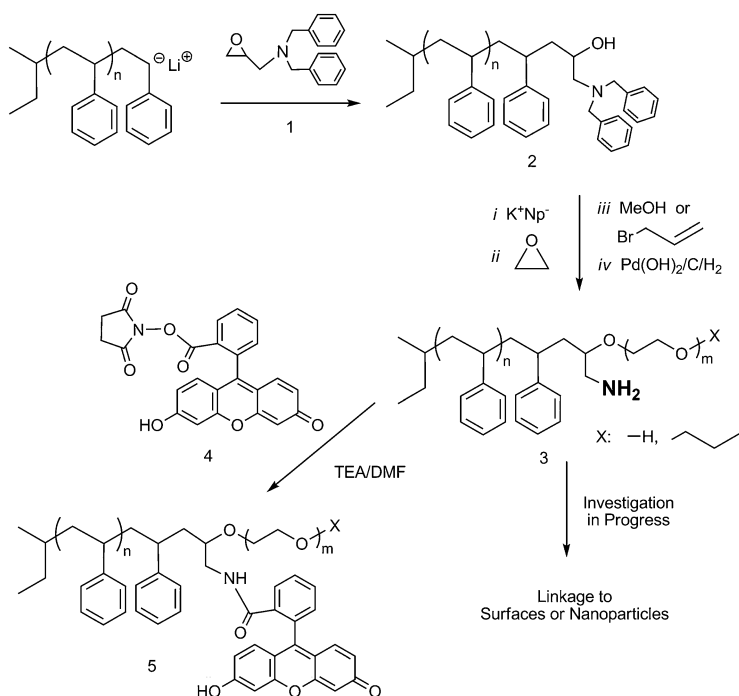


**Fig. 59** Synthetic strategy for in-chain amino-functionalized, amphiphilic block copolymers with polystyrene and poly(ethylene glycol) blocks [PS-(NH<sub>2</sub>)-*b*-PEO] via termination of the carbanionic polymerization with a benzyl-protected aminoglycidol unit (DBAG) [237b]. Numbers 1-5 refer to the compounds in the original article [237]

polymerization techniques. Allyl glycidyl ether (AGE) was utilized as an end-capping reagent for the anionic polymerization of polystyrene, achieving quantitative end-functionalization, as demonstrated by MALDI-TOF mass spectroscopy. In the next step, PS-(AGE) was used as a macroinitiator for the anionic ring-opening polymerization of ethylene oxide to afford amphiphilic PS-(AGE)-PEO block copolymers with different block ratios in the range of 6–24 kg/mol. The triethoxysilane (TEOS) anchor group for chemical grafting to silicon surfaces was introduced by hydrosilylation of PS-(AGE)-PEO leading to PS-(TEOS)-PEO (Fig. 60).

X-ray reflectivity measurements confirmed that after self-assembly and reaction of the alkoxysilyl group with the silicon oxide a 1–3 nm thick polymer layer had attached to the surface. One important issue was to clarify, whether the junction-point functional polymer was attached to the silicon surface by covalent bonds formed by the TEOS functionality, or by mere noncovalent adsorption of the PS chains at the surface. To shed light on this issue, we carried out additional deposition experiments using the allyl-functional block copolymer PS-(AGE)-PEO instead of the reactive PS-(TEOS)-PEO. X-ray reflectivity results for PS-(TEOS)-

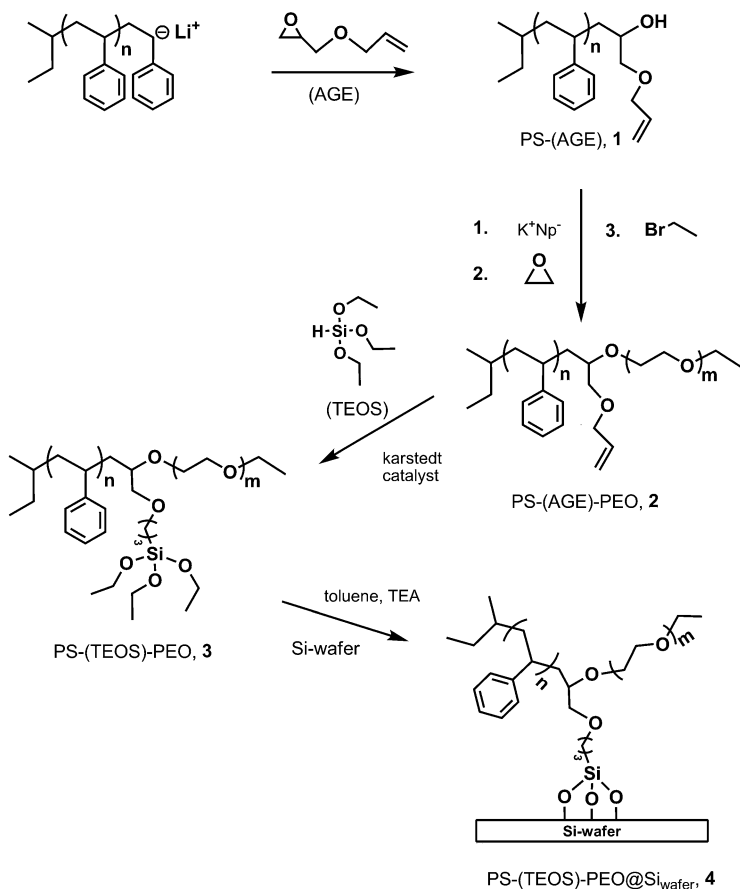


**Fig. 60** Scheme of synthesis of the junction-point reactive block copolymer PS-TEOS-PEO on a silicon wafer. AGE allyl glycidyl ether, TEOS triethoxysilane, TEA triethylamine,  $K^+Np^-$  potassium naphthalide (see text for details) [237c]

PEO@Si<sub>w</sub>afer (Fig. 61a, top) showed a fringe, whereas on PS-(AGE)-PEO@Si<sub>w</sub>afer (Fig. 61a, bottom) no fringe was detected. This confirms that layers with the TEOS anchor group could not be rinsed away by solvents as a consequence of their covalent attachment. Without TEOS, the polymer only physisorbs and can be washed away. In addition, AFM images have been recorded (Fig. 62). Fully covered, smooth surfaces on the nanometer scale were observed. The evenly distributed hydrophilic and hydrophobic polymer chains result in a homogenous thin polymer film without any visible microphase segregation, unlike conventional mixed brushes.

Figure 61b presents images showing the contact angle and the proposed chain alignments upon thermal treatment of the surface-confined diblock copolymers. The PS chain flexibility is increased during the tempering process, and the PEO

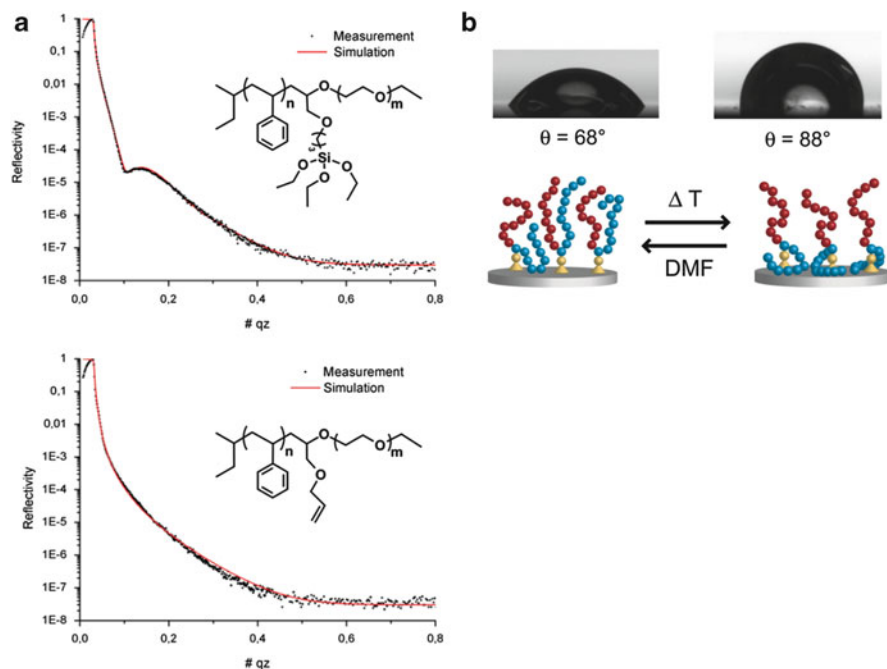


**Fig. 61** (a) X-ray reflectivity of silicon surfaces after grafting-to process with PS<sub>27</sub>-(TEOS)-PEO<sub>261</sub> (top) and PS<sub>27</sub>-(AGE)-PEO<sub>261</sub> (bottom). A fringe could only be observed in the case of block copolymers functionalized with TEOS. (b) Sessile water drop on silicon surface after grafting-to process with PS<sub>27</sub>-(TEOS)-PEO<sub>261</sub>, after tempering and treatment with DMF under reflux. A contact angle change of 20° was observed. The scheme shows PS (red) and PEO (blue) chain alignment upon thermal treatment [237c]

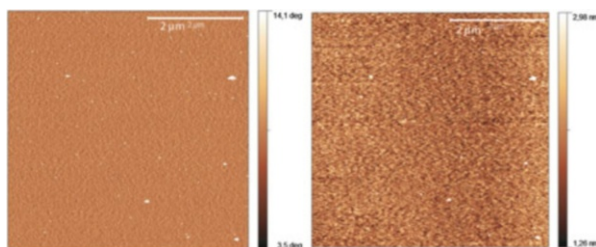


**Fig. 62** AFM (a) phase and (b) height (total  $z$  range 1.7 nm) images of surface covered with surface-confined junction-point reactive block copolymer PS-(TEOS)-PEO

chains are able to segregate on the hydrophilic substrate. This tempering results in a stratification of the polymer film, with PS on the topmost layer and with a PEO layer segregated on the silicon surface as indicated by the water contact angles of 84–88°. An analogous preference for PS over PEO towards the free surface was observed for PS-PEO diblock copolymers [240]. This is caused by the lower surface tension

of PS of 36 mN/m rather than 44 mN/m for PEO. Reversible switching of surface properties was realized by repeated solvent treatment. DMF turned out to be a suitable polar solvent, which may be related to its high boiling point of 153°C, roughly 50°C above the  $T_g$  of PS. The samples were deposited in DMF under reflux and subsequent contact angle measurements showed a decreased contact angle of 68°, indicating a regression of the mixed polymer brushes at the topmost layer, similar to the initial state.

In summary, the surface wetting shows reversible stimuli-responsive behavior when applying external stimuli (e.g., temperature and solvent), as observed via contact angle measurements. A contact angle shift of up to 23° from 61° to 84° and vice versa was observed after heating and DMF treatment, respectively (Fig. 61b).

The role of the pre-organization of the amphiphilic block copolymers in solution prior to the surface attachment, the potential of the materials with respect to achievable film thicknesses, and larger contact angle changes to switch wettability are further intriguing issues based on the structural principle of amphiphilic junction-point reactive block copolymers. In addition, hydrolytic crosslinking of the TEOS moieties in organized solution structures, such as block copolymer vesicles (cf. Sect. 5.3) at the interface may be employed to stabilize “polymersome”-type assemblies. At present, the concept of junction-point reactive block copolymers is extended to other amphiphilic block copolymers with potential use for self-cleaning, anti-fouling, and friction-reducing ultrathin polymer layers.

### 5.3 Nanoparticles Confined in a Polymersome Shell Layer

Amphiphilic block copolymers self-assemble in selective solvents such as water. Depending on parameters like overall average molecular weight, volume fraction of each block, or effective interaction energy between monomers in the blocks, vesicles with a bilayer shell and a solvent interior volume similar to liposomes are formed. They are often called polymersomes [241]. Such polymersomes in aqueous media have attracted increasing interest due to their enhanced stability compared to classical liposomes and due to the potential to control vesicle properties like bilayer thickness, permeability, or surface functionalities by appropriate chemical copolymer adjustment [242].

The block copolymer polybutadiene-*block*-poly(ethylene oxide) (PB-*b*-PEO) is frequently studied because it offers several advantages [243–246]. For example, the PEO that forms the outer part of the assembled structures in water is generally regarded as biocompatible [247, 248]. Furthermore, depending on the PB block length, the assembled polymersomes can exhibit a thicker hydrophobic membrane core and therefore higher stability compared to liposomes [249]. Additionally, this copolymer features the possibility to crosslink the PB part and thereby stabilize the assembled structure [250–252].

Amphiphilic block copolymers have been suggested as drug carriers. The concept of drug delivery is based on successful encapsulation of substrates with

different solubility parameters. Micellar structures are favored in the case of hydrophobic substrates solubilized within the hydrophobic core of the micelle [253, 254]. Hydrophilic substrates are typically encapsulated by solubilization within the water-filled cavity of liposomes or vesicles. Several block copolymers have been used, including PB-*b*-PEO [255, 256]. The hydrophobic encapsulation into the vesicle shell of various polymers has been reported recently [257–263], but most of these works address the interface by simply utilizing the amphiphilic substrate itself [264–266]. However, it has not yet been possible to verify the full hydrophobic nature of the encapsulation, especially in the case of colloidal substrates.

Considering potential pharmaceutical applications, encapsulation of different substrates at the same time is demanded but is also a scientific challenge [267]. The polymersome system presented here offers the possibility for encapsulation of both hydrophilic and hydrophobic substances at the very same time in the very same polymersome. Potential loading systems are typically limited by the lack of suitable characterization methods. We utilized fluorescence correlation spectroscopy (FCS) in combination with cryogenic TEM imaging and DLS to characterize hydrophobic loading.

In order to understand the influence of different molecular parameters on structure formation and stability, we report on the directed encapsulation of two hydrophobic model substrates inside the polymersome shell. The system both complies with requirements like water insolubility and has sufficient fluorescence intensity for monitoring. Fluorescent CdSe/CdS/ZnS core-shell quantum dots (QDs), which carry hydrophobic surface ligands, serve as a model substrate of the nanosize regime (core size approximately 6 nm). Nile Red, a lipophilic fluorescent dye, represents the molecular size regime [268–270].

Polymersome dispersions were produced following two different routes, the cosolvent method and the rehydration method:

- In the cosolvent method, small polymersomes with a narrow size distribution were obtained starting with a copolymer solution in THF and dropwise addition of water. Controlled by a syringe pump, the dropping velocity of water addition was set to 9.9 mL/h. At approximately 30 wt% THF, the addition of water was stopped and the THF evaporated over 2–3 days. Standard final polymer concentration was around 1 g/L in water. The samples were filtered through 0.45- $\mu$ m filters before proceeding. Nile Red loading of those polymersomes was achieved by the addition of dye to the starting copolymer/THF solution with different dye/copolymer weight ratios. Further treatment was done the same way.
- Employing the rehydration method, huge polymersomes with broad size distribution were obtained starting with a copolymer solution in THF or chloroform and creating a film in a Teflon vessel. After film drying at 50°C under vacuum, water was added. Film rehydration was supported by intense ultrasonic use and an elevated temperature of 50°C. The dispersions were filtered through 5  $\mu$ m filters before proceeding. For DLS and FCS, additional filtration through 0.45- $\mu$ m filters was used to remove dust and larger structures. QD loading of

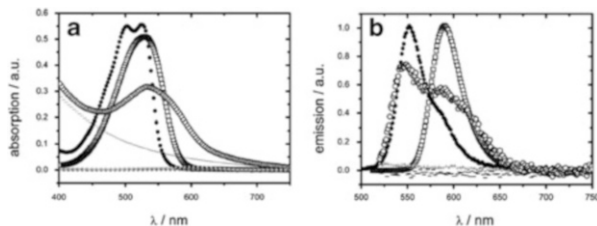


**Fig. 63** (a) Absorption and (b) emission spectra of Nile Red in THF (*squares*), Nile Red-loaded polymersomes (*circles*), blank polymersomes (*dashed line*), blind samples with no copolymer (*dark gray dots*), blind samples with just PEO polymer with molecular weight of approximately 3,500 g/mol (*light gray dots*), and Nile Red in polybutadiene (*black dots*). From [269]

polymersomes was achieved by the addition of QDs to the starting copolymer/chloroform solution at a QD/copolymer weight ratio of 1/2.8, corresponding to a molar ratio of 1/600. To load polymersomes with Nile Red, the dye was added to the starting copolymer/THF solution at a dye/copolymer weight ratio of 1/20. The rehydration procedure was performed as described above.

In order to study the potential influence of the surrounding polarity on the optical properties of an encapsulated hydrophobic dye, the hydrophobic dye Nile Red was employed to load vesicles via the “cosolvent method” starting from a solution of PB-*b*-PEO copolymer and Nile Red in THF and dropwise water addition as described above. This leads to homogeneously colored polymersome solutions with average hydrodynamic radii in the range of 40–50 nm. Typically, 500–550 dye molecules are taken up per vesicle, as determined from absorption spectra after calibration with Nile Red solutions in polybutadiene. This corresponds to an uptake of 3 mg of Nile Red per 1 g of copolymer. Blank polymersome samples without Nile Red were prepared the same way. DLS measurements showed no differences in size or size distribution of the polymersomes with or without Nile Red. Cryogenic TEM images proved the vesicular structure for both cases. Analogous to the Nile Red-loaded polymersomes, blind samples with no copolymer or with just PEO polymer with molecular weight of approximately 3,500 g/mol were prepared. Figure 63 shows absorption and emission spectra for the samples.

For  $\lambda < 500$  nm, the polymersome samples scatter light increasingly with decreasing wavelengths due to their particle size (see blank polymersome sample). The two blind samples with no copolymer or just PEO show no absorption or emission signal, respectively, thereby indicating no Nile Red uptake. In none of the samples could a fluorescence band at  $\lambda_{\text{max}} = 660$  nm originating from NR in aqueous environment be found [272]. The emission maximum of Nile Red in the vesicle is very close to the value found for Nile Red in a PB film (Fig. 63b), indicating its incorporation into the PB shell. As suggested by comparison with the Nile Red emission in THF, the increased emission intensity in the polymersome at around 600 nm might be attributed to traces of THF remaining in the hydrophobic shell from preparation. More likely are contributions of Nile Red molecules located close to the hydrophobic–hydrophilic interface.

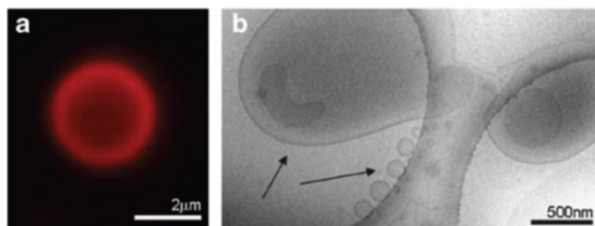


**Fig. 64** (a) Fluorescence microscopy image of Nile Red-loaded polymersome in aqueous solution and (b) cryogenic TEM image of the same solution with its broad size distribution (*arrows* mark huge and small polymersomes). From [269]

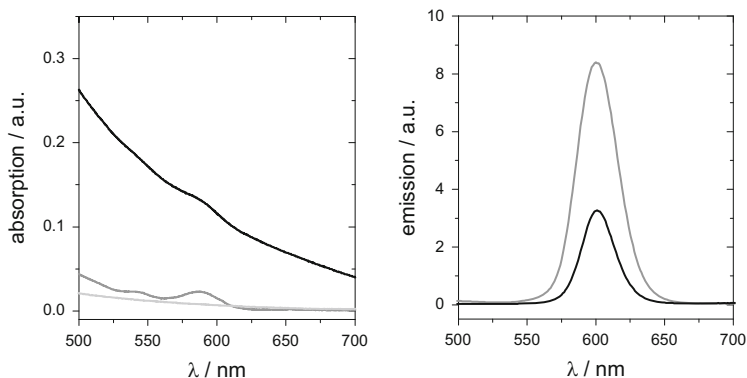


**Fig. 65** Absorption (*left*) and emission (*right*) spectra of QD-loaded polymersomes: QD-loaded vesicles via rehydration method (*black line*), QDs in chloroform (*dark grey line*), and blank polymersome solution (*light grey line*)

For further investigations, starting from a dried copolymer and Nile Red film as described above, Nile Red-loaded polymersomes were prepared via the rehydration method. This method leads to vesicles with very broad size distribution and diameters ranging from 60 up to 3  $\mu\text{m}$ . We imaged the fluorescently labeled polymersomes by fluorescence microscopy. Figure 64a shows the image of a Nile Red-loaded polymersome with a size of about 3  $\mu\text{m}$ . The high fluorescence intensity at the outer shell supports the model of hydrophobic loading into the polymersome shell and the unloaded, water-filled core. The exact position inside the inner membrane core of the shell or at the hydrophobic–hydrophilic interface cannot be determined here.

Polymersomes with diameters smaller than 2  $\mu\text{m}$  appear as nearly homogeneously fluorescing spots due to resolution limits of the microscope. Cryogenic TEM imaging of the very same solution showed vesicles over the full size distribution (Fig. 64b). In cryogenic TEM imaging, vitrified water films are typically 100–200 nm thick. Huge polymersomes with diameters of several micrometers lie only partly in those films and can therefore distort from their spherical shape in solution, as obvious in Fig. 64b.

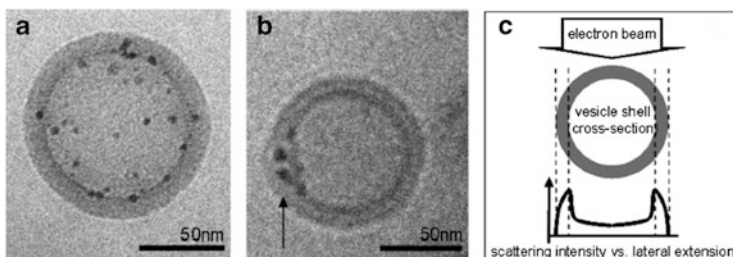


**Fig. 66** (a, b) Cryogenic TEM images of QD-loaded vesicles (prepared via rehydration method) in aqueous solution. (c) Schematic of TEM scattering intensity versus lateral extension. From [269]

The encapsulation of a larger hydrophobic model substrate was successfully realized utilizing highly fluorescent QDs. The enclosing of these nanoparticles inside the PB-*b*-PEO polymersomes was performed only via the film rehydration procedure because the preferred dispersant of QDs, chloroform, is immiscible with water and therefore not suitable for the cosolvent method. The rehydration procedure for QDs was done analogously to that for the Nile Red samples. Afterwards, filtration through 0.45- $\mu\text{m}$  filters ensured a smaller vesicle size regime, which is important for further characterization. Absorption and emission spectra indicated the presence of QDs in the vesicle solution after filtration (Fig. 65).

The quantification of QD load in the polymersomes has not yet been possible because the rehydration method never led to a complete solution of material and the QD absorption peak is drowned in the high scattering background of those huge and broadly distributed polymersomes. Furthermore, exact reference concentrations are difficult to determine for core-shell QD solutions.

Cryogenic TEM images of hydrophobically stabilized QD-containing polymersome samples are shown in Fig. 66. The PB-*b*-PEO copolymer exhibits a low scattering contrast compared to the QDs, enabling the QDs to be clearly seen as dark spots inside the vesicle structure. The TEM image represents a projection of the 3D loaded vesicle (as it is frozen in the water film) into the 2D imaging plane. Those QDs appearing in the inner core due to the projection are therefore also enclosed in the polymersome shell (Fig. 66c). Appropriate sample tilt during imaging reveals the QD position in the middle of the polymersome shell (Fig. 66b), between the two polybutadiene layers, introducing a curvature into the assembled shell. This QD/PB-*b*-PEO system is an example of hydrophobic polymersome shell loading. The phenomenon of bending around the guest particle is currently under investigation as a function of membrane thickness and incorporated nanoparticle diameter. A comparable mechanism has been observed experimentally and theoretically for the incorporation of colloids into block copolymers in the bulk [273–275].

As cryogenic TEM imaging does not necessarily represent the entire sample, FCS measurements (data not shown) were performed additionally for measuring diffusion coefficients of fluorescent particles [271, 276–280]. Light scattering yields a hydrodynamic radius of  $R_h = 67$  nm, which describes the average of the whole sample content. Nevertheless, the result is in good agreement with FCS, which yields  $R_h = 62$  nm detecting only the fluorescent sample content (in our case the loaded polymersomes). Both results are comparable to those observed with cryogenic TEM; two examples are shown in Fig. 66a, b. The agreement of DLS and FCS results shows that Nile Red and QDs were successfully incorporated into the hydrophobic part of the polymersomes.

In conclusion, the hydrophobic shell of PB-*b*-PEO polymersomes was successfully loaded with the fluorescent dye Nile Red and highly fluorescent QDs as hydrophobic model substrates. FCS showed that fluorescing signals belong to the diffusion of fluorescently loaded vesicles only, demonstrating that no other aggregation or structure stabilization occurred. Cryogenic TEM and fluorescence microscopy imaging confirmed that the hydrophobic substrates were enclosed inside the hydrophobic polymersome shell. In the case of the QD-loaded polymersomes, it has been possible by cryogenic TEM imaging to prove that the QD are located in between the two hydrophobic PB layers of the shell bilayer, introducing curvature of the copolymer layers around the guest particles. The combination of independent methods of characterization made it possible to successfully investigate the localization of the hydrophobic substrates within the hydrophobic shell of the polymersomes. Further experiments with differently sized nanoparticles will determine the limits for particle enclosing and confinement inside the shell, revealing how far the double-layer can curve before different structural assemblies are favored. Furthermore, these experiments can be nicely linked to the results obtained in other particle systems or confinement of nanoparticles in planar surfaces, as discussed in the other parts of this chapter.

## 5.4 Conclusion

The process of formation of complex block copolymer structures in 3D confinement has been elucidated for some selected PS-*b*-PMMA copolymers. Introduction of a nonsolvent into the spherical nanoparticles yielded hemispherical structures of onion-like morphology. Such structures may be viewed as a result of double confinement consisting of the outer surfactant double layer and the inner nanophase separation between the block copolymer and the nonsolvent for both blocks. This concept allows targeting the nanoparticle shape as well as the inner particle morphology (ranging from simple core-shell to onion-like to patched structures), which may find application for encapsulation of various substrates with predetermined release characteristics.

Regarding 2D confinement, newly synthesized “junction-point” block copolymers were chemically anchored onto planar substrates by their reactive junction-point moiety, forming a smooth monomolecular layer. By thermal treatment or exposure

to selective solvents for either of the blocks, the surface tension or contact angle of the coated substrate could be reversibly switched. Such adaptive surfaces may have potential applications for anti-fouling and self-cleaning surfaces.

Finally, fluorescent dye molecules as well as QDs were successfully immobilized in the hydrophobic part of the double layer of block copolymer vesicles below 100 nm in size. In the case of the QDs, the double layer was observed to strongly curve around the guest particles without becoming destabilized. The limit of stable confinement in terms of size and polarity of the guest molecules will be subject of future investigations. The presented example demonstrates that 2D confinement within a vesicle shell principally allows control of the spatial arrangement of nanoparticles in solution.

## 6 Towards Synthesis on an Insulating Surface

### 6.1 Introduction

Synthesizing macromolecules or studying the structure and dynamics of macromolecules in confining geometries is a challenging element of polymer science. A surface can also serve as confining geometry for both polymer synthesis and polymer characterization. Immobilizing polymerizable monomers on solid surfaces with suitable anchor groups and subjecting them to network formation is a well-established coating technique. A much more sophisticated approach to surface-bound polymer synthesis is the deposition of reactive monomers on conductive or insulating substrates and the promotion of light- or heat-driven polymerizations under in-situ control by scanning probe techniques. As well as the possibility of following macromolecule formation with atomic precision in real space, the surface can now also act as template by either stabilizing reactive intermediates or by pre-organizing them into a desired pattern.

In general, creating complex polymer architectures on surfaces offers a great potential for future applications, e.g., in the fields of (bio)sensors and molecular electronics. The bottom-up construction of functional devices from molecular building blocks provides utmost control in tailoring the properties and functionality of materials. Encoding the resulting structure and functionality in the molecular building blocks has been explored extensively in the field of molecular self-assembly [281]. However, because molecular self-assembly relies on weak, reversible intermolecular interactions to arrive at the (local) thermodynamic minimum, the resulting structures are inherently unstable and might not survive further processing or harsh operation conditions. Moreover, when aiming at electrically conductive structures, conjugated structures are desired because of their superior electron transport properties. To provide stability and electric conductivity, on-surface synthesis has recently been explored as a promising route to the creation of covalently linked molecular structures [282, 283]. So far, these studies have been limited to metallic

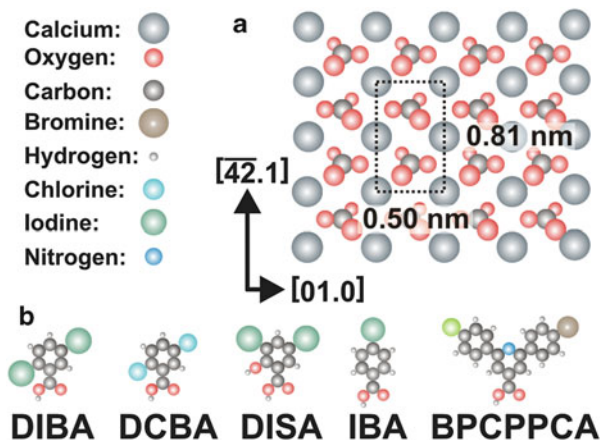


**Fig. 67** Models of (a) the calcite(10.4) surface and (b) organic molecules 4-iodo benzoic acid (IBA), 2,5-diiodo benzoic acid (DIBA), 2,5-dichloro benzoic acid (DCBA), 3,5-diiodo salicylic acid (DISA) and 2-(4-bromophenyl)-6-(4-chlorophenyl)pyridine-4-carboxylic acid (BPCPPCA). The  $\text{CaCO}_3$  (10.4) surface has a rectangular unit cell of size  $0.50 \times 0.81 \text{ nm}^2$ , consisting of two carbonate groups and two calcium ions. The carbonate groups are rotated such that one oxygen atom lies above, one in, and one below the plane spanned by the calcium ions

substrates only [284–288]. From an experimental point of view, this is motivated by the fact that most surface-sensitive techniques such as scanning tunneling microscopy, low-energy electron diffraction, or photoelectron spectroscopy require conductive samples. Moreover, when considering covalent coupling based on an Ullmann-type reaction, a metallic surface has been regarded as mandatory because it is known to act as a catalyst.

Molecular electronics applications will, however, require decoupling the electronic structure of the polymer architecture from the supporting substrate. Moreover, extending the material base from metals to the comparatively heterogeneous group of bulk insulators offers the potential for tailoring the substrate properties to the specific, application-oriented needs.

We have, therefore, explored on-surfaces synthesis on a bulk insulator surface. As a prerequisite, we investigated strategies for anchoring organic molecules to insulating surfaces in order to avoid molecule desorption upon thermal activation of the linking reaction [289]. We succeeded in presenting the first demonstration of a covalent linking reaction on an insulating surface in an ultrahigh vacuum environment [290]. We then built upon this proof-of-concept work by exploring concepts for hierarchical structure formation to pave the way for creating complex polymer architectures on surfaces [291].

Insulating materials span a wide range from weakly van-der-Waals bonded molecular crystals to covalent crystals such as diamond or titanium dioxide to ionic crystals such as potassium bromide or calcium fluoride. Therefore, a general description of molecule–surface interactions is challenging in the case of insulating substrates. However, compared to metals, the interaction of organic molecules with

prototypical insulating surfaces such as KBr(001), NaCl(001), or CaF<sub>2</sub>(111) is rather weak [292, 293]. This fact constitutes a severe challenge when aiming at complex structure formation because molecules tend to de-wet and pile up to form a 3D molecular bulk crystal.

Especially when aiming at thermal activation of an on-surface linking reaction, this rather weak molecule–surface interaction poses problems because many molecules desorb from the substrate upon annealing at temperatures well below the reaction temperature. Moreover, it is known that metal atoms act as catalysts in the dehalogenation that has been demonstrated before [285, 286]. Thus, as a first step, exploring suitable anchor groups turned out to be mandatory. Based on our previous results using the calcite as a substrate [294, 295], we identify the natural cleavage plane of calcite, namely calcite(10.4) (Fig. 67a), as an ideal substrate surface due to its comparatively high surface energy of 0.590 J/m<sup>2</sup> [295].

As simple model monomers, we explored the applicability of small benzoic acids derivatives (Fig. 67b), which were chosen for three reasons. First, these molecules are available in high purity and can readily be sublimated under ultrahigh vacuum conditions. Second, carboxylic acid groups are known to interact strongly with the calcite(10.4) surface [296]. This comparatively high molecule–substrate binding strength is employed to prevent clustering at step edges and to avoid desorption upon thermal activation of the coupling reaction. Depending on the acidity of the benzoic acid derivative, the as-deposited molecules can be deprotonated at room temperature or might require annealing for the deprotonation step to occur. We could directly follow such a deprotonation step at room temperature upon deposition of 2,5-dihydroxy benzoic acid having a pK<sub>A</sub> value of 2.97 [297]. This study gives a first estimation of the protonation state of other benzoic acid derivatives as a function of the pK<sub>A</sub> value. For all molecules shown here, deprotonation takes place on a surface held at room temperature when the pK<sub>A</sub> value is around 3 or smaller. For molecules having a higher pK<sub>A</sub> value, annealing is required to induce deprotonation. Third, by varying number and position of the halide substitution, we are able to rationally design the resulting polymer architecture.

## 6.2 *Proof of Concept: Dehalogenation and Covalent Coupling on an Insulating Surface*

For providing a proof-of-concept for covalent linking on a bulk insulator surface, we present the results of a systematic noncontact AFM study, investigating the reactions of four different halide-substituted benzoic acids. The molecules used were 4-iodo benzoic acid (IBA), 2,5-diiodo benzoic acid (DIBA), 2,5-dichloro benzoic acid (DCBA), and 3,5-diiodo salicylic acid (DISA), as shown in Fig. 67b. Within this series of systematically varied benzoic acid derivatives, IBA can be regarded as the conceptually simplest molecule. As only one halide atom is available for the linking reaction, dimer structures are expected. Based on the pK<sub>A</sub>

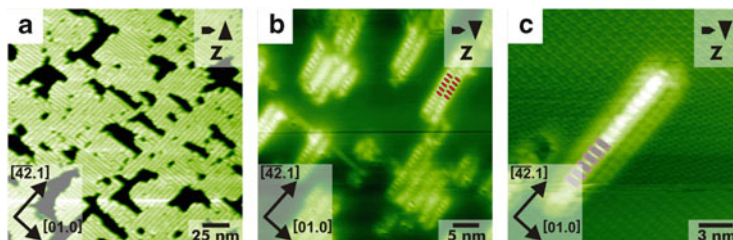


**Fig. 68** Covalent linking of IBA. (a) After annealing of the IBA-covered sample to a temperature of around 250°C, two domains are revealed. (b) Molecular structure of the IBA-covered substrate after annealing to around 310°C, showing molecular rows running along the  $[42.1]$  direction. The rows are composed of individually resolved features that are aligned side-by-side. (c) Zoom onto a single molecular row with superimposed BPCDA model molecules

value of IBA of 4.02, we expect the molecules to remain protonated when deposited onto calcite(10.4) held at room temperature. This is, indeed, the case as can be deduced from two structural transitions that are observed upon annealing. Upon deposition at room temperature, the molecules appear to be mobile. No indication is obtained for island formation on the plane terraces. Molecular islands can only be found at step edges (not shown). After a first, moderate annealing step at around 250°C, two domains of extended islands are observed with a height of 0.8 nm, which suggests upright-standing molecules (Fig. 68a). This structure is readily explained by a deprotonation step, resulting in carboxylate species. The two domains can be understood by anchoring of the carboxylate groups to the surface calcium ions [298].

The linking reaction is induced when annealing the sample to around 310°C, which is associated with a second structural change (Fig. 68b). Now, rows are revealed that are oriented along the  $[42.1]$  calcite direction. The apparent height of the rows is 0.4 nm, suggesting a transition to flat-lying molecules. The rows are composed of features that fit excellently in size with the reaction product of two IBA molecules, namely biphenyl-4,4'-dicarboxylic acid (BPDCA). The BPDCA molecules align side-by-side, as illustrated by the superimposed ellipses with the size of BPDCA molecules (Fig. 68b). A high-resolution image of a single row is shown in Fig. 68c, which also reveals atomic resolution of the underlying calcite substrate. This image elucidates the binding configuration, confirming the assumption that the carboxylate group anchors to the surface calcium ions. The presence of the carboxylate group (being a strong electron donor) is expected to weaken the phenyl-halide bond. This might give an indication as to why homolytic cleavage of this bond is favored, resulting in reactive phenyl radicals at moderate temperatures without the need of a coupling catalyst. The transition in the molecular orientation provides further evidence for the covalent linking. After the reaction, the carboxylic groups point in opposite directions, making concerted binding of the carboxylate groups to the calcite impossible. As a consequence, the dimers are expected to lie flat on the surface, which is, indeed, observed. Thus, the formation of flat-lying

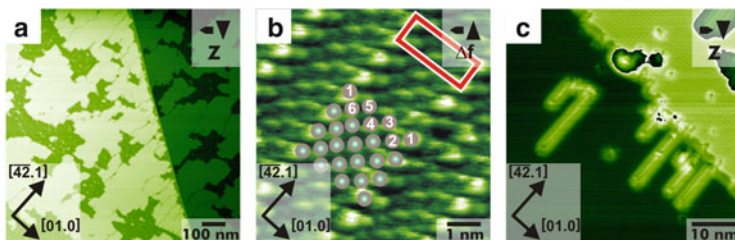


**Fig. 69** (a) Overview image of DIBA, showing two calcite terraces covered by 0.7 nm high islands. (b) Drift-corrected detail image of the inner island structure with a  $(5 \times 1)$  unit cell. (c) Structure obtained after annealing above 260°C. Molecular rows are observed that grow along the  $[42.1]$  direction

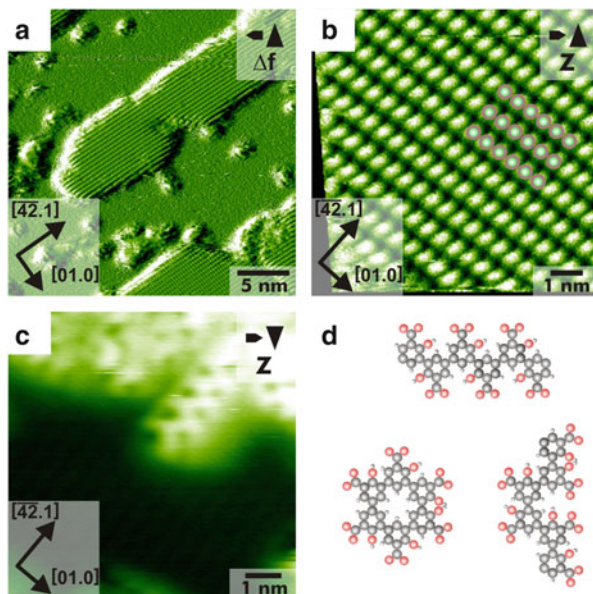
dimer species in the case of IBA monomer units constitutes the first indication of a successful covalent coupling reaction.

To arrive at extended polymeric structures, we next changed the monomer building block from having only one halide substitution to two halide atoms in *para* position. This should result in straight lines upon covalent coupling. To test this assumption, we investigated the structures observed upon deposition of DIBA. The as-deposited structure at room temperature is shown in Fig. 69a, revealing molecular islands. Based on the  $pK_A$  value of DIBA of 2.51, the molecules within the islands are expected to be deprotonated. A higher magnification image of the islands exhibits a  $(5 \times 1)$  superstructure (Fig. 69b) with a moiré pattern, which can again be understood by the anchoring of the negatively charged carboxylate group with the surface calcium ions.

For DIBA, a structural change is initiated after annealing the sample to a temperature above 260°C, as shown in Fig. 69c. After annealing, the extended islands have vanished. Instead, rows running along the  $[42.1]$  direction are observed. This structural change can be understood by the thermolytic dissociation of the two iodine atoms from the molecule and subsequent covalent linking of the radical molecules. Because the iodine atoms are substituted at opposite positions, a straight row is expected upon covalent linking, in excellent agreement with the experimental finding. This assignment is further corroborated by the experimentally obtained periodicity along the chain of 0.41 nm, which fits to the distances expected for a polymeric chain.

To provide further proof for the homolytic cleavage and covalent coupling, we changed the halide atom from iodine to chlorine. This molecule, DCBA, has basically the same  $pK_A$  value of 2.50, but a higher carbon–halide bond strength ( $\text{Cl-C}_6\text{H}_5$  399 kJ/mol versus  $\text{I-C}_6\text{H}_5$  272 kJ/mol) [299]. Therefore, a similar reaction pathway is expected for DCBA. Exclusively considering the bond strengths certainly oversimplifies the situation; however, we expect that somewhat higher temperatures are required when repeating the same experiments with DCBA instead of DIBA. When performing the same experiment with DCBA, we found similar structures to those observed before for DIBA; however, the structural

**Fig. 70** (a) Overview image of DISA deposited onto the calcite surface held at room temperature. (b) Drift-corrected detail image of an island, revealing a commensurate ( $1 \times 1$ ) structure. (c) Detail image after annealing to  $310^\circ\text{C}$ , revealing a distinctly different molecular structure. A zigzag pattern can be seen in the upper right. (d) Model of the different structures possible upon covalent linking. Besides zigzag rows, kinked and circular patterns are also possible



change only occurred when annealing above  $295^\circ\text{C}$ , which is, indeed, higher than needed for DIBA.

To explore the possibility of controlling the resulting polymer shape, we next changed the monomer building block with the idea that zigzag structures would be obtained instead of straight polymeric chains. This could be realized by changing the substitution position from *para* to *meta*. Because 3,5-diiodo benzoic acid was not available for this study, 3,5-diiodo salicylic acid (DISA) was used instead, having a  $pK_A$  of 2.07. Again, based on this  $pK_A$ , we expect the molecules to be deprotonated at room temperature.

When depositing DISA onto a calcite(10.4) surface held at room temperature, elongated islands are revealed (Fig. 70a) with a commensurate ( $1 \times 1$ ) superstructure (Fig. 70b). This structure can be explained by upright-standing molecules that again anchor with their carboxylate groups to the surface calcium ions. In the case of DISA, the reaction is induced upon annealing to approximately  $310^\circ\text{C}$ . Among the structures seen, zigzag structures are, indeed, obtained as shown in Fig. 70c. The apparent height of these structures suggests flat-lying molecules in this case. The observed transition from upright-standing molecules at room temperature to flat-lying molecules can be explained by considering the position of the carboxylate groups. Individual DISA molecules can arrange themselves with the carboxylate groups pointing towards the calcite surface. After linking, however, the carboxylate groups point in opposite directions, which prevents concerted binding of these groups to the surface. This provides the clue to understanding the transition from upright-standing to flat-lying molecules.

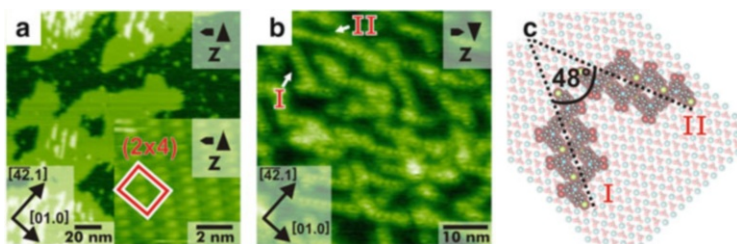


**Fig. 71** Molecular structures of BCPPCA onto calcite(10.4). (a) As-deposited, ordered island with a  $(2 \times 4)$  superstructure (*inset*). (b) Overview image after annealing the substrate to about  $300^\circ\text{C}$  for 1 h, revealing rows (labeled *I* and *II*) with two distinct angles with respect to the  $[01.0]$  direction. (c) Proposed model for the two row types on calcite(10.4)

The other structures seen can be easily understood by considering the binding possibilities of DISA. As shown in Fig. 70d, the zigzag structure is not the only possible linkage. This explains why the zigzag structure is not the only pattern that exists on the surface after annealing. With these results, we demonstrate that even shape control can be achieved by choosing rationally designed monomer building blocks.

### 6.3 Towards Hierarchical Structure Formation: Exploring Two-Step Reactions

After having demonstrated a proof-of-concept covalent linking reaction in ultrahigh vacuum [290], an important next step for creating complex structures is exploring strategies for including hierarchical control. Up to now, the structural complexity of the structures achieved by on-surface synthesis has been limited to single-step processes. Increasing the structural complexity of the resulting structures requires utmost control, with the ability to selectively induce sequential linking reactions in a hierarchical manner. This has recently been demonstrated using halide-substituted porphyrin derivatives on a Au(111) surface [300], elegantly exploiting the specific dissociation energies of the bromine–phenyl and iodine–phenyl bonds. Because the dissociation energies are associated with different activation temperatures, the linking reactions can be performed in a site-specific and sequential manner. Thus, reaction sites and sequence are encoded in the structure of the precursor molecules. The latter results have, however, been obtained on a metallic substrate, again limiting the applicability of these structures with regard to molecular electronics.

Based on the results obtained, we chose a molecule for demonstrating a site-specific and selective two-step linking process on a bulk insulator surface in ultrahigh vacuum [298]. Bromophenyl and chlorophenyl groups were chosen for inducing site-specific and sequential covalent linking based on homolytic cleavage of the halide–phenyl bonds, having dissociation energies of  $336 \text{ kJ/mol}$  ( $\text{Br-C}_6\text{H}_5$ )

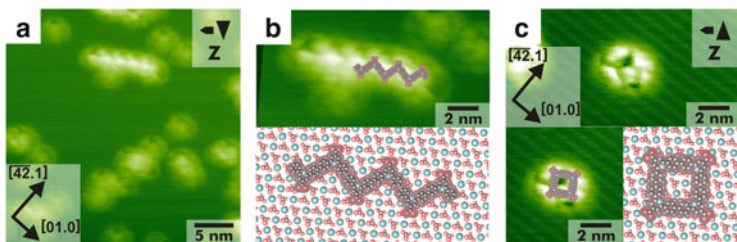


**Fig. 72** Structures observed after the second annealing step to 340 K for 1 h. (a) Chains oriented along an angle of  $+60 \pm 3^\circ$  with respect to the  $[\overline{42}.1]$  direction; ring-like features are observed to coexist on the surface. (b) Drift-corrected high-resolution image of an extended chain structure, with proposed model. (c) Drift-corrected high-resolution image of a closed ring structure, with proposed model. Note that the lines running from the *upper left* to *lower right* originate from the calcite(10.4) substrate

and 399 kJ/mol ( $\text{Cl}-\text{C}_6\text{H}_5$ ), respectively [299]. Again, a carboxylic acid moiety was chosen to provide sufficient anchoring towards the calcite surface.

When depositing a submonolayer of BCPPCA onto the calcite(10.4) surface at room temperature, ordered islands of a  $(2 \times 4)$  superstructure are formed, as shown in Fig. 71a.

A first distinct change in the molecular structure is induced upon annealing to 300°C, which can be assigned to the homolytic cleavage of the bromine–phenyl bond and subsequent covalent linking of the resulting radicals, resulting in molecular dimers. A representative image is given in Fig. 71b. Instead of ordered islands, rows are formed on the surface. Although the overall ordering is poor compared to the islands, two main orientations of the rows can be identified that span an angle of  $49 \pm 3^\circ$ . A dimer structure that is covalently linked at the former bromine position, 6,6'-[(1,1'-biphenyl)-4,4'-diyl]bis[2-(4-chloro-phenyl)isonicotinic acid], exhibits either a U- or an S-like shape. A stacking model for the S-form is given in Fig. 71c. Optimizing the intermolecular distance to allow for halogen– $\pi$  interaction can be understood as the driving force behind the lateral shift of the molecules perpendicular to the row direction. This readily results in a molecular chain that forms an angle of either  $+66^\circ$  or  $-66^\circ$  with respect to the  $[\overline{42}.1]$  mirror direction, resulting in an opening angle of  $48^\circ$ , in excellent agreement with the experimentally observed opening angle.

To induce the second reaction step, we annealed the surface to 340°C. The resulting structures are shown in Fig. 72. Most strikingly, the molecular structures that are present on the surface after the second annealing steps are, again, distinctly different from both the as-deposited ordered islands and the row structures observed after the first, moderate annealing step.

After the second annealing step, chains are oriented along an angle of  $60 \pm 3^\circ$  with respect to the  $[\overline{42}.1]$  direction and ring-like features are observed to coexist on the surface (Fig. 72a). The rows (Fig. 72b) differ in appearance and, most notably, in orientation as compared to the previously observed row structure, clearly indicating that the present chains are composed of building blocks other than

those in the previous row structures. A model can be drawn that is based on linking of the dimer to an extended row. This model is positioned onto the surface with the carboxylate groups positioned on top of the surface calcium ions. Despite this simple approach, the model fits excellently in size, in periodic repeat distance, and in the observed orientation on the surface. These three structural features together corroborate the model of a further linking of the dimer units into a zigzag polymer.

Considering the basic dimer units suggests that a second structure is feasible when linking the dimer building blocks, namely a closed ring. This structure is observed experimentally, as shown in Fig. 72c. The size of the ring-like structures fits excellently in size with a structure that is composed by further linking of the dimer molecules via cleavage of the chlorine–phenyl bond. Arranging the model such that the carboxylate groups can bind towards the calcium cations results in a well-defined angle with respect to the underlying substrate, which is exactly what is observed experimentally.

Thus, a two-step linking reaction was achieved by a sequential and selective activation of two reaction sites. Extended zigzag and closed ring structures were created upon sequential activation of homolytic cleavage of, first, the bromine–phenyl bonds and, second, the chlorine–phenyl bonds.

To conclude, we have demonstrated a proof-of-principle reaction of the covalent coupling of halide-substituted benzoic acid molecules on a bulk insulator, namely calcite(10.4). Depending on the number and position of the halide substitution, we can rationally design the structure of the resulting conjugated oligomers.

As a second step, we explored the possibility of a two-step polymerization reaction to enhance the structural control necessary to arrive at complex polymer architectures. By carefully selecting a precursor monomer that provides the encoding of the selective and sequential reaction sites, we rationally controlled a hierarchical two-step reaction process.

On-surface synthesis is expected to enhance variability when aiming at structure formation on surfaces. First, on-surface synthesis allows the creation of polymeric structures that might not be accessible from solution synthesis due to poor solubility. Second, larger structures that are difficult to transfer onto a supporting surface can be fabricated directly on the surface of interest, greatly facilitating the fabrication process. Third, due to the confinement of the molecular building blocks onto the 2D surface, fundamental new reaction pathways might be envisioned, providing further means for extending the structural complexity.

## References

1. Vögtle F (2001) Dendrimers III – design, dimension, function. In: Houk KN, de Meijere A, Kessler H, Lehn I-M, Ley SV, Schreiber SL, Thiem I, Trost BM (eds) Topics in current chemistry, vol 212. Springer, Berlin

2. Frechet JMJ, Tomalia DA (2001) Dendrimers and other dendritic polymers. In: Scheirs J (ed) Wiley series in polymer science. Wiley, New York, p 688
3. Hawker CJ, Frechet JMJ (1990) *J Am Chem Soc* 112:7638
4. Fischer M, Vogtle F (1999) *Angew Chem Int Ed* 38:885
5. Tomalia DA, Naylor AM, Goddard WA (1990) *Angew Chem Int Ed* 29:138
6. Bosman AW, Janssen HM, Meijer EW (1999) *Chem Rev* 99:1665
7. Türp D, Nguyen T-T, Baumgarten M, Müllen K (2012) *New J Chem* 36:282
8. Miller TM, Neenan TX (1990) *Chem Mater* 2:346
9. Miller TM, Neenan TX, Zayas R, Bair HE (1992) *J Am Chem Soc* 114:1018
10. Tomalia DA, Baker H, Dewald J, Hall M, Kallos G, Martin S, Roeck J, Ryder J, Smith P (1985) *Polym J* 17:117
11. Petekidis G, Vlassopoulos D, Galda P, Rehahn M, Ballauff M (1996) *Macromolecules* 29:8948
12. Buhleier E, Wehner W, Vogtle F (1978) *Synthesis-Stuttgart* 1978(2):155-158
13. Andreychenko EV, Clark CG, Bauer RE, Lieser G, Müllen K (2005) *Angew Chem Int Ed* 44:6348
14. Clark CG Jr, Wenzel RJ, Andreychenko EV, Steffen W, Zenobi R, Müllen K (2007) *J Am Chem Soc* 129:3292
15. Morgenroth F, Reuther E, Müllen K (1997) *Angew Chem Int Ed* 36:631
16. Yin M, Ding K, Gropeanu RA, Shen J, Berger R, Weil T, Müllen K (2008) *Biomacromolecules* 9:3231
17. Herrmann A, Mihov G, Vandermeulen GWM, Klok HA, Müllen K (2003) *Tetrahedron* 59:3925
18. Mondeshki M, Mihov G, Graf R, Spiess HW, Müllen K, Papadopoulos P, Gitsas A, Floudas G (2006) *Macromolecules* 39:9605
19. Mihov G, Grebel-Koehler D, Lubbert A, Vandermeulen GWM, Herrmann A, Klok HA, Müllen K (2005) *Bioconjug Chem* 16:283
20. Türp D, Wagner M, Enkelmann V, Müllen K (2011) *Angew Chem Int Ed* 50:4962
21. Mpoukouvalas K, Türp D, Wagner M, Müllen K, Butt H-J, Floudas G (2011) *J Phys Chem B* 115:5801
22. Vanderhoeven PHC, Lyklema J (1992) *Adv Colloid Interface Sci* 42:205
23. Krossing I, Raabe I (2004) *Angew Chem Int Ed* 43:2066
24. Every HA, Bishop AG, MacFarlane DR, Oradd G, Forsyth M (2004) *Phys Chem Chem Phys* 6:1758
25. Strauss SH (1993) *Chem Rev* 93:927
26. Qu JQ, Pschirer NG, Liu DJ, Stefan A, De Schryver FC, Müllen K (2004) *Chem Euro J* 10:528
27. Qu JQ, Zhang JY, Grimsdale AC, Müllen K, Jaiser F, Yang XH, Neher D (2004) *Macromolecules* 37:8297
28. Herrmann A, Weil T, Sinigersky V, Wiesler UM, Vosch T, Hofkens J, De Schryver FC, Müllen K (2001) *Chem Euro J* 7:4844
29. Weil T, Reuther E, Beer C, Müllen K (2004) *Chem Euro J* 10:1398
30. Weil T, Reuther E, Müllen K (2002) *Angew Chem Int Ed* 41:1900
31. Weil T, Vosch T, Hofkens J, Peneva K, Müllen K (2010) *Angew Chem Int Ed* 49:9068
32. Österling I, Müllen K (2007) *J Am Chem Soc* 129:4595
33. Gronheid R, Hofkens J, Kohn F, Weil T, Reuther E, Müllen K, De Schryver FC (2002) *J Am Chem Soc* 124:2418
34. Cotlet M, Gronheid R, Habuchi S, Stefan A, Barbafiga A, Müllen K, Hofkens J, De Schryver FC (2003) *J Am Chem Soc* 125:13609
35. Masuo S, Vosch T, Cotlet M, Tinnefeld P, Habuchi S, Bell TDM, Oesterling I, Beljonne D, Champagne B, Müllen K, Sauer M, Hofkens J, De Schryver FC (2004) *J Phys Chem B* 108:16686

36. Qin T, Zhou G, Scheiber H, Bauer RE, Baunigarten M, Anson CE, List EJW, Müllen K (2008) *Angew Chem Int Ed* 47:8292
37. Qin T, Wiedemair W, Nau S, Trattnig R, Sax S, Winkler S, Vollmer A, Koch N, Baumgarten M, List EJW, Müllen K (2011) *J Am Chem Soc* 133:1301
38. Nguyen T-T-T, Türp D, Wagner M, Müllen K (2013) *Angew Chem Int Ed* 52:669
39. Nguyen T-T-T, Türp D, Wang D, Noelscher B, Laquai F, Müllen K (2011) *J Am Chem Soc* 133:11194
40. Shifrina ZB, Rajadurai MS, Firsova NV, Bronstein LM, Huang XL, Rusanov AL, Müllen K (2005) *Macromolecules* 38:9920
41. Lubczyk D, Siering C, Loergen J, Shifrina ZB, Müllen M, Waldvogel SR (2010) *Sensor Actuator B* 143:561
42. Lubczyk D, Grill M, Baumgarten M, Waldvogel SR, Müllen K (2012) *Chemphyschem* 77:102
43. Gardner J, Yinon J (2003) *Electronic noses & sensors for the detection of explosives. II mathematics, physics and chemistry*. Kluwer Academic, New York
44. Newkome GR, Moorefield CN, Baker GR, Johnson AL, Behera RK (1991) *Angew Chem Int Ed* 30:1176
45. Hawker CJ, Wooley KL, Frechet JMJ (1993) *J Chem Soc Perkin Trans* 1:1287
46. Hecht S, Frechet JMJ (2001) *Angew Chem Int Ed* 40:74
47. Loi S, Butt HJ, Hampel C, Bauer R, Wiesler UM, Müllen K (2002) *Langmuir* 18:2398
48. Loi S, Wiesler UM, Butt HJ, Müllen K (2000) *Chem Commun* 1169
49. Loi S, Wiesler UM, Butt HJ, Müllen K (2001) *Macromolecules* 34:3661
50. Frechet JMJ (1994) *Science* 263:1710
51. Yin M, Feng C, Shen J, Yu Y, Xu Z, Yang W, Knoll W, Müllen K (2011) *Small* 7:1629
52. Feng CL, Yin M, Zhang D, Zhu S, Caminade AM, Majoral JP, Müllen K (2011) *Macromol Rapid Commun* 32:679
53. Yu Y, Yin M, Müllen K, Knoll W (2012) *J Mater Chem* 22:7880
54. Yin M, Shen J, Pflugfelder GO, Müllen K (2008) *J Am Chem Soc* 130:7806
55. Yin M, Shen J, Gropeanu R, Pflugfelder GO, Weil T, Müllen K (2008) *Small* 4:894
56. Dufes C, Uchegbu IF, Schatzlein AG (2005) *Adv Drug Deliv Rev* 57:2177
57. Kuan SL, Stöckle B, Reichenwallner J, Ng DYW, Wu Y, Doroshenko M, Koynov K, Hinderberger D, Müllen K, Weil T (2013) *Biomacromolecules* 14:367
58. Boas U, Heegaard PMH (2004) *Chem Soc Rev* 33:43
59. Zhang MF, Müller AHE (2005) *J Polym Sci A* 43:3461
60. Sheiko SS, Sumerlin BS, Matyjaszewski K (2008) *Progr Polym Sci* 33:759
61. Hsu H-P, Paul W, Binder K (2011) *Macromol Theor Sim* 20:510
62. Fredrickson GH (1993) *Macromolecules* 26:2825
63. Zhang B, Gröhn F, Pedersen JS, Fischer K, Schmidt M (2006) *Macromolecules* 39:8440
64. Hsu H-P, Paul W, Binder K (2008) *J Chem Phys* 129:204904
65. Hsu H-P, Paul W, Rathgeber S, Binder K (2010) *Macromolecules* 43:1592
66. Hsu H-P, Paul W, Binder K (2010) *Macromolecules* 43:3094
67. Kratky O, Porod G (1949) *J Colloid Sci* 4:35
68. Grosberg AY, Khoklov AR (1994) *Statistical physics of macromolecules*. In: Larson R, Pincus PA (eds) *AIP series in polymer and complex materials*. AIP, New York, p 382
69. Hsu H-P, Paul W, Binder K (2011) *Europhys Lett* 95:68004
70. Hsu H-P, Paul W, Binder K (2010) *Europhys Lett* 92:28003
71. Theodorakis PE, Hsu H-P, Paul W, Binder K (2011) *J Chem Phys* 135:164903
72. Gerle M, Fischer K, Roos S, Muller AHE, Schmidt M, Sheiko SS, Prokhorova S, Moller M (1999) *Macromolecules* 32:2629
73. Sun F, Sheiko SS, Möller M, Beers K, Matyjaszewski K (2004) *J Phys Chem A* 108:9682
74. Sheiko SS, Borisov OV, Prokhorova SA, Möller M (2004) *Eur Phys J E* 13:125
75. Saariaho M, Ikkala O, Szleifer I, Erukhimovich I, ten Brinke G (1997) *J Chem Phys* 107:3267

76. Elli S, Ganazzoli F, Timoshenko EG, Kuznetsov YA, Connolly R (2004) *J Chem Phys* 120:6257
77. Connolly R, Bellesia G, Timoshenko EG, Kuznetsov YA, Elli S, Ganazzoli F (2005) *Macromolecules* 38:5288
78. Subbotin A, Saariaho M, Ikkala O, ten Brinke G (2000) *Macromolecules* 33:3447
79. Nakamura Y, Norisuye T (2001) *Polym J* 33:874
80. Gerle M (1998) Dissertation, Universität Mainz
81. Wintermantel M, Gerle M, Fischer K, Schmidt M, Wataoka I, Urakawa H, Kajiwaru K, Tsukahara Y (1996) *Macromolecules* 29:978
82. Terao K, Takeo Y, Tazaki M, Nakamura Y, Norisuye T (1999) *Polym J* 31:193
83. Terao K, Nakamura Y, Norisuye T (1999) *Macromolecules* 32:711
84. Terao K, Hokajo T, Nakamura Y, Norisuye T (1999) *Macromolecules* 32:3690
85. Terao K, Hayashi S, Nakamura Y, Norisuye T (2000) *Polym Bull* 44:309
86. Hokajo T, Terao K, Nakamura Y, Norisuye T (2001) *Polym J* 33:481
87. Hsu HP, Paul W, Binder K (2013) *Polym Sci Ser C* 55:39
88. Sahl M, Muth S, Branscheid R, Fischer K, Schmidt M (2012) *Macromolecules* 45:5167
89. Cassim JY, Yang JT (1970) *Biopolymers* 9:1475
90. Gunari N, Cong Y, Zhang B, Fischer K, Janshoff A, Schmidt M (2008) *Macromol Rapid Commun* 29:821
91. Halperin A, Zhulina EB (1991) *Europhys Lett* 15:417
92. Theodorakis PE, Paul W, Binder K (2009) *Europhys Lett* 88:63002
93. Stephan T, Muth S, Schmidt M (2002) *Macromolecules* 35:9857
94. Heimann N (2004) Konformationsänderungen von zylindrischen Makromolekülen. Diploma thesis, University of Mainz
95. Zhang B, Zhang SJ, Okrasa L, Pakula T, Stephan T, Schmidt M (2004) *Polymer* 45:4009
96. Flory PJ (1953) Principles of polymer chemistry. Cornell University Press, Ithaca
97. Binder K (1994) Theories and mechanism of phase transitions, heterophase polymerizations, homopolymerization. *Addition Polym* 112:181
98. Enders S, Wolf BA (2011) Polymer thermodynamics: liquid polymer-containing mixtures. Springer, Berlin
99. Erukhimovich I, Theodorakis PE, Paul W, Binder K (2011) *J Chem Phys* 134:085101
100. Sevink GJA, Zvelindovsky AV, Fraaije J, Huinink HP (2001) *J Chem Phys* 115:8226
101. Erukhimovich I, Johner A (2007) *Europhys Lett* 79:56004
102. Stepanyan R, Subbotin A, ten Brinke G (2002) *Macromolecules* 35:5640
103. de Jong J, ten Brinke G (2004) *Macromol Theor Sim* 13:318
104. Liu YF, Abetz V, Müller AHE (2003) *Macromolecules* 36:7894
105. Hsu H-P, Paul W, Binder K (2007) *Macromol Theor Sim* 16:660
106. Hamley IW (1998) The physics of block polymers. Oxford University Press, New York
107. Leibler L (1980) *Macromolecules* 13:1602
108. Landau LD, Lifshitz EM (1958) Statistical physics. Pergamon, London
109. Hsu H-P, Paul W, Binder K (2006) *Europhys Lett* 76:526
110. Hsu H-P, Paul W, Binder K (2007) *Macromol Symp* 252:58
111. Grassberger P (1997) *Phys Rev E* 56:3682
112. Hsu H-P, Grassberger P (2011) *J Stat Phys* 144:597
113. Li CM, Gunari N, Fischer K, Janshoff A, Schmidt M (2004) *Angew Chem Int Ed* 43:1101
114. Ballauff M, Lu Y (2007) *Polymer* 48:1815
115. Akcora P, Liu H, Kumar SK, Moll J, Li Y, Benicewicz BC, Schadler LS, Acehan D, Panagiotopoulos AZ, Pyramitsyn V, Ganesan V, Ilavsky J, Thiyagarajan P, Colby RH, Douglas JF (2009) *Nat Mater* 8:354
116. Binder K, Milchev A (2012) *J Polym Sci B* 50:1515
117. Lo Verso F, Yelash L, Egorov SA, Binder K (2012) *Soft Matter* 8:4185
118. Lo Verso F, Yelash L, Egorov SA, Binder K (2011) *J Chem Phys* 135:214902
119. Lo Verso F, Egorov SA, Milchev A, Binder K (2010) *J Chem Phys* 133:184901

120. Lo Verso F, Egorov SA, Binder K (2012) *Macromolecules* 45:8892
121. Kremer K, Grest GS (1995) Entanglement effects in polymer melts and networks. In: Binder K (ed) *Monte Carlo and molecular dynamics methods in polymer science*. Oxford University Press, New York, p. 194
122. Egorov SA (2008) *J Chem Phys* 129:064901
123. Fleer GJ, Cohen Stuart MA, Scheutjens JM, Cosgrove T, Vincent B (1993) *Polymers at interfaces*. Chapman & Hall, London, p 496
124. Reith D, Milchev A, Virmau P, Binder K (2011) *Europhys Lett* 95:28003
125. Reith D, Milchev A, Virmau P, Binder K (2012) *Macromolecules* 45:4381
126. Reith D, Mirny L, Virmau P (2011) *Progr Theor Phys Suppl* 191:135
127. Halverson JD, Lee WB, Grest GS, Grosberg AY, Kremer K (2011) *J Chem Phys* 134:204904
128. Wieland T, Goldmann H, Kern W (1953) *Macromol Chem Phys* 10:136
129. Michaels AS, Miekka RG (1961) *J Phys Chem* 65:1765
130. Kabanov VA, Zezin AB, Izumrudov VA, Bronich TK, Bakeev KN (1985) *Macromol Chem Phys* 13:137-155 doi: 10.1002/macp.1985.020131985111
131. Dautzenberg H (2000) *Macromol Symp* 162:1
132. Thünemann A, Müller M, Dautzenberg H, Joanny J-F, Löwen H (2004) *Polyelectrolyte Complexes*. In: Schimidt M (ed) *Polyelectrolytes with defined molecular architecture II*. Springer, Berlin, p 113
133. Karibyants N, Dautzenberg H, Colfen H (1997) *Macromolecules* 30:7803
134. Bloomfield VA (1997) *Biopolymers* 44:269
135. Park TG, Jeong JH, Kim SW (2006) *Adv Drug Deliv Rev* 58:467
136. Haag R, Kratz F (2006) *Angew Chem Int Ed* 45:1198
137. Kabanov AV, Kabanov VA (1995) *Bioconjug Chem* 6:7
138. Bronich TK, Nguyen HK, Eisenberg A, Kabanov AV (2000) *J Am Chem Soc* 122:8339
139. Fischer D, Dautzenberg H, Kunath K, Kissel T (2004) *Intern J Pharm* 280:253
140. Katakura H, Harada A, Kataoka K, Furusho M, Tanaka F, Wada H, Ikenaka K (2004) *J Gene Med* 6:471
141. Oupicky D, Reschel T, Konak C, Oupicka L (2003) *Macromolecules* 36:6863
142. Ogris M, Steinlein P, Kurska M, Mechtler K, Kircheis R, Wagner E (1998) *Gene Ther* 5:1425
143. Boeckle S, von Gersdorff K, van der Piepen S, Culmsee C, Wagner E, Ogris M (2004) *J Gene Med* 6:1102
144. Chen W, Turro NJ, Tomalia DA (2000) *Langmuir* 16:15
145. Ottaviani MF, Sacchi B, Turro NJ, Chen W, Jockusch S, Tomalia DA (1999) *Macromolecules* 32:2275
146. Zinchenko AA, Yoshikawa K, Baigl D (2005) *Phys Rev Lett* 95:228101
147. Keren K, Soen Y, Ben Yoseph G, Gilad R, Braun E, Sivan U, Talmon Y (2002) *Phys Rev Lett* 89:088103
148. Gössl I, Shu L, Schlüter AD, Rabe JP (2002) *J Am Chem Soc* 124:6860
149. Gössl I, Shu L, Schlüter D, Rabe JP (2002) *Single Molecules* 3:315
150. Störkle D, Duschner S, Heimann N, Maskos M, Schmidt M (2007) *Macromolecules* 40:7998
151. Kuehn F, Fischer K, Schmidt M (2009) *Macromol Rapid Commun* 30:1470
152. Duschner S, Störkle D, Schmidt M, Maskos M (2008) *Macromolecules* 41:9067
153. Krohne K, Duschner S, Störkle D, Schmidt M, Maskos M (2010) *Macromolecules* 43:8645
154. Medina-Oliva A (2012) Ph.D. thesis, Dept. of Chemistry, University of Mainz, Mainz
155. Eisenriegler E (1991) *Polymers near surfaces*. World Scientific, Singapore
156. Gunari N, Schmidt M, Janshoff A (2006) *Macromolecules* 39:2219
157. Hsu H-P, Paul W, Binder K (2011) *J Phys Chem B* 115:14116
158. Winter D, Virmau P, Binder K (2009) *Phys Rev Lett* 103:225703
159. Hsu H-P, Paul W, Binder K (2010) *J Chem Phys* 133:104901
160. Brown SP, Spiess HW (2001) *Chem Rev* 101:4125
161. Brown SP (2009) *Macromol Rapid Commun* 30:688
162. Sebastiani D (2006) *Chemphyschem* 7:164

163. Tonelli AE, Schilling FC (1981) *Acc Chem Res* 14:233
164. Hansen MR, Graf R, Spiess HW (2013) *Acc Chem Res* 46:1996
165. Ober CK, Cheng SZD, Hammond PT, Muthukumar M, Reichmanis E, Wooley KL, Lodge TP (2009) *Macromolecules* 42:465
166. Spiess HW (2010) *Macromolecules* 43:5479
167. Vila JA, Scheraga HA (2009) *Acc Chem Res* 42:1545
168. Ochsenfeld C, Brown SP, Schnell I, Gauss J, Spiess HW (2001) *J Am Chem Soc* 123:2597
169. Spiess HW (2004) *J Polym Sci A* 42:5031
170. Dudenko D, Kiersnowski A, Shu J, Pisula W, Sebastiani D, Spiess HW, Hansen MR (2012) *Angew Chem Int Ed* 51:11068
171. Wüthrich K (2003) *Angew Chem Int Ed* 42:3340
172. Pannier M, Veit S, Godt A, Jeschke G, Spiess HW (2000) *J Magn Reson* 142:331
173. Spiess HW (2011) *J Magn Reson* 213:326
174. Jeschke G (2012) *Annu Rev Phys Chem* 62:419
175. Hubbell WL, Cafiso DS, Altenbach C (2000) *Nat Struct Biol* 7:735
176. Dockter C, Volkov A, Bauer C, Polyhach Y, Joly-Lopez Z, Jeschke G, Paulsen H (2009) *Proc Natl Acad Sci USA* 106:18485
177. Walton AG, Blackwell JB (1973) *Biopolymers*. Academic, New York
178. Klok H-A, Lecommandoux S (2006) Solid-state structure, organization and properties of peptide – synthetic hybrid block copolymers. In: Klok HA, Schlaad H (eds) *Peptide hybrid polymers, Advances in polymer science*, vol 202. Springer, Berlin, pp 75-111
179. Tycko R (2001) *Ann Rev Phys Chem* 52:575
180. Strobl G (2007) *The physics of polymers: concepts for understanding their structures and behavior*, 3rd edn. Springer, New York, 518
181. Floudas G, Spiess HW (2009) *Macromol Rapid Commun* 30:278
182. Floudas G (2004) *Progr Polym Sci* 29:1143
183. Wang J, Lu H, Ren Y, Zhang YF, Morton M, Cheng JJ, Lin Y (2011) *Macromolecules* 44:8699
184. Aliferis T, Iatrou H, Hadjichristidis N (2004) *Biomacromolecules* 5:1653
185. Floudas G, Papadopoulos P, Klok HA, Vandermeulen GWM, Rodriguez-Hernandez J (2003) *Macromolecules* 36:3673
186. Gibson MI, Cameron NR (2008) *Angew Chem Int Ed* 47:5160
187. Gitsas A, Floudas G, Mondeshki M, Lieberwirth I, Spiess HW, Iatrou H, Hadjichristidis N, Hirao A (2010) *Macromolecules* 43:1874
188. Graf R, Spiess HW, Floudas G, Butt HJ, Gkikas M, Iatrou H (2012) *Macromolecules* 45:9326
189. Bates FS, Fredrickson GH (1990) *Ann Rev Phys Chem* 41:525
190. Clark CG, Floudas GA, Lee YJ, Graf R, Spiess HW, Müllen K (2009) *J Am Chem Soc* 131:8537
191. Young Joo L, Clark CG Jr, Graf R, Wagner M, Müllen K, Spiess HW (2009) *J Phys Chem B* 113:1360
192. Gorelik T, Matveeva G, Kolb U, Schleuss T, Kilbinger AFM, van de Streek J, Bohle A, Brunklaus G (2010) *CrystEngComm* 12:1824
193. Gorelik TE, van de Streek J, Kilbinger AFM, Brunklaus G, Kolb U (2012) *Acta Crystallogr B* 68:171
194. Bohle A, Brunklaus G, Hansen MR, Schleuss TW, Kilbinger AFM, Seltmann J, Spiess HW (2010) *Macromolecules* 43:4978
195. Palmans ARA, Meijer EW (2007) *Angew Chem Int Ed* 46:8948
196. Metzroth T, Hoffmann A, Martin-Rapun R, Smulders MMJ, Pieterse K, Palmans ARA, Vekemans JAJM, Meijer EW, Spiess HW, Gauss J (2011) *Chem Sci* 2:69
197. Wegner M, Dudenko D, Sebastiani D, Palmans ARA, de Greef TFA, Graf R, Spiess HW (2011) *Chem Sci* 2:2040
198. Zhao DY, Feng JL, Huo QS, Melosh N, Fredrickson GH, Chmelka BF, Stucky GD (1998) *Science* 279:548

199. Ferey G, Mellot-Draznieks C, Serre C, Millange F, Dutour J, Surble S, Margiolaki I (2005) *Science* 309:2040
200. Vollmeyer J, Jester SS, Eberhagen F, Prangenberg T, Mader W, Höger S (2012) *Chem Commun* 48:6547
201. Fritzsche M, Bohle A, Dudenko D, Baumeister U, Sebastiani D, Richardt G, Spiess HW, Hansen MR, Hoeger S (2011) *Angew Chem Int Ed* 50:3030
202. Ajami D, Rebek J (2008) *Angew Chem Int Ed* 47:6059
203. Moon C, Brunklaus G, Sebastiani D, Rudzевич Y, Böhmer V, Spiess HW (2009) *Phys Chem Chem Phys* 11:9241
204. Wu JS, Pisula W, Müllen K (2007) *Chem Rev* 107:718
205. Feng X, Marcon V, Pisula W, Hansen MR, Kirkpatrick J, Grozema F, Andrienko D, Kremer K, Müllen K (2009) *Nat Mater* 8:421
206. Elmahdy MM, Mondeshki M, Dou X, Butt H-J, Spiess HW, Müllen K, Floudas G (2009) *J Chem Phys* 131: 114704
207. Herbst W, Hunger K (2004) *Industrial Organic pigments: production, properties, applications*, 3rd edn. Wiley-VCH, Weinheim, p 678
208. Schmidt-Mende L, Fechtenkötter A, Müllen K, Moons E, Friend RH, MacKenzie JD (2001) *Science* 293:1119
209. Tasios N, Grigoriadis C, Hansen MR, Wonneberger H, Li C, Spiess HW, Müllen K, Floudas G (2010) *J Am Chem Soc* 132:7478
210. Percec V, Hudson SD, Peterca M, Leowanawat P, Aqad E, Graf R, Spiess HW, Zeng X, Ungar G, Heiney PA (2011) *J Am Chem Soc* 133:18479
211. Förster S, Konrad M (2003) *J Mater Chem* 13:2671
212. Yoon J, Lee W, Thomas EL (2006) *Nano Lett* 6:2211
213. Park M, Harrison C, Chaikin PM, Register RA, Adamson DH (1997) *Science* 276:1401
214. Kikuchi M, Binder K (1994) *J Chem Phys* 101:3367
215. Shin K, Xiang HQ, Moon SI, Kim T, McCarthy TJ, Russell TP (2004) *Science* 306:76
216. Ma M, Krikorian V, Yu JH, Thomas EL, Rutledge GC (2006) *Nano Lett* 6:2969
217. Thomas EL, Reffner JR, Bellare J (1990) *J de Physique* 51:C7363
218. Higuchi T, Motoyoshi K, Sugimori H, Jinnai H, Yabu H, Shimomura M (2010) *Macromol Rapid Commun* 31:1773
219. Hales K, Chen Z, Wooley KL, Pochan DJ (2008) *Nano Lett* 8:2023
220. Crespy D, Landfester K (2007) *Macromol Chem Phys* 208:457
221. Staff RH, Rupper P, Lieberwirth I, Landfester K, Crespy D (2011) *Soft Matter* 7:10219
222. Winkler A, Statt A, Virnau P, Binder K (2013) *Phys Rev E* 87:032307
223. Statt A, Winkler A, Virnau P, Binder K (2012) *J Phys Condens Matter* 24:464122
224. Reith D, Virnau P (2010) *Comput Phys Commun* 181:800
225. Reith D, Virnau P (2011) *Comput Phys Commun* 182:1945
226. Reith D, Cifra P, Stasiak A, Virnau P (2012) *Nucleic Acids Res* 40:5129
227. Virnau P, Rieger FC, Reith D (2013) *Biochem Soc Trans* 41:528
228. Howarter JA, Youngblood JP (2007) *Adv Mater* 19:3838
229. Ghosh B, Urban MW (2009) *Science* 323:1458
230. Uhlmann P, Ionov L, Houbenov N, Nitschke M, Grundke K, Motornov M, Minko S, Stamm M (2006) *Prog Org Coat* 55:168
231. Sui ZJ, Schlenoff JB (2003) *Langmuir* 19:7829
232. Zhao B, Haasch RT, MacLaren S (2004) *J Am Chem Soc* 126:6124
233. Julthongpiput D, Lin YH, Teng J, Zubarev ER, Tsukruk VV (2003) *J Am Chem Soc* 125:15912
234. Zhulina E, Balazs AC (1996) *Macromolecules* 29:2667
235. Lin YH, Teng J, Zubarev ER, Shulha H, Tsukruk VV (2005) *Nano Lett* 5:491
236. Wang Y, Zheng JX, Brittain WJ, Cheng SZD (2006) *J Polym Sci A* 44:5608
237. Tonhauser C, Wilms D, Wurm F, Berger-Nicoletti E, Maskos M, Löwe H, Frey H (2010) *Macromolecules* 43:5582

238. Tonhauser C, Obermeier B, Mangold C, Löwe H, Frey H (2011) *Chem Commun* 47:8964
239. Tonhauser C, Golriz AA, Moers C, Klein R, Butt HJ, Frey H (2012) *Adv Mater* 24:5559
240. Neto C, James M, Telford AM (2009) *Macromolecules* 42:4801
241. Discher DE, Eisenberg A (2002) *Science* 297:967
242. Lee JCM, Bermudez H, Discher BM, Sheehan MA, Won YY, Bates FS, Discher DE (2001) *Biotechnol Bioeng* 73:135
243. Förster S, Berton B, Hentze HP, Kramer E, Antonietti M, Lindner P (2001) *Macromolecules* 34:4610
244. Antonietti M, Förster S (2003) *Adv Mater* 15:1323
245. Jain S, Bates FS (2003) *Science* 300:460
246. Maskos M (2006) *Polymer* 47:1172
247. Caliceti P, Veronese FM (2003) *Adv Drug Deliv Rev* 55:1261
248. Haag R (2004) *Angew Chem Int Ed* 116:280
249. Bermudez H, Brannan AK, Hammer DA, Bates FS, Discher DE (2002) *Macromolecules* 35:8203
250. Maskos M, Harris JR (2001) *Macromol Rapid Commun* 22:271
251. Jofre A, Hutchison JB, Kishore R, Locascio LE, Helmerson K (2007) *J Phys Chem B* 111:5162
252. Checot F, Lecommandoux S, Klok HA, Gnanou Y (2003) *Eur Phys J E* 10:25
253. Allen C, Maysinger D, Eisenberg A (1999) *Colloids Surf B* 16:3
254. Kataoka K, Harada A, Nagasaki Y (2001) *Adv Drug Deliv Rev* 47:113
255. Choucair A, Soo PL, Eisenberg A (2005) *Langmuir* 21:9308
256. Borchert U, Lipprandt U, Bilanz M, Kimpfler A, Rank A, Peschka-Suess R, Schubert R, Lindner P, Förster S (2006) *Langmuir* 22:5843
257. Lecommandoux SB, Sandre O, Checot F, Rodriguez-Hernandez J, Perzynski R (2005) *Adv Mater* 17:712
258. Krack M, Hohenberg H, Kornowski A, Lindner P, Weller H, Förster S (2008) *J Am Chem Soc* 130:7315
259. Ghoroghchian PP, Lin JJ, Brannan AK, Frail PR, Bates FS, Therien MJ, Hammer DA (2006) *Soft Matter* 2:973
260. Nardin C, Thoeni S, Widmer J, Winterhalter M, Meier W (2000) *Chem Commun* 2000:1433
261. Binder WH, Sachsenhofer R, Farnik D, Blaas D (2007) *Phys Chem Chem Phys* 9:6435
262. Binder WH, Sachsenhofer R (2008) *Macromol Rapid Commun* 29:1097
263. Lecommandoux S, Sandre O, Checot F, Perzynski R (2006) *Progr Solid State Chem* 34:171
264. Ghoroghchian PP, Frail PR, Susumu K, Park TH, Wu SP, Uyeda HT, Hammer DA, Therien MJ (2005) *J Am Chem Soc* 127:15388
265. Bockstaller MR, Lapetnikov Y, Margel S, Thomas EL (2003) *J Am Chem Soc* 125:5276
266. Chiu JJ, Kim BJ, Kramer EJ, Pine DJ (2005) *J Am Chem Soc* 127:5036
267. Ahmed F, Pakunlu RI, Brannan A, Bates F, Minko T, Discher DE (2006) *J Control Release* 116:150
268. Krishna MMG (1999) *J Phys Chem A* 103:3589
269. Hines MA, Guyot-Sionnest P (1996) *J Phys Chem* 100:468
270. Xie RG, Kolb U, Li JX, Basché T, Mews A (2005) *J Am Chem Soc* 127:7480
271. Müller W, Koynov K, Fischer K, Hartmann S, Pierrat S, Basché T, Maskos M (2009) *Macromolecules* 42:357
272. Goodwin AP, Mynar JL, Ma YZ, Fleming GR, Frechet JMJ (2005) *J Am Chem Soc* 127:9952
273. Chiu JJ, Kim BJ, Yi G-R, Bang J, Kramer EJ, Pine DJ (2007) *Macromolecules* 40:3361
274. Matsen MW, Thompson RB (2008) *Macromolecules* 41:1853
275. Kang H, Detchevery FA, Mangham AN, Stoykovich MP, Daoulas KC, Hamers RJ, Mueller M, de Pablo JJ, Nealey PF (2008) *Phys Rev Lett* 100:148303
276. Rigler R, Elson E (2001) *Fluorescence correlation spectroscopy: theory and applications*. Springer series in chemical physics, vol 65. Springer, Heidelberg
277. Hausteine E, Schwille P (2004) *Curr Opin Struct Biol* 14:531

278. Koynov K, Butt HJ (2012) *Curr Opin Colloid Interface Sci* 17:377
279. Koynov K, Mihov G, Mondeshki M, Moon C, Spiess HW, Müllen K, Butt HJ, Floudas G (2007) *Biomacromolecules* 8:1745
280. Schmidt M (1993) Dynamic light scattering. In: Brown W (ed) *Dynamic light scattering: the method and some applications*. Clarendon, Oxford, p 752
281. Whitesides GM, Mathias JP, Seto CT (1991) *Science* 254:1312
282. Franc G, Gourdon A (2011) *Phys Chem Chem Phys* 13:14283
283. Gourdon A (2008) *Angew Chem Int Ed* 47:6950
284. Hla SW, Bartels L, Meyer G, Rieder KH (2000) *Phys Rev Lett* 85:2777
285. Grill L, Dyer M, Lafferentz L, Persson M, Peters MV, Hecht S (2007) *Nat Nanotechnol* 2:687
286. Lipton-Duffin JA, Ivasenko O, Perepichka DF, Rosei F (2009) *Small* 5:592
287. Cai J, Ruffieux P, Jaafar R, Bieri M, Braun T, Blankenburg S, Muoth M, Seitsonen AP, Saleh M, Feng X, Müllen K, Fasel R (2010) *Nature* 466:470
288. Weigelt S, Busse C, Bombis C, Knudsen MM, Gothelf KV, Laegsgaard E, Besenbacher F, Linderoth TR (2008) *Angew Chem Int Ed* 47:4406
289. Rahe P, Kittelmann M, Neff JL, Nimmrich M, Reichling M, Maass P, Kühnle A (2013) *Adv Mater* 25:3948
290. Kittelmann M, Rahe P, Nimmrich M, Hauke CM, Gourdon A, Kühnle A (2011) *ACS Nano* 5:8420
291. Kittelmann M, Nimmrich M, Lindner R, Gourdon A, Kühnle A (2013) *ACS Nano* 7:5614-5620 *ACS Nano* 7:5614
292. Kunstmann T, Schlarb A, Fendrich M, Wagner T, Moller R, Hoffmann R (2005) *Phys Rev B* 71:121403
293. Schütte J, Bechstein R, Rohlfig M, Reichling M, Kühnle A (2009) *Phys Rev B* 80:205421
294. Kittelmann M, Rahe P, Kühnle A (2012) *J Phys Condens Matter* 24:354007
295. Rahe P, Lindner R, Kittelmann M, Nimmrich M, Kühnle A (2012) *Phys Chem Chem Phys* 14:6544
296. Duffy DM, Harding JH (2002) *J Mater Chem* 12:3419
297. Kittelmann M, Rahe P, Gourdon A, Kühnle A (2012) *ACS Nano* 6:7406
298. Kittelmann M, Nimmrich M, Neff JL, Rahe P, Gren W, Bouju AG, Gourdon A, Kühnle A (2013) *J Phys Chem C*, submitted
299. Luo Y-R (2007) *Comprehensive handbook of chemical bond energies*. CRC, Boca Raton
300. Lafferentz L, Eberhardt V, Dri C, Africh C, Comelli G, Esch F, Hecht S, Grill L (2012) *Nat Chem* 4:215

# Polymer Complexes in Biological Applications

**Jana Hedrich, Yuzhou Wu, Seah Ling Kuan, Frauke Kuehn, Ewelina Pietrowski, Mike Sahl, Sandra Muth, Klaus Müllen, Heiko J. Luhmann, Tanja Weil, and Manfred Schmidt**

**Abstract** This chapter summarizes the influence of polyelectrolyte topology on biological functions and biomedical applications such as cell uptake, drug delivery, and gene transfection. Polyelectrolytes utilized are spherical structures derived from dendrimers and albumin or cylindrical brushes, all of which are decorated with various polypeptide chains.

First, experiments are described that address the role of polyelectrolyte interactions on endosomal uptake and release, followed by a discussion of the novel design of albumin-based nanocarriers for anticancer drugs like doxorubicin. Finally, we describe how efficient gene transfection was accomplished with both albumin-based polycations and with cylindrical brushes having poly-L-lysine side chains.

**Keywords** Brain • Cylindrical brush polymer • Dendritic and protein polyelectrolytes • Endothelial cell • Flow cytometry • Gene transfer • Polycation • Transfection

---

J. Hedrich, E. Pietrowski and H.J. Luhmann  
Institute of Physiology and Pathophysiology, University Medical Center, Mainz, Germany

Y. Wu, S.L. Kuan and T. Weil  
Institute of Organic Chemistry III, University of Ulm, Albert-Einstein-Allee 11,  
Ulm 89081, Germany

F. Kuehn, M. Sahl, S. Muth and M. Schmidt (✉)  
Institute of Physical Chemistry, Johannes Gutenberg University, Welderweg 11, 55099 Mainz,  
Germany  
e-mail: [mschmidt@uni-mainz.de](mailto:mschmidt@uni-mainz.de)

K. Müllen  
Max Planck Institute for Polymer Research, Ackermannweg 10, Mainz 55128, Germany

## Contents

1	Exploring Cell Interactions of Dendritic and Protein Polyelectrolytes .....	213
1.1	Introduction .....	213
1.2	Polycationic and Polyanionic Core–Shell Polyphenylene Dendrimers .....	214
1.3	Polycationic Serum Albumin Proteins for Gene Delivery .....	218
1.4	Albumin Copolymer Polyelectrolytes Allow Efficient Drug Delivery .....	222
1.5	Conclusions .....	224
2	Gene Transfection Utilizing Cationic Cylindrical Brush Polymers .....	225
2.1	Introduction .....	225
2.2	Polymers for Transfection .....	226
2.3	Brush Polymer Synthesis and DNA Complexation .....	227
2.4	Transfection with Brush Polymers .....	229
2.5	Conclusions .....	230
	References .....	231

## Abbreviations

AML	Acute myeloid leukemia
ATRP	Atom transfer radical polymerization
cBSA	Cationized bovine serum albumin
DHSA	Dendronized human serum albumin
DMF	Dimethyl formamide
DOX	Doxorubicin
ECM	Extracellular matrix
EPR	Enhanced retention and permeation
GFP	Green fluorescent protein
HSA	Human serum albumin
LiBr	Lithium bromide
MRI	Magnetic resonance imaging
$M_w$	Weight-average molecular weight
NaCl	Sodium chloride
PAMAM	Polyamidoamine
PBMEC	Porcine microvascular endothelial cells
PDI	Perylene-3,4,9,10-tetracarboxdiimide
PEG	Poly(ethylene glycol)
PEI	Poly(ethylene imine)
PEO	Poly(ethylene oxide)
PLL	Poly-L-lysine
$P_n$	Number-average degree of polymerization
$P_w$	Weight-average degree of polymerization
$R_g$	Radius of gyration
$R_h$	Hydrodynamic radius

TEM	Transmission electron microscopy
$w_{\text{DNA}}$	Weight fraction of DNA
$z^+/z^-$	Molar charge ratio polycation/polyanion

## 1 Exploring Cell Interactions of Dendritic and Protein Polyelectrolytes

### 1.1 Introduction

Ionic interactions play a crucial role in many cellular processes such as membrane permeation or regulation of gene transcription [1]. The cell membrane, with its bilayer and negatively charged surface, serves as a protective barrier for the living cell towards its environment. Hydrophobic or positively charged molecules can interact with the cell membrane and can enter cells via various mechanisms [2]. In the cell nucleus, polycationic proteins and histones form complexes with DNA and regulate transcription through alteration of the charge densities of nuclear proteins and DNA [3]. Inspired by these polyelectrolytic interactions in nature, synthetic nanosized polyelectrolytes have been designed that contain multiple electrolyte groups, i.e., polycations or polyanions. Some of these polyelectrolyte carriers have already been successfully explored for biomedical applications such as gene or cancer therapy [4, 5]. With greater emphasis on defined macromolecular architectures of the materials, regularly branched cascade molecules (so-called dendrimers) and protein-based polyelectrolytes have emerged over the past decade. Their interactions with cells have been analyzed to elucidate the role of polyelectrolyte interactions in nature and to apply this knowledge for the design of efficient and biocompatible nanotransporters for the delivery of cargoes such as drugs, proteins, or nucleic acids into cells and subcellular compartments [6, 7].

Endocytosis is essential for uptake of macromolecules and nanoparticles. Thereby, the physical and chemical characteristics of the cargo and transporter complex determine the nature of the cell uptake mechanism. Particles larger than 500 nm are typically phagocytosed or macropinocytosed, whereas smaller hydrophilic molecules are internalized by any of the various endocytotic processes [2, 8]. Often, nanometer-sized transporter molecules or particles accomplish cell uptake simultaneously by several endocytotic mechanisms [9]. Clathrin-dependent endocytosis is the most widely understood pathway, which is present in nearly all mammalian cells. The clathrin pathway is considered the most important uptake mechanism for several polymers such as poly(ethylene glycol)-polylactides, poly(lactide-*co*-glycolide) (PLGA), silica-based nanoparticles, and chitosan nanoparticles [8, 10–12].

Besides clathrin-mediated cell uptake, caveolae-mediated endocytosis is another well-investigated uptake mechanism. The caveolae pathway is particularly attractive for the delivery of proteins and nucleic acids because these vesicles have neutral pH and the lysosomes, where degradation takes place, are bypassed [8, 13]. Nanoparticles

described to be mainly endocytosed by caveolae include polymeric micelles with a crosslinked anionic core, DOXIL, polysiloxanes, coated quantum dots, and Abraxane [8, 14–17].

Apart from clathrin- and caveolin-mediated endocytosis, there also exist multiple other pathways independent of clathrin and caveolin-1 that also play an important role in nanoparticle endocytosis. Exploring the clathrin- and caveolin-independent uptake mechanisms has only recently gained attention in endocytosis research, and these less-understood uptake mechanisms might have implications for drug delivery research.

In this chapter, the design of structurally defined dendritic and protein-based polyelectrolyte nanocarriers is presented and the impact of their macromolecular architectures and the presence of multiple charges and charge densities on cellular uptake, trafficking, and cell toxicity is discussed.

## ***1.2 Polycationic and Polyanionic Core–Shell Polyphenylene Dendrimers***

Polycationic proteins such as nuclear histone proteins possess high densities of the positively charged amino acids lysine and arginine located at their periphery, as well as a lipophilic interior. These “natural” polycations are able to complex and to store DNA in the cell nucleus. Based on these structural considerations, dendritic core–shell macromolecules have been designed that possess a lipophilic and relatively stiff polyphenylene scaffold that determines the size and the shape of the macromolecules, as well as a second polymer shell containing multiple positive or negative charges (Fig. 1a) [18]. The position of these charged polymer chains at the dendrimer surface is predetermined by molecular design. The approximate number of charged groups (monomer units) within the polymer chains has been varied by atom transfer radical polymerization (ATRP). In this way, structurally defined macromolecules have been obtained that allow the qualitative correlation of the impact of the architecture and the number and nature of charges of a globular macromolecule on its ability to cross biological membranes [18]. As an additional structural feature, the lipophilic inner part contains a fluorescent perylene-3,4,9,10-tetracarboxdiimide (PDI) chromophore to allow cell uptake studies by fluorescence microscopy (Fig. 1b, c). Polycationic and polyanionic shells have been achieved after polymerization of 2-*tert*-butoxycarbonylaminoethyl methacrylate or *tert*-butyl acrylate, respectively, from the inner polyphenylene core that serves as macroinitiator carrying a defined number of 2-bromo-2-methylpropionic ester groups [18]. After removal of the *tert*-butoxycarbonyl or *tert*-butyl protective groups, the synthesized core–shell macromolecules possesses good water solubility, which is essential for in vitro cell experiments.

The impact of the macromolecular architecture on cell uptake and toxicity revealed that the presence of positively charged primary amino groups is essential

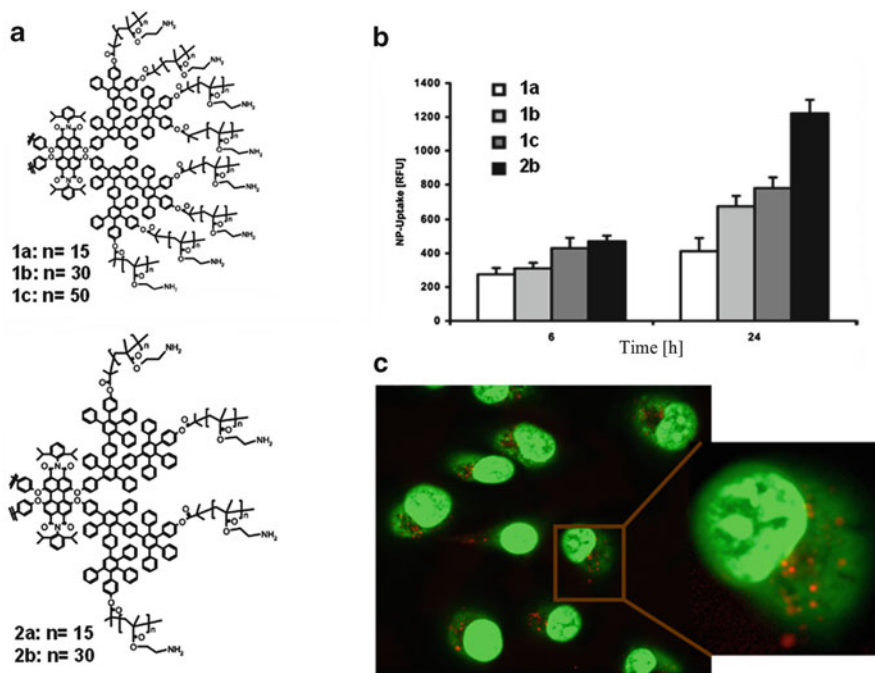


**Fig. 1** Dendritic core-shell star polymers. (a) Dendritic core-shell star polymers of different architectures with varying densities of the polycationic polymer chains grafted from the dendrimer core as well as varying numbers of positive charges along the individual polymer chains. (b) Cellular uptake of selected macromolecules by ECV-304. The bars represent relative fluorescence units (RFU) measured in individual cells. Data represent mean values ( $\pm$  SEM) after an incubation periods of 6 and 24 h. (c) Cell uptake of polycationic core-shell dendrimers into ECV-304 cells after 15 min. ECV-304 were stained using a green fluorescence cell tracker, whereas the core-shell macromolecules are shown with a red color originating from the PDI core

for efficient membrane uptake, since none of the polyanions was taken up by cells. The total number of grafted polymer chains as well as the polymer chain lengths (e.g., the number of aminoethyl groups per chain) have been varied systematically [18]. Even though all polycations were in principle able to enter cells, increasing the number of cationic repeat units (amino groups) prolonged the time required for cell uptake. In addition, the macromolecular architecture also played an important role. For those polycations with higher densities of polymer chains at the surface of the dendrimers, significantly faster cell uptake was observed but there was also more efficient exocytosis, resulting in lower intracellular concentrations compared to the polycations with lower numbers of polymer chains. In addition, all macromolecules containing a high number and high density of amino groups showed considerable cytotoxicity, most probably due to vesicle leakage and cell lysis [19], which has been reported for other polycationic macromolecules as well.

The polycationic core-shell macromolecule **4** (Fig. 2b), formed from a first-generation dendrimer with 50 monomer repeating units, revealed only minor cell

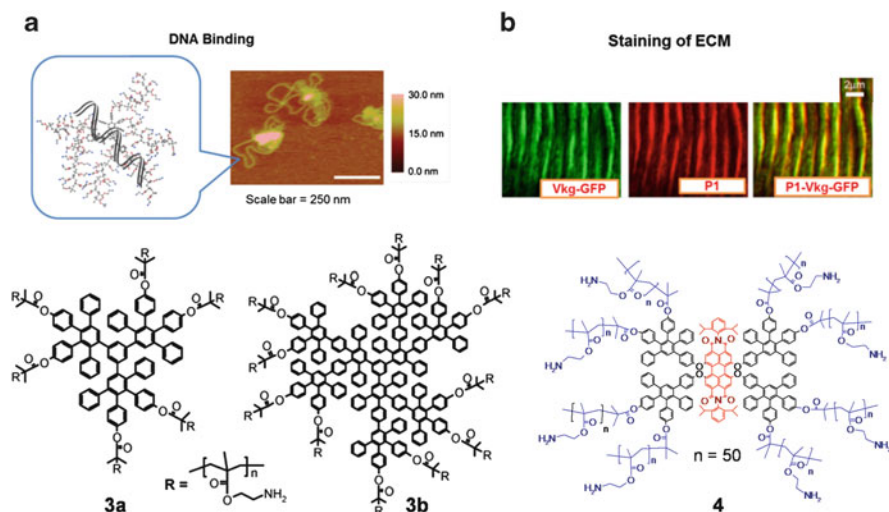


**Fig. 2** Dendritic polyelectrolyte interaction with (a) DNA and (b) the ECM (Vkg-GFP stands for the viking gene that codes for a Collagen type IV protein and localizes to membranes, green emission of the green fluorescent protein, GFP). Structures **3a** and **3b** are first and second generation dendrimers, respectively. Structure **4** is a polycationic red dye (*P1*)

toxicity and was investigated with regard to its potential to interact with subcellular structures [20]. An interaction with the highly negatively charged extracellular matrix (ECM) was observed at physiological pH [20]. Because the ECM surrounds cells and plays an important role in many aspects of cellular fate (including cell migration, stem cell differentiation, and cancer progression) specific labeling of the ECM could be attractive for cell studies. Via affinity analysis, aggrecan was identified as a major interaction partner [20]. Aggrecan is a major structural proteoglycan of cartilage ECM, with a 210–250 kDa core protein to which 100–150 chondroitin sulfate and keratan sulfate chains are attached [21, 22]. In a dot blotting assay, only negatively charged aggrecan was found to interact with the polycationic dendrimer, most probably due to the presence of multiple positive charges. Visualization of the microstructure of the ECM in both fixed and living preparations indicated strong binding to its negatively charged constituents (Fig. 2). Interestingly, the polycationic dye **4** revealed significantly increased emission intensity after binding to the ECM components, and this observation was even compatible with antibody staining, making it useful for multiple channel fluorescence imaging. Due to the observed biological specificity, such polycationic chromophores could serve as an attractive tool for specifically labeling the ECM in life science research [20].

Complex formation of polycationic core–shell macromolecules with natural polyanions such as DNA has been investigated. Three generations of core–shell polymers consisting of a dendritic polyphenylene core and an outer shell containing a defined number of primary amino groups have been synthesized via ATRP (Fig. 2a shows structures **3a** and **3b**, generations 1 and 2, respectively) [23]. All polymers

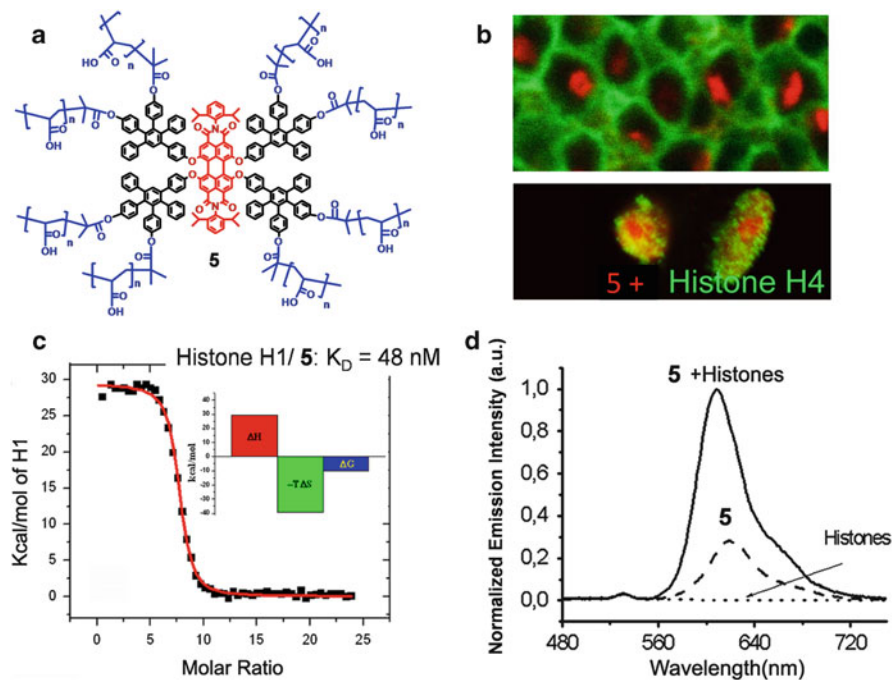


**Fig. 3** Polyanionic dendrimers interacting with histone proteins. (a) Molecular structure of the first generation polyanionic dendrimer. (b) Confocal scanning microscope images shown the co-localization of polyanionic dendrimer (**5**, red) with histone H4 proteins (green). (c) Isothermal titration calorimetry graph shows the strong interaction between histone H1 with **5**. (d) Spectral analysis of the **5**/histones

revealed tight binding to different sets of DNA fragments as well as plasmid DNA pUK19 (2,686 bp; 5,372 negative charges). Complex stoichiometries between pUK19 and the polymers were determined by isothermal titration calorimetry and it turned out that the presence of increasing numbers of amino groups within the polymer shell resulted in the formation of polyelectrolyte complexes with higher DNA contents. The average number of dendrimer molecules per pUC19 DNA helix in a complex decreased from 98 (**3a** with about 55 amino groups), to 46 (**3b** with about 116 amino groups) to 30 (third generation dendrimer with about 197 amino groups) under the assumption that neutral complexes were formed [23]. In this way, complex stoichiometries could be controlled by tuning the number of amino groups of the dendritic polycations under the formation of well-defined nanoscopic architectures. Additionally to DNA binding, the question of DNA release was also addressed in this study. A salt concentration-dependent DNA release was achieved with increasing salt concentrations from 50 mM up to 1 M, with complete DNA release at the highest concentrations. These polycationic core-shell dendrimers provide many attractive features such as multiple and adjustable positive charges, allowing high capacity binding and release of nucleic acids, which makes them an interesting tool for DNA staining, gene transfection, and DNA purification.

In contrast, polyanionic core–shell dendrimers such as **5** (Fig. 3a) did not display any cellular uptake and, therefore, it was not feasible to investigate the fate of these polyanions inside viable cells [18]. However, applying them to fixed cells allowed cell membrane uptake and specific staining of the cell nuclei in *Drosophila* tissue (Fig. 3b) [20]. In the cell nucleus, DNA wraps around histone proteins forming nucleosomes. The role of histone proteins is to pack and order DNA into structural units based on electrostatic interactions with DNA, which has an important impact for gene transcription. In the presence of the polyanionic core–shell macromolecule **5**, bearing high numbers of negatively charged carboxylate groups, DNA is most probably displaced from the complexes and polyelectrolyte complexes between **5** and the histone H1 proteins are formed due to tight interactions (Fig. 3c). **5** specifically stains the cell nucleus by binding to the positively charged nuclear proteins (Fig. 3d), and it might therefore serve as an attractive alternative to conventional fluorescent antibodies. Polyanionic core–shell dendrimers combine unique properties such as water solubility, high photochemical stability, narrow emission spectra, and cell-specific binding, making them attractive for cytochemical and histochemical studies.

### 1.3 Polycationic Serum Albumin Proteins for Gene Delivery

As discussed above, many synthetic polycations exhibit high cellular toxicities, even at low concentrations. Interestingly, polycationic proteins such as nuclear histone proteins are often much less cytotoxic, which might be due to the presence of many other functional groups within the polypeptide scaffold that potentially “dilute” the effect of the positive charges. In order to assess the impact of the positive charges of polycationic proteins on cell uptake and cell toxicity, polycationic derivatives of the abundant blood plasma protein transporter serum albumin were prepared [6]. Serum albumin is well suited to impart chemical surface modifications due to the high number of negatively charged amino acids (e.g., 100 glutamate and aspartate groups), its diameter of 4.7 nm calculated from the crystal structure [6], and the presence of lipophilic pockets that can accommodate lipophilic guest molecules. Albumin polycations have been achieved by successive conversion of carboxylic acid side chains of the negatively charged amino acids of aspartate and glutamate residues into primary amino groups (Fig. 4) [6]. Stepwise reaction of the carboxylic acid groups with increasing amounts of ethylenediamine and catalyst allowed the synthesis of albumin polycations with varying charge densities. The albumin polycations are denoted according to their modification, e.g., cBSA-147 is cationized bovine serum albumin with 147 additional primary amino groups that have been introduced by chemical modification.

With increasing charge density, more efficient cellular uptake of the polycationic BSA derivatives has been found and the highest polycationic albumin cBSA-147 revealed the most efficient uptake into A549 cells [6]. Interestingly, even at high cBSA-147 concentrations only low cytotoxicity has been found. Cell uptake proceeds

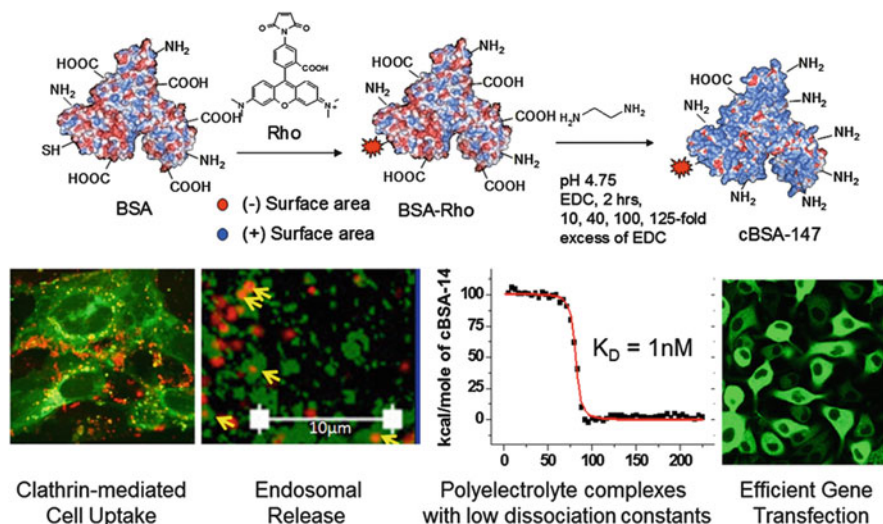


**Fig. 4** *Top*: Cationization of the protein human serum albumin carrying multiple positively charged primary amino groups. Images show that such albumin polycations (stained red) reveal efficient cellular uptake by clathrin-mediated endocytosis, endosomal release (yellow arrows), and allow gene delivery and release into cells due to tight interaction of DNA, as exemplified by the isothermal titration calorimetry graph

mostly via clathrin-mediated endocytosis, which can be inhibited with chlorpromazine hydrochloride. Rhodamine-labeled cBSA-147 escapes the endosome and is detected in the cytosol as well as in the perinuclear region (Fig. 4). With increasing numbers of primary amino groups, proteolytic stability versus trypsin or proteinase K digestion decreases. Due to the high positive net charge of the albumin polycations, complex formation with plasmid DNA encoding for the green fluorescent protein (pDNA-GFP) has been observed for cBSA-95, cBSA-113, and cBSA-147 derivatives. The latter, in particular, forms stable complexes with plasmid DNA [6]. Isothermal titration calorimetry experiments investigating complex formation were used to assess the relative stoichiometries of the protein/DNA complexes in solution (Fig. 4). Similar to the results observed for the dendritic core-shell polycations, increasing numbers of positive charges facilitated the formation of polyelectrolyte with less cBSA proteins and increased DNA contents. In addition, cBSA-147 binds pDNA-GFP very efficiently and complex dissociation constants in the low nanomolar range (below the detection limit) have been calculated. Varying the ratio of positive (cBSA) versus negative (DNA) charges (P/N) of cBSA and pDNA-GFP has an important impact on complex morphologies: at high P/N rates, DNA is tightly bound and condensed by many polycationic albumins and small, dense complexes as well as low transfection rates have been detected. Equal P/N ratios yield larger complexes containing fewer polycations and high transfection efficacies have been observed (Fig. 4). Most likely, such complexes allow more efficient release of the DNA cargo due to the formation of less densely packed

complexes. This study clearly demonstrates that high numbers of amino groups on cBSA are essential for DNA complex formation but that the number of cBSA molecules in the complexes should be low to facilitate efficient DNA transfection and release. Also, cBSA-147/DNA complexes at low P/N charge ratios reveal considerably reduced cytotoxicity compared to the commercially available transfection reagent Lipofectamine.

In addition, more sophisticated albumin polycation architectures have been designed. Serum albumins offer a single reactive thiol group that is accessible for site-directed chemistry, e.g., Michael reactions with a maleimide functionality that can react exclusively at this position. Two cBSA-147 molecules have been interconnected by a poly(ethylene oxide) (PEO) polymer linker and the successful formation of the cBSA dimers has been visualized by transmission electron microscopy (TEM). These cBSA-dimers revealed efficient cellular uptake as well as transfection of pDNA-GFP.

Furthermore, polycationic albumins have been investigated for the immobilization of viable cells based on electrostatic interactions. cBSA-147, which is readily available on a large scale, allows coating of the walls of a microchannel reactor so that bacterial cells can attach with high cell densities. These whole-cell catalysts are able to enantioselectively reduce ethyl acetoacetate to *R*-ethyl hydroxybutyrate for several days with high productivity and revealed a better profile than the standard polylysine coating [24]. In addition, giant liposomes have been immobilized on cBSA-coated surfaces, which is attractive for in vitro protein synthesis [25]. Coating of primary human cells proved to be less efficient. However, the attachment of cyclic RGD groups to cHSA (cationized human serum albumin) interacting with integrin receptors allowed the immobilization of NIH 3 T3 fibroblast cells, which could have a great impact for, e.g., coating implants with a more biocompatible human protein platform [26].

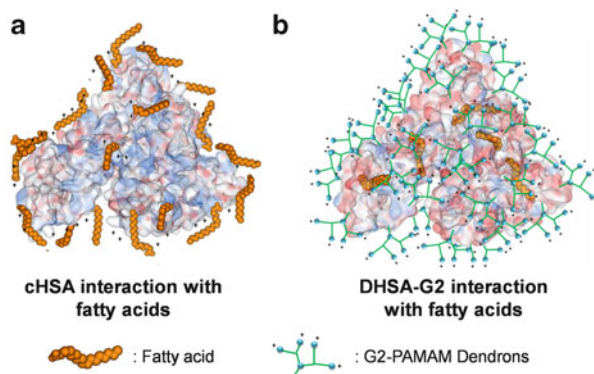
Biopolymers like cBSA offer many reactive groups suitable for multiple surface modifications, making them useful not only for gene delivery but also for drug delivery. Efficient drug delivery is still a high concern of health research because many treatment strategies are still limited by low drug concentrations at the target site or by significant side effects due to high drug doses. Drug delivery systems based on macromolecules such as polymers, dendrimers, or proteins have thus been developed for passive targeting of cancerous cells. These systems make use of the characteristic features of tumor biology that allow the macromolecules to accumulate in the tumor through the enhanced retention and permeation (EPR) effect [27]. The molecular size of the macromolecule plays an important role in tumor cell uptake and the EPR effect is typically observed for macromolecules with molecular weight greater than 20 kDa [28, 29]. Serum albumins are carriers of fatty acids in the blood and, due to their ability to bind to various exogenous and endogenous ligands, they are one of the most exploited proteins for use as a drug delivery vehicle [30, 31] in therapeutics and clinical biochemistry [32], especially for the delivery of lipophilic drug molecules and in particular lipophilic antitumor drugs. HSA drug conjugates are commercially available, e.g., as HSA nanoparticle formulations with the drug paclitacel (Abraxane) [33]. In addition, HSA–drug conjugates have been achieved that combine the drug molecule and targeting

ligands, and the potential of such modified serum albumins for receptor-mediated delivery of small lipophilic molecules has been investigated thoroughly. In this context, modified BSA and HSA molecules have been described as accommodating small drug molecules such as doxorubicin [34], camptothecin [35], and methotrexate [36].

In order to assess whether polycationic albumins still bear the lipophilic binding pockets that the native proteins offer, electron spin resonance experiments with spin-labeled fatty acids have been carried out [37]. Native HSA and BSA are able to bind about eight fatty acids within their scaffolds and their relative locations have been determined by EPR analysis. After cationization, the flexibility and mobility of the protein scaffold changed significantly, making cHSA considerably less flexible than native HSA. In addition, many fatty acid ligands are bound tightly to the surface of cHSA but none of these molecules has been found in the lipophilic binding pockets (Fig. 5a). It was speculated that the decreased mobility of the albumin scaffold might limit the capacity of cHSA to adapt to the shape of the guest molecules and that a sufficient flexibility might be required for guest uptake. However, it might be also plausible that the fatty acids are trapped on the surface of cHSA due to electrostatic interactions.

In order to dissipate the positive charges within a larger volume, polyamidoamine (PAMAM) dendrons have been attached to the HSA scaffold. PAMAM dendrimers are highly branched, structurally well-defined macromolecules with many primary amino groups within their outer shell. The dendritic branches that form a dendrimer are called dendrons. It has been shown before that PAMAM dendrimers are able to traffic into cells by clathrin-dependent endocytosis [38, 39]. The attachment of about 32 dendrons of the second and third generation to an azido-functionalized albumin by 1,3-dipolar cycloadditions yielded dendronized HSA core-shell macromolecules (DHSA-G2 and DHSA-G3) with positive net charges. Interestingly, EPR experiments indicate the accessibility of the binding pockets of albumin because five or six fatty acids were bound to DHSA-G2 and even to DHSA-G3 (Fig. 5b). In addition, due to the positive net charge of the dendrons, DHSA-G2 revealed membrane uptake, as observed by confocal microscopy. Also, the cytotoxicity of both dendronized core-shell HSA derivatives was considerably lower than that of PAMAM dendrimers with similar numbers of positive charges. This suggests that protein-based polycations and polymer polycations interact differently with cellular membranes, e.g., the latter might have a higher tendency to induce cell leakage due to hole formation in the membrane. The capacity of DHSA-G2 to accommodate and deliver the lipophilic antitumor drug doxorubicin (DOX) has been further addressed [40]. DHSA-G2 reveals a significantly higher loading compared to native HSA since about 11 DOX molecules are bound tightly even in buffer or cell culture medium. *In vitro* studies indicate a fast cellular uptake of the DHSA-G2-DOX complexes, and DOX release into the cytosol has been substantiated by the observed high cytotoxicity as well as activation of intracellular caspases 3 and 7, which ultimately leads to apoptosis. Therefore, protein dendronization could potentially be considered an attractive strategy for increasing the molecular weight of a protein to

**Fig. 5** Models of cHSA and DHSA-G2. (a) Fatty acids bind on the surface of cHSA. (b) Fatty acids bind to the hydrophobic pockets of DHSA-G2



enhance blood circulation, shield epitopes at the protein surface, reduce proteolysis by proteases, and enable drug uptake into the lipophilic interior of albumin.

However, if substantially higher drug loading is required, both the covalent attachment of drugs to the globular HSA protein as well as the non-covalent adsorption into the binding pockets are limited by the available space. In order to further increase the drug loading capacity of HSA, reactive groups within the scaffold of HSA that are normally hidden inside the protein scaffold need to become more accessible for chemical modifications.

#### **1.4 Albumin Copolymer Polyelectrolytes Allow Efficient Drug Delivery**

Further exploration of multifunctional protein polyelectrolytes requires the full use of the inner functional groups. However, unfolding of a protein's tertiary structure often leads to precipitation and destabilization. Recently, an in situ stabilization method has been developed that allows the unfolding of proteins into polypeptide chains and exposure of "hidden" functional groups. This has been achieved by controlled chemical denaturation of the native proteins and an in situ stabilization with PEO chains (Fig. 6a). Different protein precursors (e.g., HSA, BSA, and the protease lysozyme) have been studied to prove the general applicability of this approach [41, 42]. The protein-derived polypeptide side chain copolymers feature precisely defined backbone lengths, large numbers of readily available functional groups, and partially maintained secondary structure elements [41, 42]. Modification of the exposed functional groups allows successful conjugation onto the protein backbone of multiple reactive moieties such as chromophores, anticancer drugs, or MRI contrast agents [43, 44]. Due to the presence of hydrophobic patches along the protein primary sequence, the unfolded albumin-based polypeptides can efficiently interact with hydrophobic molecules. Polymeric micelles are formed where the hydrophilic groups face to the outside, and hydrophobic drug molecules are encapsulated inside

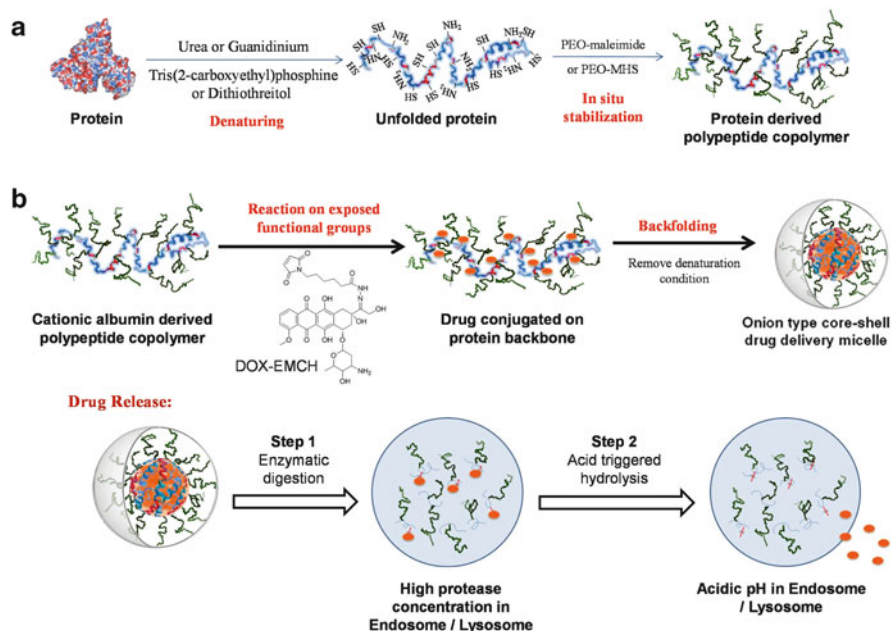


**Fig. 6** Preparation of core-shell drug delivery micelles. (a) Unfolding of globular protein to prepare protein-derived polypeptide copolymers with exposed internal functional groups. (b) Preparation of onion-type core-shell drug delivery micelles from albumin-derived polypeptide copolymers and the two step release mechanism (adopted and modified from Wu et al. [44])

these micelles [43, 44]. Via this strategy, several polycationic albumin polypeptides have been reported that displayed efficient cell uptake, low cytotoxicity, fast enzymatic degradation, and multifunctionality [41, 44, 45]. Due to their excellent biocompatibility and high drug loading capacity, they have been developed into various drug delivery systems [44, 45].

The hydrophobic effect that leads to micelle formation in the presence of lipophilic guest molecules can be further enhanced by reacting the protein side chains with additional hydrophobic groups such as ethynyl groups [43, 44]. Via this approach, the anticancer drug DOX [44, 45] and hydrophobic fluorophores such as coumarin [43] and perylenediimide [46] have been encapsulated into the interior of these polycationic micelles and efficiently delivered into cells. The DOX-encapsulating albumin micelles showed great potential as macromolecular anticancer drugs due to their fast cellular uptake, significant cytotoxicity, but low toxicity of the albumin carrier [41, 44].

Furthermore, onion-type multishell drug delivery systems offering a two-step controlled drug release have been developed by the conjugation of high numbers of DOX drug molecules into the albumin interior [44] (Fig. 6b). Specifically, HSA has been equipped with a PEO shell to ensure water solubility under denaturing conditions. Then, the HSA backbone is unfolded as described above to expose

cysteine groups for drug conjugation. The anticancer drug DOX is attached to the cysteine residues via an acid-cleavable hydrazone linker. Up to 28 DOX molecules have been uploaded per protein in a reproducible fashion. The protein backbone backfolds after drug loading to form DOX-HSA-PEO multishell micelles with (1) DOX molecules encapsulated inside the core, (2) albumin protein as the enzyme-degradable protecting shell, and (3) PE as water-soluble and immune-silencing shell. This drug delivery system exhibits a controlled two-step drug release mechanism in response to proteolysis and acidic pH environment, therefore reducing undesirable drug leakage. The cell toxicity has been examined *in vitro* as well as *in vivo*. A highly potent toxicity effect in an acute myeloid leukemia (AML) model has been observed, with an IC<sub>50</sub> in the subnanomolar range, and long-term suppression of AML growth has been observed in a mice model [44]. Furthermore, by modifying the multiple functional groups of the protein shell, additional functionalities, such as MRI contrast reagents, could be further attached to this multishell structure. For instance, the most widely used T1 MRI contrast reagent, Gd-DOTA, has been conjugated to the lysine residues of the protein backbone, thus resulting in a theranostic complex that potentially allows therapeutic drug delivery and diagnostic imaging simultaneously (our unpublished data). In the future, this system offers great potential for developing personalized anticancer therapy.

## 1.5 Conclusions

Polyelectrolyte interactions play an important role in cell biology. By introducing multiple positive charges into the periphery of fluorescently labeled polyphenylene dendrimers, charge-dependent membrane uptake and cell toxicity was found. In addition, polycationic dendrimers were able to tightly complex and release DNA and stain the extracellular matrix by interacting with the natural aggrecan polyanions. Dendritic polyanions, in contrast, were not able to pass the cellular membrane; however, in fixed cells, tight binding to histone proteins in the cell nucleus was observed, where DNA was most probably displaced from the complexes. Both the polyanionic and polycationic dendritic chromophores specifically stained cellular structures such as the ECM and the cell nucleus, based on the presence of multiple charges within a small nanoscopic volume. In addition, protein polyelectrolytes have been prepared by converting surface-exposed residues into primary amino or carboxylic acid groups. Albumin polycations revealed considerably lower cytotoxicities than their synthetic analogs as well as efficient cell uptake and intracellular release. Complex stoichiometries with DNA could be adjusted by the charge densities of the albumin polycations. Tight DNA binding and efficient transfection was achieved with the highest cationized cBSA derivative.

Cationization of albumin proteins diminished the accessibility of the albumin binding pockets. However, the attachment of positively charged dendrons allowed guest uptake into the hydrophobic binding pockets and efficient delivery of the cytotoxic drug DOX has been achieved. Denaturing the albumin backbone of

cationic albumin proteins yields polypeptides that can fold back into micelle structures in the presence of lipophilic guest molecules. These micelles can be taken up by cells due to the presence of multiple positive charges along the polypeptide backbone, which makes them attractive for drug delivery applications. A refined polycationic albumin biopolymer has been prepared that bears many drug molecules attached to the polypeptide backbone. These were protected by the polypeptide as well as by a second PEO shell, allowing a controlled two-step drug release. These polycationic polypeptides offer great potential for drug delivery and simultaneous bioimaging and have already been studied in *in vivo* experiments.

## **2 Gene Transfection Utilizing Cationic Cylindrical Brush Polymers**

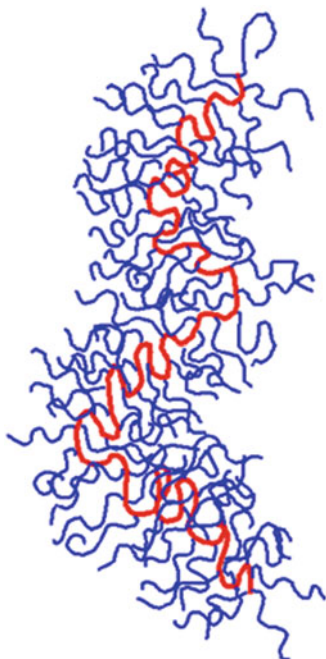
### **2.1 Introduction**

As described above, cationically modified albumin was successfully utilized in gene transfection experiments. A novel cylindrical structure of poly-L-lysine (PLL) in the form of a cylindrical brush polymer with PLL side chains has been utilized for DNA transfection. The results are compared with the transfection efficiency of flexible linear PLL/DNA complexes.

Nonviral gene transfection is a widely used *in vitro* method for studying gene effects in target cells. However, to date only few successful transfections of brain endothelial cells have been published [47–49]. For example, Zhang et al. describe the transfection of murine brain capillary endothelial cells with short polyamines containing a reducible disulfide backbone [48]. Recently, Chen and colleagues described a successful downregulation of expression (60% reduction) via targeted delivery of siRNA-loaded PLGA nanoparticles [50]. Furthermore, another study compared state-of-the-art transfection approaches and determined that only an electroporation protocol achieved efficient transfection rates of brain capillary cells (82% transfected cells) compared to lipid-based transfection (21–40% transfected cells) [49]. Hence, there is still a high demand for the development of nonviral gene delivery systems, especially for difficult-to-transfect cell lines like brain capillary endothelial cells.

Besides viruses [51–57], various synthetic and biological polycation/DNA complexes have also been utilized as vehicles for gene transport [58–66]. Among others, the effects of the polycation chemical composition, charge density, and chain topology (linear flexible coils, hyperbranched or dendritic structures, comb-like polymers) were investigated [67, 68]. Work on PLL with different chain topologies (linear, branched, dendritic) by Mannistö et al. showed no clear relation between the physicochemical properties (complex size, zeta-potential, condensation of DNA) and the transfection efficiency [69]. However, linear PLL was more efficient for transfection of D407 cell lines than the dendritic or branched polymer.

**Fig. 7** Sketch of a cylindrical brush polymer. *Thick red line*, polymethacrylate main chain; *fine blue lines*, PLL side chains. The main chain is forced into an extended conformation due to the strong steric repulsion of the densely grafted side chains



## 2.2 Polymers for Transfection

Rod-like, semiflexible, and ring-shaped polymers were claimed to be promising candidates as drug delivery vehicles, showing prolonged in vivo circulation times [70–73] and excellent accumulation in tumor cells [72, 74]. Reports on complexes of stiff polycations with DNA are rare. Besides other reports [75, 76], pullulan modified with spermine groups was reported to transfect T24 cells of a human bladder cancer cell line [77], HepG2 cells of a human hepatoma cell line [78, 79], and human microvascular endothelial cells [80].

Cylindrical brush polymers [81–88] constitute a prominent class of worm-like cylindrical polymers, which consist of a long main chain (degree of polymerization  $P_n > 500$ ) densely decorated with short polymeric side chains ( $20 < P_n < 100$ ). Due to the extremely large grafting density (typically one side chain per 0.25–0.5 nm main chain contour length) the steric repulsion of the side chains forces the main chain into an extended conformation with a persistence length comparable to that of DNA (see Fig. 7).

Such polymer topologies have not been utilized in DNA transfection studies except for one study by Liu et al. [68], who report on brush-like polymers with PEI-*b*-PEO side chains. However, in these polymers the main chain length was hardly longer than the side chain length, resulting in a spherical rather than cylindrical brush structure.

### 2.3 *Brush Polymer Synthesis and DNA Complexation*

The PLL-brush polymers were synthesized by grafting Z-protected lysine by ring-opening polymerization from a macroinitiator, as described elsewhere [87]. The total weight-average molar mass ( $M_w$ ) of the deprotected PLL brush was determined in aqueous 5 mM LiBr by light scattering to be  $1.03 \times 10^7$  g/mol, yielding an average of 55 lysine units per side chain [87]. The overall brush dimensions were  $R_g = 84.4$  nm and  $R_h = 56.7$  nm. The degree of polymerization of the macroinitiator was evaluated by light scattering to be  $P_w = 900$ . The polydispersity measured by gel permeation chromatography in dimethyl formamide (DMF) was  $M_w/M_n = 1.5$  (polystyrene calibration). Linear PLL with  $M_w = 326,000$  g/mol,  $R_g = 27$  nm, and  $R_h = 21$  nm was also utilized for complex formation and transfection studies. The DNA/polycation complexes were prepared by adding DNA (pUC19) solution dropwise to a polycation solution.

Complexes can be formed by dropwise addition of DNA solution to the polycation solution. At low excess of polycation, the radii of the complex mixture remain small, in the size regime of either the pure polycation or the DNA. In this part of the phase diagram, complexes are known to coexist with excess polycation [89–91]. When approaching the point where the molar mass and the radii of the complexes start to diverge, the excess component becomes fully incorporated into the complexes. Upon further addition of DNA, the solution becomes unstable due to bridging of the primary complexes by additional DNA. These experiments were performed with pUC19 DNA but similar results are to be expected for the larger GFP-DNA (Fig. 8). For linear PLL, this diverging point lies in the equimolar charge regime, whereas it is shifted to a bigger excess of polycation for brush molecules in qualitative agreement with our former results on similar systems [89]. Above  $z^+/z^- = 1.5$  for complexes with linear PLL and  $z^+/z^- = 2.2$  with PLL brushes, no free DNA could be detected.

For transfection experiments, these critical DNA weight fractions ( $w_{\text{DNA}}$ ) limit the choice of mixing ratios to  $0.15 < w_{\text{DNA}} < 0.2$ , because  $w_{\text{DNA}}$  should be well below the diverging point and the solution for transfection should not contain too-large an excess of uncomplexed polycation.

Typically, one complex contains 20 DNA molecules and 10 cylindrical brush molecules, whereas more than 100 linear PLL chains are involved in a complex containing similar numbers of DNA molecules.

For a successful transfection, DNA must be released from complexes. One prominent hypothesis postulates that anionic competitors, most likely polyions, could replace DNA in the complex [92, 93]. Hence, lower molar mass heparin has been established as a model for DNA release experiments, although heparin is not abundant in cells. In addition, the serum protein albumin (which is also not abundant in the cell cytoplasm) as representative of proteins with a small anionic charge, NaCl, and RNA were tested for their ability to release DNA from brush polymers and linear

**Fig. 8** Hydrodynamic radii  $R_h$  of PLL-brush/pUC19 complexes and of linear PLL/pUC19 complexes. The hydrodynamic radii  $R_h$  of PLL-brush/pUC19 complexes (*circles*) and the hydrodynamic radii of linear PLL/pUC19 complexes (*squares*) are shown as function of the weight fraction of DNA,  $w_{\text{DNA}}$ . Complexes were prepared in 150 mM NaCl with a total concentration of 10 mg/L

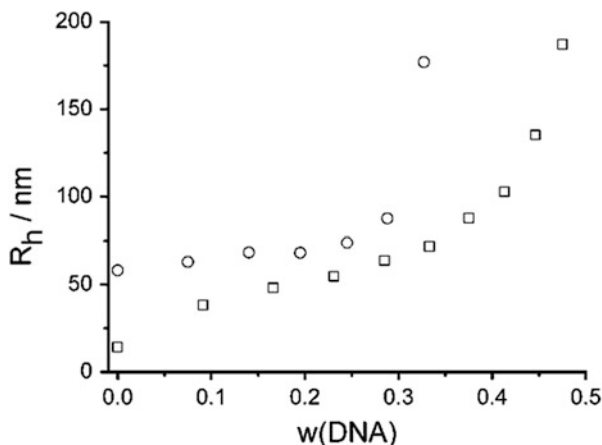


**Table 1** DNA release from polycation complexes and DNase protection

	PLL brush	Linear PLL
Heparin	Release increases with charge ratios starting at $z^-(\text{Heparin})/z^-(\text{DNA}) > 25$	No release for $z^-(\text{Heparin})/z^-(\text{DNA}) < 250$ , larger ratios not tested
BSA	Release for $z^-(\text{BSA})/z^-(\text{DNA}) > 12$	No release for $z^-(\text{BSA})/z^-(\text{DNA}) < 140$ , larger ratios not tested
NaCl	No release (up to 2 M NaCl)	No release (up to 2 M NaCl)
RNA	No release for $z^-(\text{RNA})/z^-(\text{DNA}) < 5.3$ , larger ratios not tested	No release for $z^-(\text{RNA})/z^-(\text{DNA}) < 5.3$ , larger ratios not tested
DNase protection	No	No

Conditions for DNA release from linear and cylindrical brush polycation complexes with different competitors (heparin, bovine serum albumin, RNA) and NaCl. DNase-I-mediated degradation was also measured to see whether complexation gave protection

polymers [94]. Results of the release experiments are summarized in Table 1. Complexes with linear PLL were very stable and DNA was not released by any of the applied competitors. In contrast, complexes with brush polymers were less stable and both heparin and BSA were able to release DNA, depending on the excess of competitor to DNA.

Additionally, it was investigated whether complexation of DNA with polycations could guard DNA from degradation by DNase. Degradation assays with DNase revealed that none of the complexes provided enhanced protection against DNase degradation. Recent reports on DNA protection against DNase

degradation in Lipofectamine/DNA complexes are controversial [95–98] and do not allow a detailed discussion on the importance of DNase protection on the transfection efficiency.

Whereas the release experiments clearly showed that DNA was more easily released from the cylindrical brush complexes than from linear PLL complexes, experiments with ethidiumbromide revealed that all DNA phosphate groups were complexed by the cationic charges for both linear and cylindrical brush PLLs. Thus, subtle topology-dependent enthalpic and entropic effects may play a deciding role in the DNA release out of the complexes.

## 2.4 Transfection with Brush Polymers

Prior to transfection, the question of cell cytotoxicity needs to be addressed. Porcine microvascular endothelial cell (PBMEC) viability was affected in a concentration-dependent manner and was similar for linear PLL and cylindrical PLL brushes, with a 50% cell survival concentration of 0.5 mg/mL. For comparison, the cell cytotoxicity of linear PLLs and stiff cylindrical PLL-brush polymers on fibroblasts (NIH/3T3) was also tested, which is known to be very high for linear PLL [99]. These results could be confirmed because linear as well as brush PLL polymers were found to be very toxic for fibroblasts (50% cell survival concentration 0.01 mg/mL). The differences in cytotoxicity between the two cell lines may be explained by cell type-dependent differences. Brain endothelial cells possess transport systems (efflux transporter of ABC family) characteristic for barrier endothelial cells, which constitute a physical barrier to the brain [100]. The PLL-brush polymers showed a 40% reduction in cell viability at a concentration of 0.1 mg/mL and no effect at a concentration of 0.01 mg/mL. PLL brush concentrations used for transfection were <0.1 mg/mL; hence, only moderate effects on cell viability are to be expected during transfection. Compared to the well-known cytotoxic side effects of other transfection reagents (e.g., lipofectins [101]), the moderate effects on cell viability observed here are judged to be of only minor importance.

For in vitro transfection studies, complexes of DNA and cylindrical brush PLL with PLL side chains were formed at a polycation-to-DNA charge ratio of  $z^+/z^- = 10.6$  and  $z^+/z^- = 6.3$ . [94]. Transfection was controlled by confocal microscopy and quantified by cell cytometry. Only complexes with brush PLL provided significant cell transfection of brain capillary endothelial cells (PBMEC), whereas complexes with linear PLL were not effective, as shown in Fig. 9.

It was demonstrated that cylindrical brush/DNA complexes showed the highest transfection efficiencies, even higher than for Lipofectamine controls. Quantitative analysis revealed that cylindrical brush/DNA complexes formed at an excess of 6.3 and 10.6 positive charges per negative charge ( $z^+/z^-$ ) evoked an increase in

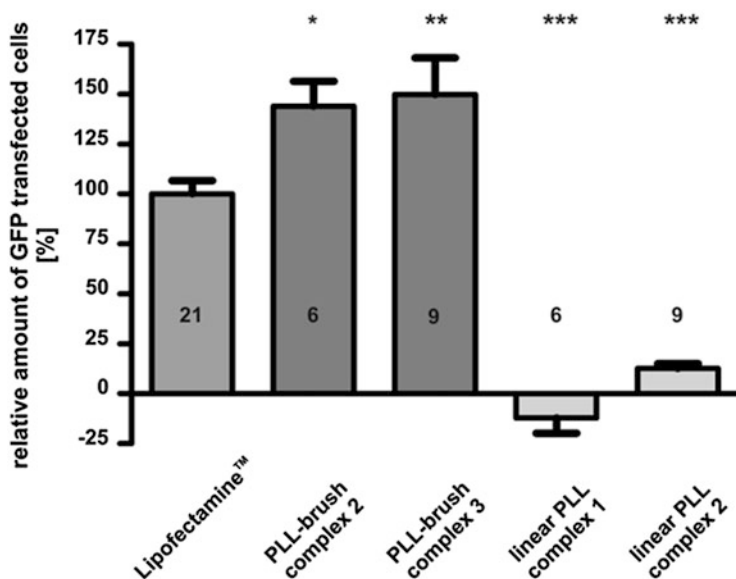


**Fig. 9** Transfection efficiency of PLL-brush/pEGFP-C3. Polymer complexes at various charge-mixing ratios with  $1.0 \mu\text{g}$  pEGFP-C3 on PBME cells: PLL-brush complex 2,  $z^+/z^- = 10.6$ ; PLL-brush complex 3,  $z^+/z^- = 6.3$ ; linear PLL complex 1,  $z^+/z^- = 8.9$ ; linear PLL complex 2,  $z^+/z^- = 6.3$ . Lipofectamine was used as a positive control and GFP expression was measured as % of total cell population, 48 h after transfection

transfection efficiency of  $50 \pm 18.2\%$  and  $44 \pm 12.4\%$  (compared to Lipofectamine) whereas similar complexes with linear PLL did not lead to any significant transfection (Fig. 9), although the size of the complexes was similar ( $80 \text{ nm} < R_h < 150 \text{ nm}$ ).

## 2.5 Conclusions

Developing an effective delivery agent for the transfection of challenging cells like capillary endothelial cells is a major experimental problem in in vitro experiments. The results of the studies described here demonstrate that the worm-like topology of synthetic polycations shows superior transfection results as compared to chemically similar linear polycations. PLL-based polycations are known to be toxic for many cell lines, although PBMEC were shown to survive amazingly high concentrations of PLL, up to  $0.1 \text{ mg/mL}$ . Accordingly, future work will aim to reduce cytotoxicity, for instance by reducing the number of cationic charges. The cylindrical brush polymers presented here have the additional advantage that they can be prepared from a variety of chemically different biocompatible and biodegradable building blocks. The latter option may eventually lead to in vivo applications, provided that the release of DNA by interaction with serum proteins can be prohibited.

## References

1. Rejman J, Conese M, Hoekstra D (2006) Gene transfer by means of lipo- and polyplexes: role of clathrin and caveolae-mediated endocytosis. *J Liposome Res* 16:237–247. doi:[10.1080/08982100600848819](https://doi.org/10.1080/08982100600848819)
2. Kumari S, Mg S, Mayor S (2010) Endocytosis unplugged: multiple ways to enter the cell. *Cell Res* 20:256–275. doi:[10.1038/cr.2010.19](https://doi.org/10.1038/cr.2010.19)
3. McGhee JD, Felsenfeld G (1980) The number of charge-charge interactions stabilizing the ends of nucleosome DNA. *Nucleic Acids Res* 8:2751–2769
4. Thomas M, Lu JJ, Zhang C et al (2007) Identification of novel superior polycationic vectors for gene delivery by high-throughput synthesis and screening of a combinatorial library. *Pharm Res* 24:1564–1571. doi:[10.1007/s11095-007-9279-3](https://doi.org/10.1007/s11095-007-9279-3)
5. Zhu J-L, Cheng H, Jin Y et al (2008) Novel polycationic micelles for drug delivery and gene transfer. *J Mater Chem* 18:4433. doi:[10.1039/b801249k](https://doi.org/10.1039/b801249k)
6. Eisele K, Gropeanu RA, Zehendner CM et al (2010) Fine-tuning DNA/albumin polyelectrolyte interactions to produce the efficient transfection agent cBSA-147. *Biomaterials* 31:8789–8801. doi:[10.1016/j.biomaterials.2010.07.088](https://doi.org/10.1016/j.biomaterials.2010.07.088)
7. Gillies ER, Fréchet MJM (2005) Dendrimers and dendritic polymers in drug delivery. *Drug Discov Today* 10:35–43. doi:[10.1016/S1359-6446\(04\)03276-3](https://doi.org/10.1016/S1359-6446(04)03276-3)
8. Rejman J, Oberle V, Zuhorn IS, Hoekstra D (2004) Size-dependent internalization of particles via the pathways of clathrin- and caveolae-mediated endocytosis. *Biochem J* 377:159–169. doi:[10.1042/BJ20031253](https://doi.org/10.1042/BJ20031253)
9. Sahay G, Alakhova DY, Kabanov AV (2010) Endocytosis of nanomedicines. *J Control Release* 145:182–195. doi:[10.1016/j.jconrel.2010.01.036](https://doi.org/10.1016/j.jconrel.2010.01.036)
10. Panyam J, Labhasetwar V (2003) Dynamics of endocytosis and exocytosis of poly(D, L-lactide-co-glycolide) nanoparticles in vascular smooth muscle cells. *Pharm Res* 20:212–220
11. Nan A, Bai X, Son SJ et al (2008) Cellular uptake and cytotoxicity of silica nanotubes. *Nano Lett* 8:2150–2154. doi:[10.1021/nl0802741](https://doi.org/10.1021/nl0802741)
12. Huang M, Ma Z, Khor E, Lim L-Y (2002) Uptake of FITC-chitosan nanoparticles by A549 cells. *Pharm Res* 19:1488–1494
13. Parton RG, Simons K (2007) The multiple faces of caveolae. *Nat Rev Mol Cell Biol* 8:185–194. doi:[10.1038/nrm2122](https://doi.org/10.1038/nrm2122)
14. Sahay G, Kim JO, Kabanov AV, Bronich TK (2010) The exploitation of differential endocytic pathways in normal and tumor cells in the selective targeting of nanoparticulate chemotherapeutic agents. *Biomaterials* 31:923–933. doi:[10.1016/j.biomaterials.2009.09.101](https://doi.org/10.1016/j.biomaterials.2009.09.101)
15. Nishikawa T, Iwakiri N, Kaneko Y et al (2009) Nitric oxide release in human aortic endothelial cells mediated by delivery of amphiphilic polysiloxane nanoparticles to caveolae. *Biomacromolecules* 10:2074–2085. doi:[10.1021/bm900128x](https://doi.org/10.1021/bm900128x)
16. Zhang LW, Monteiro-Riviere NA (2009) Mechanisms of quantum dot nanoparticle cellular uptake. *Toxicol Sci* 110:138–155. doi:[10.1093/toxsci/kfp087](https://doi.org/10.1093/toxsci/kfp087)
17. Gradishar WJ (2006) Albumin-bound paclitaxel: a next-generation taxane. *Expert Opin Pharmacother* 7:1041–1053. doi:[10.1517/14656566.7.8.1041](https://doi.org/10.1517/14656566.7.8.1041)
18. Yin M, Kuhlmann CRW, Sorokina K et al (2008) Novel fluorescent core-shell nanocontainers for cell membrane transport. *Biomacromolecules* 9:1381–1389. doi:[10.1021/bm701138g](https://doi.org/10.1021/bm701138g)
19. Parimi S, Barnes TJ, Callen DF, Prestidge CA (2010) Mechanistic insight into cell growth, internalization, and cytotoxicity of PAMAM dendrimers. *Biomacromolecules* 11:382–389. doi:[10.1021/bm9010134](https://doi.org/10.1021/bm9010134)
20. Yin M, Shen J, Gropeanu R et al (2008) Fluorescent core/shell nanoparticles for specific cell-nucleus staining. *Small* 4:894–898. doi:[10.1002/smll.200701107](https://doi.org/10.1002/smll.200701107)
21. Hedlund H, Hedbom E, Heine grd D et al (1999) Association of the aggrecan keratan sulfate-rich region with collagen in bovine articular cartilage. *J Biol Chem* 274:5777–5781

22. Hardingham TE, Fosang AJ, Dudhia J (1994) The structure, function and turnover of aggrecan, the large aggregating proteoglycan from cartilage. *Eur J Clin Chem Clin Biochem* 32:249–257
23. Yin M, Ding K, Gropeanu RA et al (2008) Dendritic star polymers for efficient DNA binding and stimulus-dependent DNA release. *Biomacromolecules* 9:3231–3238. doi:[10.1021/bm800797j](https://doi.org/10.1021/bm800797j)
24. Ng JF, Jaenicke S, Eisele K et al (2010) cBSA-147 for the preparation of bacterial biofilms in a microchannel reactor. *Biointerphases* 5:FA41–FA47. doi:[10.1116/1.3474475](https://doi.org/10.1116/1.3474475)
25. Ritz S, Eisele K, Dorn J et al (2010) Cationized albumin-biocoatings for the immobilization of lipid vesicles. *Biointerphases* 5:FA78–FA87. doi:[10.1116/1.3494039](https://doi.org/10.1116/1.3494039)
26. Ng JF, Weil T, Jaenicke S (2011) Cationized bovine serum albumin with pendant RGD groups forms efficient biocoatings for cell adhesion. *J Biomed Mater Res B Appl Biomater* 99:282–290. doi:[10.1002/jbm.b.31897](https://doi.org/10.1002/jbm.b.31897)
27. Matsumura Y, Maeda H (1986) A new concept for macromolecular therapeutics in cancer chemotherapy: mechanism of tumorotropic accumulation of proteins and the antitumor agent smancs. *Cancer Res* 46:6387–6392
28. Kratz F (2002) Drug conjugates with albumin and transferrin. *Expert Opin Ther Pat* 12:433–439. doi:[10.1517/13543776.12.3.433](https://doi.org/10.1517/13543776.12.3.433)
29. Maeda H (2001) The enhanced permeability and retention (EPR) effect in tumor vasculature: the key role of tumor-selective macromolecular drug targeting. *Adv Enzyme Regul* 41:189–207
30. Elsadek B, Kratz F (2012) Impact of albumin on drug delivery – new applications on the horizon. *J Control Release* 157:4–28. doi:[10.1016/j.jconrel.2011.09.069](https://doi.org/10.1016/j.jconrel.2011.09.069)
31. Neumann E, Frei E, Funk D et al (2010) Native albumin for targeted drug delivery. *Expert Opin Drug Deliv* 7:915–925. doi:[10.1517/17425247.2010.498474](https://doi.org/10.1517/17425247.2010.498474)
32. Varshney A, Sen P, Ahmad E et al (2010) Ligand binding strategies of human serum albumin: how can the cargo be utilized? *Chirality* 22:77–87. doi:[10.1002/chir.20709](https://doi.org/10.1002/chir.20709)
33. Paál K, Müller J, Hegedűs L (2001) High affinity binding of paclitaxel to human serum albumin. *Eur J Biochem* 268:2187–2191
34. Xu R, Fisher M, Juliano RL (2011) Targeted albumin-based nanoparticles for delivery of amphipathic drugs. *Bioconjug Chem* 22:870–878. doi:[10.1021/bc1002295](https://doi.org/10.1021/bc1002295)
35. Sun H-H, Zhang J, Zhang Y-Z et al (2012) Interaction of human serum albumin with 10-hydroxycamptothecin: spectroscopic and molecular modeling studies. *Mol Biol Rep* 39:5115–5123. doi:[10.1007/s11033-011-1307-z](https://doi.org/10.1007/s11033-011-1307-z)
36. Vis AN, Van der Gaast A, Van Rhijn BWG et al (2002) A phase II trial of methotrexate-human serum albumin (MTX-HSA) in patients with metastatic renal cell carcinoma who progressed under immunotherapy. *Cancer Chemother Pharmacol* 49:342–345. doi:[10.1007/s00280-001-0417-z](https://doi.org/10.1007/s00280-001-0417-z)
37. Akdogan Y, Wu Y, Eisele K et al (2012) Host–guest interactions in polycationic human serum albumin bioconjugates. *Soft Matter* 8:11106. doi:[10.1039/c2sm26511g](https://doi.org/10.1039/c2sm26511g)
38. Kitchens KM, Kolhatkar RB, Swaan PW, Ghandehari H (2008) Endocytosis inhibitors prevent poly(amidoamine) dendrimer internalization and permeability across Caco-2 cells. *Mol Pharm* 5:364–369. doi:[10.1021/mp700089s](https://doi.org/10.1021/mp700089s)
39. Kitchens KM, Foraker AB, Kolhatkar RB et al (2007) Endocytosis and interaction of poly(amidoamine) dendrimers with Caco-2 cells. *Pharm Res* 24:2138–2145. doi:[10.1007/s11095-007-9415-0](https://doi.org/10.1007/s11095-007-9415-0)
40. Kuan SL, Stöckle B, Reichenwallner J et al (2013) Dendronized albumin core-shell transporters with high drug loading capacity. *Biomacromolecules* 14:367–376. doi:[10.1021/bm301531c](https://doi.org/10.1021/bm301531c)
41. Wu Y, Pramanik G, Eisele K, Weil T (2012) Convenient approach to polypeptide copolymers derived from native proteins. *Biomacromolecules* 13:1890–1898. doi:[10.1021/bm300418r](https://doi.org/10.1021/bm300418r)
42. Wu Y, Weil T (2012) An efficient approach for preparing giant polypeptide triblock copolymers by protein dimerization. *Macromol Rapid Comm* 33:1304–1309. doi:[10.1002/marc.201200111](https://doi.org/10.1002/marc.201200111)

43. Wu Y, Wang T, Ng DYW, Weil T (2012) Multifunctional polypeptide-PEO nanoreactors via the hydrophobic switch. *Macromol Rapid Comm* 33:1474–1481. doi:[10.1002/marc.201200227](https://doi.org/10.1002/marc.201200227)
44. Wu Y, Ihme S, Feuring-Buske M et al (2012) A core-shell albumin copolymer nanotransporter for high capacity loading and two-step release of doxorubicin with enhanced anti-leukemia activity. *Adv Healthc Mater* 2:884–894. doi:[10.1002/adhm.201200296](https://doi.org/10.1002/adhm.201200296)
45. Wu Y, Shih EK, Ramanathan A et al (2012) Nano-sized albumin-copolymer micelles for efficient doxorubicin delivery. *Biointerphases* 7:5. doi:[10.1007/s13758-011-0005-7](https://doi.org/10.1007/s13758-011-0005-7)
46. Eisele K, Gropeanu R, Musante A et al (2010) Tailored albumin-based copolymers for receptor-mediated delivery of perylenediimide guest molecules. *Macromol Rapid Commun* 31:1501–1508. doi:[10.1002/marc.201000176](https://doi.org/10.1002/marc.201000176)
47. Zhang H, Vinogradov SV (2010) Short biodegradable polyamines for gene delivery and transfection of brain capillary endothelial cells. *J Control Release* 143:359–366. doi:[10.1016/j.jconrel.2010.01.020](https://doi.org/10.1016/j.jconrel.2010.01.020)
48. Zhang H, Mitin A, Vinogradov SV (2009) Efficient transfection of blood–brain barrier endothelial cells by lipoplexes and polyplexes in the presence of nuclear targeting NLS-PEG-acridine conjugates. *Bioconjug Chem* 20:120–128. doi:[10.1021/bc8003414](https://doi.org/10.1021/bc8003414)
49. Slanina H, Schmutzler M, Christodoulides M et al (2012) Effective plasmid DNA and small interfering RNA delivery to diseased human brain microvascular endothelial cells. *J Mol Microbiol Biotechnol* 22:245–257. doi:[10.1159/000342909](https://doi.org/10.1159/000342909)
50. Chen C, Mei H, Shi W et al (2013) EGFP-EGF1-conjugated PLGA nanoparticles for targeted delivery of siRNA into injured brain microvascular endothelial cells for efficient RNA interference. *PLoS One* 8:e60860. doi:[10.1371/journal.pone.0060860](https://doi.org/10.1371/journal.pone.0060860)
51. McTaggart S, Al-Rubeai M (2002) Retroviral vectors for human gene delivery. *Biotechnol Adv* 20:1–31
52. Verma IM, Weitzman MD (2005) Gene therapy: twenty-first century medicine. *Annu Rev Biochem* 74:711–738. doi:[10.1146/annurev.biochem.74.050304.091637](https://doi.org/10.1146/annurev.biochem.74.050304.091637)
53. Kay MA, Glorioso JC, Naldini L (2001) Viral vectors for gene therapy: the art of turning infectious agents into vehicles of therapeutics. *Nat Med* 7:33–40. doi:[10.1038/83324](https://doi.org/10.1038/83324)
54. Wong HH, Lemoine NR, Wang Y (2010) Oncolytic viruses for cancer therapy: overcoming the obstacles. *Viruses* 2:78–106. doi:[10.3390/v2010078](https://doi.org/10.3390/v2010078)
55. Nayak S, Herzog RW (2010) Progress and prospects: immune responses to viral vectors. *Gene Ther* 17:295–304. doi:[10.1038/gt.2009.148](https://doi.org/10.1038/gt.2009.148)
56. Van den Pol AN, Ozduman K, Wollmann G et al (2009) Viral strategies for studying the brain, including a replication-restricted self-amplifying delta-G vesicular stomatitis virus that rapidly expresses transgenes in brain and can generate a multicolor golgi-like expression. *J Comp Neurol* 516:456–481. doi:[10.1002/cne.22131](https://doi.org/10.1002/cne.22131)
57. Lim ST, Airavaara M, Harvey BK (2010) Viral vectors for neurotrophic factor delivery: a gene therapy approach for neurodegenerative diseases of the CNS. *Pharmacol Res* 61:14–26. doi:[10.1016/j.phrs.2009.10.002](https://doi.org/10.1016/j.phrs.2009.10.002)
58. Kabanov AV (1999) Taking polycation gene delivery systems from in vitro to in vivo. *Pharm Sci Technol Today* 2:365–372
59. El-Anead A (2004) An overview of current delivery systems in cancer gene therapy. *J Control Release* 94:1–14
60. Thomas M, Klibanov AM (2003) Non-viral gene therapy: polycation-mediated DNA delivery. *Appl Microbiol Biotechnol* 62:27–34. doi:[10.1007/s00253-003-1321-8](https://doi.org/10.1007/s00253-003-1321-8)
61. Ditto AJ, Shah PN, Yun YH (2009) Non-viral gene delivery using nanoparticles. *Expert Opin Drug Deliv* 6:1149–1160. doi:[10.1517/17425240903241796](https://doi.org/10.1517/17425240903241796)
62. Conwell CC, Huang L (2005) Recent advances in non-viral gene delivery. *Adv Genet* 53PA:1–18. doi:[10.1016/S0065-2660\(05\)53001-3](https://doi.org/10.1016/S0065-2660(05)53001-3)
63. Salcher EE, Wagner E (2010) Chemically programmed polymers for targeted DNA and siRNA transfection. *Top Curr Chem* 296:227–249
64. Ogris M (2010) Cancer gene therapies come of age. *Ther Deliv* 1:211–214

65. Yu H, Wagner E (2009) Bioresponsive polymers for nonviral gene delivery. *Curr Opin Mol Ther* 11:165–178
66. Oba M, Miyata K, Osada K et al (2011) Polyplex micelles prepared from  $\omega$ -cholesteryl PEG-polycation block copolymers for systemic gene delivery. *Biomaterials* 32:652–663. doi:[10.1016/j.biomaterials.2010.09.022](https://doi.org/10.1016/j.biomaterials.2010.09.022)
67. Bennis JM, Choi JS, Mahato RI et al (2000) pH-sensitive cationic polymer gene delivery vehicle: *N*-Ac-poly(L-histidine)-graft-poly(L-lysine) comb shaped polymer. *Bioconjug Chem* 11:637–645
68. Liu X-Q, Du J-Z, Zhang C-P et al (2010) Brush-shaped polycation with poly(ethylenimine)-b-poly(ethylene glycol) side chains as highly efficient gene delivery vector. *Int J Pharm* 392:118–126. doi:[10.1016/j.ijpharm.2010.03.043](https://doi.org/10.1016/j.ijpharm.2010.03.043)
69. Männistö M, Vanderkerken S, Toncheva V et al (2002) Structure-activity relationships of poly(L-lysines): effects of pegylation and molecular shape on physicochemical and biological properties in gene delivery. *J Control Release* 83:169–182
70. Geng Y, Dalhaimer P, Cai S et al (2007) Shape effects of filaments versus spherical particles in flow and drug delivery. *Nat Nanotechnol* 2:249–255. doi:[10.1038/nnano.2007.70](https://doi.org/10.1038/nnano.2007.70)
71. Liu Z, Davis C, Cai W et al (2008) Circulation and long-term fate of functionalized, biocompatible single-walled carbon nanotubes in mice probed by Raman spectroscopy. *Proc Natl Acad Sci U S A* 105:1410–1415. doi:[10.1073/pnas.0707654105](https://doi.org/10.1073/pnas.0707654105)
72. Fox ME, Szoka FC, Fréchet MJM (2009) Soluble polymer carriers for the treatment of cancer: the importance of molecular architecture. *Acc Chem Res* 42:1141–1151. doi:[10.1021/ar900035f](https://doi.org/10.1021/ar900035f)
73. Lee CC, Yoshida M, Fréchet MJM et al (2005) In vitro and in vivo evaluation of hydrophilic dendronized linear polymers. *Bioconjug Chem* 16:535–541. doi:[10.1021/bc0497665](https://doi.org/10.1021/bc0497665)
74. Johnson JA, Lu YY, Burts AO et al (2010) Drug-loaded, bivalent-bottle-brush polymers by graft-through ROMP. *Macromolecules* 43:10326–10335. doi:[10.1021/ma1021506](https://doi.org/10.1021/ma1021506)
75. Jo J, Okazaki A, Nagane K et al (2010) Preparation of cationized polysaccharides as gene transfection carrier for bone marrow-derived mesenchymal stem cells. *J Biomater Sci Polym Ed* 21:185–204. doi:[10.1163/156856209X415495](https://doi.org/10.1163/156856209X415495)
76. Thakor DK, Teng YD, Tabata Y (2009) Neuronal gene delivery by negatively charged pullulan-spermine/DNA anioplexes. *Biomaterials* 30:1815–1826. doi:[10.1016/j.biomaterials.2008.12.032](https://doi.org/10.1016/j.biomaterials.2008.12.032)
77. Kanatani I, Ikai T, Okazaki A et al (2006) Efficient gene transfer by pullulan-spermine occurs through both clathrin- and raft/caveolae-dependent mechanisms. *J Control Release* 116:75–82. doi:[10.1016/j.jconrel.2006.09.001](https://doi.org/10.1016/j.jconrel.2006.09.001)
78. Jo J, Ikai T, Okazaki A et al (2007) Expression profile of plasmid DNA by spermine derivatives of pullulan with different extents of spermine introduced. *J Control Release* 118:389–398. doi:[10.1016/j.jconrel.2007.01.005](https://doi.org/10.1016/j.jconrel.2007.01.005)
79. Jo J-I, Ikai T, Okazaki A et al (2007) Expression profile of plasmid DNA obtained using spermine derivatives of pullulan with different molecular weights. *J Biomater Sci Polym Ed* 18:883–899. doi:[10.1163/156856207781367756](https://doi.org/10.1163/156856207781367756)
80. Thomsen LB, Lichota J, Kim KS, Moos T (2011) Gene delivery by pullulan derivatives in brain capillary endothelial cells for protein secretion. *J Control Release* 151:45–50. doi:[10.1016/j.jconrel.2011.01.002](https://doi.org/10.1016/j.jconrel.2011.01.002)
81. Wintermantel M, Schmidt M, Tsukahara Y et al (1994) Rodlike combs. *Macromol Rapid Comm* 15:279–284. doi:[10.1002/marc.1994.030150315](https://doi.org/10.1002/marc.1994.030150315)
82. Wintermantel M, Gerle M, Fischer K et al (1996) Molecular bottlebrushes<sup>†</sup>. *Macromolecules* 29:978–983. doi:[10.1021/ma950227s](https://doi.org/10.1021/ma950227s)
83. Dziezok P, Fischer K, Schmidt M et al (1997) Cylindrical molecular brushes. *Angew Chem Int Ed* 36:2812–2815. doi:[10.1002/anie.199728121](https://doi.org/10.1002/anie.199728121)
84. Sheiko SS, Gerle M, Fischer K et al (1997) Wormlike polystyrene brushes in thin films. *Langmuir* 13:5368–5372. doi:[10.1021/la970132e](https://doi.org/10.1021/la970132e)

85. Gerle M, Fischer K, Roos S et al (1999) Main chain conformation and anomalous elution behavior of cylindrical brushes as revealed by GPC/MALLS, light scattering, and SFM<sup>‡</sup>. *Macromolecules* 32:2629–2637. doi:[10.1021/ma9816463](https://doi.org/10.1021/ma9816463)
86. Zhang B, Gröhn F, Pedersen JS et al (2006) Conformation of cylindrical brushes in solution: effect of side chain length. *Macromolecules* 39:8440–8450. doi:[10.1021/ma0613178](https://doi.org/10.1021/ma0613178)
87. Sahl M, Muth S, Branscheid R et al (2012) Helix–coil transition in cylindrical brush polymers with poly-L-lysine side chains. *Macromolecules* 45:5167–5175. doi:[10.1021/ma300377v](https://doi.org/10.1021/ma300377v)
88. Zhang B, Fischer K, Schmidt M (2005) Cylindrical polypeptide brushes. *Macromol Chem Phys* 206:157–162. doi:[10.1002/macp.200400266](https://doi.org/10.1002/macp.200400266)
89. Störkle D, Duschner S, Heimann N et al (2007) Complex formation of DNA with oppositely charged polyelectrolytes of different chain topology: cylindrical brushes and dendrimers. *Macromolecules* 40:7998–8006. doi:[10.1021/ma0711689](https://doi.org/10.1021/ma0711689)
90. Boeckle S, Von Gersdorff K, Van der Piepen S et al (2004) Purification of polyethylenimine polyplexes highlights the role of free polycations in gene transfer. *J Gene Med* 6:1102–1111. doi:[10.1002/jgm.598](https://doi.org/10.1002/jgm.598)
91. Yue Y, Jin F, Deng R et al (2011) Revisit complexation between DNA and polyethylenimine – effect of uncomplexed chains free in the solution mixture on gene transfection. *J Control Release* 155:67–76. doi:[10.1016/j.jconrel.2010.10.028](https://doi.org/10.1016/j.jconrel.2010.10.028)
92. Bertschinger M, Backliwal G, Schertenleib A et al (2006) Disassembly of polyethylenimine-DNA particles in vitro: implications for polyethylenimine-mediated DNA delivery. *J Control Release* 116:96–104. doi:[10.1016/j.jconrel.2006.09.006](https://doi.org/10.1016/j.jconrel.2006.09.006)
93. Moret I, Esteban Peris J, Guillem VM et al (2001) Stability of PEI-DNA and DOTAP-DNA complexes: effect of alkaline pH, heparin and serum. *J Control Release* 76:169–181
94. Kühn F (2010) Polykation-DNA-komplexe: eigenschaften und anwendungen in der gentransfektion. Dissertation, Johannes Gutenberg-Universität Mainz
95. Li P, Liu D, Sun X et al (2011) A novel cationic liposome formulation for efficient gene delivery via a pulmonary route. *Nanotechnology* 22:245104. doi:[10.1088/0957-4484/22/24/245104](https://doi.org/10.1088/0957-4484/22/24/245104)
96. Buzder T, Yin X, Wang X et al (2009) Uptake of foreign nucleic acids in kidney tubular epithelial cells deficient in proapoptotic endonucleases. *DNA Cell Biol* 28:435–442. doi:[10.1089/dna.2008.0850](https://doi.org/10.1089/dna.2008.0850)
97. Gadi J, Ruthala K, Kong K-A et al (2009) The third helix of the Hoxc8 homeodomain peptide enhances the efficiency of gene transfer in combination with lipofectamine. *Mol Biotechnol* 42:41–48. doi:[10.1007/s12033-008-9119-7](https://doi.org/10.1007/s12033-008-9119-7)
98. Howell DP-G, Krieser RJ, Eastman A, Barry MA (2003) Deoxyribonuclease II is a lysosomal barrier to transfection. *Mol Ther* 8:957–963
99. Fischer D, Li Y, Ahlemeyer B et al (2003) In vitro cytotoxicity testing of polycations: influence of polymer structure on cell viability and hemolysis. *Biomaterials* 24:1121–1131
100. Mahringer A, Ott M, Reimold I et al (2011) The ABC of the blood–brain barrier – regulation of drug efflux pumps. *Curr Pharm Des* 17:2762–2770
101. Uchida E, Mizuguchi H, Ishii-Watabe A, Hayakawa T (2002) Comparison of the efficiency and safety of non-viral vector-mediated gene transfer into a wide range of human cells. *Biol Pharm Bull* 25:891–897

# Computational Studies of Biomembrane Systems: Theoretical Considerations, Simulation Models, and Applications

Markus Deserno, Kurt Kremer, Harald Paulsen, Christine Peter,  
and Friederike Schmid

**Abstract** This chapter summarizes several approaches combining theory, simulation, and experiment that aim for a better understanding of phenomena in lipid bilayers and membrane protein systems, covering topics such as lipid rafts, membrane-mediated interactions, attraction between transmembrane proteins, and aggregation in biomembranes leading to large superstructures such as the light-harvesting complex of green plants. After a general overview of theoretical considerations and continuum theory of lipid membranes we introduce different options for simulations of biomembrane systems, addressing questions such as: What can be learned from generic models? When is it expedient to go beyond them? And, what are the merits and challenges for systematic coarse graining and quasi-atomistic coarse-grained models that ensure a certain chemical specificity?

---

M. Deserno (✉)

Department of Physics, Carnegie Mellon University, 5000 Forbes Ave., Pittsburgh, PA 15213,  
USA

e-mail: [deserno@andrew.cmu.edu](mailto:deserno@andrew.cmu.edu)

K. Kremer

Max-Planck-Institute for Polymer Research, Ackermannweg 10, 55128 Mainz, Germany

e-mail: [kremer@mpip-mainz.mpg.de](mailto:kremer@mpip-mainz.mpg.de)

H. Paulsen

Department of Biology, University of Mainz, Johannes-von-Müller-Weg 6, 55128 Mainz,  
Germany

e-mail: [paulsen@uni-mainz.de](mailto:paulsen@uni-mainz.de)

C. Peter

Department of Chemistry, University of Konstanz, Universitätsstraße 10, 78457 Constance,  
Germany

e-mail: [christine.peter@uni-konstanz.de](mailto:christine.peter@uni-konstanz.de)

F. Schmid

Institute of Physics, University of Mainz, Staudingerweg 9, 55128 Mainz, Germany

e-mail: [schmid@uni-mainz.de](mailto:schmid@uni-mainz.de)

**Keywords** Coarse graining · Curvature elasticity · Lipid bilayer · Mediated interactions · Multiscale · Simulation

## Contents

1	Introduction .....	238
2	Theory and Simulation of Lipid Bilayers .....	239
2.1	Basic Continuum Theory Concepts .....	239
2.2	Coarse-Grained Lipid Models .....	241
2.3	Obtaining Material Parameters .....	243
2.4	The Tension of Lipid Membranes .....	249
2.5	Membrane Heterogeneity and Lipid Rafts .....	252
3	Membrane–Protein Interactions .....	255
3.1	Hydrophobic Mismatch .....	256
3.2	Curvature-Mediated Interactions Between Proteins .....	258
4	Multiscale Modeling of Lipid and Membrane Protein Systems .....	265
4.1	Multiscale Modeling: Approaches and Challenges .....	265
4.2	The Light-Harvesting Complex .....	267
5	Conclusions .....	270
	References .....	271

## 1 Introduction

Lipid bilayers and membrane proteins are one important class of biological systems for which the relationship between single molecule properties and the behavior of complex nanoscopically structured materials has been under intense investigation for a long time. In the present review we address how approaches combining theory, simulation, and experiment may help us gain a better understanding of phenomena in biomembranes. A general overview of theoretical considerations and continuum theory of lipid membranes is given and different modeling and simulation approaches to biomembrane systems are introduced. In particular, we introduce several generic lipid simulation models and show how these models can help us understand material properties of lipid bilayers such as bending and Gaussian curvature modulus, or membrane tension. We discuss timely topics such as lipid rafts, membrane–protein interactions, and curvature-mediated interactions between proteins. These fundamental theoretical and modeling investigations are important for understanding the principles that govern the aggregation phenomena in biological membranes that lead to large superstructures such as the light-harvesting complex of green plants. In Sect. 4 of this chapter, we give an overview of multiscale modeling approaches that try to go beyond generic lipid and protein models and attempt to ensure a certain chemical specificity while still benefiting from the time- and length-scale advantages of coarse-grained simulations. The section concludes with the example of the light-harvesting complex of green plants, for which we show first steps toward a multiscale simulation model that allows one to go back and forth between a coarse-grained and an atomistic

level of resolution and therefore permits immediate comparison with atomic level experimental data.

## 2 Theory and Simulation of Lipid Bilayers

To provide a basis for both the theoretical ideas and the computational techniques that we will discuss in this chapter, we start by reminding the reader of some essential concepts. Section 2.1 reviews some basic aspects of the Helfrich Hamiltonian. Section 2.2 introduces three coarse-grained membrane models that will be used in the remainder of this chapter. In Sects. 2.3 and 2.4, we discuss the bending moduli and the surface tension of membranes in more detail, and finally comment on multicomponent membranes in Sect. 2.5.

### 2.1 Basic Continuum Theory Concepts

#### 2.1.1 Continuum Elasticity of Lipid Membranes

Lipid molecules are amphipathic: they consist of a hydrophilic head group and typically two hydrophobic (fatty acid) tails. Yet, despite their amphipathic nature, lipid molecules dissolved in water have an extremely low critical aggregate concentration (nanomolar or even smaller [1]), and thus under most common conditions lipids spontaneously aggregate. Because the roughly cylindrical shape of lipids leads to two-dimensional self-assembly, thermodynamic considerations [2] show that – in contrast to the finite size of spherical and wormlike micelles – a single macroscopic aggregate containing almost all of the lipids will form: a two-dimensional bilayer membrane. Its lateral dimensions can exceed its thickness by several orders of magnitude.

#### 2.1.2 The Helfrich Hamiltonian

If lipid membranes are subjected to lateral tension, they typically rupture at stresses of several millinewtons per meter (mN/m), with a remarkably low rupture strain of only a few percent [3]. At large scales and moderate tensions it is hence an excellent approximation to consider membranes as largely unstretchable two-dimensional surfaces. Their dominant soft modes are not associated with stretching but with bending [4–6]. Within the well-established mathematical framework developed by Helfrich [5], the energy of a membrane patch  $\mathcal{P}$ , amended by a contribution due to its boundary  $\partial\mathcal{P}$  [7], is expressible as:

$$E[\mathcal{P}] = \int_{\mathcal{P}} dA \left\{ \frac{1}{2} \kappa (K - K_0)^2 + \bar{\kappa} K_G \right\} + \oint_{\partial \mathcal{P}} \gamma. \quad (1)$$

Here,  $K = c_1 + c_2$  and  $K_G = c_1 c_2$  are the total and Gaussian curvature, respectively, and the  $c_i$  are the local principal curvatures of the surface [8, 9]. The inverse length  $K_0$  is the spontaneous bilayer curvature, showing that the first term quadratically penalizes the deviation between total and spontaneous curvature.<sup>1</sup> The parameters  $\kappa$  and  $\bar{\kappa}$  are the bending modulus and Gaussian curvature modulus, respectively, and they quantify the energy penalty due to bending. Finally, the parameter  $\gamma$  is the free energy of an open membrane edge and is thus referred to as the edge tension.

### 2.1.3 Refining the Helfrich Model

Although the Helfrich Hamiltonian provides a successful framework for describing the large-scale structure and geometry of fluid membranes, it is not designed for modeling membranes on smaller length scales, i.e., of the order of the membrane thickness. Several more refined continuum models have been proposed for amending this situation. Evidently, continuum descriptions are no longer applicable at the Ångström scale. However, they still turn out to be quite useful on length scales down to a few nanometers.

As one refinement, Lipowsky and coworkers have proposed the introduction of a separate, independent “protrusion” field that accounts for short wavelength fluctuations [10–12]. According to recent atomistic and coarse-grained simulations by Brandt et al., these protrusions seem to correspond to lipid density fluctuations within the membrane [13, 14]. Lindahl and Edholm pioneered another important refinement, which is to consider the height and thickness variations of membranes separately [15]. Continuum models for membranes with spatially varying thickness have a long-standing tradition in theories for membrane-mediated interactions between inclusions [16–27] (see also Sect. 3.1), and they can be coupled to Helfrich models for height fluctuations in a relatively straightforward manner [28–30]. In addition, one can include other internal degrees of freedom, such as local tilt [31–36], as well as membrane tension [36, 37].

In this article, we will focus in particular on the so-called coupled monolayer models [18, 20–26, 28, 29], where membranes are described as stacks of two sheets (monolayers), each with their own elastic parameters. Monolayers are bound to each other by a local harmonic potential that accounts for the areal compressibility of lipids within the membrane and their constant volume [22, 28]. Li et al. have recently compared the elastic properties of amphiphilic bilayers with those of the corresponding monolayers within a numerical self-consistent field study of

---

<sup>1</sup> Observe that  $1/K_0$  is not the optimal radius  $R_{\text{opt}}$  of a spherical vesicle. Minimizing the energy per area with respect to  $K$  shows that instead this radius is given by  $R_{\text{opt}} K_0 = 2 + \bar{\kappa}/\kappa$ .

copolymeric membranes [38]. They found that the bilayer elastic parameters can be described at an almost quantitative level by an appropriate combination of monolayer elastic parameters.

## 2.2 *Coarse-Grained Lipid Models*

The multitude of length and time scales that matter for biophysical membrane processes is mirrored in a wide spectrum of computational models that have been devised to capture these scales. These range from all-atom simulations [39–43] up to dynamically triangulated surfaces [44–47] and continuum models [48, 49]. The region in between is becoming increasingly populated by a wealth of different coarse-grained (commonly abbreviated “CG”) models, which capture different aspects of a very complex physical situation, and a number of excellent reviews exist that provide a guide to the literature [50–57].

Besides their chosen level of resolution, CG models can also be classified by the “spirit” in which they approach a physical situation: If the focus lies on generic mechanisms that are thought to be quite universal in their reach, there is no need to construct models that faithfully relate to every aspect of some particular lipid. Instead, one creates “top-down” models based on the presumed principles underlying the generic mechanisms of interest. For instance, if one wishes to understand how a bilayer membrane interacts with a colloidal particle that is much bigger than the thickness of the membrane, relevant aspects of the situation will likely include the fluid curvature–elastic response of bilayer lipid membranes, but probably not the hydrogen bonding abilities of a phosphatidylethanol head group. If, in contrast, one wishes to understand how mesoscopic membrane properties emerge from specific properties of their microscopic constituents, the aim is instead to construct “bottom-up” models whose key design parameters follow in a systematic way from those of a more finely resolved model. For instance, if one wishes to understand how those hydrogen bonding abilities of a phosphatidylethanol head group impact the mesoscopic phase behavior of mixed bilayers, it will not do to simply guess a convenient head group interaction potential, even if it is eminently plausible. The latter philosophy goes under various names, such as “systematic coarse graining” or “multiscaling” and again excellent literature and resources exist that cover this field [58–72].

The top-down and bottom-up approaches are not necessarily mutually exclusive. It is conceivable that certain aspects of the science are systematically matched, while others are accounted for in a generic way by using intuition from physics, chemistry, mathematics, or other pertinent background knowledge. Conversely, this also means that what any given model can qualitatively or quantitatively predict depends greatly on the way in which it has been designed; there is no universally applicable CG model. Stated differently, systematically coarse-grained models will not be accurate in every prediction they make, and generic models can

be highly quantitative and experimentally testable. One always needs to know what went into a given model to be able to judge the reliability of its predictions.

In Sects. 2.2.1–2.2.3, we will review the basics of three particular CG models that will feature in the remainder of this paper. The choice of models is not meant to imply a quality statement but merely reflects our own experience and work.

### 2.2.1 Cooke Model

The Cooke model [73, 74] is a strongly coarse-grained top-down lipid model in which every single lipid is represented by three linearly connected beads (one for the head group, two for the tail) and solvent is implicitly accounted for through effective interactions. It is purely based on pair interactions and therefore very easy to handle. Its main tuning parameters are the temperature and the range  $w_c$  of the effective cohesion that drives the aggregation of the hydrophobic tail beads. One might also change the relative size between head and tail beads to control the lipids' spontaneous curvature [75]. The bead size  $\sigma$  serves as the unit of length and the potential depth  $\epsilon$  as the unit of energy. For the common choice  $k_B T/\epsilon = 1.1$  and  $w_c/\sigma = 1.6$ , lipids spontaneously assemble into fluid membranes with an area per lipid of about  $1.2 \sigma^2$ , a bending rigidity of  $\kappa \approx 12.8 k_B T$  (but rigidities between  $3 k_B T$  and  $30 k_B T$  can be achieved without difficulty), and an elastic ratio of  $\bar{\kappa}/\kappa \approx -0.92$  [76].

### 2.2.2 Lenz Model

Like the Cooke model, the Lenz model [77] is a generic model for membranes, but it has been designed for studying internal phase transitions. Therefore, it puts a slightly higher emphasis on conformational degrees of freedom than the Cooke model. Lipids are represented by semiflexible linear chains of seven beads (one for the head group, six for the tail), which interact with truncated Lennard–Jones potentials. Model parameters such as the chain stiffness are inspired by the properties of hydrocarbon tails [78]. The model includes an explicit solvent, which is, however, modeled such that it is simulated very efficiently: it interacts only with lipid beads and not with itself (“phantom solvent” [79]).

The model reproduces the most prominent phase transitions of phospholipid monolayers [78] and bilayers [80]. In particular, it reproduces a main transition from a fluid membrane phase ( $L_\alpha$ ) to a tilted gel phase ( $L_{\beta'}$ ) with an intermediate ripple phase ( $P_{\beta'}$ ), in agreement with experiments. The elastic parameters have been studied in the fluid phase and are in reasonable agreement with those of saturated DPPC (dipalmitoyl-phosphatidylcholine) bilayers. Recently, the Lenz model has been supplemented with a simple cholesterol model [81]. Cholesterol molecules are taken to be shorter and stiffer than lipids, and they have a slight affinity to lipids. Mixtures of lipids and cholesterol were found to develop nanoscale raft domains

[81], in agreement with the so-called “raft hypothesis” [82]. As a generic model that reproduces nanoscale structures in lipid membranes (ripple states and rafts), simulations of the Lenz model can provide insight into the physics of nanostructure formation in lipid bilayers. This will be discussed in more detail in Sect. 2.5.

### 2.2.3 MARTINI Model

The MARTINI model for lipids [83, 84] is a hybrid between a top-down and a bottom-up model: approximately four heavy atoms are mapped to a single CG bead, and these CG beads come in a variety of types, depending on their polarity, net charge, and the ability to form hydrogen bonds. The systematic aspect of MARTINI largely derives from the fact that the nonbonded interactions between these building blocks (shifted Lennard–Jones and possibly shifted Coulomb potentials) have been parameterized to reproduce most of the thermodynamics correctly, especially the partitioning free energy between different environments, such as between aqueous solution and oil. Given a particular molecule, a judicious choice of assignments from groups of heavy atoms to MARTINI beads, together with standard bonded interactions (harmonic, angular, and dihedral potentials), leads to the CG version of a molecule.

The complete MARTINI force field encompasses more than lipids and sterols [83, 84]; it is currently also available for proteins [85], carbohydrates [86], and glycolipids [87]. The far-reaching possibilities for looking at multicomponent systems without the need to explicitly cross-parametrize new interactions have substantially contributed to the attractiveness of this force field. Of course, care must still be taken that one’s mapping onto the CG level is consistent overall and chemically meaningful: Even though the nonbonded interactions are derived from a single guiding principle, which is both conceptually attractive and computationally powerful, there is no guarantee that it will work under all circumstances for one’s particular choice of system and observable, so it is up to the user to perform judicious sanity checks. After all, with great power there must also come great responsibility [88].

## 2.3 Obtaining Material Parameters

The Hamiltonian in Eq. (1) is an excellent phenomenological description of fluid membranes, but it does not predict the material parameters entering it, which must instead come from experiment or simulation. Let us briefly list a number of ways in which this is achieved, both in experiment and in simulation.

The bending modulus  $\kappa$  is measured by techniques such as monitoring the thermal undulations of membranes [89–94], probing the low-tension stress–strain relation [95], X-ray scattering [96–99], neutron spin echo measurements [100–102] (note however the caveats raised by Watson and Brown [103]), or pulling thin

membrane tethers [104–106]. In simulations, monitoring undulations [12, 15, 28, 73, 74, 83, 107–111] or orientation fluctuations [112], measuring tensile forces in tethers [111, 113, 114], and buckling [115, 116] have been used successfully.

The Gaussian curvature modulus  $\bar{\kappa}$  is much harder to obtain because, by virtue of the Gauss-Bonnet theorem [8, 9], the surface integral over the Gaussian curvature  $K_G$  depends only on the topology and the boundary of the membrane patch  $\mathcal{P}$ . Hence, one needs to change at least one of them to access the Gaussian curvature modulus. It therefore tends to be measured by looking at the transitions between topologically different membrane phases (e.g., the lamellar phase  $L_\alpha$  and the inverted cubic phase  $Q_{II}$ ) [117–120] or the shape of phase-separated membranes in the vicinity of the contact line [121, 122] (even though the latter strictly speaking only gives access to the difference in Gaussian moduli between the two phases). In Sect. 2.3.2 we will briefly present a computational method that obtains  $\bar{\kappa}$  from the closure probability of finite membrane patches [76, 123].

To measure the edge tension requires an open edge, and in experiments this essentially means looking at pores [124–127]. This also works in simulations [73, 74, 83, 108, 109], but it tends to be easier to create straight bilayer edges by spanning a “half-membrane” across the periodic boundary conditions of the simulation box [128–131].

The spontaneous curvature  $K_0$  usually vanishes due to bilayer up–down symmetry, but could be measured by creating regions of opposing spontaneous curvature and monitoring the curvature this imprints on the membrane [132], or by measuring the shape of a spontaneously curved membrane strip [111].

Because curvature elasticity is such an important characteristic of lipid membranes, obtaining the associated moduli has always attracted a lot of attention. Let us therefore provide a few more details on some classical and some more recent computational strategies to measure them. Shiba and Noguchi [111] also provide a detailed recent review.

### 2.3.1 Bending Modulus

The shape of essentially flat membranes stretched across the periodic boundary conditions of a simulation box can be described by specifying their vertical displacement  $h(\mathbf{r})$  above some horizontal reference plane, say of size  $L \times L$ . In this so-called Monge parametrization, the bending contribution due to the total curvature term (ignoring for now on the spontaneous curvature  $K_0$ ) is given by:

$$\int dA \frac{1}{2} \kappa K^2 = \frac{1}{2} \kappa \int_{[0,L]^2} d^2r \sqrt{1 + (\nabla h)^2} \left( \nabla \cdot \frac{\nabla h}{\sqrt{1 + (\nabla h)^2}} \right)^2 \quad (2)$$

$$= \frac{1}{2} \kappa \int_{[0,L]^2} d^2r \left\{ (h_{ii})^2 - \frac{1}{2} (h_{ii})^2 h_j h_j - 2h_{ii} h_j h_{jk} h_k + \mathcal{O}(h^6) \right\}, \quad (3)$$

where the indices are short-hand for derivatives:  $h_i = \partial h / \partial r_i$ , etc. The first square root expression in Eq. (2) is the metric determinant that accounts for the increased area element if the surface is tilted. The expression following it is the total curvature in Monge gauge. Evidently, the Helfrich Hamiltonian is highly nonlinear in this parametrization! Hence, one frequently expands the integrand for small  $h$ , as is done in the second line. The first term,  $\frac{1}{2} \kappa (h_{ii})^2 = \frac{1}{2} \kappa (\Delta h)^2$  is quadratic in  $h$  and thus gives rise to a harmonic theory, which is referred to as “linearized Monge gauge.” The majority of all membrane work relies on this simplified version. However, the higher order terms occasionally matter: they are for instance responsible for the renormalization of the bending rigidity by thermal shape undulations [133–136].

Upon Fourier-transforming  $h(\mathbf{r}) = \sum_q \tilde{h}_q e^{i\mathbf{q}\cdot\mathbf{r}}$  and restricting the functional to quadratic order we obtain the transformed Hamiltonian  $E[\tilde{h}_q] = L^2 \sum_q \frac{1}{2} \kappa q^4 |\tilde{h}_q|^2$ , which shows that the modes  $\tilde{h}_q$  are independent harmonic oscillators. The equipartition theorem then implies that  $\langle |\tilde{h}_q|^2 \rangle = k_B T / L^2 \kappa q^4$ , and thus fitting to the spectrum of thermal undulations gives access to  $\kappa$ . Unfortunately, there are several difficulties with this picture (see, e.g., the recent review [137]). The simple expression can only be expected to hold for sufficiently small wave vectors because at small length scales local bilayer structure will begin to matter. For instance, it is well known that lipid tilt fluctuations contaminate the undulation spectrum [34, 35]. The situation becomes even more complicated in low temperature phases that exhibit hexatic order [138, 139] or permanent tilt [140, 141]. In such cases, the fluctuation spectrum shows no sign of a  $\langle |\tilde{h}_q|^2 \rangle \propto 1/q^4$  behavior up to length scales of at least 40 nm [142]. The most obvious way out is to simulate larger systems and thus gain access to smaller wave vectors, but unfortunately these modes decay exceedingly slowly. For overdamped Brownian dynamics with a friction constant  $\zeta = L^2 \zeta_0$ , one finds  $\zeta \dot{\tilde{h}}_q = -\partial E[\tilde{h}_q] / \partial \tilde{h}_q = -L^2 \kappa q^4 \tilde{h}_q$ , showing that modes exponentially relax with a time constant  $\tau = \zeta_0 / \kappa q^4$  that grows quartically with the wave length. Accounting for hydrodynamics turns this into a cubic dependence,  $\tau = 4\eta / \kappa q^3$  [89, 143–145], where  $\eta$  is the solvent viscosity, but the situation is still uncomfortable: when Lindahl and Edholm [15] simulated 1,024 DPPC lipids in a 20 nm square bilayer, their measured value  $\kappa = 4 \times 10^{-20}$  J implies  $\tau \simeq 3.2$  ns for the slowest (and most informative) mode, not much smaller than the overall 10 ns total simulation time.

Although measuring  $\kappa$  from the undulation spectrum is possible, there is a more basic concern with such an approach: one tries to measure a modulus with a value typically around  $20 k_B T$  by using thermal fluctuations of order  $k_B T$  to excite the bending modes, which of course makes it quite challenging to get a signal to begin

with.<sup>2</sup> An obvious alternative is to actively bend membranes and directly measure their curvature elastic response. There are clearly many ways to deform a membrane; here we will describe two possibilities that have been proposed in the past as convenient methods for obtaining the bending modulus.

Harmandaris and Deserno [113] proposed a method that relies on simulating cylindrical membranes. Imagine a membrane of area  $A$  that is curved into a cylinder of curvature radius  $R$ . Its length  $L$  satisfies  $2\pi RL = A$ , and the curvature energy per area of this membrane is:

$$e = \frac{1}{2}\kappa \frac{1}{R^2} = \frac{1}{2}\kappa \left(\frac{2\pi L}{A}\right)^2. \quad (4)$$

Because changing the length of the cylinder at constant area will also change the curvature radius, and thus the bending energy, there must be an axial force  $F$  associated with this geometry. Its value is given by:

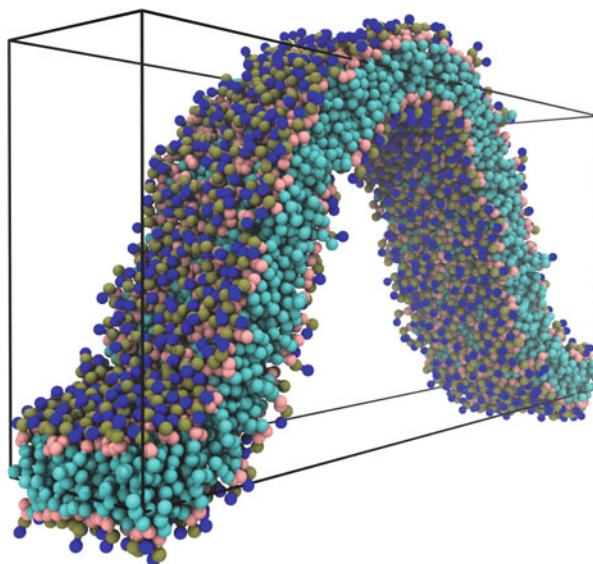
$$F = \left(\frac{\partial eA}{\partial L}\right)_A = A \kappa \frac{2\pi L}{A} \frac{2\pi}{A} = \frac{2\pi\kappa}{R}. \quad (5)$$

Hence, measuring both the axial force and the cylinder radius yields the bending modulus as  $\kappa = FR/2\pi$ . Notice that within quadratic curvature elasticity, the radius of the cylinder does not matter: Both small and large radii will lead to the same modulus. In other words,  $FR$  is predicted to be a constant. Of course, it is conceivable that higher order corrections to the Helfrich Hamiltonian Eq. (1) matter once curvatures become really strong. For the present geometry there is only one term, which enters at quartic order, and one would write a modified energy density  $e = \frac{1}{2}\kappa K^2 + \frac{1}{4}\kappa_4 K^4$ . This modified functional leads to  $FR/2\pi = \kappa + \kappa_4/R^2 \equiv \kappa_{\text{eff}}(R)$ , which can be interpreted as an effective curvature-dependent bending modulus. Simulations using different models with different levels of resolution have indeed both seen a small dependence of  $\kappa_{\text{eff}}$  on  $R$  [111, 113]. They find softening at high curvature, which would indicate that  $\kappa_4$  is negative. In contrast, Li et al. [38] recently studied the elastic properties of self-assembled copolymeric bilayers by self-consistent field theory in cylindrical and spherical geometry, and found  $\kappa_4$  to be positive. The details of nonlinear elastic corrections thus depend on the specifics of the model under study, but the present studies suggest that as long as the radius of curvature is bigger than a few times the membrane thickness, these corrections are negligible. For example, Li et al. [38] found the deviations from linear to be less than 2% both in the cylinder and sphere geometry, as long as the reduced curvature was less than  $K_0 d = 0.6$  (where  $d$  is the bilayer thickness).

---

<sup>2</sup> It is easy to see that  $\delta h \equiv \langle h(\mathbf{r})^2 \rangle^{1/2} = L\sqrt{k_B T/16\pi^3\kappa} \approx L/100$  (assuming  $\kappa \simeq 20 k_B T$ ), which is a few Ångström for typical simulation sizes.

**Fig. 1** Illustration of a buckling simulation using the MARTINI model for DMPC (which uses 10 beads per lipid) [116]. This particular membrane consists of 1,120 lipids and is compressed at a strain  $\gamma = 0.3$ , which gives it an amplitude of approximately 22% of the box length. To suppress membrane deformations in the second direction, the width of the box is chosen to be much smaller than its length



The cylinder stretching protocol appears to work very well for simple solvent-free membrane models [111, 113, 114], but with more refined models this method suffers from two drawbacks, both related to the equilibration of a chemical potential. First, the cylinder separates the simulation volume into an “inside” and an “outside.” If solvent is present, its chemical potential must be the same in these two regions, but for more highly resolved models the solvent permeability through the bilayer is usually too low to ensure automatic relaxation. Second, the chemical potential of lipids also has to be the same in the two bilayer leaflets, and again for more refined models the lipid flip-flop rate tends to be too low for this to happen spontaneously.

To circumvent this difficulty, Noguchi has recently proposed to instead simulate a buckled membrane as an example of an actively imposed deformation [115] (see Fig. 1 for an illustration). This solves both problems simultaneously: neither does the buckle divide the simulation box into two distinct compartments,<sup>3</sup> nor is lipid equilibration across leaflets a big concern because for symmetry reasons both leaflets are identical (at least for a “ground state buckle”) and thus ensuring that the same number of lipids is present in both leaflets is a good proxy. The theoretical analysis of the expected forces is a bit more complicated compared to the cylinder setup, but it can be worked out exactly, even for buckles deviating strongly from “nearly flat.” Hu et al. have recently provided systematic series expansions for the buckling forces in terms of the buckling strain. If a membrane originally has a

<sup>3</sup> Observe that the part of the membrane above the buckle and the part below the buckle can be connected through the periodic boundary of the simulation box.

length  $L$  and is buckled to a shorter length  $L_x$ , then the force  $f_x$  per length along that membrane as a function of strain  $\gamma = (L - L_x)/L$  can be written as [116]:

$$f_x = \kappa \left( \frac{2\pi}{L} \right)^2 \left[ 1 + \frac{1}{2}\gamma + \frac{9}{32}\gamma^2 + \frac{21}{128}\gamma^3 + \frac{795}{8192}\gamma^4 + \frac{945}{16384}\gamma^5 + \dots \right]. \quad (6)$$

Notice that the force does not vanish for  $\gamma \rightarrow 0$ , which is the hallmark of a buckling transition. Hu et al. [116] also estimate the fluctuation correction on this result and find it to be very small; they apply this method to four different membrane models, ranging from strongly coarse grained to essentially atomistic, and argue that it is reliable and efficient.

### 2.3.2 Gaussian Modulus

To measure the Gaussian curvature modulus  $\bar{\kappa}$  directly, the Gauss–Bonnet theorem [8, 9] forces one to either change the topology or the boundary of a membrane patch. Recently Hu et al. [76, 123] suggested a way to achieve this. Consider a circular membrane patch of area  $A$ . Being flat, its energy stems from the open edge at its circumference. The patch could close up into a vesicle in order to eliminate the open edge, but now it carries bending energy. If we imagine that transition proceeding through a sequence of conformations, each one resembling a spherical cap of curvature  $c$ , then the excess energy of such a curved patch (compared to the flat state) is given by [7, 146]:

$$\frac{\Delta E(x, \xi)}{4\pi(2\kappa + \bar{\kappa})} = \Delta \tilde{E}(x, \xi) = x + \xi \left[ \sqrt{1-x} - 1 \right]. \quad (7)$$

$\Delta E$  is scaled by the bending energy of a sphere and we defined:

$$x = (Rc)^2, \quad \xi = \frac{\gamma R}{2\kappa + \bar{\kappa}}, \quad \text{and} \quad R = \sqrt{\frac{A}{4\pi}}. \quad (8)$$

For  $\xi > 1$  the spherical state ( $x = 1$ ) has a lower energy than the flat state ( $x = 0$ ). If  $x$  is viewed as a reaction coordinate, Eq. (7) describes a nucleation process, since for  $\xi < 2$  the transition from the flat to the spherical state proceeds through an energy barrier of height  $\Delta \tilde{E}^* = (1 - \xi/2)^2$  at  $x^* = 1 - (\xi/2)^2$ . Eq. (7) shows that the functional form of the nucleation barrier depends on parameters such as moduli and system sizes only through the combination  $\xi$ , and all parameters entering  $\xi$  (with the exception of  $\bar{\kappa}$ ) can be determined ahead of time by other means. Hence, measuring  $\bar{\kappa}$  amounts to measuring the nucleation barrier (or at least the location of the maximum). Hu et al. [76, 123] do this by a dynamical process: Equilibrated but pre-curved membrane patches with some initial value for  $x$  may either flatten out or close up, depending on where on the barrier they start. The

probability for either outcome can be computed if  $\Delta E$  is known [147] and so  $\bar{\kappa}$  ends up being found through a series of patch-closure experiments.

The results of such simulations show that  $\bar{\kappa}/\kappa$  is close to  $-1$ , both for the Cooke model and for MARTINI DMPC (see Sect. 2.2 for a further discussion of these models).<sup>4</sup> This is compatible with experiments [117–122] but disagrees with the only other method that has been suggested for getting the Gaussian modulus. As first pointed out by Helfrich [148], quite general considerations suggest that the second moment of a membrane’s lateral stress profile is also equal to the Gaussian modulus [148–150]:

$$\bar{\kappa} = \int dz z^2 \Sigma(z), \quad (9)$$

where  $\Sigma(z) = \Pi_{zz} - \frac{1}{2}[\Pi_{xx}(z) + \Pi_{yy}(z)]$  is the position-resolved lateral stress through a membrane, whose integral is simply the surface tension [151]. However, when applied to the Cooke model, Hu et al. find  $\bar{\kappa}/\kappa \approx -1.7$  [76], which quite a bit more on the negative side, whereas applying it to MARTINI DMPC (at 300 K) yields  $\bar{\kappa}/\kappa \approx -0.05$ , much closer to zero; MARTINI DPPC and DOPC (dioleoylphosphatidylcholine) even lead to positive Gaussian moduli. At present it is unclear where this discrepancy originates from, but given that the values obtained from the patch-closure protocol are physically more plausible it seems likely that there is a problem with the stress approach. The latter suspicion is also supported by the fact that a more refined theory of bilayer elasticity [152] predicts corrections to the right-hand side of Eq. (2) that depend on moments of order parameter distributions.

## 2.4 The Tension of Lipid Membranes

The Helfrich Hamiltonian, Eq. (1), does not include a surface tension contribution. Free membrane patches can relax and adjust their area such that they are stress-free. In many situations, however, membranes do experience mechanical stress. For example, an osmotic pressure difference between the inside and the outside of a lipid vesicle generates stress in the vesicle membrane. Stress also occurs in supported bilayer systems, or in model membranes patched to a frame. In contrast to other quantities discussed earlier (bending stiffness etc.), and also in contrast to the surface tension of demixed fluid phases, membrane stress is not a material parameter. Rather, it is akin to a (mechanical or thermodynamic) control parameter, which can be imposed through boundary conditions.

The discussion of membrane tension is complicated by the fact that there exist several different quantities that have been called “tension” or “tension-like.” For the sake of simplicity, we will restrict ourselves to quasipolar (fluctuating)

---

<sup>4</sup>The requirement that the Hamiltonian (1) is bounded below demands that  $-2\kappa \leq \bar{\kappa} \leq 0$ .

membranes in the following. A thoughtful analysis of the vesicle case has recently been carried out by Diamant [153].

The first tension-like quantity in planar membranes is the lateral mechanical stress in the membrane, as discussed above. If the stress is imposed by a boundary condition, such as, for instance, a constraint on the lateral (projected) area of the membrane, it is an internal property of the membrane system that depends, among other parameters, on the area compressibility [36] and the curvature elasticity [154–161]. Alternatively, mechanical stress can be imposed externally. In that case, the projected area fluctuates, and the appropriate thermodynamic potential can be introduced into the Helfrich Hamiltonian, Eq. (1), in a straightforward manner:

$$G = E - \Gamma_{\text{frame}} A_p = \int_{\mathcal{P}} dA \left\{ \frac{1}{2} \kappa (K - K_0)^2 + \bar{\kappa} K_G - \Gamma_{\text{frame}} \frac{dA_p}{dA} \right\}. \quad (10)$$

Here  $\Gamma_{\text{frame}}$  is the stress or “frame tension,”  $A_p$  is the projected area in the plane of applied stress, and we have omitted the membrane edge term. Let us consider a membrane with fixed total area  $A$ . In Monge representation, one has  $dA_p/dA = 1/\sqrt{1 + (\nabla h)^2} \approx 1 - (\nabla h)^2/2 + \mathcal{O}(h^4)$ , thus the last term in Eq. (10) takes the form [37, 162]:

$$\text{const} + \frac{1}{2} \Gamma_{\text{frame}} \int_{A_p} d^2r (\nabla h)^2 + \mathcal{O}(h^4) \quad (11)$$

(with  $\text{const} = -\Gamma_{\text{frame}} A$ ). This is formally similar to a surface tension term in an effective interface Hamiltonian for liquid–liquid interfaces. The main difference is that the base  $A_p$  of the integral fluctuates. However, replacing this by a fixed base  $\langle A_p \rangle$  only introduces errors of order  $\mathcal{O}(h^4)$  [162].

From Eq. (11), it is clear that mechanical stress influences the fluctuation spectrum of membranes and, in particular, one expects a  $q^2$  contribution to the undulation spectrum,  $\langle |\tilde{h}_q|^2 \rangle^{-1} \sim \Gamma_{\text{fluc}} q^2 + \kappa q^4 + \dots$ . This introduces the second tension-like parameter in planar fluctuating membranes, the “fluctuation tension”  $\Gamma_{\text{fluc}}$ . According to Eq. (11),  $\Gamma_{\text{fluc}}$  is identical to  $\Gamma_{\text{frame}}$  up to order  $\mathcal{O}(h^2)$ .

Finally, the third tension-like parameter in membranes was introduced by Deuling and Helfrich as early as 1976 [163], and it couples to the total area of the membrane:

$$E = \int_{\mathcal{P}} dA \left\{ \frac{1}{2} \kappa (K - K_0)^2 + \bar{\kappa} K_G + \Gamma_0 \right\}. \quad (12)$$

In membranes with fixed lipid area, but variable number of lipids, the “bare tension”  $\Gamma_0$  is simply proportional the lipid chemical potential. For membranes with fixed number of lipids and variable lipid area, the physical meaning of  $\Gamma_0$  is less clear, but it can still be defined as a field that is conjugate to  $A$  in a Lagrange multiplier sense. This term also gives rise to a  $q^2$  term in the undulation spectrum, with the fluctuation tension  $\Gamma_{\text{fluc}} = \Gamma_0 + \mathcal{O}(h^2)$  [36].

At leading (quadratic) order in  $h$ , the three tension-like quantities,  $\Gamma_{\text{frame}}$ ,  $\Gamma_{\text{fluc}}$ , and  $\Gamma_0$ , thus have identical values. Nevertheless, they might differ from each other due to nonlinear corrections [90, 164–167]. For instance, the bare tension  $\Gamma_0$  is expected to deviate from the frame tension  $\Gamma_{\text{frame}}$  due to the effect of fluctuations. The exact value of the correction depends on the ensemble and differs for systems with a fluctuating number of lipids (variable number of undulating modes) or a fixed number of lipids (fixed number of modes). The former case was analyzed by Cai et al. [165] and the latter case by Farago and Pincus [168] and subsequently by a number of other authors [169–171]. Interestingly, the correction has an additive component in both cases. Hence a stress-free membrane has a finite bare tension.

Whereas the bare tension  $\Gamma_0$  is mostly of academic interest, the fluctuation tension  $\Gamma_{\text{fluc}}$  describes actual membrane conformations. The relation between  $\Gamma_{\text{fluc}}$  and  $\Gamma_{\text{frame}}$  has been discussed somewhat controversially in the past [153, 156, 162, 165, 169–174]. Cai et al. [165] and Farago and Pincus [156] have presented a very general argument for why  $\Gamma_{\text{frame}}$  and  $\Gamma_{\text{fluc}}$  should be equal. Cai et al. [165] examined the fluctuations of planar membranes with variable number of lipids and fixed lipid area and proved  $\Gamma_{\text{fluc}} = \Gamma_{\text{frame}}$  in the thermodynamic limit, if the membrane is “gauge invariant,” i.e., invariant with respect to a rotation of the “projected plane.” Farago and Pincus [156, 174] developed a similar theory for membranes with fixed number of lipids at fixed projected area. Unfortunately, these arguments – albeit appealing – are not entirely conclusive because the underlying assumptions can be questioned: The thermodynamic limit does not exist for stress-free planar membranes because they bend around on length scales larger than the persistence length [90]. In the presence of stress, the limit does not exist either, strictly speaking, because the true equilibrium state is one where the membrane has ruptured. Furthermore, high stresses break gauge invariance. Contradicting Cai et al. and Farago and Pincus [156, 165], a number of authors have claimed  $\Gamma_{\text{fluc}} = \Gamma_0$  [169–171], based on analytical arguments that, however, also rely on the existence of the thermodynamic limit and on other uncontrolled approximations [162, 172, 173].

Thus, the relation between  $\Gamma_{\text{frame}}$  and  $\Gamma_{\text{fluc}}$  remains an open question, and simulations can point at the most likely answer. For example, if  $\Gamma_{\text{fluc}} = \Gamma_{\text{frame}}$ , the fluctuation tension should vanish for stress-free membranes, i.e., the undulation spectrum should then be dominated by a  $q^4$  behavior. With a few exceptions [169, 170], this has indeed been observed in coarse-grained or atomistic simulations of stress-free lipid bilayers [12, 15, 28, 30, 109, 175] or bilayer stacks [176]. This would seem to rule out the alternative hypothesis  $\Gamma_{\text{fluc}} = \Gamma_0$ . However, it should be noted that the undulation spectra have relatively large error bars and a complex behavior at higher  $q$ , as discussed in Sect. 2.3.1. Therefore, the results also depend to some extent on the fit.

To overcome these limitations, accurate simulations of elastic infinitely thin sheets with no molecular detail are useful. Recently, a number of such simulations have been carried out in two spatial dimensions (i.e., one dimensional membranes) [162, 171, 174]. The results are found to depend on the ensemble. Fournier and Barbetta studied a membrane made of hypothetical “lipids” with freely fluctuating

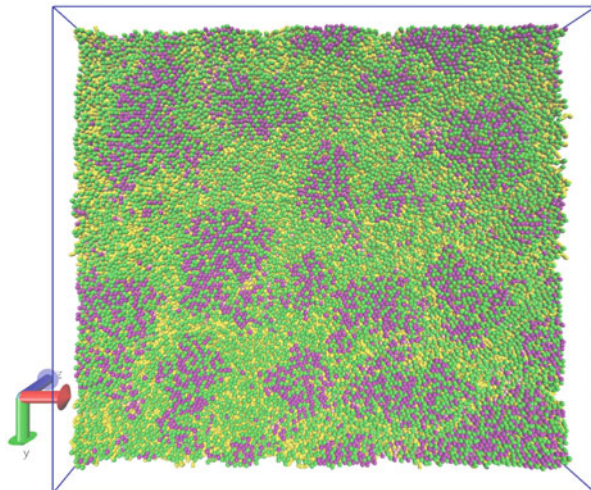
areas, only controlled by a Lagrange parameter  $\Gamma_0$ . They found that the fluctuation tension  $\Gamma_{\text{fluc}}$  displays a complex behavior and neither agrees with  $\Gamma_0$  nor with  $\Gamma_{\text{frame}}$ . Schmid [162] has considered an arguably more realistic situation where “lipids” have fixed area and either a fixed frame tension is applied or the “projected area” is kept fixed. These simulations reproduce the difference between  $\Gamma_0$  and  $\Gamma_{\text{frame}}$  and indicate with high accuracy that the fluctuation tension is given by  $\Gamma_{\text{fluc}} = \Gamma_{\text{frame}}$ . Farago [174] confirmed these findings in simulations at fixed projected area. Furthermore, he carried out reference simulations of a hypothetical membrane model that lacks gauge invariance and found that, in this case, the fluctuation tension deviates from the frame tension. These studies support the validity of the picture originally put forward by Cai et al. [165]: For rotationally invariant membranes with fixed area per lipid, the fluctuation tension is given by the frame tension.

## 2.5 Membrane Heterogeneity and Lipid Rafts

In the late 1990s, several scientists put forward the suggestion that biomembranes might not be laterally homogeneous but instead contain nanoscopic domains – soon called “lipid rafts” – which differ in their lipid composition and are important for numerous membrane-associated biological processes [177–181]. This idea quickly replaced the prevailing fluid mosaic model [182], according to which the lipid bilayer merely constitutes a two-dimensional passive solvent that carries membrane proteins. It created huge excitement due to many obvious biological implications and possibilities; at the same time it was controversial, for instance because it took time to converge on a universally accepted definition of what a raft is [82, 183–185].

According to the lipid raft concept, biomembranes are filled with locally phase-separated, cholesterol-rich, nanoscale “raft” domains, which contribute to membrane heterogeneity and play an important role in organizing the membrane proteins. Two aspects of this hypothesis are well-established: First, biological membranes are laterally heterogeneous, and heterogeneity is important for the function of membrane proteins, e.g., in signaling [186]. Second, multicomponent lipid bilayers phase separate in certain parameter regions into a “liquid disordered” (ld) and a “liquid ordered” (lo) phase [187, 188]. The hypothetical “raft state” is not phase-separated, but rather a globally homogeneous state filled with nanodomains of sizes between 10 and 100 nm. The raft concept is supported by experimental findings, e.g., on the mobility of certain membrane proteins [189]. It has been questioned mainly due to a lack of direct evidence. Rafts are too small to be visualized *in vivo* by microscopy. Moreover, it was not clear from a theoretical point of view why nanoscale rafts should be stable with respect to macrophase separation. To explain this, it was proposed that rafts might be nonequilibrium structures [190] and that rafts might be stabilized by the cytoplasm [191] or by special line-active lipids [192–194]. Alternatively, it was argued that rafts

**Fig. 2** Rafts in a two-component lipid bilayer (20,000 lipids, Lenz model). Purple (*darker*) beads correspond to cholesterol and green (*lighter*) beads to phospholipids (see [81])



might simply be a signature of critical fluctuations in the vicinity of critical points [195, 196].

Whether a thermodynamically stable nanostructured raft state could exist in simple multicomponent membranes that do not contain special line-active additives has remained unclear until recently. This theoretical question mark could be removed by recent simulations of the two-component Lenz model by Meinhardt et al. [81]. Figure 2 shows a top view of a configuration that contains microscopic cholesterol-rich domains. The simulations were carried out in a grand canonical ensemble where lipids and cholesterol can swap identities, which excludes the possibility that the finite domains simply reflect incomplete phase separation. The lateral structure factor of the membranes exhibits a peak at around  $q \sim 0.08 \text{ nm}^{-1}$ . Its existence shows that the clusters are not critical. Hence, raft-like structures can be thermodynamically stable in multicomponent membranes. The characteristic length scale of roughly 12 nm is compatible with the size commonly attributed to lipid rafts in biomembranes [82].

Two comments are in place here. First, it should be noted that typical “raft mixtures” used for studying rafts in model membranes contain at least three components. This is because three components seem necessary to bring about global lateral phase separation [188]. Meinhardt et al. report raft-like structures in simulations of a coarse-grained model for binary mixtures but, as in experiments, their systems do not show global phase separation between fluid states. Likewise, there is also some experimental evidence that nanoscopic domains may already be present in binary mixtures – in particular mixtures of saturated lipids (lipids with high main transition temperature) and cholesterol. Studies based on local techniques such as ESR, NMR, or diffusivity measurements have indicated the existence of immiscible liquid phases [188, 197, 198], whereas in fluorescence microscopy, one only observes one homogeneous phase [188]. This suggests that

these two-component membranes phase-separate on the nanoscale, while remaining homogeneous on the global scale, and that they thus feature many of the intriguing properties attributed to rafts.

Second, the characteristic length scale of the rafts is similar to the wavelength of the ripple state in one-component bilayers in the transition region between the fluid and the tilted gel  $L_{\beta'}$  state [199, 200]. Experimentally [201, 202] and in computer simulations [80, 203–207], modulated phases are observed in lipid bilayers that exhibit a tilted gel state, and they are not observed in lipid bilayers with an untilted gel state  $L_{\beta}$  [201–203, 208]. For example, in the Lenz model, rippled states occur in the standard setup with a mismatch between head and tail size [80], but they disappear if the head size is reduced such that the tilt in the gel phase vanishes [208].

Meinhardt et al. [81] have proposed a joint theoretical explanation for these findings, which is based on the coupled monolayer model (see Sect. 2.1.3). They assumed that monolayers exhibit local phase separation into two phases with different order parameter (composition or other), and that the spontaneous curvature of the monolayer depends on the local order parameter. In the strong segregation limit where different phases are separated by narrow interfaces, they showed that the line tension is reduced in the presence of a mismatch  $\Delta K_0$  between the spontaneous curvatures of the two phases. This is because monolayers with a spontaneous curvature, which are forced into being planar by the apposing monolayer, experience elastic stress, and some of that stress can be released at the domain boundaries. The resulting negative contribution to the line tension scales with  $\kappa (\Delta K_0)^2$  and should be present wherever  $\Delta K_0$  is nonzero. A more detailed calculation shows that the elastic energy is minimized for circular or stripe domains of a specific size, which is of the order of a few nanometers. This elastic mechanism could thus stabilize rafts of finite size for sufficiently large spontaneous curvature mismatch.

Meinhardt et al. also considered the weak segregation limit, where the phase separation is incomplete, the interfaces are broad, and the free energy can be expanded in powers of the order parameter  $\Phi$ . They showed that the expansion has a Landau–Brazovskii form [209]:

$$F = \int d^2r \left\{ \frac{g}{2} (\Delta + q_0^2)^2 \Phi^2 + \frac{r}{2} \Phi^2 - \frac{\gamma}{3!} \Phi^3 + \frac{\lambda}{4!} \Phi^4 \right\}, \quad (13)$$

with a characteristic wave vector of the order  $q_0 < 1/\xi$ , where  $\xi$  is the in-plane correlation length  $\xi = (\kappa t_0^2 / K_A)^{1/4}$  ( $t_0$  is the monolayer thickness and  $K_A$  the area compressibility). The Landau–Brazovskii model describes phase transitions driven by a short-wavelength instability between a disordered and one or several ordered phases. In mean-field approximation, it predicts a transition from a disordered phase to one of several ordered modulated phases (lamellar or hexagonal). Fluctuations are known to shift the order–disorder transition and to stabilize a locally structured disordered phase via the so-called Brazovskii mechanism [209]. The

correlation length  $\xi$  sets the order of magnitude and a lower limit for the characteristic wave length of the structures. Inserting typical numbers for the elastic parameters of DPPC bilayers in the fluid phase, one obtains  $\xi \sim 1$  nm.

The simple theory put forward by Meinhardt et al. accounts in a unified manner for both ripple phases and raft states in membranes. The prerequisites for the formation of such modulated phases is local phase separation (e.g., in the ripple case, between a liquid and a gel phase, or in the raft case, between a liquid disordered and a liquid ordered phase) and curvature stress in at least one of the two phases (typically the ordered one), resulting, e.g., from a size mismatch between head group and tails. In order to reproduce rippled states or rafts, coarse-grained simulation models must meet these criteria. This is often not the case. For example, the standard version of the popular MARTINI model does not have a ripple phase, because the low-temperature gel phase of saturated phospholipids is untilted.

### 3 Membrane–Protein Interactions

Biomembranes achieve their biological functions through a multitude of membrane-associated proteins. Whereas the membranes were long thought to mainly serve as a more or less inert background matrix for these proteins, the interactions between membranes and proteins have received more and more attention in recent years [210]. Membranes can affect protein function in several ways. The local lipid environment can immediately influence the function of proteins, e.g., by influencing the tilt and relative position of transmembrane domains [211] or by exerting local pressure on proteins [212]. Furthermore, membranes contribute to the effective interactions between proteins [213–215], and they can be used to tune protein clustering. In mixed membranes, the “raft hypothesis” mentioned in Sect. 2.5 asserts that nanoscale lipid domains in membranes help to organize and control protein assembly [82, 178].

Membrane–protein interactions are controlled by various factors: Local lipid packing, local lipid concentration, membrane distortion, and monolayer and bilayer elasticity. Proteins are surrounded by a shell of lipid molecules (the lipid annulus), which mostly interact nonspecifically with the protein molecules [216]. Protein–membrane interactions are thus to a large extent determined by the interactions of the annuli with the bulk, and often do not depend strongly on the details of the protein sequences. If membrane proteins locally deform the lipid bilayer to which they are bound, this can induce forces between them that are potentially long-ranged and quite universal in their characteristics. The reason is that the bilayer acts as a field that can transmit local perturbations, and thus forces, to distant regions. This is perfectly analogous to the way in which for instance an electrostatic field mediates interactions between electric charges or curved space–time mediates interactions between masses, except that a membrane seems more tangible than the other examples. However, once we look beyond

fundamental forces towards higher level emergent phenomena, very tangible fields exist everywhere. For instance, a rope can transduce a tensile force along its length, and we can describe this using continuum elasticity as the underlying “field equation.”

Just like ropes, fluid lipid membranes are continuous media at a sufficiently coarse level of description. But, their rich physical structure equips them with several properties that can take on the role of a field, for instance:

1. The membrane thickness can be considered as a spatially varying field that couples to the protein content (see Sect. 2.1.3)
2. The lipids can have a spatially varying orientation or tilt order
3. In mixed membranes, the local lipid concentrations can be viewed as a field
4. The Hamiltonian Eq. (1) associates a characteristic energy to a given shape of a membrane, thus rendering its entire geometry a field

These fields differ quite substantially in their theoretical description: concentrations are *scalar* variables, orientations are *vectors*, and differential geometry is at heart a *tensor* theory; but, all of them are known to mediate interactions. For instance, the fact that proteins might prefer one lipid composition over another and thus aggregate [217–220] is central to an important mechanism attributed to lipid rafts. Tilt-mediated protein interactions have also been studied in multiple contexts [32, 33, 159, 221–223]. It is even possible to describe all these phenomena within a common language [224], using the framework of covariant surface stresses [154, 155, 157–161]. However, in the present review we will restrict the discussion to only two examples, both related to membrane elasticity: in Sect. 3.1 we will discuss interactions due to hydrophobic mismatch, and in Sect. 3.2 we will look at interactions mediated by the large-scale curvature deformation of the membrane.

### 3.1 *Hydrophobic Mismatch*

Proteins distort or disrupt membranes, which in turn act back on proteins. Structural perturbations contribute to protein function and are among the most important sources of membrane-induced interactions between proteins. Unfortunately, perturbations or transformations of lipid bilayers due to proteins are very difficult to probe experimentally [225]. Complementary theoretical and computer simulation studies can help to elucidate the role of the lipid bilayer in processes such as protein aggregation and function.

One major source of membrane–protein interactions that has been discussed in the literature for many decades is hydrophobic mismatch [20–22, 24, 26, 28, 29, 226–233]. If the width of the hydrophobic transmembrane domain of a protein is larger than the thickness of the lipid bilayer, the system can respond in two ways: either the protein tilts [234–236] or the membrane deforms [18, 23, 24]. Both responses have biologically relevant consequences. On the one hand, the

orientation of proteins is believed to have a significant influence on their functionality, e.g., in pore formation [237]. Coarse-grained simulations by Benjamini and Smit have suggested that the cross-angle distributions of packed helix complexes are mostly determined by the tilt angle of individual helices [211]. Membrane deformation, on the other hand, induces effective protein–protein interactions and provides one way to control protein aggregation [229, 230, 238]. In experimental tilt measurements, hydrophobically mismatched proteins were sometimes found to tilt; in other cases, the reported tilt angles were surprisingly small compared to theoretical expectations [239–241]. This was partly attributed to problems with the analysis of experimental NMR (nuclear magnetic resonance) data [233] and partly to the presence of anchoring residues flanking the hydrophobic transmembrane domains, which might prevent tilting through a variety of mechanisms [236, 240, 242, 243].

However, coarse-grained simulations show that the propensity to tilt is also influenced by more generic factors. Venturoli et al. have reported that cylindrical inclusions with larger radius tilt less than inclusions with small radius [234]. Neder et al. have identified hydrophobicity as another crucial factor determining tilt [244]. In systematic studies of a variety of simple inclusions with cylindrical shape and similar radii, embedded in a model bilayer of the Lenz type, they found that the behavior of different proteins mainly depended on their free energy of insertion, i.e., their binding free energy. Weakly hydrophobic inclusions with negative binding free energies (which stayed inside the membrane due to kinetic free energy barriers) react to hydrophobic mismatch by tilting. Strongly hydrophobic inclusions with binding energies in excess of  $100 k_B T$  deform the membrane. For the probably most common weakly bound inclusions with binding energies of around  $10 k_B T$ , the situation is more complicated: upon increasing hydrophobic mismatch, inclusions first distort the bilayer and then switch to a tilted state once a critical mismatch parameter is reached. Tilting thus competes with the formation of dynamic complexes consisting of proteins and a shell of surrounding, stretched lipids, and the transition between these two states was found to be discontinuous.

In the case where the membrane is deformed, the deformation profiles can be compared to a variety of theories [16, 17, 27, 33, 245–247]. Both in coarse-grained [30, 234] and atomistic [248] simulations, it was reported that membrane thickness profiles as a function of the distance to the protein are not strictly monotonic, but exhibit a weakly oscillatory behavior. This feature is not compatible with membrane models that predict an exponential decay [16, 17, 27], but it is nicely captured by the coupled elastic monolayer models discussed earlier [22, 28, 30]. Coarse-grained simulations of the Lenz model showed that the coupled monolayer models describe the profile data at a quantitative level, with almost no fit parameters except the boundary conditions [30, 244].

In membranes containing several inclusions, the membrane thickness deformations induce effective interactions between inclusions. These have also been studied within the Lenz model [30, 249] and other coarse-grained models [250, 251]. The comparison with the elastic theory is less convincing, due to the fact that

many other factors such as local lipid packing contribute to the effective potential of mean force, which cannot easily be separated from the pure hydrophobic mismatch contribution [30]. Except for inclusions with very large radii [251], the hydrophobic mismatch contribution to the effective interactions was generally found to be attractive.

## 3.2 *Curvature-Mediated Interactions Between Proteins*

### 3.2.1 **The Mystery of the Sign**

A very striking experimental demonstration of membrane curvature-mediated interactions was given by Koltover et al. in 1999 [252]. These authors mixed micron-sized colloidal particles with giant unilamellar vesicles to which they could adhere. In the absence of vesicles, the colloidal particles showed no tendency to aggregate in solution, whereas they quickly did once they adsorbed onto the vesicles. Since it was also evident from many micrographs that the colloids induced local bending of the vesicle's membrane, the experiment strongly pointed towards membrane curvature-mediated attractions between the adhering colloids. This, however, was very surprising. Although interactions were indeed expected, the force should have been repulsive, as predicted 6 years earlier by Goulian et al. [253]. Interestingly, the prefactor of this interaction had to be corrected twice [254, 255], but this did not change the outcome: the colloids should have repelled. It was soon understood that objects that cause anisotropic deformations could in fact orient and then attract [256–258], but the colloids of Koltover et al. were isotropic (as far as one could tell experimentally).

We will try to provide a glimpse into this mystery. A big part of it has to do with careless use of the statement “theory has predicted.” Theory always deals with model systems and makes simplifying assumptions, and this particular problem is fraught with seemingly inconsequential details that could and sometimes do matter.

### 3.2.2 **The Nonlinear Ground State: Take I**

The relevant field Hamiltonian pertaining to the curvature-mediated interaction problem is Eq. (1), minus several terms that will not matter. For a start, the last term involving the edge tension  $\gamma$  does not arise in the absence of any membrane edge. The spontaneous bilayer curvature  $K_0$  usually vanishes for symmetry reasons. If lipids can flip between the two leaflets, their chemical potential must be the same in both, and if no other symmetry-breaking field is present, this means that  $K_0 = 0$ . Unfortunately, membrane curvature itself breaks the bilayer symmetry, and any existing lipid composition degree of freedom must couple to the geometry [75, 259–263]. So let us for now assume that this is not the case and take a note of

this first nontrivial assumption. Moreover, in actual biomembranes, none of this need be true because active and passive processes can maintain an asymmetric lipid composition across the two leaflets [264, 265]. Finally, the term involving the Gaussian curvature can be dropped here because we will encounter neither edges nor topology changes, and so the Gauss–Bonnet theorem will work in our favor.

What remains is the simpler Hamiltonian Eq. (2), but this looks quite formidable in Monge parametrization. To make any progress with something as forbidding as this appears quite unlikely. And yet, not all hope is lost. For a spherical particle attached to an asymptotically flat membrane, the nonlinear shape equation has an exact solution, namely, a catenoid. This is an axisymmetric minimal surface with  $K \equiv 0$  and hence obviously minimizes the left-hand side of Eq. (2). If one adds additional lateral membrane tension, the exact shape of the membrane around a single adhering spherical particle can no longer be calculated analytically, but numerical solutions are relatively easy to come by using an angle–arc length parametrization [266]. Unfortunately, we need to know the solution for two particles, and in the absence of axisymmetry this is difficult, even numerically. It has been done [267], but before we discuss this approach, let us first see what results we can analytically wrest from these equations.

Even for the full nonlinear problem, the tight link between geometry and surface stress permits one to express mediated interactions as line integrals over the equilibrium membrane geometry. For instance, picture two spherical particles bound to a membrane, held at some mutual distance. If the particles are identical, then this will give rise to a mirror-symmetric membrane shape, and it can be shown that the force between these particles can be written as [158, 159]:

$$F = \frac{1}{2} \kappa \int ds \left\{ K_{\perp}^2 - K_{\parallel}^2 \right\}, \quad (14)$$

where for simplicity we restrict to the tensionless case. The integral runs across the symmetry curve (the intersection of the membrane with the mirror plane),  $K_{\parallel}$  is the local curvature of that curve and  $K_{\perp}$  the local curvature perpendicular to that curve. The sign convention is such that a negative sign implies attraction. To obtain an interaction strength out of Eq. (14) we need these curvatures, for which we need to solve the shape equations after all. Unfortunately, not even the sign of the interaction is evident from Eq. (14), since the difference of two squares enters the integrals. Had we been curious instead about the interaction (per unit length) between two parallel rods on the membrane, we would have been in a better position: Now  $K_{\parallel}$  would be zero and the interaction would be clearly repulsive (even though we still do not quite know how strong it is). It seems that in order to make headway, we must solve the shape equation. The only hope of doing this in reasonable generality using analytical tools is to linearize it.

### 3.2.3 Linearization and Superposition Approximation

Linearizing the nonlinear geometric functional means restricting to the first term in the integrand of Eq. (3). If we add a surface tension  $\Gamma$ , this means looking at the energy density  $\frac{1}{2}\Gamma(\nabla h)^2 + \frac{1}{2}\kappa(\Delta h)^2$ , where  $\nabla$  and  $\Delta$  are the two-dimensional (flat!) surface gradient and Laplacian, respectively. A functional variation yields:

$$[-\Gamma\Delta + \kappa\Delta\Delta] h(\mathbf{r}) = 0 . \quad (15)$$

This shape equation is of fourth order, but it is linear. Unfortunately, in the present context we must solve it for a two-particle problem with finite-sized particles, and therein lies the rub: the operator in square brackets is not separable in any simple coordinate system, so we have to deal with the fact that this equation is indeed a partial differential equation.

A popular trick to avoid this problem rests on the following reasoning: If the equation is linear, one might first want to look for a solution of the one-particle problem and then simply create the two-particle solution by superposition. We can then apply Eq. (14) to calculate the force, which in the present example would yield the interaction potential [224]:

$$U(r) = 2\pi\kappa \tilde{\alpha}^2 K_0(r/\lambda) \quad \text{with} \quad \lambda = \sqrt{\frac{\kappa}{\Gamma}} \quad \text{and} \quad \tilde{\alpha} = \frac{\alpha}{K_1(r_0/\lambda)} . \quad (16)$$

Here,  $r$  is the distance between the particles,  $r_0$  is the radius of the circular contact line at which the membrane detaches from the colloid,  $\alpha$  is the angle with respect to the horizontal at which it does so, and the  $K_\nu$  are modified Bessel functions of the second kind. This solution is analytical, simple, and wrong. Or more accurately, it only holds when  $r \gg \lambda \gg r_0$ , a restriction that excludes the interesting tensionless limit in which  $\lambda \rightarrow \infty$ . The mathematical reason is that superposition in the way celebrated here is not allowed: yes, superpositions of solutions to linear equations are still solutions, but superpositions of solutions, each of which only satisfies some part of all pertinent boundary conditions, generally do not satisfy any boundary condition and are thus not the solutions we are looking for. The physical reason why the superposition ansatz in this case fails is because the presence of one colloid on the membrane, which creates a local dimple, will abet a nearby colloid to tilt, thereby changing the way in which that second colloid interacts with the membrane and, in turn, the first one.

### 3.2.4 Linearization and a Full Two-Center Solution

One way to circumvent the superposition approximation is to solve the full two-center problem. This is of course much more tedious, and in fact can only be handled as a series expansion, in which one satisfies the boundary conditions at both

particles up to some order in the multipoles, and an expansion in the smallness parameter  $r_0/r$ . This calculation has been done by Weikl et al. [268], leading to:

$$U(r) = 2\pi\kappa\left(\frac{\alpha r_0}{\lambda}\right)^2 \left\{ K_0(r/\lambda) + \left(\frac{r_0}{\lambda}\right)^2 K_2^2(r/\lambda) + \dots \right\}. \quad (17)$$

Notice that in the case  $r \gg \lambda \gg r_0$  this indeed reduces to Eq. (16), whereas in the more interesting limit in which the tension vanishes it reduces to:

$$U(r) = 8\pi\kappa\alpha^2 \left(\frac{r_0}{r}\right)^4, \quad (18)$$

which is indeed the solution of Goulian et al. [253], amended by the prefactor corrections [254, 255]. In fact, these authors have actually written down the solution for the case of two nonidentical particles 1 and 2 with detachment angles  $\alpha_1$  and  $\alpha_2$ . If we also make their radii  $r_i$  different, we find [269]:

$$U(r) = 4\pi\kappa(\alpha_1^2 + \alpha_2^2) \frac{r_1^2 r_2^2}{r^4}. \quad (19)$$

Notice that, unlike what one might have guessed from Eq. (18), the potential (and thus the force) is not proportional to the product of the two detachment angles. The actual form of the prefactor,  $\alpha_1^2 + \alpha_2^2$ , is highly suggestive of an entirely different underlying physics, as we will now see.

### 3.2.5 Linearization Using Effective Field Theory

Equations (17), (18), and (19) are expansions of the exact solution for large distance. Working out higher order terms appears reasonably forbidding, given that one has to push a difficult multicenter problem to a high order. However, there is a way to disentangle the multicenter problem from the interaction problem.

We have seen that the physical reason why the superposition approximation fails is the induced tilting of neighboring colloids. More generally, any finite particle in contact with the membrane will induce extra membrane deformations if the membrane in its vicinity is perturbed. This is simply a polarization effect: Any “incoming” field interacts with the boundary conditions imposed by the particle and these then create new “outgoing” fields. Superposition of fields would work for point particles, but these do not capture the polarization effects, unless we equip them with the requisite polarizabilities. But this of course we can do. We can write a new Hamiltonian of interacting point particles, where each of them has the same polarizabilities as the actual finite size particles of the situation we actually wish to describe. This works by adding terms to the Hamiltonian that are localized at the position of the particle and that couple to the field in the same way that a local polarizability would. For instance, if a particle at the position  $r_\alpha$  has a dipole

polarizability  $C_\alpha^{(1)}$ , we must add the term  $\frac{1}{2}C_\alpha^{(1)}[h_i(\mathbf{r}_\alpha)]^2$  to the Hamiltonian, where the index  $i$  is again a derivative. The energy increases quadratically with the gradient of the local field – exactly as for a dipole polarizability. The only remaining question is: where do we get the polarizabilities from? The answer is, just like in classical electrostatics, by calculating the response of one particle in a suitably chosen external field and comparing the full theory with the effective point particle theory.

This idea is an example of what is referred to as effective field theory [270], and it has been used for a host of vastly diverse problems, ranging from black holes in general relativity [271, 272] to finite-size radiation corrections in electrodynamics [273]. The first application in the context of fluid soft surfaces was given by Yolcu et al. [274, 275]. For two axisymmetric particles on a membrane, Yolcu and Deserno showed that Eq. (19) extends as follows [269]:

$$U(r) = 4\pi\kappa(\alpha_1^2 + \alpha_2^2) \frac{r_1^2 r_2^2}{r^4} + 8\pi\kappa \left( \frac{\alpha_1}{r_1} - \frac{\alpha_2}{r_2} \right)^2 \frac{r_1^4 r_2^4}{r^6} + \dots \quad (20)$$

Notice that the next order correction is also repulsive and in fact vanishes for identical particles (in contrast to some earlier calculations [276] that missed terms that contribute at the same order).

### 3.2.6 Fluctuation-Mediated Interactions

It has long been known that even two flat circular particles on a membrane feel an interaction because their boundaries affect the fluctuation spectrum of the membrane and thus its free energy. These forces are proportional to the thermal energy  $k_B T$  and not to the surface rigidity  $\kappa$  and are examples of Casimir interactions in soft matter systems [277]. For circular discs on a tensionless membrane the forces are attractive and, to lowest order, decay like the fourth power of distance [253, 276, 278, 279].

The true beauty of the effective field theory approach described in the previous section is that it also greatly simplifies force calculations on thermally fluctuating surfaces [269, 274, 275]. For two flat rigid particles of radii  $r_1$  and  $r_2$ , Yolcu and Deserno find [269]:

$$-\frac{U(r)}{k_B T} = 6 \frac{r_1^2 r_2^2}{r^4} + 10 \frac{r_1^4 r_2^4 + r_1^4 r_2^2}{r^6} + 3 \frac{r_1^2 r_2^2 (5r_1^4 + 18r_1^2 r_2^2 + 5r_2^4)}{r^8} + \dots \quad (21)$$

The leading order is well known,<sup>5</sup> all higher orders are new. In fact, if one restricts to identical particles, many more orders can be readily written down:

<sup>5</sup> Unfortunately, in the first paper that discusses this force, Goulian et al. [253] claim that the prefactor is 12, a mistake that is not fixed during the prefactor-fixing in [254].

$$-\frac{U(r)}{k_B T} = \frac{6}{x^4} + \frac{20}{x^6} + \frac{84}{x^8} + \frac{344}{x^{10}} + \frac{1388}{x^{12}} + \frac{5472}{x^{14}} + \frac{21370}{x^{16}} + \frac{249968}{x^{18}} \dots, \quad (22)$$

where  $x = r/r_0$ .

So here we have the first example of an attraction. Could these forces explain the aggregation observed by Koltover et al. [252]? This is difficult to say. First, in the case of almost flat membranes, which all these calculations implicitly assume by using linearized Monge gauge, the ground state repulsion, Eq. (19), overwhelms the fluctuation contribution, Eq. (21), once  $\alpha > \alpha_c = \sqrt{3k_B T/4\pi\kappa}$ . For a typical choice of  $\kappa = 20 k_B T$  this gives the rather small angle  $\alpha_c \approx 6^\circ$ . Most likely the colloids in the experiments by Koltver et al. imposed much bigger deformations, but it is hard to say what happens to both forces at larger angles. In the next section, we discuss the numerical solution of the ground state problem, but at present no calculations exist that push the Casimir force beyond the linear regime, except in the case of two parallel cylinders, for which Gosselin et al. find, rather remarkably, that the Casimir force is repulsive [280].

### 3.2.7 The Nonlinear Ground State: Take II

The various linear calculations show that two axisymmetric colloids on a membrane should repel. But, as the detachment angles  $\alpha_i$  increase, it becomes harder to justify the linearization. The expansion in Eq. (3) ultimately rests on the smallness of  $|\nabla h|$ , an expression that should be compared to  $\tan \alpha_i$ . But, once higher order terms matter, Monge parametrization not only becomes technically impenetrable, it is even incapable of dealing with membrane shapes that display overhangs. It is hence preferable to discard it in favor of a more general numerical surface triangulation.

Reynwar and Deserno [267] have studied the interaction problem for identical axisymmetric colloids with large angles  $\alpha_i$ , using the package “Surface Evolver” by Brakke [281]. For small angles  $\alpha_i$ , the large distance predictions coincide well with Eq. (18), but they break down rather abruptly as soon as  $r < 2r_0$ , which is when the particles would touch unless they could also tilt out of each other’s way. For large  $\alpha_i$ , the linear predictions substantially overestimate the repulsion. Interestingly, for the special case  $\alpha = \pi/2$  the repulsive force goes through a maximum (around  $r/r_0 \approx 1.8$ ), and it decreases upon moving the particles even close together until it vanishes at  $r/r_0 \approx 1$ . At even closer distances the particles attract. Attractive forces must also exist for detachment angles smaller than  $\pi/2$ , but Reynwar and Deserno [267] do not attempt to find the minimal angle at which this happens. Attractive forces certainly also exist for angles bigger than  $\pi/2$ , even though it might be that there is also a largest angle for which they exist. In any case, only for  $\alpha = \pi/2$  does the attraction persist all the way to  $r = 0$ .

A simple close distance approximation can be devised to understand the necessity of a sign-flip. At sufficiently close distances, the two particles tilt so much that

they almost face each other and the membrane between them assumes a shape similar to a cylinder, which is capable of transmitting tensile forces as we have seen in Sect. 2.3. For angles close to  $\pi/2$ , this theory suggests [267]:

$$\frac{Fr_0}{\pi\kappa} = \frac{1}{x^2} + \frac{1 - \sin\alpha}{x} - 1 + \mathcal{O}(x) \quad \text{with} \quad x = \frac{r}{2r_0 \cos\alpha} . \quad (23)$$

Observe that the first two terms vanish for  $\alpha = \pi/2$ , which leaves the (attractive) force  $F = \pi\kappa/r_0$ , which is half the value transmitted through a cylindrical membrane tube [see Eq. (5)]. The missing factor of 2 derives from the fact that this calculation is not made at constant area but at constant (in fact, zero) tension. The numerical calculations suggest that indeed  $F(r)$  approaches a constant as  $r \rightarrow 0$ , even though it seems slightly off from the expected value of  $-\pi\kappa/r_0$ .

### 3.2.8 Curvature-Mediated Interactions in Simulations

The experiments by Koltover et al. claim that isotropic colloids on membranes experience a surface-mediated (presumably, curvature-mediated) attraction. All theories we have discussed so far claim that the force is repulsive, unless one goes to large detachment angles. Can simulations shed more light onto the problem? If so, it will not be necessary to represent the bilayer in any greater detail because only fluid curvature elasticity needs to be captured.

Reynwar et al. have investigated this problem using the Cooke model, amended by simple generic particles with some given isotropic curvature [282]. They showed that indeed strongly membrane-deforming colloids experience attractive pair interactions. Subsequent more detailed studies revealed that these are compatible with the numerical results discussed in the previous section [267]. However, they also showed that a large number of weakly membrane deforming colloids still aggregate, in fact, that they can drive vesiculation of the membrane [282]. This is surprising because these particles exhibited detachment angles at which the ground state theory clearly insists on a repulsive pair potential.

However, just because the pair potentials are repulsive does not yet prove that aggregation cannot happen, since curvature-mediated interactions are not pairwise additive, as first pointed out by Kim et al. [283, 284]. These authors provide a general formula for an  $N$ -body interaction, and even though it is really only accurate up to the triplet level [269], it does show that the contributions beyond pairs can lower the overall repulsive energy; for instance, they show that certain multiparticle configurations are indeed marginally stable instead of being driven apart. In a later publication, Kim et al. [285] show that an infinite number of periodic lattices exist for which summing the non-pairwise interactions preserve zero membrane bending energy. Again, because their non-pairwise form is only accurate up to triplet order, it is not clear whether this result remains true if all orders are considered. Müller and Deserno have alternatively treated this problem using a cell model [286] in which a regular lattice of particles is replaced by a single particle within a cell, plus

boundary conditions that mimic the presence of other surrounding particles. They prove that within this approximation the lateral pressure between colloids is always repulsive, even in the nonlinear regime;<sup>6</sup> however, how well the cell model actually captures a multiparticle assembly is difficult to say. Auth and Gompper have also used a cell model approach [287], but they specifically apply it to a curved background membrane. They argue that even if the forces are repulsive, they might be less repulsive, and thus the free energy per colloid smaller, if the background membrane is curved because this background curvature screens the repulsion between the colloids. This could provide a driving force for creating curved vesicle buds from flat membranes studded with isotropic membrane-curving colloids, provided the average area density of colloids remains fixed. The latter is usually the case in simulations, and Auth and Gompper show that the sizes of the vesicles that detach from the parent membrane for differently curved colloids are compatible with the observations of Reynwar et al. [282]. What would fix this density in real systems is less clear, but it is conceivable that this is yet another situation where rafts come into play. If the membrane-curving particles have to stay within a finite raft, their mutual repulsion can, by virtue of the mechanism discussed by Auth and Gompper, lead to a budding of that raft domain.

In conclusion, we see that the situation is substantially more tricky than the seemingly simple question “do membrane-curving particles attract or repel?” leads one to expect. Nonlinearities, multibody interactions, fluctuations, background curvature, boundary conditions, and anisotropies are only some of the “details” that affect the answer to this question. At the moment, the situation remains not completely solved, but the results outlined in this section should provide a reliable guide for future work.

## 4 Multiscale Modeling of Lipid and Membrane Protein Systems

### 4.1 *Multiscale Modeling: Approaches and Challenges*

As we have seen in the previous sections, coarse-grained lipid models have been enormously successful for investigating phenomena in lipid bilayers and lipid bilayer/protein systems. In particular, rather coarse, generic models that reduce the lipids to their most essential features and shed almost all chemical specificity have contributed enormously to our understanding of effective interactions, generalized processes, and their driving forces. A different branch of coarse-grained models, the bottom-up models, has also progressed quite dramatically in the past

---

<sup>6</sup>They used the same techniques that also led to the exact Eq. (14), only that in the cell model case the sign is evident from the expression.

decade. These models have not been developed as stand-alone models with parameters derived to reproduce some desired experimentally known feature of the system. They were developed in a bottom-up way with the help of an underlying higher-resolution (atomistic) model. Therefore, the terms “multiscale modeling” or “systematic coarse graining” are frequently used. These models allow staying closer to an atomistic system and to retain more chemical specificity. Due to their bottom-up construction, they offer the opportunity to go back and forth between a coarse-grained and an atomistic level of resolution using so-called backmapping techniques.

It should be noted that this closeness between levels of resolution does come at a cost: upon reducing the number of degrees of freedom, the models become strongly state-point dependent and it necessarily becomes impossible to accurately represent all properties of the underlying atomistic system with the coarse-grained model. In particular, the representation of thermodynamic and structural properties is a severe challenge that has been subject of a multitude of studies over the last few years [288]. The question of representability and the unavoidable choice of parametrization target properties that has to be made has led to a number of different systematic coarse graining approaches, which are often divided into two general categories: (i) methods where the CG parameters are refined so that the system displays a certain thermodynamic behavior (typically termed “thermodynamics-based”) [83, 84, 289–291] or (ii) methods where the CG system aims at reproducing the configurational phase space sampled by an atomistic reference system (often misleadingly termed “structure-based”) [58, 59, 64, 292–301]. Representability limitations lead to the observation that a structure-based approach does not necessarily yield correct thermodynamic properties such as solvation free energies or partitioning data, whereas thermodynamics-based potentials may not reproduce microscopic structural data such as the local packing or the structure of solvation shells. Closely related are also the inevitable transferability problems of CG models: all CG models (in fact also all classical atomistic force fields) are state-point dependent and cannot necessarily (without reparametrization) be transferred to different thermodynamic conditions (temperature, density, concentration, system composition, phase, etc.) or to a different chemical or molecular environment (e.g., a certain chemical unit being part of different macromolecular chains). Structural and thermodynamic representability and state-point transferability questions are often intimately linked because the response to a change in state point corresponds to representing certain thermodynamic properties. Intensive research is currently devoted to this problem [299, 300, 302–308] because an understanding of the potential and limitations of coarse-grained models is a necessary prerequisite to applying them to complex biomolecular problems and systems such as multiprotein complexes in biomembranes. The reason for this is that CG models are usually developed based on smaller and less complex reference systems – a reference simulation of the actual target system is by construction prohibitive, otherwise the whole coarse-graining effort would not be necessary in the first place. Consequently, it is essential to understand transferability among different concentrations,

compositions, and environments to be able to put these subsystem-based models together and obtain a reliable model for the actual, more complex, target system. We will show for one example – the light-harvesting complex of green plants (LHCII) – some aspects of multiscale modeling of membrane protein systems and some of the problems that need to be addressed if one wants to go beyond generic CG models and retain a certain level of chemical specificity.

## 4.2 *The Light-Harvesting Complex*

The major light-harvesting complex (LHCII) of the photosynthetic apparatus in green plants binds more than half of the plant's chlorophyll (Chl) and is presumably the most abundant membrane protein on Earth. It has become an intensely studied model membrane protein for several reasons. Its structure is known in near-atomic detail [309, 310] and much of its biochemistry has been elaborated in the past decades [311]. Moreover, LHCII spontaneously self-organizes from its protein and pigment components *in vitro*; therefore, recombinant versions of it can easily be produced and modified almost at will [312]. The assembly of LHCII and the concomitant folding of its apoprotein has been studied in some detail [313, 314]. Both processes occur spontaneously upon combining the unfolded apoprotein and pigments in detergent solution. *In vivo*, the assembly of LHCII takes place in the lipid environment of the thylakoid membrane and, most likely, is influenced by the lipid and protein components of this membrane. This is difficult to analyze experimentally because, so far, the self-organization of LHCII cannot yet be achieved in a lipid membrane environment. Recently, the disassembly of LHCII and the role of the bound/dissociating pigments in the falling apart of LHCII trimers has also become the subject of increased interest. These pigments constitute about one third of the total mass of LHCII and, according to the structure, significantly contribute to the stability of the pigment–protein complex. The structural behavior of LHCII has been analyzed by circular dichroism (CD), fluorescence, and electron paramagnetic resonance (EPR) [312, 314–316].

One important aspect of LHCII that specifically relates to other aspects discussed in the present review is the question of how the membrane environment (lipid composition, membrane curvature, etc.) affects the association of LHCII monomers to form trimers and the assembly of these trimers into the antenna complex around the photosynthetic reaction centers. The nonbilayer-forming lipid monogalactosyldiacylglycerol (MGDG) constitutes half of the thylakoid membrane. This membrane maintains its lamellar structure only with proteins inserted, predominantly LHCII which, due to its concave shape, eases the curvature pressure exerted by MGDG. It has been suggested that this curvature pressure is a driving force for protein interaction in the membrane [317]; however, because it is not known whether, e.g., the formation of supercomplexes of LHCII trimers eases or increases curvature pressure, it is unclear whether MGDG (or other curvature

pressure-increasing lipid components) promote or inhibit the formation of such supercomplexes. Likewise, the composition of the lipid membrane and the membrane properties such as its curvature pressure most likely influence the folding of the LHCII apoprotein and its assembly with pigments.

LHCII commends itself as a useful model for studying the influence of the lipid membrane on the assembly and structural behavior of membrane proteins in general because of its known structure, its availability in a recombinant form, and its self-organization, at least in detergent micelles. Moreover, the bound Chl molecules serve as built-in fluorescence markers for monitoring the structural behavior of the pigment–protein complex. To be able to correlate experimental observations of aggregate formation with predictions from theory, recombinant LHCII has been inserted in liposomes and assayed for complex–complex distances by intercomplex FRET measurements, and for aggregate formation by quantifying aggregate-induced fluorescence quenching.

A multiscale simulation model to study the LHCII complex requires, as a first step, model parameters for all components involved. As already mentioned above, it will be neither possible nor useful to parameterize a CG model based on the actual multicomponent (lipid bilayer/protein/pigments) system but one would rather develop models for sensibly chosen subsystems. Although parameters for the protein and the lipid bilayer can typically be found in many standard force fields, a challenging first task is to obtain a reliable model for the pigments, irrespective of the level of resolution. For many biological applications, the MARTINI CG force field (described above) has become very popular and successful, in particular for lipid bilayer and protein systems. To employ the MARTINI force field for simulations of the pigmented LHCII, a CG description and model parameters for the pigment molecules needs to be added. We have developed a coarse-grained model of the chlorophyll pigments (Chl*b* and Chl*a*) that can be embedded into the existing MARTINI force field to study the pigmented LHCII trimer in the future. To do this, Chl*b* and Chl*a* were parameterized in the presence of the lipid bilayer. This reference system for parametrization was chosen for two reasons: most importantly, the Chl–lipid interactions are highly relevant for the formation and behavior of the LHCII protein–pigment complex in the lipid bilayer. About 50% of the pigment molecules in the plant are bound to the light-harvesting complex, with 42 Chl molecules per LHCII trimer. In vitro studies have shown that the folding of the LHCII apoprotein and the pigment binding to the protein are tightly coupled processes. In the LHCII monomer, many Chl pigments are situated in the outer region of the protein, effectively forming an interface between protein and lipids. Consequently, the Chl–lipid interactions are probably important for the assembly and stability of the trimer. A second reason for choosing the Chl–lipid system as reference for which the interactions between the MARTINI standard forcefield and Chl can be tuned is that it is more tractable compared to the fully pigmented LHCII membrane protein complex. The CG model for Chl*b* and Chl*a* in the DPPC bilayer was derived from a combination of a structure-based approach for bonded interaction potentials and a mixed structure-based and partitioning-based approach for

nonbonded interaction potentials to fit the thermodynamics-based MARTINI force field. The CG model for Chl molecules follows the degree of coarse graining of the MARTINI force field. Somewhat in line with the general MARTINI parameterization philosophy, which focuses on partitioning properties, the nonbonded parameters were chosen such that the distribution of the CG Chl beads between hydrophilic and hydrophobic regions in the bilayer is correctly represented, as compared to the atomistic reference simulation. Here, particular attention was paid to the interactions of the polar center of the porphyrin ring with the lipid beads and to the polarity of the aromatic ring, which needs to be carefully tuned to obtain the correct distribution between the polar headgroup and the hydrophobic tail regions of the lipid bilayer. The bonded interactions in the CG pigments were derived such that the CG model reproduces the shape and the conformational behavior of the atomistic Chl molecules. The overall shape of the porphyrin ring and the different conformations of the phytol tail are well represented in this CG model. As a last aspect of validation of the CG model, we have analyzed the propensity of the Chl pigments to aggregate in the lipid bilayer. It was found that Chl molecules do aggregate, with clusters that form and break multiple times in the course of the simulation, i.e., the aggregation is not overly strong. Qualitatively, these data are corroborated by fluorescence quenching experiments that show that chlorophylls in lipid bilayers have a tendency to aggregate at low lipid to Chl ratios of less than 1,250 lipids/chlorophyll. Summarizing the structural behavior, the distribution of the pigments in the bilayer (which are indicative of a correct balance of hydrophobicity and hydrophilicity) and the pigment association are very well represented in the CG model compared to atomistic simulations and experimental data (Debnath et al., unpublished data).

After deriving the CG model parameters for the Chl–lipid system, this new model was now combined with the MARTINI model for proteins to perform some first simulations of the pigmented LHCII complex (in trimeric as well as monomeric form). In addition, classical atomistic (explicit solvent) simulations of trimeric and monomeric LHCII in a model membrane were performed to provide a reference for validation of the CG simulations. The first CG simulations of the LHCII complex have proven to be very promising. Unlike our initial attempts without the careful parameterization of the pigments, the trimeric protein–pigment complex has been structurally stable, most notably without the presence of any artificial elastic network between the protein core and the pigments (see Fig. 3). The properties of the complex from the CG model are in excellent agreement with those from the atomistic model. In the future, this CG model will be used to study various aspects of LHCII protein–protein interactions in the lipid bilayer that, on the one hand, go beyond the time and length scales accessible to atomistic simulations alone and, on the other hand, require a more chemically realistic description of the protein/pigment/lipid system than typical generic CG models.

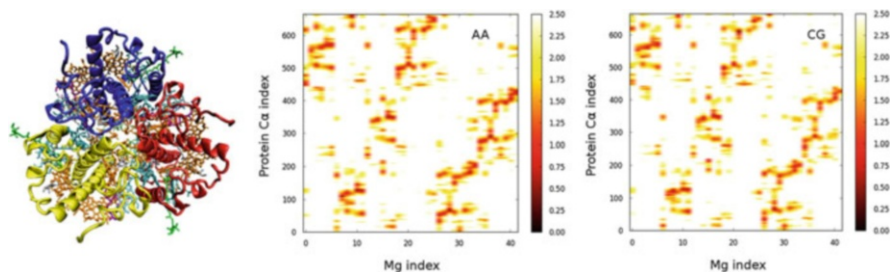


**Fig. 3** *Left*: Top view of an LHCII trimer (colors according to chain or molecule type: *blue* chain A, *red* chain B, *green* chain C, *cyan* Chl b, *pink* Chl a). *Middle and right*: Contact maps between Chl pigments and protein residues of LHCII trimer drawn as distance maps between the Ca atoms of the proteins (*y*-axis) and the Mg atoms of all Chl pigments (*x*-axis) within a 2.5 nm cut-off for atomistic (AA) simulations of 70 ns (*middle*) and coarse-grained (CG) simulations of 100 ns (*right*). The maps show that the pigments are stably located in their binding sites for both levels of resolution

## 5 Conclusions

In this chapter we have presented an overview of different approaches to the study of lipid membranes and membrane protein systems. We have reviewed theoretical and simulation approaches, and shown how generic lipid simulation models can be used to understand the principles that determine properties of lipid bilayers such as bending, Gaussian curvature modulus, and membrane tension, or fundamental phenomena such as the formation of lipid rafts or the curvature-mediated interactions between proteins. In the previous section it was outlined how multiscale modeling can in principle go a step further by ensuring a certain chemical specificity while still benefiting from the time- and length-scale advantages of coarse-grained simulations. It was noted that there are still a number of challenges in the area of systematic coarse graining that need to be addressed to be able to study complex multicomponent systems such as the light-harvesting complex of green plants. For this system, we have shown the first steps toward a multiscale simulation model that allows going back and forth between a coarse-grained and an atomistic level of resolution and therefore permits immediate comparison to atomic level experimental data.

**Acknowledgements** We would like to thank the many coworkers and colleagues who have contributed to the research reported here, in particular Ira Cooke, Jemal Guven, Vagelis Harmandaris, Gregoria Ilyia, Martin Müller, Benedict Reynwar, Ira Rothstein, Cem Yolcu, Frank Brown, Olaf Lenz, Sebastian Meinhardt, Peter Nielaba, Beate West, Ananya Debnath, Christoph Globisch, Christoph Junghans, Shahoua Ding, Sabine Wiegand, Sandra Ritz, and Eva Sinner.

## References

1. Smith R, Tanford C (1972) The critical micelle concentration of  $L_{\alpha}$ -dipalmitoylphosphatidylcholine in water and water/methanol solutions. *J Mol Biol* 67(1):75–83
2. Israelachvili JN, Mitchell DJ, Ninham BW (1976) Theory of self-assembly of hydrocarbon amphiphiles into micelles and bilayers. *J Chem Soc Faraday Trans* 72(2):1525–1568
3. Rawicz W, Olbrich K, McIntosh T, Needham D, Evans E (2000) Effect of chain length and unsaturation on elasticity of lipid bilayers. *Biophys J* 79:328–339
4. Canham PB (1970) The minimum energy of bending as a possible explanation of the biconcave shape of the human red blood cell. *J Theoret Biol* 26(1):61–81
5. Helfrich W (1973) Elastic properties of lipid bilayers—theory and possible experiments. *Z Naturforsch C* 28(11):693–703
6. Evans EA (1974) Bending resistance and chemically induced moments in membrane bilayers. *Biophys J* 14(12):923–931
7. Helfrich W (1974) The size of bilayer vesicles generated by sonication. *Phys Lett A* 50(2):115–116
8. Kreyszig E (1991) *Differential geometry*. Dover, New York
9. do Carmo M (1976) *Differential geometry of curves and surfaces*. Prentice Hall, Englewood Cliffs
10. Lipowsky R, Grotehans S (1993) Hydration versus protrusion forces between lipid bilayers. *Europhys Lett* 23:599–604
11. Lipowsky R, Grotehans S (1993) Renormalization of hydration forces by collective protrusion modes. *Biophys Chem* 49:27–37
12. Goetz R, Gompper G, Lipowsky R (1999) Mobility and elasticity of self-assembled membranes. *Phys Rev Lett* 82:221–224
13. Brandt EG, Edholm O (2010) Stretched exponential dynamics in lipid bilayer simulations. *J Chem Phys* 133:115101
14. Brandt EG, Braun AR, Sachs JN, Nagle JF, Edholm O (2011) Interpretation of fluctuation spectra in lipid bilayer simulations. *Biophys J* 100:2104–2111
15. Lindahl E, Edholm O (2000) Mesoscopic undulations and thickness fluctuations in lipid bilayers from molecular dynamics simulations. *Biophys J* 79(1):426–433
16. Owicki JC, Springgate MW, McConnell HM (1978) Theoretical study of protein–lipid interactions in bilayer membranes. *Proc Natl Acad Sci USA* 75:1616–1619
17. Owicki JC, McConnell HM (1979) Theory of protein–lipid and protein–protein interactions in bilayer membranes. *Proc Natl Acad Sci USA* 76:4750–4754
18. Huang HW (1986) Deformation free energy of bilayer membrane and its effect on gramicidin channel lifetime. *Biophys J* 50:1061–1070
19. Sperotto MM, Mouritsen OG (1991) Monte Carlo simulation of lipid order parameter profiles near integral membrane proteins. *Biophys J* 59:261–270
20. Dan N, Pincus P, Safran SA (1993) Membrane-induced interactions between inclusions. *Langmuir* 9:2768–2771
21. Dan N, Berman A, Pincus P, Safran SA (1994) Membrane-induced interactions between inclusions. *J Phys II (France)* 4:1713
22. Aranda-Espinoza H, Berman A, Dan N, Pincus P, Safran S (1996) Interaction between inclusions embedded in membranes. *Biophys J* 71:648
23. Huang HW (1995) Elasticity of lipid bilayer interacting with amphiphilic helical peptides. *J Phys II (France)* 5:1427–1431
24. Nielsen C, Goulian M, Andersen OS (2000) Energetics of inclusion-induced bilayer deformations. *Biophys J* 74:1966–1983
25. Harroun TA, Heller WT, Weiss TM, Yang L, Huang HW (1999) Theoretical analysis of hydrophobic matching and membrane-mediated interactions in lipid bilayers containing gramicidin. *Biophys J* 76:3176–3185

26. Nielsen C, Andersen OS (2000) Inclusion-induced bilayer deformations: effects of monolayer equilibrium curvature. *Biophys J* 79:2583–2604
27. Jensen MO, Mouritsen OG (2004) Lipids do influence protein function – the hydrophobic matching hypothesis revisited. *Biochim Biophys Acta* 1666:205–226
28. Brannigan G, Brown F (2006) A consistent model for thermal fluctuations and protein-induced deformations in lipid bilayer. *Biophys J* 90:1501
29. Brannigan G, Brown FLH (2007) Contributions of Gaussian curvature and nonconstant lipid volume to protein deformation of lipid bilayers. *Biophys J* 92:864–876
30. West B, Brown FLH, Schmid F (2009) Membrane-protein interactions in a generic coarse-grained model for lipid bilayers. *Biophys J* 96:101–115
31. Fournier JB (1998) Coupling between membrane tilt-difference and dilation: a new “ripple” instability and multiple crystalline inclusions phases. *Europhys Lett* 43:725–730
32. Fournier JB (1999) Microscopic membrane elasticity and interactions among membrane inclusions: interplay between the shape, dilation, tilt and tilt-difference modes. *Eur Phys J B* 11:261–272
33. Bohinc K, Kralj-Iglic V, May S (2003) Interaction between two cylindrical inclusions in a symmetric lipid bilayer. *J Chem Phys* 119:7435–7444
34. May ER, Narang A, Kopelevich DI (2007) Role of molecular tilt in thermal fluctuations of lipid membranes. *Phys Rev E* 76:021913
35. Watson MC, Penev ES, Welch PM, Brown FLH (2011) Thermal fluctuations in shape, thickness, and molecular orientation in lipid bilayers. *J Chem Phys* 135:244701
36. Watson MC, Morriss-Andrews A, Welch PM, Brown FLH (2013) Thermal fluctuations in shape, thickness, and molecular orientation in lipid bilayers II: finite surface tensions. *J Chem Phys* 139:084706 doi: 10.1063/1.4818530
37. Neder J, West B, Nielaba P, Schmid F (2010) Coarse-grained simulations of membranes under tension. *J Chem Phys* 132:115101
38. Li J, Pastor KA, Shi AC, Schmid F, Zhou J (2013) Elastic properties and line tension of self-assembled bilayer membranes. *Phys Rev E* 88:012718 doi: 10.1103/PhysRevE.88.012718
39. Scott H (2002) Modeling the lipid component of membranes. *Curr Opin Struct Biol* 12(4): 495–502
40. Saiz L, Bandyopadhyay S, Klein ML (2002) Towards an understanding of complex biological membranes from atomistic molecular dynamics simulations. *Biosci Rep* 22(2):151–173
41. Saiz L, Klein ML (2002) Computer simulation studies of model biological membranes. *Acc Chem Res* 35(6):482–489
42. Berkowitz ML (2009) Detailed molecular dynamics simulations of model biological membranes containing cholesterol. *Biochim Biophys Acta Biomembr* 1788(1):86–96
43. Niemelä PS, Hyvonen MT, Vattulainen I (2009) Atom-scale molecular interactions in lipid raft mixtures. *Biochim Biophys Acta* 1788(1):122–135
44. Gompper G, Kroll DM (1997) Network models of fluid, hexatic and polymerized membranes. *J Phys Condens Matt* 9(42):8795–8834
45. Gompper G, Kroll D (1998) Membranes with fluctuating topology: Monte Carlo simulations. *Phys Rev Lett* 81(11):2284–2287
46. Kumar PBS, Gompper G, Lipowsky R (2001) Budding dynamics of multicomponent membranes. *Phys Rev Lett* 86(17):3911–3914
47. Noguchi H, Gompper G (2004) Fluid vesicles with viscous membranes in shear flow. *Phys Rev Lett* 93(25):258102
48. Atzberger PJ, Kramer PR, Peskin CS (2007) A stochastic immersed boundary method for fluid-structure dynamics at microscopic length scales. *J Comput Phys* 224(2):1255–1292
49. Brown FLH (2008) Elastic Modeling of biomembranes and lipid bilayers. *Ann Rev Phys Chem* 59:685–712
50. Venturoli M, Sperotto MM, Kranenburg M, Smit B (2006) Mesoscopic models of biological membranes. *Phys Rep* 437(1–2):1–54
51. Müller M, Katsov K, Schick M (2006) Biological and synthetic membranes: what can be learned from a coarse-grained description? *Phys Rep* 434(5–6):113–176

52. Brannigan G, Lin L, Brown F (2006) Implicit solvent simulation models for biomembranes. *Eur Biophys J* 35(2):104–124
53. Marrink Siewert J, de Vries AH, Tieleman DP (2009) Lipids on the move: simulations of membrane pores, domains, stalks and curves. *Biochim Biophys Acta Biomembr* 1788 (1):149–168
54. Bennun SV, Hoopes MI, Xing C, Faller R (2009) Coarse-grained modeling of lipids. *Chem Phys Lipids* 159(2):59–66
55. Deserno M (2009) Mesoscopic membrane physics: concepts, simulations, and selected applications. *Macromol Rapid Comm* 30(9–10):752–771
56. Noguchi H (2009) Membrane simulation models from nanometer to micrometer scale. *J Phys Soc Jpn* 78(4):041007
57. Schmid F (2009) Toy amphiphiles on the computer: What can we learn from generic models? *Macromol Rapid Comm* 30:741–751
58. Müller-Plathe F (2002) Coarse-graining in polymer simulation: from the atomistic to the mesoscopic scale and back. *Chem Phys Chem* 3(9):754–769
59. Izvekov S, Both GA (2005) Multiscale coarse graining of liquid-state systems. *J Chem Phys* 123(13):134105
60. Praprotnik M, Delle Site L, Kremer K (2005) Adaptive resolution molecular-dynamics simulation: changing the degrees of freedom on the fly. *J Chem Phys* 123(22):224106
61. Praprotnik M, Delle Site L, Kremer K (2007) A macromolecule in a solvent: adaptive resolution molecular dynamics simulation. *J Chem Phys* 126(13):134902
62. Praprotnik M, Site LD, Kremer K (2008) Multiscale simulation of soft matter: from scale bridging to adaptive resolution. *Ann Rev Phys Chem* 59(1):545–571
63. Delgado-Buscalioni R, Kremer K, Praprotnik M (2008) Concurrent triple-scale simulation of molecular liquids. *J Chem Phys* 128(11):114110
64. Noid WG, Chu JW, Ayton GS, Krishna V, Izvekov S, Voth GA, Das A, Andersen HC (2008) The multiscale coarse-graining method. I. A rigorous bridge between atomistic and coarse-grained models. *J Chem Phys* 128(24):244114
65. Noid WG, Liu P, Wang Y, Chu JW, Ayton GS, Izvekov S, Andersen HC, Voth GA (2008) The multiscale coarse-graining method. II. Numerical implementation for coarse-grained molecular models. *J Chem Phys* 128(24):244115
66. Das A, Andersen HC (2009) The multiscale coarse-graining method. III. A test of pairwise additivity of the coarse-grained potential and of new basis functions for the variational calculation. *J Chem Phys* 131(3):034102
67. Delgado-Buscalioni R, Kremer K, Praprotnik M (2009) Coupling atomistic and continuum hydrodynamics through a mesoscopic model: application to liquid water. *J Chem Phys* 131(24):244107
68. Peter C, Kremer K (2009) Multiscale simulation of soft matter systems – from the atomistic to the coarse-grained level and back. *Soft Matter* 5:4357–4366
69. Poblete S, Praprotnik M, Kremer K, Delle Site L (2010) Coupling different levels of resolution in molecular simulations. *J Chem Phys* 132(11):114101
70. Voth GA (ed) (2008) *Coarse-graining of condensed phase and biomolecular systems*, 1st edn. CRC, Boca Raton
71. Rühle V, Jungmans C, Lukyanov A, Kremer K, Andrienko D (2009) Versatile object-oriented toolkit for coarse-graining applications. *J Chem Theory Comput* 5(12):3211–3223
72. Lu L, Voth GA (2012) The multiscale coarse-graining method. In: Rice SA, Dinner AR (eds) *Advances in chemical physics*, vol 149. Wiley, Hoboken, pp 47–81 doi: 10.1002/9781118180396.ch2
73. Cooke IR, Kremer K, Deserno M (2005) Tunable generic model for fluid bilayer membranes. *Phys Rev E* 72(1):011506
74. Cooke IR, Deserno M (2005) Solvent-free model for self-assembling fluid bilayer membranes: stabilization of the fluid phase based on broad attractive tail potentials. *J Chem Phys* 123(22):224710

75. Cooke IR, Deserno M (2006) Coupling between lipid shape and membrane curvature. *Biophys J* 91(2):487–495
76. Hu M, Briguglio JJ, Deserno M (2012) Determining the Gaussian curvature modulus of lipid membranes in simulations. *Biophys J* 102(6):1403–1410
77. Schmid F, Düchs D, Lenz O, West B (2007) A generic model for lipid monolayers, bilayers, and membranes. *Comp Phys Comm* 177(1–2):168
78. Düchs D, Schmid F (2001) Phase behavior of amphiphilic monolayers: theory and simulations. *J Phys Cond Matt* 13:4853
79. Lenz O, Schmid F (2005) A simple computer model for liquid lipid bilayers. *J Mol Liquid* 117(1–3):147–152
80. Lenz O, Schmid F (2007) Structure of symmetric and asymmetric ripple phases in lipid bilayers. *Phys Rev Lett* 98:058104
81. Meinhardt S, Vink R, Schmid F (2013) Monolayer curvature stabilizes nanoscale raft domains in mixed lipid bilayers. *Proc Natl Acad Sci USA* 12:4476–4481
82. Pike L (2006) Rafts defined: a report on the keystone symposium on lipid rafts and cell function. *J Lipid Res* 47:1597–1598
83. Marrink SJ, de Vries AH, Mark AE (2004) Coarse grained model for semiquantitative lipid simulations. *J Phys Chem B* 108(2):750–760
84. Marrink SJ, Risselada HJ, Yefimov S, Tieleman DP, de Vries AH (2007) The MARTINI force field: coarse grained model for biomolecular simulations. *J Phys Chem B* 111:7812–7824
85. Monticelli L, Kandasamy SK, Periole X, Larson RG, Tieleman DP, Marrink SJ (2008) The MARTINI coarse-grained force field: extension to proteins. *J Chem Theory Comput* 4(5):819–834
86. López CA, Rzepiela AJ, de Vries AH, Dijkhuizen L, Huenenberger PH, Marrink SJ (2009) Martini coarse-grained force field: extension to carbohydrates. *J Chem Theory Comput* 5(12):3195–3210
87. López EA, Sovova Z, van Eerden FJ, de Vries AH, Marrink SJ (2013) MARTINI force field parameters for glycolipids. *J Chem Theory Comput* 9(3):1694–1708
88. Lee S (1962) Spiderman, Amazing fantasy # 15. Marvel Comics, New York
89. Brochard F, Lennon JF (1975) Frequency spectrum of flicker phenomenon in erythrocytes. *J Phys (France)* 36(11):1035–1047
90. Brochard F, De Gennes PG, Pfeuty P (1976) Surface tension and deformations of membrane structures: relation to two-dimensional phase transitions. *J Phys (France)* 37:1099
91. Schneider MB, Jenkins JT, Webb WW (1984) Thermal fluctuations of large cylindrical phospholipid-vesicles. *Biophys J* 45(5):891–899
92. Schneider MB, Jenkins JT, Webb WW (1984) Thermal fluctuations of large quasi-spherical bimolecular phospholipid-vesicles. *Biophys J* 45(9):1457–1472
93. Faucou JF, Mitov MD, Méléard P, Bivas I, Bothorel P (1989) Bending elasticity and thermal fluctuations of lipid-membranes—theoretical and experimental requirements. *J Phys (France)* 50(17):2389–2414
94. Henriksen J, Rowat AC, Ipsen JH (2004) Vesicle fluctuation analysis of the effects of sterols on membrane bending rigidity. *Eur Biophys J* 33(8):732–741
95. Evans E, Rawicz W (1990) Entropy-driven tension and bending elasticity in condensed-fluid membranes. *Phys Rev Lett* 64(17):2094–2097
96. Liu YF, Nagle JF (2004) Diffuse scattering provides material parameters and electron density profiles of biomembranes. *Phys Rev E* 69(4):040901
97. Chu N, Kučerka N, Liu YF, Tristram-Nagle S, Nagle JF (2005) Anomalous swelling of lipid bilayer stacks is caused by softening of the bending modulus. *Phys Rev E* 71(4):041904
98. Tristram-Nagle S, Nagle JF (2007) HIV-1 fusion peptide decreases bending energy and promotes curved fusion intermediates. *Biophys J* 93(6):2048–2055
99. Pan J, Tristram-Nagle S, Kučerka N, Nagle JF (2008) Temperature dependence of structure, bending rigidity, and bilayer interactions of dioleoylphosphatidylcholine bilayers. *Biophys J* 94(1):117–124

100. Pfeiffer W, König S, Legrand JF, Bayerl T, Richter D, Sackmann E (1993) Neutron spin echo study of membrane undulations in lipid multibilayers. *Europhys Lett* 23(6):457–462
101. Takeda T, Kawabata Y, Seto H, Komura S, Ghosh SK, Nagao M, Okuhara D (1999) Neutron spin-echo investigations of membrane undulations in complex fluids involving amphiphiles. *J Phys Chem Solids* 60(8–9):1375–1377
102. Rheinstädter MC, Häußler W, Salditt T (2006) Dispersion relation of lipid membrane shape fluctuations by neutron spin-echo spectrometry. *Phys Rev Lett* 97(4):048103
103. Watson MC, Brown FLH (2010) Interpreting membrane scattering experiments at the mesoscale: the contribution of dissipation within the bilayer. *Biophys J* 98(6):L09–L11
104. Bo L, Waugh RE (1989) Determination of bilayer membrane bending stiffness by tether formation from giant, thin-walled vesicles. *Biophys J* 55(3):509–517
105. Cuvelier D, Derényi I, Bassereau P, Nassoy P (2005) Coalescence of membrane tethers: experiments, theory, and applications. *Biophys J* 88(4):2714–2726
106. Tian A, Baumgart T (2008) Sorting of lipids and proteins in membrane curvature gradients. *Biophys J* 96(7):2676–2688
107. Ayton G, Voth GA (2002) Bridging microscopic and mesoscopic simulations of lipid bilayers. *Biophys J* 83(6):3357–3370
108. Farago O (2003) “Water-free” computer model for fluid bilayer membranes. *J Chem Phys* 119(1):596–605
109. Wang ZJ, Frenkel D (2005) Modeling flexible amphiphilic bilayers: a solvent-free off-lattice Monte Carlo study. *J Chem Phys* 122:234711
110. Wang ZJ, Deserno M (2010) A systematically coarse-grained solvent-free model for quantitative phospholipid bilayer simulation. *J Phys Chem B* 114(34):11207–11220
111. Shiba H, Noguchi H (2011) Estimation of the bending rigidity and spontaneous curvature of fluid membranes in simulations. *Phys Rev E* 84:031926
112. Watson MC, Brandt EG, Welch PM, Brown FLH (2012) Determining biomembrane bending rigidities from simulations of modest size. *Phys Rev Lett* 109:028102
113. Harmandaris VA, Deserno M (2006) A novel method for measuring the bending rigidity of model lipid membranes by simulating tethers. *J Chem Phys* 125(20):204905
114. Arkhipov A, Yin Y, Schulten K (2008) Four-scale description of membrane sculpting by bar domains. *Biophys J* 95(6):2806–2821
115. Noguchi H (2011) Anisotropic surface tension of buckled fluid membranes. *Phys Rev E* 83:061919
116. Hu M, Diggins IVP, Deserno M (2013) Determining the bending modulus of a lipid membrane by simulating buckling. *J Chem Phys* 138:214110. doi:[10.1063/1.4808077](https://doi.org/10.1063/1.4808077)
117. Siegel DP, Kozlov MM (2004) The Gaussian curvature elastic modulus of n-monomethylated dioleoylphosphatidylethanolamine: relevance to membrane fusion and lipid phase behavior. *Biophys J* 87(1):366–374
118. Siegel DP (2006) Determining the ratio of the Gaussian curvature and bending elastic moduli of phospholipids from  $Q_{II}$  phase unit cell dimensions. *Biophys J* 91(2):608–618
119. Siegel DP (2008) The Gaussian curvature elastic energy of intermediates in membrane fusion. *Biophys J* 95(11):5200–5215
120. Templer RH, Khoo BJ, Seddon JM (1998) Gaussian curvature modulus of an amphiphile monolayer. *Langmuir* 14(26):7427–7434
121. Baumgart T, Das S, Webb WW, Jenkins JT (2005) Membrane elasticity in giant vesicles with fluid phase coexistence. *Biophys J* 89(2):1067–1080
122. Semrau S, Idema T, Holtzer L, Schmidt T, Storm C (2008) Accurate determination of elastic parameters for multicomponent membranes. *Phys Rev Lett* 100(8):088101
123. Hu M, de Jong DH, Marrink SJ, Deserno M (2013) Gaussian curvature elasticity determined from global shape transformations and local stress distributions: a comparative study using the MARTINI model. *Farad Discuss* 161:365–382
124. Taupin C, Dvoralitzky M, Sauterey C (1975) Osmotic-pressure induced pores in phospholipid vesicles. *Biochemistry* 14(21):4771–4775

125. Zhelev DV, Needham D (1993) Tension-stabilized pores in giant vesicles—determination of pore-size and pore line tension. *Biochim Biophys Acta* 1147(1):89–104
126. Genco I, Gliozzi A, Relini A, Robello M, Scalas E (1993) Osmotic-pressure induced pores in phospholipid vesicles. *Biochim Biophys Acta* 1149(1):10–18
127. Karatekin E, Sandre O, Guitouni H, Borghi N, Puech PH, Brochard-Wyart F (2003) Cascades of transient pores in giant vesicles: line tension and transport. *Biophys J* 84(3):1734–1749
128. Tolpekina TV, den Otter WK, Briels WJ (2004) Simulations of stable pores in membranes: system size dependence and line tension. *J Chem Phys* 121(16):8014–8020
129. Wohlert J, den Otter WK, Edholm O, Briels WJ (2006) Free energy of a trans-membrane pore calculated from atomistic molecular dynamics simulations. *J Chem Phys* 124(15):154905
130. Jiang FY, Bouret Y, Kindt JT (2004) Molecular dynamics simulations of the lipid bilayer edge. *Biophys J* 87(1):182–192
131. Wang ZJ, Deserno M (2010) Systematic implicit solvent coarse-graining of bilayer membranes: lipid and phase transferability of the force field. *New J Phys* 12:095004
132. Wang H, Hu D, Zhang P (2013) Measuring the spontaneous curvature of bilayer membranes by molecular dynamics simulations. *Commun Comput Phys* 13:1093–1106
133. Helfrich W (1985) Effect of thermal undulations on the rigidity of fluid membranes and interfaces. *J Phys France* 46(7):1263–1268
134. Peliti L, Leibler S (1985) Effects of thermal fluctuations on systems with small surface tension. *Phys Rev Lett* 54:1690–1693
135. Förster D (1986) On the scale dependence, due to thermal fluctuations, of the elastic properties of membranes. *Phys Lett A* 114(3):115–120
136. Kleinert H (1986) Thermal softening of curvature elasticity in membranes. *Phys Lett A* 114(5):263–268
137. Schmid F (2013) Fluctuations in lipid bilayers: are they understood? *Biophys Rev Lett* 8:1–20 doi:10.1142/S1793048012300113
138. Nelson DR, Peliti L (1987) Fluctuations in membranes with crystalline and hexatic order. *J Phys (France)* 48(1):1085–1092. doi:10.1051/jphys:019870048070108500
139. Le Doussal P, Radzihovsky L (1992) Self-consistent theory of polymerized membranes. *Phys Rev Lett* 69(8):1209–1211
140. Park JM, Lubensky TC (1995) Topological defects on fluctuating surfaces: general properties and the Kosterlitz–Thouless transition. *Phys Rev E* 53(3):2648–2664
141. Park JM (1996) Renormalization of fluctuating tilted hexatic membranes. *Phys Rev E* 56(7):R47–R50
142. West B, Schmid F (2010) Fluctuations and elastic properties of lipid membranes in the fluid and gel state: a coarse-grained Monte Carlo study. *Soft Matter* 6:1275–1280
143. Kramer L (1971) Theory of light scattering from fluctuations of membranes and monolayers. *J Chem Phys* 55:2097–2105
144. Seifert U, Langer SA (1993) Viscous modes of fluid bilayer membranes. *Europhys Lett* 23(1):71–76
145. Zilman AG, Granek R (1996) Undulations and dynamic structure factor of membranes. *Phys Rev Lett* 77:4788–4791
146. Fromherz P (1983) Lipid-vesicle structure: size control by edge-active agents. *Chem Phys Lett* 94:259–266
147. van Kampen NG (2007) *Stochastic processes in physics and chemistry*, 3rd edn. Elsevier, Amsterdam
148. Helfrich W (1981) *Physics of defects*. North Holland, Amsterdam
149. Helfrich W (1994) Lyotropic lamellar phases. *J Phys Condens Matter* 6:A79–A92
150. Szleifer I, Kramer D, Ben-Shaul A, Gelbart WM, Safran SA (1990) Molecular theory of curvature elasticity in surfactant films. *J Chem Phys* 92:6800–6817
151. Rowlinson JS, Widom B (2002) *Molecular theory of capillarity*, 1st edn. Dover, New York
152. Gompper G, Klein S (1992) Ginzburg–Landau theory of aqueous surfactant solutions. *J Phys II (France)* 2:1725–1744

153. Diamant H (2011) Model-free thermodynamics of fluid vesicles. *Phys Rev E* 84(6):0611203
154. Capovilla R, Guven J (2002) Stresses in lipid membranes. *J Phys A Math Gen* 35:6233–6247
155. Capovilla R, Guven J (2004) Stress and geometry of lipid vesicles. *J Phys Condens Matter* 16: S2187–S2191
156. Farago O, Pincus P (2004) Statistical mechanics of bilayer membrane with a fixed projected area. *J Chem Phys* 120:2934–2950
157. Guven J (2004) Membrane geometry with auxiliary variables and quadratic constraints. *J Phys A Math Gen* 37:L313–L319
158. Müller MM, Deserno M, Guven J (2005) Geometry of surface-mediated interactions. *Europhys Lett* 69:482–488
159. Müller MM, Deserno M, Guven J (2005) Interface-mediated interactions between particles: a geometrical approach. *Phys Rev E* 72:061407
160. Müller MM, Deserno M, Guven J (2007) Balancing torques in membrane-mediated interactions: exact results and numerical illustrations. *Phys Rev E* 76:011921. doi:[10.1103/PhysRevE.76.011921](https://doi.org/10.1103/PhysRevE.76.011921)
161. Deserno M, Müller MM, Guven J (2007) Contact lines for fluid surface adhesion. *Phys Rev E* 76:011605. doi:[10.1103/PhysRevE.76.011605](https://doi.org/10.1103/PhysRevE.76.011605)
162. Schmid F (2011) Are stress-free membranes really “tensionless”? *Europhys Lett* 95:28008
163. Deuling H, Helfrich W (1976) The curvature elasticity of fluid membranes: a catalogue of vesicle shapes. *J Phys (France)* 37:1335–1345
164. David F, Leibler S (1991) Vanishing tension of fluctuating membranes. *J Phys II (France)* 1:959–976
165. Cai W, Lubensky TC, Nelson P, Powers T (1994) Measure factors, tension, and correlations of fluid membranes. *J Phys II (France)* 4:931–949
166. Jähnig F (1996) What is the surface tension of a lipid bilayer membrane? *Biophys J* 71:1348–1349
167. Marsh D (1997) Renormalization of the tension and area expansion modulus in fluid membranes. *Biophys J* 73:865–869
168. Farago O, Pincus P (2003) The effect of thermal fluctuations on Schulman area elasticity. *Eur Phys J E* 11:399–408
169. Imperato A (2006) Surface tension in bilayer membranes with fixed projected area. *J Chem Phys* 124:154714
170. Stecki J (2008) Balance of forces in simulated bilayers. *J Phys Chem B* 112(14):4246–4252
171. Fournier JB, Barbeta C (2008) Direct calculation from the stress tensor of the lateral surface tension of fluctuating fluid membranes. *Phys Rev Lett* 100:078103
172. Fournier JB (2012) Comment on “are stress-free membranes really ‘tensionless?’” by Schmid F. *Europhys Lett* 97:18001
173. Schmid F (2012) Reply to Comment on “are stress-free membranes really ‘tensionless?’”. *Europhys Lett* 97:18002
174. Farago O (2011) Mechanical surface tension governs membrane thermal fluctuations. *Phys Rev E* 84:051944
175. Marrink SJ, Mark AE (2001) Effect of undulations on surface tension in simulated bilayers. *J Phys Chem B* 105:6122–6127
176. Loison C, Mareschal M, Kremer K, Schmid F (2003) Thermal fluctuations in a lamellar phase of a binary amphiphile-solvent mixture: a molecular-dynamics study. *J Chem Phys* 119(13): 138–13148
177. Ahmed SN, Brown DA, London E (1997) On the origin of sphingolipid/cholesterol-rich detergent-insoluble cell membranes: Physiological concentrations of cholesterol and sphingolipid induce formation of a detergent-insoluble, liquid-ordered lipid phase in model membranes. *Biochemistry* 36(36):10944–10953
178. Simons K, Ikonen E (1997) Functional rafts in cell membranes. *Nature* 387:569–572
179. Brown DA, London E (1998) Structure and origin of ordered lipid domains in biological membranes. *J Membr Biol* 164(2):103–114

180. Brown DA, London E (1998) Functions of lipid rafts in biological membranes. *Ann Rev Cell Develop Biol* 14:111–136
181. Brown DA, London E (2000) Structure and function of sphingolipid- and cholesterol-rich membrane rafts. *J Biol Chem* 275(23):17221–17224
182. Singer SJ, Nicolson GK (1972) Fluid mosaic model of structure of cell-membranes. *Science* 175(4023):720–731
183. Munro S (2003) Lipid rafts: elusive or illusive? *Cell* 115(4):377–388
184. Hancock JF (2006) Lipid rafts: contentious only from simplistic standpoints. *Nat Rev Mol Cell Biol* 7:456–462
185. Leslie M (2011) Do lipid rafts exist? *Science* 334:1046–1047
186. Vereb G, SzölloSI J, Matko J, Nagy P, Farkas T, Vigh L, Matyus L, Waldmann TA, Damjanovich S (2003) Dynamic, yet structured: the cell membranes three decades after the Singer-Nicolson model. *Proc Natl Acad Sci USA* 100:8053–8058
187. Veatch SL, Keller SL (2003) Separation of liquid phases in giant vesicles of ternary mixtures of phospholipids and cholesterol. *Biophys J* 85(5):3074–3083
188. Veatch SL, Keller SL (2005) Seeing spots: complex phase behavior in simple membranes. *Biochim Biophys Acta* 1746:172–185
189. Pralle A, Keller P, Florin EL, Simons K, Hörber JKH (2000) Sphingolipid-cholesterol rafts diffuse as small entities in the plasma membrane of mammalian cells. *J Cell Biol* 148:997–1007
190. Turner MS, Sens P, Socci ND (2005) Nonequilibrium raft-like membrane domains under continuous recycling. *Phys Rev Lett* 95:168301
191. Yethiraj A, Weisshaar JC (2007) Why are lipid rafts not observed in vivo? *Biophys J* 93:3113–3119
192. Simons K, Vaz WLC (2004) Model systems, lipid rafts, and cell membranes. *Annu Rev Biophys Biomol Struct* 33:269–295
193. Brewster R, Pincus PA, Safran SA (2009) Hybrid lipids as a biological surface-active component. *Biophys J* 97:1087–1094
194. Yamamoto T, Brewster R, Safran SA (2010) Chain ordering of hybrid lipids can stabilize domains in saturated/hybrid/cholesterol lipid membranes. *Europhys Lett* 91:28002
195. Veatch SL, Soubias O, Keller SL, Gawrisch K (2007) Critical fluctuations in domain-forming lipid mixtures. *Proc Natl Acad Sci USA* 104(17):650–655
196. Honerkamp-Smith AR, Veatch SL, Keller SL (2009) An introduction to critical points for biophysicists: observations of compositional heterogeneity in lipid membranes. *Biochim Biophys Acta* 1788:53–63
197. Ipsen JH, Karlström G, Mouritsen OB, Wennerström H, Zuckermann MJ (1987) Phase equilibria in the phosphatidylcholine-cholesterol system. *Biochim Biophys Acta* 905:162–172
198. Sankaram MB, Thompson TE (1991) Cholesterol-induced fluid-phase immiscibility in membranes. *Proc Natl Acad Sci USA* 88:8686–8690
199. Katsaras J, Tristram-Nagle S, Liu Y, Headrick RL, Fontes E, Mason PC, Nagle JF (2000) Clarification of the ripple phase of lecithin bilayers using fully hydrated, aligned samples. *Phys Rev E* 61:5668
200. Sengupta K, Raghunathan VA, Katsaras J (2003) Structure of the ripple phase of phospholipid multibilayers. *Phys Rev E* 68(3):031710
201. Koynova R, Caffrey M (1994) Phases and phase transitions of the hydrated phosphatidylethanolamines. *Chem Phys Lipids* 69:1–34
202. Koynova R, Caffrey M (1998) Phases and phase transitions of the phosphatidylcholines. *Biochimica Biophysica Acta Rev Biomembr* 1376:91–145
203. Kranenburg M, Smit B (2005) Phase behavior of model lipid bilayers. *J Phys Chem B* 109:6553–6563
204. de Vries AH, Yefimov S, Mark AE, Marrink SJ (2005) Molecular structure of the lecithin ripple phase. *Proc Natl Acad Sci USA* 102:5392–5396

205. Sun X, Gezelter JD (2008) Dipolar ordering in the ripple phases of molecular-scale models of lipid membranes. *J Phys Chem B* 112:1968–1975
206. Jamroz D, Kepczynski M, Nowakowska M (2010) Molecular structure of the dioctadecyldimethylammonium bromide (DODAB) bilayer. *Langmuir* 26(15):076–15079
207. Chen R, Poger D, Mark AE (2011) Effect of high pressure on fully hydrated DPPC and POPC bilayers. *J Phys Chem B* 115:1038–1044
208. Dolezel S (2010) Computer simulation of lipid bilayers. Diploma thesis, University of Mainz
209. Brazovskii SA (1975) Phase transitions of an isotropic system to a nonuniform state. *Soviet Phys JETP* 41:85–89
210. Marsh D (2008) Protein modulation of lipids, and vice-versa, in membranes. *Biochim Biophys Acta* 1778:1545–1575
211. Benjamini A, Smit B (2012) Robust driving forces for transmembrane helix packing. *Biophys J* 103:1227–1235
212. Cantor RS (1997) Lateral pressures in cell membranes: a mechanism for modulation of protein function. *J Phys Chem B* 101:1723–1725
213. Elliott J, Needham D, Dilger J, Haydon D (1983) The effects of bilayer thickness and tension on gramicidin single-channel lifetimes. *Biochim Biophys Acta* 735:95–103
214. Botelho AV, Huber T, Sakmar TP, Brown MF (2006) Curvature and hydrophobic forces drive oligomerization and modulate activity of rhodopsin in membranes. *Biophys J* 91:4464–4477
215. Antony B (2006) Membrane deformation by protein coats. *Curr Opin Cell Biol* 18(4):386–394
216. Lee AG (2005) How lipids and proteins interact in a membrane: a molecular approach. *Mol Biosyst* 3:203–212
217. Gil T, Sabra MC, Ipsen JH, Mouritsen OG (1997) Wetting and capillary condensation as means of protein organization in membranes. *Biophys J* 73(4):1728–1741
218. Gil T, Ipsen JH, Mouritsen OG, Sabra MC, Sperotto MM, Zuckermann MJ (1998) Theoretical analysis of protein organization in lipid membranes. *Biochim Biophys Acta* 1376(3):245–266
219. Reynwar BJ, Deserno M (2008) Membrane composition-mediated protein–protein interactions. *Biointerphases* 3:FA117–FA125
220. Machta BB, Veatch SL, Sethna JP (2012) Critical Casimir forces in cellular membranes. *Phys Rev Lett* 109:138101
221. May S, Ben-Shaul A (1999) Molecular theory of lipid-protein interaction and the L $\alpha$ -H $\text{II}$  transition. *Biophys J* 76(2):751–767
222. May S (2000) Protein-induced bilayer deformations: the lipid tilt degree of freedom. *Eur Biophys J* 29(1):17–28
223. Kozlovsky Y, Zimmerberg J, Kozlov MM (2004) Orientation and interaction of oblique cylindrical inclusions embedded in a lipid monolayer: a theoretical model for viral fusion peptides. *Biophys J* 87(2):999–1012
224. Deserno M (2009) Membrane elasticity and mediated interactions in continuum theory: a differential geometric approach. In: Faller R, Jue T, Longo ML, Risbud SH (eds) *Biomembrane frontiers: nanostructures, models, and the design of life*, vol 2. Springer, New York, pp 41–74
225. May S (2000) Theories on structural perturbations of lipid bilayers. *Curr Opin Colloid Interface Sci* 5:244–249
226. Bloom M, Evans E, Mouritsen OG (1991) Physical properties of the fluid lipid-bilayer component of cell membranes: a perspective. *Quart Rev Biophys* 24(3):293–297
227. Killian JA (1998) Hydrophobic mismatch between proteins and lipids in membranes. *Biochim Biophys Acta* 1376:401–416
228. Dumas F, Lebrun MC, Tocanne JF (1999) Is the protein/lipid hydrophobic matching principle relevant to membrane organization and functions? *FEBS Lett* 458:271–277

229. Harroun TA, Heller WT, Weiss TM, Yang L, Huang HW (1999) Experimental evidence for hydrophobic matching and membrane-mediated interactions in lipid bilayers containing gramicidin. *Biophys J* 76:937–945
230. De Planque MRR, Killian JA (2003) Protein-lipid interactions studied with designed trans-membrane peptides: role of hydrophobic matching and interfacial anchoring (review). *Mol Membr Biol* 20:271–284
231. Marsh D (2008) Energetics of hydrophobic matching in lipid–protein interactions. *Biophys J* 94:3996–4013
232. Cybulski LE, de Mendoza D (2011) Bilayer hydrophobic thickness and integral membrane protein function. *Curr Protein Pept Sci* 12:760–766
233. Strandberg E, Esteban-Martin S, Ulrich AS, Salgado J (2012) Hydrophobic mismatch of mobile transmembrane helices: merging theory and experiments. *Biochim Biophys Acta* 1818:1242–1249
234. Venturoli M, Smit B, Sperotto MM (2005) Simulation studies of protein-induced bilayer deformations, and lipid-induced protein tilting, on a mesoscopic model for lipid bilayers with embedded proteins. *Biophys J* 88:1778
235. Park SH, Opella SJ (2005) Tilt angle of a trans-membrane helix is determined by hydrophobic mismatch. *J Mol Biol* 350:310–318
236. Holt A, Killian JA (2010) Orientation and dynamics of transmembrane peptides: the power of simple models. *Eur Biophys J* 39:609–621
237. Strandberg E, Tremouilhac P, Wadhvani P, Ulrich AS (2009) Synergistic transmembrane insertion of the heterodimeric PGLA/magainin 2 complex studied by solid-state NMR. *Biochim Biophys Acta* 1788:1667–1679
238. Schmidt U, Weiss M (2010) Hydrophobic mismatch-induced clustering as a primer for protein sorting in the secretory pathway. *Biophys Chem* 151:34–38
239. Harzer U, Bechinger B (2000) Alignment of lysine-anchored membrane peptides under conditions of hydrophobic mismatch: A CD,  $^{15}\text{N}$  and  $^{31}\text{P}$  solid-state NMR spectroscopy investigation. *Biochemistry* 39(13):106–13114
240. Özdirekcan S, Rijkers DTS, Liskamp RMJ, Killian JA (2005) Influence of flanking residues on tilt and rotation angles of transmembrane peptides in lipid bilayers. a solid-state  $^2\text{H}$  NMR study. *Biochemistry* 44:1004–1012
241. Vostrikov VV, Grant CV, Daily AE, Opella SJ, Koeppe RE II (2008) Comparison of “polarization inversion with spin exchange at magic angle” and “geometric analysis of labeled alanines” methods for transmembrane helix alignment. *J Am Chem Soc* 130(12): 584–12585
242. Chiang C, Shirinian L, Sukharev S (2005) Capping transmembrane helices of MscL with aromatic residues changes channel response to membrane stretch. *Biochemistry* 44(12): 589–12597
243. Vostrikov VV, Koeppe RE II (2011) Response of GWALP transmembrane peptides to changes in the tryptophan anchor positions. *Biochemistry* 50:7522–7535
244. Neder J, Nielaba P, West B, Schmid F (2012) Interactions of membranes with coarse-grain proteins: a comparison. *New J Phys* 14:125017
245. Mouritsen OG, Bloom M (1984) Mattress model of lipid-protein interactions in membranes. *Biophys J* 36:141–153
246. Fattal DR, Ben-Shaul A (1993) A molecular model for lipid-protein interaction in membranes: the role of hydrophobic mismatch. *Biophys J* 65:1795–1809
247. Fattal DR, Ben-Shaul A (1995) Lipid chain packing and lipid–protein interaction in membranes. *Phys A* 220:192–216
248. Cordomi A, Perez JJ (2007) Molecular dynamics simulations of rhodopsin in different one-component lipid bilayers. *J Phys Chem B* 111:7052–7063
249. Neder J, West B, Nielaba P, Schmid F (2010) Membrane-mediated protein–protein interaction: a Monte Carlo study. *Curr Nanosci* 7:656–666

250. Schmidt U, Guigas G, Weiss M (2008) Cluster formation of transmembrane proteins due to hydrophobic mismatching. *Phys Rev Lett* 101:128104
251. de Meyer FJM, Venturoli M, Smit B (2008) Molecular simulations of lipid-mediated protein–protein interactions. *Biophys J* 95:1851–1865
252. Koltover I, Rädler JO, Safinya CR (1999) Membrane mediated attraction and ordered aggregation of colloidal particles bound to giant phospholipid vesicles. *Phys Rev Lett* 82:1991–1994
253. Goulian M, Bruinsma R, Pincus P (1993) Long-range forces in heterogeneous fluid membranes. *Europhys Lett* 22:145
254. Goulian M, Bruinsma R, Pincus P (1993) Long-range forces in heterogeneous fluid membranes: erratum. *Europhys Lett* 23:155
255. Fournier JB, Dommersnes PG (1997) Comment on “long-range forces in heterogeneous fluid membranes”. *Europhys Lett* 39(6):681
256. Dommersnes P, Fournier JB (1999) N-body study of anisotropic membrane inclusions: membrane mediated interactions and ordered aggregation. *Eur Phys J E* 12:9–12
257. Dommersnes P, Fournier J (2002) The many-body problem for anisotropic membrane inclusions and the self-assembly of “saddle” defects into an “egg carton”. *Biophys J* 83:2898–2905
258. Fournier JB, Dommersnes PG, Galatola P (2003) Dynamin recruitment by clathrin coats: a physical step? *C R Biol* 326:467–476
259. Wu SHW, McConnell HM (1975) Phase separations in phospholipid membranes. *Biochemistry* 14(4):847–854
260. Gebhardt C, Gruler H, Sackmann E (1977) Domain-structure and local curvature in lipid bilayers and biological membranes. *Z Naturforsch C* 32(7–8):581–596
261. Markin VS (1981) Lateral organization of membranes and cell shapes. *Biophys J* 36(1):1–19
262. Andelman D, Kawakatsu T, Kawasaki K (1992) Equilibrium shape of two-component unilamellar membranes and vesicles. *Europhys Lett* 19(1):57–62
263. Seifert U (1993) Curvature-induced lateral phase segregation in two-component vesicles. *Phys Rev Lett* 70:1335–1338
264. Bretscher MS (1972) Asymmetrical lipid bilayer structure for biological membranes. *Nature* 236(61):11–12
265. Daleke DL (2007) Phospholipid flippases. *J Biol Chem* 282(2):821–825
266. Deserno M (2004) Elastic deformation of a fluid membrane upon colloid binding. *Phys Rev E* 69:031903
267. Reynwar BJ, Deserno M (2011) Membrane-mediated interactions between circular particles in the strongly curved regime. *Soft Matter* 7:8567–8575
268. Weikl TR, Kozlov MM, Helfrich W (1998) Interaction of conical membrane inclusions: effect of lateral tension. *Phys Rev E* 57:6988–6995. doi:[10.1103/PhysRevE.57.6988](https://doi.org/10.1103/PhysRevE.57.6988)
269. Yolcu C, Deserno M (2012) Membrane-mediated interactions between rigid inclusions: an effective field theory. *Phys Rev E* 86:031906
270. Rothstein IZ (2003) TASI lectures on effective field theories. Available from arXiv.org, ArXiv:hep-ph/0308266
271. Goldberger WD, Rothstein IZ (2006) An effective field theory of gravity for extended objects. *Phys Rev D* 73:104029
272. Porto RA, Ross A, Rothstein IZ (2011) Spin induced multipole moments for the gravitational wave flux from binary inspirals to third post-newtonian order. *J Cosmol Astropart Phys* 3:009
273. Galley CR, Leibovich AK, Rothstein IZ (2010) Finite size corrections to the radiation reaction force in classical electrodynamics. *Phys Rev Lett* 105:094802
274. Yolcu C, Rothstein IZ, Deserno M (2011) Effective field theory approach to Casimir interactions on soft matter surfaces. *Europhys Lett* 96:20003
275. Yolcu C, Rothstein IZ, Deserno M (2012) Effective field theory approach to fluctuation-induced forces between colloids at an interface. *Phys Rev E* 85:011140

276. Dommersnes PG, Fournier JB (1999) Casimir and mean-field interactions between membrane inclusions subject to external torques. *Europhys Lett* 46:256
277. Kardar M, Golestanian R (1999) The “friction” of vacuum, and other fluctuation-induced forces. *Rev Mod Phys* 71:1233–1245
278. Park J-M, Lubensky TC (1996) Interactions between membrane inclusions on fluctuating membranes. *J Phys I France* 6(9):1217–1235
279. Helfrich W, Weikl TR (2001) Two direct methods to calculate fluctuation forces between rigid objects embedded in fluid membranes. *Eur Phys J E* 5:423–439
280. Gosselin HP, Morbach H, Müller MM (2012) Interface-mediated interactions: entropic forces of curved membranes. *Phys Rev E* 83:051921
281. Brakke KA (1992) The surface evolver. *Exp Math* 1:141–165
282. Reynwar BJ, Illya G, Harmandaris VA, Müller MM, Kremer K, Deserno M (2007) Aggregation and vesiculation of membrane proteins by curvature-mediated interactions. *Nature* 447:461–464
283. Kim KS, Neu J, Oster G (1998) Curvature-mediated interactions between membrane proteins. *Biophys J* 75(5):2274–2291
284. Kim KS, Neu JC, Oster GF (1999) Many-body forces between membrane inclusions: a new pattern-formation mechanism. *Europhys Lett* 48(1):99–105
285. Kim KS, Chou T, Rudnick J (2008) Degenerate ground-state lattices of membrane inclusions. *Phys Rev E* 78:011401. doi:[10.1103/PhysRevE.78.011401](https://doi.org/10.1103/PhysRevE.78.011401)
286. Müller MM, Deserno M (2010) Cell model approach to membrane mediated protein interactions. *Progr Theor Phys Suppl* 184:351–363
287. Auth T, Gompper G (2009) Budding and vesiculation induced by conical membrane inclusions. *Phys Rev E* 80:031901. doi:[10.1103/PhysRevE.80.031901](https://doi.org/10.1103/PhysRevE.80.031901)
288. Johnson ME, Head-Gordon T, Louis AA (2007) Representability problems for coarse-grained water potentials. *J Chem Phys* 126(14):144509
289. Nielsen SO, Lopez CF, Srinivas G, Klein ML (2003) A coarse grain model for n-alkanes parameterized from surface tension data. *J Chem Phys* 119:7043–7049
290. Mognetti BM, Yelash L, Virnau P, Paul W, Binder K, Müller M, Macdowell LG (2008) Efficient prediction of thermodynamic properties of quadrupolar fluids from simulation of a coarse-grained model: the case of carbon dioxide. *J Chem Phys* 128:104501
291. DeVane R, Shinoda W, Moore PB, Klein ML (2009) Transferable coarse grain nonbonded interaction model for amino acids. *J Chem Theory Comput* 5:2115–2124
292. Tschöp W, Kremer K, Batoulis J, Burger T, Hahn O (1998) Simulation of polymer melts. I. coarse-graining procedure for polycarbonates. *Acta Polym* 49(2–3):61–74
293. Lyubartsev AP, Laaksonen A (1995) Calculation of effective interaction potentials from radial-distribution functions – a reverse Monte-Carlo approach. *Phys Rev E* 52:3730–3737
294. Reith D, Putz M, Müller-Plathe F (2003) Deriving effective mesoscale potentials from atomistic simulations. *J Comp Chem* 24:1624–1636
295. Peter C, Delle Site L, Kremer K (2008) Classical simulations from the atomistic to the mesoscale: coarse graining an azobenzene liquid crystal. *Soft Matter* 4:859–869
296. Murtola T, Karttunen M, Vattulainen I (2009) Systematic coarse graining from structure using internal states: application to phospholipid/cholesterol bilayer. *J Chem Phys* 131:055101
297. Lyubartsev A, Mirzoev A, Chen LJ, Laaksonen A (2010) Systematic coarse-graining of molecular models by the Newton inversion method. *Faraday Discuss* 144:43–56
298. Savelyev A, Papoian GA (2009) Molecular renormalization group coarse-graining of electrolyte solutions: application to aqueous NaCl and KCl. *J Phys Chem B* 113:7785–7793
299. Megariotis G, Vyrkou A, Leygue A, Theodorou DN (2011) Systematic coarse graining of 4-cyano-4'-pentylbiphenyl. *Ind Eng Chem Res* 50:546–556
300. Mukherjee B, Site LD, Kremer K, Peter C (2012) Derivation of a coarse grained model for multiscale simulation of liquid crystalline phase transitions. *J Phys Chem B* 116:8474–8484

301. Shell MS (2008) The relative entropy is fundamental to multiscale and inverse thermodynamic problems. *J Chem Phys* 129:144108
302. Silbermann JR, Klapp SHL, Schoen M, Chennamsetty N, Bock H, Gubbins KE (2006) Mesoscale modeling of complex binary fluid mixtures: towards an atomistic foundation of effective potentials. *J Chem Phys* 124:074105
303. Allen EC, Rutledge GC (2009) Evaluating the transferability of coarse-grained, density-dependent implicit solvent models to mixtures and chains. *J Chem Phys* 130:034904
304. Mullinax JW, Noid WG (2009) Extended ensemble approach for deriving transferable coarse-grained potentials. *J Chem Phys* 131:104110
305. Villa A, Peter C, van der Vegt NFA (2010) Transferability of nonbonded interaction potentials for coarse-grained simulations: benzene in water. *J Chem Theory Comput* 6:2434–2444
306. Izvekov S, Chung PW, Rice BM (2010) The multiscale coarse-graining method: assessing its accuracy and introducing density dependent coarse-grain potentials. *J Chem Phys* 133:064109
307. Shen JW, Li C, van der Vegt NFA, Peter C (2011) Transferability of coarse grained potentials: implicit solvent models for hydrated ions. *J Chem Theory Comput* 7:1916–1927
308. Brini E, Marcon V, van der Vegt NFA (2011) Conditional reversible work method for molecular coarse graining applications. *Phys Chem Chem Phys* 13(10):468–10474
309. Liu Z, Yan H, Wang K, Kuang T, Zhang J, Gul L, An X, Chang W (2004) Crystal structure of spinach major light-harvesting complex at 2.72 Å resolution. *Nature* 428:287–292
310. Standfuss R, van Scheltinga ACT, Lamborghini M, Kühlbrandt W (2005) Mechanisms of photoprotection and nonphotochemical quenching in pea light-harvesting complex at 2.5 Å resolution. *EMBO J* 24:919–928
311. Schmid VH (2008) Light-harvesting complexes of vascular plants. *Cell Mol Life Sci* 65(22):3619–3639
312. Yang C, Horn R, Paulsen H (2003) The light-harvesting chlorophyll a/b complex can be reconstituted in vitro from its completely unfolded apoprotein. *Biochemistry* 42:4527–4533
313. Horn R, Grundmann G, Paulsen H (2007) Consecutive binding of chlorophylls a and b during the assembly in vitro of light-harvesting chlorophyll-a/b protein (LHCIIb). *J Mol Biol* 366:1045–1054
314. Dockter C, Volkov A, Bauer C, Polyhach Y, Joly-Lopez Z, Jeschke G, Paulsen H (2009) Refolding of the integral membrane protein light-harvesting complex II monitored by pulse EPR. *Proc Natl Acad Sci USA* 106(44):18485–18490
315. Horn R, Paulsen H (2004) Early steps in the assembly of light-harvesting chlorophyll a/b complex. *J Biol Chem* 279(43):44400–44406
316. Dockter C, Müller AH, Dietz C, Volkov A, Polyhach Y, Jeschke G, Paulsen H (2012) Rigid core and flexible terminus: structure of solubilized light-harvesting chlorophyll a/b complex (LHCII) measured by EPR. *J Biol Chem* 287:2915–2925. doi:10.1074/jbc.M111.307728
317. Garab G, Lohner K, Laggner P, Farkas T (2000) Self-regulation of the lipid content of membranes by non-bilayer lipids: a hypothesis. *Trends Plant Sci* 5(11):489–494

# Index

## A

Aggregates, 1, 66, 238, 258, 268  
Albumin, 48, 211, 225  
    gene delivery, 218  
Allyl glycidyl ether (AGE), 185  
 $\alpha$ -Hemolysin, 21  
AMBER GAFF, 31  
Amino acids, 35, 40, 168, 214, 218  
    cyclic, 34  
Aptamers, 53–56  
Arylene-ethynylene-butydiynylene, 173  
Atomic force spectroscopy (AFS), 2, 18, 53

## B

Bending modulus, 244  
Benzene-1,3,5-tricarboxamides (BTAs), 172  
Benzoylterrylene-3,4-dicarboximide, 83  
Binding pockets, 1, 52  
Biomembranes, 237  
Biopolymers, 115  
Biotin–streptavidin, 48  
Biphenyl-4,4'-dicarboxylic acid (BPDCA), 197  
Block copolymers, confinement, 176  
Bond breakage, reversible, 31  
Bottlebrush polymers, 7, 132, 140  
    cylindrical, 146  
Brain, 221  
Brazovskii mechanism, 254  
Brushes, 7, 211, 227  
    complex formation, 152  
    spherical, 154

## C

Calixarene, 28, 39, 52, 173  
    dimers, 42

Carotenoids, 82  
Catenanes, 28, 40, 52  
Chain collapse, 1  
Charged extracellular matrix (ECM), 216  
Chlorophylls, 81, 267–269  
Cholesteric phases, 61  
    liquid crystalline, 88  
Cholesterol, 242  
Clathrin-dependent endocytosis, 213  
Coarse graining, 237  
Coil-to-helix transition, 140  
Collapse, tethered single chains, 8  
Complex structure, 115  
Conformation, 115  
Cooke model, 242  
Copolymers, 115  
Copolypeptides, 169  
Coupled monolayer models, 240  
Critical adsorption point (CAP), 15  
Crossovers, 6  
Curvature elasticity, 237  
Cylindrical brush polymers, 115, 120, 132,  
    211, 226

## D

Dendrimers, 71, 99, 115, 120, 156, 211  
Dendritic core–shell star polymers, 215  
Diblock copolymers, miniemulsion droplets,  
    177  
Dinaphtho quaterrylene diimide (DNQDI), 84  
Diode lasers, 87  
Dipalmitoyl-phosphatidylcholine bilayers, 242  
DNA, 5, 18, 156, 213, 226  
    biosensors, 131  
Dodecyltrimethylammonium bromide  
    (DOTAB), 161

- Donor–acceptor dyads, electronic  
 coupling, 105  
 flexibility, 93  
 linear/kinked, 63  
 Doxorubicin (DOX), 211, 221  
 Drug delivery, 21, 131, 168, 188, 211, 220, 226  
 albumin copolymer polyelectrolytes, 222  
 Dual pulse excitation, 94  
 Dynamic force spectroscopy (DFS), 27
- E**  
 Ectoin (tetrahydro-2-methyl-4-carboxylic acid)  
 33  
 Electronic coupling, 101  
 Electronic excitation energy transfer (EET),  
 61, 93  
 Endocytosis, 213  
 Endothelial cells, 211  
 Energy transfer, 61, 98
- F**  
 Fibronectin, stretching, 33  
 Flory–Huggins parameters, 146  
 Flow cytometry, 211  
 Fluid mosaic model, 252  
 Fluorophores, 61  
 Force-clamp mode, 31  
 Force fields, 30  
 Force-induced desorption transition, 18  
 Force-induced response, 1  
 Force probe molecular dynamics simulations, 1  
 Force-ramp protocol, 31  
 Force spectroscopy, 1, 33  
 Force spectrum, 29
- G**  
 Gaussian chains, 8, 133  
 Gaussian coils, 3, 171  
 Gaussian curvature modulus, 238, 244, 248  
 Gene delivery, 218  
 Gene transfection, cationic cylindrical  
 brushes, 225  
 Gene transfer, 211  
 Grand canonical ensemble (GCE), 18  
 GROMOS G53A5 force field, 30  
 Guest molecules, 130
- H**  
 Helfrich Hamiltonian, 239, 249  
 Hexa-*peri*-hexabenzocoronene (HBC),  
 72, 97, 174
- Horseshoe brush, 144  
 Hydrogen bonds, 2, 27, 40, 49, 92, 115,  
 119, 130, 166, 241  
 Hydrophobic mismatch, membrane–protein  
 interactions, 256  
 Hydrophobic–polar (amphiphilic) copolymers  
 (HP-copolymers), 10
- I**  
 Inorganic–organic hybrid materials, 74  
 Insulating surface, 194  
 Intramolecular phase separation, 141  
 4-Iodo benzoic acid (IBA), 196  
 Ion transport, 124
- J**  
 Janus cylinders, 147  
 Junction-point reactive block  
 copolymers, 183
- K**  
 Kratky–Porod model, 5–7, 133–135
- L**  
 Landau–Brazovskii model, 254  
 Lasers, 86  
 liquid crystal, 88  
 Lasing, 61, 63, 86, 88, 92  
 Lauryl maltoside (LM), 85  
 Lenz model, 242  
 Light-emitting diodes (LEDs),  
 128, 171  
 Light-harvesting complexes, 61, 63, 81,  
 128, 267  
 Lipid bilayers, 237  
 Lipid membranes, tension, 249  
 models, coarse-grained, 241  
 Lipid rafts, 252  
 Lipofectamine, 229  
 Liposomes, 188  
 Liquid crystals, 115  
 lasers, 88  
 Liquid–liquid interfaces, selective, 10
- M**  
 MARTINI model, lipids, 243  
 Meandering brush, 144  
 Mediated interactions, 237  
 Membrane–protein systems/interactions,  
 237, 255

- Membranes, Helfrich model, 240  
heterogeneity, 252  
pores, polymer translocation, 21  
tension, 249
- Mesitylene, 46
- Methylaluminumoxanes (MAO), 128
- Micelles, 85, 189, 214, 222–225  
wormlike, 239
- Molecular dynamics (MD), 1
- Monogalactosyldiacylglycerol (MGDG), 267
- Monolayers, 254
- Monomer–monomer interactions, 4
- Multichromophores, 63  
photoswitchable, 128  
star-shaped, 71
- Multiscaling, 237
- N**
- Nanocapsules, 33, 40, 52, 177, 182
- Nanoparticles, 61, 128, 152, 177  
polymersome shell layer, 188
- NMR spectroscopy, 115
- Nucleic acids, binding pockets, small  
molecules, 52
- O**
- Oligo(*p*-benzamides) (OPBA), 171
- Oligo calix[4]arene catenanes, 33
- Oligo(phenylene) bridges, 62
- Onion-like structure, 177–183, 223  
block copolymers, 177, 193
- Opals, 87
- OPLS–AA, 31
- Organic dye molecules, 61  
functionalized, 75
- Organic electronics, 115
- Osmolytes, 33
- P**
- Pearl-necklace structure, 148
- PERM algorithm (pruned-enriched Rosenbluth  
method), 5, 149
- Persistence length, 5, 7, 38, 133, 151, 163, 169,  
226, 251
- Perylene diimide (PDI), 63  
TDI dyads, 63
- Perylenemonoimide (PMI), 72
- Photonic crystals, 86
- Pincus regime, 6
- Polybutadiene-*b*-poly(ethylene oxide)  
(PB-*b*-PEO), 188
- Polycation, 211
- Polycyclic aromatic hydrocarbons (PAH), 174
- Polyelectrolytes, 115, 211  
complexes, 156
- Polyelectrolytes, dendritic, 211
- Poly(ethylene glycol) (PEG), 171
- Polyions, wormlike, 156, 230
- Poly-L-lysine, 139, 170, 211, 225
- Polymer adsorption, 1
- Polymersomes, 188
- Polymer translocation, 1, 21
- Polymethacrylate-polystyrene brushes, 136
- Polypeptides,  $\alpha$ -helix/ $\beta$ -sheet, 139  
self-assembly, 168
- Polyphenylene dendrimers (PPDs), 120, 122  
core-shell, 214
- Poly(styrene-*b*-isoprene), 177
- Poly(styrene-*b*-methyl methacrylate)  
(PS-*b*-PMMA), 121, 177
- Poly(*tert*-butyl acrylate), 184
- Poly-2-vinylpyridinium (PVP), 141
- Porcine microvascular endothelial cell  
(PBMEC), 229
- Protein polyelectrolytes, 211
- Protein–membrane interactions, 255
- Proteins, curvature-mediated interactions, 258  
stabilization, 34
- Pruned-enriched Rosenbluth method (PERM),  
5, 149
- Pulling, reversibility, 43  
velocity, 31
- Q**
- Quantum chemistry, 61
- Quantum dots (QDs), 62  
dye complexes, 76  
oligomers, 78
- Quaterrylene dye, 84
- R**
- Raft hypothesis, lipids, 243, 252, 255
- Rhodamine maleimide, 82
- Rod–coil copolymers, 171
- Rylene dyes, 82
- Rylene tetracarboxydiimide, 62
- S**
- Scanning force microscopy (SFM), 37
- SELEX, 53
- Self assembly, 115  
PPDs, 131
- Self-avoiding walk (SAW) model, 5
- Self-consistent field (SCF), 15

Semiconductor quantum dots, 61, 75  
Serum albumin, gene delivery, 218  
Simulation, 237  
Single chains, 1  
    collapse, 8  
Single-molecule spectroscopy (SMS), 61  
Single-molecule stretching, 40  
Spectrin, 34  
Stiffness, 4, 10  
Stretching forces, 6  
Surfaces, adsorption, 162  
    insulating, 194  
Swollen coils, 3

**T**

Tenascin, 34  
Terylene diimide (TDI), 63  
Terylene monoimide monoanhydride  
    maleimide (TMIMA), 84  
Tethered chain, 8  
Tetrakis(4-ethynylphenyl)methane, 72  
Tetraphenylcyclopentadienone, 72

Thermotolerance, 34  
Titin, 34  
Toroidal structures, 4  
Transfection, 211  
    polymers, 226  
Translocation coordinate, 22  
Transmembrane domains, 255  
Transmembrane proteins, 237  
Triacetoneperoxide, 130

**U**

Unfolding, 27, 31–43, 222

**V**

van der Waals interactions, 115, 119,  
    153, 195

**W**

Worm-like chain (WLC) model, 5, 32, 38, 42,  
    133–137, 165